Essais et modélisation du cisaillement cyclique sol-struture à grand nombre de cycles. Application aux pieux

Suriyavut Pra-Ai

UNIVERSITÉ DE GRENOBLE

THÈSE
Pour obtenir le grade de
DOCTEUR DE L'UNIVERSITÉ DE GRENOBLE
Spécialite: **Matériaux Mécanique, Génie Civil, Electrochimie**
Arrêté ministériel: 7 août 2006

Présentée par

SURIYAVUT PRA-AI

Thèse dirigée par **Pierre FORAY** et
codirigée par **Marc BOULON**

préparée au sein du **Laboratoire 3S-R**
dans **l'École Doctorale Ingénierie-Matériaux Mécanique Environnement Energétique Procédés Production (I-MEP2)**

Behaviour of soil-structure interfaces subjected to a large number of cycles. Application to piles

Thèse soutenue publiquement le **28.02.2013**,
devant le jury composé de:

M. Isam SHAHROUR
Professeur à Polytech Lille, Laboratoire Génie Civil et Géo-Environnement, (Rapporteur)
M. Eric VINCENS
Maître de conférence à l'Ecole Centrale de Lyon, Laboratoire LTDS, (Rapporteur)
M. Fabrice EMERIAULT
Professeur à l'INP Grenoble, Laboratoire 3S-R, (Examinateur)
M. Jean CANOU
Chercheur à l'ENPC, Laboratoire NAVIER-CERMES, (Examinateur)
M. Alain PUECH
Directeur Scientifique à FUGRO Geo Consulting, (Invité)
Directeur Technique ANR et Programme National SOLCYP

Acknowledgements

Grenoble, there have been so many things that I have learned and so many people I have gotten to know. And this has made my life here memorable. Firstly, it has been my true honor to work with Prof. Marc Boulon and Prof. Pierre Foray. They have always believed in my potential. Without their visions, efforts and encouragements, this thesis could never have reached completion. Especially Prof. Marc Boulon, I cannot find words to express my gratitude for the helps in everything since I have been in Grenoble. My most heartfelt thanks to Prof. Isam Shahrour, Prof. Eric Vincens, Prof. Fabrice Emeriault, Prof. Jean Canou and Dr. Alain Puech, who serve as my thesis committee.

I would like to thank my officemates. They made my office a great work environment. My special appreciation is extended to my colleagues (MEMS) and other people at laboratory 3S-R. Especially Mr.Alexandre Martin for his help and guidance regarding the correction as well as the modification of the direct shear device. My gratitude also goes to Matias Silva and Bram van den Eijden, my friends who have always helped me in solving several computer problems. I would like to thank my Thai friends here at Grenoble, who have made my life here very enjoyable.

My special appreciation goes to Ariyanan Pra-ai and Parnphan Pra-ai, my wife and daughter who always stand beside me. Their love, strength, and wisdom have inspired me to be the best I can be through many difficult times. Finally, I owe my deepest gratitude to my parents, Inpan and Kanchana PRA-AI; their love is the greatest power in the world and has driven me to succeed in every goal I have dreamed of.

Suriyavut PRA-AI January, 2013

Abstract

A series of monotonic and cyclic 2D direct shear tests on sand (Fontainebleau)-rough/smooth material interfaces under constant normal load (CNL) and constant normal stiffness (CNS) conditions are presented. The aim of these tests is to simulate the situation along the shaft of piles subjected to a large number of cycles due to environmental or anthropic loadings. These cycles (typically 10^4) are of small amplitude (10, 20 and 40 kPa in terms of shear stress) as the service loads are not supposed to produce an early failure. These tests include the series of changing the cyclic amplitude in succession. The problem of loss of sand between the box and the rough plate, typical phenomenon in this type of test, receives a special attention. It is interesting to observe, according to the initial density, the position of the "center of cycles" in the stress plane (mean cyclic variables). Several factors such as initial density (I_{D0}), initial normal stress ($\sigma_{\mathrm{n\,cm0}}$), level of initial mean cyclic stress ratio (η_{cm0}), reduced cyclic amplitude ($\Delta\eta$) and imposed normal stiffness (in this thesis, k = 1000, 2000 and 5000 kPa/mm) that influence the intensity of mean cyclic normal ($[u]_{\mathrm{cm}}$) and shear ($[w]_{\mathrm{cm}}$) displacements are considered. Along CNL paths either dilation or contraction is exhibited, in agreement with the characteristic state developed by Luong. The influence of the stress path (under constant normal stress or prescribed normal stiffness) is also highlighted. It should be highlighted that CNS paths are ever contractive. The model of monotonic interface behaviour under CNL and oedometer paths is fully analytical and based on the rate-type framework with the normal relative displacement or the interface density as unique memory parameter. While the analytical formulations for identification are first proposed to describe the interface behaviour under cyclic CNL condition, the variation of cyclic amplitude and CNS condition are modeled by applying the analytical formulations for validation using finite analytical increments and introducing the notion of equivalent number of cycles. For numerical simulations by the FEM (Plaxis) these tests are interpreted and formulated according to a pseudo visco-plastic framework, the number of cycles being a fictitious time. The direct shear tests and two centrifuge pile tests (pull-out and compression) are also modeled. Recommendations are proposed for the calculation of real usual piles under cyclic loading. This thesis is one part of the national French project "ANR and National Program SOLCYP" (Research on behaviour of piles subjected to cyclic loading).

KEYWORDS: Direct shear tests, granular soil-structure interface, cyclic loading, mean cyclic path, large number of small cycles, characteristic state, pseudo visco-plasticity

Résumé

On présente tout d'abord une série d'essais de cisaillement direct 2D monotones et cycliques sur l'interface sable de Fontainebleau-plaque rugueuse et lisse, à contrainte normale constante (CNL) et à rigidité normale imposée (CNS). Le but de ces essais est de simuler la situation mécanique le long de pieux soumis à un grand nombre de cycles d'origine environnementale ou anthropique. Ces cycles (typiquement 10000) de faible amplitude (10 à 40 kPa en terme de contrainte de cisaillement) ne sont pas censés produire de rupture prématurée. Ces tests incluent une série de cycles d'amplitudes (successives) variées. Le problème de la perte de sable entre la boîte et la plaque est traité avec attention. Nous avons interprété l'effet de la position du "centre des cycles" dans le plan de contraintes (variables cycliques moyennes) et de la densité initiale. Plusieurs facteurs tels que l'indice initial de densité (I_{D0}), la contrainte normale cyclique moyenne ($\sigma_{\mathrm{n\ cm0}}$), le niveau initial moyen de contrainte de cisaillement (η_{cm0}), l'amplitude cyclique reduite ($\Delta\eta$) et la rigidité normale imposée (k qui dans cette thèse, va de 1000 à 5000 kPa/mm), influencent les déplacements relatifs cycliques moyens normal ($[u]_{\mathrm{cm}}$) et tangentiel $[w]_{\mathrm{cm}}$) et sont pris en considération. On observe soit de la dilatance, soit de la contractance en accord avec l'état caractéristique développé par Luong. L'influence du chemin de contrainte (CNL ou CNS) est également analysée. Un modèle phénomenologique et analytique de comportement d'interface sur chemins cycliques CNL est proposé. C'est également le cas pour le comportement monotone sur chemins oedométrique et CNL, la variable de mémoire unique étant la densité d'interface (sous contrainte) ou le déplacement relatif normal. Cette formulation permet de traiter, par incréments analytiques finis, les chemins comportant une variation d'amplitude cyclique, et les chemins CNS, ce qui introduit la notion de nombre de cycles équivalent. On notera que les chemins CNS sont toujours contractants. Ces essais sont utilisés pour aborder la simulation par éléments finis, avec le logiciel Plaxis, selon une approche de pseudo-visco plasticité, le nombre de cycles tenant lieu de temps fictif. L'essai de cisaillement monotone à la boîte est modélisé en densités faible et forte, ainsi que deux essais de pieux modèles centrifugés, l'un en traction, l'autre en compression. Des recommandations sont proposées pour le calcul courant des pieux sous sollicitations cycliques. Cette thèse a été soutenue par l'ANR SOLCYP et le programme national " recherches sur le comportement des pieux soumis à des sollicitations cycliques".

Mots clés : essais de cisaillement direct, interface sol granulaire-structure, chargement cyclique, chemin cyclique moyen, grand nombre de petits cycles, état caractéristique, pseudo-visco plasticité

List of Symbols

- CNL — Constant Normal Stress condition
- CNS — Constant Normal Stiffness condition
- k [kPa/mm] — Imposed normal stiffness
- τ [kPa] — Shear stress
- σ_n [kPa] — Normal stress
- τ_{cm} [kPa] — Mean cyclic shear stress
- $\sigma_{\mathrm{n\,cm}}$ [kPa] — Mean cyclic normal stress
- $[u]$ [mm] — Normal relative displacement
- $[w]$ [mm] — Shear relative displacement
- $[u]_{\mathrm{cm}}$ [mm] — Mean cyclic normal displacement
- $[w]_{\mathrm{cm}}$ [mm] — Mean cyclic shear displacement
- R_{max} [mm] — Maximum surface roughness
- R_{n} [-] — Normalised surface roughness
- t [mm] — Interface thickness
- $[u]_{\mathrm{int}}$ [mm] — Normal relative displacement of interface
- $[u]_{\mathrm{sam}}$ [mm] — Normal relative displacement of sample
- $k_{\mathrm{n\,int}}$ [kPa/mm] — Normal stiffness of interface
- $k_{\mathrm{n\,sam}}$ [kPa/mm] — Normal stiffness of sample
- $\gamma_{d0\,\sigma\,n=0}$ [kN/m^3] — Specific weight of interface without an applied normal stress
- $\gamma_{d0\,\sigma n}$ [kN/m^3] — Specific weight of interface under an applied normal stress
- γ_d [kN/m^3] — Current specific weight of interface during shear loading
- δ_{peak} [°] — Peak friction angle of interface
- δ_{crit} [°] — Critical friction angle of interface

- δ_{car} [°] Characteristic friction angle of interface
- η_{peak} [-] Peak stress ratio
- η_{crit} [-] Critical stress ratio
- η_{car} [-] Characteristic stress ratio
- η_{cm} [-] Mean cyclic stress ratio
- η_{max} [-] Maximum stress ratio
- $\Delta\tau$ [-] Cyclic amplitude in terms of shear stress
- $\Delta\eta$ [-] Reduced cyclic amplitude
- N [-] Number of cycles

Contents

General introduction

Soil-structure interfaces are commonly encountered in many geotechnical engineering problems, e.g. shallow foundations, pile foundations, cutoff walls, earth reinforcement and buried pipelines, tunnels etc. When civil engineering structures have to undergo cyclic loading conditions, the bearing capacity of structures is often reductive. Especially, many offshore oil rig works have to undergo cyclic loading conditions (wind, wave, machine operations, etc.) for a long life. The recent developments of renewable installations at sea of energy sources (offshore wind power, hydrokinetic power etc.) bring the professionals and the researchers to be interested in the effect of very large number of cycles on the soil-structure interactions. Understanding the interface behaviour subjected to cyclic loading is of significant importance. Indeed at the present time, there do not exist the methods of reliable calculation of the structure foundations subjected to this stress type and most of the experts adopt the proposed safety factors to take into account the degradations of bearing capacity due to the cycles.

The proposed subject consists in working out a model of the behaviour taking into account the effect of a large number of cycles on the elementary response of the soil and the soil-structure interface and to introduce it into a computer code by finite elements in order to be able to simulate the total behaviour of the works under this cyclic loading type.

The first part of this study will consist in developing a direct shear machine in order to carry out cyclic soil-structure interface tests with controlled boundary conditions: constant normal stress (CNL) and constant normal stiffness (CNS). Then the exhaustive test campaigns to a large number of cycles, type of surface roughness, type of sand, variation of densities, the initial normal stress condition, characteristic of shear path and characteristic of mean cyclic shearing and the amplitude of shearing will be carried out.

From cyclic triaxial test results drawn from the literature and cyclic interface tests carried out, the phenomenologic laws describing the evolution of the parameters of the soil with the number of cycles will be worked out. From numerical point of view, the accumulation of the irreversible quantities of cyclic origin (deformations, including volume in drained condition, pore water pressure in undrained condition) will be treated like a cyclic pseudo-creep, the number of cycles to be treated as a fictitious time. The established model, using a pseudo visco-plasticity (Perzyna's model) will also be tested on experiments conducted on piles model, independently of this study, in laboratory and probably in the future for cyclic loading tests of piles carried out on site. It is also interesting to simulate the phenomenon of degradation of side friction along the piles during the application of large numbers of cycles.

This project is carried out within the framework of a national research project (framework of IREX National Project) and ANR project (SOLCYP), "Research on behaviour of piles subjected to cyclic loading".

The content of this thesis is organised with the objective mentioned above.

An analysis of the interface problems consisting in various experimental methods, emphasizing the contributions made in the past by different authors is presented in Chapter 1. The element test results on high-cycle accumulation considered as a model for understanding and modeling the interface test campaigns are also reviewed. The extension of the concepts of constitutive laws based on the rate-type, elastoplastic and viscoplastic theories are then summarized.

Chapter 2 contains the statement of the testing method and the device developed to implement the interface shear tests. The description of tested materials is also discussed in detail. Monotonic CNL and CNS tests serving as the preliminary decision for cyclic interface shear tests are first outlined. Test parameters and extracted variables from the tests including the operating mode and experimental biases are also described. Then, the overall results of identification (CNL) and validation (CNL in changing cyclic amplitude and CNS) tests are presented. The influences of initial density, initial normal stress, the level of mean cyclic stress ratio and cyclic amplitude on the intensity of mean cyclic displacements are also discussed.

Chapter 3 principally devotes to the constitutive modeling of interface direct shear. The incremental (rate-type) constitutive model for monotonic soil-structure interface is first described. Then the analytical models for identification (cyclic CNL condition) by using the pseudo viscoplastic formulation (Perzyna's model) in which the number of cycles is treated instead of time are discussed in detail. The basic formulations used are analytical CNL and oedometric paths depending on the cyclic variables ($\sigma_{\mathrm{n\,cm0}}$: mean cyclic normal stress, η_{cm0}: mean cyclic stress ratio, $\Delta\eta$: cyclic amplitude, I_{D0}: density index). The integration of the constitutive model along CNS path is realised by finite analytical increments (or pre-integrated increments), with one single memory parameter: cyclic normal relative displacement ($[u]_{\mathrm{cm}}$) or interface specific weight under stress ($\gamma_{\mathrm{d}\,\sigma n}$). Subsequently, the results of the extension of analytical models for identification to validation of variation in cyclic amplitude and CNS condition are presented.

Chapter 4 presents the preliminary implementation of Plaxis FE software for modeling the interface behaviour. Monotonic interface direct shear tests (CNL and CNS) are first modeled. Then the application of analytical constitutive models to centrifuge model test of pile is presented. Monotonic pull-out/compression and cylic tests are typically described as proposed methodology.

Finally, the proposed methodology for the calculation of real piles subjected to axial cyclic loading is presented in Chapter 5.

Chapter 1

Bibliographic study of soil-structure interfaces subjected to cyclic loading

1.1 Introduction

In the field of soil mechanics applied to civil engineering, computing the bearing capacity, as the stability of deep foundations and retaining structures, is largely based on the phenomenon of skin friction between the soil and structure. This is the case of piles, anchors, retaining walls, tunnels, etc as shown in Figure 1.1. The study of frictional characteristics of the interface between granular materials and structure, developing through a thin layer of granular material, therefore plays an important role for understanding the behaviour of many geotechnical structures and also for providing more secure and cost savings in the design of structures. This subject has widely been paid attention by many researchers. Generally, the studies of soil-structure interface have been developed in various categories (e.g. fundamental and experimental studies, constitutive modeling, and application to boundary value problems). The mechanisms and characteristics were commonly determined from appropriate laboratory or field tests to describe the interface behaviour in a realistic manner. This chapter begins by reviewing the state of the art on the experimental investigations including the development of various testing devices on soil-structure interfaces. Afterwards, necessary constitutive models formulated for interface behaviour will be described.

1.2 Soil-structure interface

Soil-structure interface is the result of a phenomenon induced by the discontinuity and contrast of mechanical properties at the soil-structure contact. The interface behaviour takes place in a very thin zone around the structure which develops a strain localization caused by the transmission of tangential force of structure to the soil. A discontinuity of

mechanical properties has the important and irreversible changes in the configuration of less resistant material during shear loading. For instance, the structure of granular medium is completely altered to an extent depending on the level of existing stress. The interface zone, consisting of one part soil and some particles torn from the structure, thus has mechanical properties very different from the rest of the soil. Considering the soil-structure friction, its characteristic is due to the presence of a static part accompanied by a kinematic part in the expression of the contact law. Main observations and findings on the phenomenon based on the existence of soil-structure interfaces show the shear resistance [τ] deduced from the classical formula as:

$$\tau = \sigma \tan\delta \tag{1.1}$$

where δ is friction angle between soil and structure and σ is the normal stress exerted on a structure anchored in the soil. The stresses and strains coupled with a variation of deformations in the immediate vicinity of the structure are only meaningful in a zone of limited thickness around the inclusion. The methods for predicting the bearing capacity of piles and the laws of mobilization of skin friction along the shafts have also been proposed.

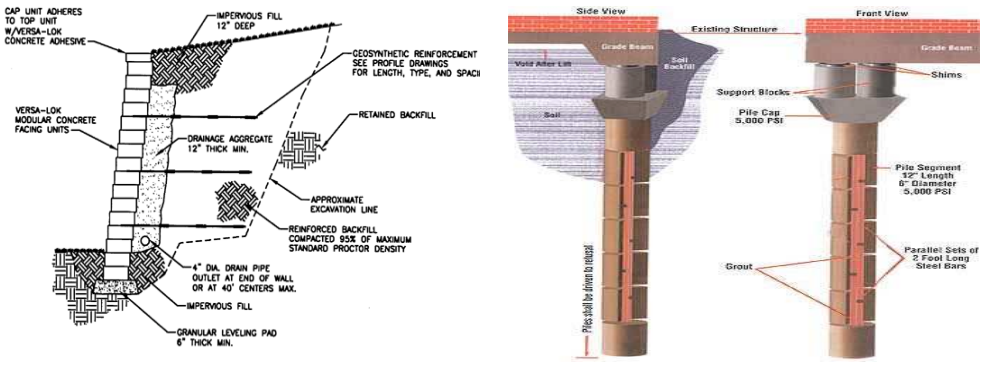

(a) (b)

Figure 1.1: Application of soil-structure friction; (a) earth retaining structures with geosynthetic reinforcement; (b) pile foundations

In most cases involving geotechnical offshore, the bearing capacity of piles are commonly designed by following the guidelines of the American Petroleum Institute API [1993]. The Coulomb failure criterion used to calculate the shaft friction of pile is defined as;

$$\tau_s = K\sigma'_n \tan\delta \tag{1.2}$$

where K is an earth pressure coefficient relating the effective normal stress acting around the piles at failure to the in situ effective over burden stress (σ'_v), $\tan\delta$ is the friction coefficient between pile and soil. The value of $K(\approx 0.8 - 1)$ is assumed constant along the

pile shaft. API method would give over or underestimation because the density of the soil surrounding the pile is not taken into account. However, this method still provides the reasonable predictions for the dimensions of piles and soil types of the used database.

Schlosser & Guilloux [1981] defined a friction coefficient, so called apparent, as a function of shear stress during the pull-out test on the strip related to the initial normal stress by the following equation;

$$\mu^* = \tau/\sigma_0 \tag{1.3}$$

with $\mu^* \geq \mu = \tau/(\sigma_0 + \delta\sigma)$; μ is the real soil-structure friction coefficient and $\Delta\sigma$ is the variation of normal stress during the pull-out test.

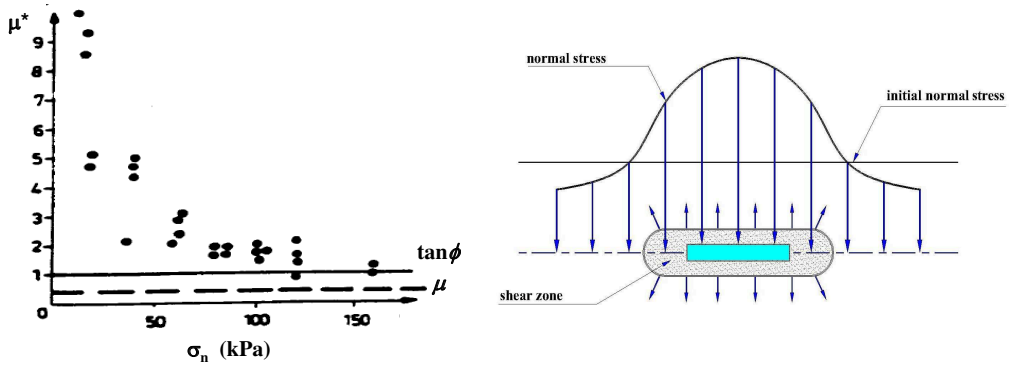

(a) (b)

Figure 1.2: Dilatancy effects in pull-out tests on strips; (a) influence of soil dilatancy on the friction coefficient; (b) local increase of normal stress as a result of dilatancy, Schlosser & Guilloux [1981]

From the experimental observations, it was commonly found that the values of the apparent friction coefficient (μ^*) were much higher than the real friction coefficient. The high value of the apparent soil-structure friction angle and the increase in normal stress, were due to dilatancy. The expansion or contraction of the soil caused by the shear loading is a phenomenon which requires the comprehension of the evolution of the interface mechanical properties. Figure 1.2 shows that a pull-out test of an inclusion embedded in the soil produces the shear stress whose values are significant only in a limited zone around the inclusion. In this area the soil tends to increase in volume due to expansion, but is partly prevented by the rest of the ground. This causes a significant increase of normal stress and consequently the friction coefficient. The roles played by the factors influencing the behavior of interface such as roughness and density have an effect on dilatancy.

1.3 Experimental investigation of interfaces

So far, the development of accurate understanding of the mechanical response of interfaces has alternatively been investigated from appropriate laboratory or field tests to describe the interface behaviour in a realistic manner. A comparison was made of their advantages and disadvantages with respect to the others. However, a number of refinements and modifications of several devices have continuously been made in order to enhance the comprehension of interface behaviour.

1.3.1 Interface shear devices

One of the most extensive studies on soil-structure interface testing has been performed by using the conventional direct shear devices whether at constant normal load (CNL) or at constant normal stiffness (CNS) condition. Figure 1.3 shows typical direct shear test which is widely used to investigate the interface behaviour (Desai et al. [1985]; Boulon [1989]; Hoteit [1990]; Al-Douri & Poulos [1992]; Tabucanon et al. [1995]; Mortara [2001]; Shahrour & Rezaie [1997]) as a result of much less technical difficulty and commonly available devices. Nevertheless, the problem arising during the test is that the stress and strain states within the sample are not homogeneous due to the effect of side wall friction. The stress non-homogeneity arises as a consequence of shear loading which is transferred through the wall of the shear box. On the condition that the interface test considered as a surface test (due to the very intense localization) instead of a volume test, therefore the homogeneity is only taken into account along the idealized displacement discontinuity surface. The shear band occurring by using direct shear test still remains at the place where it took place.

Boulon [1989] also performed a series of direct shear tests on sand-structure interfaces and proposed the idealization of soil structure interfaces. From this investigation the soil-structure interface behaviour was practically considered as a surface (or contact with friction) behavior which occurred between the two boundaries of a shear band inside the soil along the structure in bidimensional situation. A shear band or soil-structure interface cannot explicitly be separated from the surrounding soil, for this reason, the direct shear test has to be interpreted by considering two parts in the sample. Figure 1.4 also illustrates the direct shear test interpretation: the "active" lower part being in contact with the rough material, so called interface whose thickness is about 10 times the mean diameter D_{50} of the sand grains, and the "passive" upper part as thin as possible, acting as oedometer sample.

The interface variables taken into account are then vector variables: the stress vector acting on the interface (τ', σ'_n):

$$\underline{\sigma} = \begin{Bmatrix} \tau' \\ \sigma'_n \end{Bmatrix} \approx \begin{Bmatrix} \tau \\ \sigma_n \end{Bmatrix} \tag{1.4}$$

And the relative displacement vector between the two boundaries of the interface, where $[u']$ and $[w]$ are normal and tangential displacements of interface respectively:

$$\underline{[u]} = \begin{Bmatrix} [w] \\ [u'] \end{Bmatrix} \approx \begin{Bmatrix} [w] \\ [u] \end{Bmatrix} \tag{1.5}$$

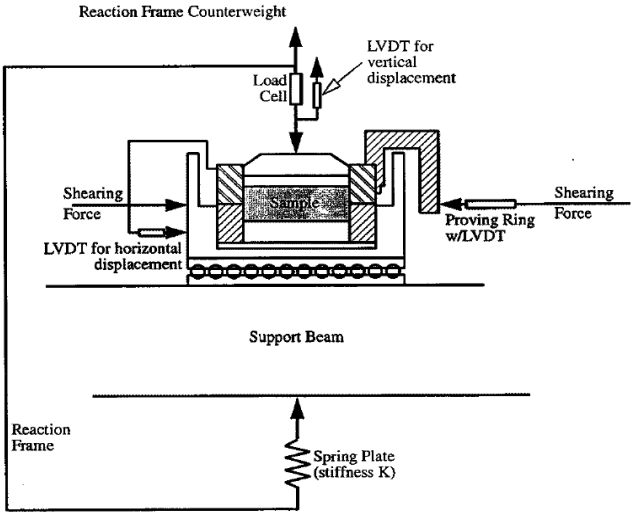

Figure 1.3: Direct interface shear apparatus, Tabucanon et al. [1995]

All the components have to be considered as mean values within the generated contact surface. In addition, the roles played by the factors influencing the behaviour of interface from various observations are roughness, normal stress level, constraint conditions, grain strength and density.

Figure 1.5 shows simple shear apparatus which can also be performed with much less difficulty in which the tangential displacement can be measured separately in terms of sliding displacement of the interface and displacement due to shear deformation of sand (Uesugi & Kishida [1986]; Kishida & Uesugi [1987]; Fakharian & Evgin [1997]). This is able to overcome the shortcoming of direct shear box. The simple interface consists of a stack of rectangular plates as the sample container placed on the plate. There are still the effect of side wall friction as well as the friction between the sample container and the plate. Moreover, this should also be taken into account the shortcomings as material loss occurring between the shear box and the plate during testing. The leakage of sample would lead to an accuracy of normal displacement. Various solutions are then used, for instance, a pair of thin steel plates inserted between the top and the bottom halves of direct shear box (Al-Douri & Poulos [1992]) and thin layer of foam and Teflon sheet pasted between the plate and the shear box (Fakharian & Evgin [1997]), were subsequently used in order to prevent the loss of material during testing.

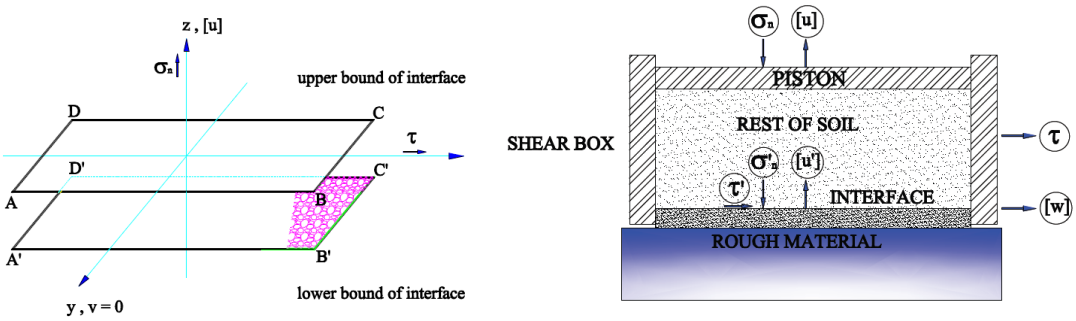

(a) (b)

Figure 1.4: Basic features of soil structure interface behavior: (a) Interface idealization; (b) Direct shear test interpretation, Boulon [1989]

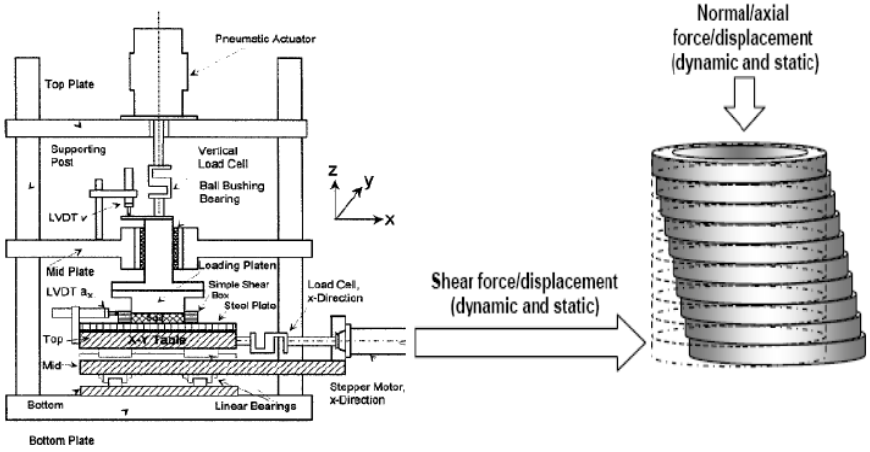

Figure 1.5: Simple shear type friction apparatus and simplified view of laterally constrained sample under simple shear conditions, Fakharian & Evgin [1997]

The ring shear would be the most efficient device to observe the interface behaviour (Yoshimi & Kishida [1981], Kelly [2001]). Because the sample is ring-shaped (i.e. there is unlimited distance for shearing), it is free from the progressive failure and the contact surface still remains constant whether the sample is sheared at a large circumferential displacement. The stress states are homogeneous through shear test. However, some disadvantages still exist, since the feature of this device is ring-shaped, it seems inconvenient to prepare the sample due to more technical difficulty. A variety of ring shear tests are presented in Figure 1.6. The sample is placed in the container below the loading ring and is sheared against the surface of loading ring. The normal load is applied through the top platen and the shear stress is determined from the applied torque.

1.3.2 Interface roughness

From experimental investigations, it has obviously been found that surface roughness of structures is a major factor affecting soil-structure friction coefficient. It was primarily quantified as a maximum height $R_{\max}$ (Yoshimi & Kishida [1981]). The roughness $R_{\max}(L = 2.50$ mm) was defined as the relative height between the highest peak and the lowest along a surface profile over 2.5 mm length. The diameter of sand particle was not considered in this definition (Figure 1.7). However, in order to correlate the surface roughness with the coefficient of interface friction, the diameter of sand particle should then be considered in evaluating the surface roughness. The diameter of sand particle can be incorporated into $R_{\max}$ by modifying the gauge length L to the 50% mean diameter of sand particle (D_{50}).

The modified roughness was represented in terms of $R_{\max}(L = 0.20$ mm) (Kishida & Uesugi [1987]), as shown in Figure 1.8. In evaluating the surface roughness of steel, a normalized roughness R_n was then defined as

$$R_n = \frac{R_{\max}(L = D_{50})}{D_{50}} \tag{1.6}$$

where $R_{\max}(L = D_{50})$ is the $R_{\max}$ value of a steel surface with gauge length $L = D_{50}$.

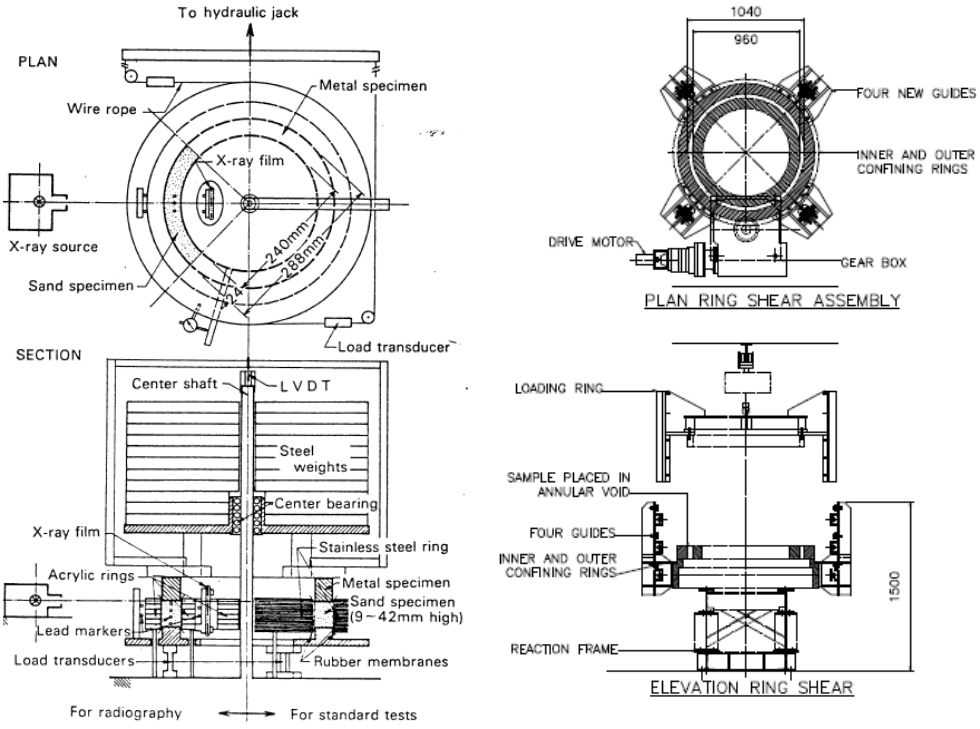

Figure 1.6: Ring shear device (left) Yoshimi & Kishida [1981], (right) Kelly [2001]

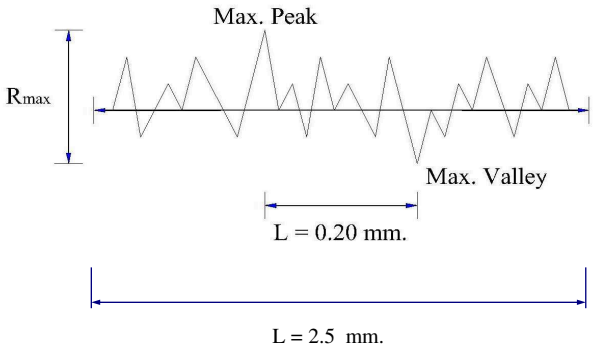

Figure 1.7: Evaluation of surface roughness and modification of surface roughness evaluation, Kishida & Uesugi [1987] and Uesugi & Kishida [1986]

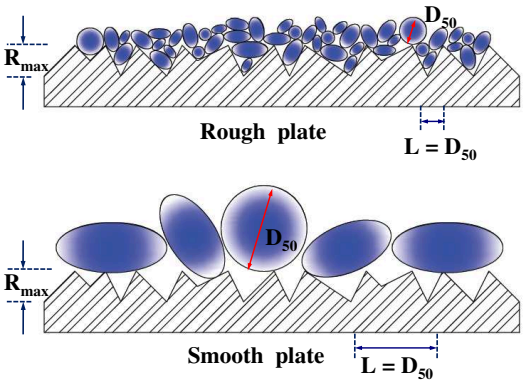

Figure 1.8: Simple interpretation of interface roughness; rough and smooth surface, Uesugi & Kishida [1986] and Mortara et al. [2007]

The normalized roughness is used to distinguish the type of the roughness in terms of smooth interface or rough interface. The value of critical roughness (R_{crit}) is therefore used to classify these terms of the interface. Available investigations (Uesugi & Kishida [1986], Uesugi et al. [1989], Hu & Pu [2004]) indicate that the critical roughness (R_{crit}) is defined in the range of 0.1-0.13, i.e. $R_n < R_{\text{crit}}$ (smooth interface) and $R_n > R_{\text{crit}}$ (rough interface). Figure 1.9 also shows typical influence of the normalized roughness. As can be seen in this figure, the peak shear stress is a function of normalized roughness. The dilative behaviour can be observed on the test with high value of normalized roughness.

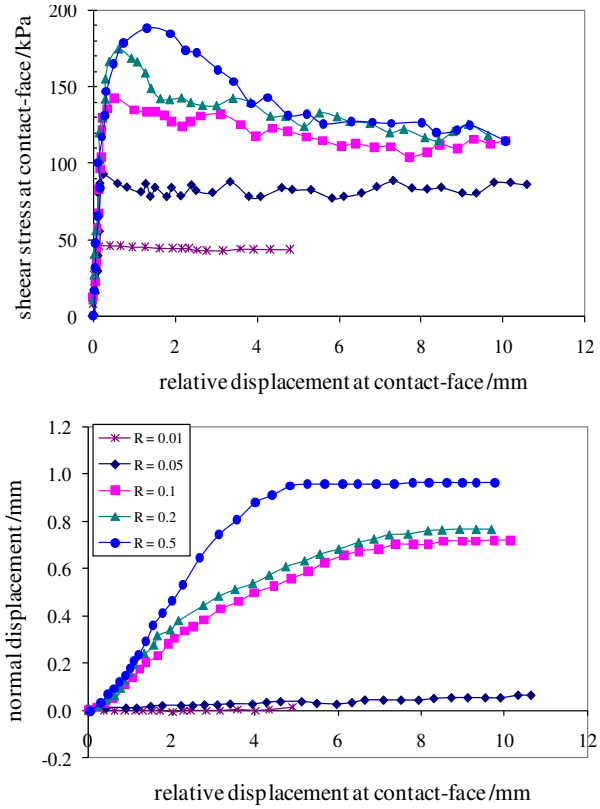

Figure 1.9: Influence of roughness surface (R ; see definition 1.6 hereabove) on interface CNL sand (silica)-structure tests ($D_r = 90\%$, $\sigma_n = 200$ kPa), Hu & Pu [2004]

1.3.3 Interface thickness

The evaluation of the thickness of the soil-structure interface has been the subject of several studies carried out using different methods. It is worth noting that to define the exact interface thickness is quite delicate and requires a high quality measurement. For instance, Hoteit [1990] evaluated the interface thickness by using the stereophotogrammetry while Dejong et al. [2003] investigated the shear deformation and volume change taking place within the shear band by using particle image velocimetry (PIV). However, the parameters discussed and identified by different authors have qualitatively the same influence. In general, the grain size, as well as the roughness surface, influences the interface thickness. The grain size influences the interface thickness as an increasing function of average grain diameter. From several observations, the range of 7-14D_{50} is generally taken into account for estimating interface thickness.

The thickness of the shear band tends to decrease when the initial density increases. Many experimental results show that the relative displacements as well as the rotations of grains in loose sand-structure interface are higher than that in the case of dense sand (Figure 1.10). This is explained by the fact that the grains of loose sand have a greater freedom of

movement than that of dense sand. From the investigation carried out by Hammad [1991], the interface thickness for loose sand was in the range of 6-7D_{50} while for dense sand the range of 4-5D_{50} was observed with rough interface.

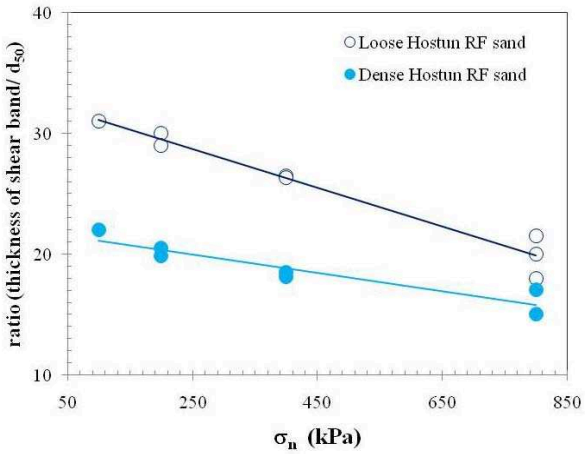

Figure 1.10: Thickness of shear bands relative to the grain size (D_{50}) as a function of confining stress (σ_n), Hammad [1991]

1.4 Cyclic CNL interface shear tests

The development of cyclic testing has widely been conducted on sand-structure interfaces, whether by using modified direct shear tests or simple shear tests on various sands. Several investigations have been carried out by varying amplitude of displacement, amplitude of shear stress and normal stress, number of loading cycles, initial relative density of sand and surface roughness (Desai et al. [1985]; Al-Douri & Poulos [1992]; Fakharian & Evgin [1997]; Mortara [2001]; Shahrour & Rezaie [1997]; Oumarou & Evgin [2005]).

Figure 1.11 and Figure 1.12 show monotonic and cyclic interface shear tests, on loose (D_r = 35%) and dense (D_r = 85%) Toyoura sand, respectively, performed by Mortara [2001]. The applied cycles are symmetric in terms of shear displacement. For smooth interface, it could be seen that the variation on peak shear stress was not significant whether the interface was subjected to cyclic loading on loose sample or dense sample. Considering the evolution of normal displacement, the contracting interface behaviour (u>0) was observed on both samples. On the other hand, rough interfaces exhibited the increase of maximum shear resistance mobilized in the post cyclic phase providing this is tested on dense sample. Moreover, a contracting behaviour followed by dilation at each stress reversal on dense sample was significantly observed. The contractive accumulation rate decreased with an increase of the number of cycles. In addition, the post cyclic behavior exhibited an obvious dilation because cyclic loading at constant normal stress leads to the progressive densification of the interface and the dilatancy angles consequently increase (Mortara [2001]; Shahrour & Rezaie [1997]).

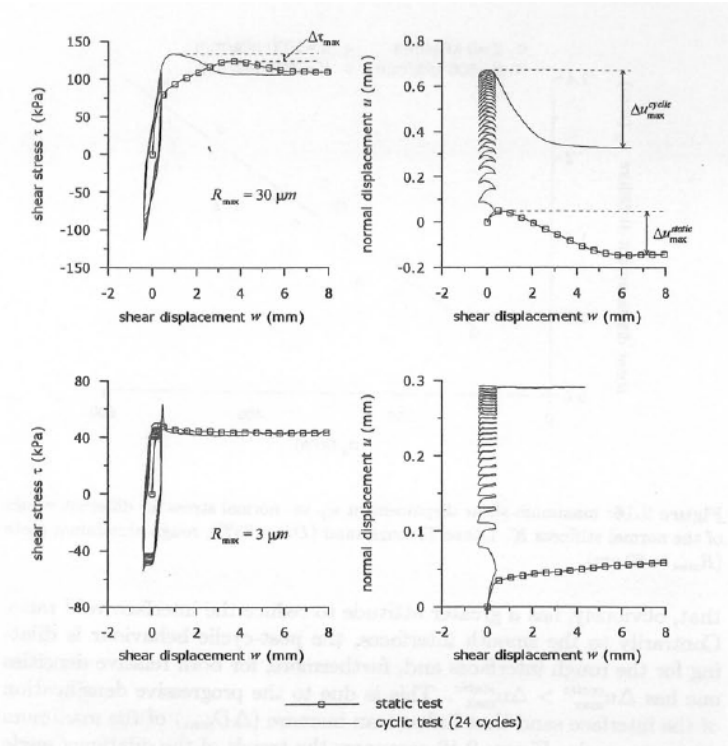

Figure 1.11: Comparison between monotonic and cyclic CNL interface shear tests on smooth and rough surface, Toyoura (silica) sand (D_r = 35%, σ_n = 150 kPa) u > 0 contraction, Mortara [2001]

The amplitude of cyclic loading also influences the behaviour of interfaces. Figure 1.13 shows the intensity of normal displacements of interface subjected to cyclic loading with different amplitudes of cycles (A) on loose Toyoura sand (D_r = 35%). With increasing amplitude of cycles (in the range of A = 0.4-0.8 mm), the normal displacement tended to be more contractive (Mortara [2001]).

1.5 CNS interface shear tests

1.5.1 Several shear paths

The study of interface behaviour has been specified in the conventional interface experiments in which the applied normal stress is controlled to be constant (CNL) during the process of shearing. Especially when interfaces subjected to cyclic loading, numerous experimental investigations have been reported that the interface responses turn into a progressive densification with increasing number of cycles and stiffening rate decreases as a function of number the cycles. This leads to the mobilized shear stress (Desai et al. [1985]; Al-Douri & Poulos [1992]; Shahrour & Rezaie [1997]; Oumarou & Evgin [2005]).

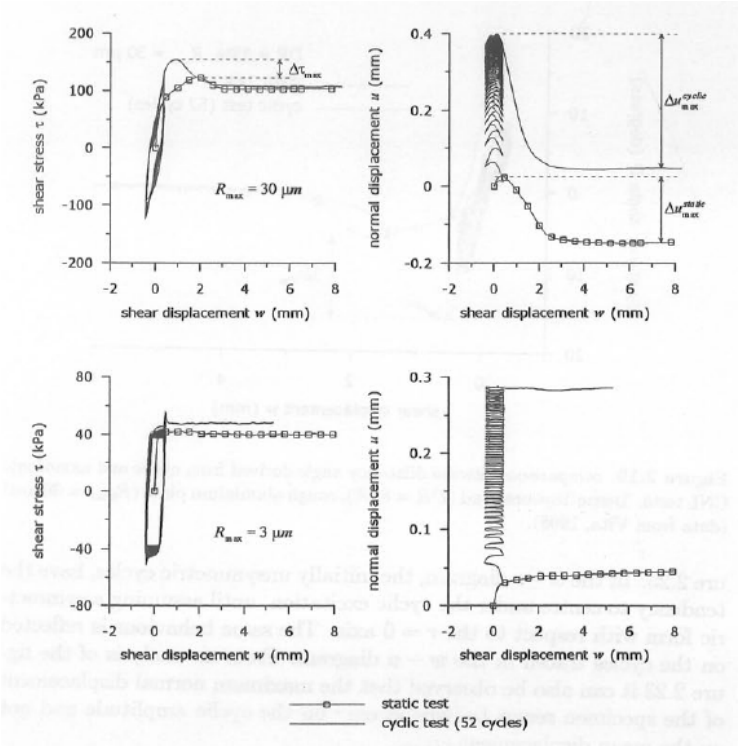

Figure 1.12: Comparison between monotonic and cyclic CNL interface shear tests on smooth and rough surface, Toyoura (silica) sand (D_r = 90%, σ_n = 150 kPa) u > 0 contraction, Mortara [2001]

Nevertheless, from pull-out test of a model-pile embedded in sand performed by Puech et al. [1979] the results obtained indicate that the variations of shaft friction coefficients (K) during the loading correspond to the tendency of soil close to the pile whether to dilate or to contract during the localized shear. For instance, the dilatancy is partially impeded by the surrounding soil mass and then leads to an increase in lateral stress. Boulon & Foray [1986] performed cyclic pull-out test of model-pile in sand. From this investigation, the skin friction decreased as a function of number of cycles as shown in Figure 1.14. This can be attributed that cyclic loading induces a contraction of the sand adjacent to pile. A decrease in volume of sand leads to a progressive decrease in lateral stress, and consequently a decrease of shear resistance.

Boulon & Foray [1986] also proposed the boundary conditions of direct shear tests in which the stiffness of surrounding soil was represented by a pressuremetric modulus in order to simulate the elementary mechanism of mobilization of lateral friction at the pile-soil interface. This boundary condition, so called constant normal stiffness (CNS), has been situated between the two extreme conditions, first the constant normal load (CNL) as mentioned before. The other assuming no-volume change has not been realistic because of considering the mass of the surrounding soil beyond the sheared zone as radially perfectly rigid. Figure 1.15 shows how the interface behaved under two extreme conditions at high

and low initial normal stress respectively. The obvious difference between the two tests can be observed, especially the mobilized normal stress on constant volume test.

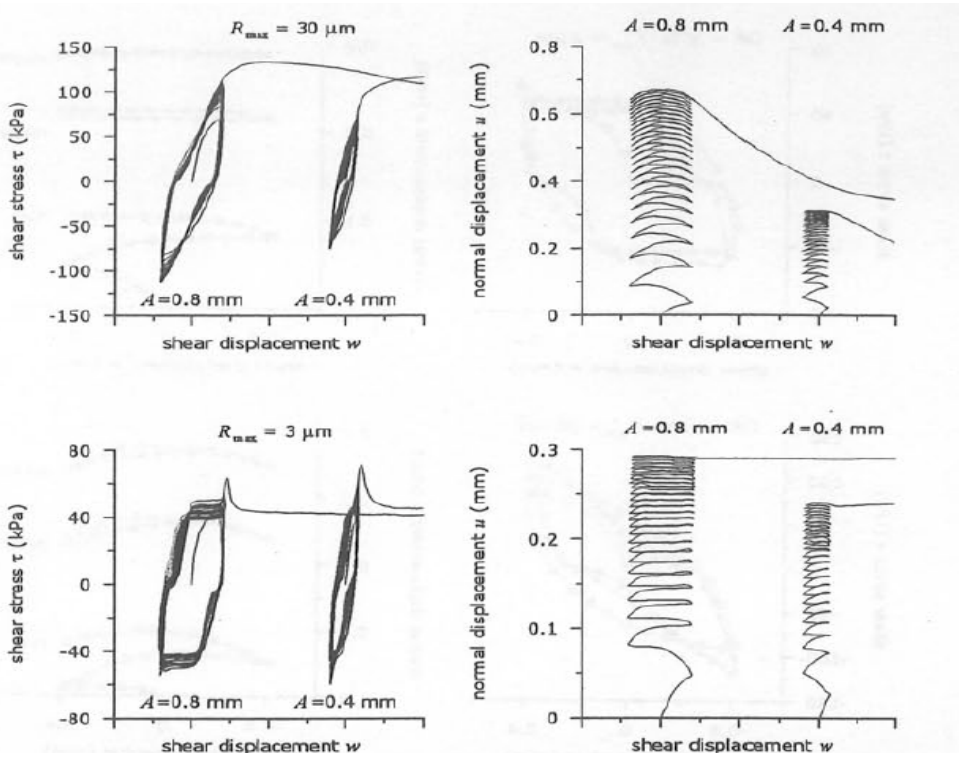

Figure 1.13: Influence of different amplitude on cyclic CNL interface shear tests on smooth and rough surface, Toyoura (silica) sand (D_r = 35%, σ_n = 150 kPa) u > 0 contraction, Mortara [2001]

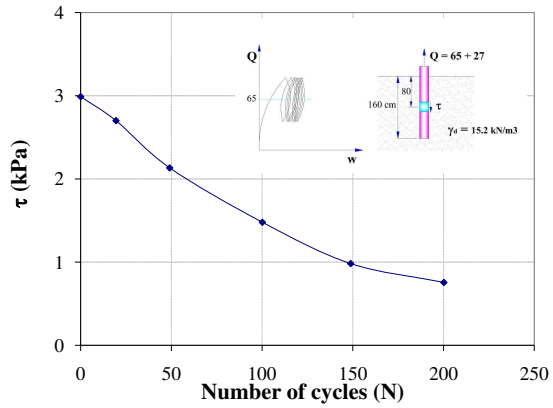

Figure 1.14: Shear stress degradation with increasing number of cycles on cyclic pull-out test of model-pile embedded in Hostun (silica) sand; mean unit skin friction, Boulon & Foray [1986]

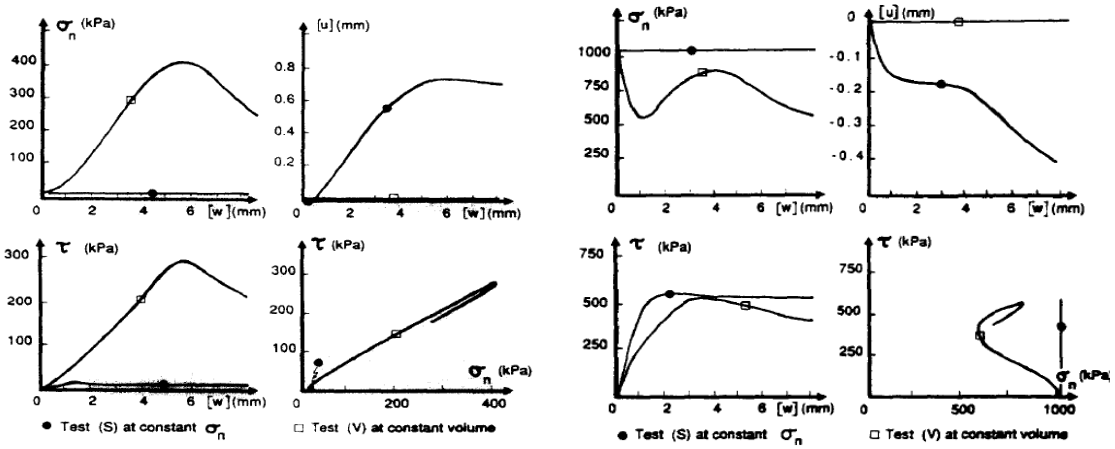

(a) (b)

Figure 1.15: Extreme interface direct shear tests on Hostun (silica) sand; (a) at low initial normal stress $\sigma_n = 12$ kPa on dense sample; (b) at high initial normal stress σ_n =1061 kPa on loose sample, Boulon [1989] and Boulon & Foray [1986]

1.5.2 Definition of Constant Normal Stiffness (CNS)

A laboratory test of pile-soil interface can simply be interpreted as an interface under constant normal stiffness (CNS) condition. Considering a pile with radius R_0, embedded in soil with a pressuremetric modulus E_p, and the thickness of the interface layer (e) mobilized during the large localized shear (e $<<$ R_0). The normal stiffness imposed to the interface (k) according to Boulon & Foray [1986] results from the definition of the pressuremetric modulus E_p (Figure 1.16, $\Delta V/V_0$ = relative volume change):

$$E_p = \frac{\Delta\sigma}{-2\Delta V/V_0} \cong \frac{\Delta\sigma}{-2\Delta[u]}(R_0 + e) \cong \frac{\Delta\sigma}{-2\Delta[u]}(R_0) \tag{1.7}$$

Consequently;

$$\frac{\Delta\sigma}{-\Delta[u]} = \frac{2E_p}{R_0} = k \tag{1.8}$$

where $\Delta\sigma$ represents the variation of normal stress acting on the interface, $\Delta[u]$ the variation of normal displacement.

Figure 1.16 shows the analogy between the localized shear along a pile and a direct shear test with an imposed normal stiffness. In this case the normal stress acting on the interface was applied by a spring with and appropriate stiffness. The values of the stiffness can be distinguished in three typical boundary conditions.

- case I: $k = 0, \Delta\sigma = 0, \Delta[u] \neq 0$(constant normal stress)

- case II: $k = \infty, \Delta\sigma \neq 0, \Delta[u] = 0$(constant volume)
- case III: $k =$ constant, $\Delta\sigma \neq 0, \Delta[u] \neq 0$(constant normal stiffness)

For instance, in case I, the normal stress applied on the interface is controlled to be constant throughout shearing. For case II, the volume of the sample remains constant during shearing. Case III in which the normal stress and the normal displacement vary proportionally to $\Delta\sigma_n/\Delta u = k$, as shown in Figure 1.17.

Boulon & Foray [1986] also illustrated a comparison of direct shear tests with imposed stiffness (k) existing intermediately between the extreme conditions as shown in Figure 1.18. Furthermore, grading characteristics of sand and crushability of sand grains could also been found to be the major factors on interfaces. Figure 1.19 shows a comparison between interface direct shear tests under CNS condition performed on siliceous and on calcareous sands. For a given stiffness, the mobilization of normal stress associated with shear stress observed on calcareous sand is lower than that on siliceous sand, as a result of the high crushability of sand grains on calcareous.

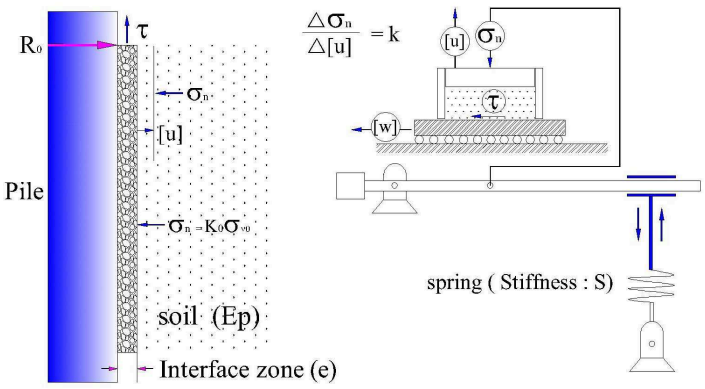

Figure 1.16: Analogy between the localized shear along pile and a direct shear test with an imposed normal stiffness, Boulon & Foray [1986]

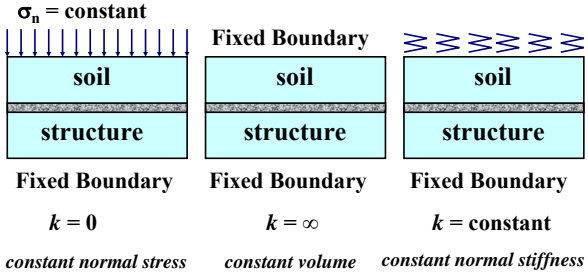

Figure 1.17: Boundary condition in direction normal to interface, Fakharian & Evgin [1997]

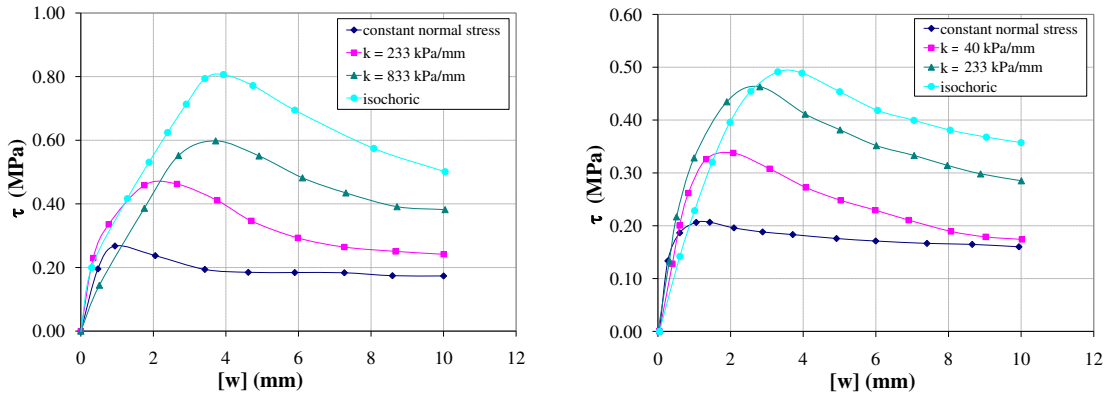

(a) (b)

Figure 1.18: Hostun (silica)sand-structure interface direct shear tests with three different boundary conditions; (a) dense samples; (b) loose samples, with σ_{n0} =354 kPa, Boulon & Foray [1986]

Using CNS direct shear apparatus to investigate the behaviour of soil-structure interface, many researchers have investigated the effect of different constant normal stiffness on the response in both static and cyclic conditions and the variation of interface roughness to cover the whole range of soil-structure interfaces.

Johnston et al. [1987] used CNS direct shear testing techniques to investigate the factors which could control the behavior of rough concrete-rock interfaces and to develop more rational methods for the prediction of side shear resistance in rock-socketed piles (Figure 1.20). This observation can explain that the dilation of the socket causes an increase in the stress acting normal to the pile shaft and the relative movement between the pile and the rock mass is controlled by CNS conditions as opposed to the more conventionally encountered conditions of constant normal load (CNL) referring to the at rest K_0 state.

Several monotonic CNS direct shear tests performed, for instance, by Hoteit [1990]; Tabucanon et al. [1995] and Mortara [2001] obviously showed the influence of the stiffness on interface behaviour. Figure 1.21 shows that the larger CNS value on rough/dense sample could cause a mobilization of the stresses acting on interface. It can be said that during shearing phase, the interface exhibited a dilation and then led to an increase in normal stress associated with shear stress. The normal displacements reduced for increasing values of the normal stiffness. On the other hand loose samples showed a significant degradation of the stresses as a result of the contractive behavior of interfaces. For smooth interface, the peak shear stresses were very low due to the normal stress decreased rapidly. The normal stiffness had little influence on the response as shown in Figure 1.22. From this observation, the normal stress could vanish for small shear displacement (15-20 mm.), depending on the conditions. This is due to the fact that smooth interface always exhibits contractive behavior and sliding then occurs along the contact surface between sand-structure (Uesugi & Kishida [1986]).

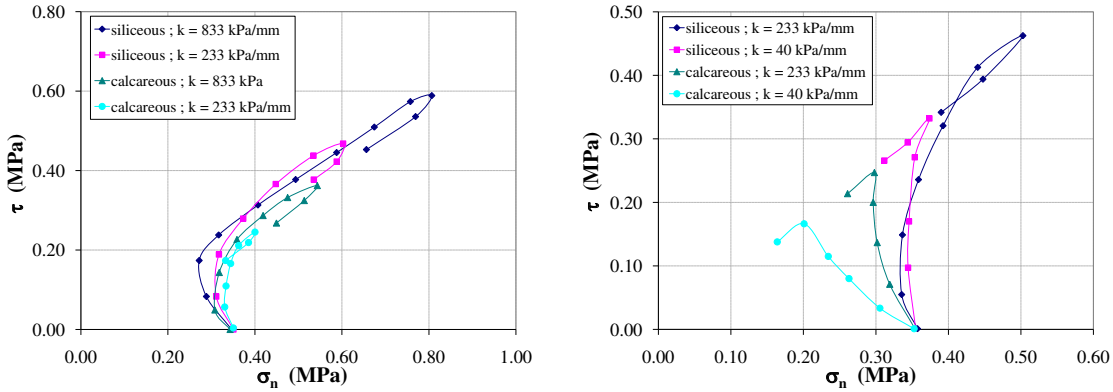

(a) (b)

Figure 1.19: Sand-structure interface direct shear tests with imposed stiffness on siliceous and calcareous sand; (a) dense samples; (b) loose samples, with σ_{n0} =354 kPa, Boulon & Foray [1986]

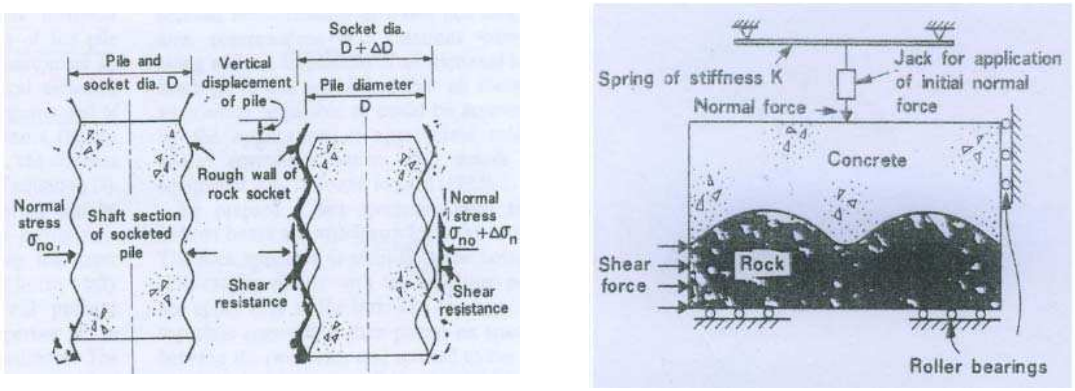

(a) (b)

Figure 1.20: Behaviour of pile socketed in rock (a) displacement behavior; (b) principle of the CNS test technique, Johnston et al. [1987]

1.5.3 Cyclic CNS interface shear tests

The effects of normal stiffness (k) on the cyclic interface behaviour performed by either direct shear or simple shear tests are more significant than that on monotonic interface behavior. The main characteristic of cyclic interfaces under CNS condition is the degradation of normal stress accompanied with the degradation of shear stress as a result of the progressive densification. Figure 1.23 shows the typical results of cyclic CNS tests on dense/rough interface performed on direct shear test by Airey et al. [1992].

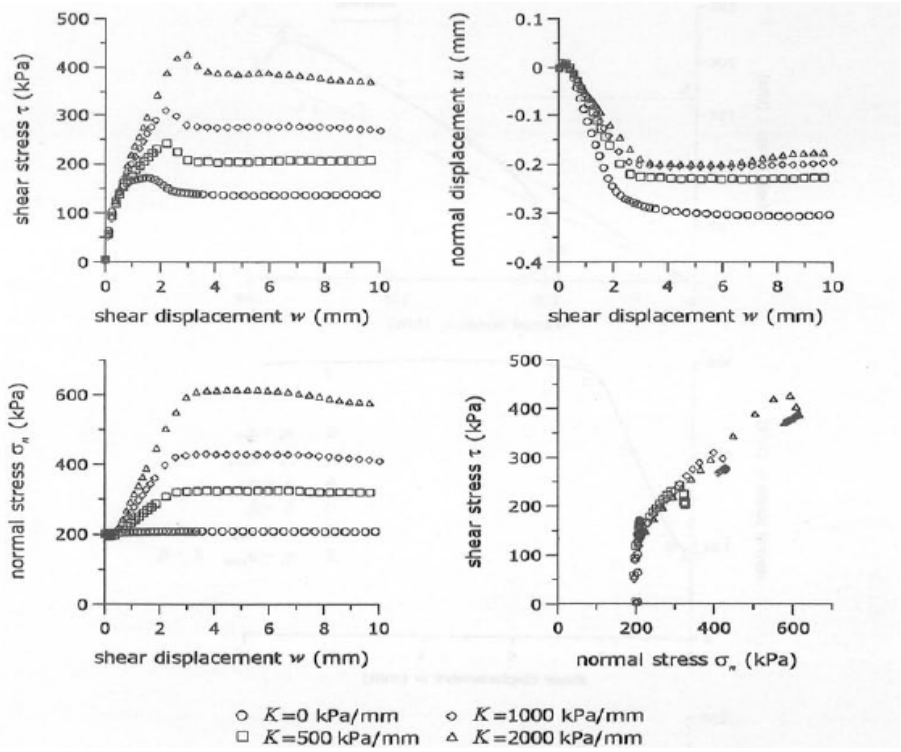

Figure 1.21: Interface test results for different values of the normal stiffness. Dense Toyoura (silica) sand,(D_r = 85%, σ_n = 200 kPa, rough surface $R_{max} = 60\mu m$), u > 0 contraction Mortara [2001]

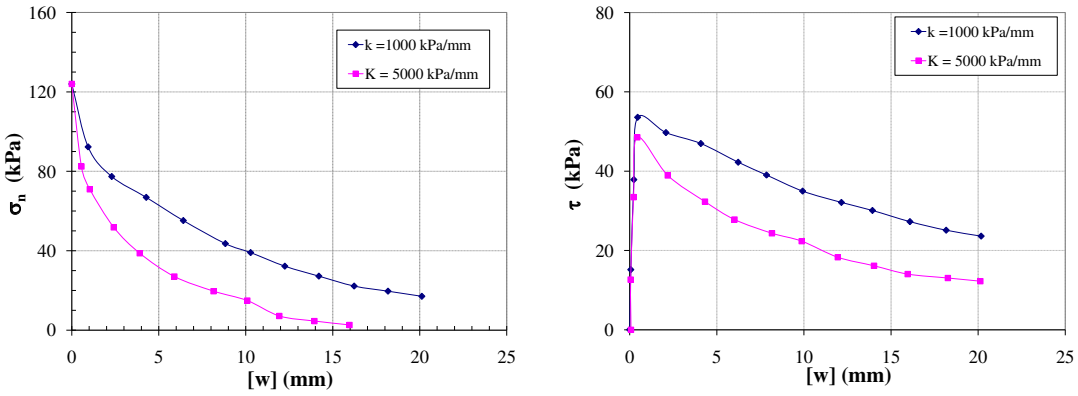

Figure 1.22: Interface test results for different values of the normal stiffness on loose Calcareous sand-smooth surface, σ_n = 125 kPa, Hoteit [1990]

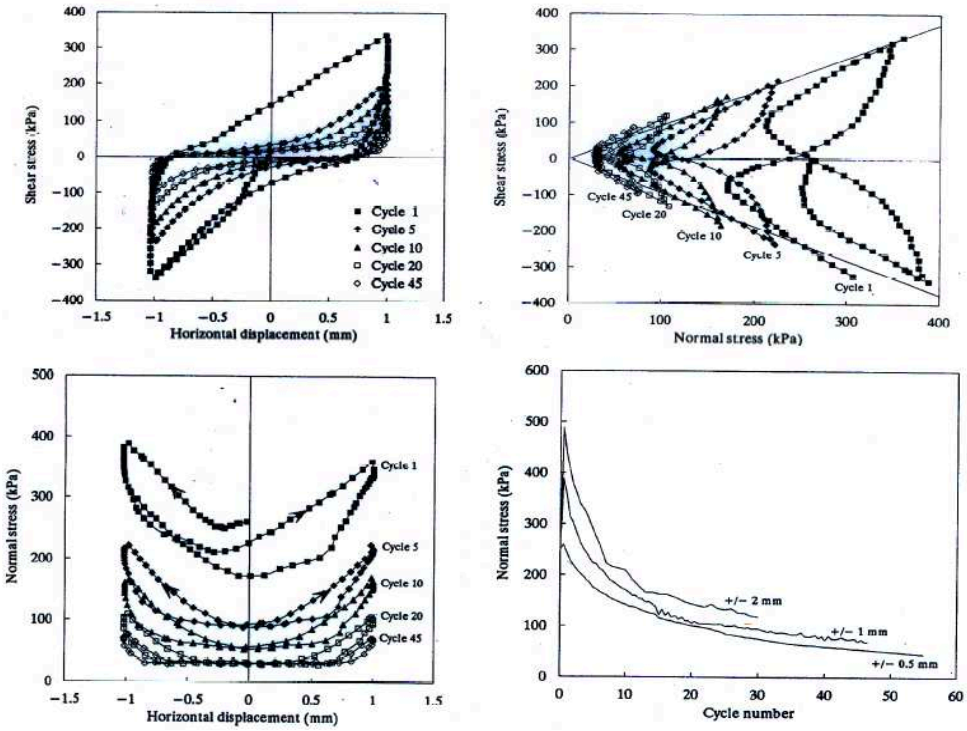

Figure 1.23: Typical cyclic CNS shear test with $k = 1600$ kPa/mm on dense calcareous sand/rough surface, $\sigma_n = 250$ kPa, Airey et al. [1992]

Fakharian & Evgin [1997] also reported the effect of magnitude of normal stiffness on dense/rough interface by means of simple shear test. From this experimental investigation the normal and shear stresses decreased rapidly as a function of N with increasing the normal stiffness (k) as shown in Figure 1.24. The amplitude of cycles also influenced the stress gradation. If the amplitude of tangential displacement was large enough (0.75mm, in this observation) to be able to reach the peak stress ratio with certain cycles, then a degradation of stresses led to the failure of interface as shown in Figure1.25(a). The stress path illustrated in Figure 1.26 also shows a gradual decrease in normal stress associated to shear stress with cycles in case of cyclic amplitude = 0.75 mm. The stress path cycles evolved inside the peak envelope before the failure. After touching the failure envelope (cycle 11) the stress path subsequently bounced back inward and stabilized on the residual envelope. For small amplitude of tangential displacement (0.25 mm), Figure 1.25(b), the reduction of normal stress associated with small reduction in maximum shear stress could hardly lead to failure. The failure of interface did not occur if the sliding displacement did not accumulate with cycles.

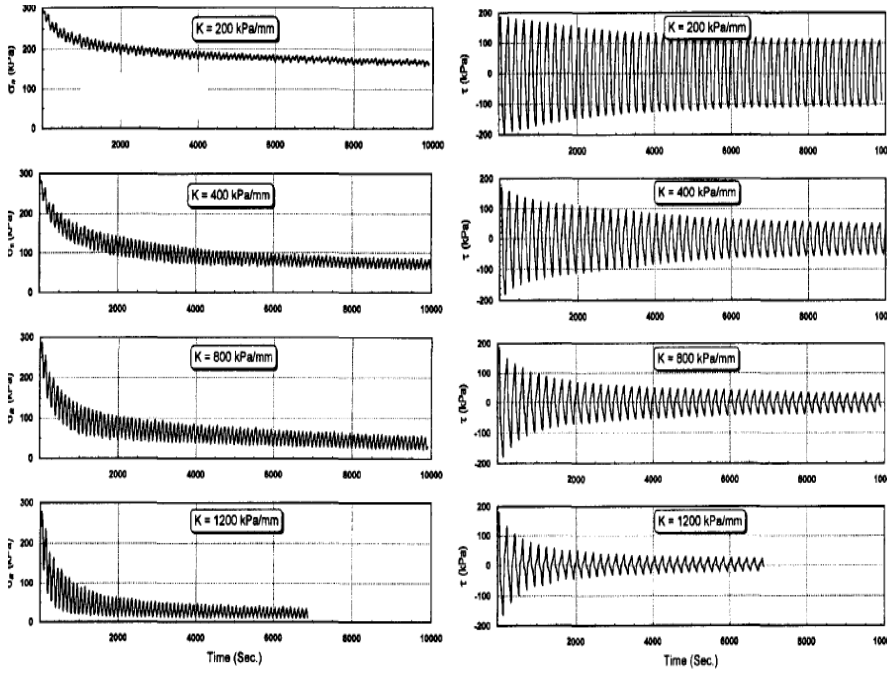

Figure 1.24: Variation of normal and shear stress during cyclic CNS shear test with different values of k (prescribed normal stiffness) on dense silica sand/rough surface, $\sigma_n = 300$ kPa, Fakharian & Evgin [1997]

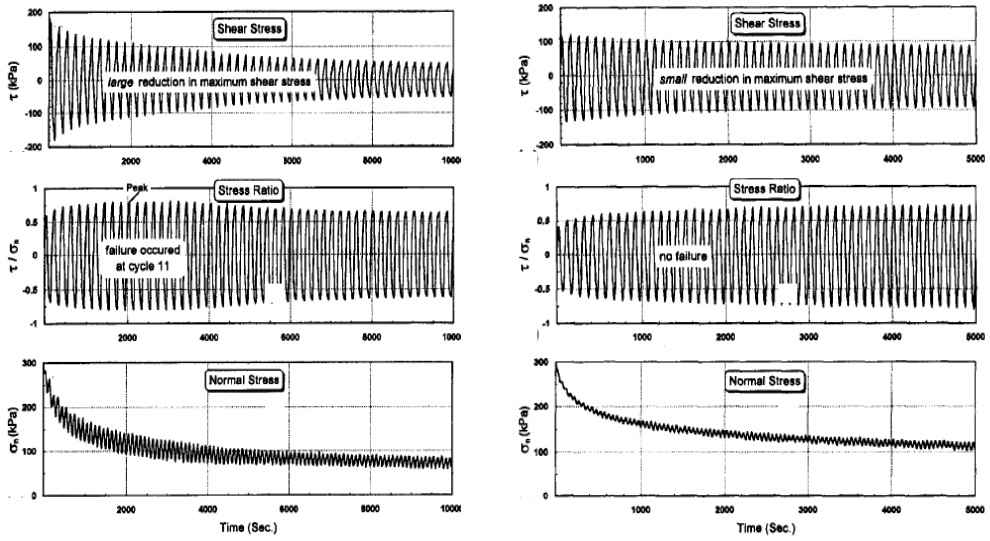

(a) (b)

Figure 1.25: Variation of normal and shear stress during cyclic CNS shear test with different amplitudes of cycles on dense silica sand/rough surface, $\sigma_n = 300$ kPa; (a) 0.75 mm; (b) 0.25 mm , Fakharian & Evgin [1997]

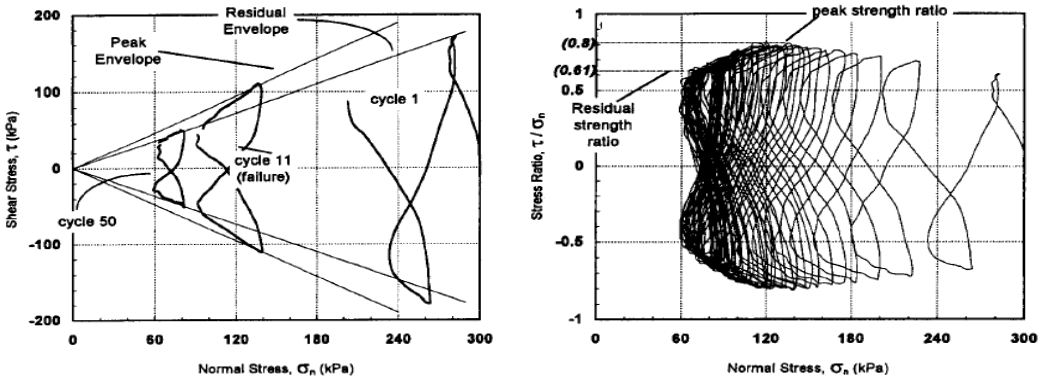

Figure 1.26: Stress path touching the failure (N=11) during cyclic CNS shear test with amplitudes of cycles 0.75 mm on dense silica sand/rough surface, $\sigma_n = 300$ kPa, Fakharian & Evgin [1997]

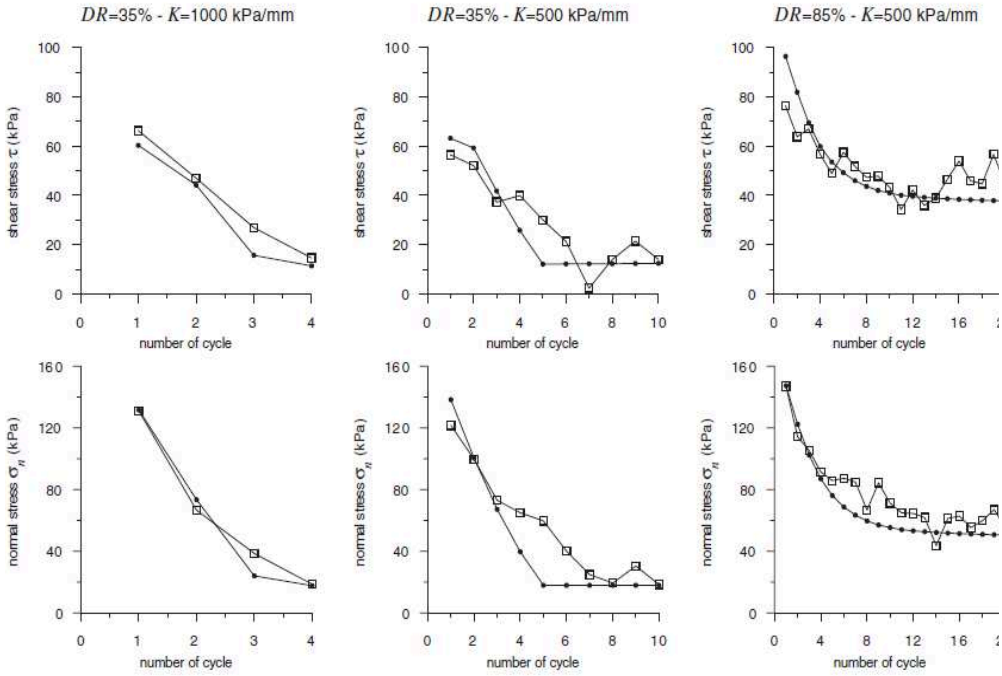

Figure 1.27: Shear and normal stress degradation on cyclic CNS interface tests on Toyoura (silica) sand with rough surface, $\sigma_n = 150$ kPa, Mortara et al. [2002]

Mortara [2001] and Mortara et al. [2002] also reported an important influence of normal stiffness on cyclic interface especially on loose sample. Figure1.27 shows the significant degradation of normal and shear stresses with an increase of normal stiffness on loose

sample. In this case, on rough interface with $k = 1000$ kPa/m three cycles were sufficient for the normal stress dropped rapidly to a minimum value. On the other hand dense samples exhibiting low tendency to contract required a higher number of cycles to reach the critical condition.

The effect of normal stiffness (k) on different roughness has also been reported by Mortara et al. [2007] as shown in Figure 1.28. The alternating phases of compression followed by dilation were significant on rough interface. In this case, the overall behaviour still exhibited contraction and therefore normal and shear stresses decreased. Furthermore, the post cyclic phase showed a recovery of normal and shear stresses as a result of dilative behaviour. On the other hand smooth roughness showed the progressive contraction without dilative phase. For this reason there was no recovery of stresses in post cyclic phase.

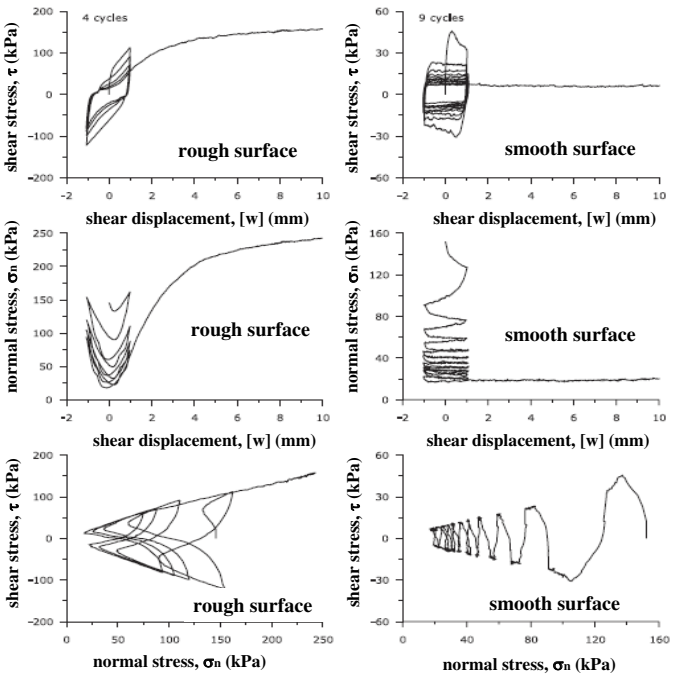

Figure 1.28: Comparison between cyclic shear displacement controlled CNS tests with different values of roughness on Toyoura (silica) sand, $\sigma_n = 150$ kPa, Mortara et al. [2007]

1.6 Element tests on high-cycle accumulation

The element test results performed on triaxial tests will be presented in the following sections. These are not related to interfaces but to volume behaviour. However, these very interesting results should be considered as a model for understanding and modeling a part of cyclic interface tests. Boulon & Nova [1990] illustrated the similarity in the interface behaviour exhibited with respect to sand behaviour on triaxial path. It is obvious to describe that the terms of deviatoric stress (q), deviatoric strain (ε_1), confining pressure (p') and volume strain (ε_v) from triaxial paths are respectively substituted by the terms of τ , $[w]$, σ_n and $[u]$ from interface direct shear tests as shown in Figure 1.29.

Considerable deformations in soils due to the accumulation of irreversible strain under the effect of cyclic loading can lead to many problems. Even though the amplitude is very small (e.g. $\varepsilon^{ampl} < 10^{-3}$, Wichtmann [2005]) but a great number of cycles (e.g. $N > 10^3$) would lead to significantly harmful phenomena. In drained condition cyclic loading leads to the accumulation of irreversible deformation either in contraction or in dilation and the modification of soil modulus due to variation of density. Therefore, these issues are of practical importance.

In this study the term "accumulation" is used in such a way that it means either an increase or decrease of state variables. A cyclic loading is able to lead to either residual strains or change of stress, depending on the boundary conditions applied. Figure 1.30 shows typical accumulation phenomenon under cyclic loading. If stress cycles are applied, this can lead to an occurrence of cyclic pseudo-creeps (Figure1.30a) and if strain cycles applied then a phenomenon of stress-relaxation can be observed (Figure 1.30b). Both conditions, pseudo-relaxation and pseudo-creep, may occur simultaneously in the case of mixed-controlled tests (Figure 1.30c).

Most of ideal approaches should be capable of simulating all the features of soil behaviour. There are two main categories for calculating the accumulation of stress and strain caused by cyclic loading: the "implicit" method and the "explicit" method.

The implicit or incremental method requires several (100) increments per cycle which may lead to an accumulation of unavoidable numerical error and inaccurate results for a high number of cycles, in general this method is appropriate for $N < 50$.

Thus it is obvious that the importance of explicit models is proposed, especially for a high number of cycles, in such a way that only one or the first few cycles are calculated using an incremental computation, and the rest of cycles will be treated as a cyclic pseudo-creep. The first cycle whose shape is irregular may differ from the following ones. Therefore in this method the accumulation is determined from the second cycle in which the number of cycles (N) is taken into account instead of time (t) as shown in Figure 1.31(a). Several studies have been conducted in the process of establishing patterns of cyclic behavior of materials and especially to estimate the accumulated strain (pseudo-creep), which also causes an accumulation of stress.

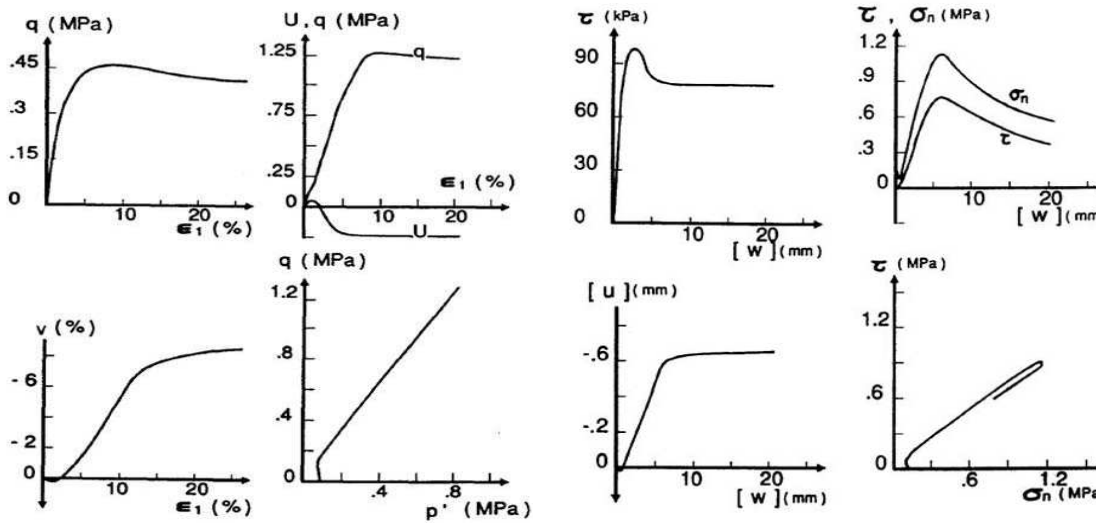

(a) (b)

Figure 1.29: Similarity in sand behavior on triaxial paths exhibited with respect to the interface behavior; (a) triaxial tests; (b) interface direct shear tests, Boulon & Nova [1990]

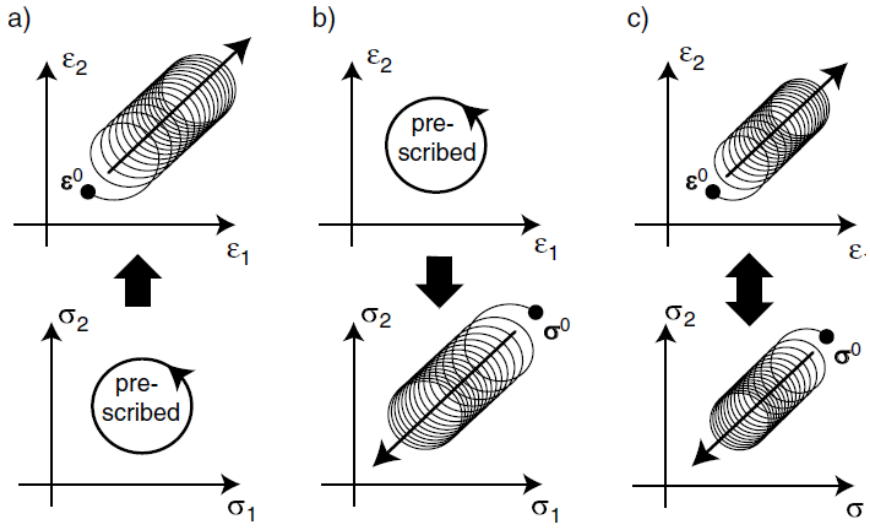

Figure 1.30: Accumulation of stress or strain illustrated for the two-dimensional case; (a) strain accumulation due to stress cycles applied; (b) stress accumulation due to strain cycles applied; (c) mixed control tests, Wichtmann [2005]

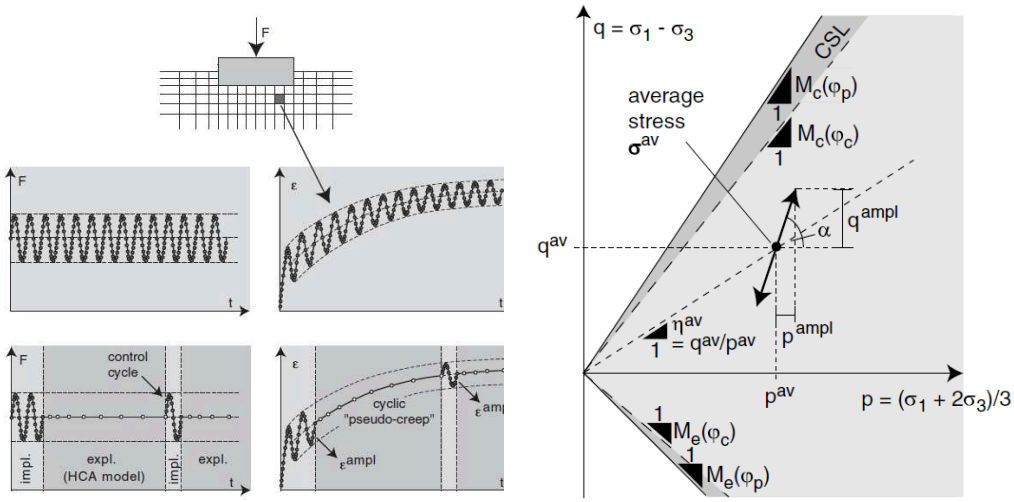

(a) (b)

Figure 1.31: (a) Basic idea of explicit calculation strategies of the cumulative deformation; (b) State of stress in cyclic triaxial test , Wichtmann [2005] and Wichtmann et al. [2005]

Wichtmann [2005], Wichtmann et al. [2005] and Wichtmann et al. [2010] performed several series of drained tests with triaxial compression and uniaxial stress cycles with large number of cycles ($10^3 - 10^6$) and relative small amplitudes. Figure 1.31 illustrates the state of stress in cyclic triaxial test in which;

- The effective Cauchy stress σ_n (positive for compression) are used according to Roscoe invariants p (mean pressure) and q (deviatoric stress) as:

$$p = (\sigma_1 + 2\sigma_3)/3 \tag{1.9}$$

$$q = (\sigma_1 - \sigma_3)/ \tag{1.10}$$

- The strain in axial direction is denoted with ε_1 and the one in radial direction $\varepsilon_2 = \varepsilon_3$. The strain invariants can therefore be expressed as:

$$\varepsilon_v = \varepsilon_1 + 2\varepsilon_3 \tag{1.11}$$

$$\varepsilon_q = 2/3(\varepsilon_1 - 2\varepsilon_3) \tag{1.12}$$

- The critical friction angle is denoted by φ_c and the other one at peak as φ_p.

- The critical state lines in compression and extension tests are denoted by M_c and M_e as:

$$M_c = \frac{6\sin(\varphi_c)}{3-\sin(\varphi_c)} \quad and \quad M_e = \frac{6\sin(\varphi_e)}{3-\sin(\varphi_e)} \tag{1.13}$$

- The average mean stress p^{av} was kept constant and the axial stress component σ_1 was cyclically varied with amplitude σ_1^{ampl}. The normalized size of the stress amplitude can be described as the ratio of:

$$\xi = \frac{\sigma_1^{ampl}}{p^{av}} \; = \; \frac{q^{ampl}}{p^{av}} \tag{1.14}$$

- The strain accumulation and the direction of strain accumulation (cyclic flow rule) are denoted respectively as:

$$\varepsilon^{acc} = \|\varepsilon^{acc}\| \; = \; \sqrt{(\varepsilon_1^{acc})^2 + 2(\varepsilon_3^{acc})^2} \tag{1.15}$$

$$\omega = \varepsilon_v^{acc}/\varepsilon_q^{acc} \tag{1.16}$$

where ε_v^{acc} and ε_q^{acc} are the cumulative volumetric and deviatoric strain components respectively.

In attempt to understand the high-cycle accumulation deformation, principal remarks drawn from this work are the following:

1.6.1 Influence of the strain amplitude

The effect of the strain amplitude ε^{ampl} on the accumulation rate showed that number of cycles caused a decrease of strain amplitude, ε^{ampl}. This decrease can obviously be observed within the first 100 cycles for larger amplitudes. The accumulated strain increased proportionally with the logarithm of number of cycles. In addition the higher amplitudes of cycles caused larger accumulation rates ε^{acc} (Figure 1.32). At higher values of the strain amplitude ε^{ampl}, the ratio of the cumulative volumetric strain to the cumulative deviatoric strain,$\omega = \varepsilon_v^{acc}/\varepsilon_q^{acc}$, is independent of ε^{ampl}. For small values of strain amplitude, the accumulated volumetric strain and deviatoric strain are small which results in the inaccuracy of ω . This suggests that the direction of accumulation is independent of the amplitude of the deformation (Figure 1.33).

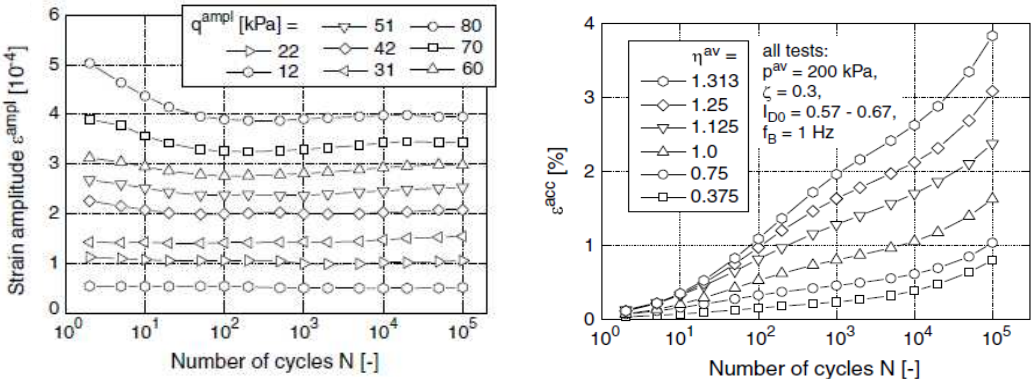

(a) (b)

Figure 1.32: (a) Strain amplitude; (b) Accumulation of strain as a function of number of cycles N , Wichtmann [2005]

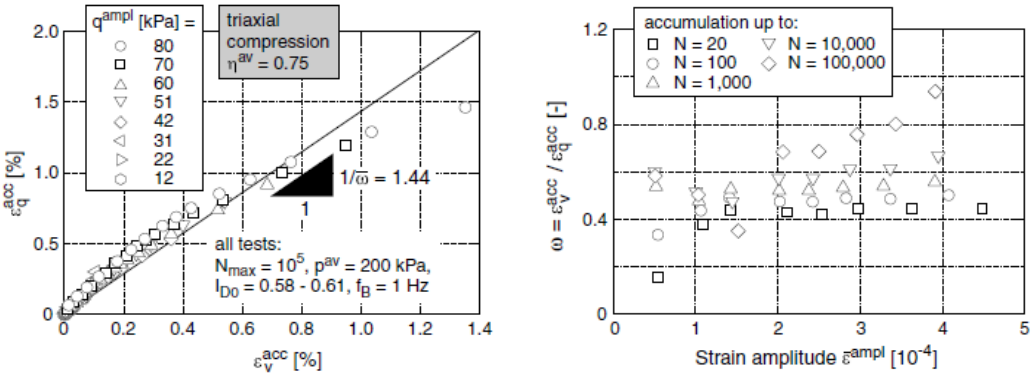

(a) (b)

Figure 1.33: Direction of strain accumulation in tests with different amplitudes of cycles, $\varepsilon_v > 0$ (contraction); (a) ε_q^{acc} - ε_p^{acc} strain paths; (b) ratio $\omega = \varepsilon_v^{acc}/\varepsilon_q^{acc}$ as a function of strain amplitude ampl, Wichtmann [2005]

1.6.2 Influence of initial density, I_{D0}

The behaviour of soils under any loading conditions is strongly influenced by many factors. It is obvious that the initial density is one of the most important factors on strain accumulation. The results obtained from variation of initial void ratio showed that the strain accumulation increased as a function of void ratio. This is due to the decrease in stiffness which can be attributed to an increase in void ratio. The direction of accumulation (ω) was also found to be independent of the void ratio as shown in Figure 1.34

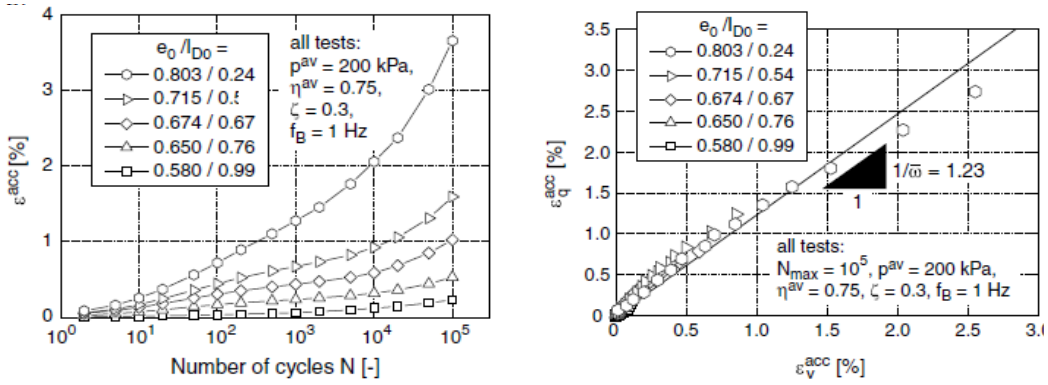

(a) (b)

Figure 1.34: (a) Strain accumulation ε^{acc} as a function of N in tests with different densities, $\varepsilon_v > 0$ (contraction); (b) ε_p^{acc} - ε_q^{acc} strain paths, Wichtmann [2005]

1.6.3 Influence of of loading frequency

Whatever load frequencies in the low range were used, there was no variation on strain accumulation. It can be said that the loading frequency did not influence the strain accumulation as well as the direction of accumulation as shown in Figure 1.35.

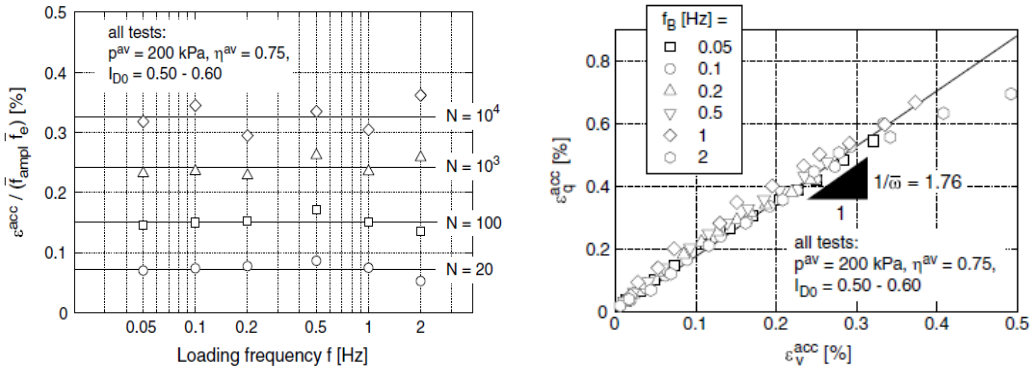

(a) (b)

Figure 1.35: (a) Strain accumulation ε^{acc} as a function of loading frequency, $\varepsilon_v > 0$ (contraction); (b) ε_p^{acc} - ε_q^{acc} strain paths, Wichtmann [2005]

1.6.4 Influence of of the average stress

In case of constant stress ratio (η^{av}) as well as the constant amplitude of stress ratio $\xi = q^{ampl}/p^{av}$ but different mean pressures (p^{av}), the strain amplitude slightly increased as a

function of mean pressures. The strain accumulation (ε^{acc}) significantly increased with decrease in average mean pressure. With low average mean pressures, the dependence on pressure was significant for large number of cycles (N) as shown in Figure 1.36. Considering the direction of strain accumulation, however, effect of mean pressure could not be observed.

Keeping p^{av} constant while varying η^{av}, the strain amplitude (ε^{ampl}) slightly decreased with increasing p^{av} whereas the strain accumulation (ε^{acc}) increased as a function of η^{av} (Figure 1.37). The stress ratio (η^{av}) was obviously found to influence the direction of strain accumulation. The strain ratio (ω) obviously decreased with the variation of (p^{av}), the curve showed that above a critical value of (η^{c}), so called characteristic threshold (η^{car}), the behaviour of the material passed from the contraction to dilation phase. This was in accordance with that performed by Luong [1980]. The characteristic threshold (CT) was proposed by Luong in such a way that stress state below this line leads to contractive phase or that stress state above this line leads to dilative phase (Figure1.38). This line was also shown to be independent of p^{av}, stress amplitude and the density.

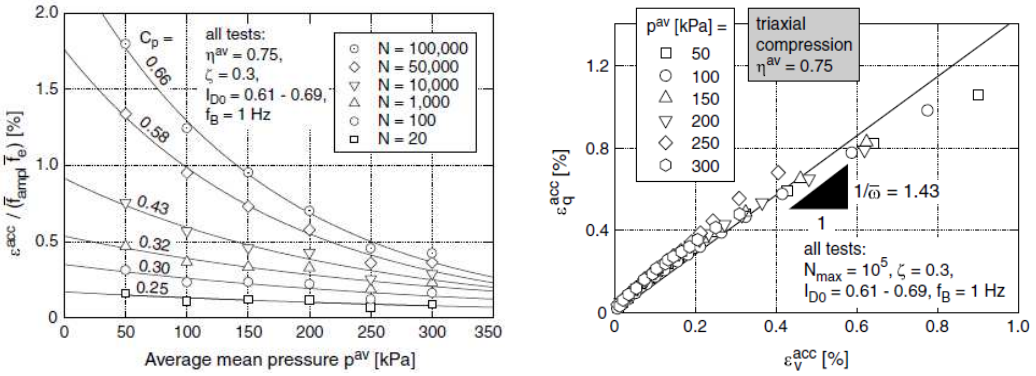

(a) (b)

Figure 1.36: (a) Strain accumulation ε^{acc} as a function of average mean stress p^{av}, $\varepsilon_v > 0$ (contraction); (b) ε_p^{acc} - ε_q^{acc} strain paths, Wichtmann [2005]

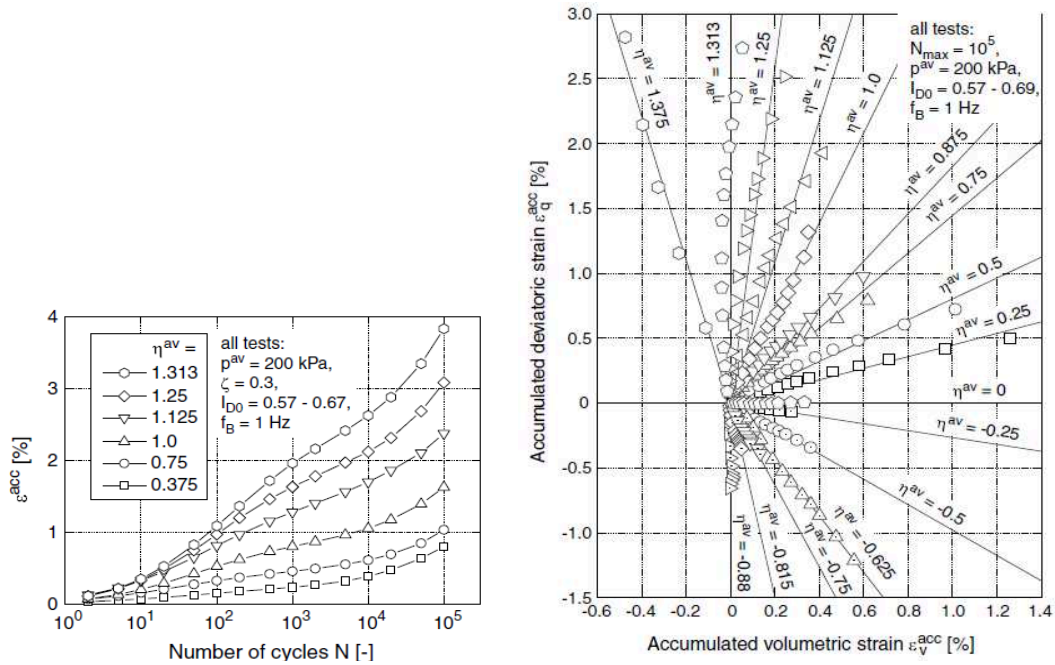

(a) (b)

Figure 1.37: (a) Strain accumulation ε^{acc} as a function of of N in tests with different η^{av}, $\varepsilon_v > 0$ (contraction); (b) ε_p^{acc} - ε_q^{acc} strain paths, Wichtmann [2005]

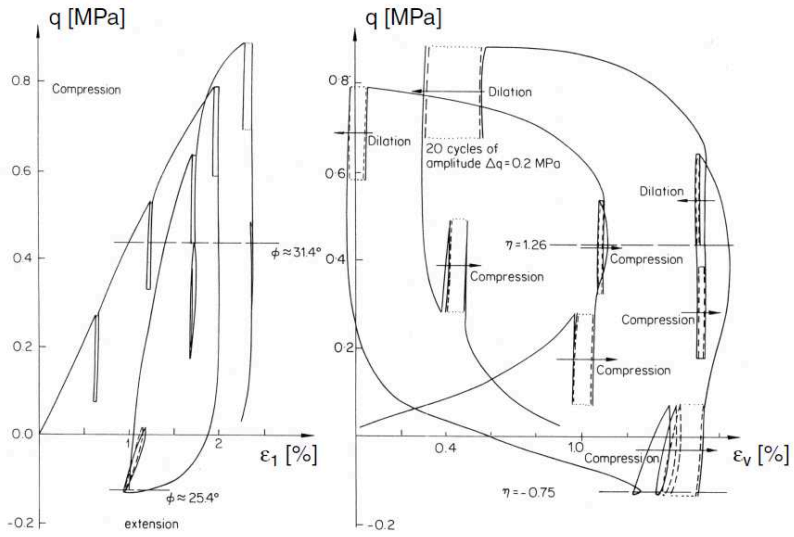

Figure 1.38: Compression and dilation as a result of average stress under cyclic loading, Luong [1980]; Wichtmann [2005]

In case of changing average stress q^{ampl} between consecutive packages of cycles, this can represent a random cyclic loading (variation of cyclic amplitudes). Generally, it is difficult to calculate the strain accumulation due to a random cyclic loading. Then, the packages of cycles containing a constant amplitide are replaced instead (as commonly found in practice, e.g., wind or wave loading acting on off-shore foundation, etc.). In the experimenal observation carried out by Wichtmann [2005] and Wichtmann et al. [2010], several series of four consecutive packages, each with 25,000 cycles, were performed. The deviatoric stress amplitudes q^{ampl} = 20, 40, 60 and 80 kPa were tested in different sequences whereas the average stress p^{av} = 200 kPa and stress ratio $\eta^{av} = q^{ampl}/p^{av}$ = 0.75 were kept constant. The total strain accumulation turned out to be independent of the sequence of these packages application. The direction of strain accumulation (ω) was hardly influenced by the consecutive packages as shown in Figure1.39. However, if the significant changes of average stress packages especially q^{ampl} closed to CT line were applied, these would lead to different results. Further investigations are then necessary to overcome this ambiguity (Wichtmann et al. [2010]).

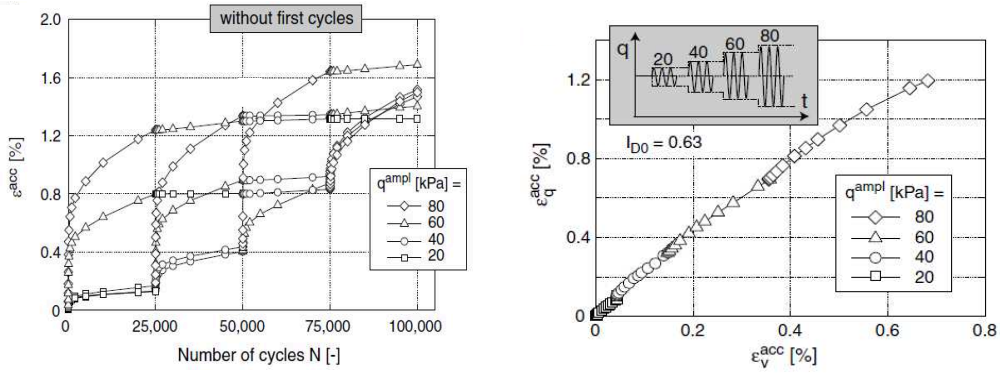

(a) (b)

Figure 1.39: (a) Strain accumulation ε^{acc} as a function of N with changing the consecutive packages of cycles, $\varepsilon_v > 0$ (contraction); (b) ε_p^{acc} - ε_q^{acc} strain paths, Wichtmann [2005]

1.7 Constitutive models

1.7.1 Introduction

From experimental investigations as mentioned in previous section, it has turned out that the interface subjected to whether monotonic or cyclic shearing load experienced a completely changed structure leading to hardening or degradation (softening). Interfaces enable either localized dilation or contraction behaviour to occur (depending on several factors e.g. the initial density, the local stress level and surface roughness). Various types of constitutive law have continuously been proposed to describe the interface behaviour. One of them, the simplest law used to describe the frictional contact between two solids is a rigid perfectly plastic Coulomb condition. However, this law is not appropriate for granular soils because the constraint on contact stress is essentially considered whereas the interface zone is only strained in the tangential direction. Desai et al. [1985] and Desai & Nagaraj [1988] proposed the law taking interface zone as a thin continuum into account. However, this law may cause some problems in which the thickness of the interface should be specified. Even though the interface thickness is commonly related to the grain size of soils, it would still be ambiguous to specify the exact thickness of interface; moreover, the interface thickness is significantly small in comparison with the size of the boundary.

Boulon [1989] then proposed the law in which the interface zone is considered as a two dimensional continuum. This law does not require the constitutive parameter of interface thickness because it is directly embodied in the constitutive equation chosen to model the behavior of interface. It can be said that the interface is considered as a zone of zero thickness. Subsequently, Boulon & Nova [1990] compared an incremental model with an elastoplastic model based on general model initially proposed for sand, Nova & Wood [1979], and successfully conformed to interfaces by changing stress and strain variables.

Appropriate and accurate constitutive models have so far been developed for characterizing the mechanical response of interfaces which are of importance for reliable solution of the associated boundary problems. The constitutive laws governing the mechanical interfaces include various phenomena which can be classified according to Coulomb friction, finite friction, interface elastoplasticity, strain softening and hardening interface, and time dependent in terms of viscoplasticity and creep.

The objective of this section is to describe the concepts of constitutive laws and how they may be formulated for the use in interface analysis. This section begins by considering the variety of constitutive models that have been, and still are, used to represent interface behavior. The remainder of the section is then devoted to the extended formulations based on, respectively, the elastoplastic and viscoplastic theories.

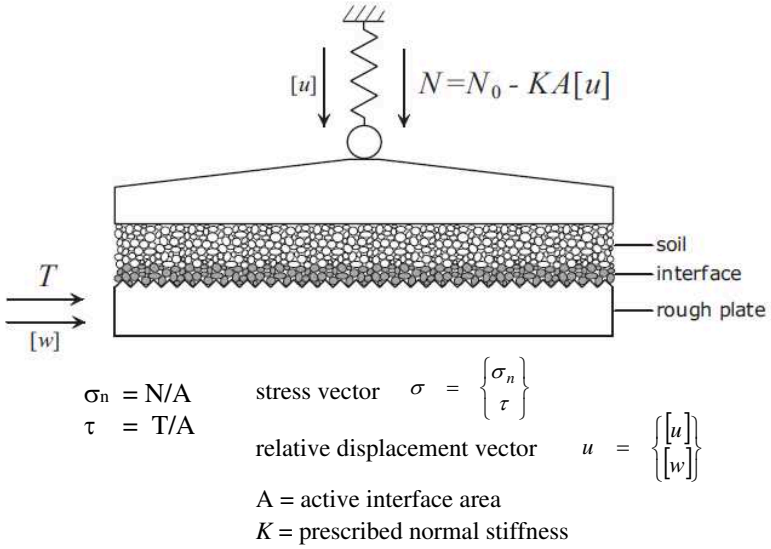

Figure 1.40: Basic variable involved in an interface test, Mortara et al. [2002]

1.7.2 Interface constitutive models

Considering general approach of interface constitutive models in 2-D case, the basic state variables taken into account are then vector variables:

$$\sigma_n = \frac{N}{A} \ , \ \tau = \frac{T}{A} \tag{1.17}$$

where N and T are respectively the normal and tangential forces acting on the interface with an area A. The kinematic state variables are the normal, $[u]$, and tangential, $[w]$, relative displacements. The normal stress is considered as positive in compression and dilatancy (increase in volume) is considered as positive (Figure 1.40).

Referring to Boulon & Nova [1990] and Boulon et al. [1995], these vectors variables can be expressed as follows:

$$\underline{t} = \{\tau \quad \sigma_n\}^T \tag{1.18}$$

$$[\underline{u}] = \{[w] \quad [u]\}^T \tag{1.19}$$

The time derivatives of these state variables are then expressed:

$$\dot{\underline{t}} = \{\dot{\tau} \quad \dot{\sigma_n}\}^T \tag{1.20}$$

$$[\dot{\underline{u}}] = \{[\dot{w}] \quad [\dot{u}]\}^T \tag{1.21}$$

For any possible state of tangent loading path and the relative displacement being supposed to be small, the constitutive equation is then given by the following relation:

$$\dot{\underline{t}} = \underline{\underline{d}}\,(\texttt{loading state})\,[\dot{\underline{u}}] \tag{1.22}$$

The matrix $\underline{\underline{d}}$ containing the stiffness of interface is expressed by:

$$\underline{\underline{d}} = \begin{bmatrix} k_s & k_{sn} \\ k_{ns} & k_n \end{bmatrix} \tag{1.23}$$

The diagonal components k_s and k_n are respectively the "internal" shear and normal stiffness. The off diagonal components k_{sn} and k_{ns} express the coupling between shear and normal phenomena. This coupling is activated by the dilative behaviour occurring on the material with high relative density. However, in case the interface model is considered in terms of uncoupled behaviour of the interface in the normal and tangential directions, the component k_{sn} and k_{ns} are then supposed to be omitted, consequently, the dilative behaviour cannot be described.

In general the basic features of interface constitutive model in terms of incremental or tangent path can be expressed, for instance, as;

- Interface shear test at constant σ_n, (CNL);

prescribed path: $[\dot{w}] = \left[\overline{\dot{w}_0}\right] \;\; ; \;\; \dot{\sigma_n} = 0$

response deduced from the constitutive equation: $[\dot{u}] = -\frac{k_{ns}}{k_n} \cdot \left[\overline{\dot{w}_0}\right]$, $\dot{\tau} = \left[k_s - \frac{k_{sn} \cdot k_{ns}}{k_n}\right][\dot{w}]$

- Interface shear test at constant volume (CV);

prescribed path: $[\dot{w}] = \left[\overline{\dot{w}_0}\right]$, $[\dot{u}] = 0$

response deduced from the constitutive equation: $\dot{\tau} = k_s \cdot \left[\overline{\dot{w}_0}\right]$, $\dot{\sigma_n} = k_{ns} \cdot \left[\overline{\dot{w}_0}\right]$

- Interface shear test at constant normal stiffness k_e, e $\Leftrightarrow$ external, (CNS);

prescribed path: $[\dot{w}] = \left[\overline{\dot{w}_0}\right]$, $\frac{\dot{\sigma_n}}{[\dot{u}]} = k_e$

response deduced from the constitutive equation: $\dot{\tau} = \frac{k_s}{k_e - k_n} \left[\overline{\dot{w}_0}\right]$, $\dot{\tau} = \left[k_{ns} + \frac{k_{sn} \cdot k_{ns}}{k_e - k_n}\right] \cdot \left[\overline{\dot{w}_0}\right]$

In terms of interface modeling approach, it can be deduced that the elastic perfectly plastic law is primarily used to describe the interface mechanism. The constitutive relations and

associated quantities are now briefly reviewed. As the simplicity of this framework, then certain functions such as yield (or loading) function and flow rule have to be specified.

A yield function with a non-associated flow rule is governed by Mohr-Coulomb function:

$$f = \tau - \sigma_n \tan\delta \tag{1.24}$$

$$g = \tau - \sigma_n \tan\psi \tag{1.25}$$

The yield function (f) is defined by the frictional angle between the soil and structure (δ) without considering the cohesion of soils. The plastic potential (g) in which the flow rule is allowed to use the interface dilatancy angle (ψ), can be used to reproduce the volumetric behaviour during interface tests.

The constitutive matrix of interface behaviour can then be described by:

$$\begin{Bmatrix} \dot{\tau} \\ \dot{\sigma_n} \end{Bmatrix} = \frac{1}{k_s + k_n \cdot \Gamma} \begin{bmatrix} k_s^2(1-\alpha) + k_s k_n \Gamma & \alpha k_s k_n \tan\delta \\ \alpha k_s k_n \tan\psi & k_s k_n k_n^2 (1-\alpha) \end{bmatrix} \begin{Bmatrix} [\dot{w}] \\ [\dot{u}] \end{Bmatrix} \tag{1.26}$$

where $\Gamma = \tan\delta \tan\psi$. From this relation, if $\alpha = 0$ then this matrix provides the elastic behaviour, or $\alpha = 1$ the plastic behaviour will occur instead. However, some shortcomings can be found in this simple model. For instance, the first one is the appearance of tension in the case of cohesive materials. The occurrence of tensile stress with the magnitude of a.tanδ can be handled by the set of extra tension cut-off yield surface (Figure 1.41b) or by introducing a new yield surface (Figure 1.41c). By using a curved yield surface ($f = 0$), then a non-linear plastic potential function has to be described. The second one is that the gradual dilation still exists during shearing load. Clearly, from experimental investigations the dilation will vanish corresponding to the critical void ratio as shown in Figure 1.42. The dilatancy cut-off criterion is consequently required to describe realistic feature.

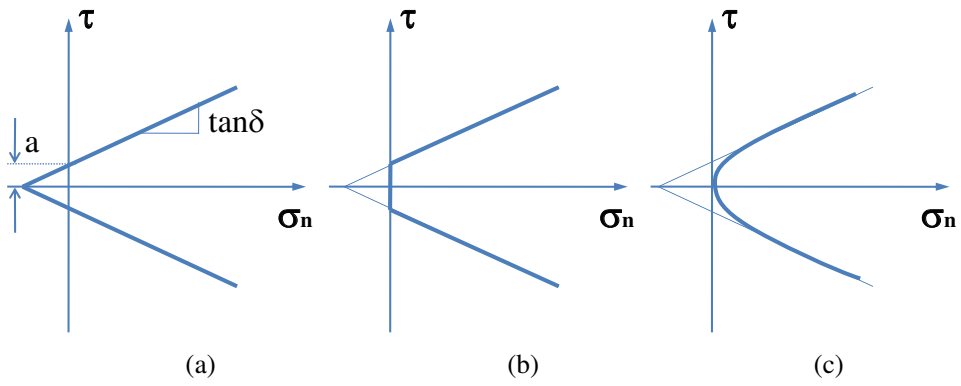

Figure 1.41: Coulomb type yield surface extension , Boulon et al. [1995]

In case of $\psi = 0$, the elastoplastic behaviour of the interface (1.26) comes out irrelevant to $[\dot{w}]$ and the constitutive matrix can then be given as follows:

$$\left\{ \begin{array}{c} \dot{\tau} \\ \dot{\sigma_n} \end{array} \right\} = \frac{1}{k_s} \begin{bmatrix} k_s^2(1-\alpha) & \alpha k_s k_n \tan\delta \\ 0 & k_s k_n \end{bmatrix} \left\{ \begin{array}{c} [\dot{w}] \\ [\dot{u}] \end{array} \right\} = \begin{bmatrix} k_s(1-\alpha) & \alpha k_n \tan\delta \\ 0 & k_n \end{bmatrix} \left\{ \begin{array}{c} [\dot{w}] \\ [\dot{u}] \end{array} \right\} \tag{1.27}$$

However, this linear equation within the concept of perfect plasticity mentioned above may be in lack of some laws describing the reasonable mechanism of interfaces. Consequently, hardening and softening plasticity have to be required in order to provide the full set of interface mechanism.

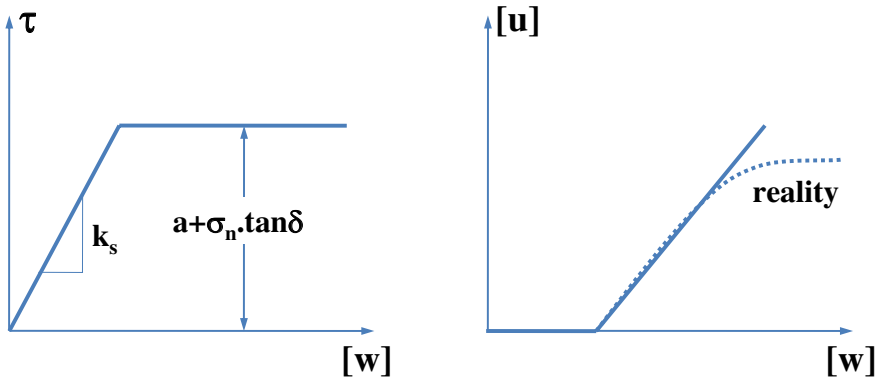

Figure 1.42: Performance of Mohr-Coulomb model in test with constant normal stress, Boulon et al. [1995]

1.7.3 Incremental models (Implicit in the sense of Wichtmann(2005))

As mentioned in the experimental interface section, Boulon [1989] proposed the basic concept for describing a general direct shear paths which can govern the set of possible responses of the interface in case of two-dimensional condition. The basic feature of this constitutive equation is based on the non linear relation between the incremental loadings:

$$[\underline{\dot{u}}]\, dt = \left\{ \begin{array}{c} [\dot{w}] \\ [\dot{u}] \end{array} \right\} dt \tag{1.28}$$

and the corresponding incremental response:

$$\underline{\dot{\sigma}} dt = \left\{ \begin{array}{c} \dot{\tau} \\ \dot{\sigma_n} \end{array} \right\} dt \tag{1.29}$$

where dt is an infinitesimal time step, the set of incremental loadings and responses normalized from the initial state can then be expressed as:

$$\|[\underline{\dot{u}}]\|\, dt = \left([\dot{w}]^2 + [\dot{u}]^2\right)^{1/2} dt \tag{1.30}$$

Supposing (λ ,μ) is an arbitrary space in which the possible incremental loading paths can be described as the points of the unit circle. The corresponding points of the incremental response space (ξ , η) depend on two parameters (λ and μ) connected by one relation (λ^2 + $\mu^2 = 1$). The direction of incremental loading and the corresponding response are then defined as follows:

$$\left\{ \begin{array}{c} \lambda \\ \mu \end{array} \right\} = \frac{1}{\|[\underline{\dot{u}}]\|} \cdot \left\{ \begin{array}{c} [\dot{w}] \\ [\dot{u}] \end{array} \right\} \tag{1.31}$$

$$\left\{ \begin{array}{c} \xi \\ \eta \end{array} \right\} = \frac{1}{\|[\underline{\dot{u}}]\|} \cdot \left\{ \begin{array}{c} \dot{\tau} \\ \dot{\sigma} \end{array} \right\} \tag{1.32}$$

The interface material is also supposed to exhibit the continuous incremental behaviour for loading direction. From the initial state, the directional incremental parameters λ and μ enable the set of possible loading and the response to be mapped in the corresponding incremental spaces. Then the approximation of possible incremental responses can be set up by interpolation, just knowing a small number N of basic incremental responses:

$$\left\{ \begin{array}{c} \xi \\ \eta \end{array} \right\} = \sum_{i=1}^{N} W_i \left\{ \begin{array}{c} \xi_i \\ \eta_i \end{array} \right\} \longrightarrow \left\{ \begin{array}{c} \dot{\tau} \\ \dot{\sigma} \end{array} \right\} = \left\{ \begin{array}{c} \dot{\tau}([\dot{w}]\,, [\dot{u}]\,, \text{initial state}) \\ \dot{\sigma}([\dot{w}]\,, [\dot{u}]\,, \text{initial state}) \end{array} \right\} \tag{1.33}$$

where W_i are interpolation functions (e.g., polynomial, trigonometric).

The incremental paths based on three different conditions (e.g., constant normal load (CNL), constant volume (CV) and constant normal stiffness (CNS)) are then obtained by derivation of analytical expressions in which, for instance, τ and $[u]$ can be represented as a function of $[w]$ (e.g., $\tau([w])$, $[u]([w])$, etc.) in case of CNL tests. Figure1.43 illustrates typical key parameters for describing the basic direct shear tests.

In case of CNL test, considering the phase of $[w] \leq [w]_{CNL+}$ and $[w] \geq [w]_{CNL+}$, as shown in Figure 1.43(a) and (b), where $[w]_{CNL+}$ is the tangential displacement corresponding to the ultimate state $(\tau/\sigma_{n0})_+$, $[w]_p$ and $[u]_p$ are respectively the tangential and normal displacements at peak stress ratio, the parameters can be given as follows:

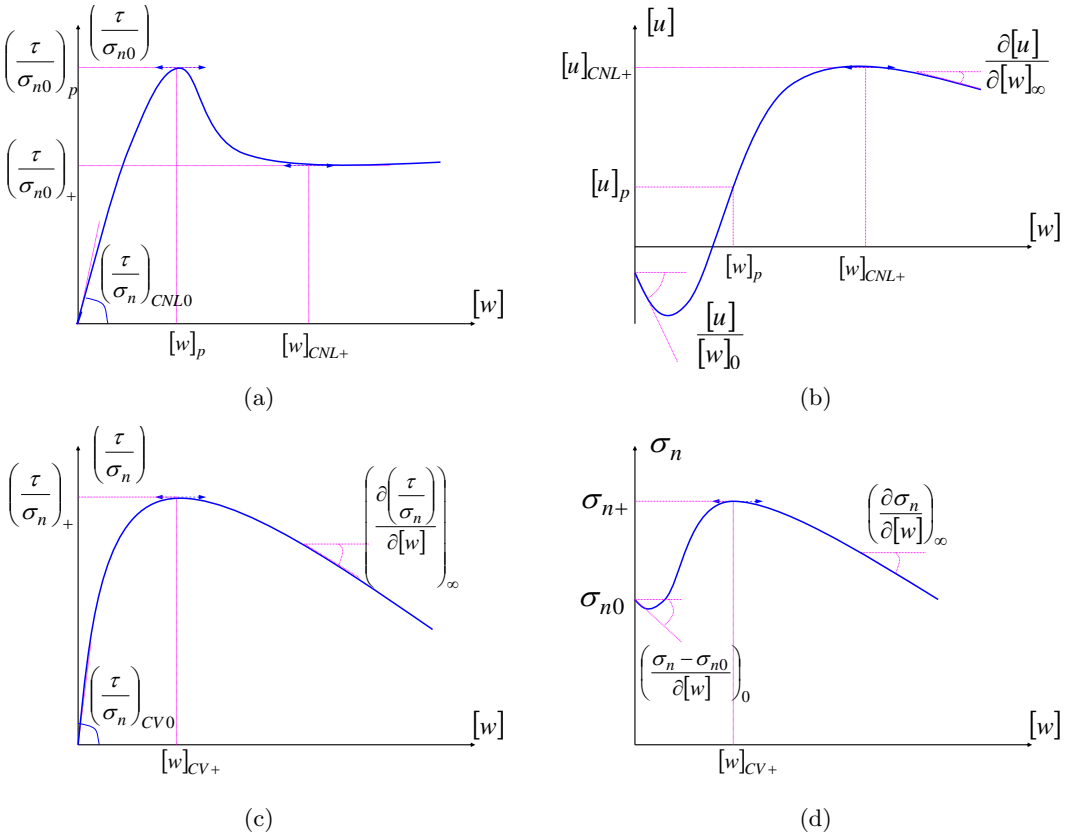

Figure 1.43: Key parameters for description of the basic direct shear tests; (a), (b) constant normal load (CNL); (c), (d) constant volume test (CV), Boulon & Nova [1990]

- phase of $[w] \leq [w]_{CNL+}$

$$\frac{\tau}{\sigma_{n0}} = f_{CNL}\left[\left(\frac{\tau}{\sigma_n}\right)_{CNL0}, [w]_p, \left(\frac{\tau}{\sigma_{n0}}\right)_p, [w]_{CNL+}, \left(\frac{\tau}{\sigma_{n0}}\right)_+\right] \tag{1.34}$$

$$[u] - [u]_0 = g_{CNL}\left[\left(\frac{[u]}{[w]}\right)_0, [w]_p, [u]_p, [w]_{CNL+}, [u]_{CNL+}\right] \tag{1.35}$$

- phase of $[w] > [w]_{CNL+}$

$$\frac{\tau}{\sigma_{n0}} = \left(\frac{\tau}{\sigma_n}\right)_+ \tag{1.36}$$

$$[u] - [u]_+ = \left(\frac{\partial [u]}{\partial [w]}\right)_\infty \cdot ([w] - [w]_{CNL+}) \tag{1.37}$$

Similarly, in the case of CV or CNS (Figure 1.43(c) and (d)) in which the normal stress varies during shearing load, where $[w]_{CV+}$ is tangential displacement corresponding to the

peak state $(\tau/\sigma_{n0})_+$, the parameters can also be given as follows:

- phase of $[w] \leq [w]_{CV+}$

$$\frac{\tau}{\sigma_{n0}} = f_{CV}\left[\left(\frac{\tau}{\sigma_n}\right)_{CV0}, [w]_{CV+}, \left(\frac{\tau}{\sigma_n}\right)_{+}\right] \tag{1.38}$$

$$\sigma_n - \sigma_{n0} = g_{CV}\left[\left(\frac{\sigma_n - \sigma_{n0}}{[w]}\right)_0, [w]_{CV+}, \sigma_{n+}\right] \tag{1.39}$$

- phase of $[w] > [w]_{CV+}$

$$\frac{\tau}{\sigma} - \left(\frac{\tau}{\sigma_n}\right)_{+} = \left(\frac{\partial\left(\frac{\tau}{\sigma_n}\right)}{\partial[w]}\right)_{\infty} \cdot ([w] - [w]_{CV+}) \tag{1.40}$$

$$\sigma_n - \sigma_{n+} = \left(\frac{\partial \sigma_n}{\partial[w]}\right)_{\infty} \cdot ([w] - [w]_{CV+}) \tag{1.41}$$

It can be noted that for defining the entire set of incremental responses, unloading incremental paths are then assumed to have the initial slopes ($[w] = 0$) of the corresponding loading incremental paths. In the final manner, the constitutive equation can formally be written via Euler's theorem for homogeneous functions:

$$\left\{ \begin{array}{c} \dot{\tau} \\ \dot{\sigma_n} \end{array} \right\} = \begin{bmatrix} \frac{\partial \dot{\tau}}{\partial[\dot{w}]} & \frac{\partial \dot{\tau}}{\partial[\dot{u}]} \\ \frac{\partial \dot{\sigma_n}}{\partial[\dot{w}]} & \frac{\partial \dot{\sigma_n}}{\partial[\dot{u}]} \end{bmatrix} \left\{ \begin{array}{c} [\dot{w}] \\ [\dot{u}] \end{array} \right\} \tag{1.42}$$

1.7.4 Elastoplastic models (Implicit in the sense of Wichtmann(2005))

The majority of interface models have so far been devoted to elastoplastic framework incorporating whether hardening or softening law. These models are based on classical soil mechanics and are able to reproduce the prominent behaviour of interfaces. The plastic function of the model is now taken to be a generalization of yield function as a hardening parameter (Aubry et al. [1990] ; Mortara [2001] ; Gennaro & Frank [2002] ; Mortara et al. [2002] ; Shahrour & Rezaie [1997] ; Boulon et al. [2003] ; D'Aguiar et al. [2008] ; D'Aguiar et al. [2011]).

Following Mortara [2001] , Mortara et al. [2002] , Boulon et al. [2003], the normalized displacement $[w_n]$ is defined in incremental form as;

$$[w_n] = \int_t [\dot{w}_n]\, dt \tag{1.43}$$

where $[\dot{w}_n]$ is the ratio between the plastic tangential displacement rate $[\dot{w}^p]$ and the plastic tangential displacement at failure $[w_p]$ corresponding to the peak value of the stress ratio η_p .

$$[\dot{w}_n] = \frac{[\dot{w}^p]}{[w_p]} \tag{1.44}$$

From the definition of normalized displacement, the locus of the stresses at failure corresponds to the plastic function for $[w_n] = 1$. The plastic functions of the model are then given as:

$$f = \sqrt{\tau^2} - \alpha\sigma_n = 0 \tag{1.45}$$

where α is a hardening-softening function which defines the rule of expansion and contraction of the plastic function. Function α then represents the slope of the stress envelopes for the value of $[w_n] = 1$ (Figure 1.44).

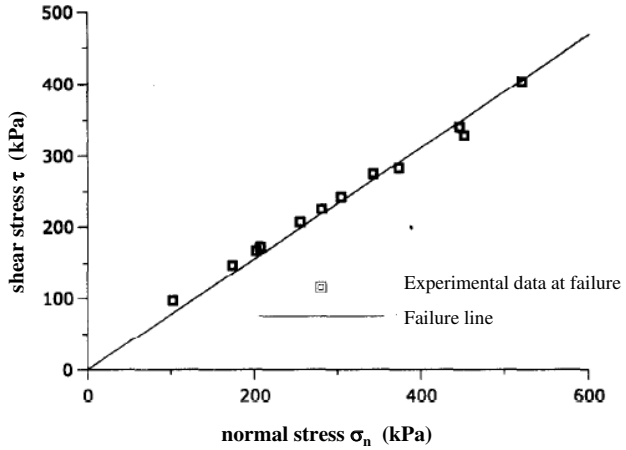

Figure 1.44: Exprimental data at failure and plastic function for $[w_n] = 1$, interface test on Toyoura (silica) sand ($D_r = 85\%$) with roughness $R_{max} = 60$ μm, Mortara et al. [2002] , Boulon et al. [2003]

Figure 1.45 also shows the α functions in dependence on $[w_n]$ utilized to interpolate α_{exp} values. The function $\alpha([w_n]$ is given by the following equation:

$$\alpha\left([w_n]\right) = \alpha_c \left[(\omega[w_n] + 1)^{\psi} - 2\right] exp\left\{-L[w_n]^M\right\} + \alpha_c \tag{1.46}$$

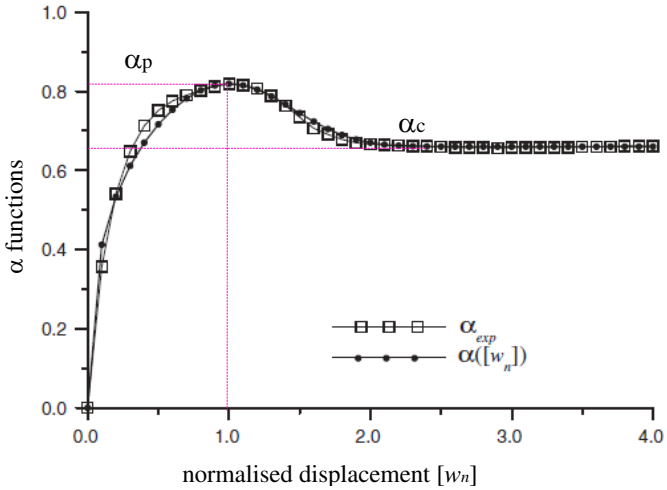

Figure 1.45: Exprimental and model a values, interface test on Toyoura (silica) sand ($D_r = 85\%$) with roughness $R_{max} = 60$ μm, Mortara et al. [2002] , Boulon et al. [2003]

where α_c is the asymptotic value of the function $\alpha([w_n])$, ω and ψ are curve fitting parameters. By defining the conditions in $\alpha([w_n])$ as:

$$\alpha|_{[w_n]=1} = \alpha_p \quad , \quad \frac{d\alpha}{d[w_n]}|_{[w_n]=1} = 0 \tag{1.47}$$

where α_p is the peak value of $\alpha([w_n])$ function as shown in Figure1.45. For L and M, these can now be generated:

$$L = \ln\left\{\frac{\alpha_c}{\alpha_p - \alpha_c}\left[(\omega+1)^{\psi} - 2\right]\right\} \tag{1.48}$$

$$M = \left(\frac{\alpha_c}{\alpha_p - \alpha_c}\right)\frac{\omega\psi}{L\exp\{L\}}(\omega+1)^{\psi-1} \tag{1.49}$$

According to the classical theory of plasticity, the derivatives of plastic potential g surface provide the relative magnitudes of plastic displacement rates:

$$[\dot{w}^p] = \dot{\lambda}\frac{\partial g}{\partial \tau} \quad , \quad [\dot{u}^p] = \dot{\lambda}\frac{\partial g}{\partial \sigma_n} \tag{1.50}$$

where $[\dot{w}^p]$ and $[\dot{u}^p]$ are respectively the plastic rate of normal and tangential displacements and $\dot{\lambda}$ is a scalar plastic multiplier. Based on the orthogonality of the plastic incremental displacement vector to the plastic potential, it is possible to examine the plastic displacement by considering the variation of dilatancy with stress ratio. The dilatancy (d) can therefore be written as:

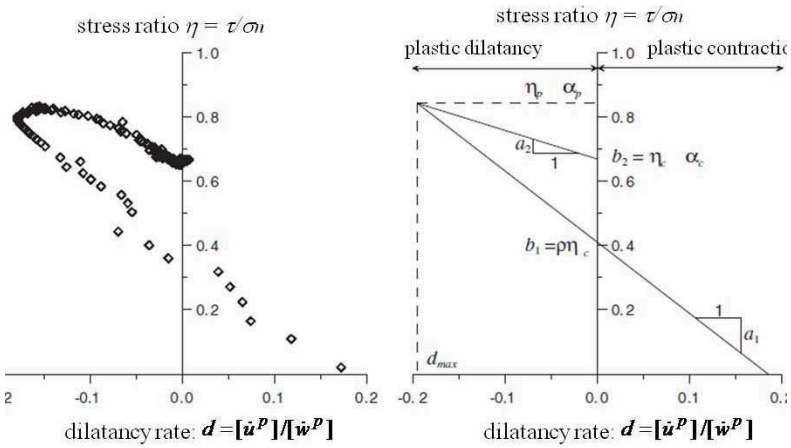

Figure 1.46: Flow rule of an interface test on Toyoura (silica) sand ($D_r = 85\%$) with roughness $R_{max} = 60$ μm, Mortara et al. [2002] , Boulon et al. [2003]

$$d = -\frac{[\dot{u}^p]}{[\dot{w}^p]} \quad , \quad -\frac{d\tau}{d\sigma_n} \tag{1.51}$$

Rewriting this relation in term of η and d gives:

$$\frac{d\sigma_n}{\sigma_n} = \frac{d\eta}{d+\eta} \tag{1.52}$$

Figure 1.46 shows the typical stress-dilatancy relation for an interface test. The flow rule observed can be considered as a bilinear relation which can be described for hardening and softening conditions, respectively, as:

$$\eta = a_1 d + b_1 \quad \text{for} \quad [w_n] \leq 1 \tag{1.53}$$

$$\eta = a_2 d + b_2 \quad \text{for} \quad [w_n] \geq 1 \tag{1.54}$$

where a_1 , b_1, a_2 and b_2 are respectively the slopes and the interceptions of the pre-peak and post-peak flow rule in the stress-dilatancy plane. The convergence of flow rules at the peak of direct shear test, $[w_n]$ =1, is then given as:

$$\eta_p \;=\; a_1 d_{\max} + \rho\eta_c \quad = \quad a_2 d_{\max} + \rho\eta_c \tag{1.55}$$

where η_p and η_c are respectively the stress ratio for peak and ultimate conditions, and $d_{\max}$ is the maximum dilatancy. The parameter ρ is the ratio between the stress ratios corresponding to the condition $d = 0$ in hardening and softening conditions. The expression of plastic potential which satisfies the required conditions is:

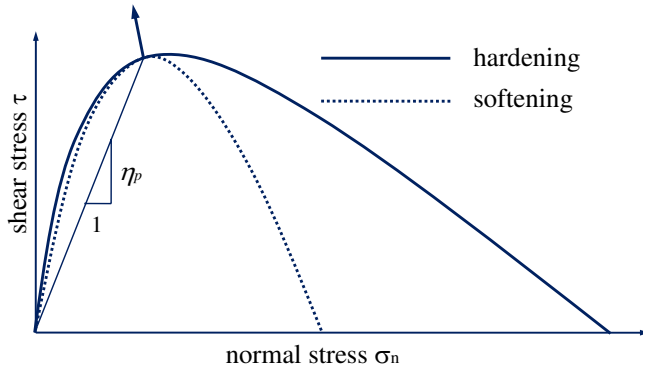

Figure 1.47: Plastic potential for failure conditions; interface test on Toyoura (silica) sand ($D_r = 85\%$) with roughness $R_{max} = 60$ μm, Mortara et al. [2002] , Boulon et al. [2003]

$$g \;=\; \sqrt{\tau^2} - \frac{b}{1+a}\sigma_n \left[1 + a\left(\frac{\sigma_n}{\sigma_c}\right)^{-(1+a)/a}\right] \;=\; 0 \tag{1.56}$$

where a and b are the generic slope and the interception of the flow rule in the $\eta - d$ diagram and σ_c is the normal stress corresponding to $d = 0$. This plastic potential is similar to that of Nova & Wood [1979] and is shown in Figure 1.47 for failure conditions.

In elastic domain, the shear stiffness is proportional to the normal stiffness with a constant, C_K:

$$k_s^e \;=\; C_K k_n^e \tag{1.57}$$

It can be noted that the elastic constant does not influence the response provided the modeling is satisfactory by having an accurate order of magnitude.

For monotonic interface shear test, the simple elastoplastic or incremental models can be used to simulate the interface mechanism with sufficient accuracy. However, for more complex loading programs involving cyclic loading, more complex rules should be examined in order to describe more realistically the effects occurring for these loading conditions. The applicability of the model can be extended by formulating a cyclic surface (f_0) subjected to kinematic rotational hardening inside the isotropic plastic surface (absolute limit surface, f). Cyclic surface which separates domains of active loading and elastic unloading is described by

$$f_0 \;=\; \sqrt{\overline{\tau}^2} - \alpha_0 \overline{\sigma}_n \;=\; 0 \tag{1.58}$$

Where $\overline{\tau}$ and $\overline{\sigma}_n$ are the stresses in a reference system with the surface (1.58) rotated by an angle θ with respect to axis $\tau = 0$, Figure 1.48;

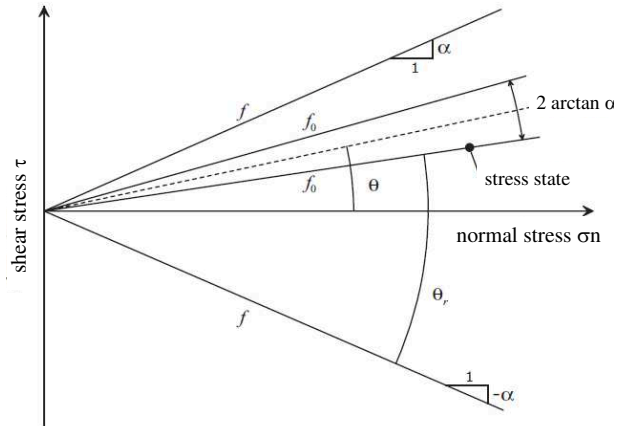

Figure 1.48: Isotropic and kinematic surfaces of the model, Mortara et al. [2002] , Boulon et al. [2003]

$$\overline{\sigma}_n = \sigma_n \cos\theta + \tau \sin\theta \tag{1.59}$$

$$\overline{\tau} = -\sigma_n \sin\theta + \tau \cos\theta \tag{1.60}$$

where α_0 is hardening-softening function cyclic mechanism which specifies the cyclic mechanism, and is supposed to be a constant proportion of the maximum amplitude of the isotropic surface:

$$\arctan\alpha_0 = C_\alpha \arctan\alpha_p \tag{1.61}$$

where C_α is a parameter of the model which has to be interpreted numerically. The angular distance θ_r between the isotropic plastic surface (f) and cyclic surface (f_0) as shown in Figure 1.48 is given by:

$$\theta_r = \arctan\alpha - \mathrm{sgn}\left(\frac{\partial f_0}{\partial \tau}\right) \arctan\frac{\tau}{\sigma_n} \tag{1.62}$$

The hardening modulus for plastic state within the isotropic plastic surface is given by an interpolation function:

$$H = H_\alpha + h\frac{\theta_r}{\theta_{r0} - \theta_r} \tag{1.63}$$

where H_α is the hardening modulus relative to the isotropic mechanism and the angle θ_{r0} is the value of θ_r corresponding to the reversal loading. Function h which describes the dependency of hardening modulus on shear stress mobilization and of irreversible normal displacement and relative position of two surfaces is given by:

$$h = \frac{\alpha_p \sigma_n}{[w_p]} \gamma [w_n]^\delta R_{\alpha\theta}^{n\theta_{r0}} \left(1 + \chi_h \frac{[u^p_{\max}]}{s_0}\right) \tag{1.64}$$

where γ , δ , n and χ_h are parameters of the model while s_0 is an arbitrary reference displacement. The quantity $R_{\alpha\theta}$ is given by:

$$R_{\alpha\theta} = \frac{2(\arctan\alpha - \arctan\alpha_0)}{\theta_{r0}} \tag{1.65}$$

With the condition $R_{\alpha\theta} \neq 1$, this means that the reloading proceeds without reaching isotropic plastic surface (f).

To indicate how the above concepts of cyclic interface behaviour work, Figure 1.49 can clearly illustrate the typical paths of cyclic CNL test in $\tau - \sigma_n$ and $\tau - [w]$ planes. Initially, the two domains move solidly on first loading along path AB and the interface response is governed by the external surface. Once the first reverse loading occurs, the behaviour is elastic on initial unloading (AB) and is sufficient to invoke the cyclic surface. Along BC the interface behaves elastoplastically and the hardening modulus is governed by the equation in (1.63). The next reverse of shear loading at C produces an elastic response. With further loading the interface behaviour is still defined by the cyclic domain until the stress state reaches E which coincides with A on the isotropic domain. Further loading EF will eventually invoke the isotropic domain.

The interface subjected to cyclic loading usually exhibits a progressive densification which leads to an important role in determining the cyclic degradation of shear resistance under CNS tests. For increasing number of cycles, the cyclic flow rule undergoes a progressive variation that can be schematized as a parallel translation in comparison with that of static condition. The following form of $\eta = a_1 d + b_1$ is then proposed for cyclic condition:

$$\eta = ad + b + \Delta b \quad = \quad ad + b + \chi_b \frac{[u^p_{\max}]}{s_0} \tag{1.66}$$

where χ_b is a parameter of the model. However, the direction of incremental displacement which is executed from isotropic potential (Pastor et al. [1985]) has to be defined when a loading reversal takes place. During cyclic loading the following definition is given as:

$$\varphi = \operatorname{sgn}\left(\frac{\partial f_0}{\partial \tau}\frac{\partial g}{\partial \tau}\right) \;=\; \left\{ \begin{array}{c} 1 \text{ for Loading (L)} \\ -1 \text{ for Unloading(U)} \end{array} \right\} \tag{1.67}$$

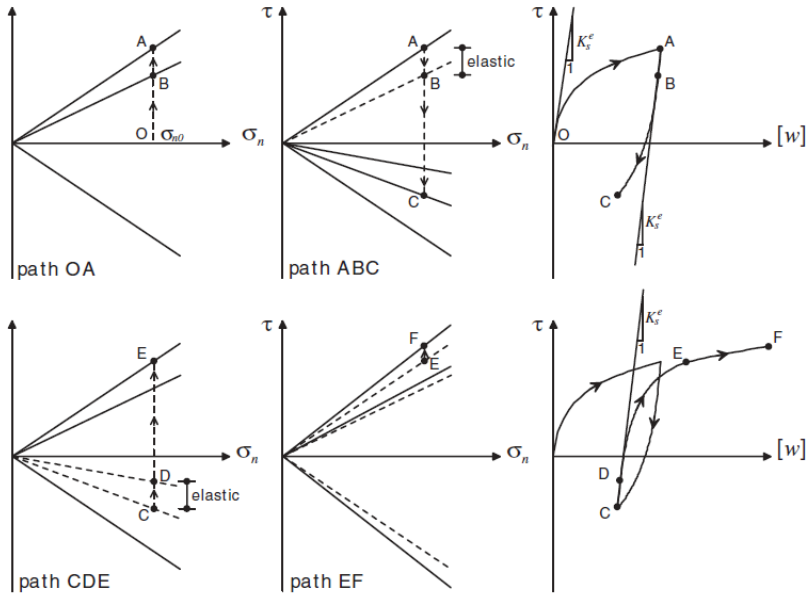

Figure 1.49: Behaviour of the cyclic model under CNL condition , Mortara et al. [2002]

which can govern whether hardening or softening conditions. With gradients of plastic potential and plastic functions:

$$n = \begin{bmatrix} \frac{\partial f}{\partial \sigma_n} \\ \frac{\partial f}{\partial \tau} \end{bmatrix} , \; n_0 = \begin{bmatrix} \frac{\partial f_0}{\partial \sigma_n} \\ \frac{\partial f_0}{\partial \tau} \end{bmatrix} , \; v_L = \begin{bmatrix} \frac{\partial g}{\partial \sigma_n} \\ \frac{\partial g}{\partial \tau} \end{bmatrix} , \; v_U = \begin{bmatrix} \left| \frac{\partial g}{\partial \sigma_n} \right| \\ -\frac{\partial g}{\partial \tau} \end{bmatrix} , \tag{1.68}$$

the elastoplastic matrices of the isotropic plastic surface (D) and cyclic surface (D_0) are then given by the following relations:

$$D = D^e - \frac{D^e v_L n^T D^e}{H_\alpha + n^T D^e v_L} , \; D_0 = D^e - \frac{D^e v_{L/U} n_0^T D^e}{H + n_0^T D^e v_{L/U}} \tag{1.69}$$

where $v_{L/U} = v_L$ for $\varphi = 1$ and $v_{L/U} = v_U$ for $\varphi =$ -1.

1.7.5 Pseudo-creep models (Explicit in the sense of Wichtmann(2005))

Appropriate model describing the interface mechanism is a major object in engineering applications. One of the considerable conditions is the time rate effect in which the conventional theory of plasticity cannot describe the interface mechanism adequately. This time rate effect is closely related to a degradation of properties which can be revealed by creep and relaxation phenomena and by the influence of strain rates. Furthermore, the interface

behaviour can significantly be crucial when time-dependence is taken into account. A further condition in which time rates plays an important role is that when the interface is subjected to dynamic transient loading. For instance, interfaces subjected to cyclic loading, even with small amplitude, may lead to a significant long term plastic displacement. As an experimental observation the yield function of material under high strain rates can be greater than that under the low (quasi-static) value.

However, interface investigations have rarely taken time-dependence into account. In order to define the interface mechanism realistically, the theory of viscoplasticity providing a unified approach to the problem of creep and plasticity has to be proposed. In general, a widely-used viscoplastic formulation is the Perzyna model, Perzyna [1966].

The major concept of this model, so called overstress, is that the yield surface does not have a limit on the possible stress states and then viscous effects related to the stress component can exceed this yield surface. Figure 1.50 describes the definition of the overstress which is defined as the distance in stress space between the current stress state P and the static yield surface f_s. The dynamic loading surface f_d on which the current stress state P is located depends on the stress state and viscoplastic work. The direction of viscoplastic strain rate is perpendicular to the plastic potential surface g. In Perzyna's overstress theory, viscous effects are negligible in elastic domain, e.g. no viscous strains take place within the static yield surface which corresponds to the classical yield surface associated with time-independent plasticity. So far, the characteristics as well as numerical formulations of Perzyna model have been devoted by many authors, e.g. Owen & Hinton [1980]; Flavigny & Nova [1987]; Samtani et al. [1996]; Heeres et al. [2002]; Hicher & Shao [2002]; Liingaard et al. [2004]; Yin [2006]; Stijn et al. [2007]; Yin & Karstunen [2008]; Karstunen et al. [2008].

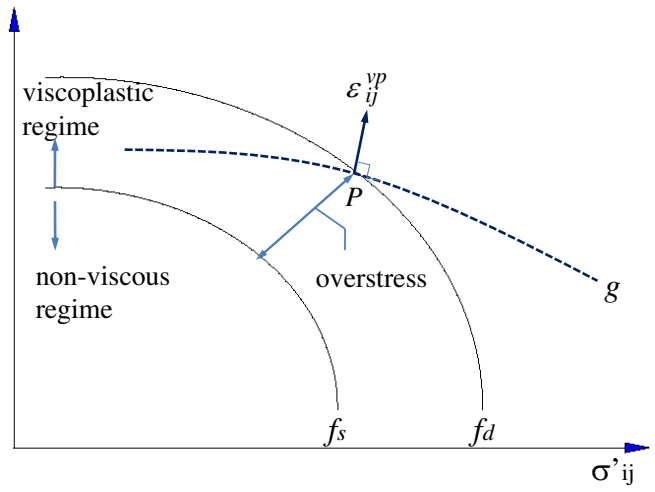

Figure 1.50: Overstress F is defined as the distance between current stress state P on the dynamic yield surface f_d and the static yield surface f_s , Liingaard et al. [2004]

In view of elasto-viscoplastic model of soil-structure interface, the proposed constitutive model requires the simplest possible formulation which can qualitatively reproduce the entire feature of experimental observation. Referring to Samtani et al. [1996] and Armand et al. [1998], the displacement vector can be additively decomposed into elastic and viscoplastic components:

$$s = \left\{ \begin{array}{c} [\dot{u}] \\ [\dot{w}] \end{array} \right\} = \left\{ \begin{array}{c} [\dot{u}^e] \\ [\dot{w}^e] \end{array} \right\} + \left\{ \begin{array}{c} [\dot{u}^{vp}] \\ [\dot{w}^{vp}] \end{array} \right\} \tag{1.70}$$

where the superimposed dot denotes the time derivative. Additionally, if the shear stress and normal responses are taken to be uncoupled, the elastic part of velocity vector is then related to stress rate vector as follows:

$$\left\{ \begin{array}{c} [\dot{u}^e] \\ [\dot{w}^e] \end{array} \right\} = \begin{bmatrix} k_s & 0 \\ 0 & k_n \end{bmatrix} \left\{ \begin{array}{c} \dot{\tau} \\ \dot{\sigma_n} \end{array} \right\} \tag{1.71}$$

where k_s and k_n are the elastic normal and shear stiffness of the interface which are expressed as follows:

$$k_n = \frac{d\sigma_n}{d[u]} \quad , \quad k_s = \frac{d\tau}{d[w]} \tag{1.72}$$

By following Perzyna's original approach, the viscoplastic velocity vector is defined by a viscoplastic flow rule of the formulation:

$$\dot{s}^{vp} = \gamma \Phi \left(F \right) \frac{\partial g}{\partial \sigma} \tag{1.73}$$

In this formulation the viscoplastic potential g gives the direction of $\dot{s}^{vp}$, the viscous nucleus Φ is a scalar function of the yield function F and γ is a material constant which is known as the fluidity parameter with the dimension of inverse time. Adopting anisotropic (for forward and reversal shear loading) Mohr-Coulomb plasticity model, the yield surface F (Figure 1.51), according to Armand et al. [1998] and Papadopoulos et al. [1998], is given as:

$$F_{1,2} = \tau + \left(r \pm k \right) \sigma_n \tag{1.74}$$

with the definition of

$$r = \frac{1}{2} \left(\mu_1 - \mu_2 \right) \tag{1.75}$$

$$k = \frac{1}{2} \left(\mu_1 + \mu_2 \right) \tag{1.76}$$

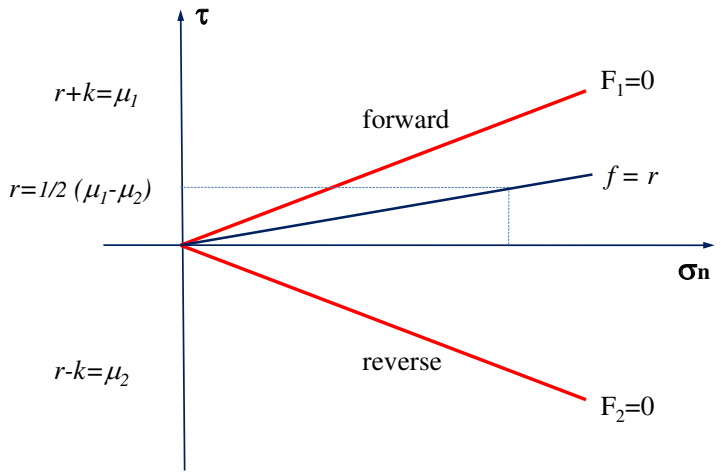

Figure 1.51: Yield surface representation, Armand et al. [1998]

where μ_1 and μ_2 are friction coefficients ($\mu = \tan \delta$) in forward and reversal direction in a parallel manner. The plastic potential in which the dilatancy angle (ψ) is described is then given as:

$$g_{1,2} = \tau + \tan(\psi_{1,2})\,\sigma_n + \text{const} \tag{1.77}$$

The viscous nucleus $\Phi(F)$ describes the evolution of the viscoplastic strain vector. By using the Macauley bracket $\langle\ \rangle$, a simple representation of viscous nucleus is then given as:

$$\Phi(F) = \left\langle \frac{F}{-\sigma_n} \right\rangle = \begin{cases} -F/\sigma & \text{if } F > 0 \\ 0 & \text{if } F \leq 0 \end{cases} \tag{1.78}$$

or it can be rewritten as:

$$\Phi(F) = \begin{cases} f + \mu_{1,2} & \text{if } f_{1,2} \geq 0 \text{ with } f = \frac{F}{-\sigma} \\ 0 & \text{else} \end{cases} \tag{1.79}$$

The definition of viscous nucleus $\Phi(F)$ can implicitly be described that the viscoplastic velocity is not zero even if the current state of stress lies outside the considering yield surface. The material constant introduces the physical time dimension into the problem. Considering for the limit $\gamma \to \infty$, the constitutive model turns out to be plastic and its time dependency then disappears.

Following the element tests on high-cycles accumulation, several studies on the cyclic behaviour of sand concerning a large number of cycles ($N > 10^3$) were carried out in the approach to predict the accumulated deformations (pseudo-creep). In general, there are two main approaches for describing the accumulation due to cyclic loading. The most

conventional one, so-called implicit (elastoplastic) model, is capable of describing the accumulation for $N < 10^2$. For instance, the numerical error which normally occurs in modeling would increase significantly during an application of a large number of cycles. This denotes the importance of the explicit model in which the number of cycles N is treated instead of time.

Niemunis et al. [2005] and Wichtmann et al. [2005] proposed the rate of strain accumulation ($\mathbf{D}^{acc}$) based on the cyclic triaxial tests as:

$$\mathbf{D}^{acc} = \mathbf{m} f_{\text{ampl}} \dot{f}_N f_p f_Y f_e f \pi \tag{1.80}$$

with the following functions which describe the influence on the rate of strain accumulation;

- f_{ampl}: amplitude, shape and polarization of the strain loop, summerized in the scalar $\varepsilon^{\text{ampl}}$
- f_p: average mean stress p^{av}
- f_Y: average stress ratio $\overline{Y}^{av}$
- f_e: average void ratio e
- $\dot{f}_N$: number of cycles N, if $\varepsilon^{\text{ampl}}$ = constant.
- f_π: polarization changes

$\mathbf{m}$ is the unit tensor expressing the direction of accumulation(flow rule) which is only dependent of average stress ratio (η^{av}). Table1.1 shows the definition of these functions except f_π.

Table 1.1: Summary of the partial functions f_i for triaxial tests performed by Niemunis et al. [2005]

Function	Mat. Constants
$f_{\text{ampl}} = \left(\varepsilon^{\text{ampl}}/\varepsilon^{\text{ampl}}_{\text{ref}}\right)^2$	$\varepsilon^{\text{ampl}}_{\text{ref}}$
$\dot{f}_N = \frac{C_{N1}C_{N2}}{1+C_{N2}N} + C_{N1}C_{N3}$	C_{N1}, C_{N2}, C_{N3}
$f_p = \exp\left[C_P\left(\frac{p^{av}}{p_{\text{ref}}} - 1\right)\right]$	C_P, p_{ref}
$f_Y = \exp\left(C_Y \overline{Y}^{av}\right)$	C_Y
$f_e = \frac{(C_e-e)^2}{1+e}\frac{1+e_{\text{ref}}}{(C_e-e_{\text{ref}})^2}$	C_e, e_{ref}
$f_\pi = 1$ if polarization of the strain loop = constant	

Messast et al. [2006] formulated a simple model describing the volumetric strain accumulation (ε^c_{vN}). This formulation is based on the cyclic parameters of the first cycle:

$$\varepsilon_{vN}^{c} = \frac{N}{\frac{1}{\varepsilon_{v1}^{c}} + \frac{N-1}{\varepsilon_{v\infty}^{c}}} \tag{1.81}$$

where ε_{v1}^{c} and $\varepsilon_{v\infty}^{c}$ are the strain accumulation when $N = 1$ and $N \to \infty$, respectively. The volumetric strain accumulation at $N \to \infty$, $\varepsilon_{v\infty}^{c}$, can be expressed as a function of $\Delta\eta$ and η^{av}:

$$\varepsilon_{v\infty}^{c} = \varepsilon_{v0}^{\infty} \frac{\left(\frac{\eta^{av}}{\eta^{car}} - 1\right)}{\left(1 - \frac{\eta^{av}}{\eta^{peak}}\right)} \tag{1.82}$$

As can be seen in Figure 1.52, the function can then be written in the following form:

$$\varepsilon_{v0}^{\infty} = \frac{C_1 \Delta\eta}{\Delta\eta + C_2} \tag{1.83}$$

where C_1 and C_2 are the coefficients depending on η^{av} and the void ratio.

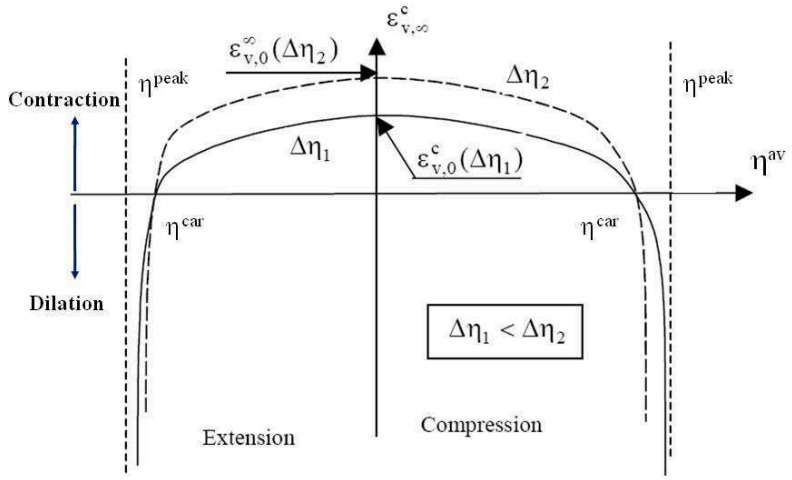

Figure 1.52: Strain accumulation at infinity $\varepsilon_{v\infty}^{c}$ as a function of $\Delta\eta$ and Δ^{av} , Messast et al. [2006]

1.8 Conclusions

The behaviour of interfaces has widely been the subject of experimental studies. The majority of earlier studies dealt with the monotonic behaviour of interfaces. The behaviour of interfaces was found to depend on the soil properties and surface roughness. Subsequently, experimental studies on cyclic behaviour of interfaces were performed to understand the

mechanics of the interaction. From these studies, it is possible to conclude that the cyclic interface behaviour is influenced by the amplitude of tangential displacement, normal stress, density of sample, number of loading cycles, position and amplitude of the cycles within the stress space.

The use of a constant normal stiffness to investigate the behaviour of soil-structure interfaces is based on the observation that soil deformation is concentrated in a thin region close to the structure. In model pile tests, cyclic loading has been found to decrease the frictional resistance of the surrounding soil. This phenomenon has been attributed to a decrease in the normal stress due to cumulative contraction of the soil within the interface shear zone. It can be concluded that the reduction in normal stress associated with shear stress is not only due to the normal stiffness, but also due to the increasing amount of shear displacement at the interface with an increase in number of cycles.

On high cycle accumulation the intensity of strain accumulation depends on several factors, e.g. initial density, initial confining stress (p^{av}), amplitude of average stress (q^{ampl}) and the stress ratio (η^{av}). But the direction of strain accumulation (ω) depends exclusively on the stress ratio (η^{av}).

The concept of such models aiming at reproducing soil-structure interface behaviour is formulated by using the same physical principles as those of soil mechanic models. The interface models which have been described can provide a satisfactory and consistent formulation of interface behaviour. However, the progress in modeling interface behaviour is still required in order to achieve a more realistic overview.

Chapter 2

Interface direct shear tests

2.1 Introduction

The work presented in this chapter focuses on the identification and characterization of granular soil-structure interface behaviour, and more particularly of interface behaviour concerning a large number of cycles (typically 10^4) with small amplitude of cycles in terms of shear stress. The purpose of this section is the presentation of an innovative direct shear device developed at laboratory 3S-R. This device is specifically designed to access the domains of soil-structure interfaces whether under constant normal stress or unit load (CNL) or at constant normal stiffness (CNS) conditions (Hoteit [1990]; Moutraji [1992]).

Therefore, a large part of this chapter is devoted to the illustration of the experimental facilities implemented during this study and the interpretation of the data delivered. Most of interface direct shear tests carried out in this work focus on rough plate under CNL and CNS conditions. For smooth plate, some tests are additionally presented. The results, analyzed and processed, from the various experimental campaigns are presented and summarized in the following sections.

2.2 Interface direct shear devices

The mechanism of interface soil-structural materials was studied in detail by several researchers at 3S-R laboratory at which the tests with constant normal stress (CNL) and constant volume (CV) are carried out by using a modified direct shear test. Hoteit [1990] carried out a complete direct shear test to impose normal stiffness by using two types of sand and two different values of roughness. Moutraji [1992] later performed and modified interface ditrect shear tests on silt-steel by measuring relative displacement and stresses in normal and tangential directions. For interface direct shear box used in this study, the lower half-box is replaced by a plate whose roughness is variable (smooth, rough) according to the tests and the purpose which are to simulate the side surface of the structural materials anchored in the soil. The sample box which is of cylindrical form is placed at a calibrated

distance of the plate. The normal stress (σ_n) is then applied vertically via a piston (top cap), while the tangential stress (τ) is obtained by a horizontal relative movement (tangential displacement [w]) of the plate. Contrary to more traditional tests which are carried out only under both constant normal stress (CNL) and constant volume (CV) conditions, the system of current loading allows the realization of various conditions, in particular the constant normal stiffness (CNS) condition.

The direct shear apparatus used in this study is shown in Figure 2.1. The main aspect of ϕ 60 mm shear box apparatus was modified to enable the normal load to be applied by a generating engine to provide the constant normal stiffness condition. The conditions with constant normal stress (CNL) and constant volume (CV) can be regarded as "extreme" conditions, framing the real paths followed by the interface during the mobilization of side friction along a pile, according to the simplified model suggested by Boulon [1989]. This test, direct shearing with imposed normal stiffness, is carried out by using a control between the variation of normal stress (σ_n) acting on the sample and the normal displacement ([u]) at the top part of sample box.

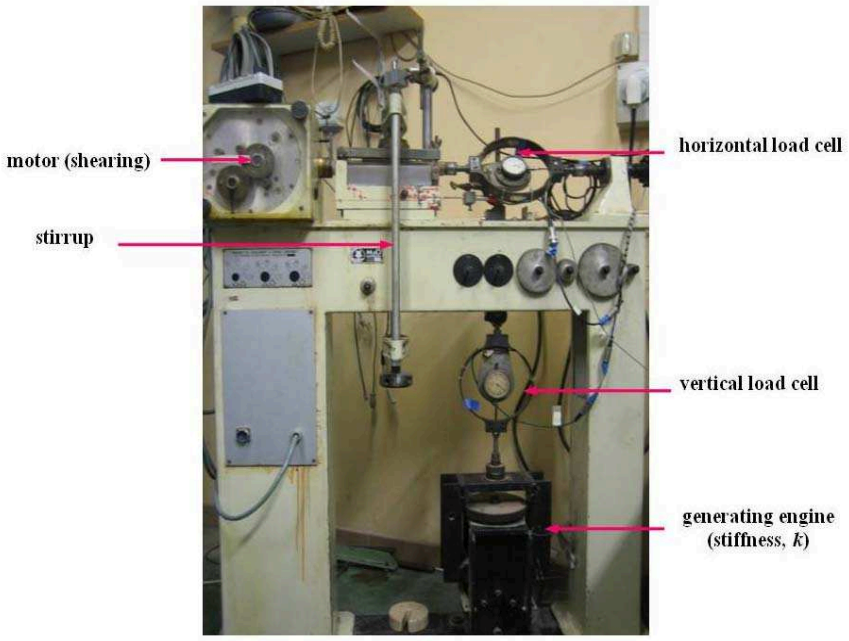

Figure 2.1: Direct shear apparatus used in this research

The generating engine is employed to apply the normal load on the interface. The operation of this generating engine is controlled by a computer to impose a constant normal stress ($k = 0$) or a constant stiffness ($k \neq 0$) conditions. It consists in controlling the variations of the normal stress (σ_n) to normal relative displacement [u] according to the relation:

$$C = \Delta\sigma_n - k\Delta\,[u] \tag{2.1}$$

Indeed, to measure the values of different stress and displacement transducers in real time, one is able to control a physical value measured at an imposed set over time. Therefore, this allows the performance of tests with different stress paths. Possible paths of direct shear according to value of k are:

- Case I. $k = 0$; constant normal stress
- Case II. $k = \infty$; constant volume
- Case III. $k > 0$; constant normal stiffness (k)

Figure 2.2 shows a schematic illustration of the control system. The generation of normal stress is ensured by traditional micro engine in two directions, ensuring loading or unloading of the sample. During shearing, the set (2.1), where k is the imposed normal stiffness, is applied with a precision of 0.1 kPa. This is capable of following the most general path of direct shear tests. Shearing is induced on the sample by tangential displacement of the structural surface which can directly be controlled by the system. Using the shear rate with low range, it is assumed that there is no influence of shear rate on test results. In this study, the compatible maximum $[\dot{w}]$ with a sufficient data acquisition is then used with a shear displacement rate of 0.5 mm/min. In case of cyclic tests under controlled shear stress, two thresholds (high and low, adjustable) of shear stress are prescribed, causing a reversal of shear direction when they are reached. Electrical displacement transducers, monitored by a computer system, are used to measure displacements and the applied loads in calibrated proving rings.

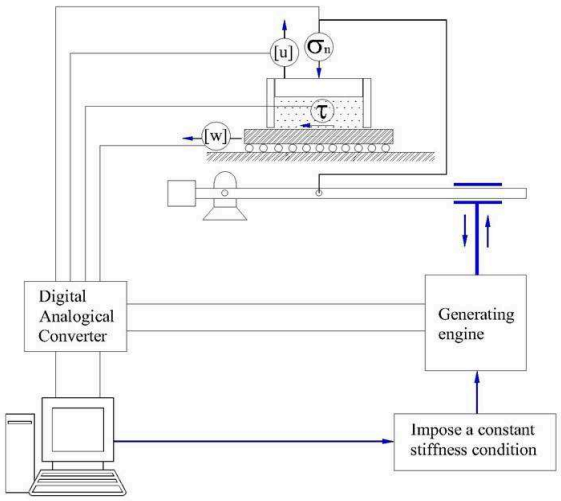

Figure 2.2: Principle of the direct shear test to impose normal stiffness (k), Hoteit [1990]

The calibration of transducers based on displacement transducer (LVDT) and load cells is a procedure which converts an electrical value into a physical quantity. This electrical value varies according to the amount of the physical quantity which is under the measure. For calibrating the load cells, as the load placed upon the load cell, the electrical resistance changed due to the flexion of the cell under loading. The electrical value produced by the load cell was picked up by a digital-analogical converter, and then sent to a computer for displaying and recording. To compute the calibration constants, the relationship between the change of electrical values and loads is obtained from the slope of linear regression line. The calibration of LVDTs (resolution 0.01 mm) can be done on the same way. Figure 2.3 shows typical calibrations of these transducers.

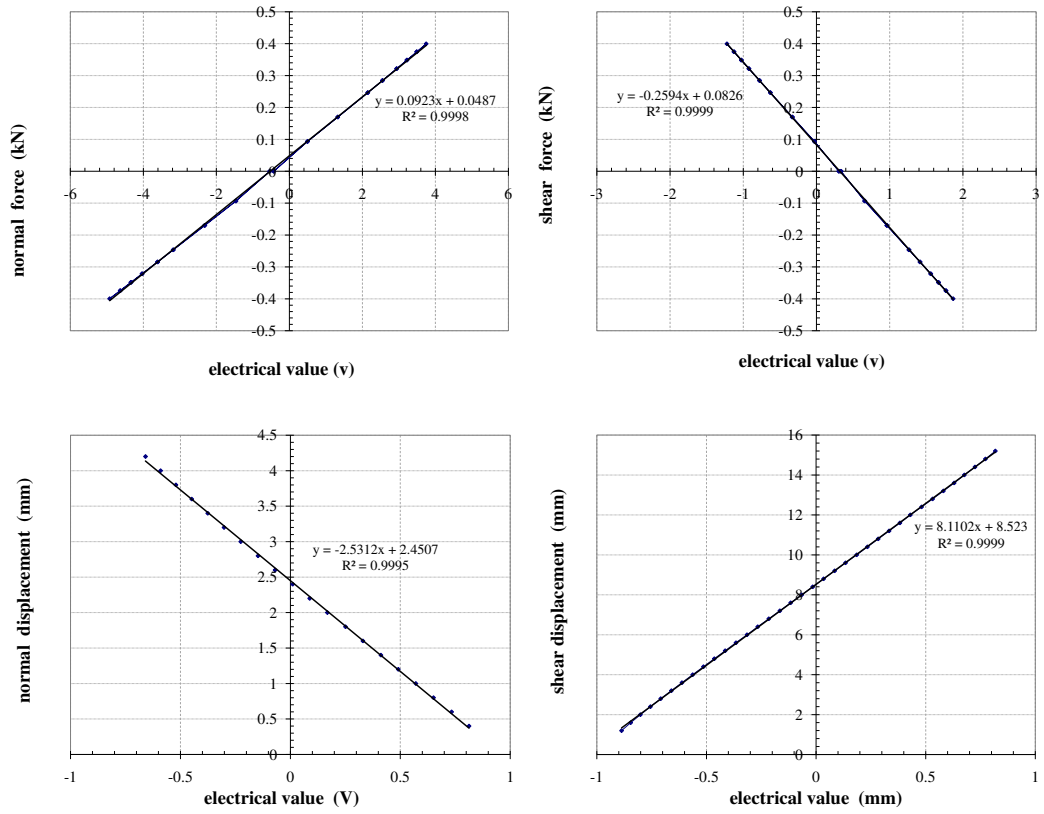

Figure 2.3: Calibration of force and displacement transducers

During interface direct shear tests, the signal of all sensors were recorded every five seconds by means of a data acquisition system. The measured and recorded variables are the stress vector applied to the interface (normal, σ_n (> 0 in compression) and shear, τ components and the displacement vector on soil-structure (components normal $[u] > 0$ dilating) and tangential $[w]$). Table 2.1 shows the relationships of state variables in data acquisition system.

Table 2.1: Relationships of interface variables of direct shear test in data acquisition system

State variable	Relation
τ	$-(\Delta V)0.2594/A$
σ_n	$((\Delta V)0.0923 + c)4.76/A$
[u]	$2.5312(\Delta V)$
[w]	$8.1102(\Delta V) - 0.00272727\tau$
[v]	$-1.9239(\Delta V)$

where ΔV is the change of electical values recorded from the beginning. A is a cross section area of shear box. Taking into account the vertical movement of load cell, the coefficient c is then described as $c = 0.0026$[v]. The vertical movement of shear box, [v], is additionally measured in order to find the solution of leakage of sample which will be discussed later.

However, the LVDTs used for measuring the displacements have the range limits. For instance, the LVDTs for measuring the normal and tangential displacements provide high precision and accuracy in the ranges of ± 2 mm and ± 6.5 mm, respectively. In some cases of cyclic interface shear tests, especially in CNS test series, the horizontal relative movement of the plate would exceed the range of 13 mm but the tangential displacement is still recorded in the range of 13 mm. This provides the partial measurement error of tangential displacement. Installation of these sensors on the apparatus is shown in Figure 2.4.

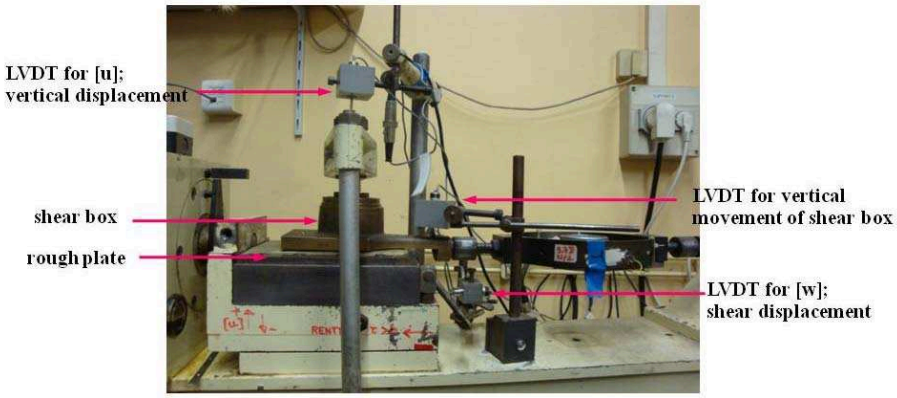

Figure 2.4: Position of three LVDTs on direct shear apparatus

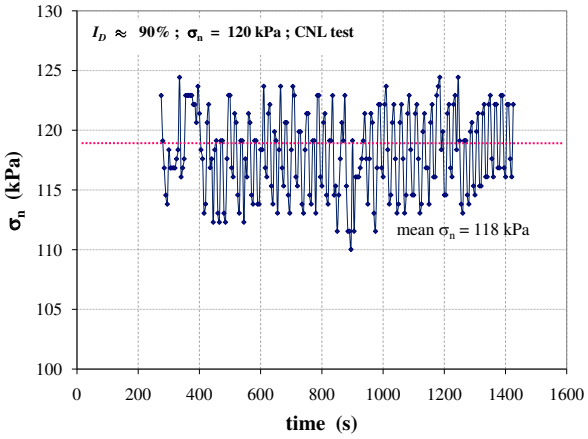

Figure 2.5: Typical normal stress applied to the sample, $\sigma_n = 120$ kPa, $I_{D0} = 90$ % under CNL condition

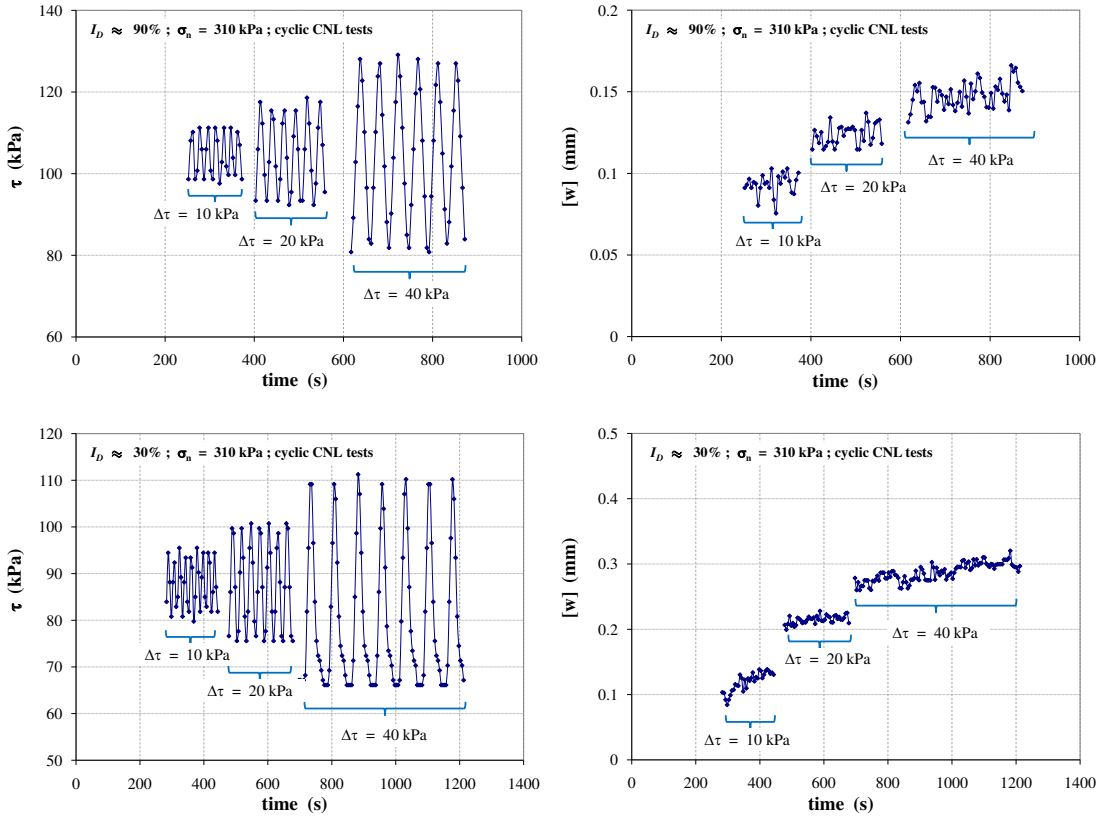

Figure 2.6: Typical shear stress applied to the sample and shear displacement $[w]$ output on cyclic CNL tests, $\sigma_n = 310$ kPa with cyclic amplitude $\Delta\tau$ of 10, 20 and 40 kPa

The typical normal stress applied to the sample during shear loading, in case of CNL condition, from the generating engine is shown in Figure 2.5. Even though this test is under CNL condition, there is still a variation in normal stress (typically in the range of $\Delta\sigma = \pm$ 5 kPa). This small variation of the normal stress is due to the generating engine in two directions. In case of cyclic tests, the cycles are carried out between two shear stress thresholds (shear stress-controlled tests). Even though the cyclic forms are not somehow uniform (Figure2.6), depending on the level of mean cyclic stress ratio (η_{cm}) and density index (I_{D0}), these cyclic tests still provide the reasonable results on the ground that the mean cyclic paths are principally considered.

2.3 Tested materials

2.3.1 Standard Fontainebleau sand

In several laboratories in France, standard Fontainebleau sand is commonly utilized. This sand is siliceous sand. It has a color that ranges between grey and white. The characteristics of standard Fontainebleau sand which was used in this research are shown in Table 2.2. For Fontainebleau sand NE34, SOLCYP* Project provides the values of $e_{\text{min}} = 0.545$ and $e_{\text{max}} = 0.866$, which may be fairly representative and usable in our first approach to define three states (loose ($I_{D0} = 40\%$), medium ($I_{D0} = 65 - 70\%$) and dense ($I_{D0} = 90\%$)). These values correspond to maximum and minimum dry densities of 1.72 g/cm^3 and 1.42 g/cm^3 respectively (the specific gravity of the material G is taken equal to 2.65 g/cm^3, practically pure silica). It is worth noting that these values should then compare to those that have been obtained by using the standard in a rigorous way (proposed by A. Puech and J. Garnier, Fugro Geotechnical laboratory), which we take as the reference. The measurements of e_{min} and e_{max} on the sample of Fontainebleau performed by Fugro Geotechnical Laboratory following the French standard with $G = 2.70$ g/cm^3 are 0.50 and 0.89, respectively. Maximum dry density is close to that found by SOLCYP Project, whereas minimum dry density is farther. However, a good correspondence still exists between these values.

An important element of the characterization of a set of grains is the grading curve. Figure 2.7 shows two curves of particle size distribution obtained by two different methods. A typical curve obtained by sieving method still serves as a reference curve for defining the characteristics of the material. The other method by laser granulometry provides an estimate of the average size of each particle. This method thus shows a shift of the grading curve to the right (larger diameter). The difference between these curves is due to the sieving method taking into account the weight of sand whereas laser granulometry method which takes into account the volume mass of sand provides the average particle size. However, these two methods still provide the parallel curves (the same uniformity). The mean grain size D_{50} is identified to be 0.23 mm for sieving method and 0.25 mm for laser granulometry. With the uniformity coefficient ($C_u = D_{60}/D_{10}$), from sieving method $C_u \leq 4$, this sand can be considered to be poorly graded or uniform.

Table 2.2: Properties of standard Fontainebleau sand according to SOLCYP* Project

D_{50} (mm)	G (g/cm^3)	$\rho_{\text{d max}}$ (g/cm^3)	$\rho_{\text{d min}}$ (g/cm^3)	$e_{\max}$	$e_{\min}$	$C_{\text{u}} = D_{60}/D_{10}$
0.23	2.65	1.72	1.42	0.866	0.545	1.72

* Research on behaviour of piles subjected to cyclic loading Project (French National Program)

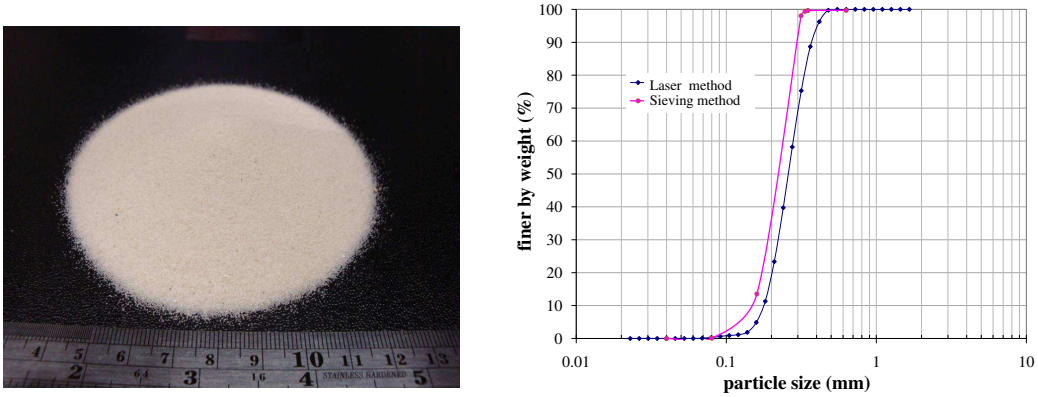

Figure 2.7: Fontainebleau sand and grain size distribution

With the minimum and maximum void ratios ($e_{\min}, e_{\min}$) or minimum and maximun dry densities ($\rho_{\text{d min}}, \rho_{\text{d max}}$), the density index ($I_{D0}$) used to classify the dense or loose sample in this study was then given as:

$$I_{D0} = \frac{e_{\max} - e_0}{e_{\max} - e_{\min}} = \frac{\rho_{\text{d max}}(\rho_{\text{d0}} - \rho_{\text{d min}})}{\rho_{\text{d0}}(\rho_{\text{d max}} - \rho_{\text{d min}})} \tag{2.2}$$

where e_0 and ρ_{d0} are respectively the void ratio and the dry density at the beginning of a test (before applying normal stress). Within this study, two distinct densities $I_{D0} = 90 \pm 3\%$ and $I_{D0} = 30 \pm 3\%$ represent dense ($\gamma_{\text{d0}} \approx 16.55\ kN/m^3$) and loose ($\gamma_{\text{d0}} \approx 14.74\ kN/m^3$) samples respectively.

2.3.2 plates

Having mentioned in the previous chapter, the surface roughness of structural materials were quantified as the modified roughness in term of a maximum height $R_{\max}$, $L = 0.20$ mm (Uesugi & Kishida [1986]), which is the relative height between the highest peak and the lowest valley along a surface profile over the gauge length $L = 0.20$ mm. In this study, the

rough plates mainly used to describe the interface behaviour were made by gluing on a steel plate 1 cm thick layer of 0.2 mm from a mixture of araldite (epoxy) and Fontainebleau sand (30 g of araldite per 100 g of sand passing the sieve with mesh size of 630 μm and retained on the sieve with mesh size of 315 μm), this method then represents a high roughness (Figure2.8). The value of roughness ($R_{\max}$) can effectively be quantified by morphology method.

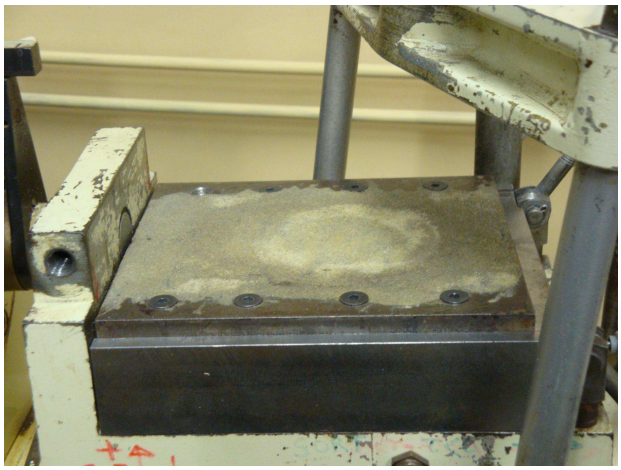

Figure 2.8: Rough surface positioned on direct shear test

At 3S-R laboratory, a measurement system in contact surface known as asperities to a certain degree has been experienced. Most of the ealier works were performed on the measurement of the evolution of morphology of rock joints by using a laser beam (Armand et al. [1998] , Hans & Boulon [2003]). This method is well appropriate to describe the asperities surface. In accordance with this approach, the surface roughness can be directly measured. This device as described in Figure 2.9 is composed of a laser scan fixed on a platform motorized by two stepper motors generating two orthogonal displacements controlled by two LVDTs from the PC. The morphology is obtained by scanning the surface by a series of parallel profiles with a constant step. By this way a map of altitude of steel surface, consisting in 128 profiles of each one 128 points for a maximum size of plate of 80 mm x 80 mm, is then obtained. Every scan of the surface is referred to the origin point of the plate as shown in Figure 2.10. In this way the relative position of the origin point and each point on the steel plate is precisely defined in the three orthogonal systems (X, Y, Z). Figure 2.11 shows typical measurement of the morphology of rough plate used in this study. The surface roughness as defined by $R_{\max} = 0.2$ mm is the average measurement obtained from morphology method. Taking into account the normalized roughness ($R_n = R_{\max}/D_{50}$) proposed by Uesugi & Kishida [1986], with particle diameter D_{50} of Fontainebleau sand ($D_{50} = 0.23$ mm), these rough plates then represent $R_{\mathrm{n}} = 0.87$ which can be attributed to be very rough. From available references on surface roughness definition, $R_{\mathrm{n}} \geq 0.10$ would be able to stand for rough surface: Uesugi & Kishida [1986]; Uesugi et al. [1989]; Hu & Pu [2004].

A comparison was also performed between the two different kinds of surface roughness. For

the steel plate (so-called "smooth plate"), some of test series were additionally conducted. All monotonic tests with smooth plate under CNL and CNS conditions describing the main characteristics of interface will be prestented. The surface roughness of this plate delivered from SOLCYP is intended to be similar to that of steel pile model tests. It is found that $R_{\max}$ of this plate is about 14 μm. This surface roughness has not been determined by morphology method, but has been derived from SOLCYP. Considering the normalized roughness (R_n), the value of $R_{\max} = 14$ μm is very much less than D_{50} of Fontainebleau sand. Therefore, it can be concluded that the surface of this plate ($R_n = 0.06$) is fairly smooth (Figure 2.12).

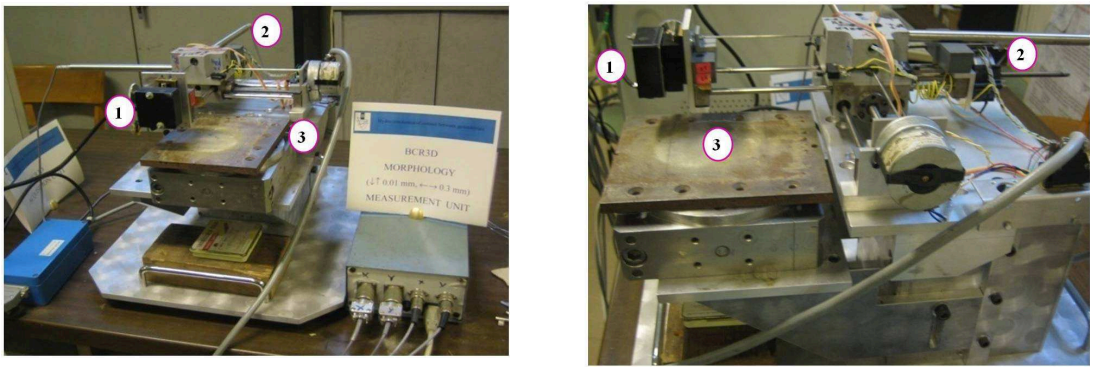

Figure 2.9: View of the apparatus of morphology measurement: (1) Laser beam; (2) LVDT displacement sensors of the laser beam (3) rough plate

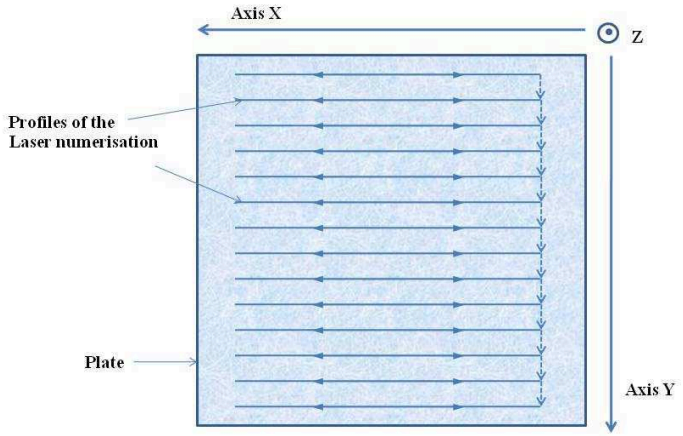

Figure 2.10: Scheme of measurement of the morphology of surface roughness, Hans & Boulon [2003]

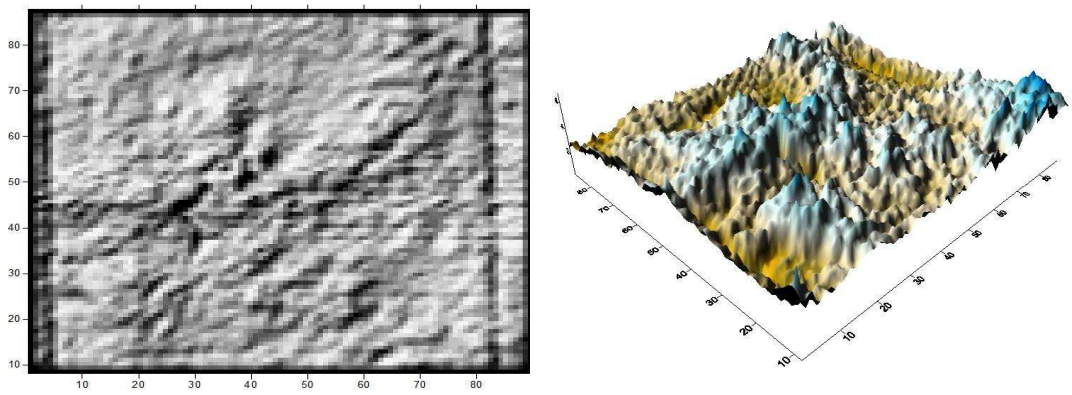

Figure 2.11: Map of altitude of surface obtained from morphology of the rough material,(left) shaded relief map, (right) 3D surface.

For the purpose of the sample preparation, having known the mean diameter of Fontainebleau sand ($D_{50} = 0.23$ mm), the maximum gap between the shear box and bottom plate should not be over 0.3 mm in order to prevent the leakage of fine particles of sand from this gap, especially during the cyclic loading tests. Therefore, a spacing of 0.3 mm, created by a pair of brass foils, was arranged between the plate and the 1/2 box (see Figure 2.13) during the construction of the sand sample to the desired density. Furthermore, this gap was set in order to avoid having the direct friction between half shear box and the rough plate.

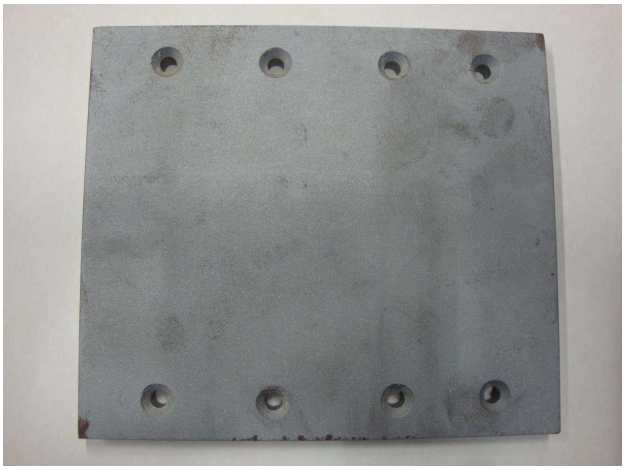

Figure 2.12: Smooth plate delivered from SOLCYP

In this study all tests were performed as dry tests, i.e. completely drained tests. With much less technical difficulty of direct shear device, the sample preparation began with the setup of a pair of brass foils and the shear box, serving as a container of the material, on the rough plate (see Figure 2.14). The sample was set up by simple pluviation in the air with a low-high fall. Once the density index was fixed, the weight of sample was required to achieve the

desired sample height. The average height of the samples before application of σ_n was 20 $\pm$ 0.5 mm. At this stage of sample preparation, different fabrication processes of the sample were used. Loose sample was achieved by a simple pluviation method in the air with a low-high fall. The tamping and vibration methods for obtaining dense sample were therefore used. After each layer of sand deposited by simple pluviation and having flattened the soil surfacee, the load piston (top cap) was then placed. The sample underwent densification by using the tamping and vibration methods. Before running the test, the load piston has not to be in contact with the stirrup (load hanger) for applying the normal stress in order to be sure that there is no load applying to the sample. After turning on the control system, the stirrup was positioned on the load piston (top cap) which induced a small normal stress acting on the sample (about 5-10 kPa). This small normal stress was also recorded. Then the normal stress was continuously applied by the control system until reaching the required value, after that shear stress was applied.

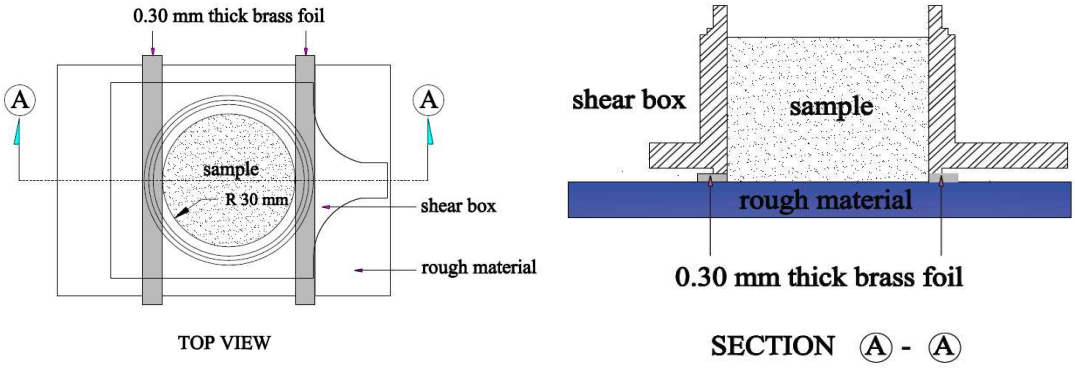

Figure 2.13: Setup of shear box with a pair of brass foils

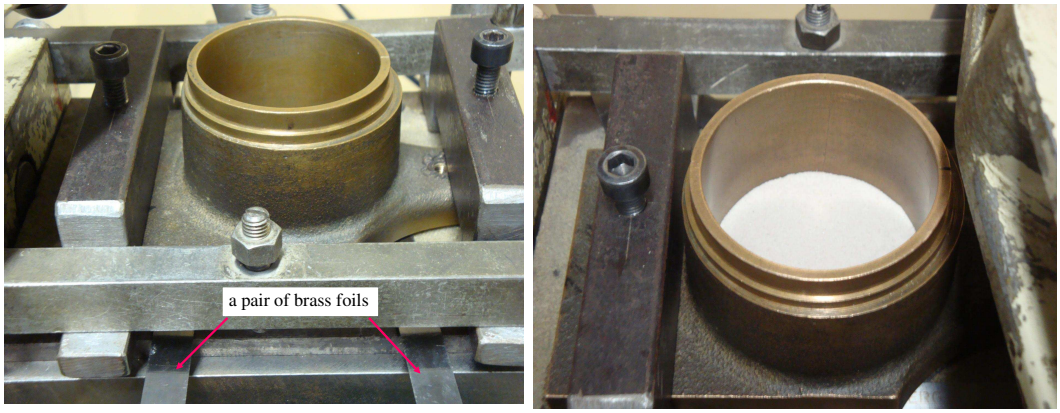

Figure 2.14: Preparation of a sample for interface shear test

2.4 Monotonic interface direct shear tests

2.4.1 Interpretation of interface shear test

As mentioned in the previous chapter, a shear band or the soil-structure interface cannot explicitly be separated from the surrounding soil. Let us recall the direct shear test by using stereophotogrammetry to display the evolution of the field of the soil-rough plate relative displacement (Hoteit [1990]). Figure 2.15 displays the progressive localization of the field of incremental relative displacements. At the beginning of shearing, a diffused convex zone is created at the contract of the rough plate. Very quickly after this initial phase, this zone turns into a precise thin layer of constant thickness within the shear box. This experiment and some others by different authors motivate our subsequent choice by considering the direct shear sample composed of two parts. During soil-structure direct shear test, the sample is schematically composed of two parts subjected to two different stresses. Two parts of direct shear test have to be interpreted by considering:

- The "active" lower part being in contact with the rough material is a so-called interface.
- The "passive" upper part as the rest (most) of the sample overcoming this interface is practically subjected to compression oedometer.

From the interface interpretation proposed by Boulon [1988], in case of constant σ_n (CNL), the normal stress acting on the interface (σ'_n) and the normal relative displacement of interface ([u']) are considered within the generated interface (interface thickness, $t \approx 10D_{50}$) as shown in Figure 2.16. The compression oedometer has no influence in this case. However, on different paths (including CNS condition), it would be appropriate to consider an oedometer correction of the normal relative displacement measured. Whereas σ_n is variable, the variation of normal displacement of interface ($\Delta[u']$) is due to the contribution of the passive part ($\Delta[u]_{\text{oedometer}}$) and the variation of the sample height (Δh) as:

$$\Delta[u'] = \Delta h - \Delta[u]_{\text{oedometer}} \tag{2.3}$$

Boulon [1988] also performed an oedometer correction at CV condition and found that there was no much difference on the maximum shear stress with the height of sample of 20 mm. For this reason, all components in this study can be considered as mean values within the generated interface without taking into account the oedometer correction, according to moderate changes in σ_n.

The normal stiffness of interface ($k_{n\,\text{int}}$) measured in the shear box is different from the normal stiffness on the full sample of sand ($k_{n\,\text{sam}}$). This sfiffness is formed along the interface and part of oedometer sample. The entire sample (sample height, h) is mobilized during the implementation of the initial normal stress (path at constant normal stress, the most common). However, only the interface (thickness t) is then mobilized when shearing load is applied (Figure 2.17). The relationship between interface thickness (t) and sample height (h) can be expressed by:

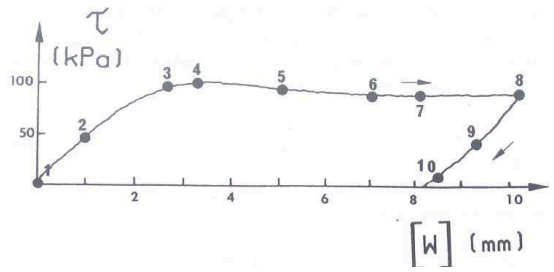

(a)

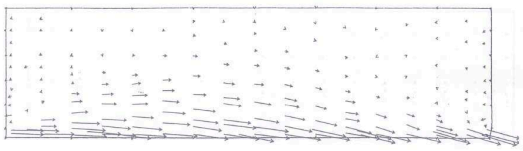

(b)

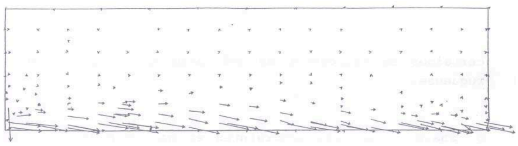

(c)

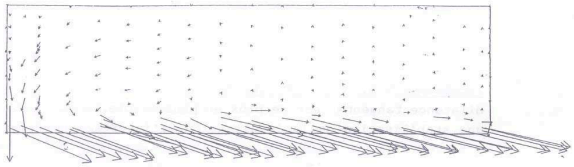

(d)

Figure 2.15: 2-D CNL test, Hostun sand-rough plate, $\sigma_n = 100$ kPa, Hoteit [1990]. Parallelepipedic shear box (6 cm x 20 cm x 20 cm); (a) Shear stress - shear displacement curve (b) Relative displacement vectors, increment 1-2 (c) Relative displacement vectors, increment 2-3 (d) Relative displacement vectors, increment 3-4

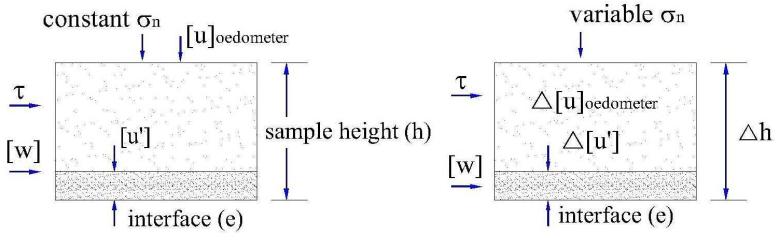

Figure 2.16: Direct shear test interpretation, Boulon [1988]

$$\frac{[u]_{\text{int}}}{t} = \frac{[u]_{\text{sam}}}{h} \quad \Rightarrow \quad k_{n\,\text{int}} = k_{n\,\text{sam}} \frac{h}{t} \tag{2.4}$$

where $[u]_{\text{int}}$ and $[u]_{\text{sam}}$ are the normal displacement of interface (t) and of sample (h), respectively.

Or the normal stiffness (k_n) can be considered as;

$$\Delta\sigma_n = k_{n\,\text{sam}}[u]_{\text{sam}} = k_{n\,\text{int}}[u]_{\text{int}} = k_{n\,\text{sam}} \frac{h}{t}[u]_{\text{int}} \tag{2.5}$$

The normal stiffness (necessarily secant) will be taken into account in the calculation of specific weight under applied stress. But the normal relative displacement can aso be taken into account. Considering at beginning of the test, when the normal stress is applied, the vertical displacement is then measured for the entire sample. The relative displacement of interface is only proportional to t/h of the vertical displacement measured. At this stage, the normal stiffness of interface ($k_{n\,\text{int}}$) resulting from an application of normal stress is taken into account. The current unit weight, specific weight ($\gamma_{d0\,\sigma_n}$), of interface under an applied normal stress is then expressed by

$$\gamma_{d0\,\sigma_n} = \gamma_{d0\,\sigma_n=0} \cdot \frac{1}{\left(1 - \frac{\sigma_n}{t \cdot k_{n\,\text{int}}}\right)} \tag{2.6}$$

or it can be expressed in terms of proportion of normal displacement

$$\gamma_{d0\,\sigma_n} = \gamma_{d0\,\sigma_n=0} \cdot \frac{1}{\left(1 + \frac{[u]_{\text{int}\,\sigma_n}}{t}\right)} \quad = \quad \gamma_{d0\,\sigma_n=0} \cdot \frac{1}{\left(1 + \frac{[u]_{\text{sam}\,\sigma_n}}{h}\right)} \tag{2.7}$$

where $\gamma_{d0\,\sigma_n=0}$ is the initial unit weight without taking into account the normal stress. $[u]_{\text{int}\,\sigma_n}$ and $[u]_{\text{sam}\,\sigma_n}$ are respectively the normal displacement of interface and of sample due to an application of normal stress.

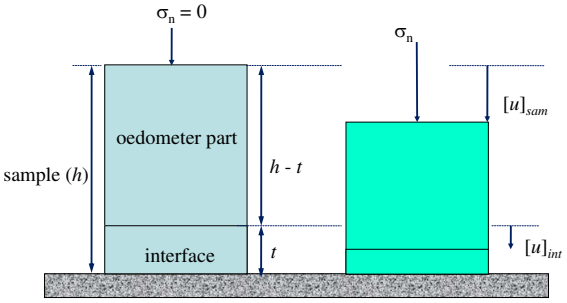

Figure 2.17: Interpretation of full sample and interface during the application of the initial normal stress

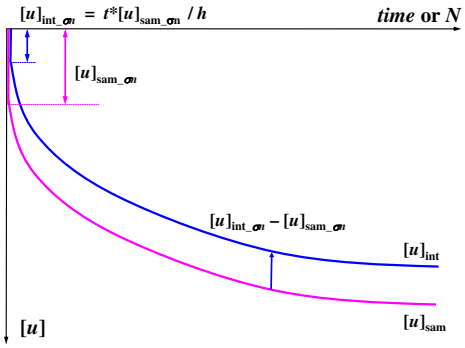

Figure 2.18: Full sample and interface during the application of the initial normal stress, then during the monotonic or cyclic direct shear

However, when following whether nonotonic or cyclic direct shear tests (at constant normal stress), the global normal displacement at any time is expressed as $[u]_{\text{sam}}$, but only the interface contributes to the normal relative displacement (Figure 2.18). During shear loading, the additional relative displacement of interface coincides with the additional relative displacement of the sample, but both relative normal displacements are different. Therefore, the normal relative displacement of the interface at any given time or number of cycles, $[u]_{\text{int}}$, can be expressed by

$$[u]_{\text{int}} = [u]_{\text{sam}} - [u]_{\text{sam }\sigma_n} \cdot \left(1 - \frac{t}{h}\right) \tag{2.8}$$

In the following, for the sake of simplicity $[u]$ stands for the normal relative displacement of the interface instead of $[u]_{\text{int}}$

2.4.2 Test results of monotonic interface shear test

Preliminarily to cyclic interface shear tests, monotonic interface shear tests on two different values of roughness whether under CNL or CNS conditions, as shown in Table 2.3, were first performed in order to determine the peak friction angle (δ_{peak}) between granular soil and structure as well as the critical angle (δ_{crit}) and the characteristic angle (δ_{car}) separating the contractive and dilative domains, and main characteristics of the interface. Two distinct densities, dense ($I_{D0} = 90 \pm 3\%$) and loose sand ($I_{D0} = 30 \pm 3\%$) were performed under CNL and CNS conditions. In case of CNS condition, three different values of the normal stiffness (k = 1000, 2000 and 5000 kPa/mm) were performed.

Table 2.3: Tests for primary validation (monotonic tests)

I_{D0} (%)	type of plate	γ_{d0} (kN/m^3)	Path (kPa/mm)	σ_n (kPa)
30	rough , smooth	≈ 14.74	0 (CNL)	60, 120, 310
90	rough , smooth	≈ 16.55	0 (CNL)	60, 120, 310
30	rough , smooth	≈ 14.74	1000(CNS)	60, 100, 310
30	rough	≈ 14.74	2000(CNS)	60, 100, 310
30	rough , smooth	≈ 14.74	5000(CNS)	60, 100, 310
90	rough , smooth	≈ 16.55	1000(CNS)	60, 100, 310
90	rough	≈ 16.55	2000(CNS)	60, 100, 310
90	rough , smooth	≈ 16.55	5000(CNS)	60, 100, 310

In accordance with the interface interpretation, the objective of accessing the density (specific gravity) of the soil-structure interface connected with the normal relative displacement observed is necessary. However, there are different ways to access this approach. Some attempts have been made to get a good correspondence between the interface thickness and the density. Having known that the critical density depends only on the level of normal stress, each of these stress levels with the hypothesis of interface thikness which might differ according to initial compaction should be considered. Since the normal relative displacement is measured, the critical density could be expressed as a function of the normal stress.

First considering rough plate, after the application of the normal stress, the vertical displacement was then measured for the entire sample (Figure 2.19(a)). Indeed, the normal displacement of interface is only in proportion to the interface thickness (t) and sample height (h), which can be expressed as $[u]_{\text{int}} = [u]_{\text{sam}} \cdot (t/h)$. Considering the interface thickness within the range of $10D_{50} - 12D_{50}$, Figure 2.19(b) shows the normal displacement of interface on both densities after applying the normal stress. These values of interface thickness also led to the evaluation of critical density. Taking into account the interface

thickness ($t = 10D_{50}$) on both densities, there was a small dispersion of the trend in critical density as a function of initial normal stress. In the range of $t = 10D_{50} - 12D_{50}$, this small dispersion still existed (Figure 2.20(a)). The value of $11D_{50}$ would be reasonable to represent the interface thickness. However, the interface thickness was then considered according to Hammad [1991]'s investigation. This investigation showed that the thickness of the shear band had a tendency to decrease when the initial density increased. This can be concluded that the relative displacements as well as the rotations of grains in the loose sand-structure interface are more independent than that in the case of the dense sand-structure interface. Dejong et al. [2003] also reported that the thickness of the localized shear zone varied with the test conditions and increased with the accumulative displacement. From monotonic CNL tests, the interface thickness on dense and loose samples were then defined as $10D_{50}$ and $12D_{50}$, respectively (Figure 2.20(b)) .

The interface test results on smooth suface are also presented in a similar way. Nevertheless, the interpretation of interface thickness seems very difficult because smooth plate provides very thin thickness or no interface thickness. In general, as can be seen in available observations on smooth plate, the slippage occurs along the contact surface between the structural material and granular soil instead of the intense shear zone as can be seen on rough plate (Uesugi & Kishida [1986]). Considering the $R_n = 0.07$ of this plate, even though this value can be attributed to the smooth surface according to the criterion of surface classification ($R_{crit} \approx 0.1$), this would provide fairly thin thickness. The interface thickness can then be defined, in accordance with the critical density (Figure 2.21(b)), as $3D_{50}$ for dense sand and $9D_{50}$ for loose sand. It would be said that there is a good correspondence between smooth and rough plate in critical density. Figure 2.21(a) shows the normal displacement of sample $[u]_{\text{sam}}$ and of interface $[u]_{\text{int}}$ after applying initial normal stress. With very thin thickness of interface on dense sand ($3D_{50}$), the normal displacement due to the application of normal stress is then very small.

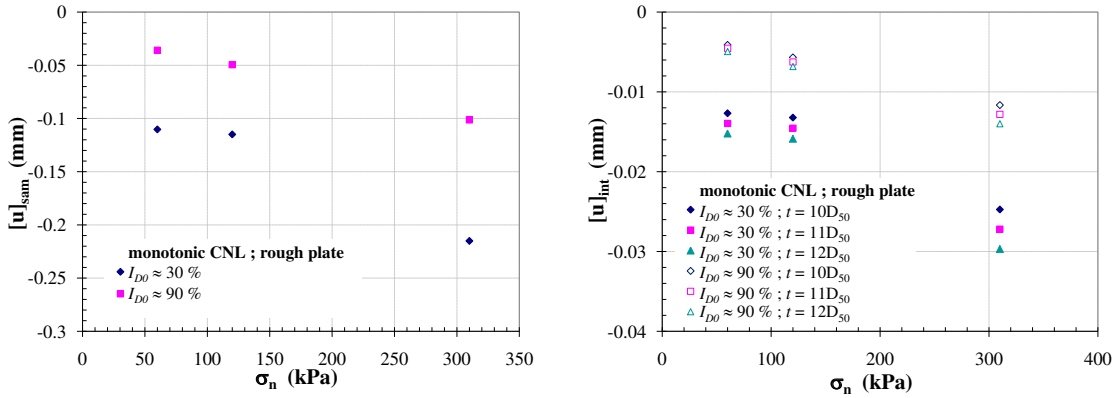

(a) (b)

Figure 2.19: Normal relative displacement measured due to application of normal stress:(a) sample ; (b) interface with t = 10-12D_{50}

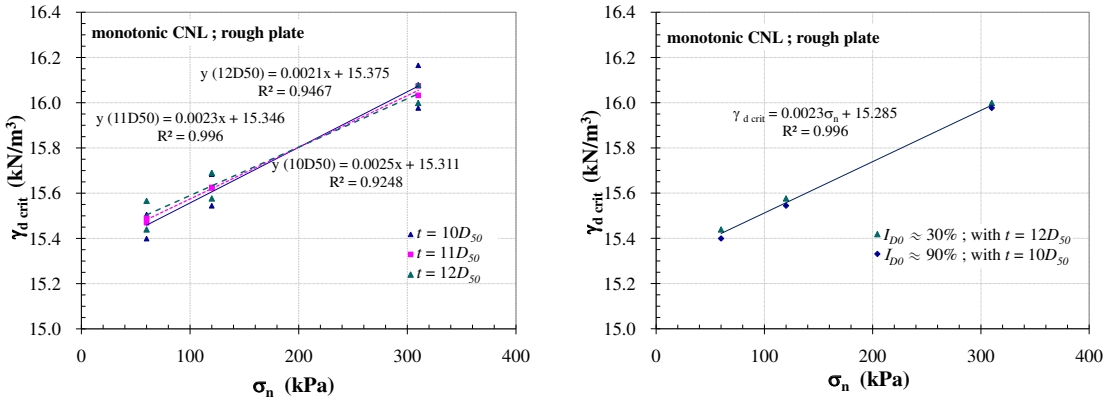

Figure 2.20: Critical density of interface shear tests according to monotonic CNL direct shear tests on rough plate: (a) with different values of interface thickness ; (b) with $t = 10D_{50}$ for dense sample and $t = 12D_{50}$ for loose sample

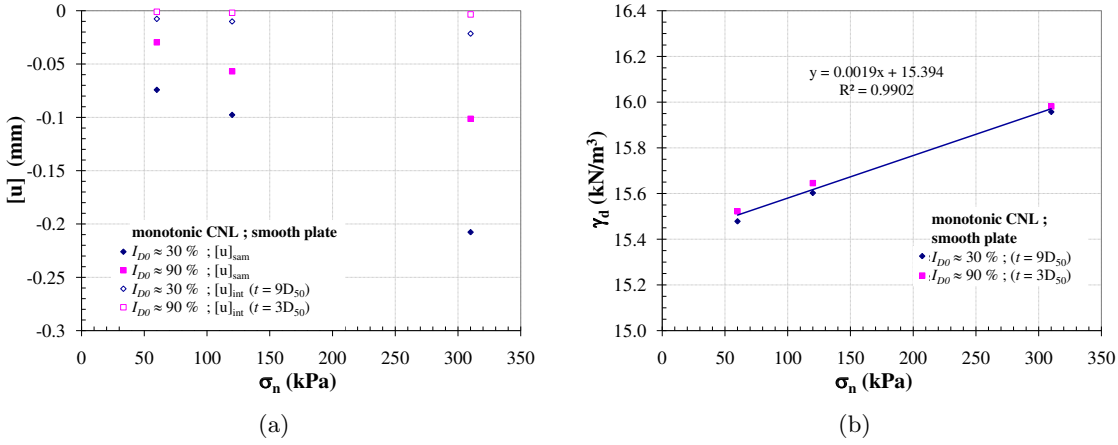

Figure 2.21: Interpretation of monotonic CNL interface test on smooth plate: (a) normal relative displacement measured due to application of normal stress ; (b) Critical density in accordance with the interface thickness

Figure 2.22 shows the typical monotonic interface results under CNL condition with rough plate on both densities. As can be seen, the interface shear tests on dense sample ($I_{D0} \approx 90\%$) obviously showed dilative behaviour ($[u] > 0$) which was higher for $\sigma_n = 60$ kPa than the other ones. It was also found that the shear stress increased with the shear relative displacement $[w]$ until reaching a peak value and then decreased (softening behaviour) to a residual shear stress (critical state). With high σ_n, the softening phase was significantly observed. The peak stress ratio ($\eta_{\text{peak}} = \tau_{\text{peak}}/\sigma_n$) for $\sigma_n = 60$ kPa was higher than that for $\sigma_n = 310$ kPa. This is due to the decrease in dilation rate as a function of normal stress. In case of loose sample ($I_{D0} \approx 30\%$), the shear stress increased continuously with relative shear

displacement [w] and had slight softening. The interface behaved contractively throughout the test on loose sample.

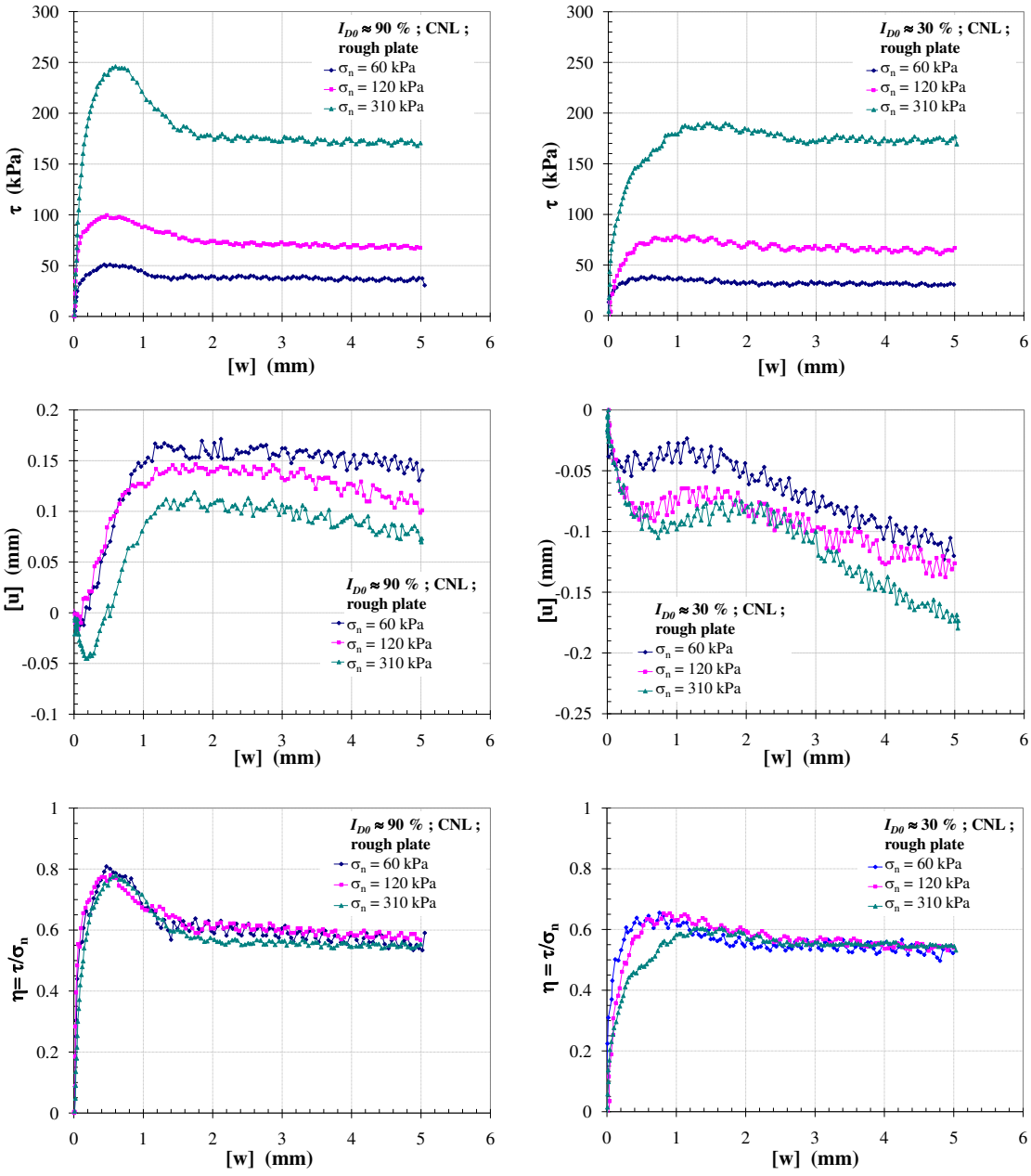

Figure 2.22: Monotonic CNL interface tests with rough plate, σ_n = 60, 120 and 310 kPa on dense sand ($I_{D0} \approx 90\%$) and on loose sand ($I_{D0} \approx 30\%$)

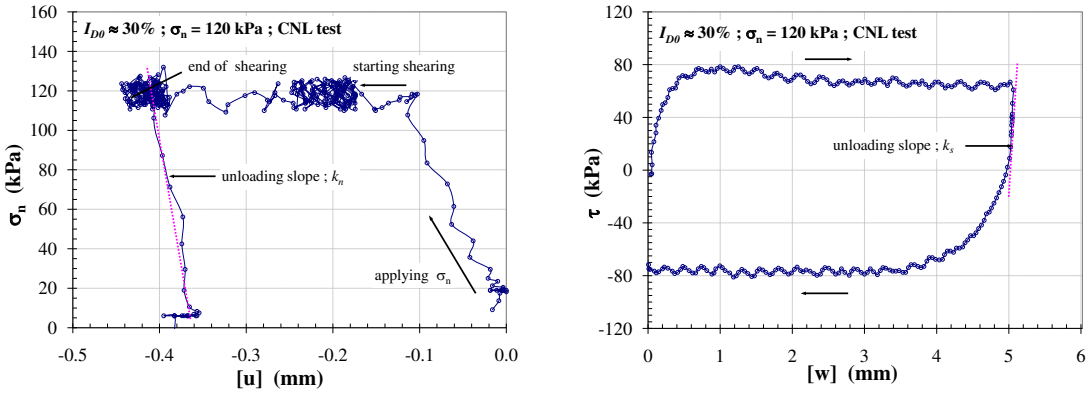

(a) (b)

Figure 2.23: Typical determination of interface stiffnesses on loose sample with rough plate, σ_n = 120 kPa: (a) normal stiffness (k_n); (b) shear stiffness (k_s)

On evaluating the stiffness of the interface, Figure 2.23 shows typical determination of normal and shear stiffnesses on loose sample. The slopes of the unloading curves from σ_n-$[u]$ and τ-$[w]$ diagrams give the values of k_n and k_s, respectively. However, as mentioned above, the unloading slope of k_n from σ_n-$[u]$ diagram which is determined from the entire sample has to be interpreted due to the normal displacement and the thickness of the interface. While the interface thickness has no influence on shear stiffness, this stiffness can directly be obtained from unloading curve of τ-$[w]$ diagram.

Figure 2.24 also shows the typical monotonic CNL interface results with smooth plate on both densities. Obviously, the surface roughness strongly influenced the interface test results. The shear stress whether on dense sample or on loose sample increased with the relative shear displacement $[w]$ until reaching a peak value and then continued to a residual shear stress (critical state) without showing any softening phase. As can be seen, the interface shear tests show that the peak and critical values of shear stress with smooth plate are obviously less than those with rough plate. It is found that the peak shear stress observed from smooth plate is about 60 - 70 % of that from rough plate. This is due to the effect of dilative behaviour found on rough plate. Smooth plate, contrary to rough plate, did not show a significant dilation phase during shear loading. The normal relative displacement $[u]$ of smooth plate was then less contractive than that of rough plate.

In general, the interface behaviour under constant normal stress condition (CNL) is well capable of describing the problems involving the slope stability and retaining walls. It is very important to understand the condition in which the normal stress acting on the interface varies during shear loading which can be found in case of pile foudations. In this case, the soil adjacent to the pile induces a normal stiffnes (k), depending on the diameter of pile (D) and shear modulus of soil (G) expressed as $k = 4G/D$, which leads to the variation of normal stress acting on the interface. This variation of normal stress is attributed to the tendency of soil whether to contract or to dilate. This shows the great interest of the loading paths with an imposed stiffness.

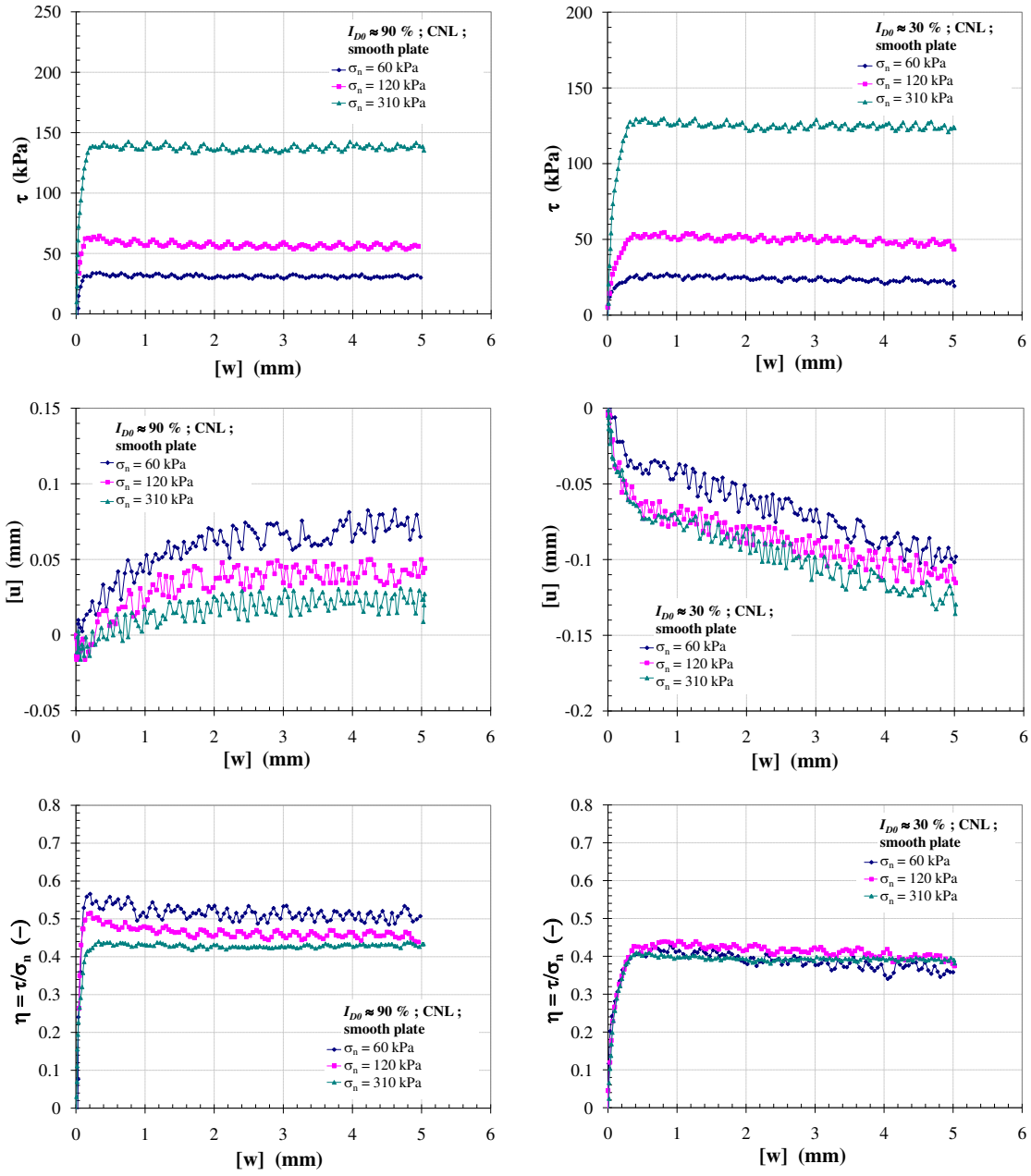

Figure 2.24: Monotonic CNL interface tests with smooth plate, $\sigma_n = 60$, 120 and 310 kPa on dense sand ($I_{D0} \approx 90\%$) and on loose sand ($I_{D0} \approx 30\%$)

Therefore, to illustrate how the interface behaves under CNS condition, the monotonic interface shear tests under CNS condition were performed with the three different values of normal stiffness (k = 1000, 2000 and 5000 kPa/mm) and initial normal stress σ_{n0} = 60, 100 and 310 kPa. The effect of normal stiffness was also observed on two different values of surface roughness.

Figure 2.25 illustrates the test results on dense sample ($I_{D0} \approx 90\%$) as well as on loose sample ($I_{D0} \approx 30\%$) with initial normal stress (σ_{n0} = 100 kPa), it was found that the normal stiffness significantly influenced the interface behaviour. On dense sample, at the beginning of shearing phase, the normal stress (σ_n) slightly decreased due to contractive phase while the shear stress (τ) still evolved and afterward the normal stress associated with shear stress increased as a result of dilative phase. The increase of stress state evolved with the shear displacement [w] until reaching the peak value of stress ratio (τ/σ_n) and then decreased to the critical state. The increase of normal stiffness (k) caused a significant increase in peak normal and shear stresses. Dense samples showed dilative behaviour which decreased with increasing normal stiffness (k).

The behaviour of interface under CNS condition on loose samples was significantly different from that observed on dense samples. When loose sand was subjected to shear loading under CNS conditon, the main charateristic of the inteface was that the normal stress (σ_n) associated with shear stress (τ) decreased significantly. The effect of increasing the normal stiffness (in this study k = 5000 kPa/mm) was evident. At the beginning of shearing phase, the interface showed significant contraction and consequently led to the significant degradation of normal stress. During shearing phase, the interface behaved contractively and the degradation of normal stress accompanied with the degradation of shear stress evolved continuously.

Comparisons between the tests performed under various conditions of the inital normal stress (σ_{n0}) and normal stiffness (k) are also presented. Figure 2.26 and 2.27 show the influence of initial normal stress (σ_{n0}) as well as the normal stiffness (k) on dense sand ($I_{D0} \approx 90\%$) and on loose sand ($I_{D0} \approx 30\%$), respectively. On dense sand, the normal stress associated with shear stress increased considerably as a function of normal stiffness. The increase in normal stress (σ_n) during shearing phase was due to the the dilative behaviour. With imposing the low value of stiffness (k) the dilative behaviour was more evident. The high value of imposed normal stiffness induces the reduction of dilation rate according to the relation of $k = \Delta\sigma/\Delta[u]$. On the other hand, loose sand significantly showed the contractive behaviour throughout shearing phase which led to the significant degradation of normal stress associated with shear stress. In particular, with σ_{n0} = 60 kPa and k = 5000 kPa/mm, the stress state could only evolve in a small range ([w] $\approx$ 0.5 - 0.8 mm) due to the rapid degradation of normal stress. With high value of imposed normal stiffness, in this case k = 5000 kPa/mm which could be high enough to represent the constant volume condition (CV), the normal relative displacement [u] of interface was almost constant throughout shearing phase.

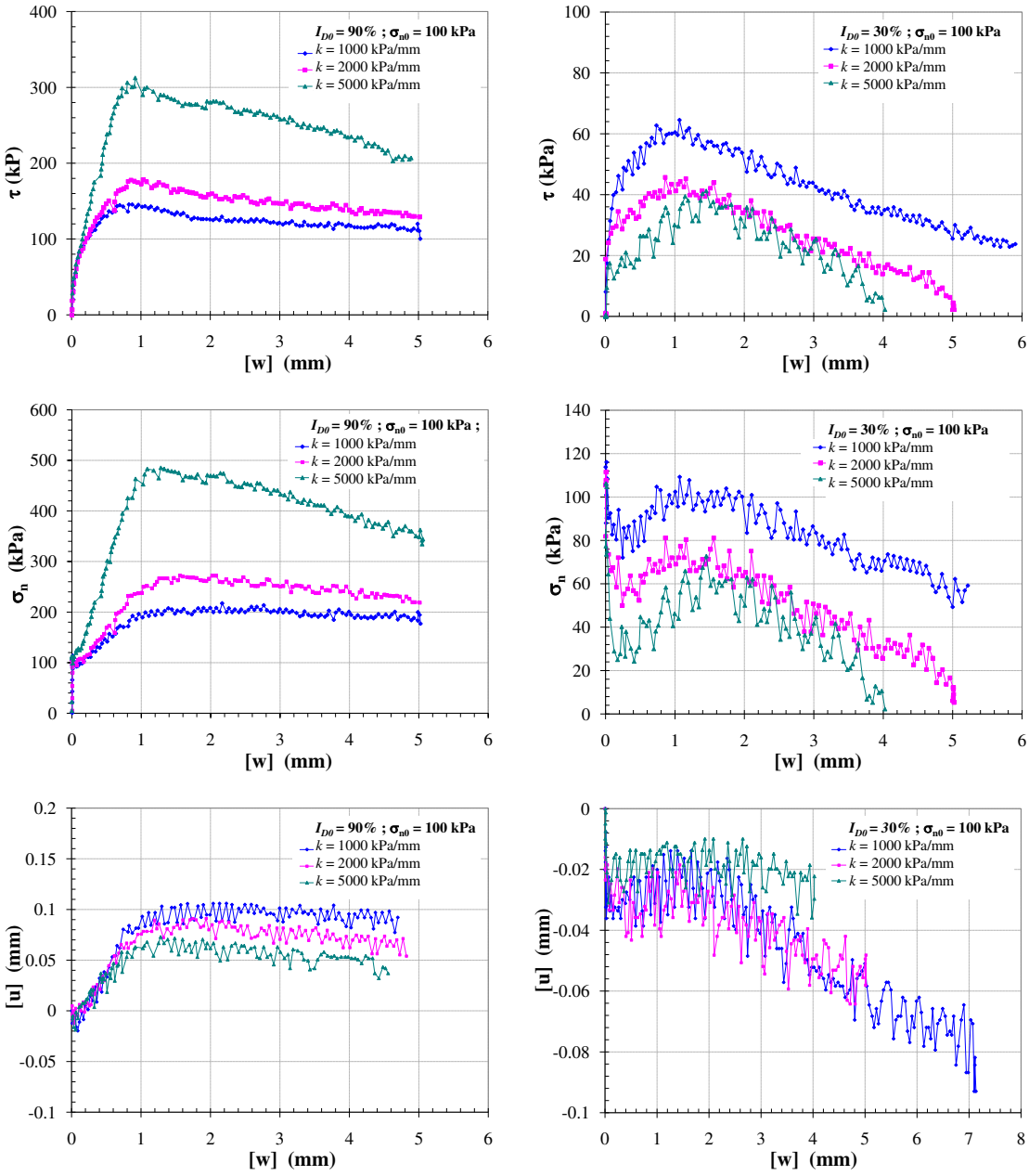

Figure 2.25: Monotonic CNS interface tests with three different normal stiffnesses (k), for the "rough plate", $\sigma_{n0} = 100$ kPa on dense sand ($I_{D0} \approx 90\%$) and on loose sand ($I_{D0} \approx 30\%$)

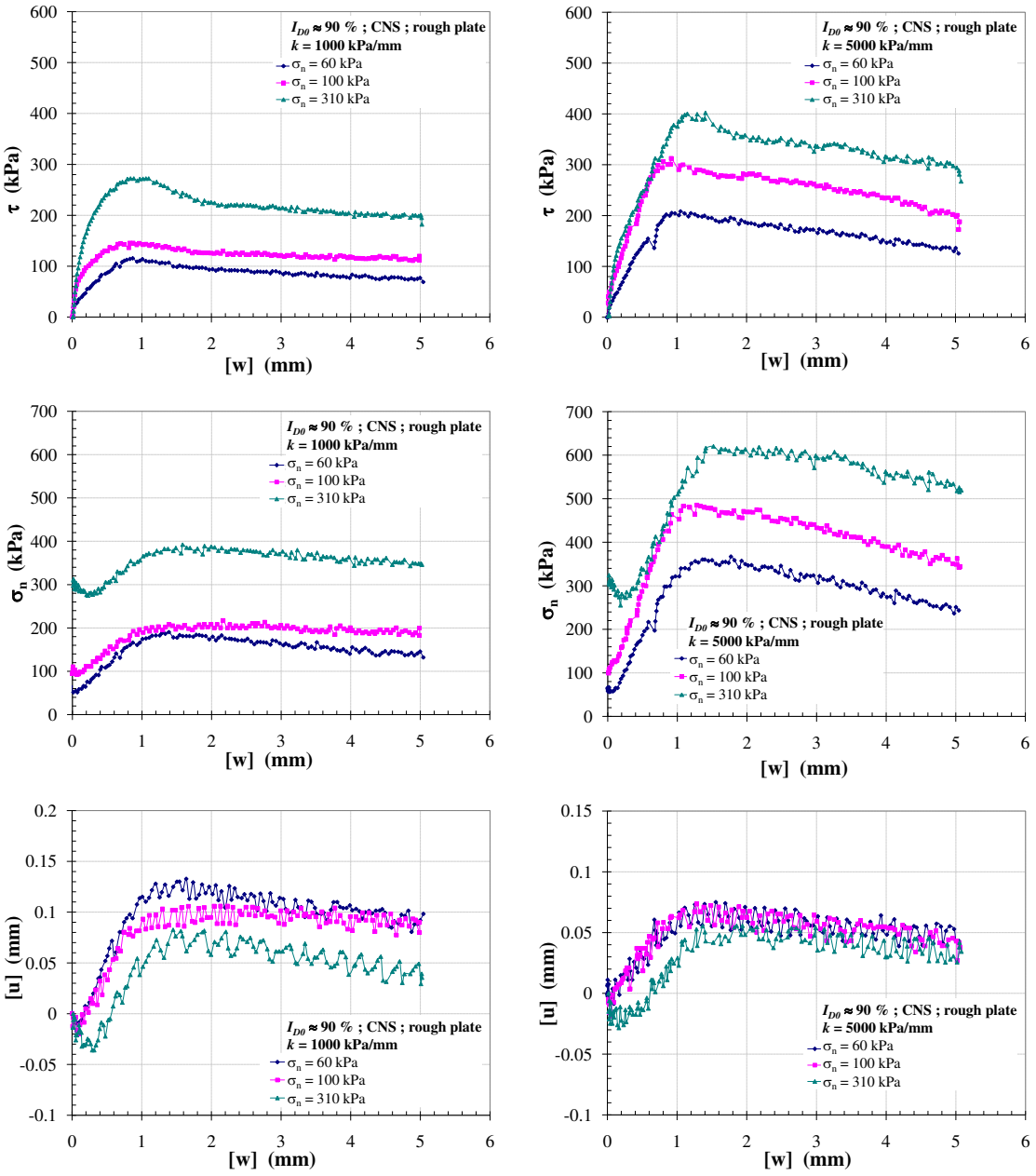

Figure 2.26: Monotonic CNS interface tests with rough plate on dense sand ($I_{D0} \approx 90\%$), $k = 1000$ and 5000 kPa/mm

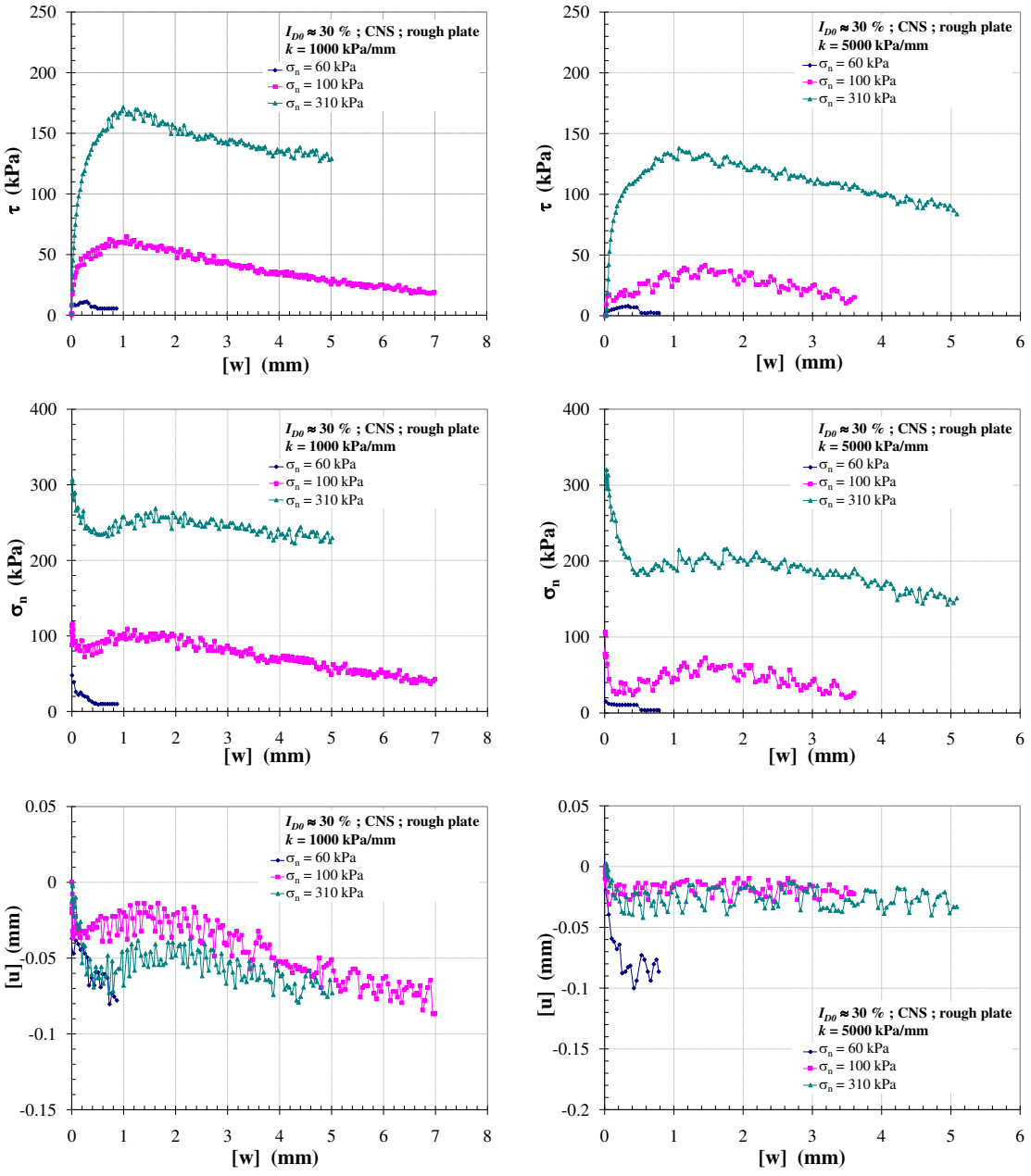

Figure 2.27: Monotonic CNS interface tests with rough plate on loose sand ($I_{D0} \approx 30\%$), k = 1000 and 5000 kPa/mm

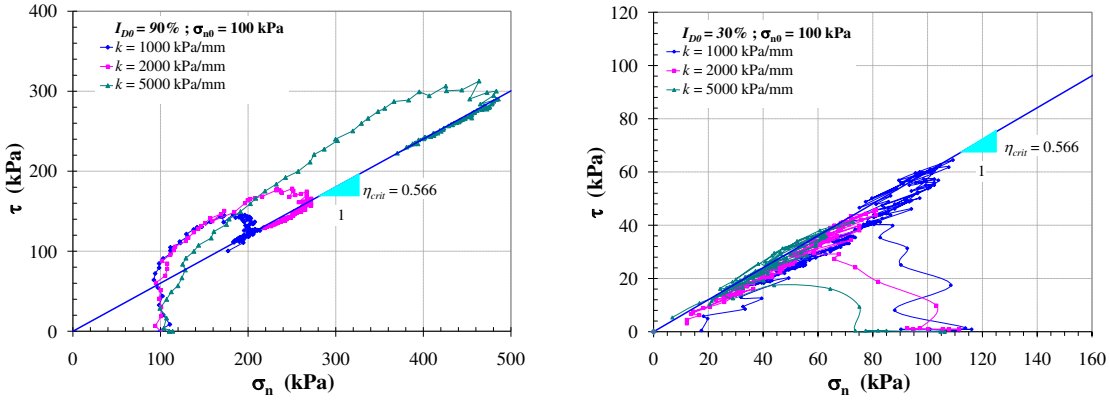

Figure 2.28: Stress paths of monotonic CNS interface tests with rough plate, $\sigma_{n0} = 100$ kPa; (a) dense sand ($I_{D0} \approx 90\%$); (b) loose sand ($I_{D0} \approx 30\%$)

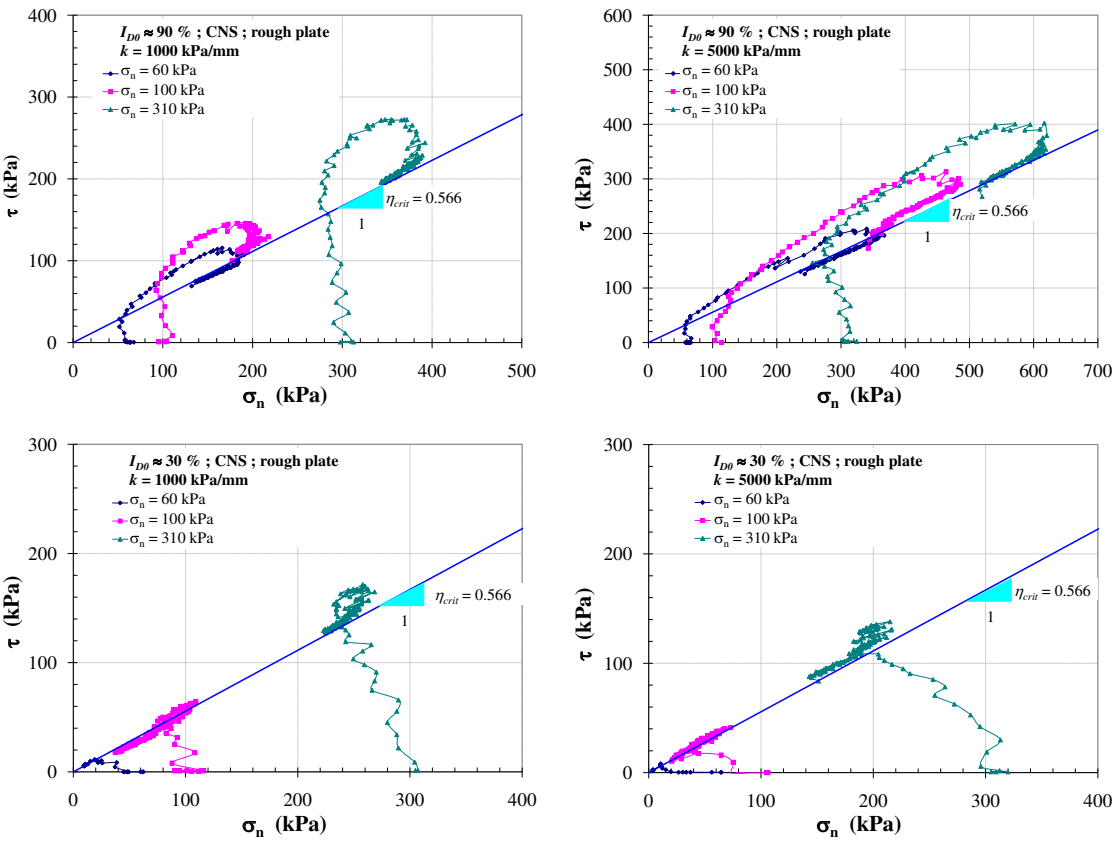

Figure 2.29: Stress paths of monotonic CNS interface tests with rough plate, $k = 1000$ and 5000 kPa/mm

Figure 2.28 and 2.29 also show the stress paths of monotonic CNS tests with various initial conditions. Even though different values of normal stiffness (k) were applied, the interface tests still mobilized the same critical stress ratio ($\eta_{\text{crit}} = \tau_{\text{crit}}/\sigma_n \approx 0.566$). This observation is in accordance with that observed by Tabucanon et al. [1995]. The peak shear stress ratio ($\eta_{\text{peak}} = \tau_{\text{peak}}/\sigma_n$) slighly decreased with an increase function of normal stress and an imposed normal stiffness. The stress paths of different values of normal stffness whether on dense sand or loose sand also showed the similar trend of stress ratio (η) after reaching the peak stress ratio η_{peak} which lied on the critical stress ratio (η_{crit}).

To verify the regularity of imposed normal stiffness, Figure 2.30 shows the relationship between the variation of normal stress $\Delta\sigma_n$ and of normal relative displacement $\Delta[u]$ during shear loading. The scatter of these tests resulted from the applied normal stress from generating engine in two directions as described in the section of interface direct shear devices. It should be noticed that the loose tests (CNL as well as CNS) are less stable, due to the occurrence of oscillation, than dense tests. This was evident when performing the tests with low inital normal stress ($\sigma_{n0} = 60$ kPa) and high value of imposed normal stiffness ($k = 5000$ kPa/mm).

Figure 2.31 shows the critical and peak stress envelopes of the test results with rough plate on both densities. The envelopes of these stress states for CNS tests corresponded well to that for CNL tests. These envelopes were fit with the power functions as can also be seen in Mortara [2001]. It would be said that the value of the normal stiffness has no influence on these envelopes.

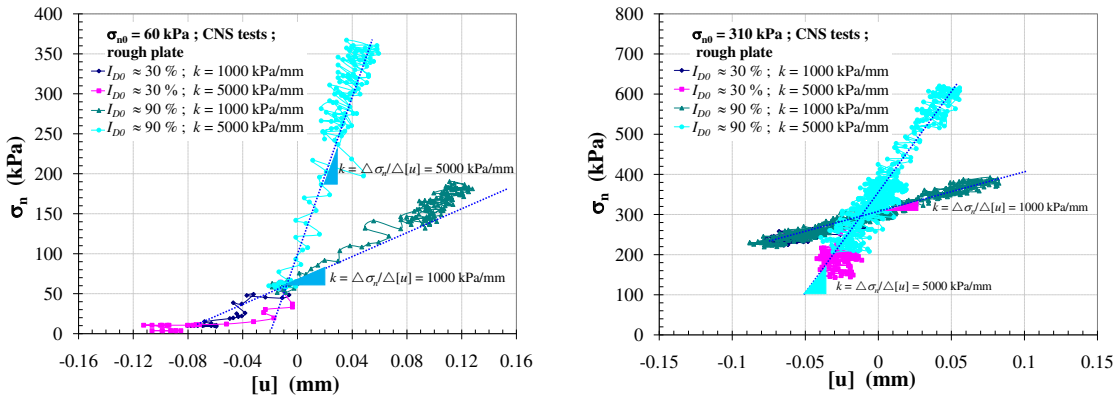

(a) (b)

Figure 2.30: Relationship of imposed normal stiffness during monotonic tests with rough plate on loose and dense sands: (a) $\sigma_{n0} = 60$ kPa ; (b) $\sigma_{n0} = 310$ kPa

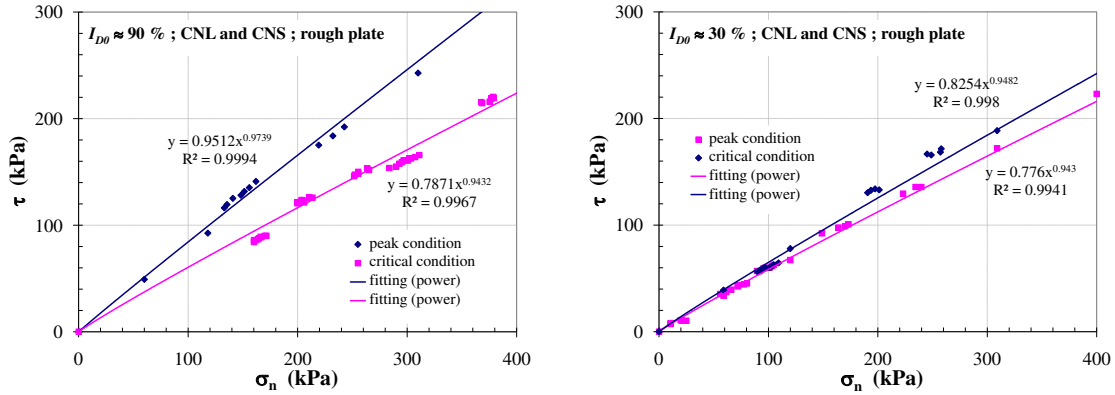

(a) (b)

Figure 2.31: Envelopes of peak and critical stress states for monotonic CNL and CNS interface shear tests with rough plate : (a) dense sand ($I_{D0} \approx 90\%$) ; (b) loose sand ($I_{D0} \approx 30\%$)

With smooth plate, the test results also showed the influence of imposed normal stiffness. A similar trend, as can be observed with rough plate, was expected during shearing. However, it was found that the tests results obtained from smooth plate were different from those obtained from rough plate. As can generally be observed from monotonic CNL tests on smooth plate as well as rough plate, the surface roughness strongly influenced the test results. Especially under CNS condition, the dilative behaviour which could significantly be observed, depending on σ_{n0} as well as k, on rough plate provided the significant variation of normal stress associated with shear stress. On the other hand, Figure 2.32 shows that smooth plate did not show the significant dilation and therefore the stress state did not show significant variation. The normal stress slighly increased during shearing phase (this could only be found in case of $\sigma_{n0} = 310$ kPa and $k = 5000$ kPa/mm). Consequently, the shear stress evolved continuously whithout showing softening phase. Figure 2.33(a) also shows stress paths of monotonic CNS tests on dense sand. The different values of imposed normal stiffness ($k = 1000$ and 5000 kPa/mm) slighly influenced the interface behaviour on smooth plate. With moderate value of initial normal stress ($\sigma_{n0} = 60$ and 100 kPa) the different values of k seemed to have no influence on the test results. It was clear that the volumetric behaviour of interface was not influenced by the imposed normal stiffness. The normal relative displacement ($[u]$) from various conditions were almost constant during shearing phase. The dilative behaviour could hardly be observed on smooth plate.

On loose sand, it was found that the influence of imposed normal stiffness observed on smooth plate was similar to rough plate (the significant degradation in σ_n). During shearing, the interface behaved contractively and then the degradation of normal stress increased significantly. This also led to the degradation of shear stress. As can be seen on rough plate, the rate of normal stress degradation significantly increased as a function of imposed normal stiffness on loose sand. It was also found that the rate of stress degradation on smooth plate was higher than rough plate. Obviously, on smooth plate with $k = 5000$ kPa/mm, $\sigma_{n0} =$

310 kPa the normal stress decreased from 310 kPa to 100 kPa in the range of $[w] = 1$ mm whereas on rough plate the normal stress decreased from 310 kPa to 200 kPa. The stress paths on smooth plate (Figure 2.33) also showed the trend of stress degradation rate when increasing the imposed normal stiffness. The normal relative displacement under various conditions on smooth plate showed that the imposed normal stiffness had no influence on the volumetric behaviour of the interface.

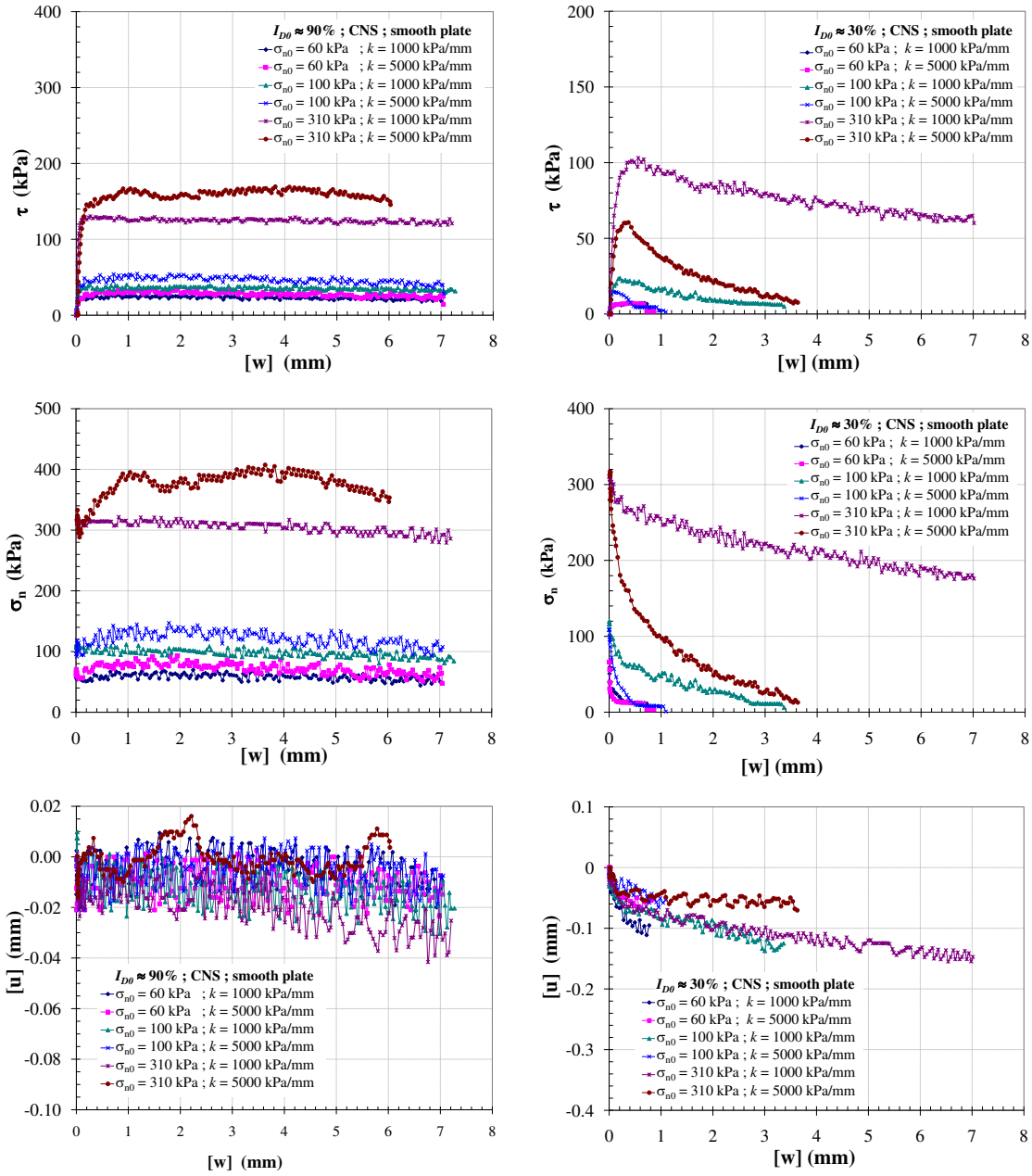

Figure 2.32: Monotonic CNS interface tests with smooth plate, $k = 1000$ and 5000 kPa/mm

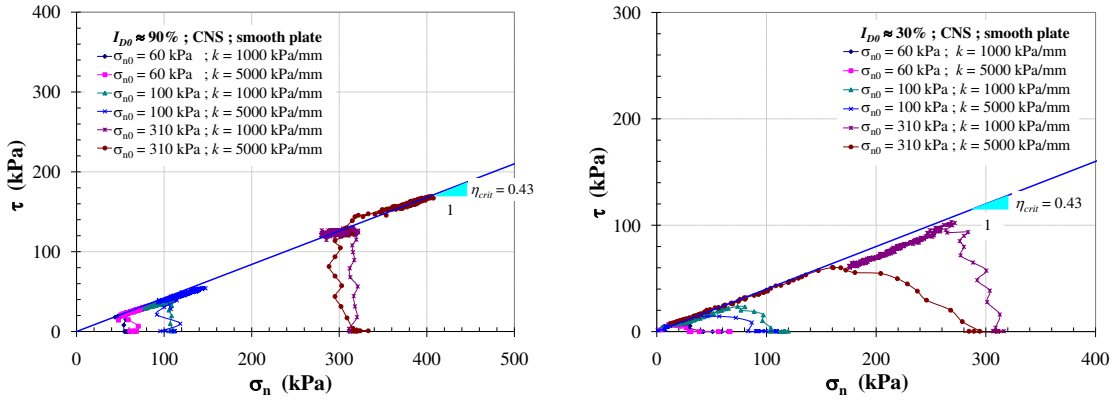

Figure 2.33: Stress paths of monotonic CNS interface tests with smooth plate, $k = 1000$ and 5000 kPa/mm : (a) dense sand ($I_{D0} \approx 90\%$) ; (b) loose sand ($I_{D0} \approx 30\%$)

After finishing the test, additional observation of the grain breakage within interface shear zone was carried out. Generally, shear loading causes a substantial disruption of grains within the shear zone which depends on several factors such as grain size, grain shape, σ_{n0}, I_{D0} and the surface roughness of structure. From many observations relevant to soil-structure interface and the measurement of interface thickness in this study, it is evident that the approximate interface thickness for granular materials is about $10 - 12D_{50}$. In this study, with $D_{50} = 0.23$ mm of Fontainebleau sand resulting from sieving method, the approximate layer of 2 - 3 mm, depending on the initial density and type of plate, of sand adjacent to the plate was therefore carried out by means of sieving method.

The extension of this purpose is to describe the specific energy (W) which allows a first approach of the level of grain breakage within the interface during shear loading. It is expressed by using the following formula;

$$W = \int_{\text{time}} (\tau \cdot [\dot{w}] - \sigma_n[\dot{u}])\ d\text{time} \tag{2.9}$$

This energy is also used in the modeling of interface behaviour in the form of nonlinear incremental law (Garnica-Anguas [1993]). It is comprehensible that with sufficient energy induced during shear loading the particles within the localized shear zone can be crushed. The grain breakage also depends on the crushability of grains (Uesugi et al. [1989]). Figure 2.34 and 2.35 show typical curves representing the specific energy from interface shear tests on rough and smooth plates, respectively. For CNL tests on rough and smooth plates, the specific energy increased as a function of σ_n and it was found that this specific energy was nearly independent of I_{D0}. As can be seen, the smooth plate obviously provided less specific energy than rough plate.

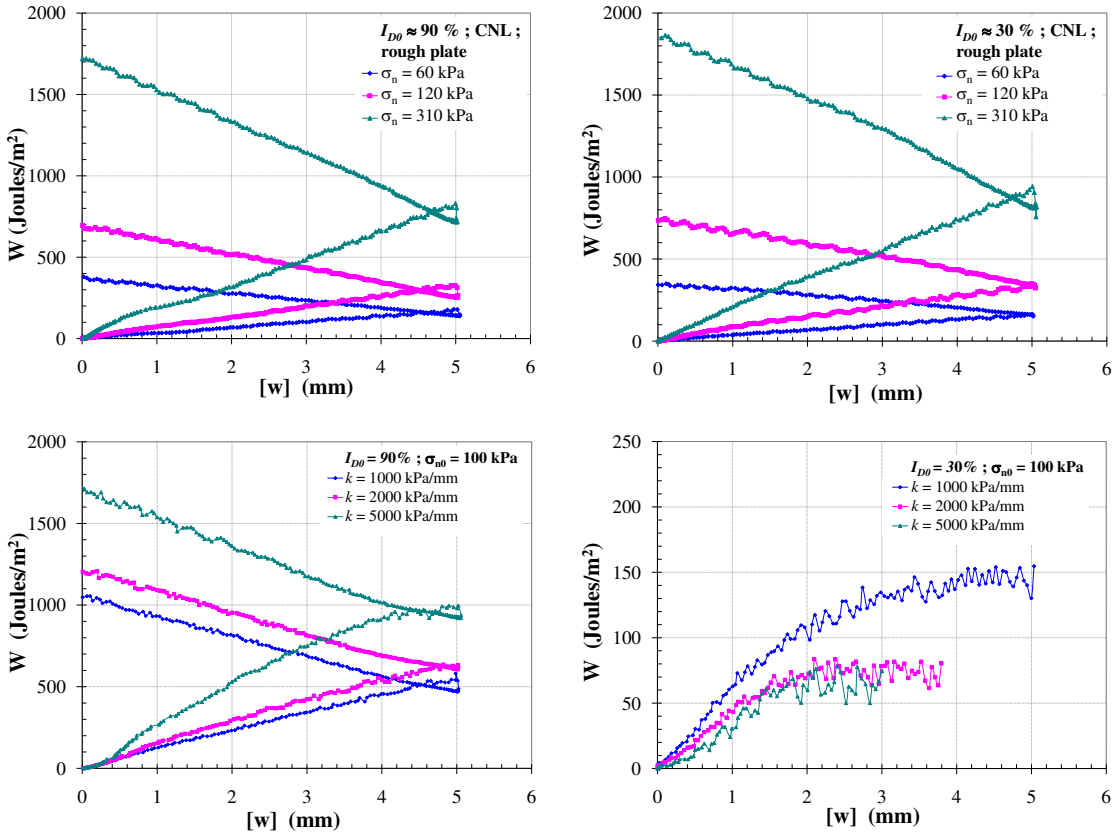

Figure 2.34: Specific energy from monotonic CNL and CNS tests on rough plate

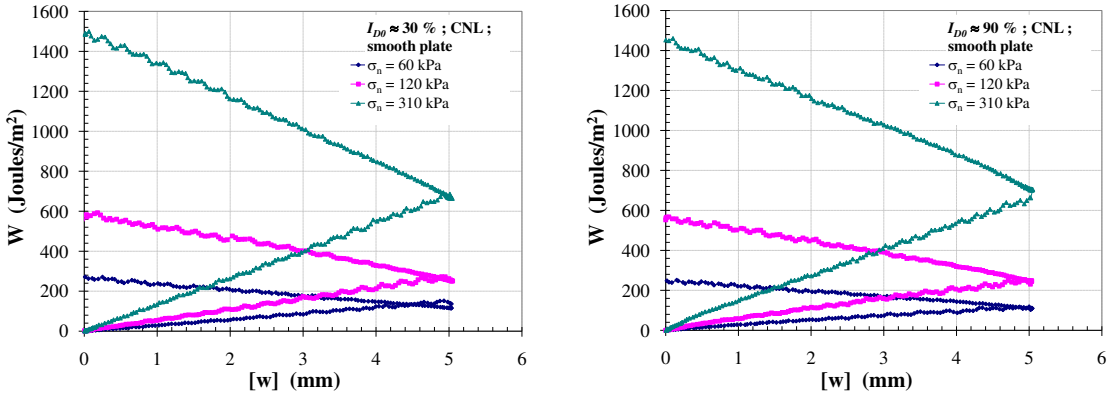

(a) (b)

Figure 2.35: Specific energy from monotonic CNL tests on smooth plate: (a) loose sand ($I_{D0} \approx 30\%$) ; (b) dense sand ($I_{D0} \approx 90\%$)

For CNS tests, dense sand also showed an increase of specific energy as a function of normal stiffness (k) due to the siginificant increase in normal stress associated shear stress. On the other hand, loose sand showed different trend of specific energy. An increase of the normal stiffness for the same initial normal stress induced the degradation of stress. The shear stress passed a peak value and then decreased, while the normal stress significantly decreased during shear loading. This can be said that with small amount of specific energy the particles within the inteface would not be crushed (Uesugi et al. [1989]).

Figure 2.36 - 2.38 show typical grain size distribution curves after testing by means of sieving method. On rough plate, it turned out that the particle size (D_{50}) after testing under CNL condition did not changed so much, in comparison with the curve of initial state resulting from sieving method, (see Figure 2.36) even with high initial normal stress and high initial density. However, when considering the fine particle size (D_{10}), at high value of normal stress (σ_n = 310 kPa), there were small variations of fine particle size (D_{10}), a shif of grading curves to the left. This variation from initial state on dense sample was more evident than on loose sample. Even though the specific energy of dense sand was almost the same as loose sand but the tendency of grain to be crushed on dense sand would be higher than that on loose sand. With low initial normal stress (σ_n = 60 kPa) especially on low density, the grain breakage could hardly be observed.

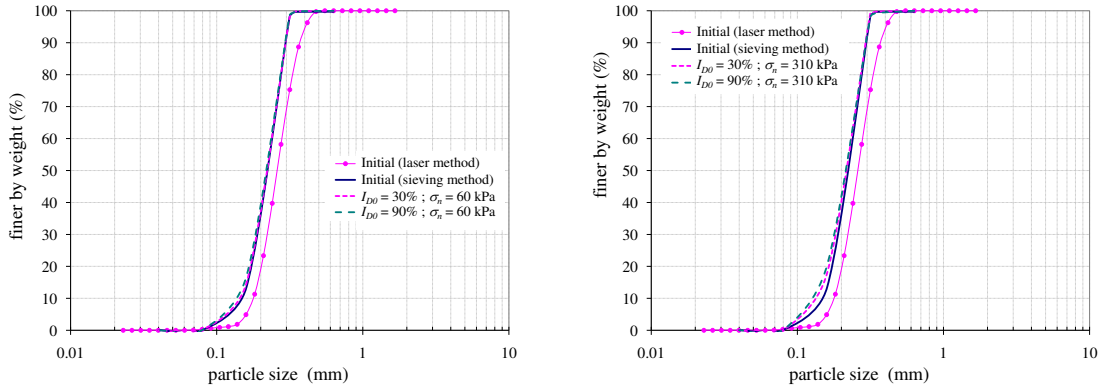

(a) (b)

Figure 2.36: Grain size distribution of sand after testing of monotonic CNL tests on rough plate: (a) with normal stress σ_n = 60 kPa ; (b) with normal stress σ_n = 310 kPa

Under CNS condition, the variation of normal stress associated with the shear stress induced the grain breakage within the localized shear zone differing from that as observed under CNL condition. On dense sand, with increasing the value of imposed normal stiffness (k) the dilative behaviour which could be observed with rough plate resulted in the significant increase in normal stress associated with shear stress. Therefore, the specific energy as a product of shear stress and shear displacement increased significantly. However, grain size distribution curves still provided the small vriation of particle size (D_{50}). Following the same procedure in which the the fine particle (D_{10}) was considered, the variation of D_{10} observed from CNS tests was more evident than that from CNL condition. The change in

fine particle size described by D_{10} was considerable for increasing the initial normal stress and imposed normal stiffness as shown in Figure 2.37.

On the other hand, loose sand showed the contractive behaviour throughout shearing tests which consequently led to the degradation of normal stress associated with shear stress. Therefore, the particle within interface shear zone could not considerably be crushed. With $\sigma_{n0} = 310$ kPa, the variation of fine particle size (D_{10}) could fairly be observed. For low initial normal stress $\sigma_{n0} = 60$ kPa, the interface tests which could only performed in a small range ($[w] \approx 1$ mm) due to the significant reduction of stress state showed no variations in grain size distribution curves.

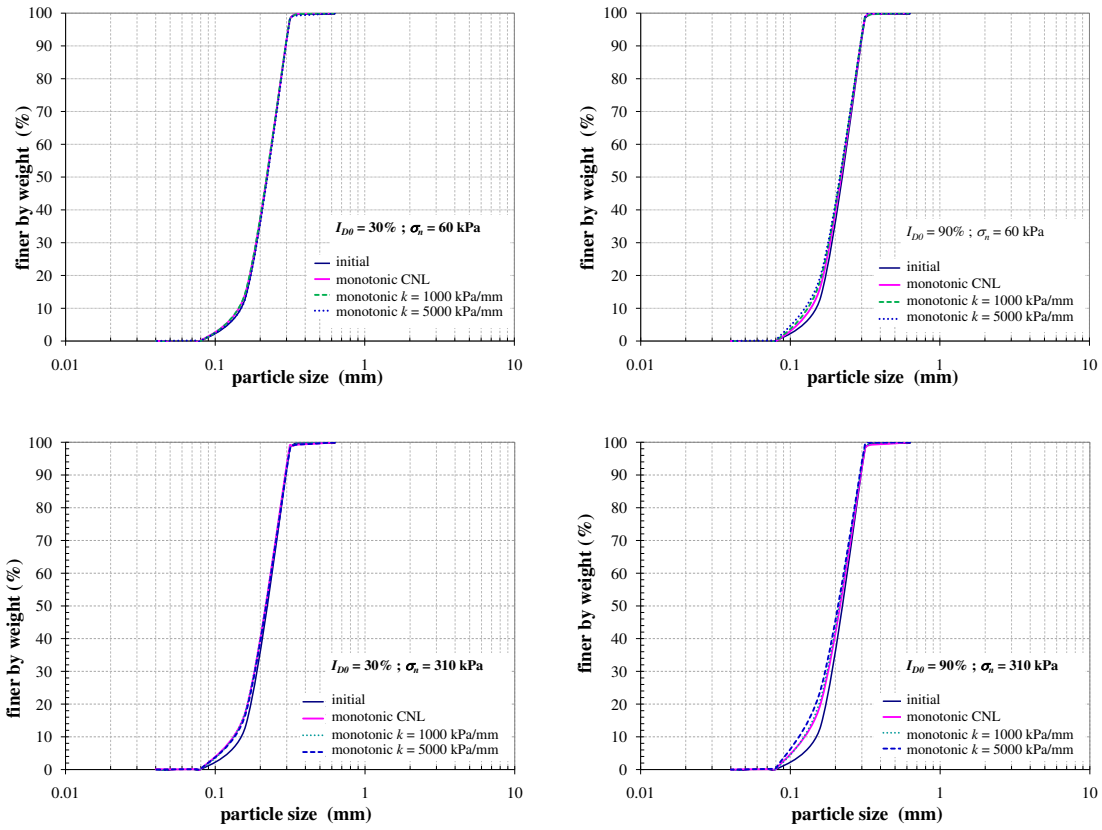

Figure 2.37: Grain size distribution of sand after testing of monotonic CNS tests on rough plate with initial normal stress $\sigma_{n0} = 60$ and 310 kPa

On smooth plate, the trend of grain size distibution curves was not much different from that observed on rough plate. The fine particle size (D_{10}) was still considered. It was found that the trend of grain breakage on smooth plate was less evident than rough plate. With $\sigma_{n0} = 60$ kPa the change of fine particle size from the initial state (a shift of grading curve) could hardly observed. This can be attributed to the interface mechanism on two distinct surfaces. If the stress state is high enough, the localized shear zone constitued along the sand-rough plate interface induces grain breakage (Uesugi et al. [1989]). In the same

condition, sand-smooth plate that the slippage normally occurrs along the contact surface shows less grain breakage.

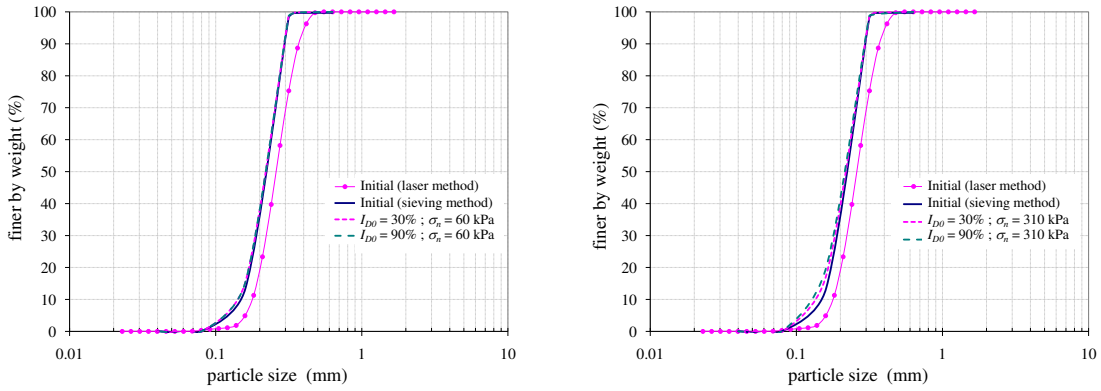

(a) (b)

Figure 2.38: Grain size distribution of sand after testing of monotonic CNL tests on smooth plate: (a) with normal stress $\sigma_n = 60$ kPa ; (b) with normal stress $\sigma_n = 310$ kPa

From these monotonic tests under CNL condition, the peak friction (δ_{peak}), critical (δ_{crit}) and characteristic (δ_{car}, separating dilative and contractive domain) angles were then determined. These angles were used to design the cyclic test campaign. It was found that the peak friction angle obviously depended on the initial density as well as the surface roughness. Figure 2.39 and 2.40 respectively show the peak shear stresses (τ_{peak}) of all tests in $\tau - \sigma_n$ plane of rough and smooth plates. The peak, critical and characteristic lines arose from the fitting of a linear function through the origin. The peak friction angle (δ_{peak}) was calculated from the ratio between the maximum shear stress along the inclusion and initial normal stress (Schlosser & Guilloux [1981]) as:

$$\tan \delta_{\text{peak}} = \frac{\tau_{\text{peak}}}{\sigma_n} \tag{2.10}$$

Then the peak friction angle with rough plate on dense and loose samples $\delta_{\text{peak}} = 38.3°$ ($\eta_{\text{peak}} = 0.79$) and $\delta_{\text{peak}} = 31.4°$ ($\eta_{\text{peak}} = 0.61$) were approximately held, respectively. Similarly, the critical (δ_{crit}) and the characteristic angles (δ_{car}) which were taken into account as the average values for dense and loose samples were $\delta_{\text{crit}} = 29.5°$ ($\eta_{\text{crit}} = 0.566$) and $\delta_{\text{car}} = 29°$ ($\eta_{\text{car}} = 0.555$), respectively. These two angles seemed to be the same value. According to the definition of the characteristic angles (δ_{car}) proposed by Luong [1980], it is found to be independent of the density and the confined stress. The characteristic and critical states were very similar. For loose sand at high confined stress the failure which generally occurs at the critical state would be attributed to the characteristic state as well.

For smooth surface, the peak friction angle on dense and loose samples $\delta_{\text{peak}} = 26.1°$ ($\eta_{\text{peak}} = 0.49$) and $\delta_{\text{peak}} = 23.3°$ ($\eta_{\text{peak}} = 0.43$) were held, respectively. In the same way, the critical and characteristic angles on dense sameple were 23.3° ($\eta_{\text{crit}} = 0.43$) and 18.8° ($\eta_{\text{car}}$

= 0.34), respectively. Because smooth plate did not show softening behaviour, the peak and critical values of stress ratio were almost the same on loose sample. Therefore, the critical angle on loose sample was 23.3° ($\eta_{\text{crit}} = 0.43$).

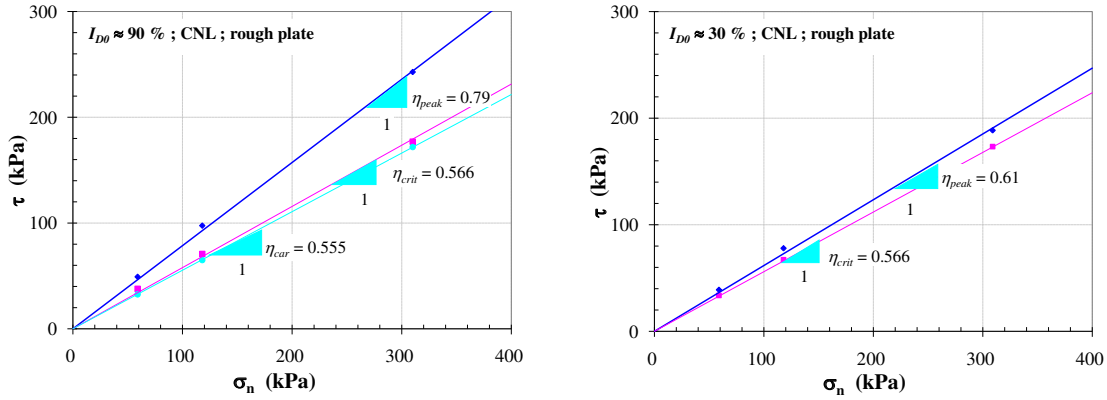

(a) (b)

Figure 2.39: Peak and characteristic stress in $\tau - \sigma_n$ plane from monotonic CNL interface tests on rough plate; (a) dense sand ($I_{D0} \approx 90\%$); (b) loose sand ($I_{D0} \approx 30\%$)

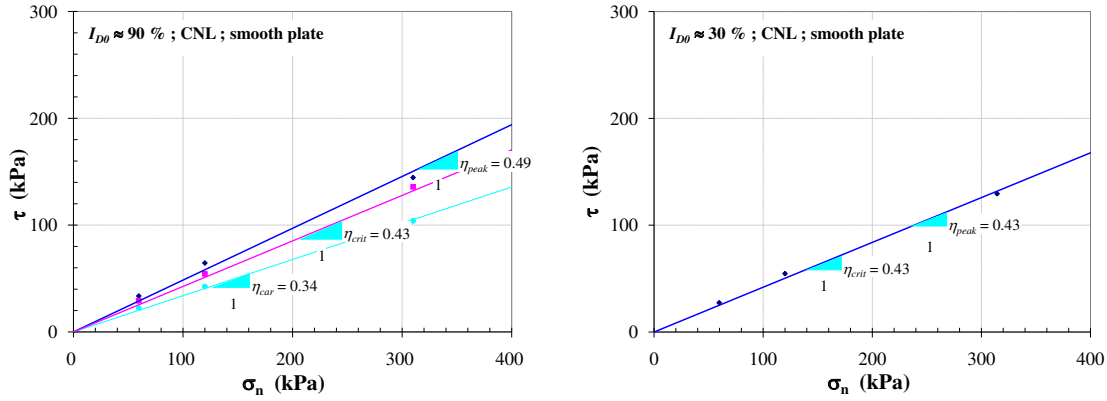

(a) (b)

Figure 2.40: Peak and characteristic stress in $\tau - \sigma_n$ plane from monotonic CNL interface tests on smooth plate; (a) dense sand ($I_{D0} \approx 90\%$) ; (b) loose sand ($I_{D0} \approx 30\%$)

It was also found that the peak interface friction angle (δ_{peak}) on rough plate was comparatively lower than the internal friction angle of Fontainebleau sand (φ_{peak}) as shown in Figure 2.41. These internal friction angles of Fontainebleau sand were obtained from available observations in triaxial tests. Tabucanon et al. [1995] also reported that the interface friction angle was lower than internal friction angle on standard shear box for Bass Strait calcareous sand, however both friction angles mobilized the same critical friction angle. They concluded that the shear resistance of interface was controlled by the deformation

of sand adjacent to the rough plate which was lower than that mearsured in sand-sand on standard shear box. For smooth plate the interface friction angle was obviously lower than those obtained from rough pate and the internal friction angle. This could be said that on smooth plate the sand slipped at the interface and the volume change could hardly be observed.

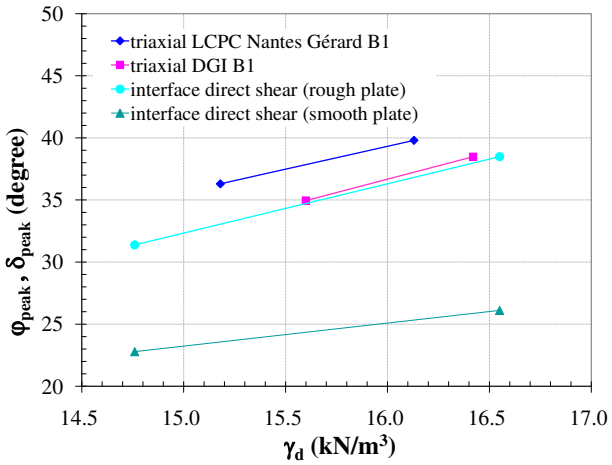

Figure 2.41: Peak interface friction angle (δ_{peak}) with rough and smooth plates in comparison with peak internal friction angle (φ_{peak}) of Fontainebleau sand

2.5 Test parameters and extracted variables from the tests

The objective of this study is to clarify the main trends (extrapolated to other interfaces) of the behaviour of granular soil-structure interface under cyclic loading with a large number of cycles. In order to formulate the results of this test campaign in a visco-plastic constitutive model in which the number of cycles (N) is the fictitious time (t), and the mean cyclic path during the regular cycles ($N > 1$) is considered more than the detail of each cycle, see Figure 2.42. So far the most salient observations in cyclic loading domain with a large number of cycles (e.g. Niemunis et al. [2005], Wichtmann [2005], Wichtmann et al. [2005]) show that the explicit method is suitable to describe the accumulation of granular soil deformation. The fist (irregular) cycle and the subsequent (regular) cycles are different due to the deformation at the beginning of cyclic loading. Therefore, the regular cycles ($N \geq 2$) are more representative for an analysis of the accumulated deformation.

All the tests are set at $N = 10^4$ cycles, at least if the failure is not reached before this objective. Moreover, as indicated before, the cycles are carried out between two shear stress thresholds (shear stress-controlled test). The data aimed in these tests are the mean cyclic paths or irreversible relative displacements as well as the interface stiffness modification, and finally the interface resistance modification during the cycles. In the $\tau - \sigma_n$, the interface variables used in the cyclic test campaign are therefore defined as (Figure 2.43):

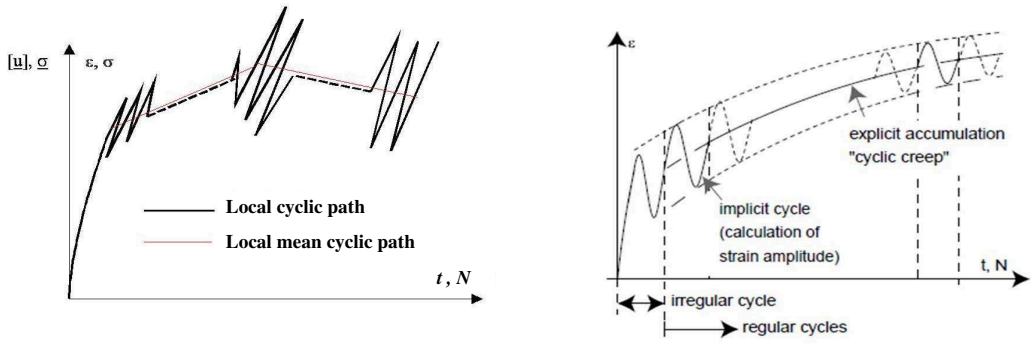

(a) (b)

Figure 2.42: (a) mean cyclic path for cyclic interface shear test; (b) calculation procedure of explicit models, Wichtmann et al. [2005]

- δ_{peak} and η_{peak} are respectively the peak friction angle (resistance) and the peak stress ratio.
- δ_{car} $(0 < \delta_{\text{car}} < \delta_{\text{peak}})$ is the characteristic angle of soil-structure interface (separating cyclic contracting and dilating domains).
- $\sigma_{\text{n cm}}$ is the level of mean cyclic normal stress in CNL tests and $\sigma_{\text{n cm0}}$ is the level of initial mean cyclic normal stress in CNS tests.
- τ_{cm} is the level of mean cyclic shear stress.
- $\Delta\tau$ is the amplitude of the cycles in terms of shear stress.
- η_{cm} is the level of mean cyclic stress ratio.

In the following, the subscript "cm" denotes the mean cyclic path. The soil-structure friction angle (δ) and mean cyclic stress ratio (η_{cm}) are expressed as:

$$\eta_{\text{cm}} = \tan\delta_{\text{cm}} = \frac{\tau_{\text{cm}}}{\sigma_{\text{n cm}}} \tag{2.11}$$

The possible maximum stress ratio (η_{max}) that can be carried out in the campaign of experimental observation is defined as:

$$\eta_{\text{max}} = \frac{\eta_{\text{cm}} + \frac{\Delta\eta}{2}}{1 - \eta_{\text{cm}}\frac{\Delta\eta}{2}} \leq \eta_{\text{peak}} \tag{2.12}$$

where $\Delta\eta = \frac{\Delta\tau}{\sigma_{\text{n cm}}}$

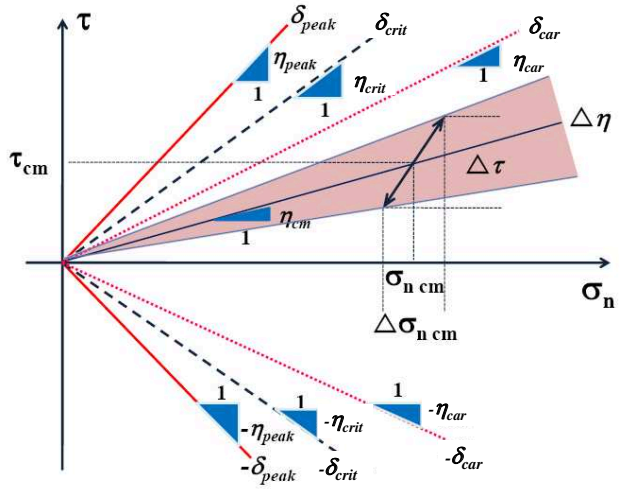

Figure 2.43: Characterization of the implemented cycles

The expected results were the displacement vectors as mean cyclic tangential $[w]_{\mathrm{cm}}$ and mean cyclic normal $[u]_{\mathrm{cm}}$ relative displacements. In addition, the evolution of normal k_{n} and tangential k_{s} stiffnesses as well as interface resistance δ_{peak} of the interface after cyclic shear loading were also expected:

$$[w]_{\mathrm{cm}} = [w]_{\mathrm{cm}}(I_{D0}, \sigma_{\mathrm{n\ cm}}, \eta_{\mathrm{n\ cm}}, N) \tag{2.13}$$

$$[u]_{\mathrm{cm}} = [u]_{\mathrm{cm}}(I_{D0}, \sigma_{\mathrm{n\ cm}}, \eta_{\mathrm{n\ cm}}, N) \tag{2.14}$$

$$k_{\mathrm{n}} = k_{\mathrm{n}}(I_{D0}, \sigma_{\mathrm{n\ cm}}, \eta_{\mathrm{n\ cm}}, N) \tag{2.15}$$

$$k_{\mathrm{s}} = k_{\mathrm{s}}(I_{D0}, \sigma_{\mathrm{n\ cm}}, \eta_{\mathrm{n\ cm}}, N) \tag{2.16}$$

$$\delta_{\mathrm{peak}} = \delta_{\mathrm{peak}}(I_{D0}, \sigma_{\mathrm{n\ cm}}, \eta_{\mathrm{n\ cm}}, N) \tag{2.17}$$

Finally, the grain breakage within interface shear zone was then observed by means of sieving method.

2.6 Operating mode and experimental biases

The procedure of cyclic test campaign in this study follows the required data set in the previous section, but induces experimental biases inherent to the direct shear test. However, testing is never ideal and therefore not completely corresponding to the wishes of the operator.

2.6.1 Operating mode

Taking into account the collection of expected information, the test procedure consisted of 5 consecutive phases:

- 1^{st} Phase: the application of normal stress since the neutral state until $\sigma_{\mathrm{n\ cm}}$
- 2^{nd} Phase: the application of shear loading until τ_{cm}
- 3^{rd} Phase: the application of N cycles of small amplitude of controlled shear stress $\Delta\tau$
- 4^{th} Phase: one great cycle of shear (after N cycles were reached) to failure
- 5^{th} Phase: discharge in shear stress (τ) and then the normal stress until $\sigma_{\mathrm{n}} = 0$, respectively.

Figure 2.44 also illustrates the scheme of the test procedure. The 2^{nd} and 3^{rd} phases were automatically controlled by the system. Additionally, the 4^{th} phase was carried out in order to characterize the change of interface resistance (δ_{peak}) due to cyclic loading. This phase could not be carried out in case of η_{cm} close to η_{peak} due to the early termination (stress state tended towards critical state).

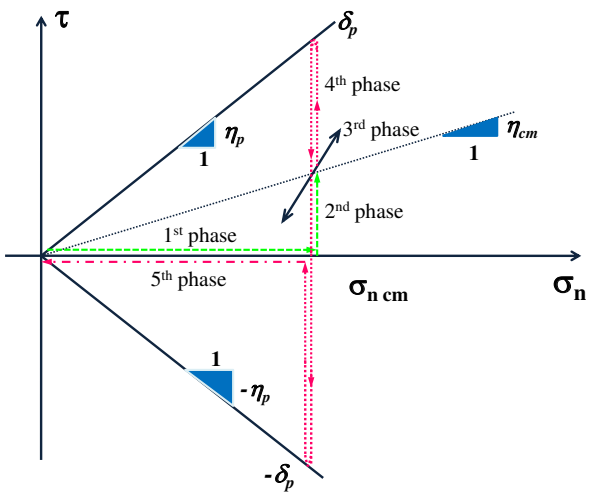

Figure 2.44: Procedure of cyclic interface direct shear tests

2.6.2 Experimental bias

The rough plates used in this study have roughness amplitude (R_{max}) of about 0.2 mm. So that the upper half shear box did not rub directly on the rough plate, a spacing of 0.3 mm, created by a pair of brass foils, was arranged between the plate and the $\frac{1}{2}$ box during the

construction of the sand sample to the desired density. Furthermore, this gap between the shear box and rough plate has to be taken into account because the leakage of sand from shear box would take place (Figure 2.45). Additional verification of this gap was that a continuous measurement of the level of the box was also recorded for all purposes by using LVDT (see Figure 2.45(b)). Thus a certain "leakage of sample" took place during the test between the $\frac{1}{2}$ box and the rough plate (Figure 2.46), equivalent to contraction interference. This loss of material, very small (approximately, 0.2 - 2 g depending on I_{D0}, σ_n, η_{cm}), was measured at end of tests. However, this leakage also occurred during the 4^{th} phase which led to the gradual leakage of sand as increasing the shear displacement $[w]$. Consequently, cyclic CNL tests without 4^{th} phase were carried out to specifically isolate the leakage of sand due to the cycles. From experimental point of view, three possible assumptions to affect the leakage of sand were;

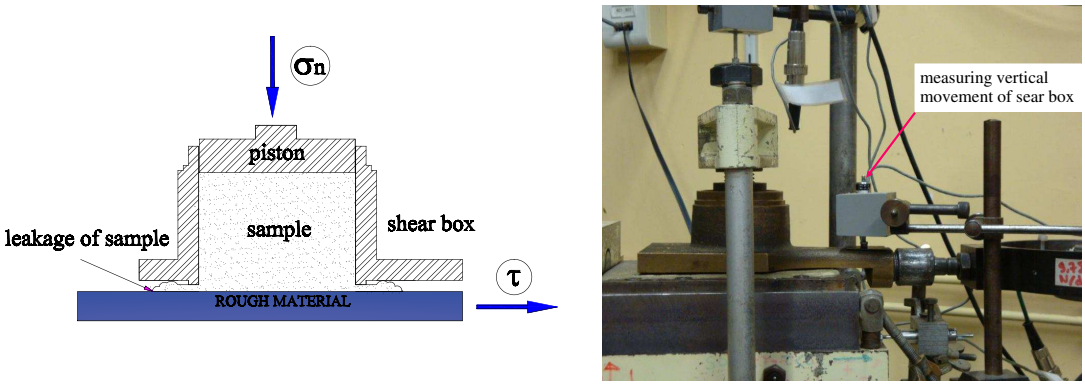

(a) (b)

Figure 2.45: (a) Leakage of sample during cyclic interface shear tests; (b) Additional verification of vertical movement of shear box

- proportional to time or number of cycles during the tests.
- proportional to accumulated $[w]$
- proportional to $[w]$ and the vertical displacement of the box.

However, the effect of the vertical relative displacement of the box compared to the rough plate was difficult to quantify. Figure 2.47 illustrates two possibilities of fictitious contractions for correcting the normal displacement $[u]$. The first one which was proportional to the number of cycles or time led to too much fictitious contraction, especially, in case of cyclic test with final shear phase (final great cycle). When taking into account the normal relative displacement measured and the fictitious contraction, the normal displacement refined became too much dilative. This would be inaccurate in some cases of dense sand. Whereas the test without final shear phase would be reasonalbe when taking into account the fictitious contraction proportional to the number of cycles or time. The second one was proportional to the accumulation of tangential displacement of cyclic loading phase including the post-cyclic phase (final great cycle). This method provided less fictitious con-

traction than the previous one and the refined normal displacement seemed proper for any conditions. Therefore, the reasonable solution found in this study was that the leakage of sand was proportional to the accumulated $[w]$. A simple inclusive correction can then be performed by considering the loss of sand as the fictitious contraction $[u]_{\text{loss}}$:

$$[u]_{\text{loss}} = -\frac{m_{\text{loss}} g}{\gamma A} \cdot \frac{[w]_{\text{cm Nf}}}{[w]_{\text{acc}}} \tag{2.18}$$

where:

m_{loss} : total mass of lost sand measured at the end of test;

γ : average specific gravity of sand at the interface during the test;

A : the interface area;

g : gravity acceleration;

$[w]_{\text{cm Nf}}$: mean cyclic shear displacement $[w]$ at the final cycle;

$[w]_{\text{acc}}$: accumulated shear displacement $[w]$, taking into account the post-cyclic phase (final great cycle);

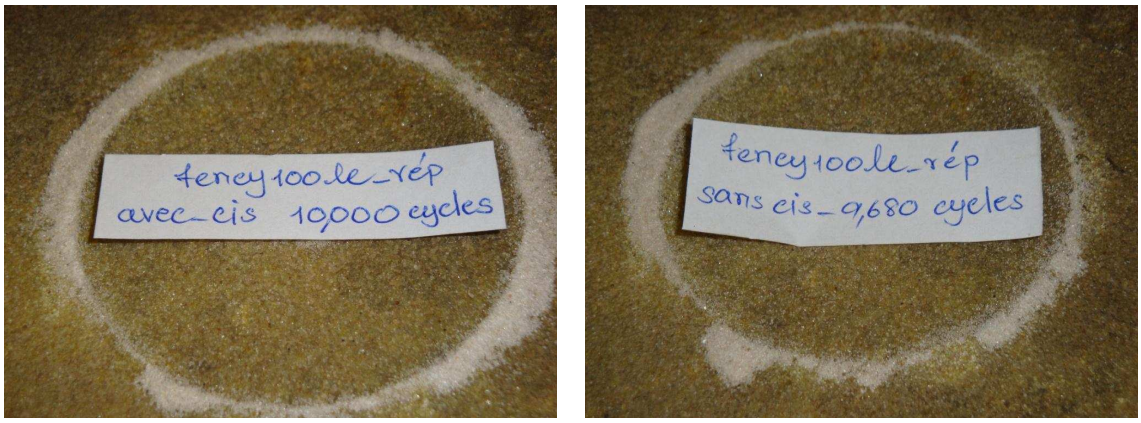

(a) (b)

Figure 2.46: Examples of loss of material after testing with $\sigma_n = 120$ kPa on loose sand ($I_{D0} \approx 30\%$); (a) loss of material after testing with post-cyclic phase; (b) loss of material after testing without post-cyclic phase

Consequently, correction of $[u]_{\text{cm}}$ was systematically applied to unrefined results $[u]_{\text{unrefined}}$ as:

$$[u]_{\text{cm}} = [u]_{\text{cm unrefined}} - [u]_{\text{loss}} \cdot \frac{[w]_{\text{cm}}}{[w]_{\text{acc}}} \tag{2.19}$$

Figure 2.48 shows the typical $[u]_{\mathrm{cm}}$ corrected from the assumption of lost sand proportional to the accumulated $[w]$ on dense sand with $\sigma_n = 120$ kPa and $\eta_{\mathrm{cm}} \approx \frac{1}{2}\eta_{\mathrm{peak}}$ ($45 < \tau < 55$ kPa). This example also illustrates the reproducibility of cyclic CNL interface shear tests by the results of two tests of which the first one included the post-cyclic phase and the other excluded the post-cyclic phase. In the same way, the shear displacement $[w]_{\mathrm{cm}}$ are also presented. The reproducibility of cyclic CNL interface shear tests was satisfactory.

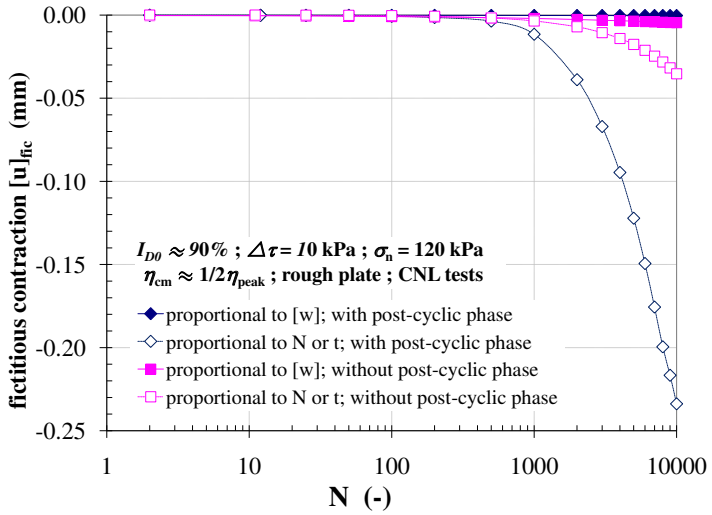

Figure 2.47: Example of fictitious contractance proportional to $[w]$ and N or t for cyclic CNL test on dense sand ($I_{D0} \approx 90\%$) with $\sigma_n = 120$ kPa, $\eta_{\mathrm{cm}} \approx \frac{1}{2}\eta_{\mathrm{peak}}$, $\Delta\tau = 10$ kPa

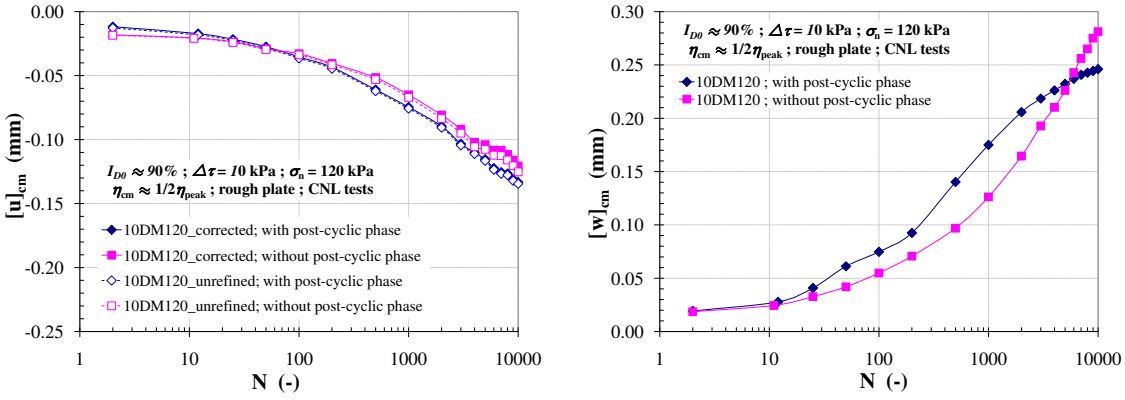

Figure 2.48: Cyclic CNL test on dense sand ($I_{D0} \approx 90\%$) with $\sigma_n = 120$ kPa, $\eta_{\mathrm{cm}} \approx \frac{1}{2}\eta_{\mathrm{peak}}$, $\Delta\tau = 10$ kPa (a) Correction of $[u]_{\mathrm{cm}}$ proportional to $[w]$ as a function of N; (b) Evolution of $[w]_{\mathrm{cm}}$ as a function of N

2.7 Identification tests (cyclic CNL tests on rough plate)

A test program was conceived according to the philosophy of the experimental design. These tests were classified into two groups for two purposes:

- Identification series aimed to study the interface behaviour sujected to cyclic loading under CNL conditions. The influence of initial normal stress (σ_n), amplitude of cycles ($\Delta\tau$), level of mean cyclic stress ratio (η_{cm}) on the intensity of displacement was observed.
- Validation series aimed to highlight the phenomena of interface under CNS condition and by changing the consecutive package of cycles.

The latter will be described in the following section.

The main parameters of cyclic CNL tests in this study are the initial density of sand (I_{D0}), the level of mean cyclic normal stress ($\sigma_{\mathrm{n\,cm}}$), the level of mean cyclic shear stress ($\tau_{\mathrm{n\,cm}}$) and the cyclic amplitude ($\Delta\tau$). In terms of normal stress level, the cyclic tests were guided by the sizes of the current piles as well as by the prescribed limits of the direct shear device. The small normal stress levels were forbidden for the reason of precision of the tests. In addition, the same shear box (ϕ = 60 mm) was used for the whole series of tests. In this study, the minimum normal stress level was 60 kPa while the maximum normal stress level was 310 kPa which corresponds to a depth of about 40 m for a bored pile and to 15-20 m for a driven pile.

Having known the peak (η_{peak}) and characteristic (η_{car}) stress ratios from monotonic CNL tests, three levels of mean cyclic stress ratio (η_{cm}) were decided to perform, i.e. low ($\eta_{\mathrm{cm}} = 0$), medium ($\eta_{\mathrm{cm}} \approx \frac{1}{2}\eta_{\mathrm{peak}}$) and high (as close as possible to η_{peak}; $\eta_{\mathrm{cm}} \approx 9/10\eta_{\mathrm{peak}}$). These tests allowed to get the overview on the cyclic interface response. In case of high level of η_{cm} ($\eta_{\mathrm{cm}} \approx 9/10\eta_{\mathrm{peak}}$), η_{cm} varied in the range $0.50 < \eta_{\mathrm{cm}} < 0.73$ depending on σ_n, I_{D0} and cyclic amplitude ($\Delta\tau$). Moreover, four supplementary tests with $\Delta\tau$ = 40 kPa for σ_n = 310 kPa were performed in order to properly describe the influence of cyclic amplitude (at $\eta_{\mathrm{cm}} = \frac{1}{2}\eta_{\mathrm{peak}}$ and $\eta_{\mathrm{cm}} \approx 9/10\eta_{\mathrm{peak}}$). All tests were planned to 10^4 cycles, unless early termination was reached. This early termination was found in case of η_{cm} close to η_{peak}. These tests are summarized in Table 2.4.

The designation of these cyclic CNL tests is as follows:

- The first two digits of the test (e.g. 10, 20 and 40) indicate the amplitude of cycles in terms of shear stress ($\Delta\tau$).
- The first capital letter denotes the type of initial density, "L" for loose sand and "D" for dense sand.
- The following capital letter denotes the level of mean cyclic stress ratio (η_{cm}): "L" (low, $\eta_{\mathrm{cm}} = 0$), "M" (medium, $\eta_{\mathrm{cm}} \approx \frac{1}{2}\eta_{\mathrm{peak}}$) and "H" (high, $\eta_{\mathrm{cm}} \approx 9/10\eta_{\mathrm{peak}}$)
- The last two or three digits of the test (e.g. 60, 120 and 310) indicate the initial normal stress (σ_n).

Table 2.4: Tests for identification, CNL path, parameters

N°	I_{D0} (%)	σ_n (kPa)	level of η_{cm} (-)	τ (kPa)	η_{cm} (-)	$\Delta\tau$ (kPa)
10LL60	30	60	0	$-5 < \tau < 5$	0	10
10LM60	30	60	$\approx 1/2\eta_{\text{peak}}$	$10 < \tau < 20$	0.25	10
10LH60	30	60	$\approx 9/10\eta_{\text{peak}}$	$25 < \tau < 35$	0.50	10
10LL120	30	120	0	$-5 < \tau < 5$	0	10
10LM120	30	120	$\approx 1/2\eta_{\text{peak}}$	$30 < \tau < 40$	0.29	10
10LH120	30	120	$\approx 9/10\eta_{\text{peak}}$	$55 < \tau < 65$	0.50	10
10LL310	30	310	0	$-5 < \tau < 5$	0	10
10LM310	30	310	$\approx 1/2\eta_{\text{peak}}$	$83 < \tau < 93$	0.28	10
10LH310	30	310	$\approx 9/10\eta_{\text{peak}}$	$170 < \tau < 180$	0.57	10
10DL60	90	60	0	$-5 < \tau < 5$	0	10
10DM60	90	60	$\approx 1/2\eta_{\text{peak}}$	$15 < \tau < 25$	0.33	10
10DH60	90	60	$\approx 9/10\eta_{\text{peak}}$	$32 < \tau < 42$	0.62	10
10DL120	90	120	0	$-5 < \tau < 5$	0	10
10DM120	90	120	$\approx 1/2\eta_{\text{peak}}$	$45 < \tau < 55$	0.40	10
10DH120	90	120	$\approx 9/10\eta_{\text{peak}}$	$85 < \tau < 95$	0.75	10
10DL310	90	310	0	$-5 < \tau < 5$	0	10
10DM310	90	310	$\approx 1/2\eta_{\text{peak}}$	$100 < \tau < 110$	0.34	10
10DH310	90	310	$\approx 9/10\eta_{\text{peak}}$	$50 < \tau < 60$	0.71	10
20LL60	30	60	0	$-10 < \tau < 10$	0	20
20LM60	30	60	$\approx 1/2\eta_{\text{peak}}$	$5 < \tau < 25$	0.25	20
20LH60	30	60	$\approx 9/10\eta_{\text{peak}}$	$15 < \tau < 25$	0.42	20
20LM120	30	120	$\approx 1/2\eta_{\text{peak}}$	$25 < \tau < 45$	0.29	20
20LL310	30	310	0	$-10 < \tau < 10$	0	20
20LM310	30	310	$\approx 1/2\eta_{\text{peak}}$	$78 < \tau < 98$	0.28	20
20LH310	30	310	$\approx 9/10\eta_{\text{peak}}$	$160 < \tau < 180$	0.55	20
20DL60	90	60	0	$-10 < \tau < 10$	0	20
20DM60	90	60	$\approx 1/2\eta_{\text{peak}}$	$10 < \tau < 30$	0.33	20
20DH60	90	60	$\approx 9/10\eta_{\text{peak}}$	$25 < \tau < 45$	0.58	20
20DM120	90	120	$\approx 1/2\eta_{\text{peak}}$	$35 < \tau < 55$	0.37	20
20DL310	90	310	0	$-10 < \tau < 10$	0	20
20DM310	90	310	$\approx 1/2\eta_{\text{peak}}$	$95 < \tau < 115$	0.34	20
20DH310	90	310	$\approx 9/10\eta_{\text{peak}}$	$210 < \tau < 230$	0.71	20
40LM310	30	310	$\approx 1/2\eta_{\text{peak}}$	$68 < \tau < 108$	0.28	40
40LH310	30	310	$\approx 9/10\eta_{\text{peak}}$	$140 < \tau < 180$	0.52	40
40DM310	90	310	$\approx 1/2\eta_{\text{peak}}$	$85 < \tau < 125$	0.34	40
40DH310	90	310	$\approx 9/10\eta_{\text{peak}}$	$190 < \tau < 230$	0.68	40

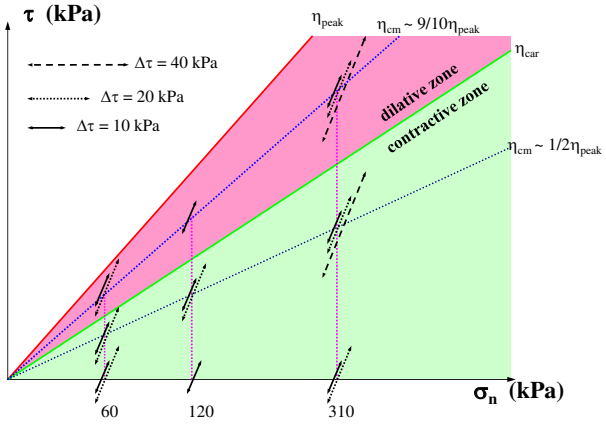

Figure 2.49: Tests of identification series with CNL path on dense sand ($I_{D0} \approx 90\%$), $\Delta\tau$ = 10, 20 and 40 kPa

Figure 2.49 also shows the scheme of identification tests on both densities ($I_{D0} \approx 90\%$) with the amplitude of cycles $\Delta\tau = 10$, 20 and 40 kPa.

From the results obtained during this campaign, the first analysis concerns the global behaviour of the sample. With a large number of cycles, according to Wichtmann [2005] and Wichtmann et al. [2005], the fist (irregular) cycle and the subsequent (regular) cycles are distinguished due to the significant difference in displacements at the beginning of cyclic loading. Figure 2.50 and 2.51 show respectively the typical $\tau - [w]$ as well as $[u] - [w]$ diagrams and selected number of cycles of cyclic CNL test on loose and dense samples with $\sigma_n = 120$ kPa, at $\eta_{\text{cm}} = 0$, $\frac{1}{2}\eta_{\text{peak}}$ and $9/10\eta_{\text{peak}}$, $\Delta\tau = 10$ kPa.

From typical test results on both densities, it was clear that the first cycle obviously differed from the subsequent ones. On loose sand the contractive behaviour was observed through the test. The intensity of relative displacements obviously depended on the level of η_{cm}. On dense sand, the existence of characteristic state, passage from contractive to dilative behaviour, proposed by Luong [1980] was observed when η_{cm} was in the range of $\eta_{\text{car}} < \eta_{\text{cm}} < \eta_{\text{peak}}$, otherwise the interface behaved contractively in the range of $\eta_{\text{cm}} < \eta_{\text{car}}$. This characteristic state obviously depended on the level of stress ratio (η_{cm}) as can be seen in "$10DH120$" test. The shear displacement at low level of stress ratio ($\eta_{\text{cm}} = 0$) was hardly observed. At high level of η_{cm} on both densities, after reaching certain number of cycles with large enough shear displacement $[w]$, the shear stress could not evolve the next cycle even though the normal stress was kept constant (the shear stress tended to the critical state), consequently, the evolution of normal displacement $[u]$ was almost constant (critical state). It should be noticed that $[u]$ and $[u]_{\text{cm}}$ are physically limited due to the mandatory contact between the grains, which is not the case for $[w]$ and $[w]_{\text{cm}}$

In this study the mean paths during cycles were considered more than the detail of each cycle. The mean cyclic displacements $[u]_{\text{cm}}$ and $[w]_{\text{cm}}$ were then taken into account from $N = 2$. Due to the amplitudes of cycles in terms of shear stress applied ($\Delta\tau$) were small,

whether $\Delta\tau$ = 10, 20, 40 kPa, which led to some ambiguities of corresponding response (see Figure 2.6). Therefore, certain of the consecutive cycles would be more representative. In the following figures, $[u]_{\mathrm{cm}}$ and $[w]_{\mathrm{cm}}$ in dependence of the number of cycles (N) represent the mean cyclic path of ten consecutive cycles (e.g., N = 2, 12, 25 and 50... represent respectively the mean path of N = 2-11, 12-21, 25-34 and 50-59...).

From the experimental observations performed in the identification series and those from the complete literatures, it is possible to distinguish the main features of the intrinsic behaviour and the factors influencing the overall behaviour of granular soil-structure interface under cyclic loading.

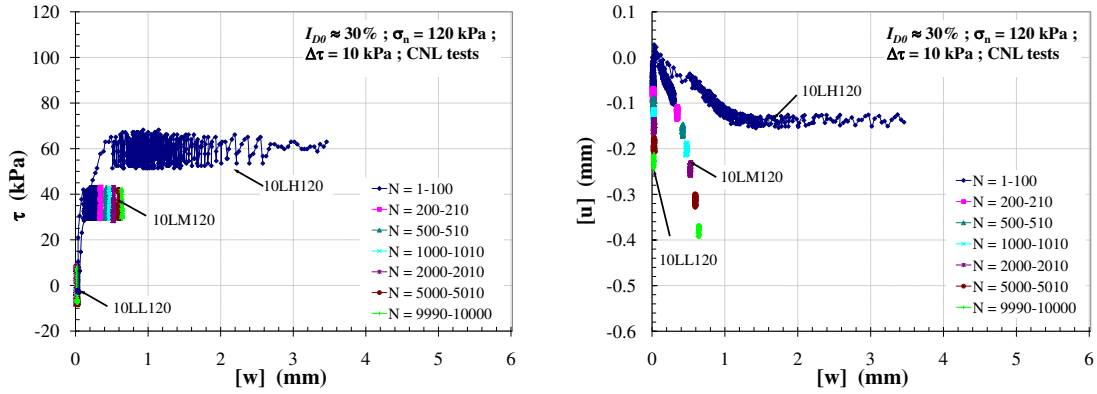

(a) (b)

Figure 2.50: Typical cyclic CNL tests on loose sand ($I_{D0} \approx 30\%$) with σ_n = 120 kPa, $\Delta\tau$ = 10 kPa

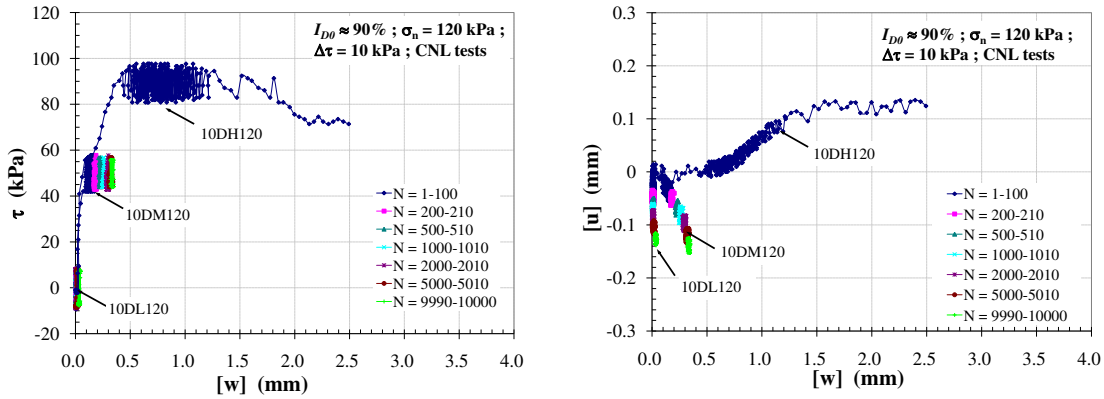

(a) (b)

Figure 2.51: Typical cyclic CNL tests on dense sand ($I_{D0} \approx 90\%$) with σ_n = 120 kPa, $\Delta\tau$ = 10 kPa

2.7.1 Influence of density (I_{D0})

The influence of density was observed on two distinct densities ($I_{D0} \approx 30\%$ and $I_{D0} \approx 90\%$). Under cyclic CNL condition, the structure of sand-structure interface varied as a result of the progressive densification due to cycles. For instance, Figure 2.52 and 2.53 show respectively the mean cyclic normal $[u]_{\text{cm}}$ and shear $[w]_{\text{cm}}$ displacements with the number of cycles during the cycles $N > 1$ on loose and dense samples with $\sigma_n = 120$ kPa, three levels of mean cyclic stress ratio, η_{cm} (i.e. 0, $\approx \frac{1}{2}\eta_{\text{peak}}$ and $\approx 9/10\eta_{\text{peak}}$) with a cyclic amplitude of $\Delta\tau = 10$ kPa. At low density the interface behaved contractively for all levels of η_{cm}. The reduction rate in contraction increased as a function of N. On the other hand, for high density, a dilative behaviour occurred at η_{cm} close to η_{peak} in the range between η_{car} and η_{peak} whereas the interface behaved contractively in the range between $0 < \eta_{\text{cm}} < \eta_{\text{car}}$.

Considering the evolution of $[w]_{\text{cm}}$ in dependence on the number of cycles (N), these two figures qualitatively provide the same information for loose and dense sands. There was an exponential acceleration of $[w]_{\text{cm}}$ when η_{cm} tended towards η_{peak}. At the level of η_{cm} close to η_{peak}, the interface underwent the significant increase of $[w]_{\text{cm}}$ and then the stress state could not evolve the next cycle due to the experimental limit of $[w]_{\text{cm}}$.

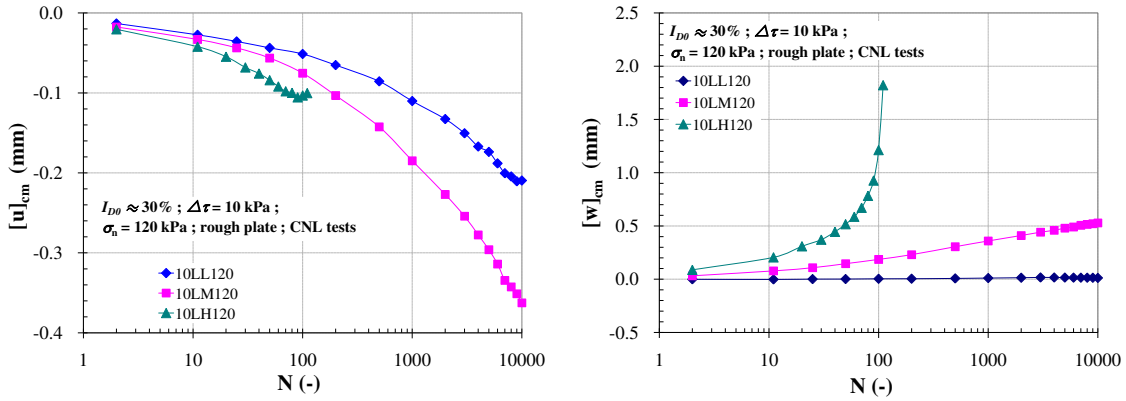

(a) (b)

Figure 2.52: Evolution of $[u]_{\text{cm}}$ and $[w]_{\text{cm}}$ in dependence on the number of cycles (N) for cyclic CNL tests on loose sand ($I_{D0} \approx 30\%$), rough plate, $\sigma_n = 120$ kPa, $\Delta\tau = 10$ kPa

In case of $\eta_{\text{cm}} = 0$ ($10LL120$ and $10DL120$), $[w]_{\text{cm}}$ was observed to be very small. This was generally found in the range of $\pm$ 0.10 - 0.16 mm (depending on σ_n and I_{D0}). Therefore, it would be concluded that the interface behaviour had no prominent shear displacement ($[w]_{\text{cm}}$) at $\eta_{\text{cm}} = 0$. In modeling part which will be described in the following chapter $[w]_{\text{cm}}$ is deduced to be zero for $\eta_{\text{cm}} = 0$. With increasing I_{D0}, the rate of $[u]_{\text{cm}}$ and $[w]_{\text{cm}}$ obviously decreased.

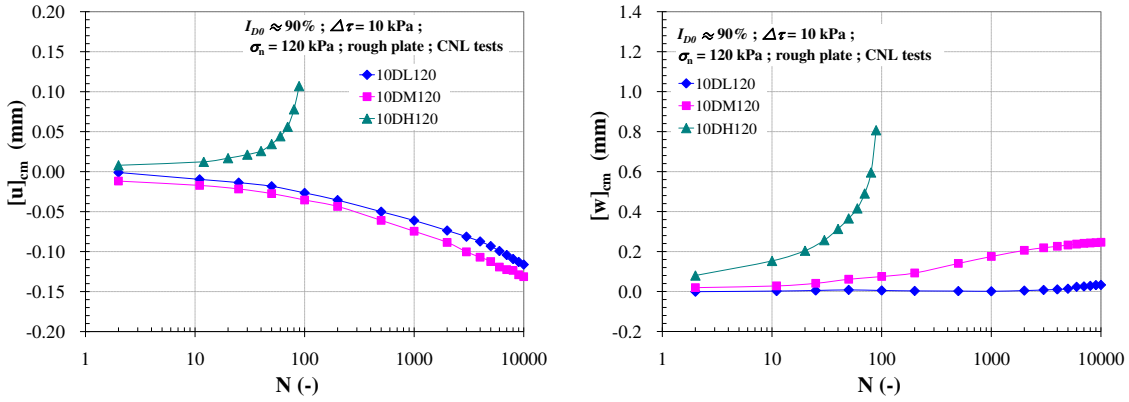

Figure 2.53: Evolution of $[u]_{\mathrm{cm}}$ and $[w]_{\mathrm{cm}}$ in dependence on the number of cycles (N) for cyclic CNL tests on dense sand ($I_{D0} \approx 90\%$), rough plate, $\sigma_n = 120$ kPa, $\Delta\tau = 10$ kPa

Figure 2.54 and 2.55 show the evolution of the local tangent stiffness (k_s) and normal stiffnesses (k_n), corresponding to η_{cm}, on loose and dense sands (with $\sigma_n = 120$ kPa, $\Delta\tau = 10$ kPa), respectively. The evolution of both kinds of stiffness resulted from cyclic loading application. Generally, the shear as well as the normal stiffnesses of interface evolving during the cyclic loading can be expressed as:

$$k_s = \frac{d\tau}{d[w]} \quad ; \quad k_n = \frac{d\sigma}{d[u]} \tag{2.20}$$

However, with the stiffness relation expressed above, it seemed ambiguous in evaluating the evolution of stiffness during the consecutive cycles. This was due to the ambiguous response when applying the cyclic shear stress as mentioned before. This ambiguity, especially the shear stiffness k_s, would obviously arise from the tests performed at $\eta_{\mathrm{cm}} = 0$. At this level ($\eta_{\mathrm{cm}} = 0$) the evolution of shear displacement was not steady during cyclic shearing or it could be negligible. To properly achieve this purpose, the evolution of stiffness relavent to the density would be considered. Therefore, with the small amplitude of cycles and the mean cyclic path was considered more than the detail of each cycle in this study, the evolution of stiffness during cyclic loading can therefore be defined in terms of the evolution of density:

$$k_s = k_{\mathrm{s\ mono}} \cdot \left(\frac{\gamma_{\mathrm{d}}}{\gamma_{\mathrm{d0}}}\right)^n \quad ; \quad k_n = k_{\mathrm{n\ mono}} \cdot \left(\frac{\gamma_{\mathrm{d}}}{\gamma_{\mathrm{d0}}}\right)^n \tag{2.21}$$

where the subscript "mono" denotes the stiffness derived from monotonic tests, γ_{d} and γ_{d0} are respectively the current and initial density. The power "n" is supposed to be constant, in this study $n = 0.50$ is used for both kinds of stiffness.

The evolution of normal stiffness (k_n) was obviously higher than that of shear stiffness (k_s). This was due to the interface thickness being taken into account for evaluating the normal

stiffness. For both kinds of stiffness, a stiffening of the interface for the low values of η_{cm} ($\eta_{\mathrm{cm}} = 0$ and $\approx \frac{1}{2}\eta_{\mathrm{peak}}$) could be observed on both densities. The stiffening of the interface increased as a function of η_{cm} within the range of $\eta_{\mathrm{cm}} < \eta_{\mathrm{car}}$. On the other hand a violent softening, the consequence of the dilative behaviour when η_{cm} tended towards η_{peak}, was significant on dense sample.

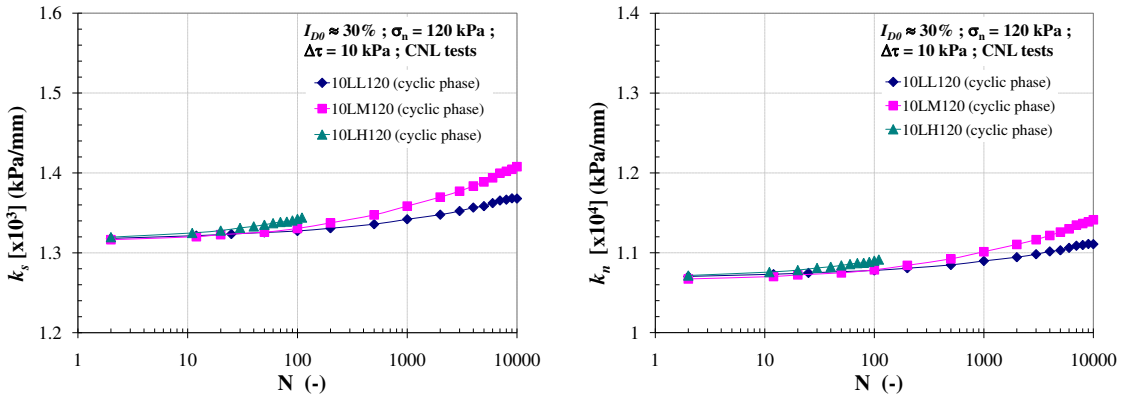

(a) (b)

Figure 2.54: Evolution of local stiffness in dependence on the number of cycles (N) for cyclic CNL tests on loose sand ($I_D \approx 30\%$), rough plate, $\sigma_n = 120$ kPa, $\Delta\tau = 10$ kPa; (a) tangent stiffness (k_s); (b) normal stiffness (k_n)

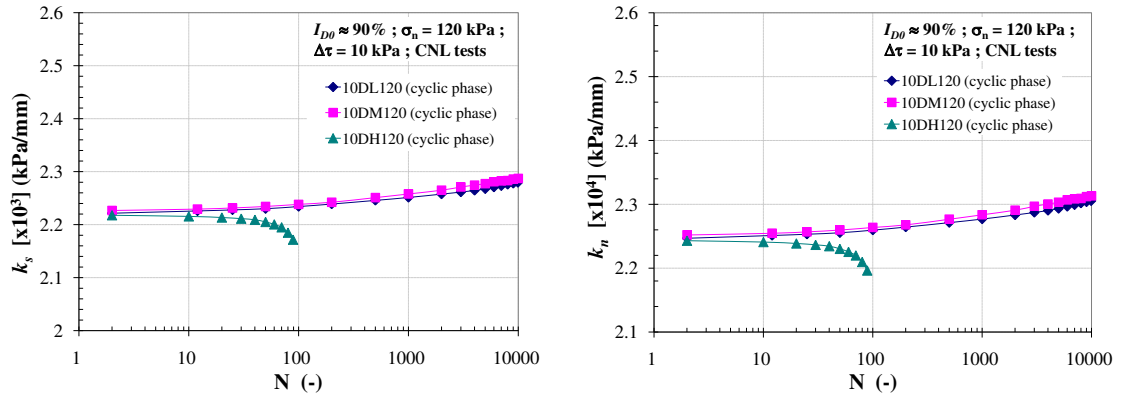

(a) (b)

Figure 2.55: Evolution of local stiffness in dependence on the number of cycles (N) for cyclic CNL tests on dense sand ($I_{D0} \approx 90\%$), rough plate, $\sigma_n = 120$ kPa, $\Delta\tau = 10$ kPa; (a) tangent stiffness (k_s); (b) normal stiffness (k_n)

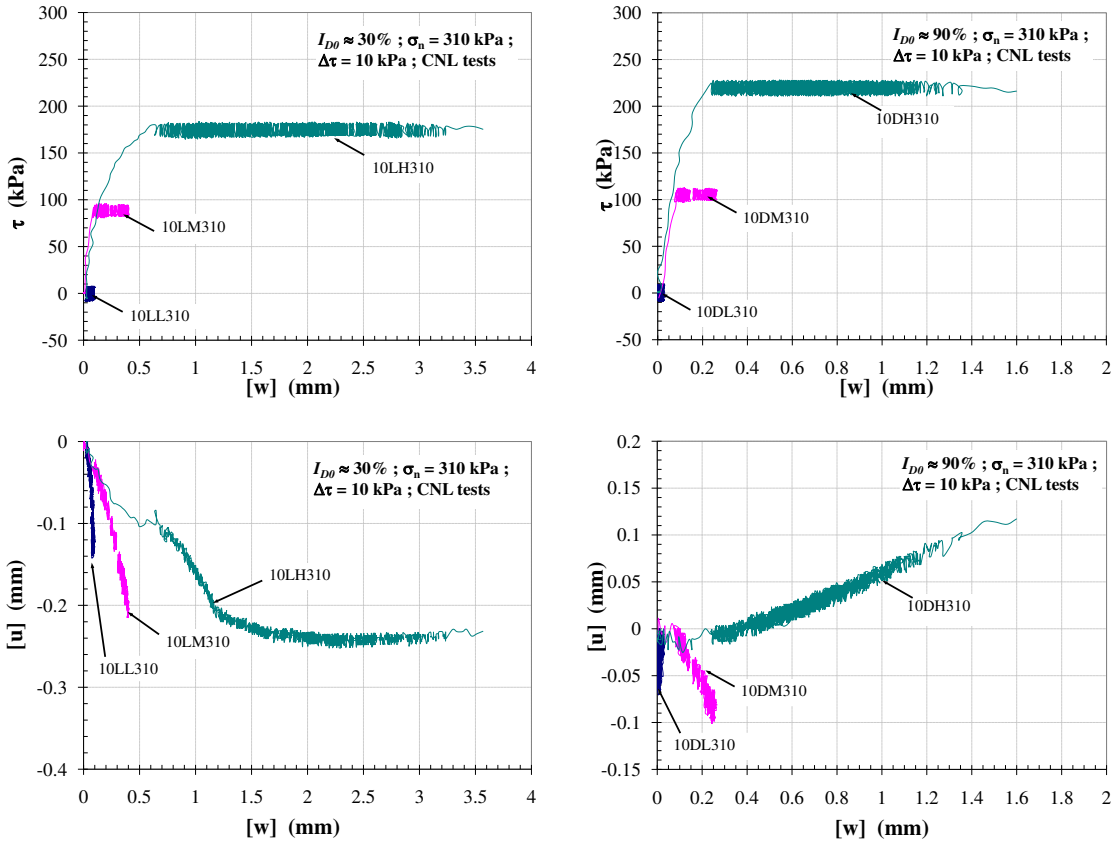

Figure 2.56: Typical cyclic CNL tests with rough plate, $\sigma_n = 310$ kPa, $\Delta\tau = 10$ kPa, on loose sand ($I_{D0} \approx 30\%$) and dense sand ($I_{D0} \approx 90\%$)

2.7.2 Influence of initial normal stress (σ_n)

The dependence of the intensity of $[u]_{\text{cm}}$ and $[w]_{\text{cm}}$ on the initial normal stress was studied in three different values of σ_n (60, 120 and 310 kPa). Figure 2.56 shows typical cyclic CNL tests with $\sigma_n = 310$ kPa, $\Delta\tau = 10$ kPa on both densities. Similarly, the overview response of these tests showed the similar trend as can be seen in the tests with $\sigma_n = 120$ kPa. The existence of characteristic state could be observed when η_{cm} was close to η_{peak} on dense sand.

Figure 2.57 shows the evolution of $[u]_{\text{cm}}$ and $[w]_{\text{cm}}$ in dependence on N (at level of $\eta_{\text{cm}} \approx \frac{1}{2}\eta_{\text{peak}}$) with three values of initial normal stress ($\sigma_n = 60$, 120 and 310 kPa), cyclic amplitude $\Delta\tau = 10$ kPa on both densities. With high value of σ_n the interface was restrained to expand during cyclic shearing, therefore the rate of $[u]_{\text{cm}}$ and $[w]_{\text{cm}}$ in case of $\sigma_n = 310$ kPa obviously decreased on both densities.

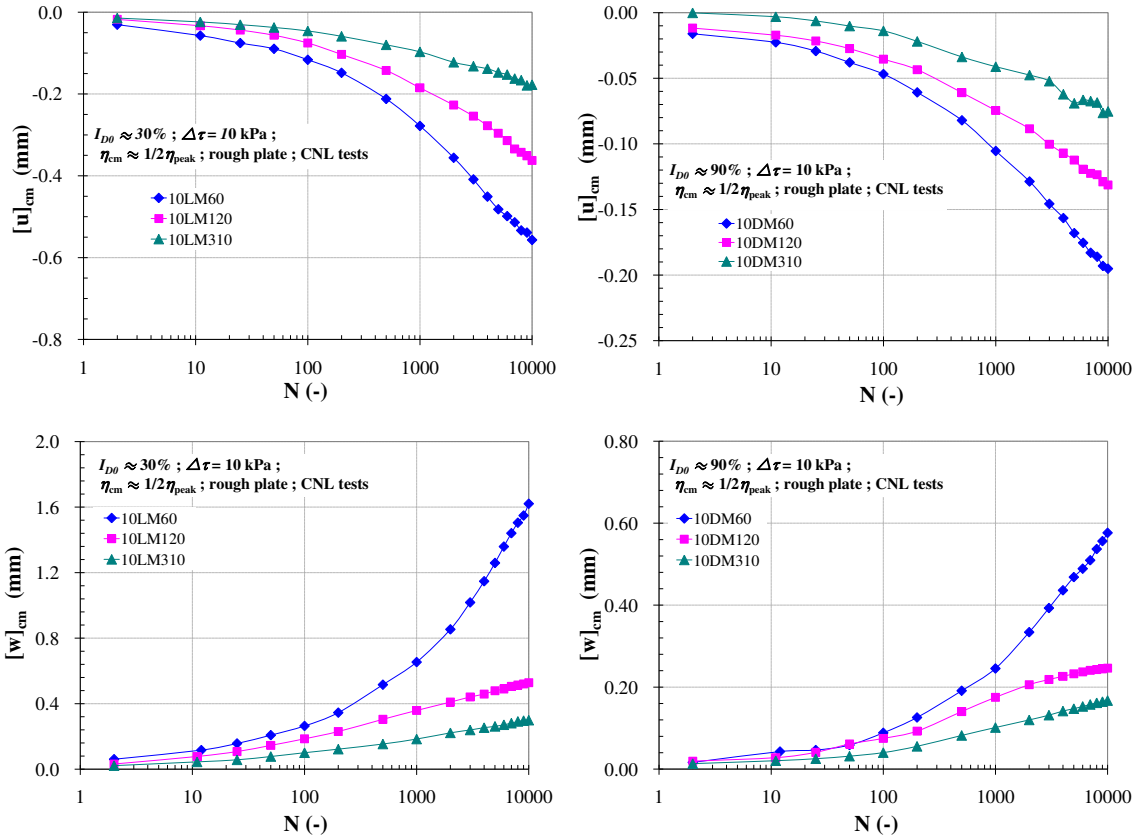

Figure 2.57: Evolution of $[u]_{\mathrm{cm}}$ and $[w]_{\mathrm{cm}}$ in dependence on the number of cycles (N) for cyclic CNL tests on loose sand ($I_{D0} \approx 30\%$) and dense sand ($I_{D0} \approx 90\%$) with $\sigma_n = 60$, 120 and 310 kPa, $\eta_{\mathrm{cm}} \approx \frac{1}{2}\eta_{\mathrm{peak}}$, $\Delta\tau = 10$ kPa

In case of η_{cm} close to η_{peak}, Figure 2.58 also shows the evolution of $[u]_{\mathrm{cm}}$ and $[w]_{\mathrm{cm}}$ as a function of number of cycles (N) for three values of initial normal stress (σ_n) at $\eta_{\mathrm{cm}} \approx 9/10\eta_{\mathrm{peak}}$, $\Delta\tau = 10$ kPa. On loose sand, the contractive behaviour was evident. It was found that a number of cycles for reaching the critical state (the state that the cyclic loading could not evolve the next one) mainly depended on the stress state (e.g. η_{cm} and $\Delta\tau$ in $\tau - \sigma$ plane). Although the level of $\eta_{\mathrm{cm}} = 0.50$ ($25 < \tau < 35$ kPa) in case of $10LH60$ was slighly lower than $\eta_{\mathrm{cm}} = 0.57$ ($170 < \tau < 180$ kPa) in case of $10LH310$, but the ampltitude of cycles normalized with normal stress as expressed by $\Delta\eta = \Delta\tau/\sigma_n$ would have more influence for reaching the critical state in case of $10LH60$ than $10LH310$. A number of cycles for reaching the critical state in $10LH60$ (324 cycles) were less than those in $10LH310$ (3,230 cycles). On dense sand, the dilative behaviour was evident which the rate of dilation decreased with increasing σ_n. The intensity rate of $[w]_{\mathrm{cm}}$ at this level decreased when σ_n and I_{D0} increased. At low density as well as low normal stress, the interface could reach farther $[w]_{\mathrm{cm}}$ (e.g. $[w]_{\mathrm{cm}} > 6$mm for $\sigma_n = 60$ kPa on $I_{D0} = 30\%$).

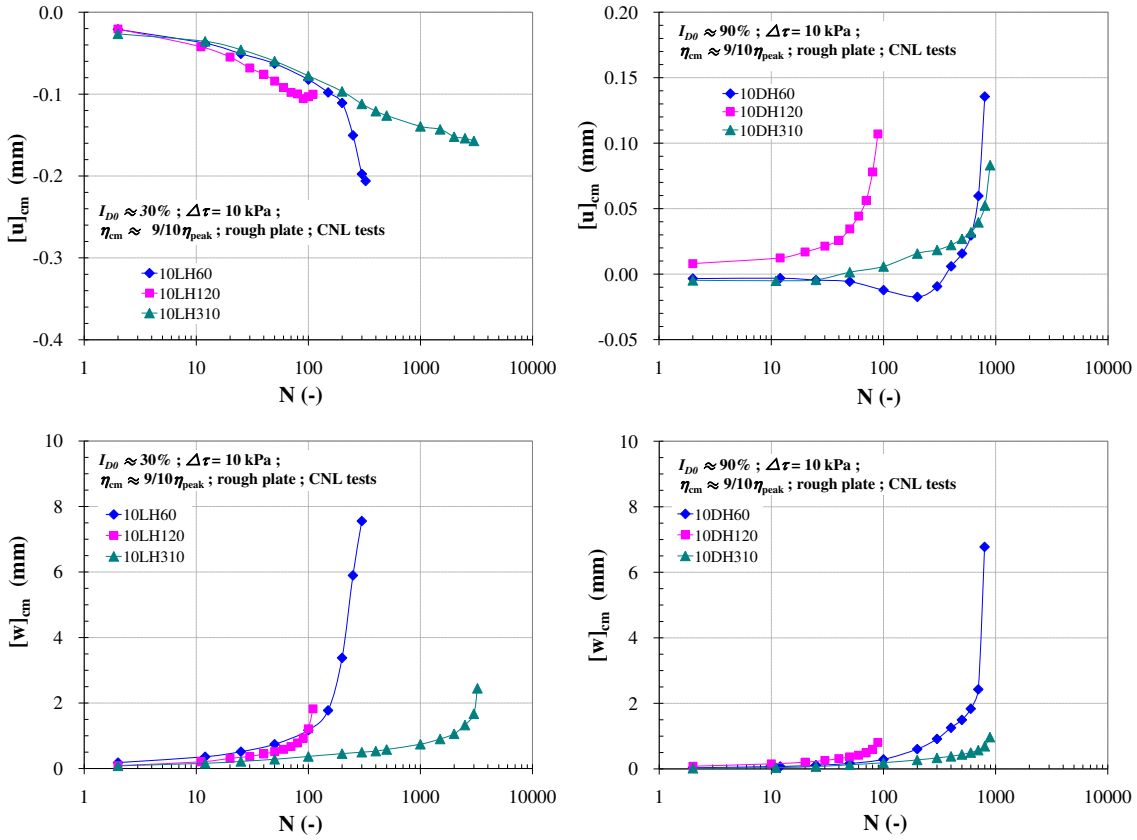

Figure 2.58: Evolution of $[u]_{\mathrm{cm}}$ and $[w]_{\mathrm{cm}}$ in dependence on the number of cycles (N) for cyclic CNL tests on loose sand ($I_{D0} \approx 30\%$) and dense sand ($I_{D0} \approx 90\%$) with $\sigma_n = 60$, 120 and 310 kPa, $\eta_{\mathrm{cm}} \approx 9/10\eta_{\mathrm{peak}}$, $\Delta\tau = 10$ kPa

2.7.3 Influence of mean cyclic stress ratio η_{cm}

The effect of mean cyclic stress ratio is typically presented by the tests of $\sigma_n = 120$ kPa for three levels of η_{cm} (i.e. 0, $\approx \frac{1}{2}\eta_{\mathrm{peak}}$ and $\approx 9/10\eta_{\mathrm{peak}}$) with a cyclic amplitude $\Delta\tau = 10$ kPa (see also Figure 2.52 and 2.53). In case of η_{cm} close to η_{peak}, η_{cm} was chosen according to σ_n, I_{D0} and cyclic amplitude $\Delta\tau$ (e.g. $\eta_{\mathrm{cm}} = 0.73$ on dense sand and $\eta_{\mathrm{cm}} = 0.50$ on loose sand were chosen for $\sigma_n = 120$ kPa) as shown in Figure 2.59. The intensity of relative displacements significantly depended on the level of η_{cm}.

For loose sand, see Figure 2.52, the rate of $[u]_{\mathrm{cm}}$ and $[w]_{\mathrm{cm}}$ obviously increased with increasing the level of η_{cm}. However, for the level of η_{cm} close to η_{peak} ($\eta_{\mathrm{cm}} = 0.50$) even below η_{car} ($\eta_{\mathrm{car}} = 0.555$), the interface could reach the critical state with a certain number of cycles. This was due to the significant increase of $[w]_{\mathrm{cm}}$ as a function of N. With a significant increase of $[w]_{\mathrm{cm}}$ as a function of N, $[w]_{\mathrm{cm}}$ evolved until exceeding the limit in which the cyclic loading could not evolve further. On loose sand, the interface behaved contractively and could undergo further $[w]_{\mathrm{cm}}$ than that on dense sand.

In case of dense sand, see Figure 2.53, within the domain of $\eta_{\mathrm{cm}} < \eta_{\mathrm{car}}$, the intensity of $[u]_{\mathrm{cm}}$ and $[w]_{\mathrm{cm}}$ also increased with increasing the level of η_{cm} unless η_{cm} was close to η_{peak}. When η_{cm} was in the range between η_{car} and η_{peak}, contrary to those tests mentioned above, the dilative behaviour took place and consequently the interface could reach the critical state with a certain number of cycles.

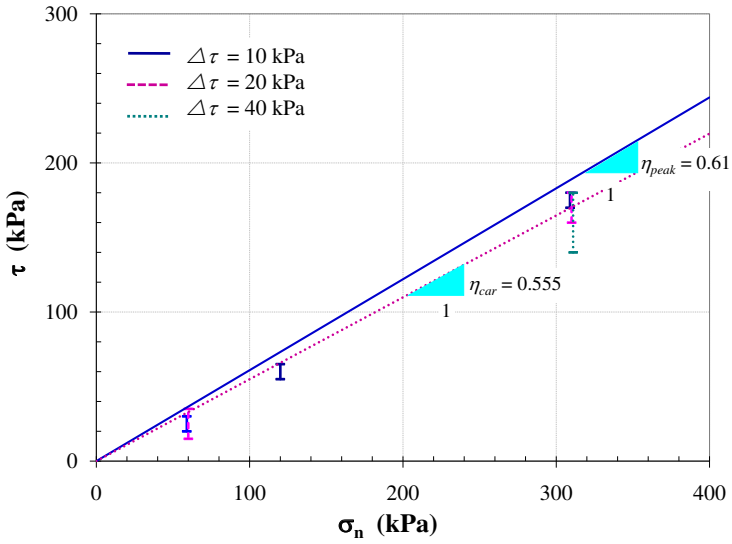

(a)

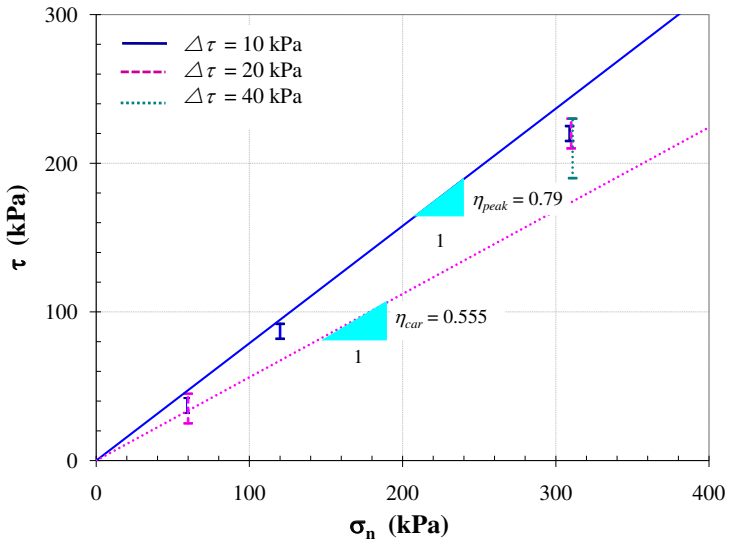

(b)

Figure 2.59: Cyclic CNL tests at $\eta_{\mathrm{cm}} \approx 9/10\eta_{\mathrm{peak}}$, depending on σ_n and I_{D0}, $\Delta\tau = 10$ kPa; (a) on loose sand ($I_{D0} \approx 30\%$) ; (b) on dense sand ($I_{D0} \approx 90\%$)

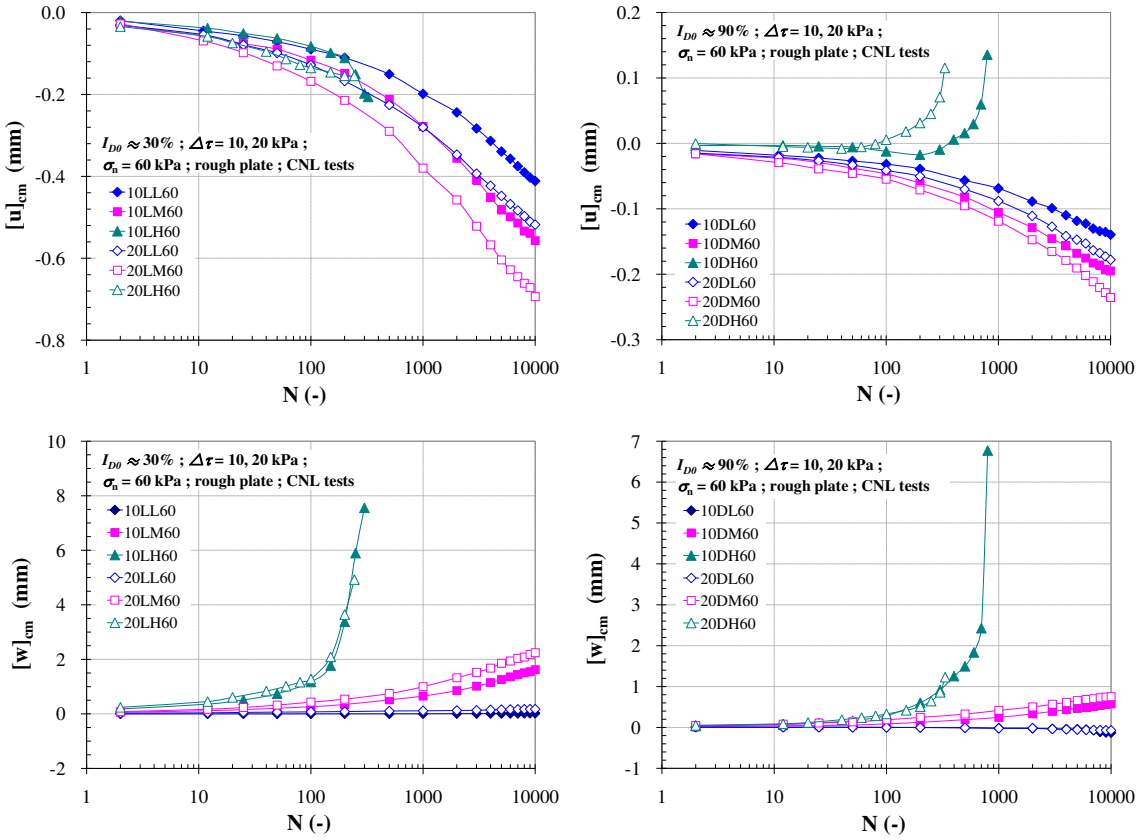

Figure 2.60: Influence of cyclic amplitude ($\Delta\tau = 10$ and 20 kPa) on intensity of $[u]_{\text{cm}}$ and $[w]_{\text{cm}}$ in dependence on the number of cycles (N) for cyclic CNL tests on loose sand ($I_{D0} \approx 30\%$) and dense sand ($I_{D0} \approx 90\%$) with $\sigma_n = 60$ kPa

2.7.4 Influence of cyclic amplitude $\Delta\tau$

The tests on the effect of cyclic amplitude were also performed, $\Delta\tau = 10$ and 20 kPa, for three values of initial normal stress. The influence of cyclic amplitude with $\sigma_n = 60$ kPa on loose and dense samples is first presented. Figure 2.60 shows the intensity of $[u]_{\text{cm}}$ and $[w]_{\text{cm}}$ in dependence of N on both densities. For loose sand as for dense sand at $\eta_{\text{cm}} = 0$ and $\eta_{\text{cm}} \approx \frac{1}{2}\eta_{\text{peak}}$, the intensity of $[u]_{\text{cm}}$ and $[w]_{\text{cm}}$ increased with increasing the cyclic amplitude. The rate of the intensity decreases as a function of N. The interface underwent the gradual contraction with an increasing function of cyclic amplitude within the range of $\eta_{\text{cm}} < \eta_{\text{car}}$. At $\eta_{\text{cm}} = 0$, although the amplitude of $\Delta\tau = 20$ kPa was applied, the mean cyclic path of $[w]_{\text{cm}}$ was still almost zero. In case of η_{cm} close to η_{peak}, on loose sand the contraction still existed whereas on dense sand the dilative behaviour occurred. It was found that the dilation of the smaller amplitude ($10DH60$) was more cosiderable than that of the bigger one. A number of cycles for reaching the critical state decreased with increasing the cyclic amplitude. In case of smaller amplitude ($\Delta\tau = 10$ kPa) the interface could undergo farther

than the bigger one ($\Delta\tau = 20$ kPa), e.g. $[w]_{\text{cm}} \approx 6.8$ mm for $10DH60$.

Figure 2.61 shows the same trend of the influence of the cyclic amplitude on both densities with the initial normal stress $\sigma_n = 310$ kPa. On loose sand, within the range of $\eta_{\text{cm}} < \eta_{\text{car}}$ the rate of $[u]_{\text{cm}}$ and $[w]_{\text{cm}}$ was obviously less than that observed with $\sigma_n = 60$ kPa. At η_{cm} close to η_{peak}, with $\Delta\tau = 20$ kPa ($20LH310$, $160 < \tau < 180$) this test could reach the critical state with 443 cycles whereas in case of $\Delta\tau = 10$ kPa ($10LH310$, $170 < \tau < 180$) the interface could evolve more than 3,000 cycles. This could be said that even though the stress ratio η_{cm} of $10LH310$ was more closer to η_{peak} than that of $20LH310$, the interface could undergo farther with smaller amplitude. On dense sand, the influence of cyclic amplitude induced an increase of the intensity of $[u]_{\text{cm}}$ and $[w]_{\text{cm}}$ in the range of $\eta_{\text{cm}} < \eta_{\text{car}}$. In case of η_{cm} close to η_{peak} the dilative behaviour also occurred. The smaller amplitude ($10DH310$) provided more considerable dilation than the bigger one ($20DH310$).

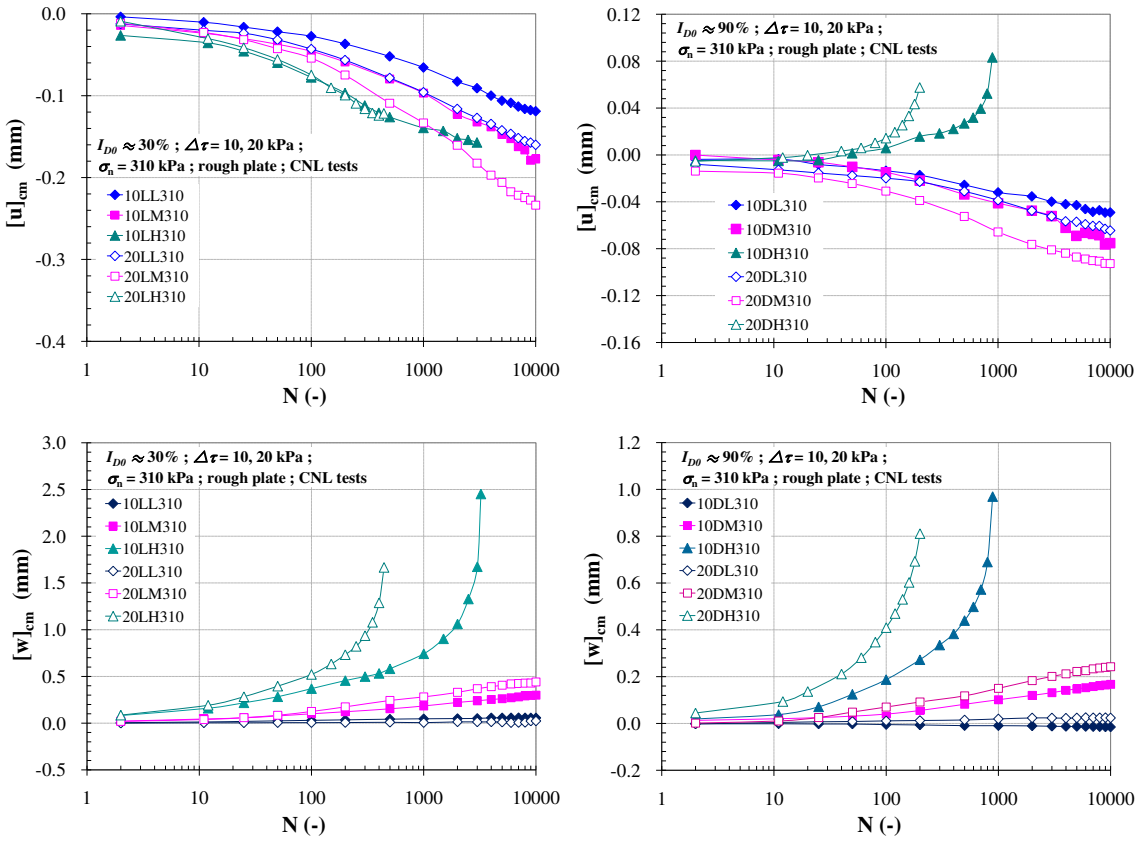

Figure 2.61: Influence of cyclic amplitude ($\Delta\tau = 10$ and 20 kPa) on intensity of $[u]_{\text{cm}}$ and $[w]_{\text{cm}}$ in dependence on the number of cycles (N) for cyclic CNL tests on loose sand ($I_{D0} \approx 30\%$) and dense sand ($I_{D0} \approx 90\%$) with $\sigma_n = 310$ kPa

For the purpose of describing properly on amplitude-dependence, the supplementary tests with $\Delta\tau = 40$ kPa were performed for $\sigma_n = 310$ kPa at the level of $\eta_{\text{cm}} \approx \frac{1}{2}\eta_{\text{peak}}$ and $\eta_{\text{cm}} \approx 9/10\eta_{\text{peak}}$. Again, Figure 2.62 shows the evolution of $[u]_{\text{cm}}$ and $[w]_{\text{cm}}$ in dependence of

N for $\sigma_n = 310$ kPa on both densities. Within the range of $\eta_{\text{cm}} < \eta_{\text{car}}$, the rate of $[u]_{\text{cm}}$ and $[w]_{\text{cm}}$ increased with increasing the cyclic amplitude. It is also interesting to consider the influence of cyclic ampltitude when η_{cm} close to η_{cm}. First, considering the increase of cyclic amplitude on loose sand, with $\Delta\tau = 40$ kPa ($40LH310$, $140 < \tau < 180$), it could be seen that η_{cm} of this test was farther away from η_{peak} than those with $\Delta\tau = 10$ and 20 kPa (see Figure 2.59(a)). Each of these tests η_{max} was kept constant while increasing the amplitude of cycles, η_{cm} then decreased. Since η_{cm} of $40LH310$ was lower than that of $20LH310$ ($\Delta\tau = 20$ kPa), the interface could then undergo farther. This could be attributed to the influence of η_{cm}. In case of $40LH310$, η_{cm} was in the contractive zone. However, it could be deduced that with increasing cyclic amplitude a number of cycles for reaching the critical state decreased. This became evident when the increase of cyclic amplitude was applied on dense sand. At the level of η_{cm} close to η_{peak}, η_{cm} of these three tests were in the range of $\eta_{\text{car}} < \eta_{\text{cm}} < \eta_{\text{peak}}$ (see also Figure 2.59(b)). A number of cycles for reaching the critical state therefore decreased with increasing the cyclic amplitude. The dilative behaviour which was found in the cases of η_{cm} close to η_{peak} was considerable when the test was performed with the smaller amplitude.

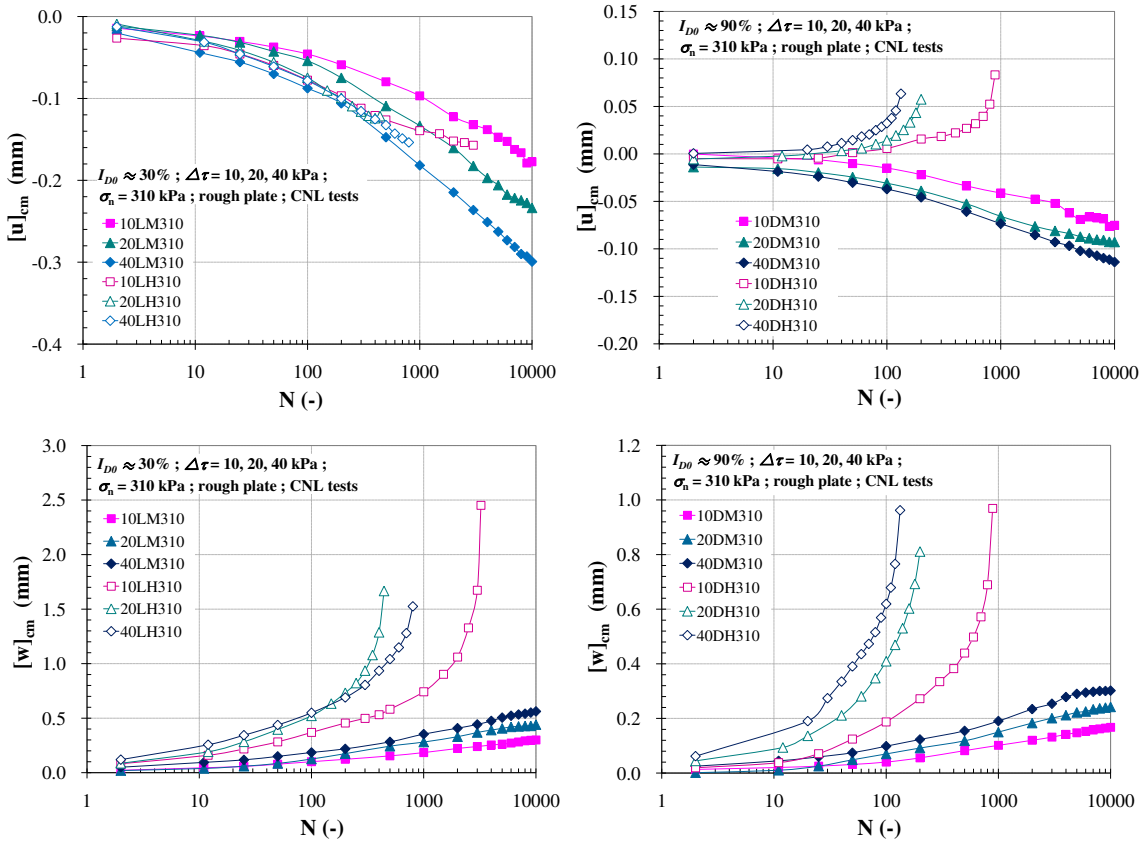

Figure 2.62: Influence of cyclic amplitude ($\Delta\tau = 20$ and 40 kPa) on intensity of $[u]_{\text{cm}}$ and $[w]_{\text{cm}}$ in dependence on the number of cycles (N) for cyclic CNL tests on loose sand ($I_D \approx 30\%$) and dense sand ($I_D \approx 90\%$) with $\sigma_n = 310$ kPa, $\eta_{\text{cm}} \approx \frac{1}{2}\eta_{\text{peak}}$ and $\eta_{\text{cm}} \approx 9/10\eta_{\text{peak}}$

2.7.5 Post-cyclic interface behaviour

One of the most important phases of the cyclic tests in the identification series is the post-cyclic phase. This phase can be carried out by one single large cycle after the cyclic phase (4^{th} phase in Figure 2.44) in order to characterize the change of interface resistance (δ_{peak}) due to cyclic loading. This post-cyclic phase could not be carried out for η_{cm} close to η_{peak} due to the early termination. As can be dedeuced from experimental observations, within the range of $\eta_{\text{cm}} < \eta_{\text{car}}$ the principal characteristic of interface subjected to cyclic loading under CNL condition was the progressive contraction.

Figure 2.63 shows the typical $\tau/\sigma - [w]$, $[u] - [w]$ and $\sigma_n - [u]$ diagrams of cyclic interface direct shear test for $\sigma_n = 120$ kPa, $\eta_{\text{cm}} \approx \frac{1}{2}\eta_{\text{peak}}$, $\Delta\tau = 10$ kPa on loose ($10LM120$) and dense ($10DM120$) sands after cyclic loading phase. On loose sand, within the range of $\eta_{\text{cm}} < \eta_{\text{car}}$, after cyclic phase the interface became denser and consequently the peak stress ratio (η_{peak}) of cyclic test was slightly higher than that of monotonic test. The interface showed slightly dilative behaviour at the post-cyclic phase. On dense sand as long as $\eta_{\text{cm}} < \eta_{\text{car}}$, the interface behaved contractively the peak stress ratio after cyclic loading phase was not much different from monotonic test. At post-cyclic phase, the interface exhibited dilative behaviour as a result of gradual densification. In comparison with the monotonic tests, the normal stiffness, k_n (slope of $\Delta\sigma/\Delta[u]$ in $\sigma_n - [u]$ diagrams) of cyclic tests after discharging σ_n slighly increased. This was due to the cyclic loading phase inducing more densification on both densities.

Figure 2.64 shows the post-cyclic behaviour for $\sigma_n = 60$ kPa on loose sand with $\Delta\tau = 10$ and 20 kPa. As can be observed, the values of peak stress ratio (η_{peak}) of both amplitudes after cyclic phase were slightly higher than that of monotonic test. Considering the volumetric behaviour, $[u] - [w]$ diagrams in Figure 2.64, loose sand which became denser after undergoing cyclic loading exhibited variations of $[u]$ (slightly dilative behaviour). With increasing the level of η_{cm} and $\Delta\tau$, the peak stress ratio (η_{peak}) increased slightly as a result of more progressive densification. Nevertheless, in case of $\Delta\tau = 20$ kPa at $\eta_{\text{cm}} \approx \frac{1}{2}\eta_{\text{peak}}$ ($20LM60$) which provided more progressive contraction, η_{peak} was lower than those of the other ones. This might be attributed to either the evolution of grain breakage or the high evolution of $[w]_{\text{cm}}$ during cyclic phase exceeding $[w]$ corresponding to peak stress ratio of monotonic test. Uesugi et al. [1989] concluded that one of the main factors in the degradation of maximum shear stress was the magnitude of sliding displacement of interface. Fakharian & Evgin [1997] also explained that under cyclic loading with a sufficient increase in sliding displacement or slip at interface, the shear stress which mobilized to the peak value decreased to a residual stress. Considering the specific energy (see Figure 2.65), the specific energy of grain breakage during cyclic phase at $\eta_{\text{cm}} \approx \frac{1}{2}\eta_{\text{peak}}$ with $\Delta\tau = 20$ kPa was higher than those of the other ones in cyclic tests, this would lead to the reduction rate of peak stress ratio. However, this specific energy was still small, the peak stress ratio at post-cyclic phase of this case was so slightly higher than that of monotonic test.

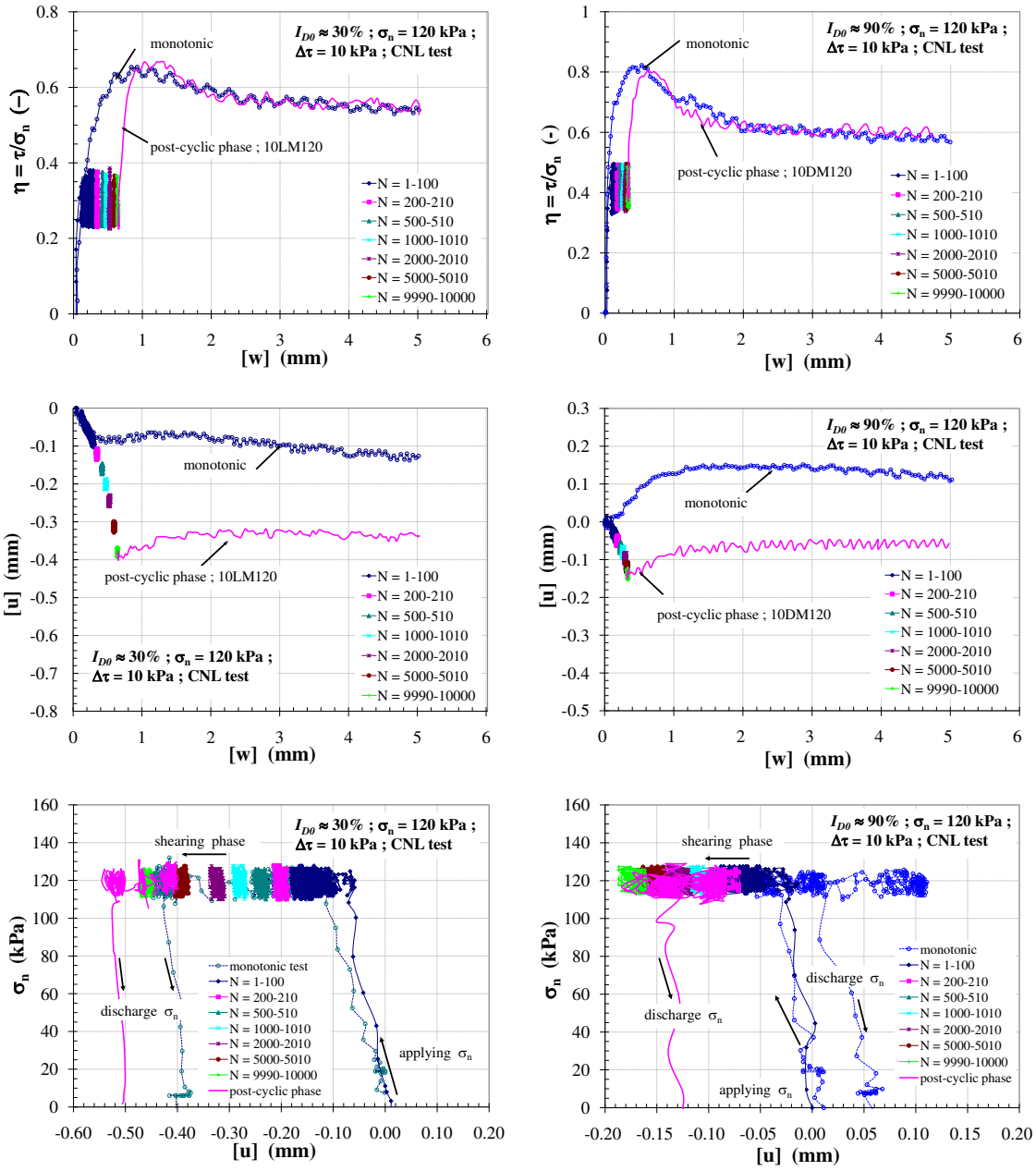

Figure 2.63: Post-cyclic phase for cyclic CNL tests with rough plate, $\sigma_n = 120$ kPa, $\eta_{\text{cm}} \approx \frac{1}{2}\eta_{\text{peak}}$, $\Delta\tau = 10$ kPa on loose ($I_{D0} \approx 30\%$) and dense ($I_{D0} \approx 90\%$) sands

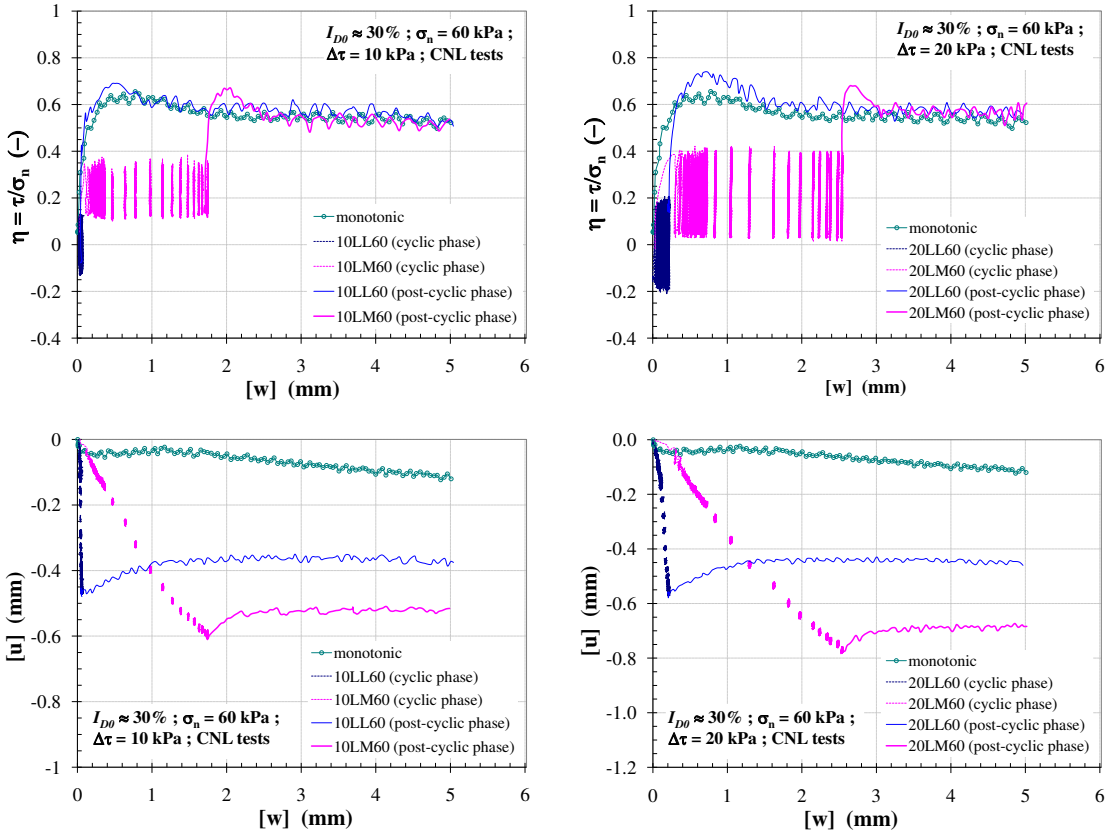

Figure 2.64: Post-cyclic phase for cyclic CNL tests with rough plate, $\sigma_n = 60$ kPa, $\eta_{\text{cm}} = 0$ and $\approx \frac{1}{2}\eta_{\text{peak}}$, $\Delta\tau = 10$ and 20 kPa on loose sand ($I_{D0} \approx 30\%$)

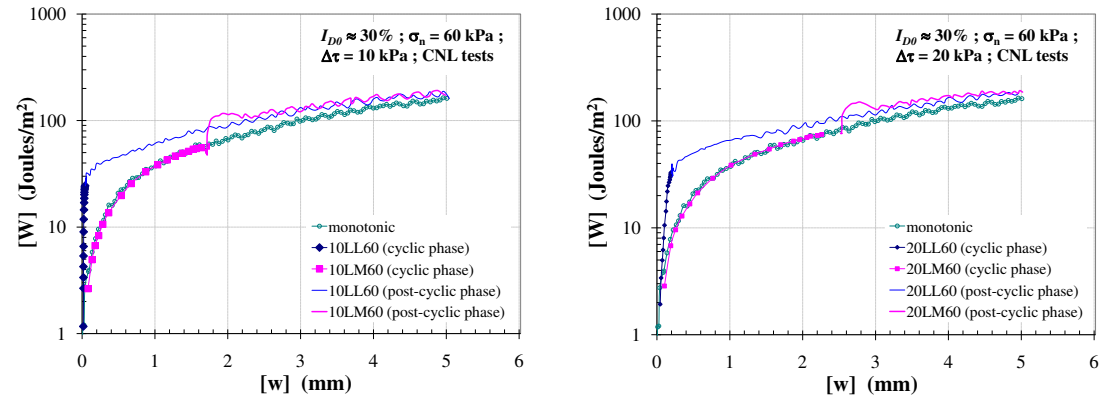

(a) (b)

Figure 2.65: Evolution of specific energy during cyclic loading (CNL tests) with rough plate, $\sigma_n = 60$ kPa, $\eta_{\text{cm}} = 0$ and $\approx \frac{1}{2}\eta_{\text{peak}}$ on loose sand ($I_{D0} \approx 30\%$); (a) $\Delta\tau = 10$ kPa; (b) $\Delta\tau = 20$ kPa

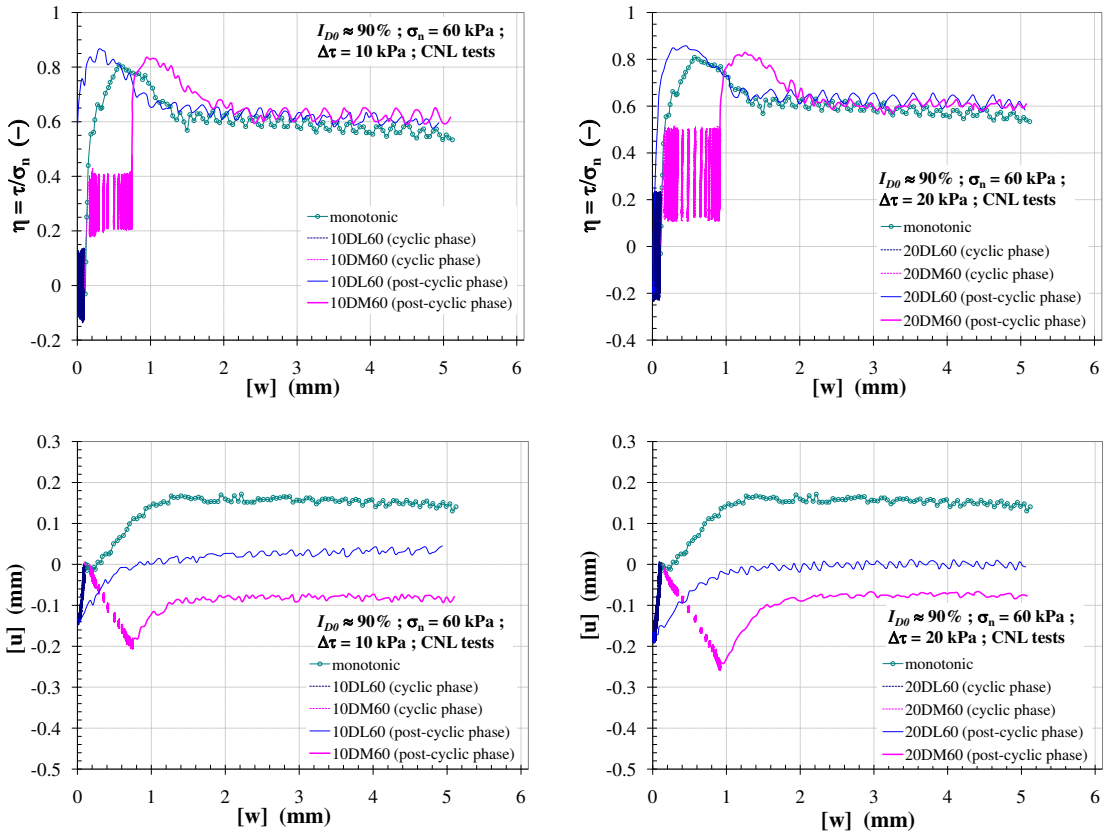

Figure 2.66: Post-cyclic phase for cyclic CNL tests with rough plate, $\sigma_n = 60$ kPa, $\eta_{\text{cm}} = 0$ and $\approx \frac{1}{2}\eta_{\text{peak}}$, $\Delta\tau = 10$ and 20 kPa on dense sand ($I_{D0} \approx 90\%$)

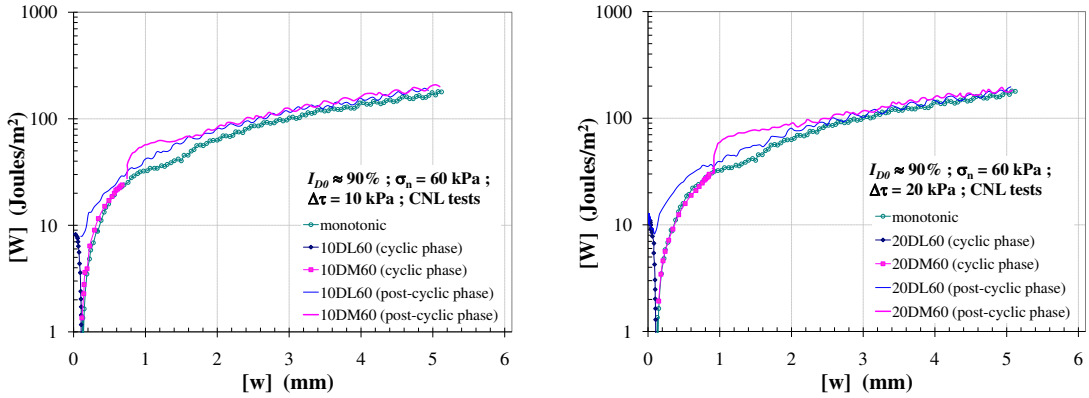

(a) (b)

Figure 2.67: Evolution of specific energy during cyclic loading (CNL tests) with $\sigma_n = 60$ kPa, $\eta_{\text{cm}} = 0$ and $\approx \frac{1}{2}\eta_{\text{peak}}$ on dense sand ($I_{D0} \approx 90\%$); (a) $\Delta\tau = 10$ kPa; (b) $\Delta\tau = 20$ kPa

On dense sand as shown in Figure 2.66, the post-cyclic phase also provided the slight increase of peak stress ratio (η_{peak}). Within the range of $\eta_{\text{cm}} < \eta_{\text{car}}$ the interface behaved contractively, the peak stress ratio at this phase seemed to decrease as a function of η_{cm} although a gradual densification during cyclic loading was observed. The dilative behaviour ($[u] - [w]$ diagrams) observed at this phase was not so much different from monotonic test. Figure 2.67 also shows the evolution of specific energy during cyclic phase as well as post-cyclic phase. At the beginning of post-cyclic phase, the specific energy increased significantly and was higher than that of monotonic test afterward increased continuously and then coincided with that of monotonic test.

In case of $\sigma_n = 310$ kPa, Figure 2.68 shows the behaviour of post-cyclic phase on loose sand which exhibited slight variation of peak stress ratio among those tests. With $\Delta\tau =$ 10 kPa, in case of $\eta_{\text{cm}} = 0$ and $\approx \frac{1}{2}\eta_{\text{peak}}$, there was not a significant increase of the peak stress ratio (η_{peak}) at post-cyclic phase even though $\eta_{\text{cm}} \approx \frac{1}{2}\eta_{\text{peak}}$ ($10LM310$) provided more densification during cyclic phase. Again, at the level of $\eta_{\text{cm}} \approx \frac{1}{2}\eta_{\text{peak}}$ with increasing $\Delta\tau$, ($\Delta\tau = 10$, 20 and 40 kPa), despite the gradual densification that accompanied cyclic loading there was not the significant increase of peak stress ratio. Furthermore, the peak stress ratio of these three tests at post-cyclic phase seemed to be similar to that of monotonic test. On loose sand, the contractive behaviour during cyclic loading resulted in interface densification (increasing as a function of $\Delta\tau$) but the significant variation of volumetric behaviour ($[u] - [w]$ diagrams) could hardly be observed during post-cyclic shearing.

On dense sand as shown in Figure 2.70, with $\Delta\tau = 10$ kPa, an increase of η_{cm} which practically induced more densification had no variations of peak stress ratio. Moreover, at $\eta_{\text{cm}} \approx \frac{1}{2}\eta_{\text{peak}}$, the peak stress ratio at post-cyclic phase decreased slightly with increasing $\Delta\tau$ ($\Delta\tau = 10$, 20 and 40 kPa). Even though an increase of $\Delta\tau$ induced more gradual contraction, there was not significant variation of normal displacement $[u]$ (dilation rate) at post-cyclic phase. This phenomenon might be attributed to the crushing and wear of the grains resulting from an increase of inter-granular particles in the localized shear zone between sand and rough plate during cyclic phase (Al-Douri & Poulos [1992], Tabucanon et al. [1995]). However, this contribution seems to be in contrast with that concluded by Uesugi & Kishida [1986]. They concluded that during cyclic loading an increase of crushing paricles due to the high intensity of stress state increasing the normalized the surface roughness (R_n) of the soil-structure interface then led to the higher coefficient of friction. Nevertheless, they also concluded that the characteristics of sand (e.g. shape of grains, hardness etc.) and the sliding displacement at the interface mainly influenced the coefficient of friction.

Considering the specific energy, see Figure 2.69, with high value of σ_n, η_{cm} and $\Delta\tau$, an increase of specific energy after cyclic loading phase would lead to gradual crushing and wear of grains, especially in case of dense sand. Consequently, the peak stress ratio of interface (η_{peak}) at post-cyclic phase was slightly lower than that of monotonic test.

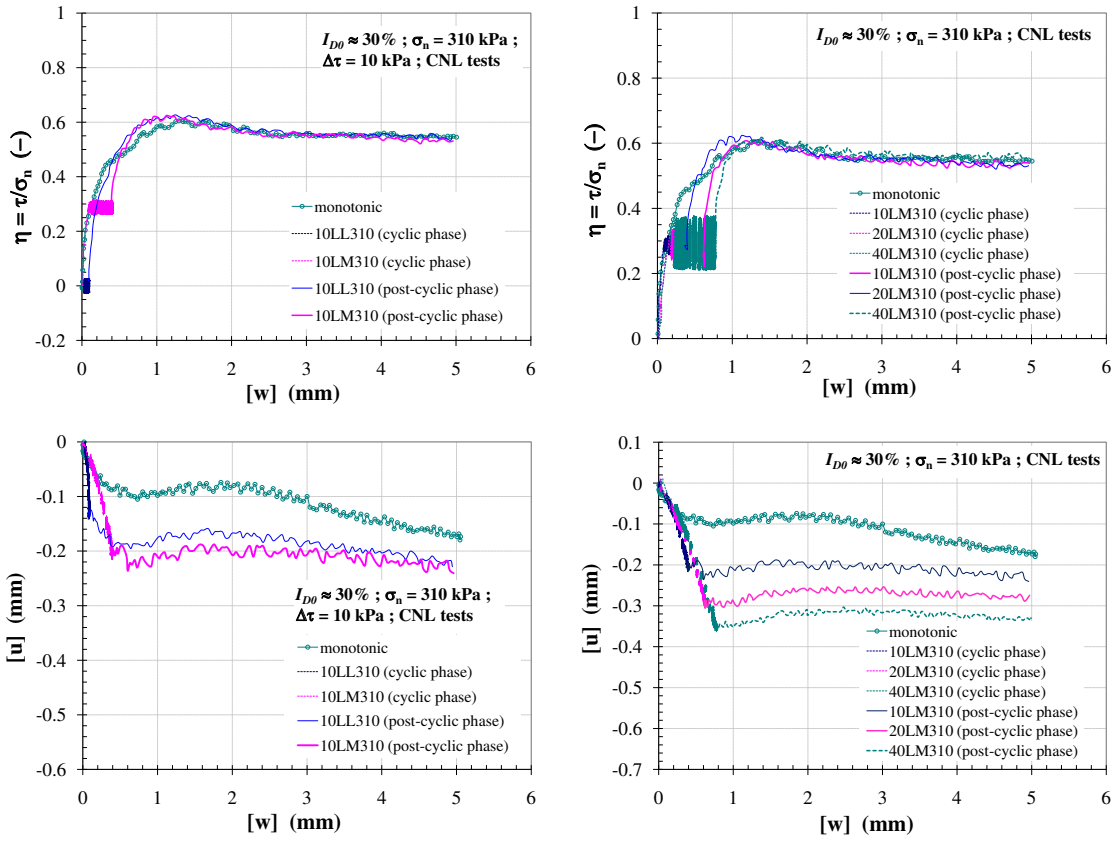

Figure 2.68: Post-cyclic phase for cyclic CNL tests with rough plate, $\sigma_n = 310$ kPa, $\Delta\tau = 10$, 20 and 40 kPa on loose sand ($I_{D0} \approx 30\%$)

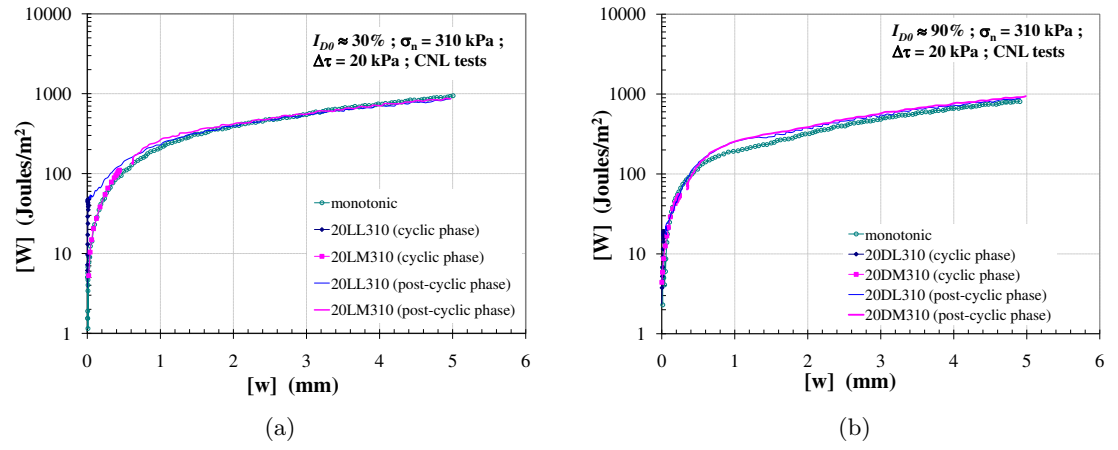

(a) (b)

Figure 2.69: Evolution of specific energy during cyclic loading (CNL tests) with rough plate, $\sigma_n = 310$ kPa, $\eta_{\text{cm}} = 0$ and $\approx \frac{1}{2}\eta_{\text{peak}}$, $\Delta\tau = 20$ kPa; (a) on loose sand ($I_{D0} \approx 30\%$); (b) on dense sand ($I_{D0} \approx 90\%$)

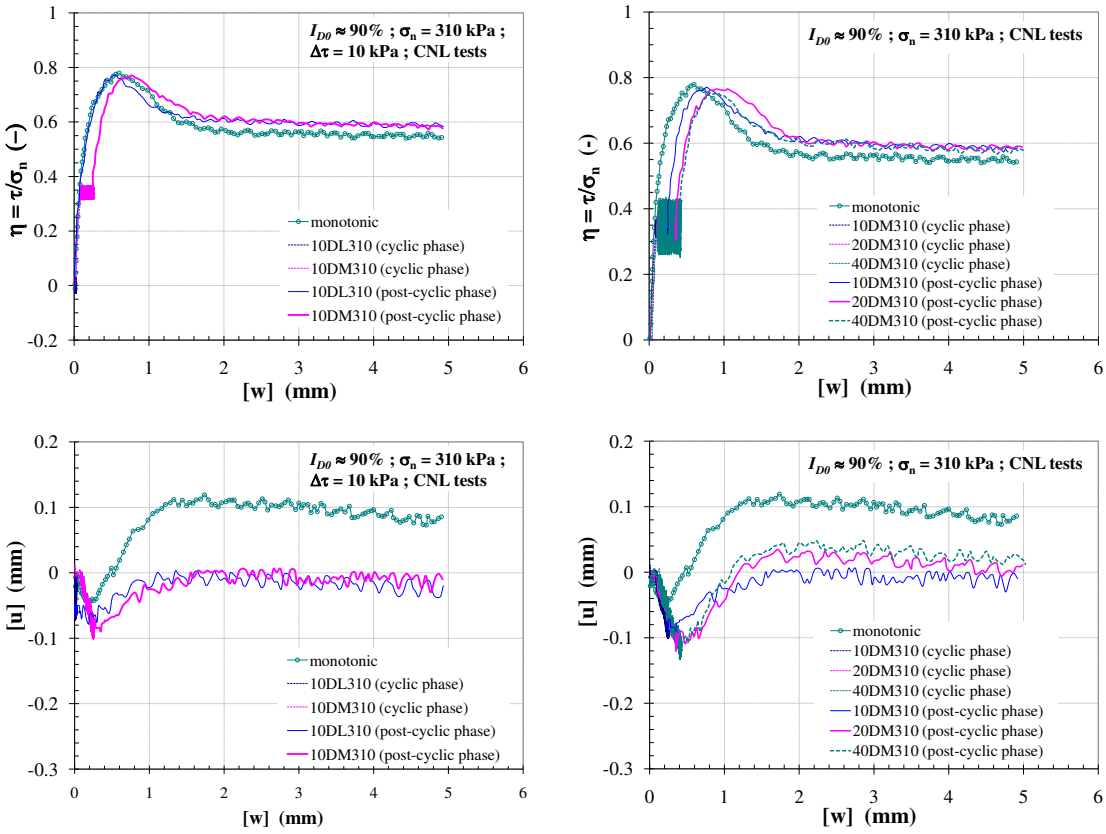

Figure 2.70: Post-cyclic phase for cyclic CNL tests with rough plate, $\sigma_n = 310$ kPa, $\Delta\tau = 10$, 20 and 40 kPa on dense sand ($I_{D0} \approx 90\%$)

The observation of the grain breakage within the interface was also carried out after finishing the cyclic tests. As can be seen in monotonic tests, there were many factors that influenced the grain breakage. Again, the same procedure (sieving method) was still carried out in order to investigate the influence of cyclic loading on grain breakage. Figure 2.71 and 2.72 show typical gains size distribution curves resulting from monotonic and cyclic interface shear tests with various conditions of $\sigma_n = 60$ and 310 kPa, respectively.

In comparison with monotonic tests, cyclic tests resulted in more grain breakage within the localized shear zone between sand and rough surface. However, in cyclic test series the particle size (D_{50}) still did not change so much but this would be considerable when taking into account the fine particle size (D_{10}). At low value of normal stress ($\sigma_n = 60$ kPa), there was a small variation of fine particle size (D_{10}) on dense sand whereas the variation of paticle size could hardly be observed on loose sand. On dense sand, with increasing η_{cm} and $\Delta\tau$, the small variation of fine grains (D_{10}) could be observed (Figure 2.71(b)). In case of $\sigma_n = 310$ kPa (see Figure 2.72), the steady shear stress at a high value as well as the continuous contraction in cyclic CNL tests resulting in an increase in the specific energy induced an intense grain breakage and the formation of fine particles (resulting in a drop

in particle size of the material). Although the specific energy during cyclic phase on loose sand was slighly higher than that on dense sand, the energy on both densities then evolved in the same value during post-cyclic phase. Indeed, dense sand has more tendency of grain breakage within the localized shear zone than loose sand. The abrasion between the grains and the surface roughness of plate on dense sand therefore provided an increase in crushing and wear of grains.

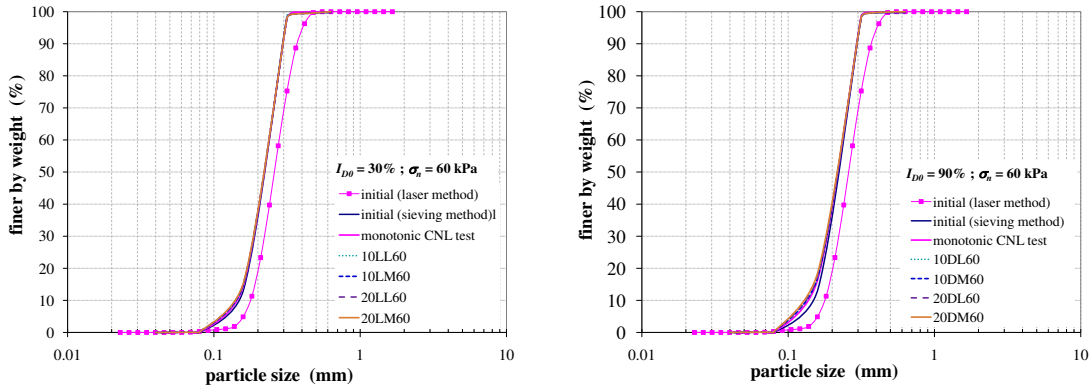

(a) (b)

Figure 2.71: Grain size distribution of sand after testing with various CNL conditions, rough plate, $\sigma_n = 60$ kPa; (a) on loose sand ($I_{D0} \approx 30\%$); (b) on dense sand ($I_{D0} \approx 90\%$)

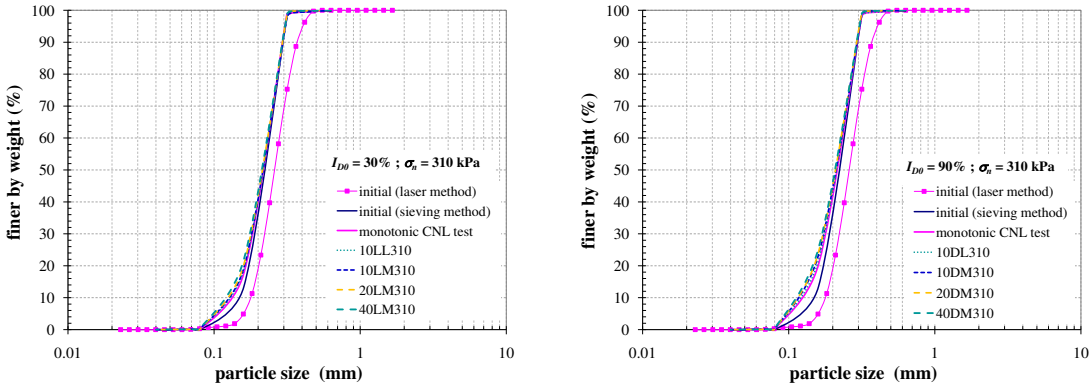

(a) (b)

Figure 2.72: Grain size distribution of sand after testing with various CNL conditions, rough plate, $\sigma_n = 310$ kPa; (a) on loose sand ($I_{D0} \approx 30\%$); (b) on dense sand ($I_{D0} \approx 90\%$)

The change in particle size described by D_{10} (a shift of grading curve to the left) was greater for increasing I_{D0}, σ_n, η_{cm} and $\Delta\tau$. The small amplitude of cycle ($\Delta\tau = 10$ kPa) can even lead to the crushing and wear of the sand particles if the interface undergoes a large number of cycles (as can be seen in this study, $N = 10^4$). This may contribute to the

small degradation of the peak stress ratio at post-cyclic phase. The fine grains resulting from crushing grains during cyclic loading then replaced the void within the interface zone. Consequently, this led to further contraction of interface.

2.8 Validation tests (cyclic CNS tests on rough plate)

In this study, some validation tests were performed in order to investigate the interface behaviour subjected to cyclic loading under constant normal stiffness (CNS) condition. This would be more realistic to study the behaviour of habitual problems often encontered in practice such as pile foundations, soil nailing etc. The first series of validation tests was to test the cyclic pseudo-creep CNS path with three values of normal stiffness (k) and initial normal stress (σ_{n0}). The second series was intended to test the memory parameters of the constitutive law, which made it possible to connect the cycles of different characteristics. These tests were performed by changing the amplitude of cycles in succession. The detail of the tests in this series is summarized in Table 2.5

2.8.1 Influence of normal stiffness (k)

In case of cyclic CNS tests, all tests were performed with σ_{n0} = 60, 100 and 310 kPa on both densities while the stress ratio (η_{cm0}) varied according to I_{D0} and the normal stiffness (k). In this section, three values of normal stiffness k = 1000, 2000 and 5000 kPa/mm are focused. From our experience, an interface behaviour with an imposed normal stiffness of 5000 kPa/mm is not far from the "constant volume" condition at least for the current normal stress levels (< 500 kPa). In addition, ever from our experience, the normal stiffness corresponding to the current piles, cast in situ as well as driven, is much less than 5000 kPa/mm. The main factors that influence the interface behaviour (i.e. I_{D0}, σ_{n0}, η_{cm0} and $\Delta\tau$) were the same as those presented under CNL condition.

The influence of normal stiffness on the cyclic interface was more significant than that on monotonic interface behaviour. The principal characteristic of cyclic interfaces under CNS condition was the gradual degradation of normal stress accompanied with the degradation of shear stress as a result of the progressive contraction of soil adjacent to the structural material. Figure 2.73 illustrates the relationship between the variation of normal stress ($\Delta\sigma_n$) and the variation of normal displacement ($\Delta[u]$) to represent the imposed normal stiffness (k) during cyclic loading in case of k = 1000 and 2000 kPa/mm on both densities. Although there were somewhat many scatters during the test, the trend fitted through the data indicated that the overall test data correlated well with this relationship. The scatters were mainly due to the applied normal stress from generating engine in two directions. Moreover, taking into account the fictitious contraction due to the leakage of sand during cyclic tests which induced less contraction also led to some of the scatters (as can be seen in the phase of towards critical state). The important feature during all these cyclic tests was that the stress ratio (η_{cm}) increased (because of the degradation of σ_n) from η_{cm0} prescribed at the beginning of the test to the critical value (η_{crit}).

Table 2.5: Tests for validation, CNS path, parameters

N°	I_{D0} (%)	σ_n (kPa)	k (kPa/mm)	level of η_{cm0} (-)	τ (kPa)	η_{cm} (-)	$\Delta\tau$ (kPa)
10LM60_1000k	30	60	1000	$\approx 1/2\eta_{\text{peak}}$	$13 < \tau < 23$	0.30	10
10LM100_1000k	30	100	1000	$\approx 1/2\eta_{\text{peak}}$	$25 < \tau < 35$	0.30	10
20LM100_1000k	30	100	1000	$\approx 1/2\eta_{\text{peak}}$	$20 < \tau < 40$	0.30	20
10LM100_2000k	30	100	2000	$\approx 1/3\eta_{\text{peak}}$	$15 < \tau < 25$	0.20	10
10LL100_5000k	30	100	5000	$\approx 1/4\eta_{\text{peak}}$	$10 < \tau < 20$	0.15	10
20LL100_5000k	30	100	5000	$\approx 1/4\eta_{\text{peak}}$	$5 < \tau < 25$	0.15	20
10LM310_1000k	30	310	1000	$\approx 1/2\eta_{\text{peak}}$	$88 < \tau < 98$	0.30	10
10DM60_1000k	90	60	1000	$\approx 1/2\eta_{\text{peak}}$	$16 < \tau < 26$	0.35	10
10DH60_1000k	90	60	1000	$\approx 1/2\eta_{\text{peak}}$	$20 < \tau < 30$	0.42	10
10DM100_1000k	90	100	1000	$\approx 1/2\eta_{\text{peak}}$	$30 < \tau < 40$	0.35	10
10DH100_1000k	90	100	1000	$\approx 2/3\eta_{\text{peak}}$	$45 < \tau < 55$	0.50	10
20DM100_1000k	90	100	1000	$\approx 1/2\eta_{\text{peak}}$	$25 < \tau < 45$	0.35	20
10DM100_2000k	90	100	2000	$\approx 1/2\eta_{\text{peak}}$	$30 < \tau < 40$	0.35	10
10DH100_2000k	90	100	2000	$\approx 2/3\eta_{\text{peak}}$	$45 < \tau < 55$	0.50	10
10DM100_5000k	90	100	5000	$\approx 1/2\eta_{\text{peak}}$	$30 < \tau < 40$	0.35	10
10DH100_5000k	90	100	5000	$\approx 2/3\eta_{\text{peak}}$	$45 < \tau < 55$	0.50	10
20DM100_5000k	90	100	5000	$\approx 1/2\eta_{\text{peak}}$	$25 < \tau < 45$	0.35	20
10DM310_1000k	90	310	1000	$\approx 1/2\eta_{\text{peak}}$	$105 < \tau < 115$	0.35	10
10DH310_1000k	90	310	1000	$\approx 2/3\eta_{\text{peak}}$	$150 < \tau < 160$	0.50	10
10_20LM120	30	120	CNL	$\approx 1/2\eta_{\text{peak}}$	$30 < \tau < 40$	0.29	10
					$25 < \tau < 45$	0.29	20
20_10LM120	30	120	CNL	$\approx 1/2\eta_{\text{peak}}$	$25 < \tau < 45$	0.29	20
					$30 < \tau < 40$	0.29	10
10_20DM120	30	120	CNL	$\approx 1/2\eta_{\text{peak}}$	$45 < \tau < 55$	0.40	10
					$40 < \tau < 60$	0.40	20
20_10DM120	30	120	CNL	$\approx 1/2\eta_{\text{peak}}$	$35 < \tau < 55$	0.37	20
					$40 < \tau < 50$	0.37	10

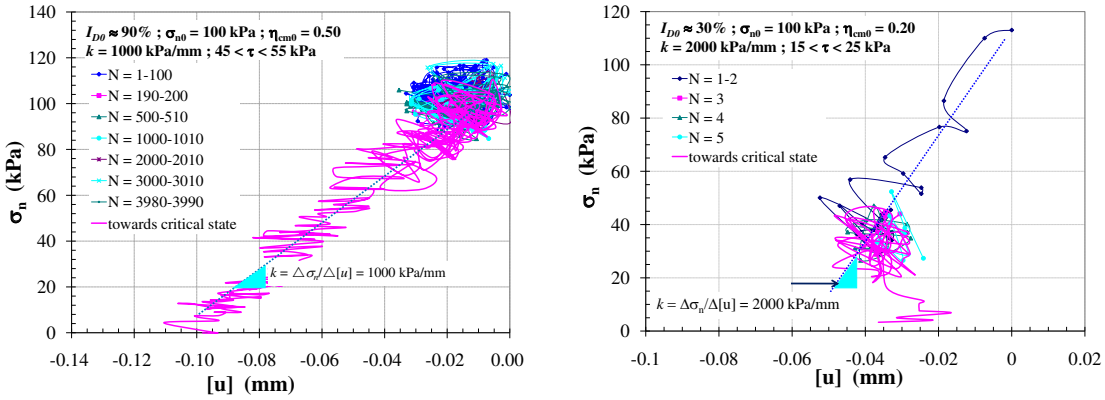

(a) (b)

Figure 2.73: Relationship of imposed stiffness during cyclic CNS tests, with rough plate, σ_{n0} = 100 kPa, $\Delta\tau$ = 10 kPa ; (a) k = 1000 kPa/mm, η_{cm0} = 0.50 on dense sand $I_{D0} \approx$ 90%; (b) k = 2000 kPa/mm, η_{cm0} = 0.20 on loose sand $I_{D0} \approx$ 30%

On loose sand, as can be seen in the preliminary series of monotonic tests, the significant degradation of normal stress associated with shear stress was observed as a result of contraction during shearing. In cyclic condition, the significant degradation of normal stress (σ_n) as a result of more progressive contraction accompanied with N led to the critical state easily. An increase of normal stiffness on loose sand induced the stress state to accelerate towards the critical state. Figure 2.74 shows a comparison of stress paths and the degradation of σ_n during cyclic CNS tests with the initial normal stress σ_{n0} = 100 kPa, $\Delta\tau$ = 10 kPa on loose sand. The first one was performed with k = 1000 kPa/mm at η_{cm0} = 0.30 while the second one was performed with k = 5000 kPa/mm at η_{cm0} = 0.15. As can be observed on $\tau - \sigma_n$ and $\sigma_n - [w]$ planes, the influence of k was evident on loose sand. Althoughh the value of η_{cm0} was small (η_{cm0} = 0.15) there was a significant degradation of σ_n with k = 5000 kPa/mm. In this case, in spite of small $[w]$ the normal stress decreased rapidly during the first two cycles (from 100 to 20 kPa) until the 6^{th} cycle, while the mean shear stress was kept constant (τ_{cm} = 15 kPa), after that the stress state could not evolve to the next cycle and consequently moved towards the critical state line.

A comparison between the distinction of σ_{n0} (σ_{n0} = 60 and 310 kPa) was also performed at the same level of η_{cm0} (η_{cm0} = 0.30), k = 1000 kPa/mm on loose sand. The test with σ_{n0} = 60 kPa was performed at 13 < τ < 23 kPa (Figure 2.75) while the case of σ_{n0} = 310 kPa was performed at 88 < τ < 98 kPa (Figure 2.76). Obviously, with low initial normal stress the stress state could undergo only two cycles whereas the latter the stress state could undego more than 2,000 cycles. The degradation rate of normal stress with σ_{n0} = 60 kPa increased rapidly during the first two cycles and then the stress state could not evolve to the next one. This indicates that whenever the interface subjected to cyclic loading under CNS condition with low initial normal stress on loose sand, it can easily reach the critical state due to the initial stress state close to the critical state line.

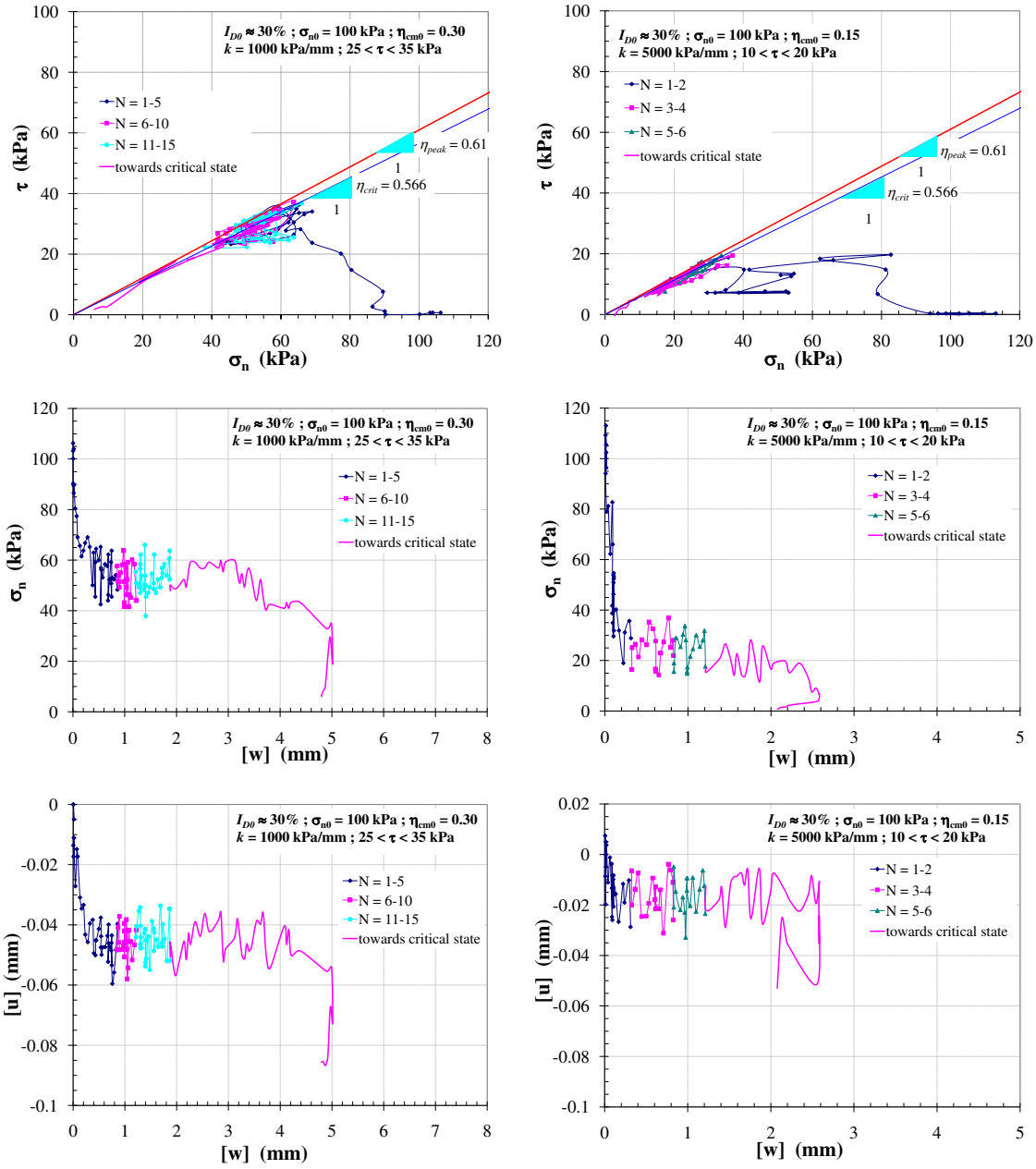

Figure 2.74: Cyclic CNS tests on loose sand ($I_{D0} \approx 30\%$) with rough plate, $\sigma_{n0} = 100$ kPa, $\Delta\tau = 10$ kPa; (left) $k = 1000$ kPa/mm, $\eta_{\mathrm{cm0}} = 0.30$; (right) $k = 5000$ kPa/mm, $\eta_{\mathrm{cm0}} = 0.15$

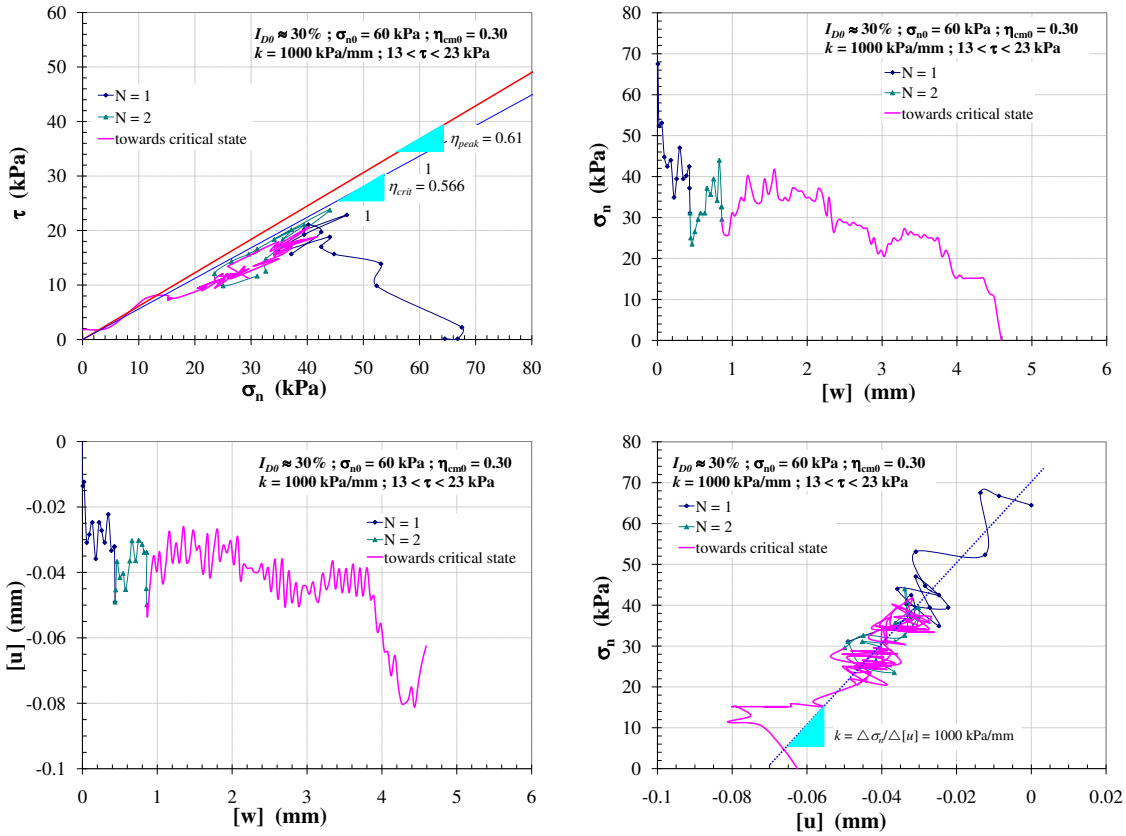

Figure 2.75: Cyclic CNS tests on loose sand ($I_{D0} \approx 30\%$) with rough plate, $\sigma_{n0} = 60$ kPa, $k = 1000$ kPa/mm, $\Delta\tau = 10$ kPa at $13 < \tau < 23$ kPa

On the other hand, dense sand exhibiting low attitude to contract required a greater number of cycles as well as the tangential displacement $[w]$ to reach the critical state. Figure 2.77 shows the typical results of cyclic CNS tests on dense sand with $\sigma_{n0} = 100$ kPa, $\eta_{\text{cm0}} = 0.35$, $\Delta\tau = 10$ kPa, for $k = 1000$ and 5000 kPa/mm. During cyclic loading the interface showed continuous contraction which induced the degradation in normal stress. This contraction continued as a function of number of cycles which associated with the shear displacement ($[w]$) and then led to more degradation in σ_n as a result of the interface densification (see $\sigma_n - [w]$ and $[u] - [w]$ planes in Figure 2.77). Subsequently, with large shear displacement the interface showed more contraction and then the stress state moved towards the critical line as shown in $\tau - \sigma_n$ plane. After reaching the critical state the cycles could not evolve to the next one, the stress state then decreased continuously and coincided the critical state line.

In case of $k = 1000$ kPa/mm with $\eta_{\text{cm0}} = 0.35$, while the stress state was in critical condition the stress path did not coincide the critical line in $\tau - \sigma_n$ plane. This was due to the limitation of the shear displacement transducer (LVDT) as mentioned before in the section of interface direct shear device. Generally, the horizontal relative movement of the plate

was set up in the range of ±6.5 mm in accordance with the limitation of LVDT. In this case the interface could undergo farther (more than 10 mm with N = 11,972) and reached the limitation of horizontal movement, subsequently the plate was obstructed while the stress state decreased continuously.

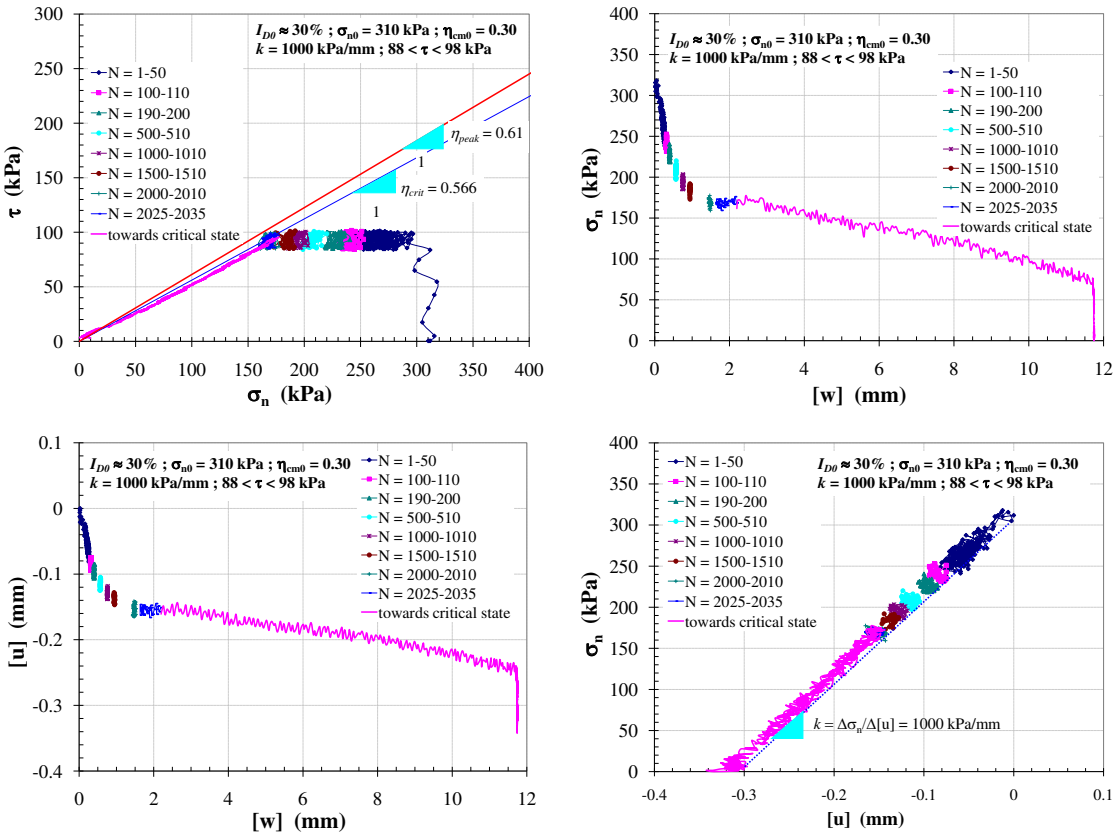

Figure 2.76: Cyclic CNS tests on loose sand ($I_{D0} \approx 30\%$) with rough plate, σ_{n0} = 310 kPa, k = 1000 kPa/mm, $\Delta\tau$ = 10 kPa at 88 < τ < 98 kPa

To describe the evolution of the mean cyclic stress state (represented by $\eta_{\mathrm{cm}} = \tau_{\mathrm{cm}}/\sigma_{\mathrm{n\,cm}}$) tending towards the critical state, the $\eta_{\mathrm{cm}} - [w]$ and $\eta_{\mathrm{cm}} - N$ diagrams of the tests with σ_{n0} = 100 kPa as shown in Figure 2.78 are then prensented. During the interface subjected to cyclic loading, the shear stress was kept constant while the normal stress decreased as a function of N as well as $[w]$ then the mean cyclic stress ratio η_{cm} which started from the beginning (η_{cm0} = 0.35) increased and then moved to the critical state line. An increase of normal stiffness induced more degradation of normal stress, consequently the mean cyclic stress ratio η_{cm} increased significantly. Obviously, a number of cycles for reaching the critical state with high value of k (k = 5000 kPa/mm) were less than those with the other ones. However, in case of k = 2000 and 5000 kPa/mm the interface could almost undergo the same value of shear displacement ($[w]$) but difference in N for reaching the critical state line. Unlike those tests in case of k = 1000 kPa/mm the interface could undergo farther

with a large number of cycles.

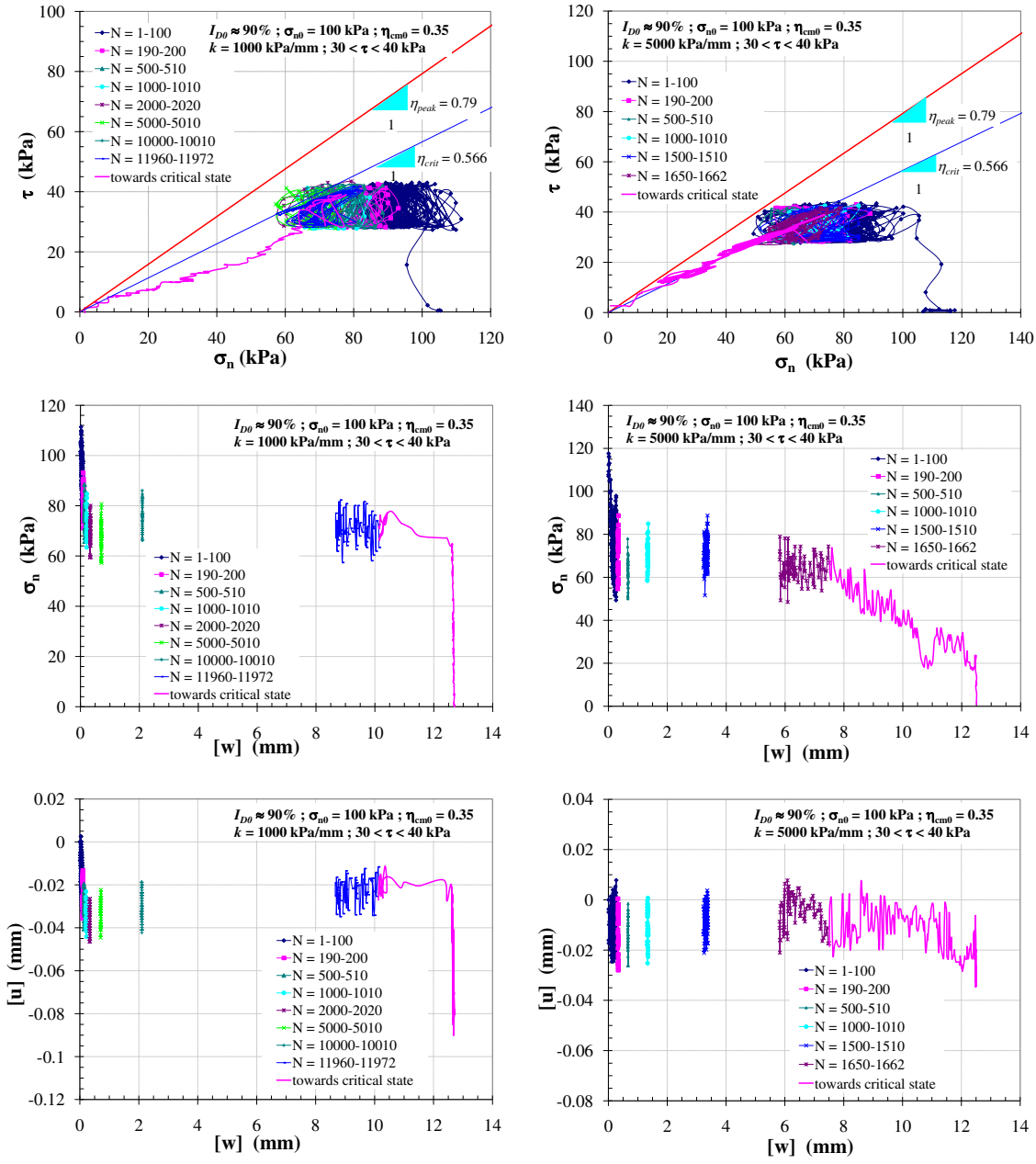

Figure 2.77: Cyclic CNS tests on dense sand ($I_{D0} \approx 90\%$) with rough plate, $\sigma_{n0} = 100$ kPa, $\Delta\tau = 10$ kPa; (left) $k = 1000$ kPa/mm, $\eta_{\mathrm{cm0}} = 0.35$; (right) $k = 5000$ kPa/mm, $\eta_{\mathrm{cm0}} = 0.35$

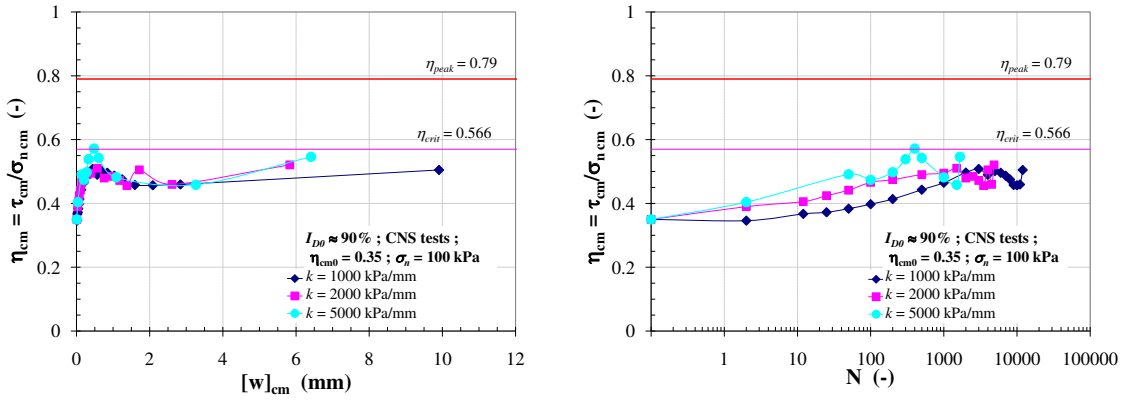

(a) (b)

Figure 2.78: Evolution of η_{cm} as a function of N and $[w]_{cm}$ of cyclic CNS tests, $\sigma_{n0} = 100$ kPa on dense sand ($I_{D0} \approx 90\%$)

In case of $k = 5000$ kPa/mm which may be attributed to very high value of stiffness (approximately constant volume condition), the volumetric behaviour of interface represented by $[u] - [w]$ diagrams in Figure 2.74 and 2.77 showed the contractive behaviour which seemed to be constant during cyclic loading on both densities.

2.8.2 Influence of η_{cm0}

The series of validation also covered the influence of η_{cm0} in CNS condition. First, this observation is typically represented by the tests carried out with $\sigma_{n0} = 100$ kPa, $\Delta\tau = 10$ kPa, $k = 2000$ kPa/mm on two levels of η_{cm0} ($\eta_{\text{cm0}} = 0.35$ and 0.50). Figure 2.79 illustrates how the level of η_{cm0} influenced the interface behaviour under cyclic CNS condition. An increase of η_{cm0} obviously resulted in less number of cycles for reaching the critical condition. However, the degradation rate of normal stress accompanied with $[w]$ at $\eta_{\text{cm0}} = 0.50$ was less than that at $\eta_{\text{cm0}} = 0.35$ (see $\sigma - [w]$ diagram). During $N = 1500$ - 2000 the normal stress of $\eta_{\text{cm0}} = 0.50$ slightly increased as a result of more densification and then decerased as a function of $[w]$ and N. The stress state of high η_{cm0} which was close to η_{crit} at the beginning of cyclic loading moved towards critical state line earlier than that of low η_{cm0} as can be seen in $\tau - \sigma_n$ plane.

When considering the influence of η_{cm0} with $\sigma_{n0} = 60$ kPa, these two cyclic tests were performed which η_{cm0} was not much different. The first one was performed at $\eta_{\text{cm0}} = 0.35$ ($16 < \tau < 26$ kPa) while η_{cm0} of the second one was 0.42 ($20 < \tau < 30$ kPa) as shown in Figure 2.80. A number of cycles for reaching the critical state at $\eta_{\text{cm0}} = 0.42$ kPa were significantly less than those at $\eta_{\text{cm0}} = 0.35$. In case of $\eta_{\text{cm0}} = 0.42$ the stress state could reach the critical state and evolved until $N = 178$ whereas $\eta_{\text{cm0}} = 0.35$ the stress state could undergo more than 1,000 cycles. As can be seen in $\tau - \sigma_n$ plane, at the beginning of cyclic shearing phase, the stress state at $\eta_{\text{cm0}} = 0.42$ was close to the critical state line and the stress state could move to the critical state line during the first 20 cycles.

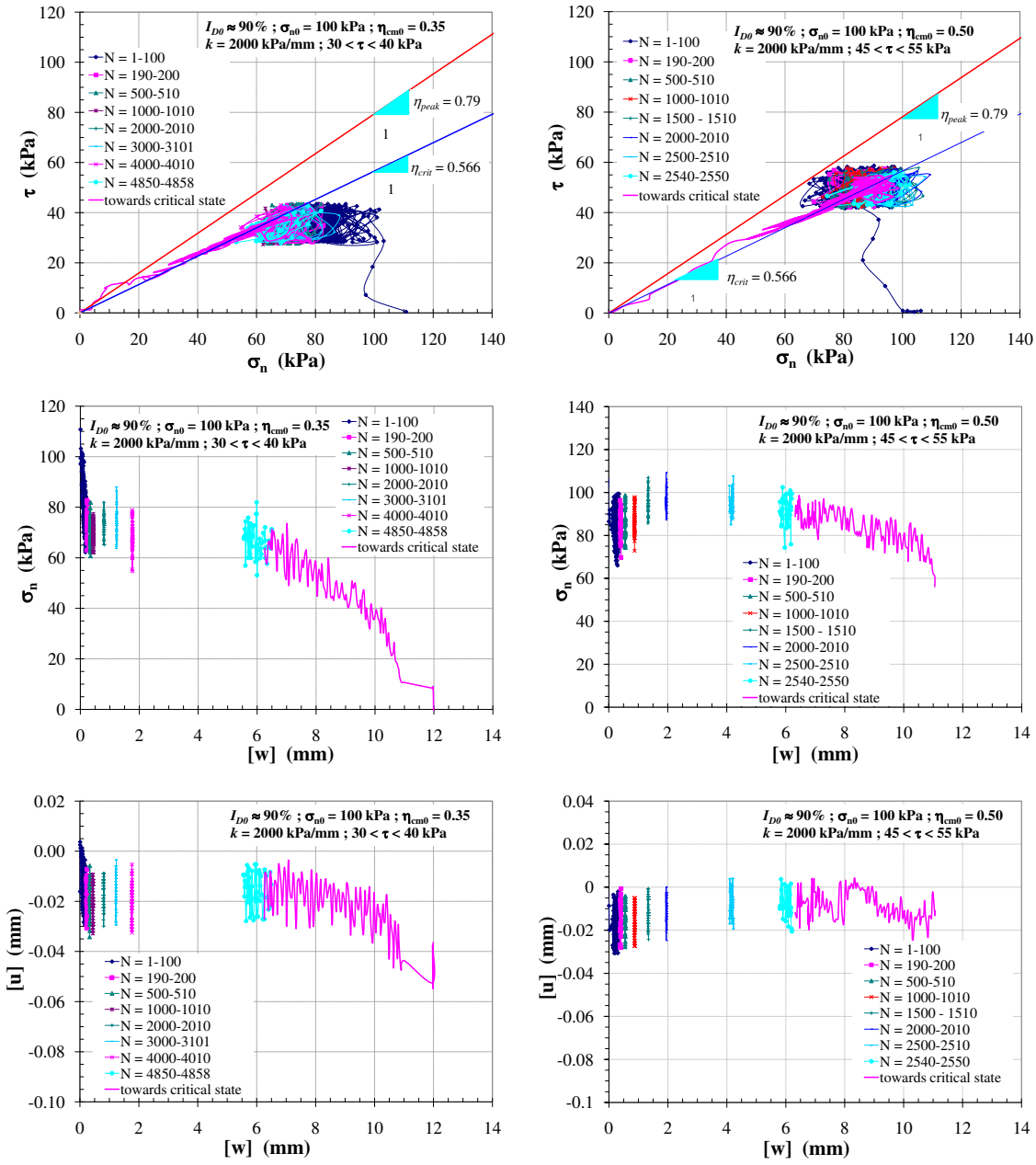

Figure 2.79: Cyclic CNS tests on dense sand ($I_{D0} \approx 90\%$) with rough plate, $\sigma_{n0} = 100$ kPa, $\Delta\tau = 10$ kPa, $k = 2000$ kPa/mm, $\eta_{\mathrm{cm0}} = 0.35$ and 0.50

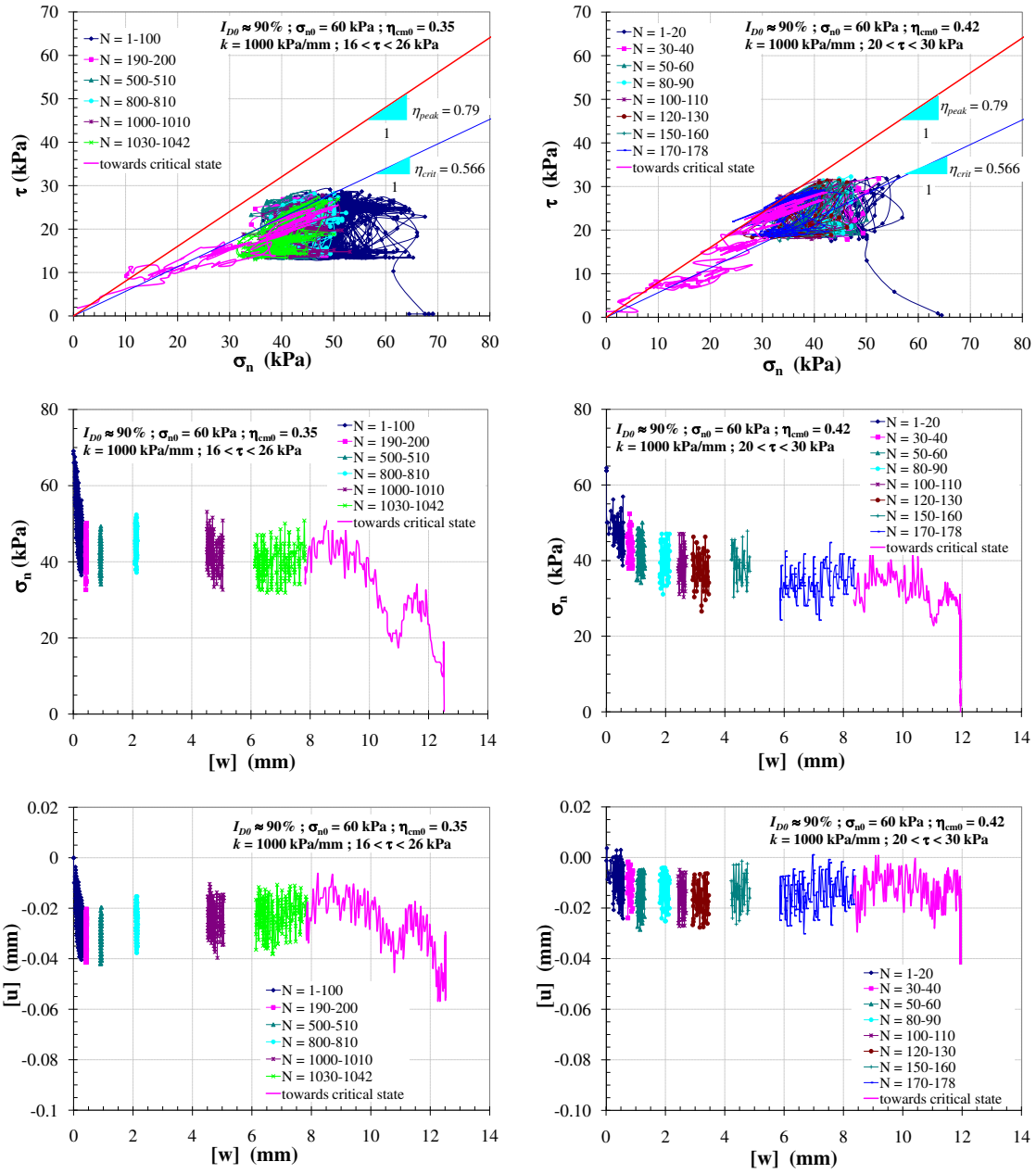

Figure 2.80: Cyclic CNS tests on dense sand ($I_{D0} \approx 90\%$) with rough plate, $\sigma_{n0} = 60$ kPa, $\Delta\tau = 10$ kPa, $k = 1000$ kPa/mm, $\eta_{\mathrm{cm0}} = 0.35$ and 0.42

It is also interesting to investigate the influence of η_{cm0} on the interface behaviour under CNS condition with high value of initial normal stress. Figure 2.81 shows the result of cyclic CNS test with $\sigma_{n0} = 310$ kPa, $k = 1000$ kpa/mm at $\eta_{\text{cm0}} = 0.50$ ($150 < \tau < 160$ kPa). Although this test was performed with high η_{cm0} a number of cycles for reaching the critical state were more than 17,800 cycles (in comparison with $\sigma_{n0} = 100$ kPa at the same level of η_{cm0} which $N \approx 3900$). The degradation rate of normal stress increased slowly until $[w] \approx 4$ mm, subsequently the stress state tended to the critical state.

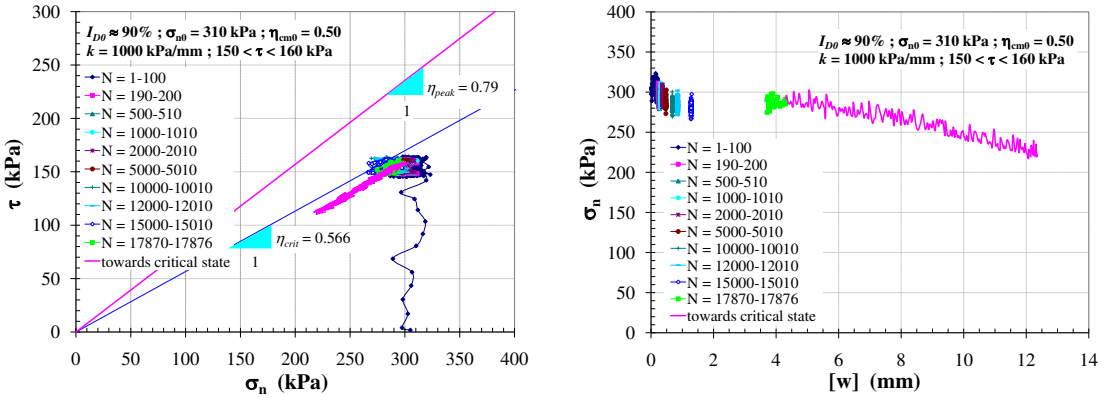

(a) (b)

Figure 2.81: Cyclic CNS tests on dense sand ($I_{D0} \approx 90\%$) with rough plate, $\sigma_{n0} = 310$ kPa, $\Delta\tau = 10$ kPa, $k = 1000$ kPa/mm, $\eta_{\text{cm0}} = 0.50$

In case of $\sigma_{n0} = 310$ kPa at $\eta_{\text{cm0}} = 0.35$ ($105 < \tau < 115$ kPa), this test was performed until $N = 32669$ while the stress state was still so far from the critical line, subsequently the post-cyclic phase was performed instead (Figure 2.82). In this case, the degradation of normal stress as a function of N increased very slow. Considering the evolution of mean cyclic stress ratio η_{cm} as a function of N, during cyclic phase η_{cm} increased with a very slow rate. With $N = 32669$ the interface could only undergo $[w] \approx 0.30$ mm (see Figure 2.84). This can be descriebed that with high σ_{n0} and low level of η_{cm0} the initial stress state was so far from the critical state line, then the stress state was able to evolve further. Consequently, a large number of cycles were required to reach the critical state. Figure 2.83 also illustrates a comparison between the the degradation of mean cyclic normal stress ($\sigma_{\text{n cm}}$) and the evolution of mean cyclic stress ratio (η_{cm}) as a function of N of these two tests. As can be seen, although the degradation rate of σ_n at $\eta_{\text{cm0}} = 0.50$ was less than that of $\eta_{\text{cm0}} = 0.35$ the evolution of η_{cm} of the former evolved close to the critical state line (η_{crit}) and finally reached η_{crit}. This can clearly be described in Figure 2.83(b) when considering the evolution of η_{max} which can be expressed as

$$\eta_{\text{max}} = \frac{\eta_{\text{cm}} + \frac{\Delta\eta}{2}}{1 - \eta_{\text{cm}}\frac{\Delta\eta}{2}}$$

The evolution of η_{max} in case of $\eta_{\text{cm0}} = 0.35$ continued without having the trend to reach

the critical state line whereas $\eta_{\max}$ of the test with $\eta_{cm0} = 0.50$ could reach this critical state line.

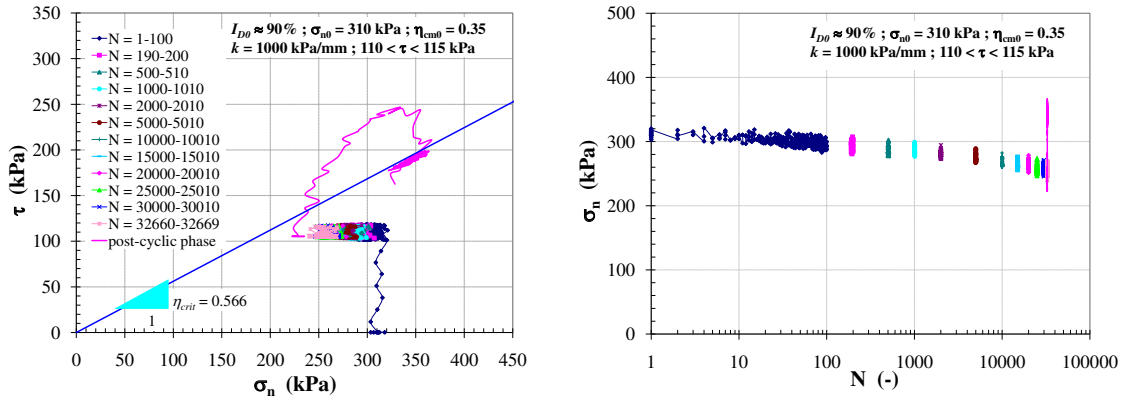

(a) (b)

Figure 2.82: Cyclic CNS tests on dense sand ($I_{D0} \approx 90\%$) with rough plate, $\sigma_{n0} = 310$ kPa, $\Delta\tau = 10$ kPa, $k = 1000$ kPa/mm, $\eta_{cm0} = 0.35$

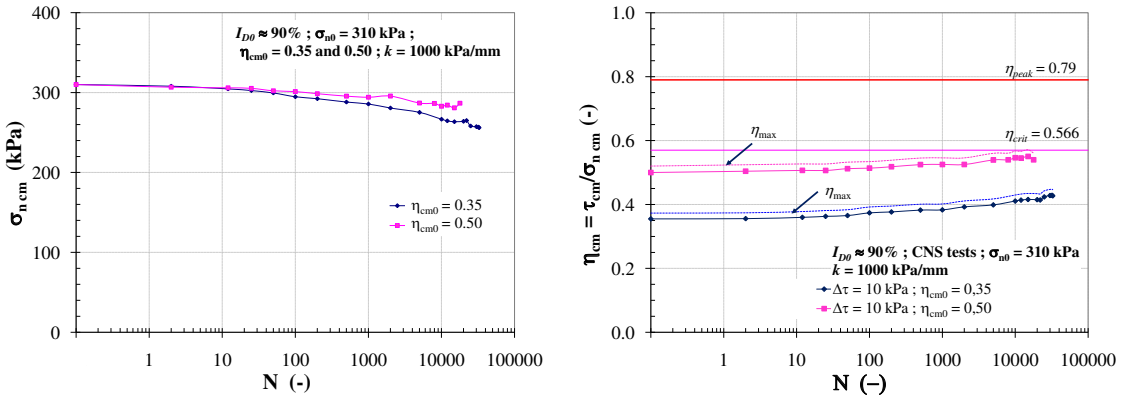

(a) (b)

Figure 2.83: Effect of the level of η_{cm0} with $\sigma_{n0} = 310$ kPa, $\Delta\tau = 10$ kPa, $k = 1000$ kPa/mm on dense sand ($I_D \approx 90\%$), rough plate; (a) the degradation rate of normal stress ; (b) evolution of $\eta_{\max}$

Considering the post-cyclic phase in case of $\eta_{cm0} = 0.35$ ($\sigma_{n0} = 310$ kPa), this phase started at $\sigma_n \approx 230$-240 kPa as shown in Figure 2.84. In comparison with the stress path that obtained from monotonic CNS test with $\sigma_{n0} = 310$ kPa, the peak shear stress ($\tau_{\max}$) at post-cyclic phase was obviously lower than that of monotonic CNS test. However, when considering the peak stress ratio (η_{peak}), η_{peak} after cyclic loading was slightly lower than those obtained whether from monotonic CNS or CNL tests. Although the cyclic loading induced more densification of interface, there was not a large difference in dilation between

the post-cyclic phase and monotonic CNS test (see $[u]-[w]$ diagram in Figure 2.84). This is in accordance with Tabucanon et al. [1995]'s investigation. They also reported that there was a lower stress recovery during post-cyclic response and the loss of strength increased with increasing the number of cycles due to the smaller volume change accompanying shear loading of the interface.

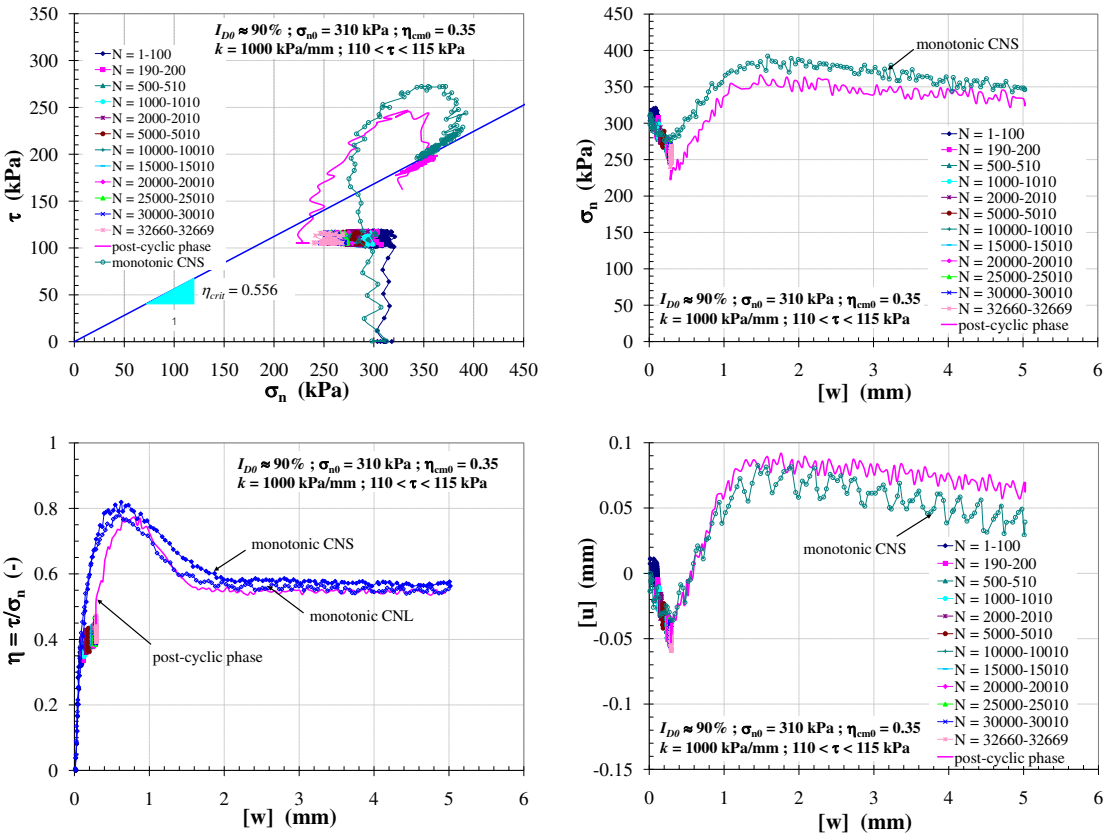

Figure 2.84: Comparison between post-cyclic CNS and monotonic CNS tests on dense sand ($I_{D0} \approx 90\%$) with rough plate, $\sigma_{n0} = 310$ kPa, $\Delta\tau = 10$ kPa, $k = 1000$ kPa/mm, $\eta_{\mathrm{cm0}} = 0.35$

2.8.3 Influence of cyclic amplitude ($\Delta\tau$)

Two cyclic amplitudes ($\Delta\tau = 10$ and 20 kPa) were performed on both densities with $k = 1000$ and 5000 kPa/mm. Figure 2.85 illustrates the influence of cyclic amplitude ($\Delta\tau$) on dense sand with $k = 5000$ kPa/mm, $\sigma_{n0} = 100$ kPa at $\eta_{\mathrm{cm0}} = 0.35$. As can be conceived that an increase of $\Delta\tau$ at the same level of η_{cm0} induced the interface trending towards more progressive densification and consequently the gradual degradation in normal stress. Therfore, the critical state could be reached with a few number of cycles. With smaller amplitude of cycle $\Delta\tau$, in contrast, a large number of cycles for reaching the critical state would be required. In comparison between these two tests, with $k = 5000$ kPa/mm a

number of cycles for reaching the critical state were not much different (i.e. $N = 1662$ with $\Delta\tau = 10$ kPa and $N = 1176$ with $\Delta\tau = 20$ kPa). In this study, it was found that the influence of cyclic amplitude was significant when performing the tests with $k = 1000$ kPa/mm, $\sigma_{n0} = 100$ kPa. In case of $\Delta\tau = 10$ kPa at $\eta_{\mathrm{cm0}} = 0.35$ ($30 < \tau < 40$ kPa) as can be seen before (see Figure 2.77), a number of cycles for reaching the critical state were 11,972 cycles. Figure 2.86 shows the result of cyclic CNS test with $\Delta\tau = 20$ kPa ($25 < \tau < 45$ kPa) which provided the significant degradation in number of cycles for reaching the critical state (i.e. $N = 3630$ for reaching η_{crit}). Figure 2.87 can illustrate how the stress state in case of $\Delta\tau = 20$ kPa can reach the critical state early than $\Delta\tau = 10$ kPa. Although the rate of the evolution of η_{cm} as a function of N in case of $\Delta\tau = 20$ kPa was slower than that of $\Delta\tau = 10$ kPa the maximum stress ratio (η_{max}) of a bigger amplitude could reach the critical state line early. Some of the main factors influencing the cyclic interface (e.g. σ_{n0}, η_{cm0} and $\Delta\tau$) are presented in Figure 2.88 in the form of the evolution of η_{cm} as well as the degradation of σ_n in dependence of N. As can be seen during cyclic CNS tests, the degradation of σ_n as a function of N induced an increase in η_{cm} which evolved and subsequently moved towards the critical state line.

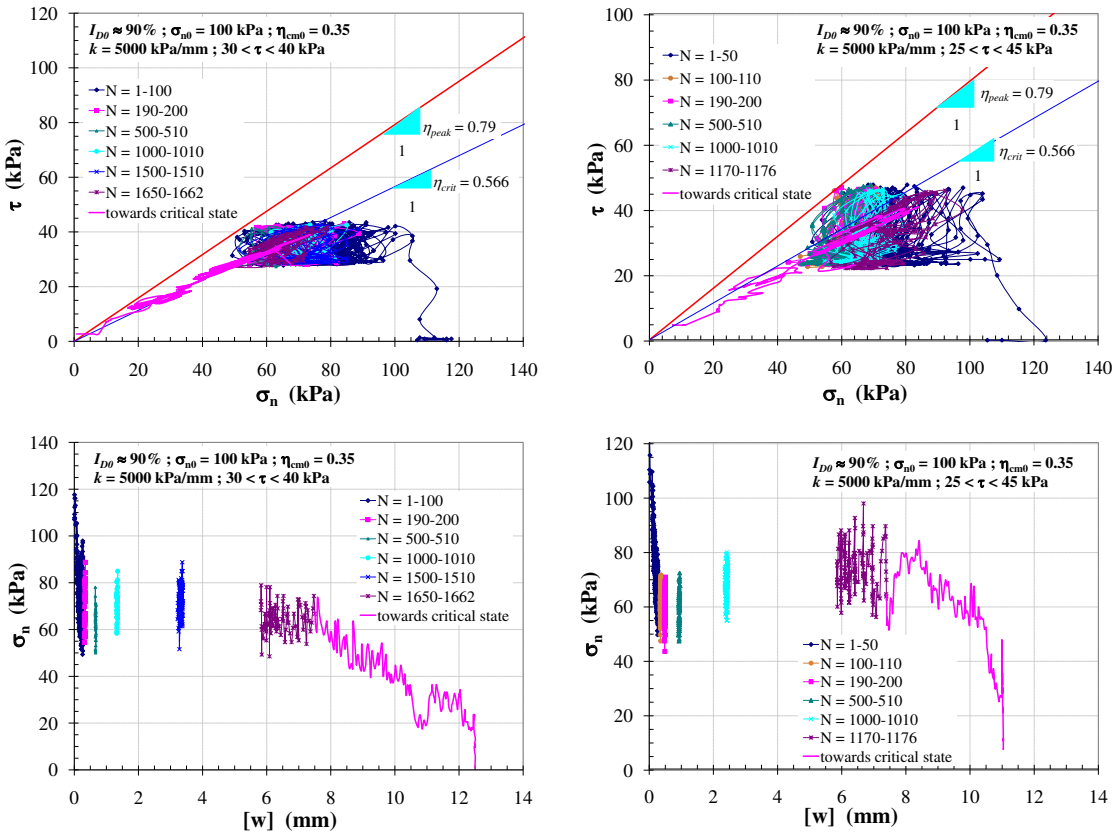

Figure 2.85: Influence of $\Delta\tau$ on normal stiffness ($k = 5000$ kPa/mm) of cyclic CNS tests with rough plate, $\sigma_{n0} = 100$ kPa, $\eta_{\mathrm{cm0}} = 0.35$ on dense sand ($I_{D0} \approx 90\%$)

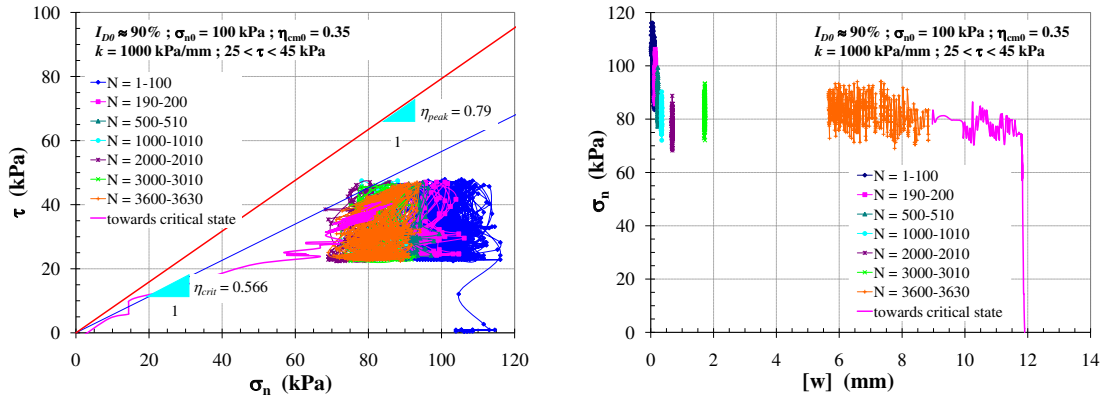

(a) (b)

Figure 2.86: Cyclic CNS tests on dense sand ($I_{D0} \approx 90\%$) with rough plate, $\sigma_{n0} = 100$ kPa, $\Delta\tau = 20$ kPa, $k = 1000$ kPa/mm, $\eta_{\mathrm{cm0}} = 0.35$

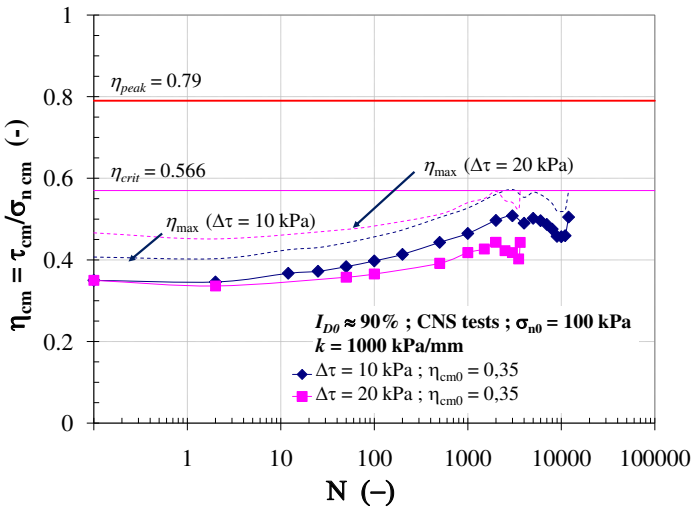

Figure 2.87: Comparison between the evolution of η_{cm} as a function of N of cyclic CNS tests with $\Delta\tau = 10$ and 20 kPa on dense sand ($I_{D0} \approx 90\%$) with rough plate, $\sigma_{n0} = 100$ kPa, $k = 1000$ kPa/mm, $\eta_{\mathrm{cm0}} = 0.35$

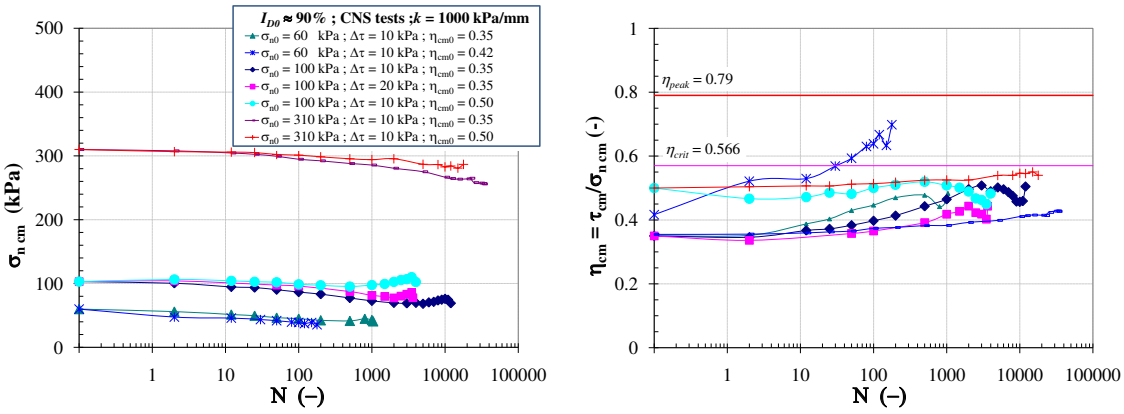

(a) (b)

Figure 2.88: Influence of σ_{n0}, η_{cm0} and $\Delta\tau$ on cyclic CNS tests with rough plate, dense sand ($I_{D0} \approx 90\%$); (a) degradation of σ_n as a function of N ; (b) evolution of η_{cm} as a function of N

For loose sand the increase of cyclic amplitude led to the significant degradation of normal stress as a result of gradual contraction. In comparison with the case of $\sigma_{n0} = 100$ kPa, $\Delta\tau = 10$ kPa as presented in Figure 2.74, an increase of k as well as $\Delta\tau$ could lead to the critical state rapidly. In case of $\Delta\tau = 20$ kPa as shown in Figure 2.89, both tests ($k = 1000$ kPa/mm at $\eta_{\mathrm{cm0}} = 0.30$ and $k = 5000$ kPa/mm at $\eta_{\mathrm{cm0}} = 0.15$) could undergo only 2 cycles. It was found that σ_n dropped significantly during the first two cycles afterwards the stress state could not evolve to the next cycle.

From many cyclic tests under CNS condition described above, it can be concluded that the worse condition is the test being performed with high level of η_{cm0}, large-amplitude of cycle, high value of k, low initial normal stress (σ_{n0}) on loose sand. This conclusion can clearly be explained by the evolution of η_{cm} in dependence of N on loose sand for various conditions as shown in Figure 2.90. All tests in this figure started from $\eta_{\mathrm{cm}} = 0.30$, the test with low initial normal stress ($\sigma_{n0} = 60$ kPa) and the case of $\sigma_{n0} = 100$ kPa with $\Delta\tau = 20$ kPa, η_{cm} moved rapidly towards the critical state line with a few number of cycles.

Considering the grain breakage after testing, Figure 2.91 shows typically the grain breakage represented by the grain size distribution curves of the tests with $\sigma_{n0} = 310$ kPa, $\Delta\tau = 10$ kPa, $k = 1000$ kPa/mm on both densities. It was found that the fine particle (D_{10}) after cyclic CNS loading on dense sand showed the variation of grading curves from the initial state (the shift of grading curves to the left). With low level of η_{cm0} ($10DM310\_1000k$), the grain breakage was considerably observed. Because the interface underwent cyclic shearing for a long period ($N \approx 32600$), the grains within the intense shear were able to be crushed. On loose sand, the grading curve of the cyclic CNS test did not show the significant variation from the initial state.

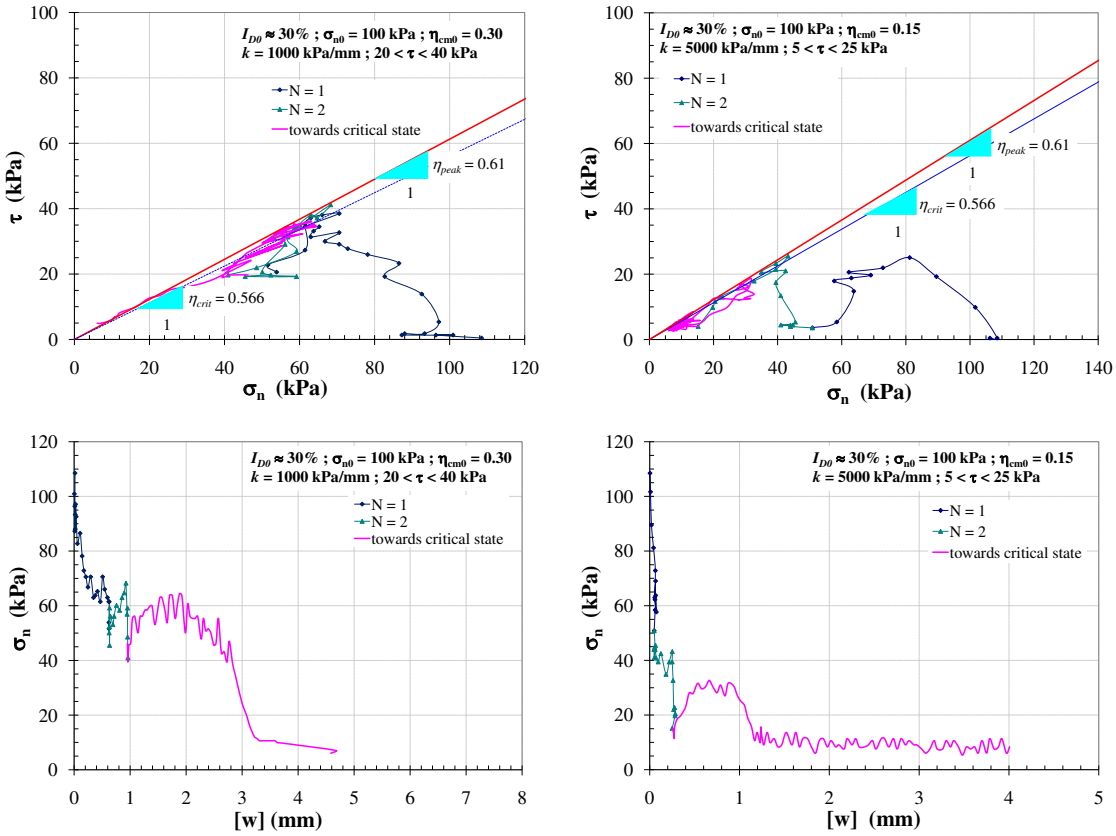

Figure 2.89: Influence of $\Delta\tau$ and k on cyclic CNS tests with rough plate, $\sigma_{n0} = 100$ kPa, on loose sand ($I_{D0} \approx 30\%$)

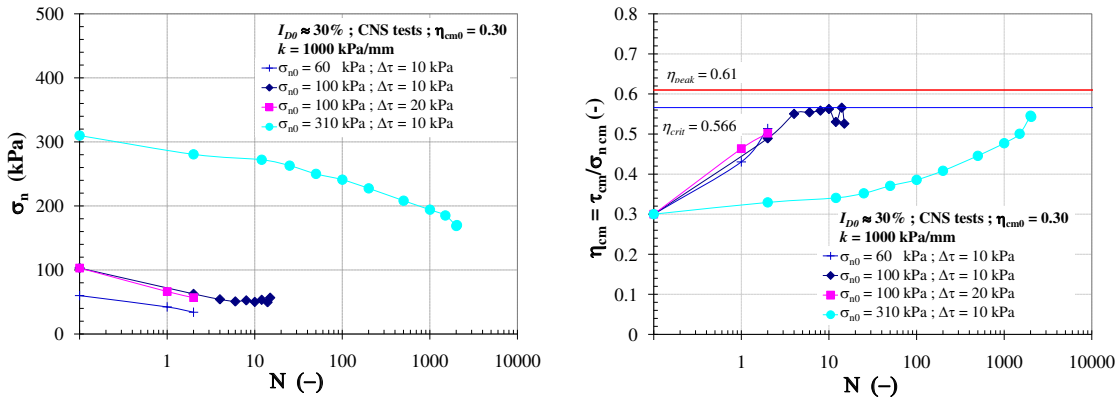

(a) (b)

Figure 2.90: Influence of σ_{n0}, and $\Delta\tau$ on cyclic CNS tests with rough plate, dense sand ($I_{D0} \approx 30\%$); (a) degradation of σ_n as a function of N ; (b) evolution of η_{cm} as a function of N

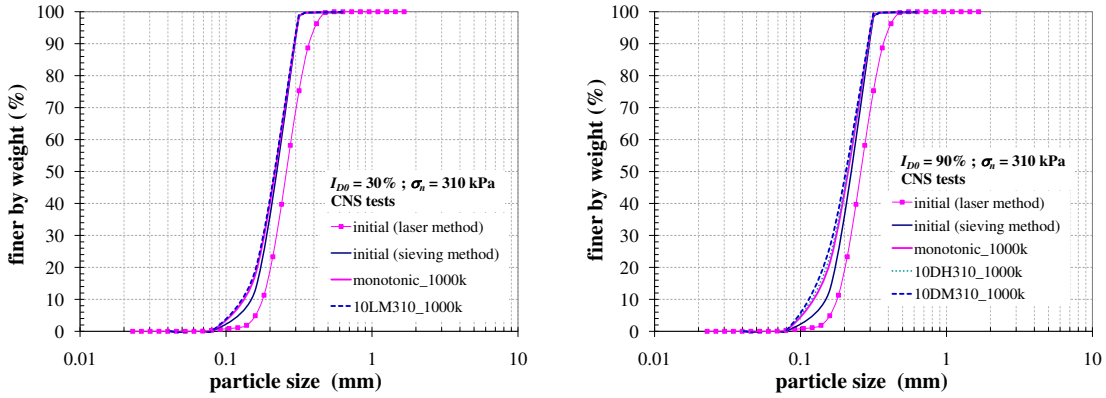

(a) (b)

Figure 2.91: Grain size distribution of sand after testing with various CNS conditions, rough plate, $\sigma_n = 310$ kPa, $k = 1000$ kPa/mm, $\Delta\tau = 10$ kPa ; (a) on loose sand ($I_{D0} \approx 30\%$); (b) on dense sand ($I_{D0} \approx 90\%$)

2.9 Validation tests (cyclic CNL tests by changing cyclic amplitude)

This series was carried out by changing the sequence and amplitude of two consecutive packages ($\Delta\tau = 10$ and 20 kPa), each with 5,000 cycles, in CNL condition with $\sigma_n = 120$ kPa, $\eta_{\text{cm}} \approx \frac{1}{2}\eta_{\text{peak}}$. These tests were still in the range of $\eta_{\text{cm}} < \eta_{\text{car}}$. Figure 2.92 illustrates the typical $\tau - [w]$ and $[u] - [w]$ diagrams of cyclic CNL direct shear interface by changing the amplitude of cycles on loose sand. These two tests were performed by changing the package with $\Delta\tau = 10$ ka at $\eta_{\text{cm}} = 0.30$ ($30 < \tau < 40$ kPa) and $\Delta\tau = 20$ ka at $\eta_{\text{cm}} = 0.30$ ($25 < \tau < 45$ kPa) vice versa. These diagrams show, for each package, the first 100 cycles of cyclic loading and 10 consecutive cycles at N= 200, 500, 1000, 2000 and 5000.

Figure 2.92 also illustrates that when the package of cycles with small amplitude ($\Delta\tau = 10$ kPa) was first applied, the subsequent package with large amplitude ($\Delta\tau = 20$ kPa) then induced the reduction of displacement rate. However, the subsequent package with large amplitude ($\Delta\tau = 20$ kPa) was applied, the first cycle of this package did not significantly differ from the following ones as can be observed from the ordinary tests. It can be said that the precedent package with $\Delta\tau = 10$ kPa caused gradual densification and consequently induced a reduction in rate of $[u]$ and $[w]$.

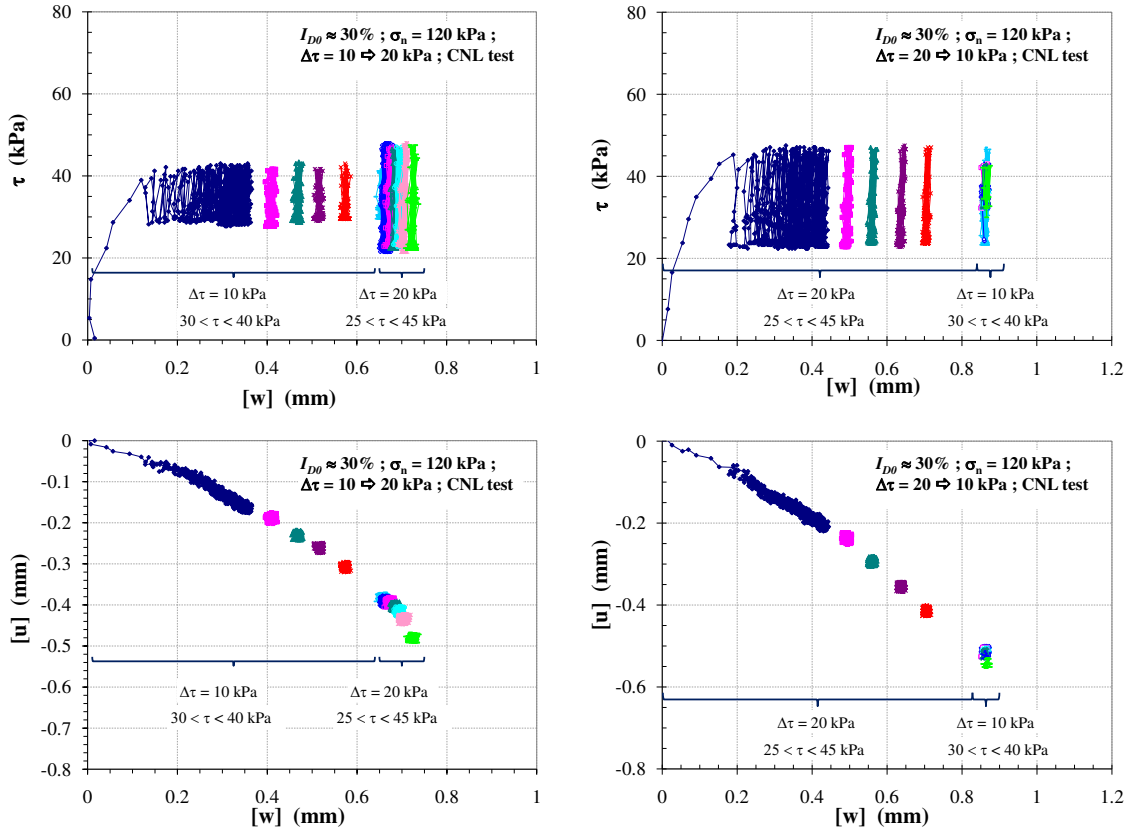

Figure 2.92: $\tau - [w]$ and $[u] - [w]$ diagrams of cyclic CNL tests by changing the amplitude of cycles, 5000 cycles of each amplitude, with rough plate on loose sand ($I_{D0} \approx 30\%$), σ_{n0} = 120 kPa, $\eta_{\text{cm}} \approx \frac{1}{2}\eta_{\text{peak}}$

When starting with large amplitude ($\Delta\tau$ = 20 kPa), the displacements, $[u]$ and $[w]$, caused by this package were more prominent than those with $\Delta\tau$ = 10 kPa. The displacements during the subsequent package of $\Delta\tau$ = 10 kPa evolved hardly. The first package with $\Delta\tau$ = 20 kPa resulted in more progressive densification and led to the significant reduction of displacement rate when the subsequent package of $\Delta\tau$ = 10 kPa was applied. The total displacements at N = 10000 of the test starting with $\Delta\tau$ = 20 kPa were larger than those with $\Delta\tau$ = 10 kPa. This was due to the larger displacement in the first package with large amplitude.

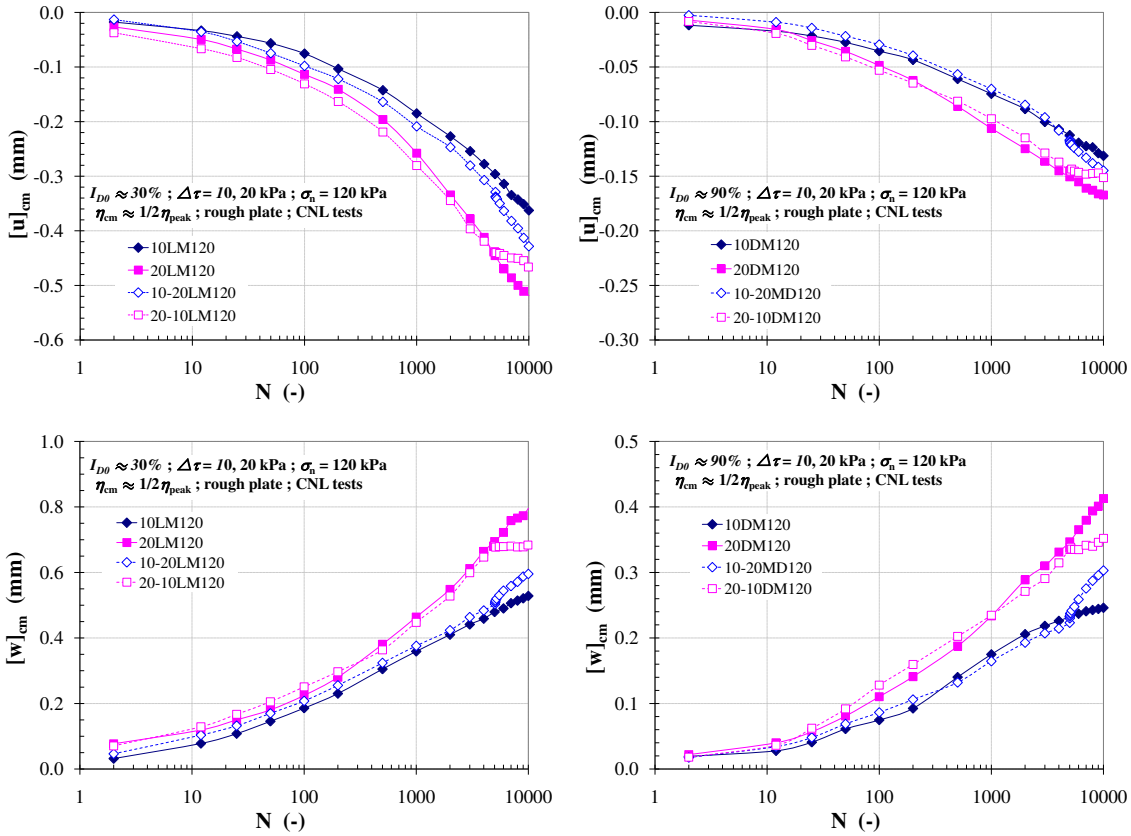

Figure 2.93: Evolution of mean cyclic displacements $[u]_{\mathrm{cm}}$ and $[w]_{\mathrm{cm}}$ in dependence of N of cyclic CNL tests with rough plate, σ_{n0} = 120 kPa, $\eta_{\mathrm{cm}} \approx \frac{1}{2}\eta_{\mathrm{peak}}$; (left) on loose sand ($I_{D0} \approx 30\%$) ; (right) on dense sand ($I_{D0} \approx 90\%$)

However, after excluding the first cycle of each package, the mean cyclic displacements ($[u]_{\mathrm{cm}}$ and $[w]_{\mathrm{cm}}$) in dependence of N on loose and dense sand were presented in Figure 2.93. The tests with steady amplitude ($\Delta\tau$ = 10 and 20 kPa in the identification series) were also presented. In comparison with the steady amplitude of $\Delta\tau$ = 10 and 20 kPa, the evolution of $[u]_{\mathrm{cm}}$ and $[w]_{\mathrm{cm}}$ of the tests by changing the amplitude of cycles on both densities were in the range of this boundary condition. In case of starting with amplitude of cycle $\Delta\tau$ = 20 kPa, the mean cyclic displacements $[u]_{\mathrm{cm}}$ and $[w]_{\mathrm{cm}}$ at N =10000 were slightly larger than that with $\Delta\tau$ = 10 kPa. Therefore, this can be attributed that the change of amplitude of cycles between consecutive packages has no influence on the total mean cyclic displacements $[u]_{\mathrm{cm}}$ and $[w]_{\mathrm{cm}}$. Since this series was performed in the range of $\eta_{\mathrm{cm}} < \eta_{\mathrm{car}}$, if the significant change of amplitude of cycles, especially in case of η_{cm} close to η_{car} is applied, this would lead to different results (Wichtmann et al. [2010]).

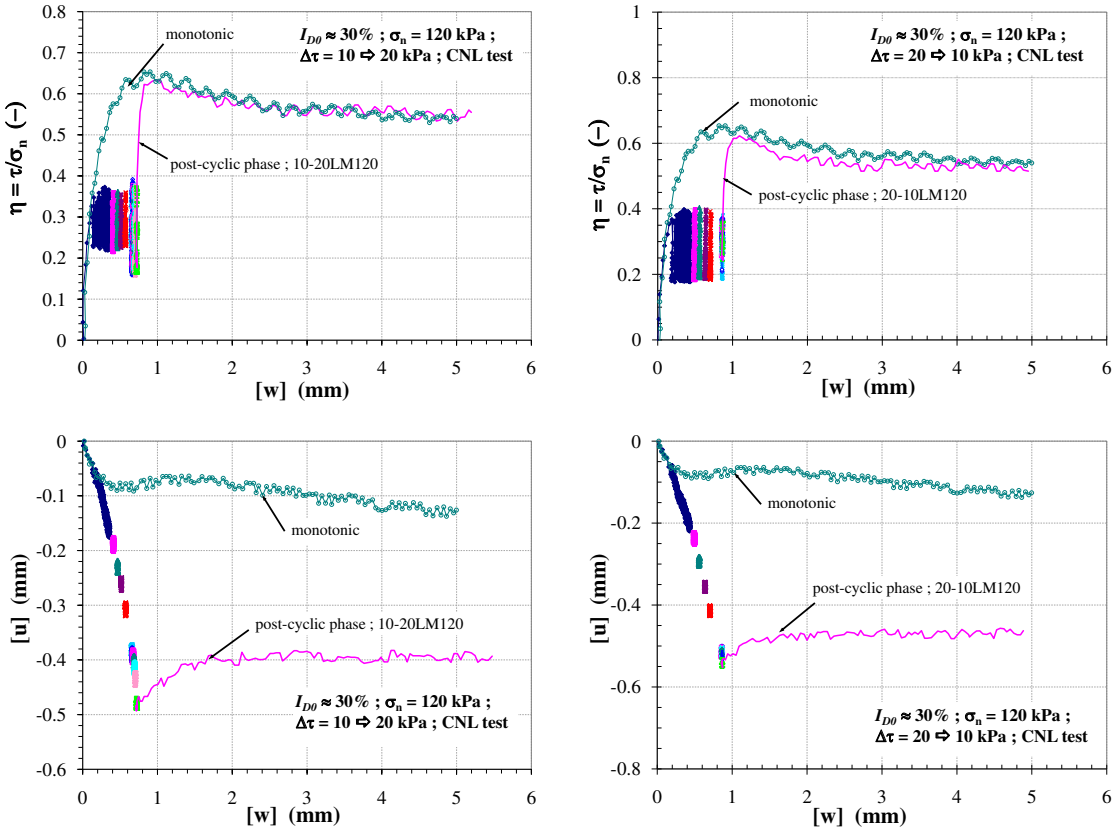

Figure 2.94: Post-cyclic phase of cyclic CNL tests by changing the amplitude of cycles on loose sand ($I_{D0} \approx 30\%$) with rough plate, $\sigma_{n0} = 120$ kPa, $\eta_{\text{cm}} \approx \frac{1}{2}\eta_{\text{peak}}$

After cyclic phase, the post-cyclic phase was then carried out. Figure 2.94 and 2.95 show respectively the post-cyclic behaviour of interface on losse and dense sands. The values of peak stress ratio (η_{peak}) at post-cyclic phase of these tests on both densities were not different so much from those in monotonic tests. Most of them were slightly lower than those in monotonic CNL tests. Altough during cyclic phase the interface behaved contractively which induced more densification on loose sand (the occurence of slight dilation rate at the beginning of post-cyclic phase) there was not the significant difference in η_{peak}. The slight decrease in η_{peak} at post-cyclic phase on loose sand may be attributed to the high evolution of $[w]_{\text{cm}}$ during cyclic phase (the magnitude of sliding displacement of interface, Uesugi et al. [1989] and Fakharian & Evgin [1997]). Dense sand on which the interface behaved contractively during cyclic loadig exhibited dilative behaviour at post-cyclic phase. The dilation rate at post-cyclic phase was not so much different from monotonic test. The slight decrease in η_{peak} was also found at post-cyclic phase. This would be attributed to an increase in crushing and wear of grains within the interface shear zone on dense sand.

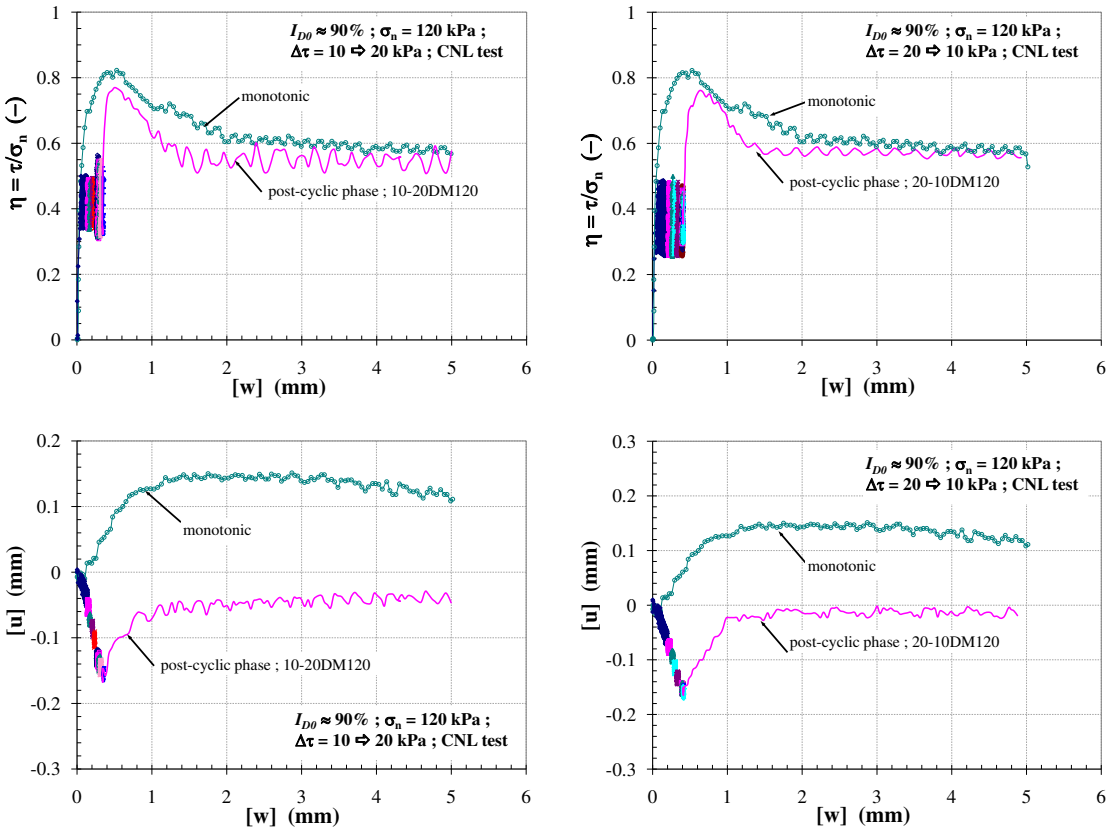

Figure 2.95: Post-cyclic phase of cyclic CNL tests by changing the amplitude of cycles on dense sand ($I_{D0} \approx 90\%$) with rough plate, $\sigma_{n0} = 120$ kPa, $\eta_{\text{cm}} \approx \frac{1}{2}\eta_{\text{peak}}$

2.10 Cyclic interface direct shear tests on smooth plate

Cyclic interface direct shear tests on smooth plate were supplementarily performed in oder to compare to those on rough plate. This series was mainly focused in CNS condition (Table 2.6). In case of cyclic CNS condition on loose sand with $\sigma_{n0} = 60$ kPa, there was not any possible way to perform the tests whether with $k = 1000$ or 5000 kPa/mm. From experimental observations in monotonic tests on smooth plate, the peak stress ratio η_{peak} on loose sand is very small. Obviously, under CNS condition the test with $\sigma_{n0} = 60$ kPa, these tests were only performed in a short period of time ($\tau_{\text{peak}} \approx 9$ kPa at $[w] \approx 0.80$ mm). Some of cyclic CNL tests were performed by observing some factors influencing on the interface behaviour.

Table 2.6: Cyclic tests on smooth plate

N°	I_{D0} (%)	σ_n (kPa)	k (kPa/mm)	level of η_{cm0} (-)	τ (kPa)	η_{cm} (-)	$\Delta\tau$ (kPa)
10LL120	30	120	CNL	0	$-5 < \tau < 5$	0	10
10LM120	30	120	CNL	$\approx 1/2\eta_{\text{peak}}$	$20 < \tau < 30$	0.21	10
10LH120	30	120	CNL	$\approx 9/10\eta_{\text{peak}}$	$40 < \tau < 50$	0.38	10
20LM120	30	120	CNL	$\approx 1/2\eta_{\text{peak}}$	$15 < \tau < 35$	0.21	20
10DL120	90	120	CNL	0	$-5 < \tau < 5$	0	10
10DM120	90	120	CNL	$\approx 1/2\eta_{\text{peak}}$	$28 < \tau < 38$	0.28	10
10DH120	90	120	CNL	$\approx 9/10\eta_{\text{peak}}$	$50 < \tau < 60$	0.46	10
20DM120	90	120	CNL	$\approx 1/2\eta_{\text{peak}}$	$23 < \tau < 43$	0.28	20
10LL100_1000k	30	100	1000	0	$5 < \tau < 15$	0.10	10
10LL100_5000k	30	100	5000	0	$0 < \tau < 10$	0.05	10
10LM310_1000k	30	310	1000	$\approx 1/2\eta_{\text{peak}}$	$42 < \tau < 52$	0.15	10
10LM310_1000k	30	310	1000	$\approx 2/3\eta_{\text{peak}}$	$88 < \tau < 98$	0.30	10
10DM60_1000k	90	60	1000	$\approx 1/2\eta_{\text{peak}}$	$10 < \tau < 20$	0.25	10
10DM100_1000k	90	100	1000	$\approx 1/2\eta_{\text{peak}}$	$15 < \tau < 25$	0.20	10
10DM100_1000k	90	100	1000	$\approx 2/3\eta_{\text{peak}}$	$30 < \tau < 40$	0.35	10
10DH100_5000k	90	100	5000	$\approx 2/3\eta_{\text{peak}}$	$30 < \tau < 40$	0.35	10
20DH100_1000k	90	100	1000	$\approx 2/3\eta_{\text{peak}}$	$25 < \tau < 45$	0.35	20
20DH100_5000k	90	100	5000	$\approx 2/3\eta_{\text{peak}}$	$25 < \tau < 45$	0.35	20
10DH310_1000k	90	310	1000	$\approx 2/3\eta_{\text{peak}}$	$105 < \tau < 115$	0.35	10

2.10.1 Cyclic CNL tests

Figure 2.96 shows the test results of cyclic interface tests under CNL condition on both densities. As can be observed, the mean cyclic displacements ($[u]_{\text{cm}}$ and $[w]_{\text{cm}}$) obtained from smooth plate were considerable than those from rough plate. Considering the normal displacement $[u]_{\text{cm}}$, unlike monotonic test it was found that cylic CNL tests on smooth plate provided more contraction than rough plate did. The contractive behaviour was found in the range of $\eta_{\text{cm}} < \eta_{\text{car}}$. However, this was in contrast to those derived from available investigations in which the normal displacement of rough plate was greater than that of smooth plate (the effect of dilative behaviour which was mainly found on rough plate influenced the volumetric behaviour and consequently resulted in more variation of $[u]$).

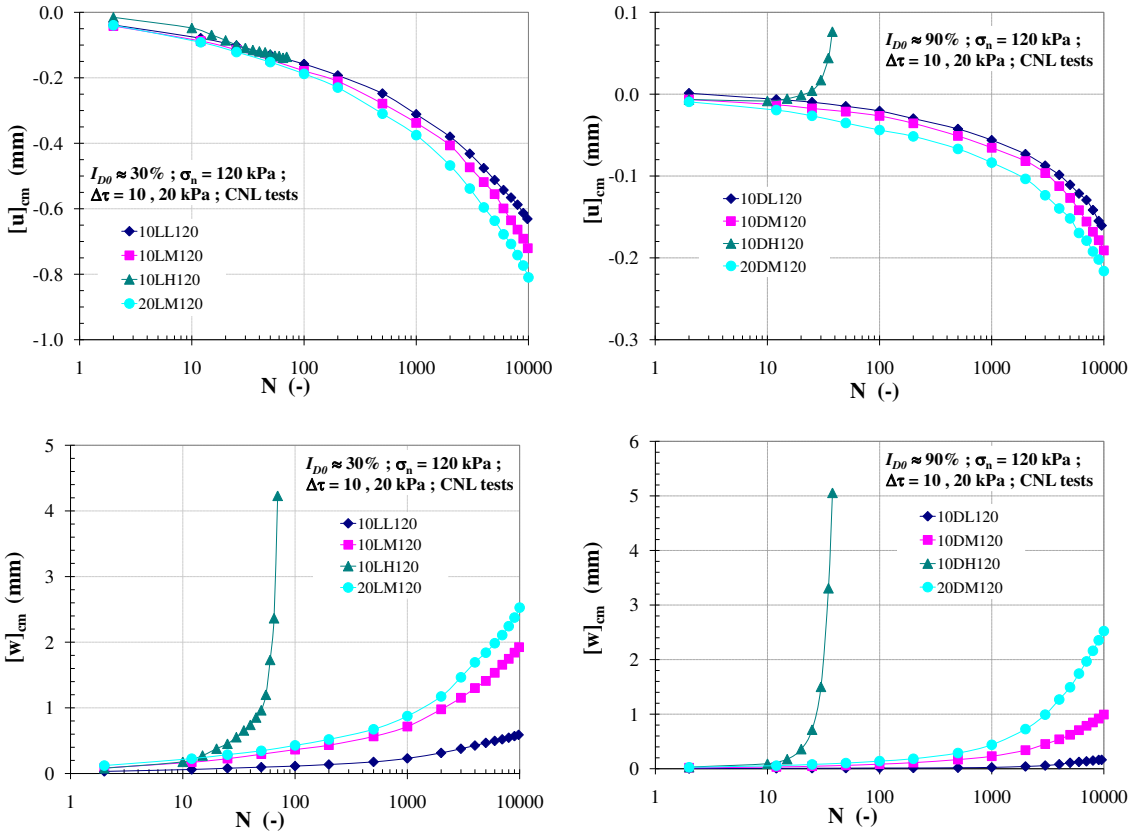

Figure 2.96: Evolution of mean cyclic displacements $[u]_{\mathrm{cm}}$ and $[w]_{\mathrm{cm}}$ in dependence of N of cyclic CNL tests, $\sigma_{n0} = 120$ kPa with smooth plate; (left) on loose sand ($I_D \approx 30\%$) ; (right) on dense sand ($I_{D0} \approx 90\%$).

For instance, Mortara [2001], Shahrour & Rezaie [1997] and Mortara et al. [2007] reported that under cyclic CNL condition the normal displacement $[u]$ from rough plate was larger than that from smooth plate due to the effect of dilative behaviour. However, those observations were in displacement-controlled tests whereas this study was carried out by shear stress-controlled tests. With displacement-controlled tests, a contracting behaviour followed by dilation at each cycle was observed on rough plate (more evident on dense sand). Considering the shear stress-controlled tests, an evolution of accumulative displacements as a function of N was obtained. In this study, it was found that the accumulation of dispacements mainly depended on many factors such as initial normal stress (σ_{n0}), initial density (I_{D0}), mean cyclic stress ratio (η_{cm}) and amplitude of cycle ($\Delta\tau$). When comparing two different types of surface roughness, although the tests were performed at the same level of η_{cm} (but η_{cm} of smooth plate was closer to η_{peak} as a result of lower friction angle), the evolution of mean cyclic shear displacement $[w]_{\mathrm{cm}}$ on smooth plate was more significant than that on rough plate and consequently led to more contraction. This displacement ($[w]_{\mathrm{cm}}$) arose considerably, thought $\eta_{\mathrm{cm}} = 0$ as shown in Figure 2.96. This can be deduced that the smooth plate allowed the interface to slide than rough plate (the freedom in movement

of soil adjacent to the structure). The significant increase of mean cyclic shear displacement $[w]_{\mathrm{cm}}$ therefore induced more contractive behaviour (an increase in $[u]_{\mathrm{cm}}$). Within the range of $\eta_{\mathrm{cm}} < \eta_{\mathrm{car}}$, the increase of cyclic amplitude ($\Delta\tau$) induced the increasing rate of displacement intensity. In case of high level of η_{cm} on dense sand, the dilative behaviour on smooth plate was less evident than that on rough plate.

At post-cyclic phase, the peak stress ratio (η_{peak}) was found to be slightly less than that of monotonic test on both densities (Figure 2.97). It was also found that there was not significant difference in peak stress ratio when performing the tests in different conditions. Despite the increase in contraction during cyclic loading, the volumetric behaviour at post-cyclic phase did not show any significant variation. Indeed, in the range of $\eta_{\mathrm{cm}} < \eta_{\mathrm{car}}$ cyclic loading which induces more densification within the interface would at least lead to the variation of volumetric behaviour at post-cyclic phase. This can be attributed to the effect of dilative behaviour which can hardly be observed on smooth plate.

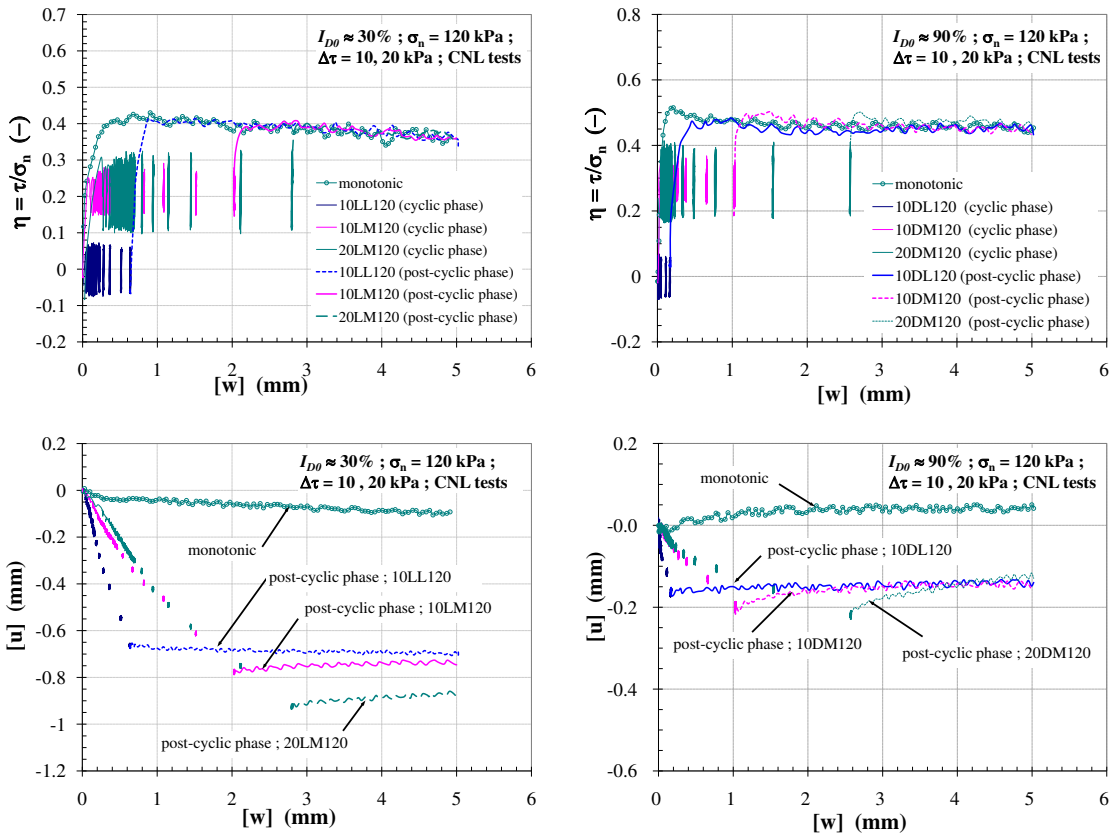

Figure 2.97: Post-cyclic phase of cyclic CNL tests, $\sigma_{n0} = 120$ kPa with smooth plate; (left) on loose sand ($I_{D0} \approx 30\%$) ; (right) on dense sand ($I_{D0} \approx 90\%$).

Similarly to rough plate, the examination of grain breakage after testing was also carried out. As can be well conceived that the smooth has less abrasive surface than rough plate and the slippage generally occurs along the contact surface between smooth plate and sand (Uesugi & Kishida [1986]). The tendency for grain crushing, due to the abrasion between grains and smooth plate, within the localized shear zone would be hardly found. After cyclic loading tests, it was found that smooth plate did not provide noticeable grain breakage. Figure 2.98 shows the grading curves of the tests performed on smooth plate in various conditions. On loose sand the variation of grading curves representing the grain breakage could hardly observed even considering the fine particle (D_{10}) whereas slight variation of grading curves could observed on dense sand.

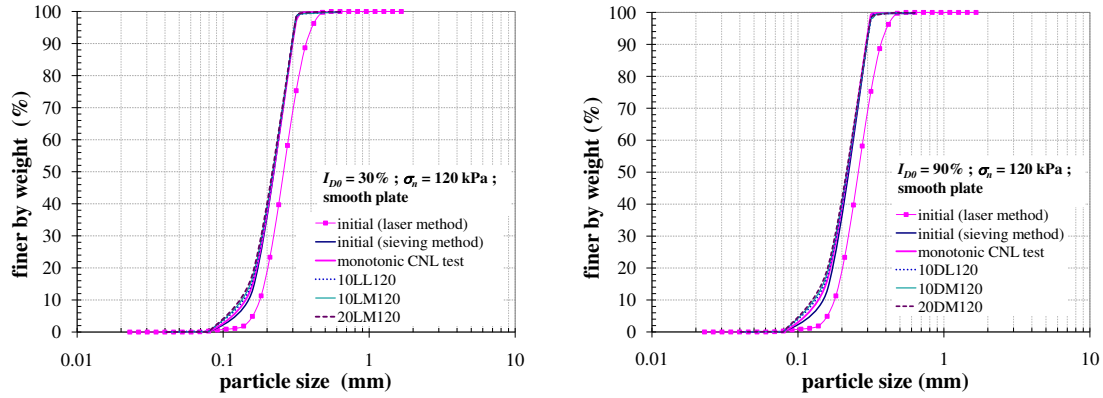

(a) (b)

Figure 2.98: Grain size distribution of sand after testing with various CNL conditions on smooth plate, σ_n = 120 kPa; (a) on loose sand ($I_{D0} \approx 30\%$); (b) on dense sand ($I_{D0} \approx 90\%$)

2.10.2 Cyclic CNS tests

An important feature of cyclic interface tests is the CNS condition in which the degradation of normal stress is described. Smooth plate also showed that the degradation of normal stress was the main characteristic which was similar to that on rough plate. Having known from experimental evidences, the significant degradation of normal stress was due to the contraction within the interface. As can be seen on rough plate, there were many factors that influenced the interface behaviour such as k, I_{D0}, σ_{n0}, η_{cm0}, $\Delta\tau$.

The results for cyclic CNS tests with smooth plate, σ_{n0} = 100 kPa on dense sand are typically presented as the diagrams of $\tau - \sigma_n$, $\sigma_n - [w]$ and $[u] - [w]$ in Figure 2.99. These results show the strong influence of k (k = 1000 and 5000 kPa/mm) on cyclic interface behaviour. These can be compared with the tests given in Figure 2.77 for rough plate. On dense sand, although these tests were performed at the same level of $\eta_{\text{cm0}} = 0.35$, it was evident that a number of cycles for reaching the critical state with smooth plate were significantly less than those with rough plate. Considering the rate of degradation in normal

stress as a result of the progressive contraction, it was found that this rate of smooth plate was slighly lower than that of rough plate. On rough plate, for instance in case of $k = 1000$ kPa/mm, σ_n dropped from 100 to 60 kPa during the first 100 cycles whereas σ_n dropped from 100 to 80 kPa on smooth plate. However, the interesting feature of the degradation in normal stress (and consequently the critical state was reached) was the level of initial mean cyclic stress ratio (η_{cm0}).

While the critical state line of smooth plate is obviously lower than that of rough plate ($\eta_{\text{crit}} = 0.43$ for smooth plate whereas $\eta_{\text{crit}} = 0.566$ for rough plate), with starting the same level of η_{cm}, the stress state of smooth plate moves towards the critical state line due to the degradation of normal stress and then early reaches the lower value of critical state line. These two plates did not show the significant difference in volumetric behaviour ($[u] - [w]$ diagrams) especially in case of $k = 5000$ kPa/mm in which the normal displacement can be deduced to be almost constant during cyclic loading.

To illustrate some of the main factors (i.e. σ_{n0}, η_{cm0} and $\Delta\tau$) influencing the cyclic CNS interface, first the tests performed with different values of initial normal stress (σ_{n0}) are presented. Figure 2.100 shows the test results performed with $\sigma_{n0} = 60$ kPa at $\eta_{\text{cm0}} = 0.25$ and $\sigma_{n0} = 310$ kPa at $\eta_{\text{cm0}} = 0.35$ on dense sand. The influence of σ_{n0} can well be understood by considering the test results on rough plate as shown in Figure 2.80 and 2.82. Obviously, the test performed with $\sigma_{n0} = 60$ kPa provided less number of cycles for reaching the critical state. A simimilar trend was also observed on smooth plate. With $\sigma_{n0} = 60$ kPa, $\eta_{\text{cm0}} = 0.25$ on smooth plate, a number of cycles for reaching the critical state were $N = 19$ (in case of rough plate $N = 1042$ at $\eta_{\text{cm0}} = 0.35$).

The effect of σ_{n0} was more considerable when performing with $\sigma_{n0} = 310$ kPa at the same level of η_{cm0} (e.g. $\eta_{\text{cm}} = 0.35$). As can be seen in Figure 2.82, the tendency to reach the critical state on rough plate was hardly found (this test was performed until $N = 32669$ and then the post-cyclic phase was applied) whereas the smooth plate required 4,710 cycles for reaching the critical state. The noticeable difference in number of cycles for reaching the critical state of these two plates can be attributed to the difference in peak (η_{peak}) and critical (η_{crit}) stress ratios. These two stress ratios obtained from smooth plate allowed the stress state to reach the critical state early than rough plate did.

The effect of cyclic amplitude was also observed. Again, the effect of cyclic amplitude was observed with $\Delta\tau = 10$ ($30 < \tau < 40$) and 20 ($25 < \tau < 45$) kPa, $\sigma_{n0} = 100$ kPa, $\eta_{\text{cm0}} = 0.35$, $k = 1000$ and 5000 kPa/mm. Figure 2.101 typically shows the test results in case of $\Delta\tau = 20$ ($25 < \tau < 45$) kPa with $k = 5000$ kPa/mm. As can be seen on rough plate, since the increase in amplitude of cycle was applied, a number of cycles for reaching the critical state decreased obviously. In case of $k = 5000$ kPa/mm, $\Delta\tau = 20$ kPa, a number of cycles $N = 48$ were required for reaching the critical state while $N = 121$ for $\Delta\tau = 10$ kPa. The rate of degradation in normal stress was almost similar, the normal stress dropped from 100 to 80 kPa, but the stress state in case of $\Delta\tau = 20$ kPa could reach the critical state early because of the size of cycles (see $\tau - \sigma_n$ planes).

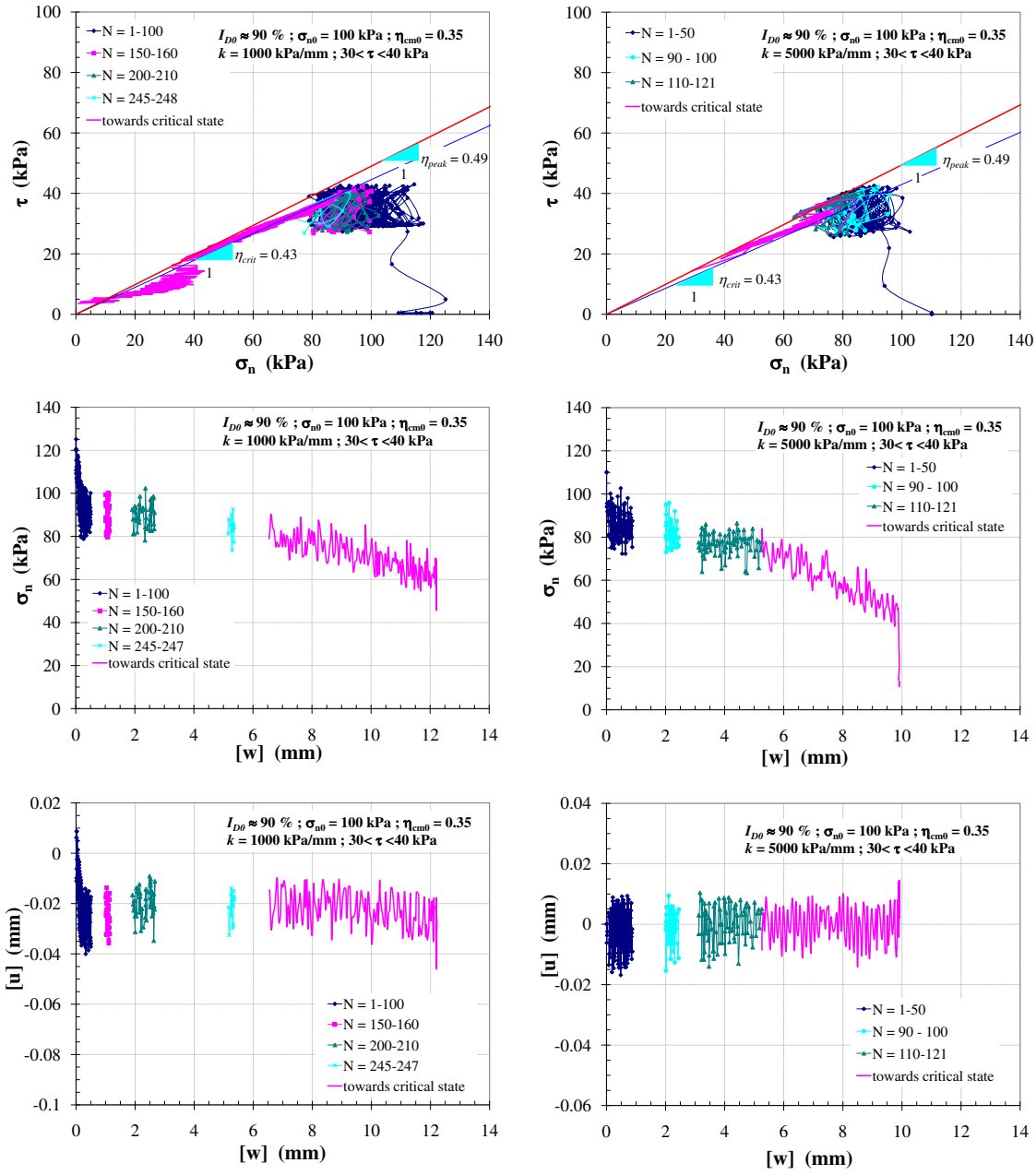

Figure 2.99: Influence of k on cyclic CNS tests, $\sigma_{n0} = 100$ kPa, $\eta_{\mathrm{cm0}} = 0.35$ on dense sand ($I_{D0} \approx 90\%$) with smooth plate; (left) $k = 1000$ kPa/mm; (right) $k = 5000$ kPa/mm

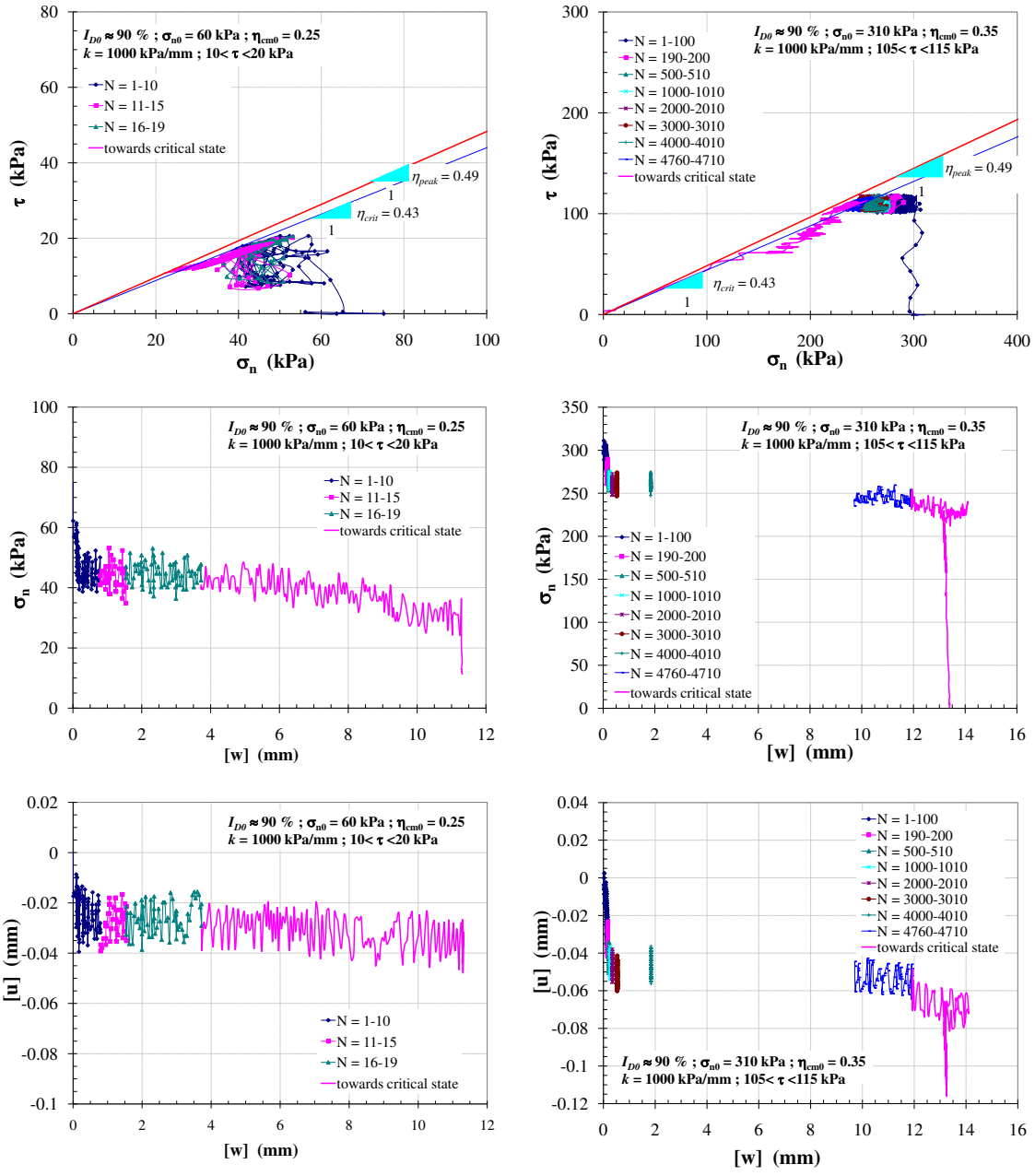

Figure 2.100: Influence of σ_{n0} on cyclic CNS tests, $k = 1000$ kPa/mm, on dense sand ($I_{D0} \approx 90\%$) with smooth plate; (left) $\sigma_{n0} = 60$ kPa at $\eta_{\mathrm{cm0}} = 0.25$; (right) $\sigma_{n0} = 310$ kPa at $\eta_{\mathrm{cm0}} = 0.35$

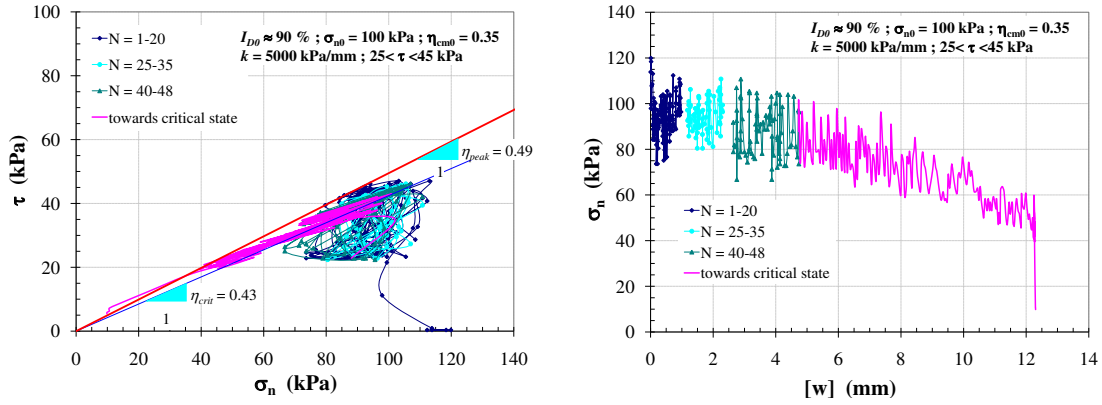

(a) (b)

Figure 2.101: Cyclic CNS test on smooth plate, $\sigma_n = 100$ kPa, $\Delta\tau = 20$ kPa, $k = 1000$ kPa/mm on dense sand ($I_{D0} \approx 90\%$); (a) $\tau - \sigma_n$ plane; (b) $\sigma_n - [w]$ plane

When considering the evolution of η_{cm} during cyclic phase, Figure 2.102 illustrates how the stress state represented by η_{cm}, corresponding to the degradation of normal stress, moves towards the critical state line. The evolution of η_{cm} corresponding to the degradation of σ_{cm} as a function of N as well as $[w]_{\text{cm}}$ clearly explains how the critical state of the interface is reached under various conditions. Similarly to cyclic CNS tests on rough plate, the degradation in normal stress increased as a function of N and $[w]_{\text{cm}}$. When comparing this degradation between the tests performed at different levels of η_{cm} (e.g. the tests with $\sigma_{n0} = 100$ kPa at $\eta_{\text{cm0}} = 0.20$ and 0.35), the rate of normal stress deradation at $\eta_{\text{cm0}} = 0.35$ was lower than that at $\eta_{\text{cm0}} = 0.20$ but the stress state at $\eta_{\text{cm0}} = 0.35$ could reach the critical state with $N = 248$ whereas in case of $\eta_{\text{cm0}} = 0.20$ required 294 cycles. The test performed with low initial stress ratio (η_{cm0}) required a large number of cycles for reaching the critical state line.

On loose sand, smooth plate provided the significant degradation of σ_n as a result of the progressive contraction. Figure 2.103 shows typical results due to the effect of imposed normal stiffness on loose sand with $\sigma_{\text{n0}} = 100$ kPa, $\Delta\tau = 10$ kPa. These two tests were performed at almost the same level of η_{cm0} ($k = 1000$ kPa/mm at $\eta_{\text{cm0}} = 0.10$, $5 < \tau < 15$ and $k = 5000$ kPa/mm at $\eta_{\text{cm0}} = 0.05$, $0 < \tau < 10$). Although the levels of η_{cm0} of these two tests were very small, the stress state could evolve only 3 cycles for $k = 1000$ kPa/mm whereas in case of $k = 5000$ kPa/mm the stress state could evolve only one cycle. The significant degradation of normal stress in these two tests dropped rapidly during the first cycle (especially in case of $k = 5000$ kPa/mm, σ_n dropped from 100 to 40 kPa) and consequently the stress state moved to the critical state line.

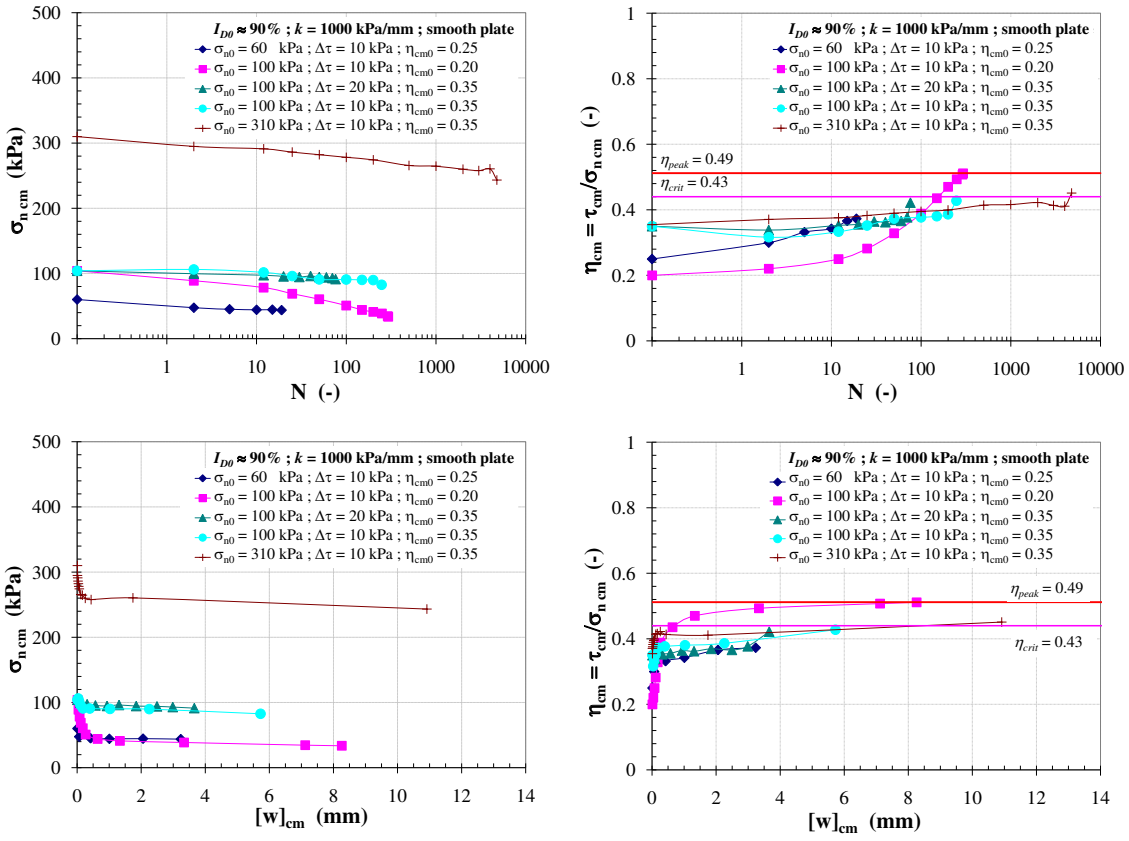

Figure 2.102: Degradation of $\sigma_{n\,cm}$ corresponding to the evolution of η_{cm} of cyclic CNS tests on dense sand ($I_{D0} \approx 90\%$) with smooth plate

The influence of η_{cm0} with the same value of σ_{n0} on loose sand was also observed by performing cyclic CNS tests with σ_{n0} = 310 kPa, k = 1000 kPa/mm, the first one was performed at η_{cm0} = 0.30 as described on rough plate (see Figure 2.76). This was evident in number of cycles for reaching the critical state (see Figure 2.104). On smooth plate, the normal stress decreased rapidly during the evolution of the first cycle (σ_n dropped to 230 kPa) and then the stress state could not evolve the next cycle whereas on rough plate the normal stress decreased continuously until σ_n = 165 kPa at N = 2035. This can clearly be described by the peak and critical stress ratios (η_{peak} and η_{crit}) of smooth plate which are lower than those of rough plate. On smooth plate, since the stress state was closed to the critical state line at the beginning of cyclic loading phase, it could move quickly to the critical state line during the first cycle. However, when performing the test at η_{cm0} = 0.15, σ_{n0} = 310 kPa on smooth plate it was found that the normal stress decreased continously as a function of N and $[w]$ until σ_n = 120 kPa at N = 481.

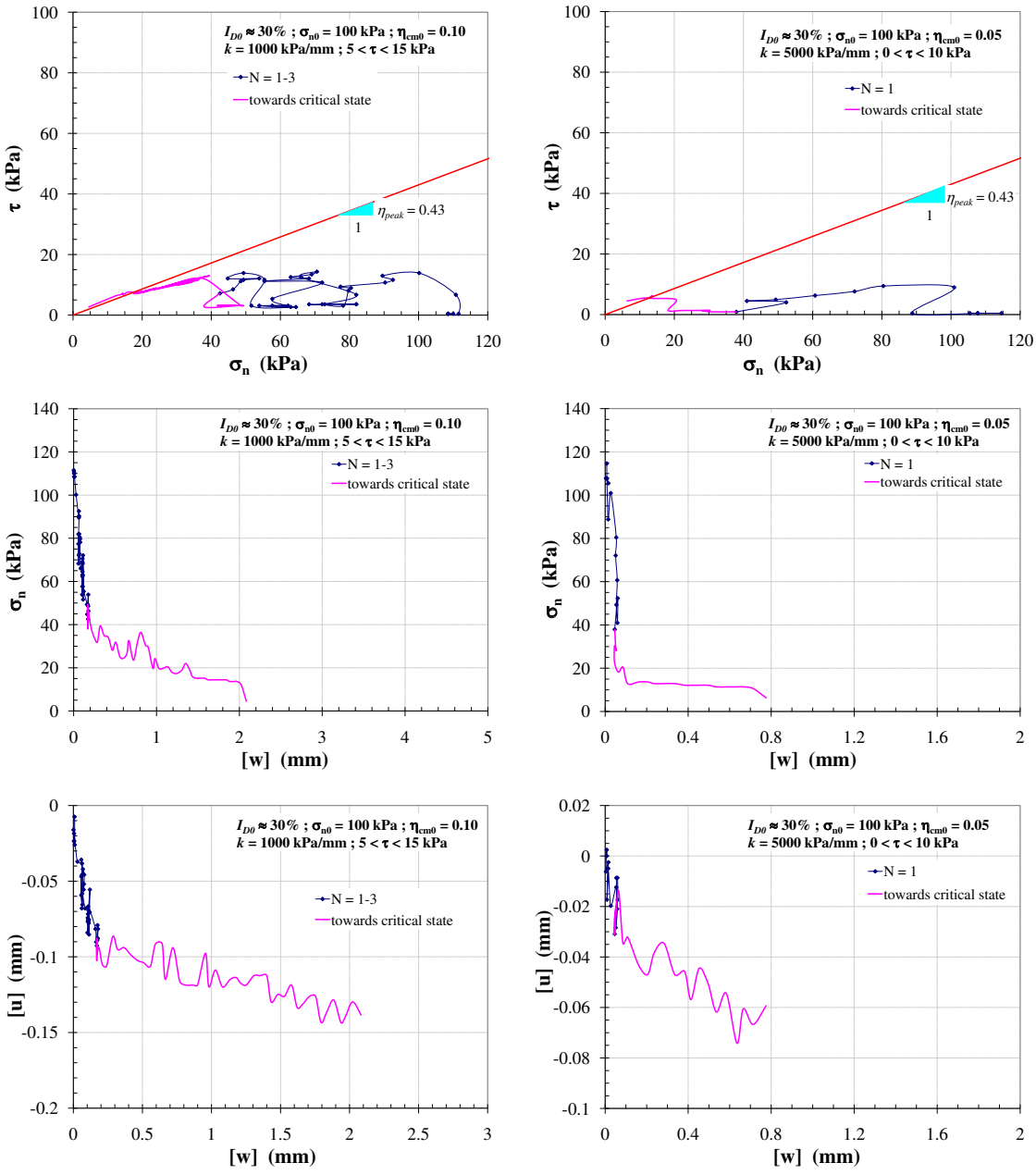

Figure 2.103: Influence of k on cyclic CNS tests, $\sigma_{n0} = 100$ kPa, loose sand ($I_{D0} \approx 30\%$) with smooth plate; (left) $k = 1000$ kPa/mm at $\eta_{\mathrm{cm0}} = 0.10$; (right) $k = 5000$ kPa/mm at $\eta_{\mathrm{cm0}} = 0.05$

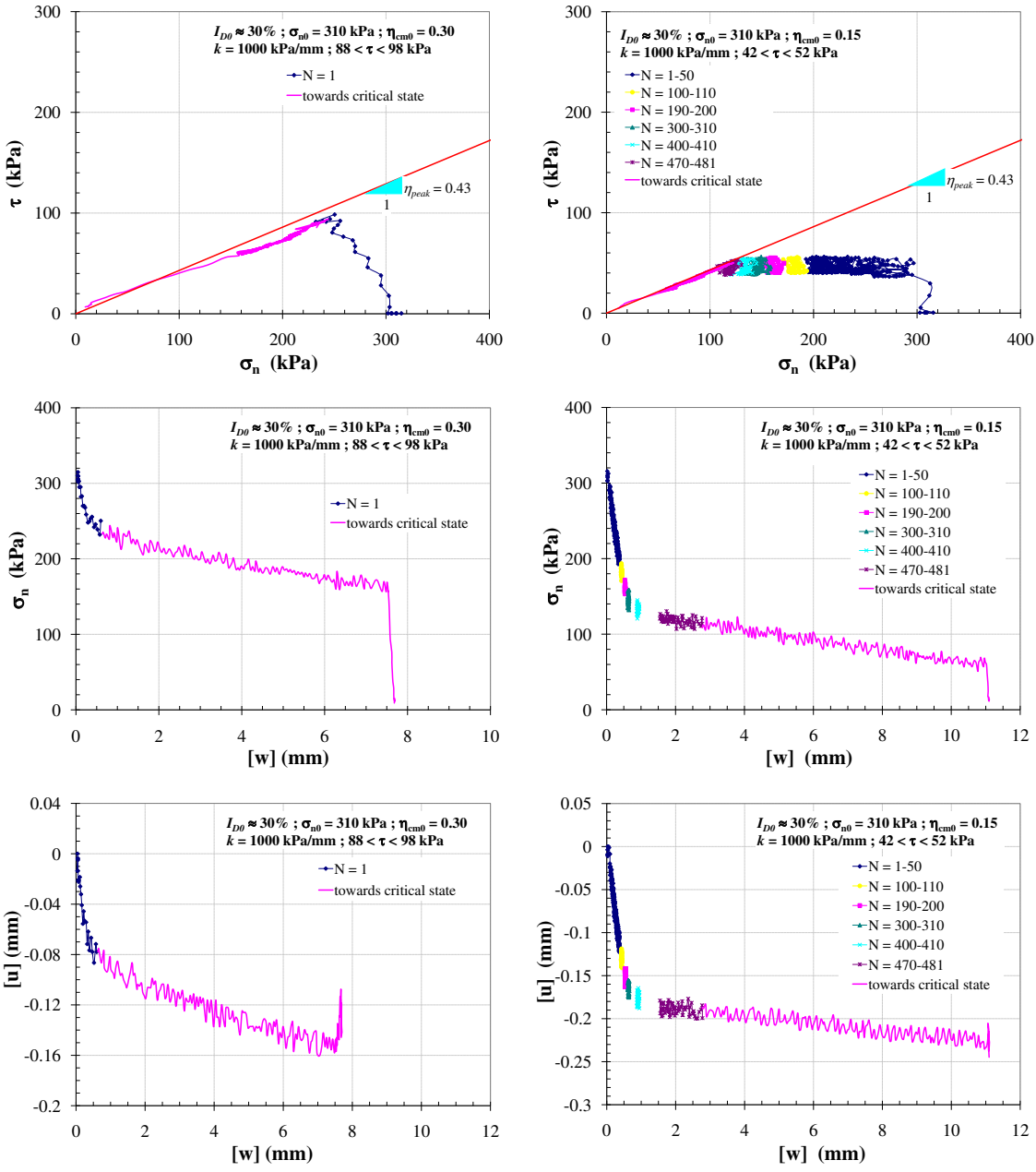

Figure 2.104: Influence of η_{cm0} on cyclic CNS tests, $\sigma_{n0} = 310$ kPa, loose sand ($I_{D0} \approx 30\%$) with smooth plate; (left) at $\eta_{\mathrm{cm0}} = 0.30$; (right) at $\eta_{\mathrm{cm0}} = 0.15$

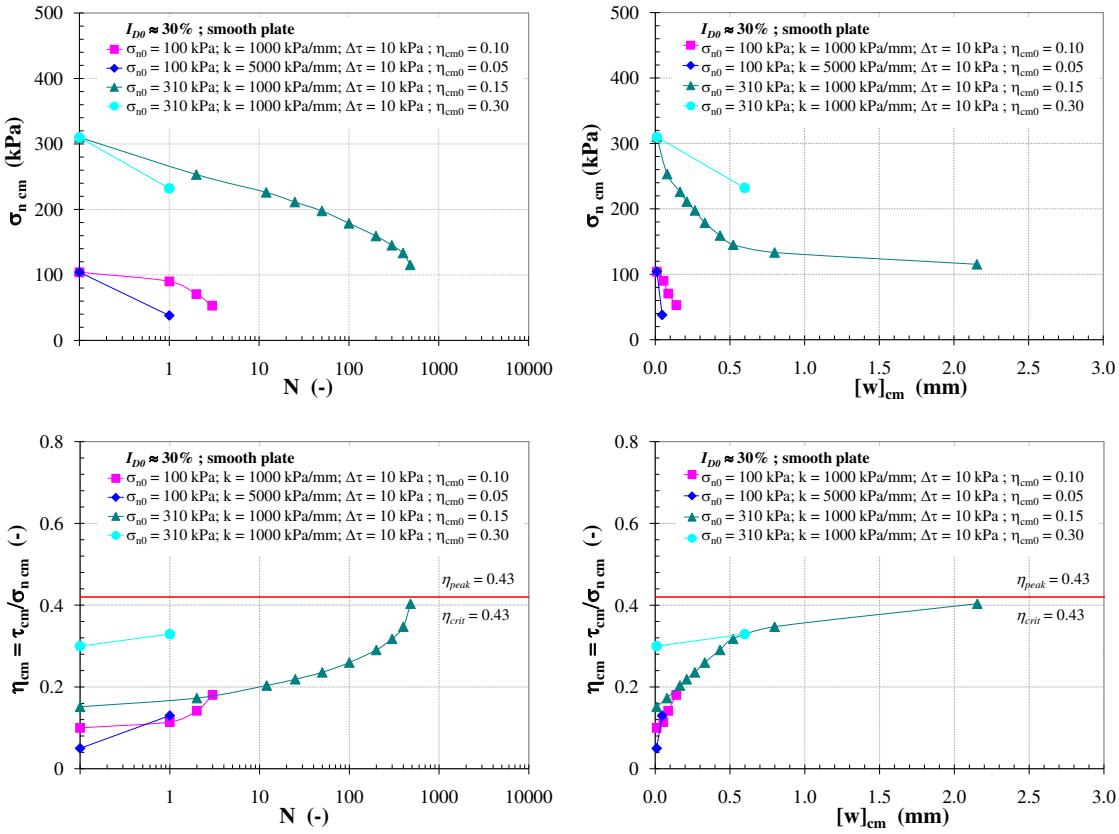

Figure 2.105: Degradation of $\sigma_{\mathrm{n\ cm}}$ corresponding to the evolution of η_{cm} of cyclic CNS tests on loose sand ($I_{D0} \approx 30\%$) with smooth plate

Again, the degradation of σ_n on loose sand corresponding to the evolution of η_{cm0} as shown in Figure 2.105 can clarify the effect of k in various conditions. Since the rate of degradation in normal stress increased as a function of N and $[w]$ and then the stress state represented by η_{cm} moved towards critical state line. From experimental observations, it can be deduced that the worse condition of cyclic CNS interface shear tests is the test performing with smooth plate, low initial normal stress, high level of η_{cm0} and high value of k.

2.11 Conclusions

Experimental campaigns carried out in this study mainly focus on cyclic direct shear tests on sand (Fontainebleau)/rough material interface under constant normal load (CNL) and constant normal stiffness (CNS) conditions. These tests were intended to simulate the situation along the shaft of piles subjected to a large number of cycles due to environmental or anthropic loadings. The rough plates which were mainly used in this study were made by gluing on a steel plate of a mixture of araldite (epoxy) and Fontainebleau sand. In case of smooth plate, in comparison with rough plate, some tests were additionally performed.

Monotonic tests preliminarily performed in order to determine the peak (δ_{peak}), critical (δ_{crit}) and characteristic (δ_{car}, separating contractive and dilative domains) friction angle allowed us to decide the cyclic test campaigns. Three levels of mean cylic stress ratio (η_{cm}, e.g. $\eta_{\text{cm}} = 0$, $\approx \frac{1}{2}\eta_{\text{peak}}$ and $\approx 9/10\eta_{\text{peak}}$) were then performed.

The cyclic tests (the shear stress-controlled tests) were classified into two groups for two purposes:

- Identification, CNL (constant normal stress) tests
- Validation of constitutive law, CNS (constant normal stiffness) tests

All tests were planned to 10^4 cycles, unless early termination occurred (this phenomenon was found in case of η_{cm} close to η_{peak}).

In particular, a special care in analysing the leakage of material during the test was then devoted in order to get the proper results. In a reasonable manner, a simple inclusive correction was then be performed by considering the leakage of sand as the fictitious contraction proportional to the accumulated $[w]$.

The cyclic tests performed with various conditions provided the deep insight of interface behaviour. From experimental observations in this study, the main factors playing an important role in cyclic interface shear tests, whether under CNL or CNS conditions, can be summarized as follows:

- Cyclic CNL condition

With rough plate, it was found that the interface behaved contractively within the range of $\eta_{\text{cm}} < \eta_{\text{car}}$ whether on loose or dense sands. The intensity of mean cyclic displacements ($[u]_{\text{cm}}$ and $[w]_{\text{cm}}$) increased as a function of η_{cm} and $\Delta\tau$ (when performing the tests at η_{cm} close to η_{car}, this would lead to different results). The volumetric behaviour of cyclic test where 10^4 cycles were reached was more contractive than monotonic test. The rate of the intensity of $[u]_{\text{cm}}$ and $[w]_{\text{cm}}$ decreased as a function of N as well as I_{D0}. The tests performed with high value of σ_n provided less intensity of $[u]_{\text{cm}}$ and $[w]_{\text{cm}}$ because the interface was restrained to expand when applying the high value of σ_n. In case of η_{cm} close to η_{peak}, dense sand showed the existence of characteristic state (passage from contractive to dilative behaviour) proposed by Luong [1980]. A number of cycles for reaching the critical state (the state that the cycles could not evolve anymore) decreased when increasing the amplitude of cycles ($\Delta\tau$).

The post-cyclic phase under CNL condition showed slight variation of peak stress ratio (η_{peak}) in comparison with that from monotonic test. When performing with low initial normal stress, η_{peak} at post-cyclic phase was slightly higher than that from monotonic test while high initial normal stress provided slighly lower η_{peak}. Considering the grain breakage within the interface shear zone represented by the grain size distribution curves (sieving method), it was found that the fine particle size (D_{10}) would be appropriate to represent the change in grain breakage analysis. Within the range of $\eta_{\text{cm}} < \eta_{\text{car}}$, an increase in σ_n, η_{cm} and I_{D0} provided more grain breakage (a shift of grading curves to the left).

In case of cyclic CNL tests by changing the sequence and amplitude of two consecutive packages ($\Delta\tau$ = 10 and 20 kPa), it was found that the change of amplitude of cycles between consecutive packages had no influence on the total mean cyclic displacements $[u]_{\text{cm}}$ and $[w]_{\text{cm}}$. However, if the significant change of amplitude of cycles, especially in case of η_{cm} close to η_{car} is applied, this would lead to different results.

With smooth plate, there existed the similar trend as can be found on rough plate. The intensity of $[u]_{\text{cm}}$ and $[w]_{\text{cm}}$ still increased as a function of η_{cm} and $\Delta\tau$ within the range of $\eta_{\text{cm}} < \eta_{\text{car}}$ on both densities. However, the intensity of the displacement with smooth plate was found to be more considerable than that with rough plate. This was in contrast to the available investigations in which the normal displacement of rough plate was greater than that of smooth plate due to the influence of dilative behaviour which was mainly found on rough plate. In comparison between two different types of surface roughness, smooth plate which provided lower friction angle allowed the mean cyclic shear displacement ($[w]_{\text{cm}}$) to evolve considerably (due to η_{cm} close to η_{peak}). Therefore, the significant increase of $[w]_{\text{cm}}$ induced more contractive behaviour (an increase in $[u]_{\text{cm}}$). In case of high level of η_{cm} on dense sand, the dilative behaviour on smooth plate was less evident than that on rough plate.

Smooth plate showed slight decrease in peak stress ratio (η_{peak}) at post-cyclic phase on both densities. Altough during cyclic phase the interface behaved contractively and consequently the interface exhibited more densification, there was not any significant variation in volumetric behaviour at post-cyclic phase. The examination of grain breakage after testing was found that the variation of grading curves could hardly observed on loose sand even considering the fine particle (D_{10}) whereas slight variation of grading curves could observed on dense sand. This is due to less abrasive surface of smooth plate. Generally, the slippage occurs along the contact surface between smooth plate and sand instead of an intense shear zone.

- Cyclic CNS condition

The great interest of the loading paths with an imposed stiffness (k) is the variation of normal stress acting on the interface. This variation of the normal stress mainly depends on the volumetric behaviour of the granular soil adjacent to the structure (either to contract or to dilate). Under cyclic CNS loading, the significant degradation in normal stress associated with the degradation in shear stress was observed as a result of contraction during shearing. With rough plate, the significant degradation of normal stress as a result of the progressive contraction accompanied with N and $[w]$ led to the critical state easily. From experimental

observations in this study, an increase of normal stiffness (k), cyclic amplitude ($\Delta\tau$) and level of mean cyclic stress ratio (η_{cm}) induced the gradual degradation in normal stress and consequently the stress state moved towards the critical state. The interface could reach the critical state easily (with a few number of cycles) on loose sand whereas dense sand which exhibited low attitude to contract required a large number of cycles for reaching the critical state.

During cyclic shearing, the degradation of σ_n as a function of N and $[w]$ induced an increase in η_{cm} which evolved and consequently moved towards the critical state line.

Smooth plate which obviously showed lower value in peak friction angle (the effect of dilative behaviour) provided less number of cycles for reaching the critical state. The significant difference in number of cycles for reaching the critical state of two different plates was found when performing the tests with the same condition. The worse condition which the interface could reach the critical state easily was that the test was performed on loose sand with low initial normal stress (σ_{n0}), high value in normal stiffness (k), high level in mean cyclic stress ratio (η_{cm}) and large-amplitude cycles ($\Delta\tau$).

Considering the grain breakage within the interface after testing, because most of the tests in cyclic CNS condition could be performed in a short period the grain breakage represented by the change in fine particle size (D_{10}) could hardly be observed (especially on loose sand). However, when performing the test with rough plate, high initial normal stress (σ_{n0}), low value in normal stiffness (k) and low level in mean cyclic stress ratio (η_{cm}) on dense sand, the test could continuously be performed and then provided the grain breakage (the shift of grading curves to the left).

Chapter 3

Constitutive modeling of direct shear tests

3.1 Introduction

The constitutive modeling of element tests generally refers to elasto-plasticity, elasto-visco-plasticity, rate-type approach, defined by relations between time derivation of loading and time derivative of response and related evolution of state or memory parameters. These relations are integrated by the increments of time in order to build any finite paths, the measurable variables being stresses, strains and relative displacements, i.e. Desai et al. [1985] ; Aubry et al. [1990] ; Shahrour & Rezaie [1997] ; Mortara [2001] ; Gennaro & Frank [2002] ; Mortara et al. [2002] ; Boulon et al. [2003] ; D'Aguiar et al. [2008] ; D'Aguiar et al. [2011] including the others, a generalized plasticity (Liu et al. [2006] ; Liu & Ling [2008]).

The traditional approach which has been developed in Lab 3S-R is the rate-type (after called incremental) analysis proposed by Boulon [1989].

In this study, a rate-type approach limited to some special paths in case of soil-structure interaction is developed: the direct shear paths at constant normal stress (CNL) and at prescribed normal stiffness (CNS, prescribed normal stiffness k) are previleged. It is noticed that the CNL paths are in fact CNS paths with $k = 0$.

Considering only special paths, Boulon [1988] tried to model no more infinitesimal increments, but if possible finite increments, as large as possible in order to make possible finite element computations with a limited volume and time of calculation.

In case of monotonic CNL and CNS tests, it has been possible to directly model analytically entire path. Each path is defined by 3 parameters: the initial density (I_{D0}), the initial normal stress (σ_{n0}) and the prescribed normal stiffness (k). In addition, the length of the path in terms of tangential displacement ($[w]_{\max}$) is also considered.

In case of cyclic CNL and CNS tests, the situation is much more complex, due to the number of parameters to be taken into account (i.e. initial density (I_{D0}), the initial mean cyclic

normal stress ($\sigma_{\mathrm{n\ cm0}}$), the initial mean cyclic shear stress (τ_{cm0}), the amplitude of cyclic shear stress ($\Delta\tau$), and the number of cycle N). In this study, the initial mean cyclic stress ratio ($\eta_{\mathrm{cm0}} = \frac{\tau_{\mathrm{cm0}}}{\sigma_{\mathrm{n\ cm0}}}$) instead of τ_{cm0}, and the amplitude of cyclic stress ratio ($\Delta\eta = \frac{\Delta\tau}{\sigma_{\mathrm{n\ cm0}}}$) would be preferable.

It has been possible to model analytically the CNL tests while the CNS tests have been modeled by finite analytical increments according to the following principle. One CNS finite increment is a summation of a CNL finite increment and of a finite increment in compression or extension (Figure 3.1).

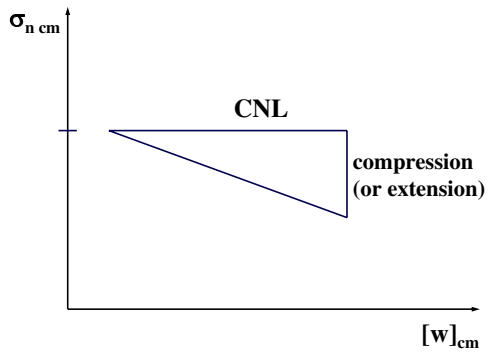

Figure 3.1: Derivation of CNS path from a CNL finite increment

In addition, the memory variable allowing to chain the finite increments is the mean cyclic normal relative displacement [u_{cm}] which is equivalent to the interface weight density under normal stress ($\gamma_{\mathrm{d}\ \sigma n}$).

In this chapter, one of the principal categories of constitutive modeling is detailed. The incremental (rate type) model is first introduced and discussed. This model serves as the implicit approach for describing the monotonic interface behaviour. After that, a study on modeling the visco-plastic behaviour of the interface subjected to a large number of cycles is proposed. The so-called explicit model (Wichtmann [2005], Wichtmann et al. [2010], Niemunis et al. [2005]) in which the number of cycles N is treated instead of time is then detailed. However, the strategy of model calibration is only detailed and provides a first step to check the consistency of the model on rough plates. Simulations of interface behaviour are then compared with experimental results and discussed.

3.2 Monotonic tests

3.2.1 Incremental (rate type) constitutive models

A constitutive relation within the framework of non-linear incremental (or rate type) law has successively been carried out at laboratory 3S-R (e.g. Boulon [1989] ; Hoteit [1990] ;

Boutrif [1993] ; Garnica-Anguas [1993]). In this frame work, unlike elasto-plastic law, the interface is considered as being a surface of kinematic discontinuity. The interface thickness is not taken into account as a constitutive parameter. In general, the interface thickness is assumed to be proportional to the value of D_{50}. In other words, it would be said that the interface is considered as a zero thickness within the non-linear incremental framework (Boulon & Nova [1990], Boulon et al. [1995]).

Having mentioned in the first chapter (Constitutive models section), the incremental interface model is capable of describing a general direct shear paths which can govern the set of possible responses of the interface in case of two-dimensional condition.

By definition, a constitutive law is a functional relation which allows to express the internal forces (stress vector for the interface, $[\underline{\sigma}]$), depending on the kinematic discontinuities at the contact (relative displacement vector to the interface, $[\underline{u}]$) that describe the complex deformations of the medium;

$$[\underline{u}] = \left\{ \begin{array}{c} [w] \\ [u] \end{array} \right\} \quad \text{and} \quad [\underline{\sigma}] = \left\{ \begin{array}{c} \tau \\ \sigma_n \end{array} \right\}$$

Again, the basic feature of this constitutive equation based on the non-linear relation between the incremental loadings and the corresponding incremental response shown in (1.33) is expressed by:

$$\left\{ \begin{array}{c} \dot{\tau} \\ \dot{\sigma} \end{array} \right\} = \left\{ \begin{array}{c} \dot{\tau}([\dot{w}], [\dot{u}], \text{memory parameters}) \\ \dot{\sigma}([\dot{w}], [\dot{u}], \text{memory parameters}) \end{array} \right\}$$

Several kinds of interpolation fucntion (e.g. polynomial, trigonometric, exponential functions etc. proposed by Boulon [1989] ; Boutrif [1993] ; Garnica-Anguas [1993]) are then described for constructing an approximate incremental response.

Finally, the constitutive equation can formally be written via Euler's theorem for homogeneous functions (1.42):

$$\left\{ \begin{array}{c} \dot{\tau} \\ \dot{\sigma_n} \end{array} \right\} = \left[\begin{array}{cc} \frac{\partial \dot{\tau}}{\partial [\dot{w}]} & \frac{\partial \dot{\tau}}{\partial [\dot{u}]} \\ \frac{\partial \dot{\sigma_n}}{\partial [\dot{w}]} & \frac{\partial \dot{\sigma_n}}{\partial [\dot{u}]} \end{array} \right] \left\{ \begin{array}{c} [\dot{w}] \\ [\dot{u}] \end{array} \right\}$$

3.2.2 Analytical approach

- **Key parameters**

In this approach, the basic key parameters which are obtained by the derivation of interface direct shear paths (representing $\eta = \tau/\sigma_n$ and $[u]$ as a function of $[w]$ for CNL condition; τ and σ_n as a function of $[w]$ for monotonic CNS condition) are presented by Figure 3.2 and 3.3, respectively.

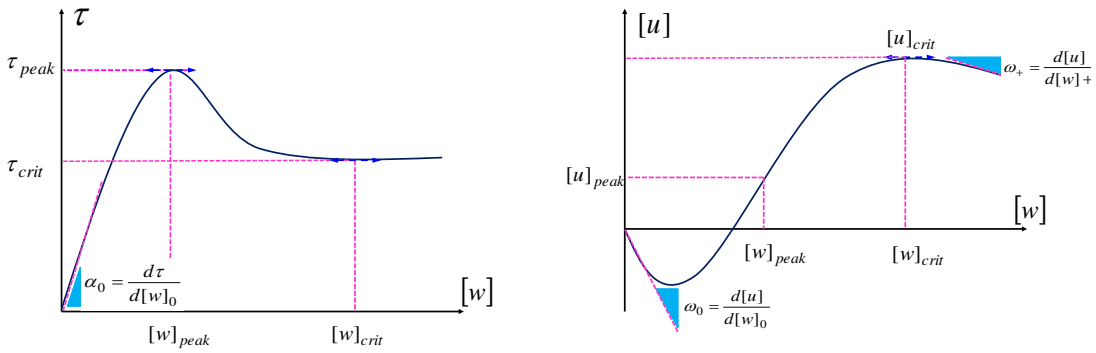

(a) (b)

Figure 3.2: Key parameters for description of CNL test

To highlight the physical phenomena commonly encountered during shear loading (the dilatancy, the evolution of friction angle, the grain breakage, etc.), these two figures show the dependence of the evolution of the interface behaviour. They express the existence of two phases of concurrent behaviour and seem difficult to separate:

1. The first phase is the phase before peak stress ratio ($\eta_{\text{peak}} = \tau_{\text{peak}}/\sigma_n$) where the evolution of the tangential relative displacement ($[w]$) is not dominant.
2. The second phase corresponds to the post-peak (η_{peak}) and the interface behaviour evolves as a function of the tangential relative displacement ($[w]$) for both conditions.

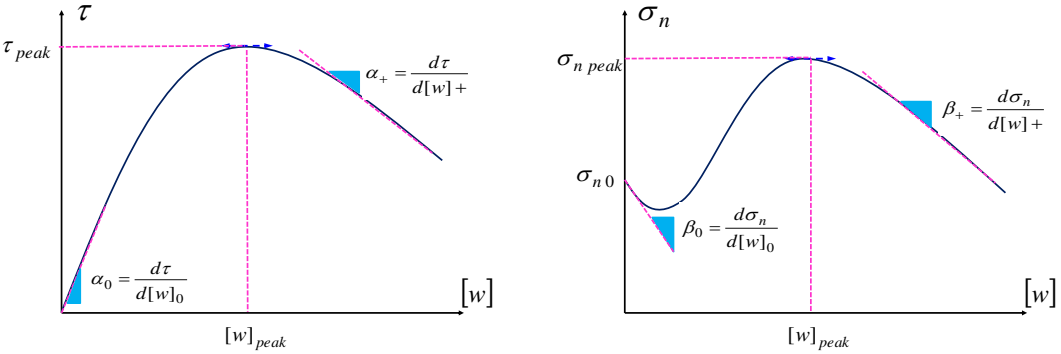

(a) (b)

Figure 3.3: Key parameters for description of CNS test

- at constant normal stress (CNL), the presence of the critical state of shear stress (τ_{crit}) preceeded by softening behaviour and a continuous evolution of the normal displacement ($[u]$) at large tangential displacement ($[w]$) can be observed.
- at an imposed normal stiffness (CNS), τ and σ_n tend to decrease or increase and

the interface exhibits either a contractive or dilative behaviour (depending on the initial density) with the reduction rate as a function of tangential relative displacement.

In general, there exists a stabilisation of the normal displacement ($[u]$, without dilation or contraction) at large tangential displacement ($[w]$) in accordance with a critical state concept. However, from typical interface test results, it is found that the feature of $[u]$-$[w]$ and $\sigma_n - [w]$ diagrams are almost the same under CNS condition. The principal characteristics of the interface are the initial contraction or dilation (depending on the initial density) due to the rearrangement of the particles of the sand and the decrease after the peak. The last one would probably be due to either a degradation related to the grains breakage within the interface or the loss of material during the test (Boulon [1988]).

Therefore, during shear loading, the interface behaviour would be considered in two parts:

- The first part, due to rearrangement of the particles of the sand within the interface shear zone during shear loading (contraction-dilation), is only a function of shear relative displacement.
- The second part is due to the grain breakage linked with the specific interface energy, W. After the peak, normal stress allows a linear slope (β_+) with respect to W.

However, in a certain area of W, the slope $\beta_+ = \partial\sigma_n/\partial[w]_+$ seems constant for an initial normal stress (σ_{n0}) and initial density (I_{D0}). In other words, the energy as a result of shear loading is not high enough to allow the grain breakage. The influence of grain breakage on the path of σ_n can be illustrated by Figure 3.4.

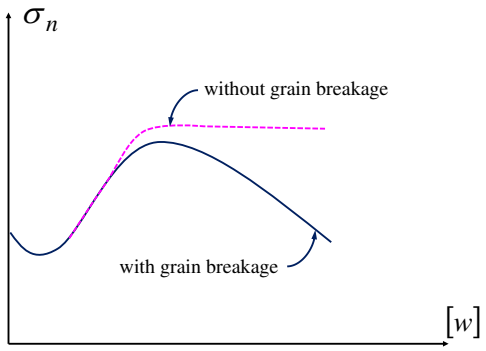

Figure 3.4: Interface direct shear test under CNS condition

With the hypothesis that the grains within the localized shear zone has a tendency to be crushed during shearing load, and then the progress of crushing grains leads to more contraction. Garnica-Anguas [1993] proposed the originality of the formulation describing the grain breakage within the interface. This formulation can be expressed as:

$$\sigma_r = \beta_+ (\sigma_{n0}, I_{D0})\, W \tag{3.1}$$

where:

σ_r is the normal stress due to the grain breakage.

β_+ is the slope ($\partial\sigma_n/\partial[w]_+$) at large tangential displacement.

W is the specific energy.

Figure 3.5 illustrates some of typical key parameters chosen to describe the interface behaviour under both conditions. From data of a typical interface direct shear tests shown in $[u]-[w]$ diagram (see also $[u]-[w]$ diagram in the previous chapter), it is also worth mentioning that the presence of the slight evolution of normal displacement ($[u]$) at large tangential displacement ($[w]$) is observed. This may lead to a controversy with that of critical state concept in which the normal displacement is almost constant. However, with the concept of grain breakage, this can be satisfactory for describing the interface behaviour.

When first considering the direct shear path under CNL condition, basic key parameters are proposed to describe these curves;

- Before-peak phase:
  - the initial modulus of $\eta([w])$, α_0 : $\alpha_0 = \partial\eta/\partial[w]_0$
  - peak stress ratio, η_{peak}
  - shear relative displacement corresponding to η_{peak}, $[w]_{\eta\ \text{peak}}$
  - the initial dilatancy, ω_0 : $\omega_0 = \partial[u]/\partial[w]_0$
- Post-peak phase:
  - critical stress ratio, η_{crit}
  - the normal relative displacement at critical state, $[u]_{\text{crit}}$
  - the dilatancy, ω_+, corresponding to the post-peak phase: $\omega_+ = \partial[u]/\partial[w]_+$

Similarly, under CNS condition the basic key parameters describing the evolution of shear (τ) and normal σ_n stresses are then defined:

- Before-peak phase:
  - the initial modulus of $\eta([w])$, α_0 : $\alpha_0 = \partial\eta/\partial[w]_0$
  - peak stress ratio, η_{peak}
  - peak normal stress, $\sigma_{\text{n peak}}$
  - shear relative displacement corresponding to η_{peak} and $\sigma_{\text{n peak}}$, $[w]_{\eta\ \text{peak}}$ and $[w]_{\sigma\ \text{peak}}$
  - the initial modulus of $\sigma_n([w])$, β_0 : $\beta_0 = \partial\sigma_n/\partial[w]_0$
  - the initial dilatancy, ω_0 : $\omega_0 = \partial[u]/\partial[w]_0$

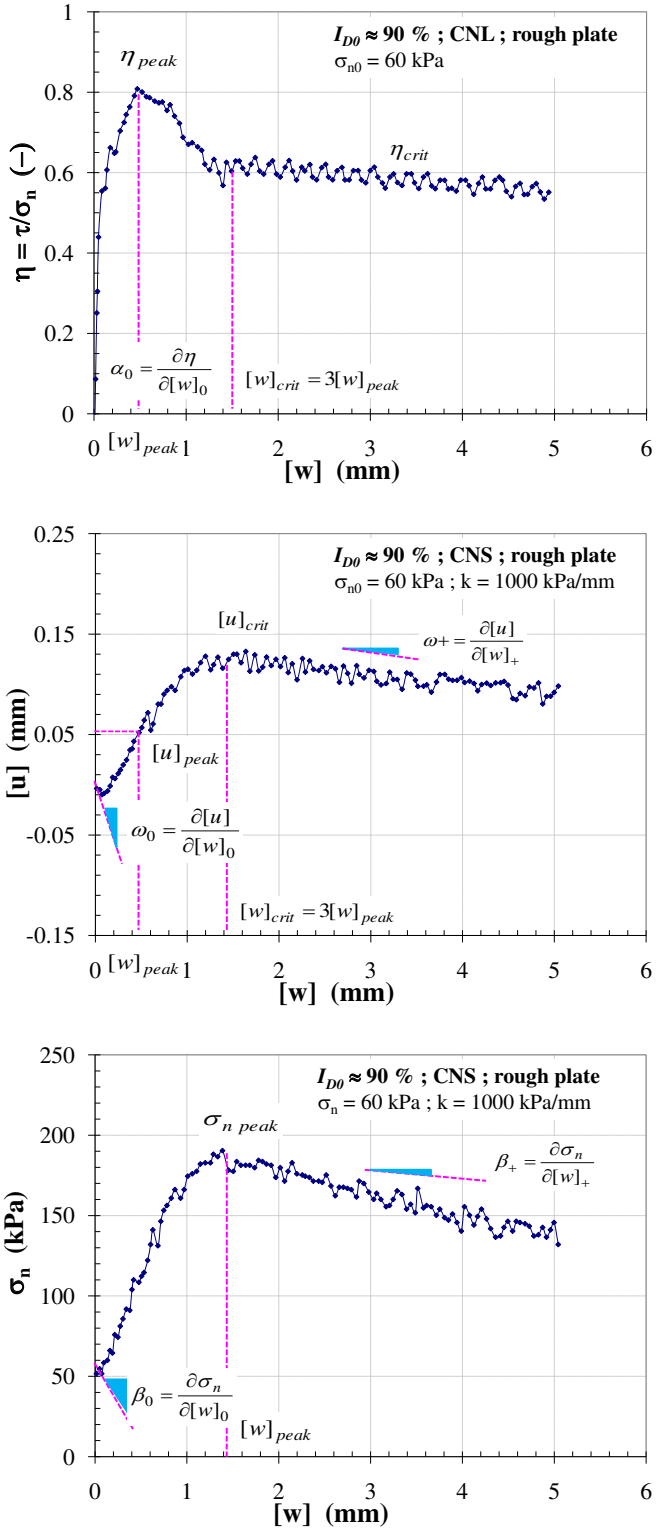

Figure 3.5: Illustration of typical key parameters on dense sand ($I_{D0} \approx 90\%$), $\sigma_n = 60$ kPa, CNL and CNS ($k = 1000$ kPa/mm) with rough plate

- Post-peak phase:
  - critical stress ratio, η_{crit}
  - the modulus of $\sigma_n([w])$, β_+, corresponding to the post-peak phase : $\beta_+ = \partial\sigma_n/\partial[w]_+$
  - the normal relative displacement at critical state, $[u]_{\text{crit}}$
  - the dilatancy, ω_+, corresponding to the post-peak phase: $\omega_+ = \partial[u]/\partial[w]_+$

To begin with the formulation of an incremental model, the monotonic CNL and CNS interface shear tests are considered. Figure 3.6 typically shows the values of η_{peak}, $[w]_{\eta\ \text{peak}}$, $\sigma_{\text{n peak}}$ and $[u]_{\text{crit}}$ derived from monotonic CNL and CNS tests on dense sand. These key parameters on loose sand are evaluated in the same way.

On dense sand, η_{peak} obviously decreases as a function of σ_n and k. The effect of k seems to have more influence on η_{peak} with low initial stress than high initial stress. $\sigma_{\text{n peak}}$ increases as a function of σ_n and k. $[w]_{\eta\ \text{peak}}$ also increases as a function of σ_n, whereas the effect of k seems to have no influence on $[w]_{\eta\ \text{peak}}$. An increase of k and σ_n totally or partially prevents the change in volume, and consequently leads to the reduction rate of $[u]_{\text{crit}}$).

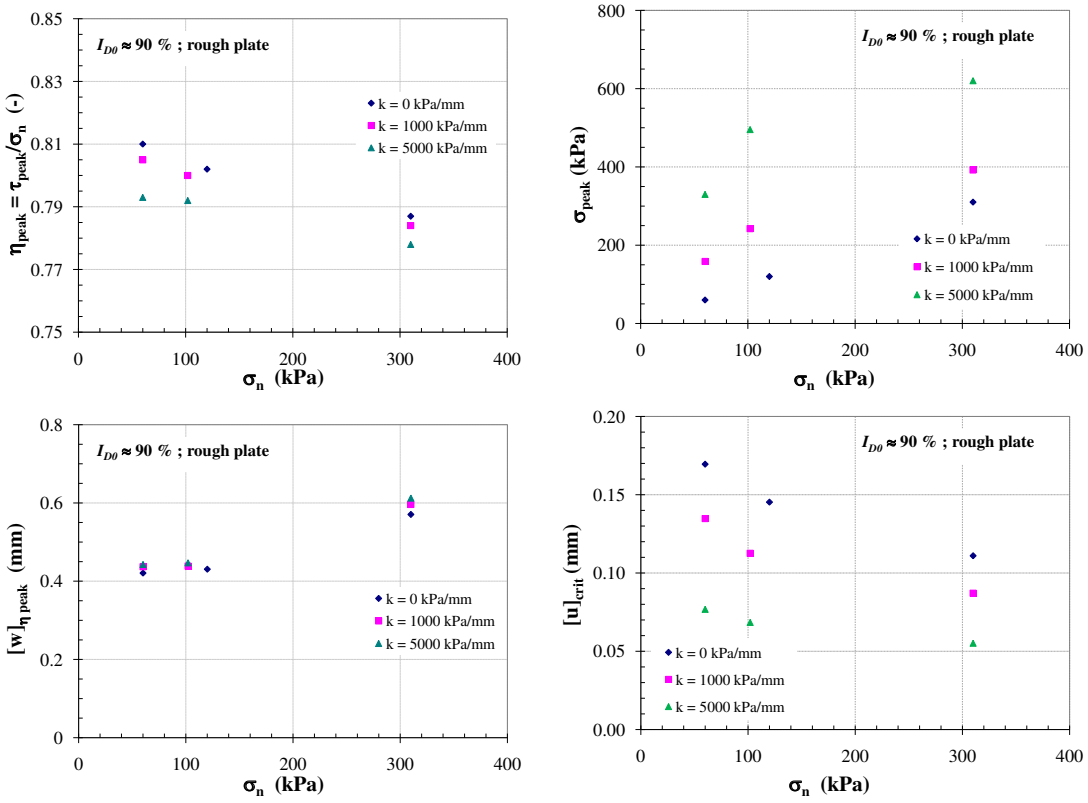

Figure 3.6: Typical peak and critical values of key parameters on dense sand ($I_{D0} \approx 90\%$), rough surface with different values of k

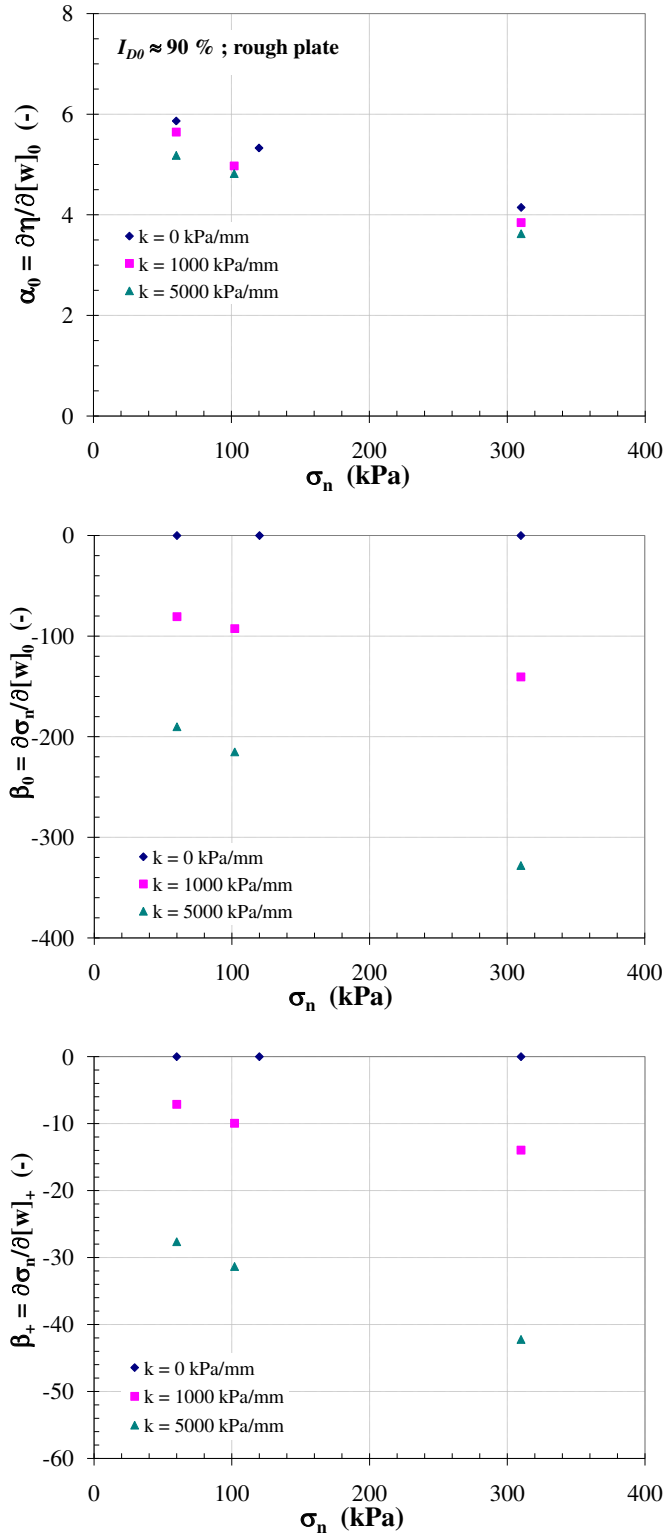

Figure 3.7: Typical moduli of key parameters on dense sand ($I_{D0} \approx 90\%$), rough surface with different values of k

The other figures which deserve to mention at this point, for describing some of the major parameters which are to properly be interpreted in order to reach the satisfactory model, are Figure 3.7 and 3.8. These two figures also show the initial slope (the initial moduli and dilatancy e.g. $\partial\eta/\partial[w]_0$, $\partial\sigma_n/\partial[w]_0$ and $\partial[u]/\partial[w]_0$) as well as the slope corresponding to the post-peak phase ($\partial\sigma_n/\partial[w]_+$ and $\partial[u]/\partial[w]_+$).

Considering before-peak phase, $\partial\eta/\partial[w]_0$ decreases as function of σ_n and k. As can be observed in CNS tests, σ_n decreases at the beginning of the test to overcome the contractive behaviour and the rate of $\partial\sigma_n/\partial[w]_0$ increases as a function of σ_n and k. Unlike $\partial\sigma_n/\partial[w]_0$, $\partial[u]/\partial[w]_0$ has a different tendency in which an increase of k totally or partially prevents the volume variation.

After reaching the peak value, the stress ratio decreases (softening behaviour) and subsequently evolves to the critical state. As can be observed in the previous chapter, the interface shear tests can be concluded to evolve the same critical stress ratio ($\eta_{\text{crit}} = \tau_{\text{crit}}/\sigma_n \approx 0.566$ on rough plate) on both densities. The imposed normal stiffness has no influence on the critical stress ratio. The rate of $\partial\sigma_n/\partial[w]_+$ still increases as a function of σ_n and k. The trend of dilatancy rate at post peak phase is similar to that at before peak phase.

These basic key parameters are then formulated as a simple function of k and σ_n for each density. Table 3.1 shows the summary of peak and critical values of the key parameters on both densities. The moduli and the dilatancy of the interface (before and post-peak phases) are then presented on Table 3.2.

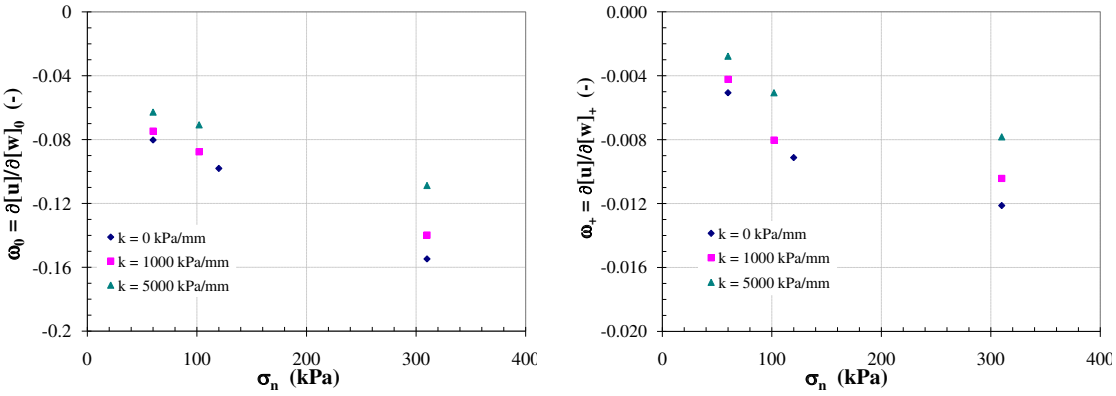

(a) (b)

Figure 3.8: Key parameters for the description of dilatancy on dense sand

Table 3.1: Summary of the peak and critical values of the key parameters on rough plate

Key parametrs	Function	
	$I_{D0} \approx 30$ %	$I_{D0} \approx 90$ %
$\eta_{\text{peak}} = \text{a}\cdot\exp(\text{b}.k)$		
a	-8E-05σ_n + 0.6477	-9E-05σ_n - 0.8127
b	6E-08σ_n + 3E-07	7E-09σ_n - 4E-06
$[w]_{\eta\ \text{peak}} = \text{a}\cdot\exp(\text{b}.k)$		
a	0.0014σ_n + 0.5836	6E-04σ_n + 0.3796
b	-9E-08σ_n - 4E-05	1E-08σ_n - 5E-06
$\sigma_{n\ \text{peak}} = \text{a}\cdot k^2 + \text{b}\cdot k + \text{c}$		
a	1E-08σ_n - 2E-07	2E-08σ_n - 1.3E-05
b	-1E-04σ_n - 0.0036	-1E-04σ_n + 0.134
c	σ_n	σ_n
$[w]_{\sigma n\ \text{peak}} = \text{a}\cdot\exp(\text{b}.k)$		
a	0.0027σ_n + 0.5105	0.0011σ_n + 1.225
b	2E-08σ_n + 3E-06	-9E-09σ_n + 9E-06
$[u]_{\text{crit}} = \text{a}\cdot k^2 + \text{b}\cdot k + \text{c}$		
a	-7E-12σ_n - 3E-09	-4E-12σ_n + 4E-09
b	7E-08σ_n - 2E-05	4E-08σ_n - 4E-05
c	-1E-04σ_n - 0.0654	-2E-04σ_n + 0.1753

- **Analytical formulation of the base paths**

In this study, the analytical formulations for the base paths are then presented. These formulations were first described by Boutrif [1993] and Garnica-Anguas [1993]. The interpolations of the base paths were made from the initial state and the current state of the interface.

Each of these base paths can analytically be defined from the initial state of the interface which is characterized by an initial density (I_{D0}), initial tangential relative movement ($[w] = 0$), an initial normal stress (σ_n), and from the current state due to a certain number of parameters which have been defined in several ways.

For the interface direct shear tests whether in CNL or CNS conditions, the analytical formulation of the base paths are presented in the space of the incremental response at different stages of shear loading. These paths can be used to assess the behaviour of the law in all cases of possible loading. In each phase, analytical formulations of the paths are written in the function of $[w]$ (the intergration step). Several interpolation functions (e.g. cubic polynomial, exponential, etc.) are then described. In τ/σ_n - $[w]$, σ_n - $[w]$ and $[u]-[w]$ diagrams, the interpolation functions are given by the following:

Table 3.2: Summary of the moduli of the key parameters on rough plate

Key parametrs	Function	
	$I_{D0} \approx 30$ %	$I_{D0} \approx 90$ %
$\alpha_0(\partial\eta/\partial[w]_0) = \mathrm{a}\cdot\exp(\mathrm{b}.k)$		
a	-0.0027σ_n + 2.6132	-0.0076σ_n + 6.0382
b	5E-08σ_n + 5E-06	4E-08σ_n - 4E-05
$\beta_0(\partial\sigma_n/\partial[w]_0) = \mathrm{a}\cdot k^2 + \mathrm{b}\cdot k$		
a	4E-08σ_n + 7E-06	7E-09σ_n + 7E-06
b	-3E-04σ_n - 0.0816	-2E-04σ_n - 0.056
$\beta_+(\partial\sigma_n/\partial[w]_+) = \mathrm{a}\cdot k^2 + \mathrm{b}\cdot k$		
a	3E-09σ_n + 2E-07	4E-09σ_n + 6E-07
b	-2E-05σ_n - 0.004	-3E-05σ_n - 0.00875
$\omega_0(\partial[u]/\partial[w]_0) = \mathrm{a}\cdot k^2 + \mathrm{b}\cdot k + \mathrm{c}$		
a	-2E-12σ_n - 3E-10	-4E-12σ_n - 7E-10
b	5E-08σ_n + 9E-06	4E-08σ_n + 7E-06
c	-2E-04σ_n - 0.129	-3E-04σ_n - 0.0647
$\omega_+(\partial[u]/\partial[w]_+) = \mathrm{b}\cdot k + \mathrm{c}$		
b	5E-09σ_n + 8E-07	5E-09σ_n + 6E-07
c	-2E-05σ_n - 0.00612	-2E-05σ_n - 0.005

- Before-peak phase ; $[w] \leq [w]_{\mathrm{peak}}$

In this phase, with the peak values and initial moduli, inluding the initial dilatancy, all of the interface direct shear paths can be written in the same formula as;

$$\begin{aligned}\tau/\sigma_n = &\left(\frac{\alpha_0}{[w]^2_{\eta\ \mathrm{peak}}} - 2\frac{\eta_{\mathrm{peak}}}{[w]^3_{\eta\ \mathrm{peak}}}\right)\cdot[w]^3 \\ &+\left(-2\frac{\alpha_0}{[w]_{\eta\ \mathrm{peak}}} + 3\frac{\eta_{\mathrm{peak}}}{[w]^2_{\eta\ \mathrm{peak}}}\right)\cdot[w]^2 + \alpha_0\cdot[w]\end{aligned} \tag{3.2}$$

$$\begin{aligned}\sigma_n = &\left(\frac{\beta_0}{[w]^2_{\sigma\ \mathrm{peak}}} - 2\frac{\sigma_{\mathrm{peak}}-\sigma_n}{[w]^3_{\sigma\ \mathrm{peak}}}\right)\cdot[w]^3 \\ &+\left(-2\frac{\beta_0}{[w]_{\sigma\ \mathrm{peak}}} + 3\frac{\sigma_{\mathrm{peak}}-\sigma_n}{[w]^2_{\eta\ \mathrm{peak}}}\right)\cdot[w]^2 + \beta_0\cdot[w] + \sigma_n\end{aligned} \tag{3.3}$$

$$
\begin{aligned}
[u] = & \left(\frac{\omega_0}{[w]^2_{[u]\text{crit}}} - 2\frac{[u]_{\text{crit}}}{[w]^3_{[u]\text{crit}}} \right) \cdot [w]^3 \\
& + \left(-2\frac{\omega_0}{[w]_{[u]\text{crit}}} + 3\frac{[u]_{\text{crit}}}{[w]^2_{[u]\text{crit}}} \right) \cdot [w]^2 + \omega_0 \cdot [w]
\end{aligned}
\tag{3.4}
$$

where:

$[w]_{\eta\ \text{peak}}$ and $[w]_{\sigma\ \text{peak}}$ are the shear displacement corresponding to η_{peak} and σ_{peak}, respectively.

$[w]_{[u]\ \text{crit}}$ is the shear displacement corresponding to $[u]_{\text{crit}}$ which $[w]_{\sigma\ \text{peak}} = [w]_{[u]\ \text{crit}}$.

- Post-peak phase ; $[w] > [w]_{\text{peak}}$

The path of $\tau/\sigma_n([w])$ which shows the reduction from peak to critical condition at large displacement is written as:

$$
\begin{aligned}
\tau/\sigma_n = & \left(\frac{\tau}{\sigma_n} \right)_{\text{crit}} \\
& + \left[\left(\frac{\tau}{\sigma_n} \right)_{\text{peak}} - \left(\frac{\tau}{\sigma_n} \right)_{\text{crit}} \right] \cdot \exp\left(-\frac{\ln(0.02)}{(3[w]_{\eta\ \text{peak}})^2} \cdot ([w] - [w]_{\eta\ \text{peak}})^2 \right)
\end{aligned}
\tag{3.5}
$$

Because the feature of $\sigma_n([w])$ is similar to $[u]([w])$, these two paths are then written in the same formula:

$$
\begin{aligned}
\sigma_n = & \sigma_{\text{peak}} + \ \beta_+ \cdot ([w] - [w]_{\sigma\ \text{peak}}) \\
& - \beta_+ \cdot \left(\frac{[w]_{\sigma\ \text{peak}}}{2.9957} \right) \cdot \left[1 - \exp\left(([w] - [w]_{\sigma\ \text{peak}}) \cdot \frac{2.9957}{[w]_{\sigma\ \text{peak}}} \right) \right]
\end{aligned}
\tag{3.6}
$$

$$
\begin{aligned}
[u] = & [u]_{\text{crit}} + \ \omega_+ \cdot \left([w] - [w]_{[u]\text{crit}} \right) \\
& - \omega_+ \cdot \left(\frac{[w]_{[u]\text{crit}}}{2.9957} \right) \cdot \left[1 - \exp\left(([w] - [w]_{[u]\text{crit}}) \cdot \frac{2.9957}{[w]_{[u]\text{crit}}} \right) \right]
\end{aligned}
\tag{3.7}
$$

The integration of the interface law requires that the base paths, whether at constant normal stress (CNL) or constant normal stiffness (CNS), have some "coherences" in their formulation. The detail of these formulas is provided in Appendix **A**.

Figure 3.9 shows a comparison between the experimental results and the model predictions of monotonic CNL tests with $\sigma_n = 120$ kPa on both densites. The comparisons of experimental results and model predictions with different values of initial normal stress at CNL on loose and dense sands are presented in Figure 3.10 and 3.11, respectively.

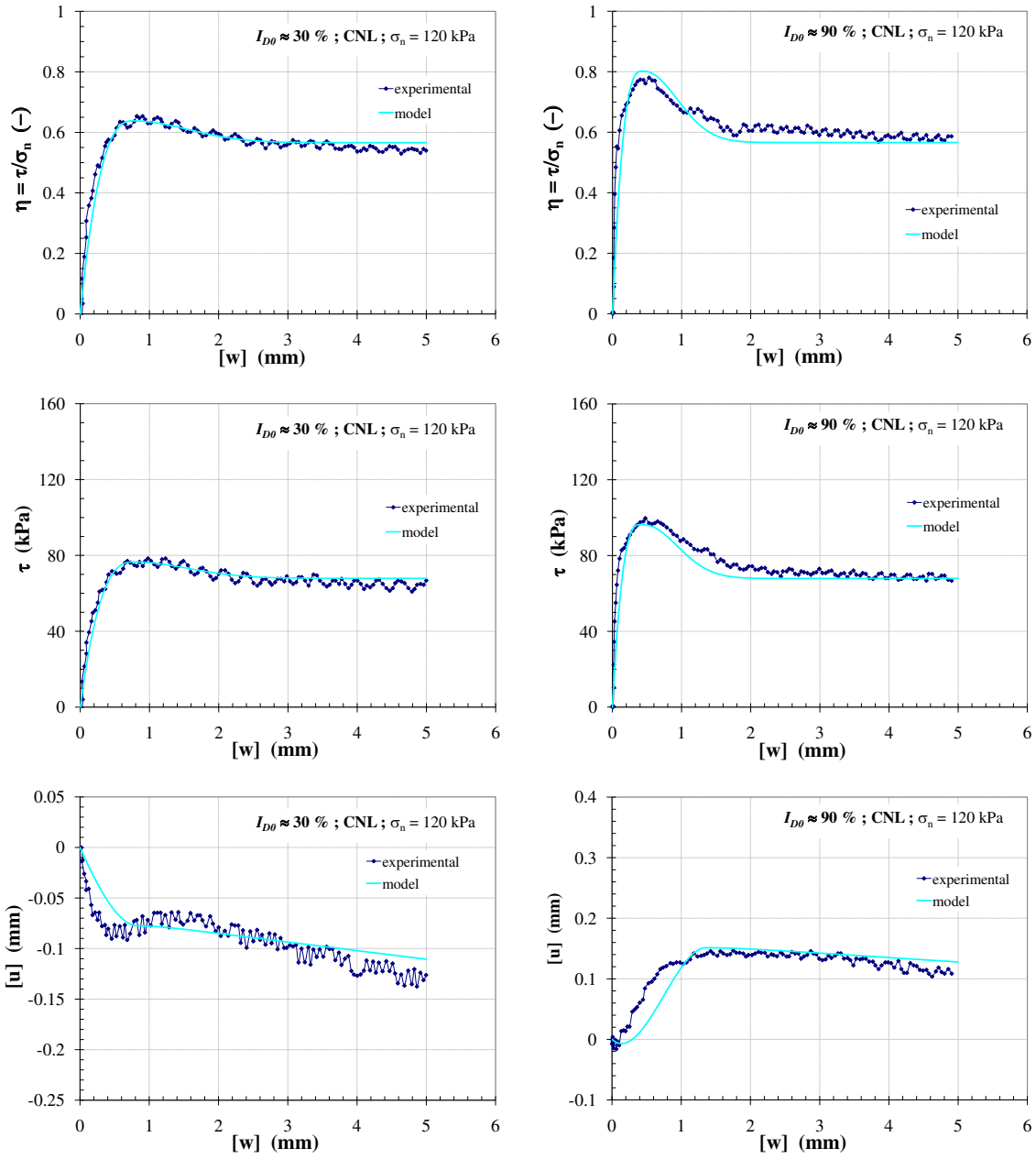

Figure 3.9: Comparison between experimental data and the model predictions, $\sigma_n = 120$ kPa, CNL tests with rough plate : (left) loose sand ($I_{D0} \approx 30\%$) ; (right) dense sand ($I_{D0} \approx 90\%$)

In case of CNS test, Figure 3.12 shows the comparison between the experimental tests and model predictions of monotonic CNS tests with σ_{n0} = 100 kPa, k = 1000, 2000 and 5000 kPa/mm on loose and densed sands, respectively. Results from the model predictions with various conditions, which cover the main factors influencing the interface behaviour under CNS condition (e.g. I_{D0}, σ_{n0} and k), are also shown in Figure 3.13. The model includes the features of interface model formulated in terms of the incremental stresses and of the incremental relative displacements. The capability of the proposed model to reproduce the experimental observations in laboratory is satisfactory. It is also found that the proposed model can well reproduce the interface behaviour, especially in CNS condition in which the degradation of normal stress associated with shear stress can well be described at large tangential displacement. All features of interface model are shown in Appendix **B**

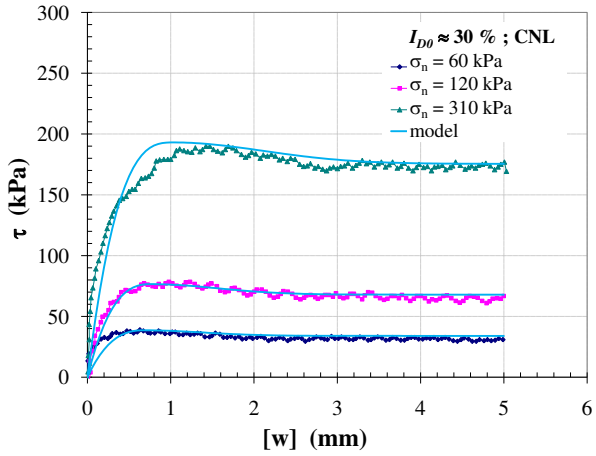

Figure 3.10: Comparison between experimental data and the model predictions, CNL tests on loose sand ($I_{D0} \approx 30\%$) with rough plate

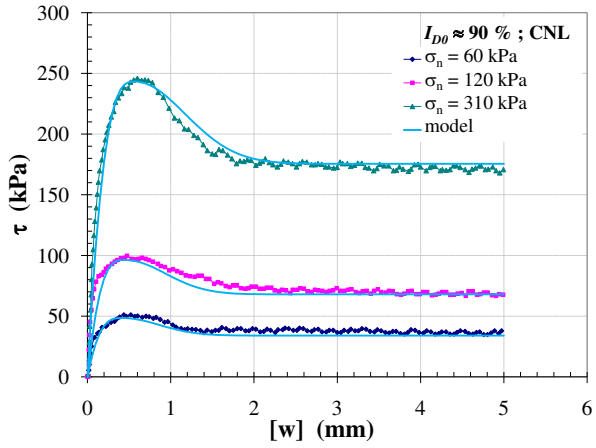

Figure 3.11: Comparison between experimental data and the model predictions, CNL tests on dense sand ($I_{D0} \approx 90\%$) with rough plate

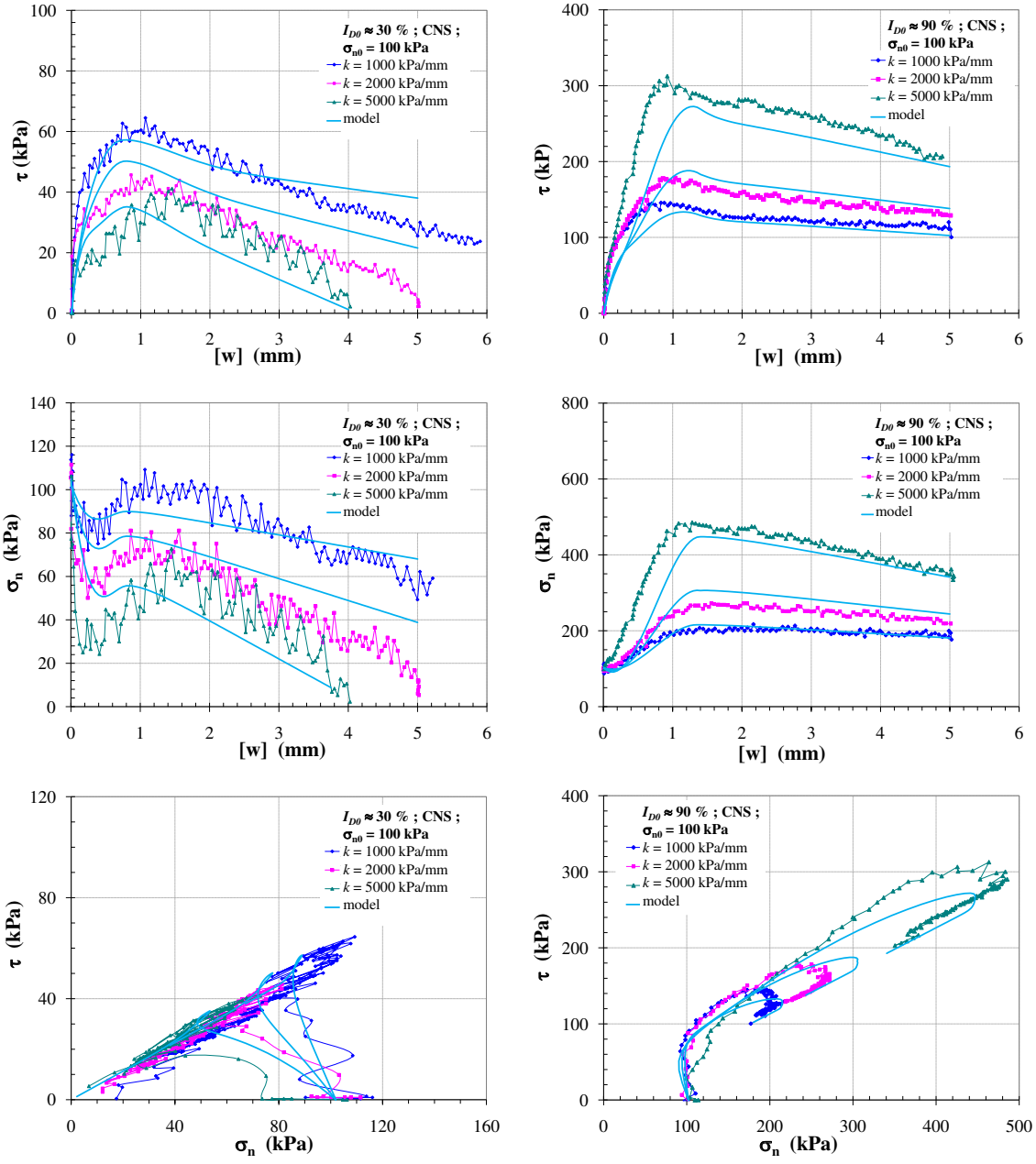

Figure 3.12: Comparison between experimental data and the model predictions, $\sigma_n = 100$ kPa, $k = 1000$, 2000 and 5000 kPa/mm with rough plate : (left) loose sand ($I_{D0} \approx 30\%$) ; (right) dense sand ($I_{D0} \approx 90\%$)

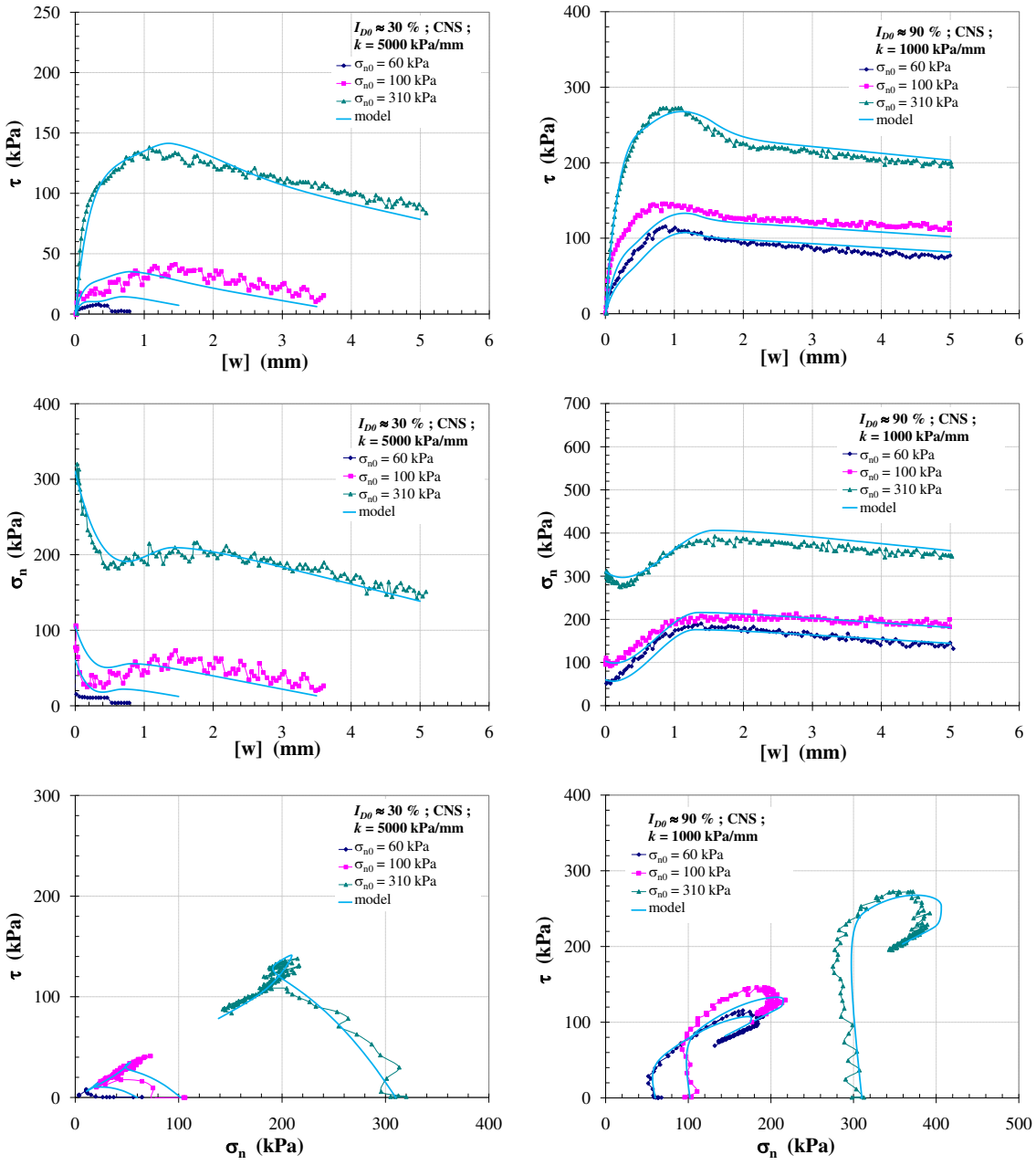

Figure 3.13: Comparison between experimental data and the model predictions, $\sigma_{n0} = 60$, 100 and 310 kPa with rough plate : (left) $k = 5000$ kPa/mm on loose sand ($I_{D0} \approx 30\%$) ; (right) $k = 1000$ kPa/mm on dense sand ($I_{D0} \approx 90\%$)

3.3 Cyclic tests

A constitutive model for the granular material subjected to a large number of cycles proposed by Wichtmann [2005], Wichtmann et al. [2005] and Niemunis et al. [2005] is devoted to the explicit method in which the number of cycles is considered instead of time. In the domain of soil-structure interface, whether under constant normal stress (CNL) or constant normal stiffness (CNS), a general formulation is expressed as:

$$d\left[\underline{u}\right] = d\left[\underline{u}\right]_{\mathrm{e}} + d\left[\underline{u}\right]_{\mathrm{cm}} \tag{3.8}$$

where $d\left[\underline{u}\right]_{\mathrm{e}}$ describes the elastic part of which the increment of elastic displacements is related to that of stresses according to

$$d\left[\underline{u}\right]_{\mathrm{e}} = D_{\mathrm{e}}^{-1} d\underline{\sigma} \tag{3.9}$$

where D_{e} is the elasticity matrix expressed as:

$$D_{\mathrm{e}} = \begin{bmatrix} k_t & 0 \\ 0 & k_n \end{bmatrix} \tag{3.10}$$

While the viscoplastic part a widely-used viscoplastic formulation, so-called Perzyna model Perzyna [1966], is expressed as

$$d\left[\underline{u}\right]_{\mathrm{cm}} = \Gamma \left\langle \Phi(F) \right\rangle \frac{\partial G}{\partial \underline{\sigma}} dN \tag{3.11}$$

in which a fluidity parameter (Γ) and the function of $\langle \Phi(F) \rangle$ describe the intensity of $d\left[\underline{u}\right]_{\mathrm{cm}}$. A plastic potential $G = G(\underline{\sigma})$ of which $\frac{\partial G}{\partial \underline{\sigma}}$ describes the direction of $d\left[\underline{u}\right]_{\mathrm{cm}}$.

During cyclic tests the variables measured in each test are, in addition to the components of the stress vector (σ_{cm}, τ_{cm}):

- The mean cyclic relative displacement vector, normal $[u]_{\mathrm{cm}}$ and tangential $[w]_{\mathrm{cm}}$ components.
- The initial normal and tangential stiffnesses of the soil-structure interface, k_{ni} and k_{ti}.
- The strength of sand-interface structure due to one great cycle of shear stress to failure after cyclic loading phase.

To clarify the interface behaviour under cyclic loading, a representation of stress plane (σ_n, τ) is useful, with the mean cyclic stress vector (σ_{cm}, τ_{cm}), and the mobilisation of mean cyclic stress ratio ($\eta_{\mathrm{cm}} = \frac{\tau_{\mathrm{cm}}}{\sigma_{\mathrm{cm}}}$), cyclic amplitude ($\Delta\eta = \frac{\Delta\tau}{\sigma_{\mathrm{cm}}}$). The remarkable statements involving the characteristic (δ_{car}), critical (δ_{crit}) and peak (δ_{peak}) angles, or their respective tangents (η_{car}, η_{crit} and η_{peak}), depending on the initial density, and their opposite counterparts are also described. These parameters are derived from monotonic direct shear tests.

Figure 3.14 shows the behaviour of the soil-structure interface under cyclic loading which is characterized into three main poles (in terms of the stress state). In this figure, the pole here means that the dilating / contracting character is maximum on the level of this pole (identified in term of η_{cm}), and this character decreases in the vicinity of the pole, when the stress state goes away from this one. It can be distinguished as:

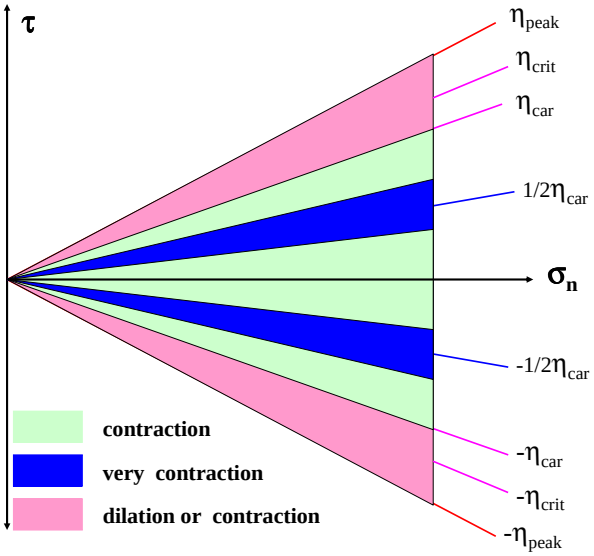

Figure 3.14: Behaviour of sand-structure interface under cyclic loading, poles in the stress plan

- 2 poles showing slowly (in term of number of cycles) very contractive domain, regardless of the initial density of the sand, and the amplitude of the cycles, for η_{cm} close to $\pm\frac{1}{2}\eta_{\text{car}}$.
- 1 pole showing slowly (in term of number of cycles) less contraction, regardless of the initial density of the sand, and the amplitude of the cycles, for η_{cm} close to 0.
- 2 poles driving rapidly (in term of number of cycles) to critical state, regardless of the initial density of the sand, and the amplitude of the cycles, for η_{cm} close to $\pm\eta_{\text{peak}}$. This behaviour is always dilative in the case of the dense sand, it is dilative or contractive in the case of the loose sand, according to the initial density, in comparison with the critical density.

Besides, an increasing amplitude of the cycles amplifies the observed phenomenon.

In shear stress-controlled cyclic tests, the application of the mean cyclic stresses provides an accumulation of displacements. At first, the model is proposed to properly and simply describe the mean cyclic displacements ($[u]_{\text{cm}}$ and $[w]_{\text{cm}}$), from the initial state in density ($I_{D0} \approx 30$ or 90 %) and for the maximum number of cycles ($N = 10000$) carried out in laboratory, possibly by extrapolating in a higher number of cycles ($N > 20000$). However,

it will be necessary to question the parameters of cyclic interface behaviour. The current density is the first one of these parameters, but it seems that the initial density before cycles is also relevant, as far as the grains have the difference in freedom from a low density or from a high density, except passing through the critical state (mobilizing in the same critical-density).

There are three main steps in this approach, making extensive use of successive and progressive interpolations, which consist of:

- modeling $[u]_{cm}$ path at constant normal stress (CNL)
- modeling $[w]_{cm}$ path at constant normal stress (CNL)
- processing the imposed constant normal stiffness (CNS) paths, still contracting, and leading to the critical state after a certain number of cycles (as η_{cm} increases from η_{cm0}, as a correction with respect to the paths at constant normal stress)

It can be noted that the first two steps are in the identification phase whereas the last one is in the validation phase.

3.3.1 Modeling $[u]_{\mathbf{cm}}$ path at constant normal stress (CNL)

A logical first step of modeling $[u]_{\mathrm{cm}}$ path is to reach the density (specific weight, γ_{d}) of the soil-structure interface to connect to the normal relative displacement ($[u]_{\mathrm{cm}}$) observed. Thereby, this approach allows the difference between the initial density and the final denstiy during cyclic loading by considering the normal relative displacement to be interpreted according to:

$$\gamma_{\mathrm{d}} = \gamma_{d0\,\sigma_n} \left(\frac{1}{1 + \frac{[u]_{\mathrm{cm}}}{t}} \right) \tag{3.12}$$

where

γ_{d} is the current specific weight of interface.

$\gamma_{d0\,\sigma_n}$ is the initial specific weight of interface under an applied normal stress.

$[u]_{\mathrm{cm}}$ is the mean cyclic normal displacement.

t is the interface thickness depending on the initial density ($t = 12D_{50}$ for $I_{D0} \approx 30\%$, and $t = 10D_{50}$ for $I_{D0} \approx 90\%$).

To validate the model, the global effect η_{cm} subjected to the attractions of various poles, on the specific weight (γ_{d}) to 10,000 cycles, is first treated. Then the influence of cyclic amplitude ($\Delta\eta = \Delta\tau/\sigma_n$) on the specific weight and finally the influence of the number of cycles on the evolution of the specific weight at 10,000 cycles are described.

- **The global effect of $\eta_{\mathbf{cm}}$**

Let us examine at first the position of the cyclic loading for each reference of normal stress (σ_n = 60, 120 and 310 kPa). Figure 3.15 shows the overview of cyclic CNL tests performed in this study. The tests with high values of η_{cm} (i.e., "LH" or "DH") are partly positioned below and partly beyond the characteristic state (contracting and dilating zone under cycles, respectively). As such, they lead towards the critical state.

The global effect of the cyclic loading depends mainly on the trends identified in five poles (5 nodes in terms of interpolation) mentioned above:

$$\underline{\eta_{\text{cm}}} = (-\eta_{\text{peak}}, -\eta_*, 0, \eta_*, \eta_{\text{peak}}) \tag{3.13}$$

where $\eta_* = \frac{\eta_{\text{car}}}{2}$

From these discrete data, the behaviour of soil-structure interface will be generated. Initially, $[u]_{\text{cm}}$ as a function of the number and characteristics of cycles, for any value of η_{cm}, by the interpolation of the behaviour on these discreet data will be described.

- **Constitutive interpolations (weight functions)**

  Two interpolation functions for describing the principal behaviour of interface are chosen, with regard to η_{cm}:

  1. Term of W_c, "contraction" : there are five important conditions of the contraction:
     - For $\eta_{\text{cm}} = 0 \rightarrow W_c = \bar{a}$ with $0 < \bar{a} < 1$ (contacting for $\eta_{\text{cm}} = 0$)
     - For $|\eta_{\text{cm}}| = \eta_* \rightarrow W_c = 1$
     - For $|\eta_{\text{cm}}| = \eta_{\text{peak}} \rightarrow W_c = 0$
     - For $|\eta_{\text{cm}}| = \eta_* \rightarrow W_c' = 0$
     - For $|\eta_{\text{cm}}| = \eta_{\text{peak}} \rightarrow W_c' = 0$

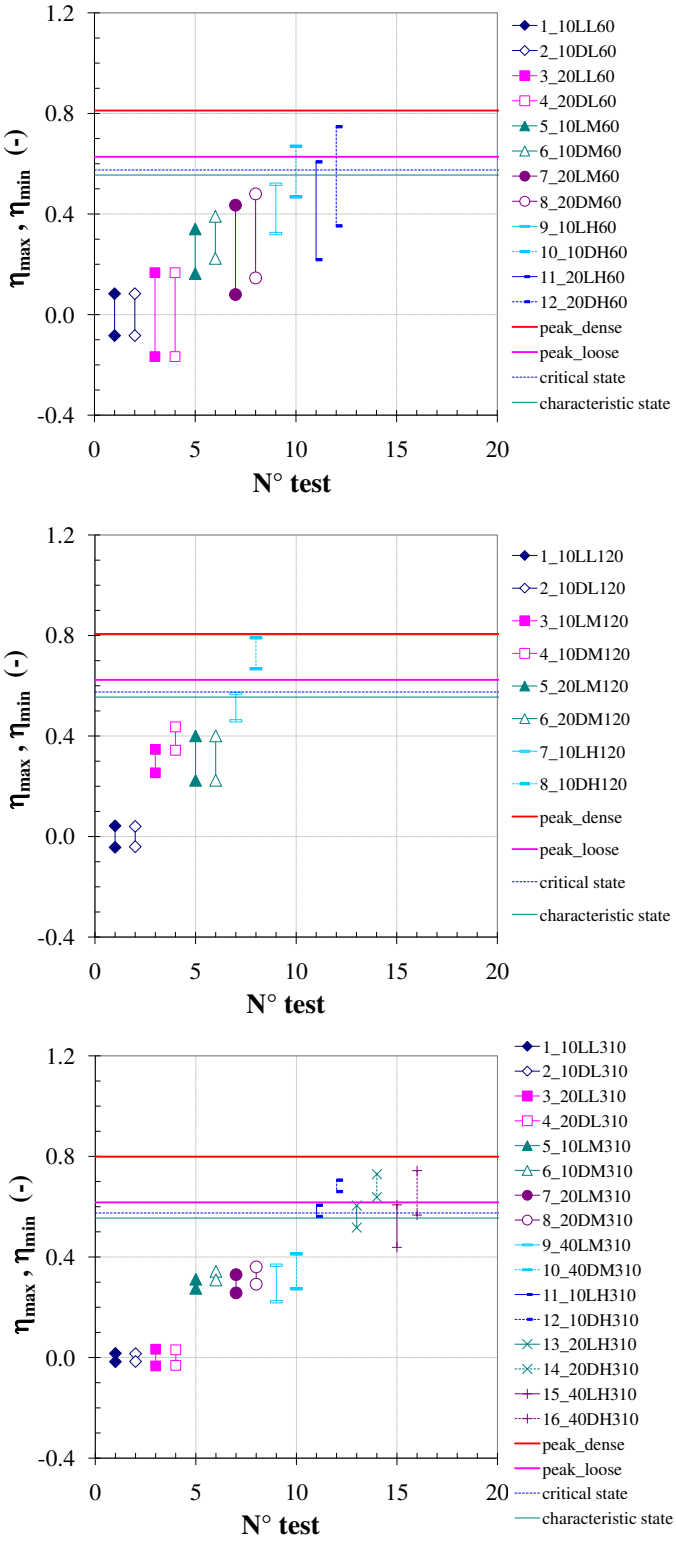

Figure 3.15: Position of the cycles with regard to the remarkable parameters on cyclic interface CNL direct shear tests

where W_c (see Appendix **C.1** for details) is given as:

$$\begin{aligned} W_c = & \frac{e}{4}\eta_{\text{cm}}^4 + \frac{|\eta_{\text{cm}}^3|}{3}\left(f + e\left(\eta_{\text{peak}} + \eta_*\right)\right) \\ & + \frac{\eta_{\text{cm}}^2}{2}\left(e\eta_{\text{peak}}\eta_* - f\left(\eta_{\text{peak}} + \eta_*\right)\right) + \eta_{\text{cm}} f \eta_{\text{peak}}\eta_* \end{aligned} \tag{3.14}$$

the parameters e and f are expressed as:

$$e = \frac{4}{(\eta_{\text{peak}} - \eta_*)^3}\left[\frac{(1-\bar{a})(3\eta_* - \eta_{\text{peak}})}{\eta_*^2} + \frac{\bar{a}(3\eta_{\text{peak}} - \eta_*)}{\eta_{\text{peak}}^2}\right] \tag{3.15}$$

$$f = -\frac{2}{(\eta_{\text{peak}} - \eta_*)^3}\left[\frac{(1-\bar{a})\eta_{\text{peak}}(2\eta_* - \eta_{\text{peak}})}{\eta_*^2} + \frac{\bar{a}\eta_*(2\eta_* - \eta_{\text{peak}})}{\eta_{\text{peak}}^2}\right] \tag{3.16}$$

2. Term of W_d, "dilation" : similarly, 5 conditions imply the following:
   - For $\eta_{\text{cm}} = 0 \rightarrow W_d = 0$
   - For $|\eta_{\text{cm}}| = \eta_* \rightarrow W_d = 0$
   - For $|\eta_{\text{cm}}| = \eta_{\text{peak}} \rightarrow W_d = 1$
   - For $\eta_{\text{cm}} = 0 \rightarrow W_d' = 0$
   - For $|\eta_{\text{cm}}| = \eta_{\text{peak}} \rightarrow W_d' = 0$

   The expression of W_d is:

$$W_d = e\eta_{\text{cm}}^2\left(|\eta_{\text{cm}} - \eta_*|\right)\left(|\eta_{\text{cm}}| - f\right) \tag{3.17}$$

where

$$f = \eta_{\text{peak}}\frac{4\eta_{\text{peak}} - 3\eta_*}{3\eta_{\text{peak}} - 2\eta_*} \tag{3.18}$$

$$e = -\frac{3\eta_{\text{peak}} - 2\eta_*}{\eta_{\text{peak}}^3(\eta_{\text{peak}} - \eta_*)^2} \tag{3.19}$$

This interpolation gives, as examples, the following results (Figure 3.16 and 3.17 for $I_{D0} \approx 30\%$, $\sigma_n = 120$ kPa and $I_{D0} \approx 90\%$, $\sigma_n = 310$ kPa; and $\bar{a} = 0.30$ in both cases, respectively).

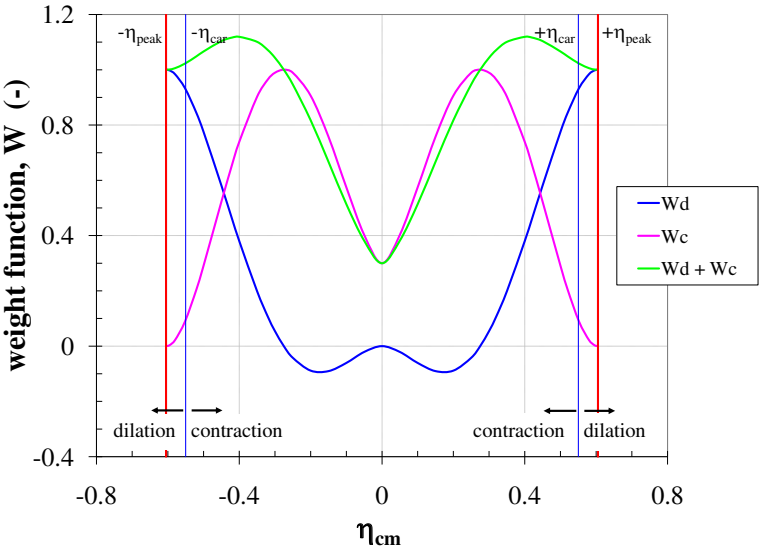

Figure 3.16: Interpolation functions on η_{cm}, $I_{D0} \approx 30\%$, $\sigma_n = 120$ kPa, the summation of $W_c + W_d = 1.119$ and the minimum of W_d = -0.0904

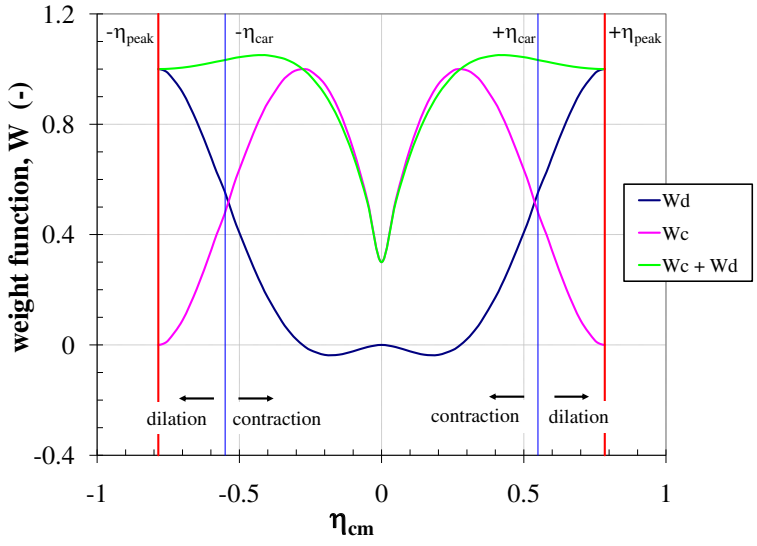

Figure 3.17: Interpolation functions on η_{cm}, $I_{D0} \approx 90\%$, $\sigma_n = 310$ kPa, the summation of $W_c + W_d = 1.048$ and the minimum of W_d = -0.0347

- **Interpolation corrections**

Unfortunately, it is found that these interpolations still present a defect, because their summation of W_c and W_d is not equal to unity $\forall \eta_{\text{cm}}$. Therefore, some corrections are necessary to be treated. However, the range of $-\eta_* < \eta_{\text{cm}} < \eta_*$ and the range of $\eta_* < |\eta_{\text{cm}}|$

$< \eta_{\text{peak}}$ are considered differently.

In the range of $-\eta_* < \eta_{\text{cm}} < \eta_*$, it is necessary that W_d is zero, because η_{cm} is in the contraction area, regulated by W_c and $\bar{a}$ only.

While in the range of $\eta_* < |\eta_{\text{cm}}| < \eta_{\text{peak}}$, depending on W_c and W_d, it would be satisfactory if the summation is equal to unity. The error with respect to these requirements still seems to be quite low, but this should still make a correction to W_c and W_d. Therefore, the so-called $W_{c\,\text{cor}}$ and $W_{d\,\text{cor}}$ will be constructed for the correction of W_c and W_d, respectively. Two corrective coefficients ("cfc" and "cfd") are then described as:

$$\text{cfd} = -0.5 + \text{sgn}\left(|\eta_{\text{cm}}| - \eta_*\right) \exp(-\,||\eta_{\text{cm}}| - \eta_*|)^{0.2} \tag{3.20}$$

with

$$\text{cfc} = \text{cfd} + 1 \tag{3.21}$$

where "cfc" and "cfd" are the corrective coefficients of contractive and dilative zones, respectively. Figure 3.18 shows these two corrective coefficients as a funcion of η_{cm} on both densities.

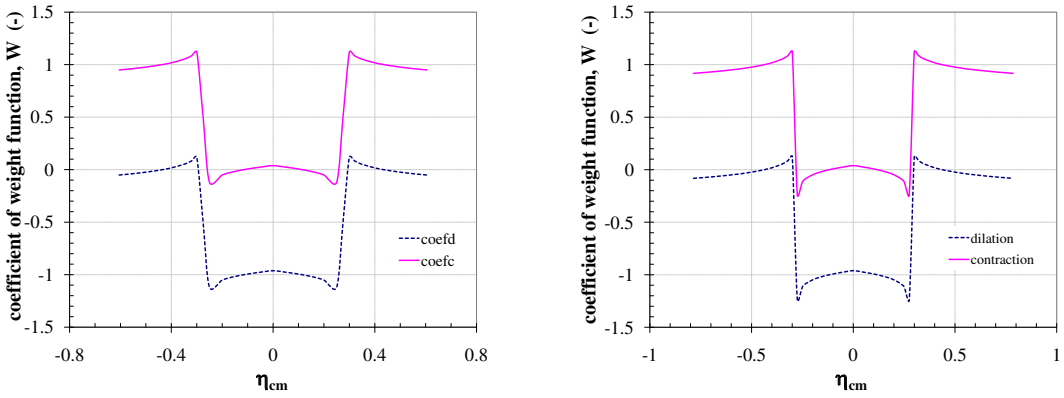

(a) (b)

Figure 3.18: Corrective coefficients of W_c and W_d: (a) in case of loose sand ; (b) in case of dense sand

Then the correction of $W_{c\,\text{cor}}$ and $W_{d\,\text{cor}}$ can be written as:

$$W_{d\,\text{cor}} = \frac{W_d(1 + \text{cfd})}{\text{cfx}} \tag{3.22}$$

$$W_{c\,\text{cor}} = W_c - \text{cfc}(W_c + W_{d\,\text{cor}} - 1) \tag{3.23}$$

where "cfx" is the maximum value of $W_d(1 + \text{cfd})$. The value of "cfx" can be given in the following:

$$\text{cfx} = \begin{cases} 0.9089(\sigma_n)^{0.0016} & \text{for dense sand} \\ 0.9424(\sigma_n)^{0.0014} & \text{for loose sand} \end{cases} \tag{3.24}$$

As a result, Figure 3.19 and 3.20 show again the interpolation functions for $I_{D0} \approx 30\%$, σ_n = 120 kPa and $I_{D0} \approx 90\%$, σ_n = 310 kPa in which the summation of $W_{c\,\text{cor}}$ and $W_{d\,\text{cor}}$ is unity.

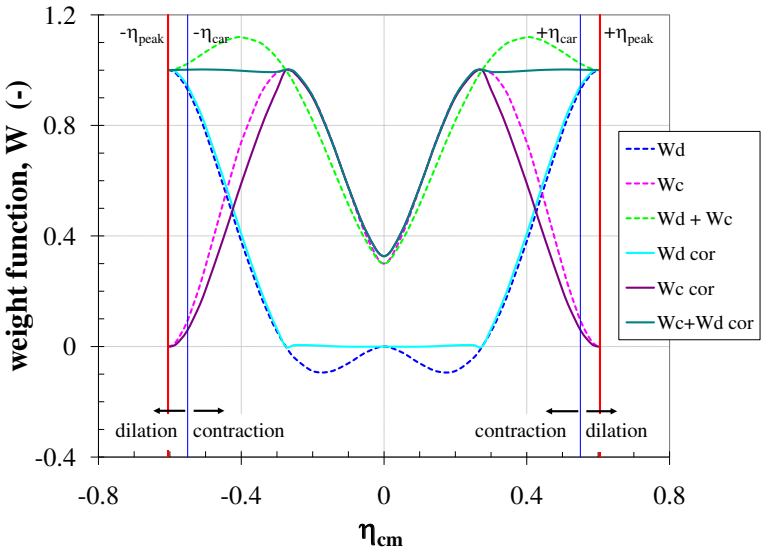

Figure 3.19: Interpolation functions on η_{cm}, $I_{D0} \approx 30\%$, σ_n = 120 kPa

In view of the simulations, these interpolations are effective for η_{cm} taken away from η_{peak}. On the other hand, η_{cm} can never exactly approach η_{peak} unless $\Delta\eta \approx 0$. It is therefore necessary to consider the position of η_{max} in comparison with η_{peak}, because, unlike η_{cm}, η_{max} can exactly approach η_{peak}. The case of $\eta_{\text{cm}} > 0$ will be first considered, it will be necessary to revise η_{max} and η_{min} later so as to incorporate the case of $\eta_{\text{cm}} < 0$ because η_{min} can approach $-\eta_{\text{peak}}$. The correction is obtained by "amplifying" η_{cm} in a controlled manner, becoming η_{cm2} in the direction of η_{peak}, according to the following strategy;

- if $\frac{\eta_{\text{max}}}{\eta_{\text{peak}}}$ is very small $\rightarrow \eta_{\text{cm2}} \approx \eta_{\text{cm}}$
- if $\frac{\eta_{\text{max}}}{\eta_{\text{peak}}} \rightarrow 1$ then $\eta_{\text{cm2}} \rightarrow \eta_{\text{peak}}$

Finally, the expression of η_{cm2} is given (see Appendix **C.2** for details) as:

$$\eta_{\text{cm2}} = \eta_{\text{cm}} + (\eta_{\text{peak}} - \eta_{\text{cm}}) \left[-\frac{33}{4} \left(\frac{\eta_{\text{max}}}{\eta_{\text{peak}}} \right)^4 + \frac{29}{2} \left(\frac{\eta_{\text{max}}}{\eta_{\text{peak}}} \right)^3 - \frac{21}{4} \left(\frac{\eta_{\text{max}}}{\eta_{\text{peak}}} \right)^2 \right] \tag{3.25}$$

This correction is then applied by using η_{cm2} instead of η_{cm}.

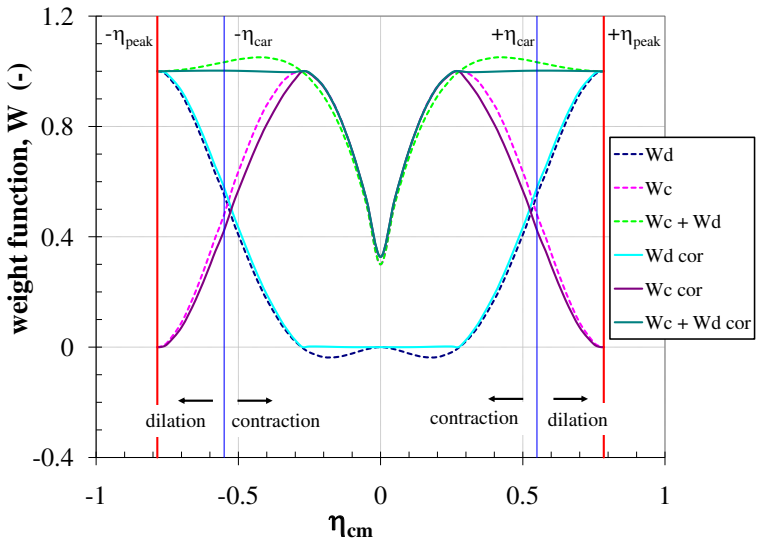

Figure 3.20: Interpolation functions on η_{cm}, $I_{D0} \approx 90\%$, $\sigma_n = 310$ kPa

During a cyclic loading, $[u]_{\mathrm{cm}}$ results from variations of the specific weight of interface. This specific weight of interface evolves between its initial value (expressed under the application of stress) $\gamma_{d0\,\sigma n}$ and its value at the end of cyclic loading (N_{f}), i.e. $N_{\mathrm{f}} = 10000$ in the general case, and $N_{\mathrm{f}} < 10000$ in the case of a cyclic loading leading to the critical state. From experimental point of view, the evolution of specific weight ends up with $N_{\mathrm{f}} \leq 10000$ ($\gamma_{d\,\sigma n\,\mathrm{Nf}}$) in the general case.

$\gamma_{d\,\sigma n\,\mathrm{Nf}}$ is then calculated as the weighted value between:

- a maximum value ($\gamma_{d\mathrm{max}\,\sigma n\,\mathrm{Nf}}$) observed in the neighborhood of the very contracting poles $\pm\eta_*$,
- and a critical value ($\gamma_{d\mathrm{crit}\,\sigma n}$) mostly observed in the neighborhood of the dilating poles $\pm\eta_{\mathrm{peak}}$,

The weighting coefficients are respectively the functions $W_{c\,\mathrm{cor}}$ and $W_{d\,\mathrm{cor}}$ previously described as a function of η_{cm}. And then the specific weight for a given N ($\gamma_{d\,\mathrm{N}}$) can be expressed as:

$$\gamma_{d\,\mathrm{N}} = \gamma_{d0\,\sigma n} + W_{c\,\mathrm{cor}}\,(\gamma_{d\mathrm{max}\,\sigma n\,\mathrm{Nf}} - \gamma_{d0\,\sigma n}) + W_{d\,\mathrm{cor}}\,(\gamma_{d\mathrm{crit}\,\sigma n} - \gamma_{d0\,\sigma n}) \tag{3.26}$$

- **Influence of cyclic amplitude $\Delta\eta$**

Let us consider the influence of $\Delta\eta$ on $\gamma_{d\mathrm{max}\,\sigma n\,\mathrm{Nf}}$ in the neighborhood of the very contracting pole ($\eta_{\mathrm{cm}} \approx \frac{\eta_{\mathrm{car}}}{2}$). A power formulation of $\gamma_{d\mathrm{max}\,\sigma n\,\mathrm{Nf}}$ is given as:

$$\gamma_{d\max\,\sigma n\,\mathrm{Nf}} = \gamma_d^*(\Delta\eta)^n \tag{3.27}$$

The performance of this formulation for three normal stresses has served as a reference. The parameters γ_d^* and n relative in $\eta_{\mathrm{cm}} \approx \frac{\eta_{\mathrm{car}}}{2}$ are represented in Figure 3.21. The analytical formulations for each density are given by

- for loose sand

$$\gamma_d^* = 24.4\exp(-0.0009\sigma_n) \tag{3.28a}$$
$$n = 0.1567\exp(-0.0043\sigma_n) \tag{3.28b}$$

- for dense sand

$$\gamma_d^* = 19.37\exp(-0.00023\sigma_n) \tag{3.29a}$$
$$n = 0.0311\exp(-0.003\sigma_n) \tag{3.29b}$$

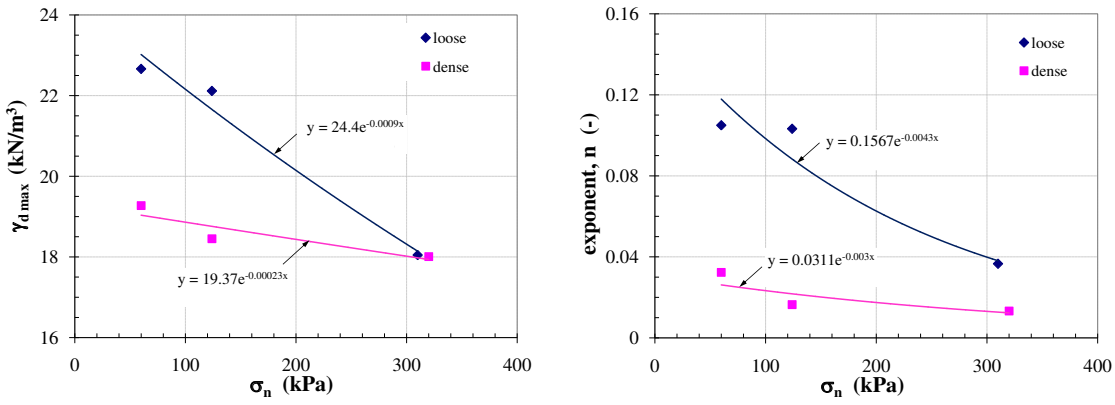

(a) (b)

Figure 3.21: Parameters γ_d^* and n, representation of $\gamma_{d\max\,\sigma n\,\mathrm{Nf}}$ relative in $\eta_{\mathrm{cm}} \approx \frac{\eta_{\mathrm{car}}}{2}$

Let us examine now the influence of $\Delta\eta$ on $\gamma_{d\,\sigma n\,\mathrm{Nf}}$ for the high values of η_{cm} which does not allow further testing until $N = 10000$, because the critical state is reached for a small number of cycles, with large tangential relative displacement. The specific weight at this state is then taken into account as $\gamma_{d\mathrm{crit}\,\sigma n}$. The evolution between initial specific weight (after the application of normal stress) and final specific weight in case of high values of η_{cm} is represented in Figure 3.22. It is found that the specific weight at critical state from monotonic tests is slightly lower than that from cyclic tests. As mentioned in the previous chapter, the thickness of interface deduced from monotonic tests (with a very good coefficient of correlation) is lower in high initial density ($t = 10D_{50}$) than in low initial density ($t = 12D_{50}$). The influence of $\Delta\eta$ on $\gamma_{d\mathrm{crit}\,\sigma n}$ is generally low, but requires further analysis.

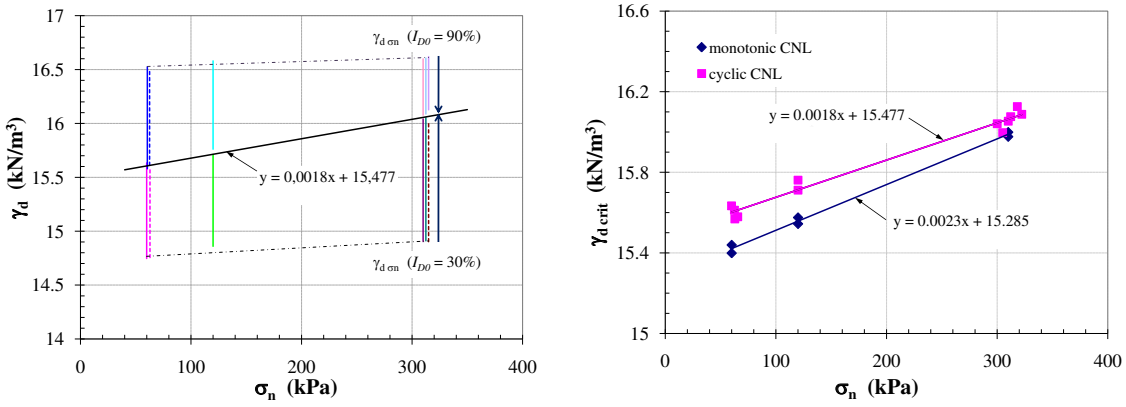

(a) (b)

Figure 3.22: (a) Cyclic tests with high values of η_{cm}, evolution between initial and final specific weights; (b) Critical specific weights from monotonic and cyclic tests

- **Evaluation of the parameter $\bar{a}$ characterizing the moderately contractive pole ($\eta_{\text{cm}} = 0$)**

The formulation of $\bar{a}$ relates $\gamma_{d\,\sigma n\,\text{Nf}}$ in the vicinity of $\eta_{\text{cm}} = 0$ and $\eta_{\text{cm}} \approx \frac{1}{2}\eta_{\text{peak}}$. This parameter mainly influences on the low value of η_{cm}. The ratio of $\bar{a}$ is derived from the difference of $\gamma_{d\,\sigma n\,\text{Nf}}$ between $\eta_{\text{cm}} = 0$ and $\eta_{\text{cm}} \approx \frac{1}{2}\eta_{\text{peak}}$. It is worth mentioning that since $\bar{a}$ is the interpolation coefficient of W_c, the other one (W_d) is then zero. The variations of $\bar{a}$ as a function of σ_n can be given as:

$$\bar{a} = \begin{cases} 0.8329(\sigma_n)^{-0.0423} & \text{for loose sand} \\ 0.844(\sigma_n)^{-0.0509} & \text{for dense sand} \end{cases} \tag{3.30}$$

- **Rate of cyclic pseudo-creep evolution (constant $N_{50\%}$)**

The rate of cyclic pseudo-creep evolution is set by the function of the number of cycles $f(N)$. Initially, two functions are used to describe this rate (cyclic pseudo-creep) in each of the poles (contraction and dilation):

$$f_c(N) = \frac{N}{Cte1 + N} \tag{3.31a}$$

$$f_d(N) = 1 - \exp(-Cte2 \cdot N) \tag{3.31b}$$

where $f_c(N)$ and $f_d(N)$ are respectively the functions applying to the contractive and dilative poles. These functions are represented and parametrized in Figure 3.23. As can be seen, the hyperbolic function (f_c) practically reaches the unity for approximately 5,000 cycles with $Cte1 = 670$, whereas the exponential function (f_d) practically reaches the unity for approximately 1000 cycles with $Cte2 = 0{,}003912$.

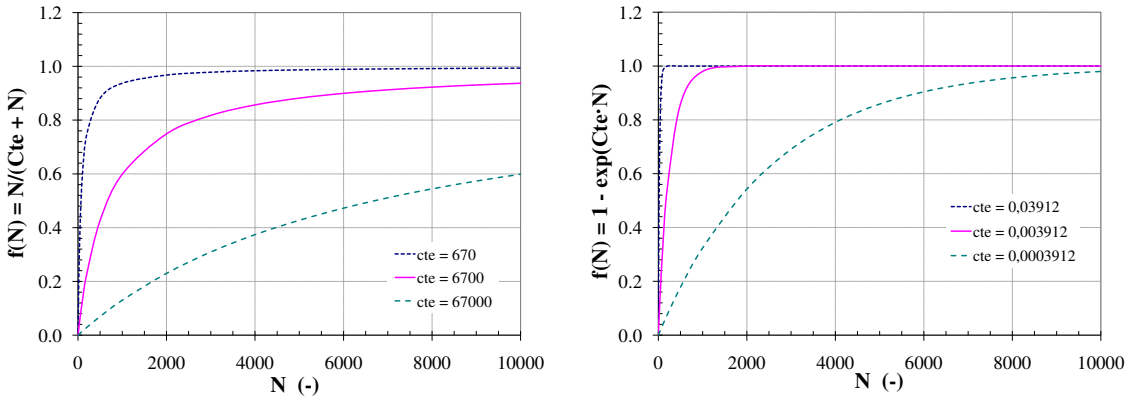

(a) (b)

Figure 3.23: (a) Hyperbolic function of the number of cycles $f(N)$; (b) Exponential function of the number of cycles $f(N)$

Regarding the results of cyclic tests, the evolutions of contraction are relatively slow, whereas the evolutions of dilation (or towards the critical state) are rather fast. This remark allows the choice of the functions and the constants, according to the values of σ_n, η_{cm}, etc.

The hyperbolic function $f_c(N) = \frac{N}{Cte1+N}$ seems more properly applicable, because the direction of the constant is easy to identify. Figure 3.24 shows the direction of Cte from hyperbolic function. It is clear that the $Cte = N_{50\%}$ is appropriate to use.

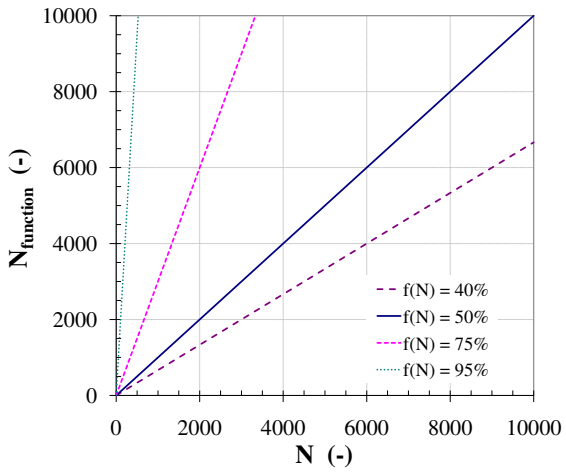

Figure 3.24: Direction of constant hyperbolic function

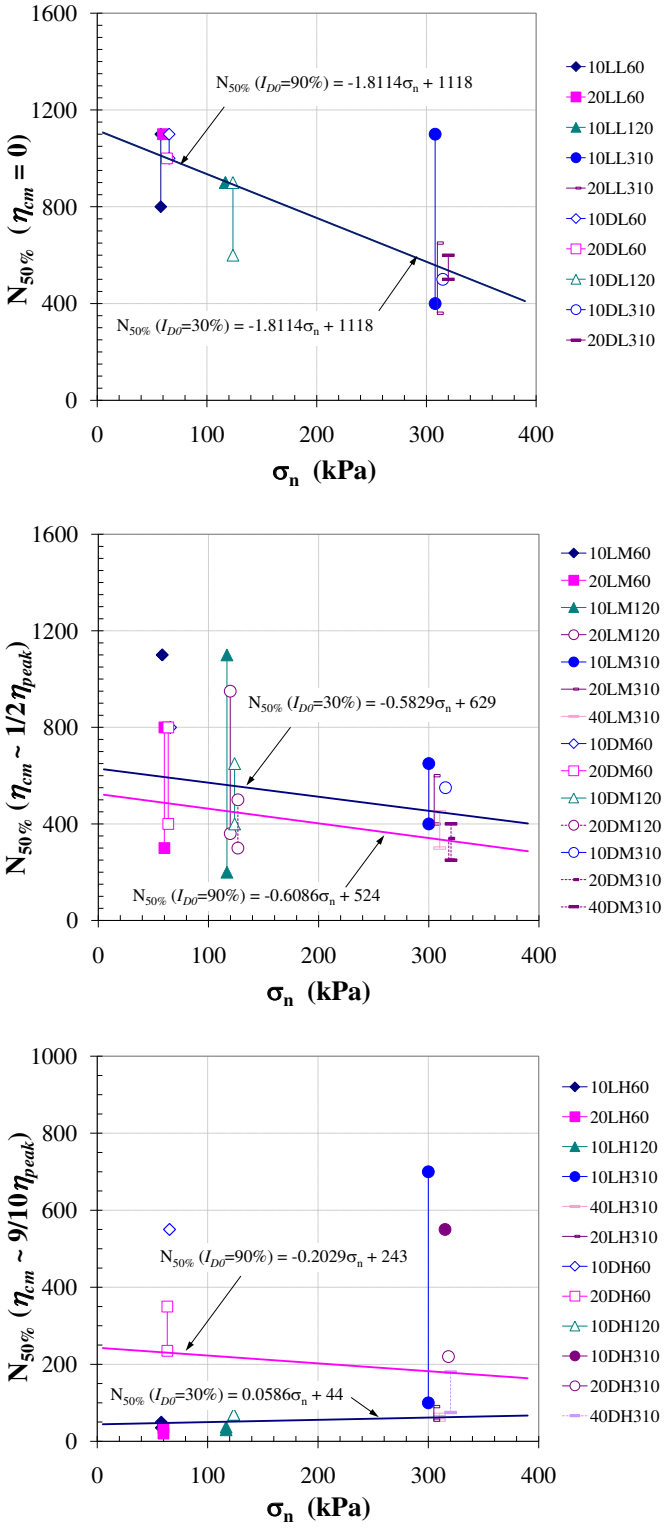

Figure 3.25: Evaluation of the number of cycles $N_{50\%}$ to achieve 50% of $[u]_{\mathrm{cm}}$ reached in N_f ($N_f = 10000$ for low and medium values of η_{cm}, less for high value of η_{cm})

Therefore, it is a question of allocating a constant to each test by considering the rate of evolution of the test. Figure 3.25 gives an evaluation of the degree of evolution of $[u]_{\text{cm}}$ with N (the number of cycles, $N_{50\%}$, allowing to reach 50% of $[u]_{\text{cm}}$ reached in N_f). From this degree of evolution, the hyperbolic constant $N_{50\%}$ is then be held. The average lines for each of 3 typical values of $\eta_{\max}/\eta_{\text{peak}}$ as a functions of σ_n are then taken into account as shown in Figure 3.26. And hence a trend of the intercept and slope of these average lines as a function of $\eta_{\max}/\eta_{\text{peak}}$ is obtained.

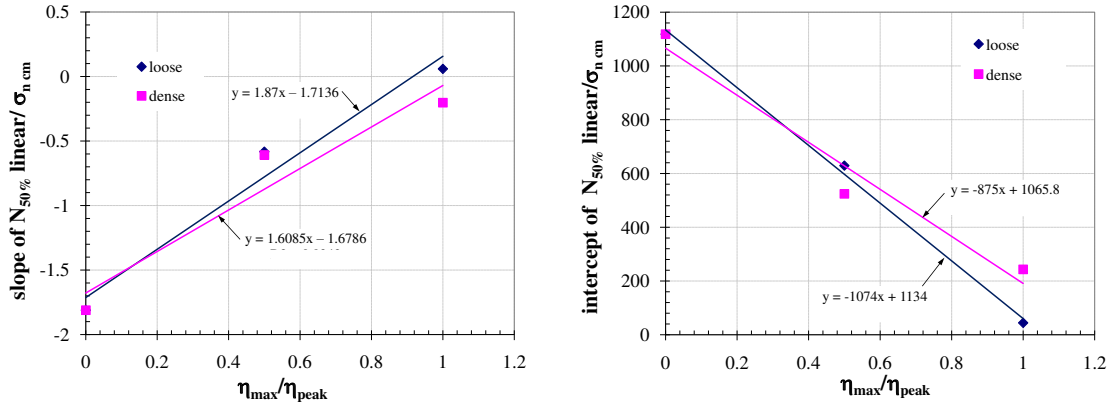

Figure 3.26: Slope and intercept of linear approximations of $N_{50\%}(\sigma_n)$ as a function of $\eta_{\max}/\eta_{\text{peak}}$

The formulation of the constant $N_{50\%}$ is then expressed as:

$$\text{for loose sand} \quad f(N_{50\%}) = (-1074\frac{\eta_{\max}}{\eta_{\text{peak}}} + 1134) + (1.87\frac{\eta_{\max}}{\eta_{\text{peak}}} - 1.7136)\sigma_n \tag{3.32a}$$

$$\text{for dense sand} \quad f(N_{50\%}) = (-875\frac{\eta_{\max}}{\eta_{\text{peak}}} + 1065.8) + (1.6085\frac{\eta_{\max}}{\eta_{\text{peak}}} - 1.6786)\sigma_n \tag{3.32b}$$

Therefore, from (3.26) the evolution of specific weight during cyclic loading is given:

$$\begin{aligned}\gamma_{d\,\text{N}} = \gamma_{d\,\sigma n} + f(N_{50\%})W_{c\,\text{cor}}\,(\gamma_{d\max\,\sigma n\,\text{Nf}} - \gamma_{d0\,\sigma n}) \\ + f(N_{50\%})W_{d\,\text{cor}}\,(\gamma_{d\text{crit}\,\sigma n} - \gamma_{d0\,\sigma n})\end{aligned} \tag{3.33}$$

Figure 3.27 shows typical prediction of the evolution of specific weight during cyclic loading for $\sigma_n = 120$ kPa, $I_{D0} \approx 30\%$ and $\sigma_n = 310$ kPa, $I_{D0} \approx 90\%$ with $\Delta\tau = 10$ kPa. Therefore, the evolution of the normal displacement $[u]_{\text{cm}}$ as a function of N is achieved.

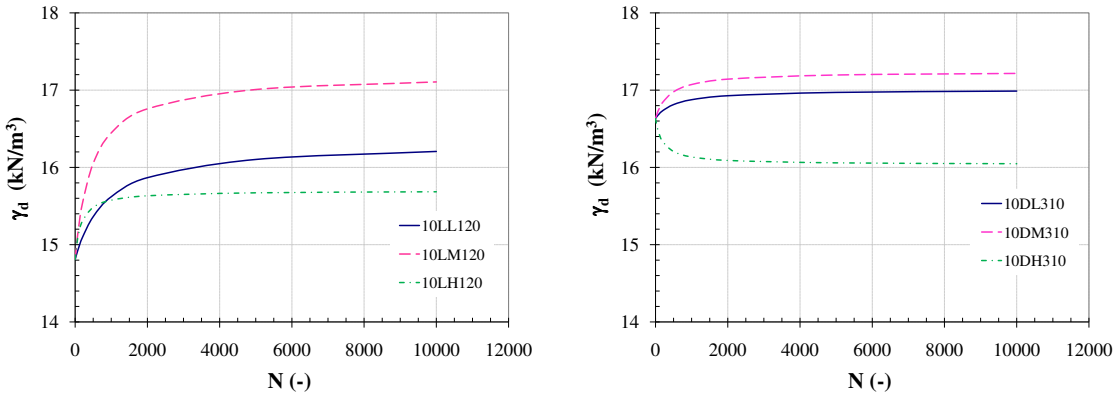

(a) (b)

Figure 3.27: Evolution of specific weight during cyclic loading: (a) $\sigma_n = 120$ kPa, $I_{D0} \approx 30\%$; (b) $\sigma_n = 310$ kPa, $I_{D0} \approx 90\%$

3.3.2 Modeling $[w]_{\mathbf{cm}}$ path at constant normal stress (CNL)

The evolution of $[w]_{\text{cm}}$ depending on the number of cycles is similar to that of the creep (Figure 3.28): it is the cyclic pseudo-creep. In the case of soil-structure interfaces studied, three main characteristics can be observed:

- no pseudo-cyclic creep for a very low value of η_{cm} (i.e. $\eta_{\text{cm}} \approx 0$)
- primary and secondary creep for the medium values of η_{cm} (i.e. $\eta_{\text{cm}} \approx \eta_*$)
- primary and then secondary then tertiary creep for the high values of η_{cm} (i.e. η_{cm} close to η_{peak})

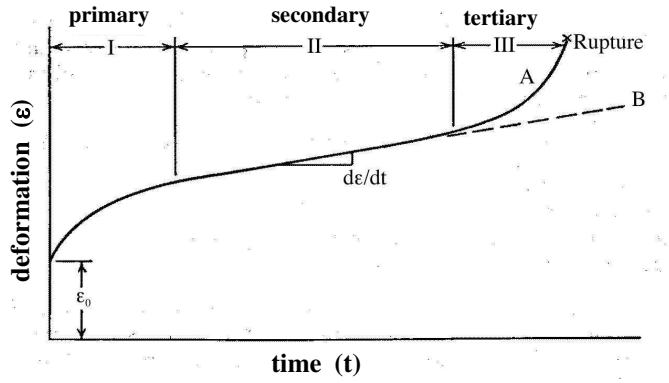

Figure 3.28: The classical view of creep

The evolution of $[w]_{\text{cm}}$ will be treated by a function of the number of cycles (as described in the part of $[u]_{\text{cm}}$). First, the expression of the limits, for medium and high values of η_{cm} has to be described. The estimation of the oblique asymptotes of $[w]_{\text{cm}}(N)$, and the rate of evolution towards these asymptotes will then be treated separately. Figure 3.29 then represents these estimated asymptotes, for medium value of η_{cm} (so-called secondary creep).

Let us now separate the slope and intercept of the asymptotes.

- **Slope of the asymptote of $[w]_{\text{cm}}(N)$ for the medium values of η_{cm}**

It is here about secondary pseudo-creep. Figure 3.30 represents the slope m of the estimated asymptotes of $[w]_{\text{cm}}(N)$ on loose and dense sands, with a parameter $\Delta\eta$. A formulation of this slope which takes into account, at the same time, the level of the normal stress and the cyclic amplitude is determined. The effect of stress level on the slope of the asymptote, in case of loose sand, can be expressed in a power law as:

$$m_{[w]\text{cm/cycle}} = 0.0457(\sigma_n)^{-1.691} \qquad (\text{mm/cycle}) \tag{3.34}$$

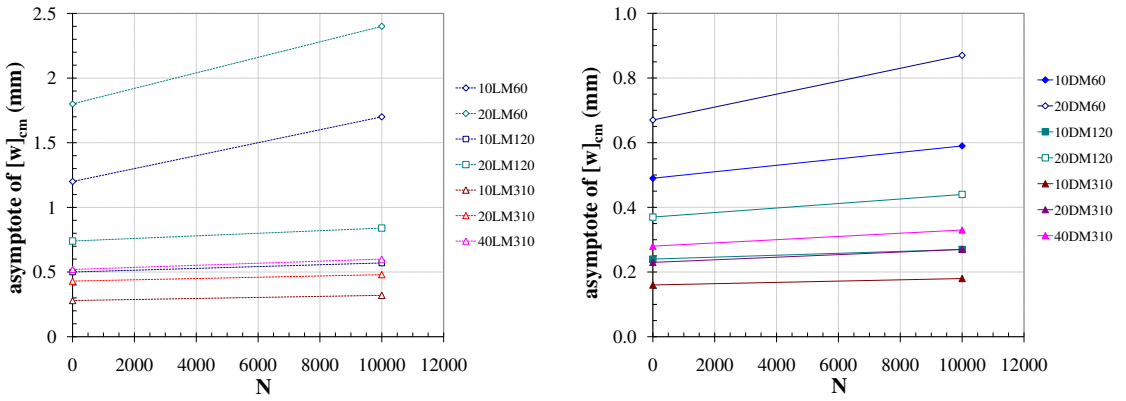

(a) (b)

Figure 3.29: Estimation of asymptotes in case of medium value of η_{cm}: (a) loose sand, $I_{D0} \approx 30\%$; (b) dense sand, $I_{D0} \approx 90\%$

In case of dense sand, the slope of the asymptote is still expressed in a power law:

$$m_{[w]\text{cm/cycle}} = 6E-05(\sigma_n)^{-0.427} \qquad (\text{mm/cycle}) \tag{3.35}$$

Taking into account the influence of $\Delta\eta$ on $m_{[w]\text{cm/cycle}}$ in power law, a coefficient c describing the ratio of m for each $\Delta\eta$ has to be presented. Figure 3.31 shows the coefficient (c) as a function of $\Delta\eta$ for loose and dense sands. This can be written as:

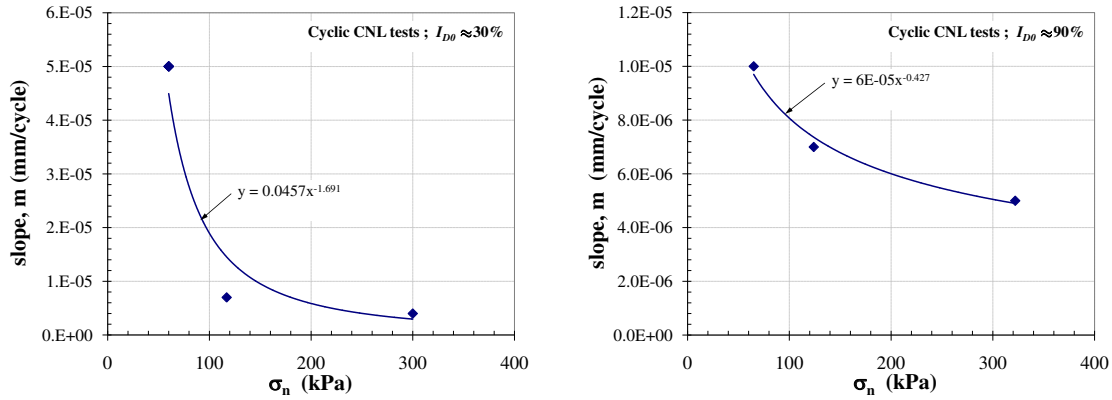

(a) (b)

Figure 3.30: Estimated slope of the asymptote $[w]_{\mathrm{cm}}(N)$ in case of medium value of η_{cm}: (a) loose sand, $I_{D0} \approx 30\%$; (b) dense sand, $I_{D0} \approx 90\%$

$$\text{for loose sand} \quad c = -9.468\Delta\eta^2 + 7.3472\Delta\eta - 0.0107 \tag{3.36a}$$

$$\text{for dense sand} \quad c = 1.5405\Delta\eta^2 + 5.9432\Delta\eta + 0.0005 \tag{3.36b}$$

Finally, the slope of the asymptote for the medium values of η_{cm} can be written as:

$$\text{for loose sand} \quad m_{[w]\mathrm{cm/cycle}} = 0.0457(\sigma_n)^{-1.691}(-9.468\Delta\eta^2 + 7.3472\Delta\eta - 0.0107) \tag{3.37a}$$

$$\text{for dense sand} \quad m_{[w]\mathrm{cm/cycle}} = 6E-05(\sigma_n)^{-0.427}(1.5405\Delta\eta^2 + 5.9432\Delta\eta + 0.0005) \tag{3.37b}$$

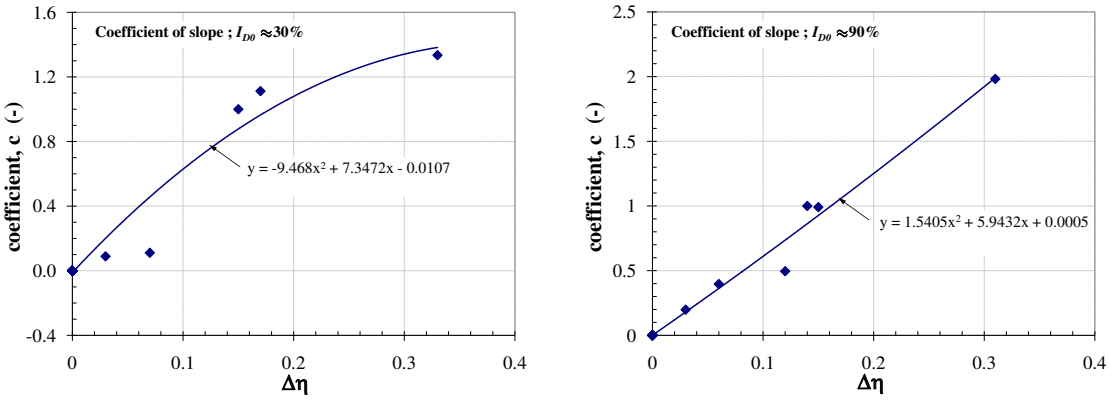

(a) (b)

Figure 3.31: Coefficient "c" of the slope of asymptote in case of medium value of η_{cm}: (a) loose sand, $I_{D0} \approx 30\%$; (b) dense sand, $I_{D0} \approx 90\%$

It is worth noting that $m_{[w]\text{cm/cycle}} \neq 0$ for $\Delta\eta = 0$, which is not physical, but very low, however, this results from the approximation mode.

- **Intercept of the asymptote of $[w]_{\mathbf{cm}}(N)$ for the medium values of $\eta_{\mathbf{cm}}$**

Similarly to the slope of asymptote, the estimated intercept of the asymptote ($b_{[w]\text{cm}}$) as a function of normal stress level can be expressed in both cases:

$$\text{for loose sand} \quad b_{[w]\text{cm}} = 20.019(\sigma_n)^{-0.6281} \tag{3.38a}$$

$$\text{for dense sand} \quad b_{[w]\text{cm}} = 2.5742(\sigma_n)^{-0.3584} \tag{3.38b}$$

A coefficient c taking into account the influence of $\Delta\eta$ on $b_{[w]\text{cm}}$ can be given in power law as:

$$\text{for loose sand} \quad c = 1.6359\Delta\eta^{0.2944} \tag{3.39a}$$

$$\text{for dense sand} \quad c = 1.6676\Delta\eta^{0.287} \tag{3.39b}$$

And then the intercept of the asymptote for the medium values of η_{cm} can be written as:

$$\text{for loose sand} \quad b_{[w]\text{cm}} = 20.019(\sigma_n)^{-0.6281}(1.6359\Delta\eta^{0.2944}) \tag{3.40a}$$

$$\text{for dense sand} \quad b_{[w]\text{cm}} = 2.5742(\sigma_n)^{-0.3584}(1.6676\Delta\eta^{0.287}) \tag{3.40b}$$

- **Evolution of $[w]_{\mathbf{cm}}(N)$ with N for the medium values of $\eta_{\mathbf{cm}}$**

The evolution of $[w]_{\text{cm}}(N)$ is described by using a hyperbolic formulation. The oblique asymptote is formulated according to the slope and intercept of the estimation.

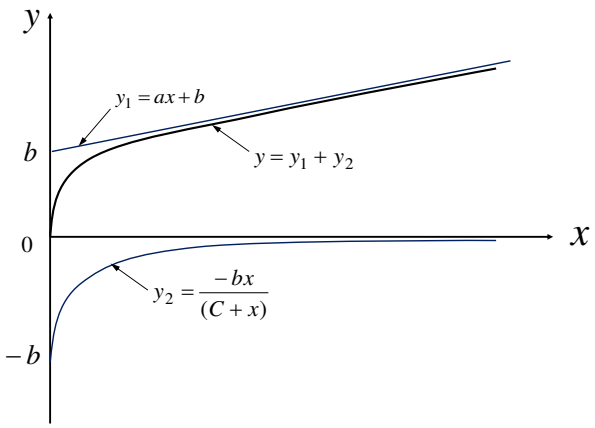

Figure 3.32: Evolution of $[w]_{\text{cm}}(N)$ with N, linear + hyperbolic functions

$$[w]_{\text{cm-asymp}} = m_{[w]\text{cm/cycle}} \cdot N + b_{[w]\text{cm}} \tag{3.41}$$

The evolution of $[w]_{\text{cm}}$ as a function of N is written as:

$$[w]_{\text{cm}} = [w]_{\text{cm-asymp}} - b_{[w]\text{cm}} \cdot \left(1 - \frac{N}{Cte + N}\right) \tag{3.42}$$

or it can be rewritten in

$$[w]_{\text{cm}} = m_{[w]\text{cm/cycle}} \cdot N + b_{[w]\text{cm}} \cdot \frac{N}{Cte + N} \tag{3.43}$$

The constant Cte is comparable to $N_{50\%}$ as mentioned in the rate of cyclic pseudo-creep evolution. In fact, the evolution of $[w]_{\text{cm}}$ is slower than that of $[u]_{\text{cm}}$. The set of constant Cte is decided to be:

$$Cte = 2N_{50\%} \tag{3.44}$$

- **Modeling of $[w]_{\text{cm}}$ for high value of η_{cm}**

In case of tertiary pseudo-creep (high value of η_{cm}), the estimation of slopes and intercepts is more difficult and subjective than in the case of the secondary pseudo-creep (medium value of η_{cm}). In addition, the evolution of hyperbolic formulation as a function of N is no longer appropriate because the curve $[w]_{\text{cm}}(N)$ contains an inflexion point (at the beginning of the so called tertiary creep).

In the hypothesis of high value of η_{cm}, the model parameters of cyclic CNL tests mainly depend on σ_n, η_{cm} and $\Delta\eta$.

Let us see how this evolution will be modeled. Two linear formulations (as shown in Figure 3.33) are first chosen as:

$$y_1 = y'_0 \cdot x \tag{3.45a}$$

$$y_2 = a \cdot x + c \tag{3.45b}$$

These two linear formulations are based on:

- a and b the slope and intercept of the asymptote
- y'_0 the slope passing through the origin
- horizontal interpolation between these two lines

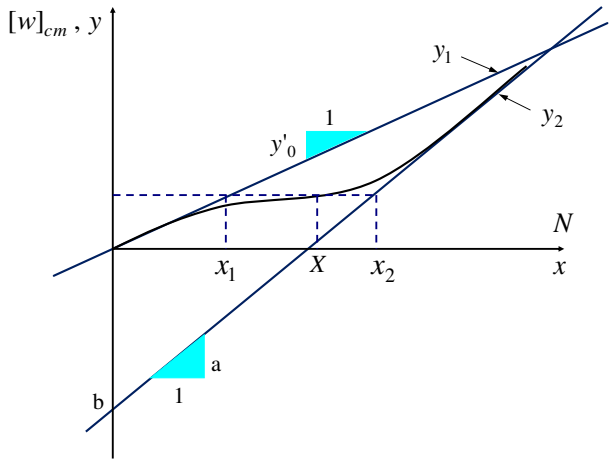

Figure 3.33: Evolution of $[w]_{\text{cm}}(N)$ with N at high value of η_{cm}, linear function

For a given y , the formulation can commonly be written as:

$$N = H_1 x_1 + H_2 x_2 \tag{3.46}$$

where $x_1 = \frac{y_1}{y'_0}$, $x_2 = \frac{y_2 - b}{a}$ and $0 \leq H_1, H_2 \leq 1$.

The function H_1 and H_2 are given in the following:

$$H_1 = \exp(-Ay^2) \tag{3.47a}$$

$$H_2 = 1 - \exp(-Ay^2) \tag{3.47b}$$

where "A" is a parameter describing the inflexion point, so-called "$[w]_{\text{cm inf}}$", which can be expressed as:

$$A = \frac{1}{[w]_{\text{cm inf}}^{1/2}} \tag{3.48}$$

Substitution of H_1 and H_2 into 3.46 gives:

$$X = \frac{y}{y'_0} \exp(-Ay^2) + \frac{y - b}{a} \left[1 - \exp(-Ay^2)\right] \tag{3.49}$$

or it can be rewritten in $[w]_{\text{cm}} - N$ form:

$$N = \frac{[w]_{\text{cm}}}{y'_0} \exp(-A[w]_{\text{cm}}^2) + \frac{[w]_{\text{cm}} - b}{a} \left[1 - \exp(-A[w]_{\text{cm}}^2)\right] \tag{3.50}$$

To be able to use two linear formulations, the determination of a, b and y'_0 has to be described. Before handling these parameters, the so-called $\Delta\eta_{\max}$ which describes the feasible condition that the tests can be carried out is considered. $\Delta\eta_{\max}$ principally depends on η_{cm} which can be expressed as (see Appendix **C.3** for details):

$$\Delta\eta_{\max} = 2\frac{\eta_{\text{peak}} - |\eta_{\text{cm}}|}{1 + \eta_{\text{peak}} \cdot |\eta_{\text{cm}}|} \tag{3.51}$$

From the above expression, it turns out that

$$\Delta\eta_{\max} = \begin{cases} 0 & \text{if } |\eta_{\text{cm}}| \to \eta_{\text{peak}} \\ 2\eta_{\text{peak}} & \text{if } |\eta_{\text{cm}}| \to 0 \end{cases}$$

Then, the current parameter p for describing these tests are proposed.

Let p be:

- the slope and intercept of the asymptote, a and b
- or the slope passing through the origin, y'_0
- or the inflexion point, A

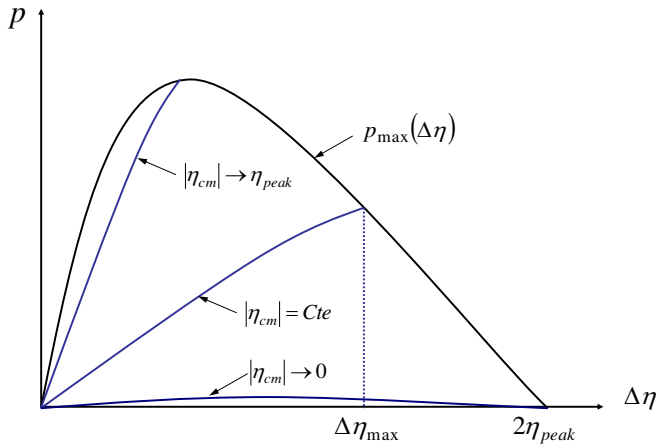

Figure 3.34: Limit of $p_{\max}(\Delta\eta)$ for a given $|\eta_{\text{cm}}|$

The determination of these parameters can be represented in $p - \Delta\eta$ plane for each level of η_{cm} as shown in Figure 3.34. It can be noted that the curves $p(\Delta\eta,\ |\eta_{\text{cm}}|)$ are limited by the curve $p_{\max}(\Delta\eta)$, corresponding to $\Delta\eta = \Delta\eta_{\max}$ for a given $|\eta_{\text{cm}}|$. The expression is then given as:

$$p = p_{\max} \cdot \frac{\Delta\eta}{\Delta\eta_{\max}} \left(2 - \frac{\Delta\eta}{\Delta\eta_{\max}}\right) \tag{3.52}$$

And then the maximum feasible conditions of a, b and y'_0 (later called $a_{\max}$, $b_{\max}$ and $y'_{0\,\max}$, respectively), corresponding to $\eta_{\rm cm}$ are determined for each level of σ_n:

$$a_{\max} = a_1 \Delta\eta_{\max} + b_1 - \frac{b_1 c_1}{c_1 - \Delta\eta_{\max}} \tag{3.53}$$

$$b_{\max} = a_2 \Delta\eta_{\max} + b_2 - \frac{b_2 c_2}{c_2 - \Delta\eta_{\max}} \tag{3.54}$$

$$y'_{0\,\max} = a_3 \Delta\eta_{\max} + b_3 - \frac{b_3 c_3}{c_3 - \Delta\eta_{\max}} \tag{3.55}$$

where a_i, b_i, and c_i are the parameters which only depend on σ_n.

Figure 3.35 shows typical parameters a_i, b_i, and c_i derived from the estimation in case of $\sigma_n = 310$ kPa on dense sand. Although certain points are beyond the maximum criterion (e.g. a_i), the evolution of theses parameters coresponding to $\eta_{\rm cm}$ is still reliable.

However, to obtain the proper formulation, the elaboration of these parameters, by considering the size of the cycle in term of the ratio of $\Delta\eta/\eta_{\max}$ and $\eta_{\rm peak}/\Delta\eta$, is still required. The multiplicative factors ($C_{a\,\max}$, $C_{b\,\max}$ and $C_{y'0\,\max}$) are then taken into account, depending on the initial density, and these factors can be given as the following:

- in case of loose sand

$$C_{a\,\max} = \frac{\Delta\eta}{\eta_{\max}} \left[1 - \frac{1}{100}\left(3.8592 \frac{\eta_{\rm peak}}{\Delta\eta}\right)\right] \tag{3.56a}$$

$$C_{b\,\max} = \frac{\Delta\eta}{\eta_{\max}} \left[1 - \frac{1}{100}\left(-15.096 \frac{\eta_{\rm peak}}{\Delta\eta} - 19.245\right)\right] \tag{3.56b}$$

$$C_{y'0\,\max} = \frac{\Delta\eta}{\eta_{\max}} \left[1 - \frac{1}{100}\left(-20 + 1.5 \frac{\eta_{\rm peak}}{\Delta\eta}\right)\right] \tag{3.56c}$$

- in case of dense sand

$$C_{a\,\max} = \frac{\Delta\eta}{\eta_{\max}} \left[1 - \frac{1}{100}\left(-30 + 4 \frac{\eta_{\rm peak}}{\Delta\eta}\right)\right] \tag{3.57a}$$

$$C_{b\,\max} = \frac{\Delta\eta}{\eta_{\max}} \left[1 - \frac{1}{100}\left(-53.177 \frac{\eta_{\rm peak}}{\Delta\eta} - 5\right)\right] \tag{3.57b}$$

$$C_{y'0\,\max} = \frac{\Delta\eta}{\eta_{\max}} \left[1 - \frac{1}{100}\left(0.886 + 1.931 \frac{\eta_{\rm peak}}{\Delta\eta}\right)\right] \tag{3.57c}$$

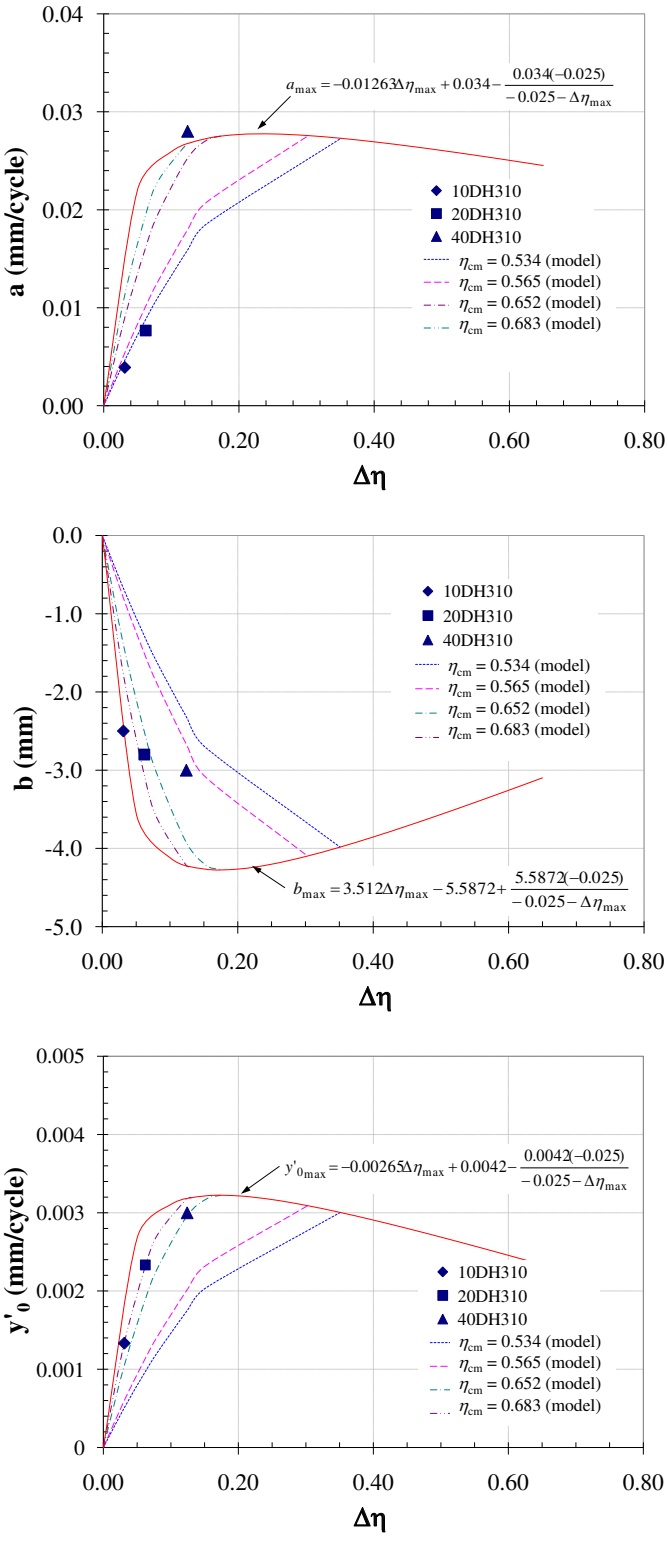

Figure 3.35: Estimation of a_i, b_i, and c_i for high value of η_{cm}, $\sigma_n = 310$ kPa on dense sand

The inflexion points ($[w]_{\text{cm inf}}$) which mainly depend on σ_n and the ratio of $\frac{\Delta\eta}{\eta_{\text{peak}}}$ are determined from experimental data. Figure 3.36(a) shows the typical derivation of $[w]_{\text{cm inf}}$ in case of loose sand. The influence of cyclic amplitude represented by $\frac{\Delta\eta}{\eta_{\text{peak}}}$ on the inflexion of $[w]_{\text{cm}}(N)$ is also presented in Figure 3.36(b).

From taking into account the influence of σ_n and $\frac{\Delta\eta}{\eta_{\text{peak}}}$, the expression of inflexion points ($[w]_{\text{cm inf}}$) on both densities can be given as:

$$\text{for loose sand; } [w]_{\text{cm inf}} = (-0.499\ln\sigma_n + 3.5571)\left(-0.0364\frac{1}{0.0536}\frac{\Delta\eta}{\eta_{\text{peak}}} + 1.031\right) \quad (3.58a)$$

$$\text{for dense sand; } [w]_{\text{cm inf}} = (-0.731\ln\sigma_n + 5.624)\left(-0.0892\frac{1}{0.0389}\frac{\Delta\eta}{\eta_{\text{peak}}} + 1\right) \quad (3.58b)$$

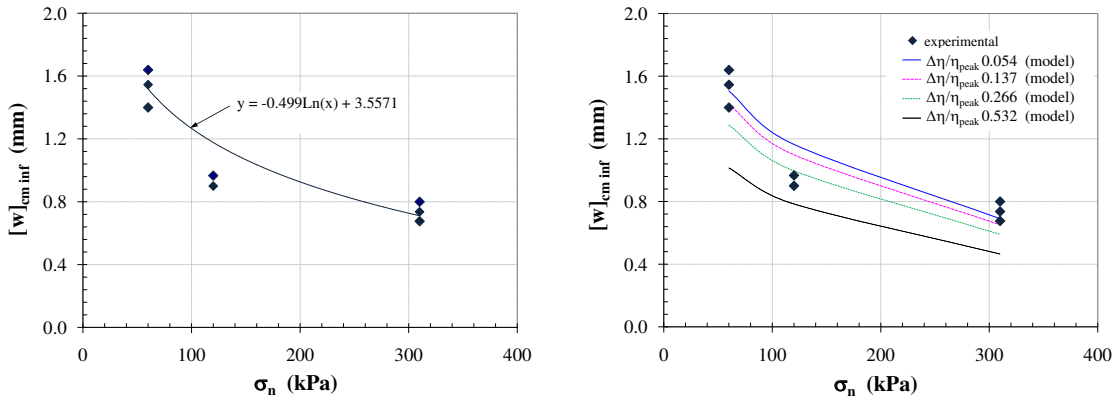

(a) (b)

Figure 3.36: Typical inflexion of $[w]_{\text{cm}}(N)$ for the high values of η_{cm} on loose sand

Combining (3.43), called $[w]_{\text{cm}\,1}$, and (3.49), called $[w]_{\text{cm}\,2}$, with the constitutive functions $W_{c\,\text{cor}}$ and $W_{d\,\text{cor}}$, respectively, the formulation of $[w]_{\text{cm}}$ for a given η_{cm} is written as:

$$[w]_{\text{cm}} = [w]_{\text{cm}\,1}(W_{c\,\text{cor}}) + [w]_{\text{cm}\,2}(W_{d\,\text{cor}}) \quad (3.59)$$

From experimental data, $[w]_{\text{cm}}$ at $\eta_{\text{cm}} = 0$ is not prominent. This also means that $W_{c\,\text{cor}}$ and $W_{d\,\text{cor}}$ for modeling $[w]_{\text{cm}}$ should be zero when η_{cm} is close to zero. Therefore, $W_{c\,\text{cor}}$ and $W_{d\,\text{cor}}$ additionally require multiplicative factors, which can respectively be written as:

$$W_{mc\,\text{cor}} = W_{c\,\text{cor}}\left[\exp\left(-\left|2.42\frac{(\eta_{\text{cm}} - \eta_{\text{peak}})}{\eta_{\text{peak}}}\right|^8\right)\right] \quad (3.60a)$$

$$W_{md\,\text{cor}} = W_{d\,\text{cor}}[1 - \exp(-92.1034\eta_{\text{cm}})] \quad (3.60b)$$

3.3.3 Checking of the proposed analytical models for identification

To check the validation of the proposed models, Figure 3.37 - 3.40 show typical comparisons between experimental observations and analytical model predictions of cyclic CNL tests by considering the overall factors (e.g. I_{D0}, σ_n, η_{cm} and $\Delta\tau$). Generally, the proposed models are capable of reproducing the interface behaviour under cyclic loading. In the range of 0 $< \eta_{\text{cm}} < \eta_{\text{car}}$, the capability of the proposed models is satisfactory. However, in case of η_{cm} close to η_{peak}, it is difficult to properly reproduce the cyclic interface behaviour. The early termination of these tests provides a deficient description of the rate of cyclic pseudo-creep evolution. At high level of η_{cm} close to η_{peak}, during cyclic shearing the model cannot properly reproduce $[u]_{\text{cm}}$ especially on dense sand. All features of interface model in CNL condition are summarized in Appendix **D**.

In addition, the proposed models are verified by interpolating wheteher on I_{D0}, η_{cm} or σ_n. Figure 3.41 first shows the model predictions of cyclic CNL tests on I_{D0} = 60%, σ_n = 310 kPa. In this case the medium sand shows approximately contractive behaviour at η_{cm} close to η_{peak}. It is noted that the sign of η_{cm} ($\pm\eta_{\text{cm}}$) only indicates the direction of shear displacement while this has no influence on normal displacement. The interpolation of σ_n = 200 kPa also confirms the validity of the proposed models as shown in Figure 3.42.

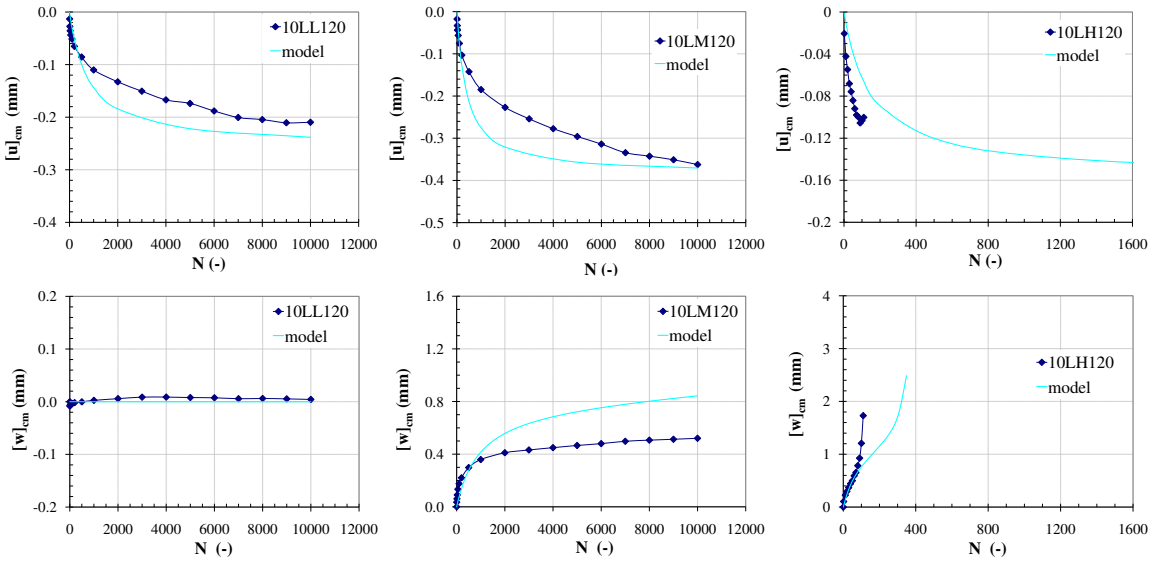

Figure 3.37: Comparison between experimental data and the model prediction, σ_n = 120 kPa, cyclic CNL tests on loose sand ($I_{D0} \approx 30\%$), $\Delta\tau$ = 10 kPa with rough plate

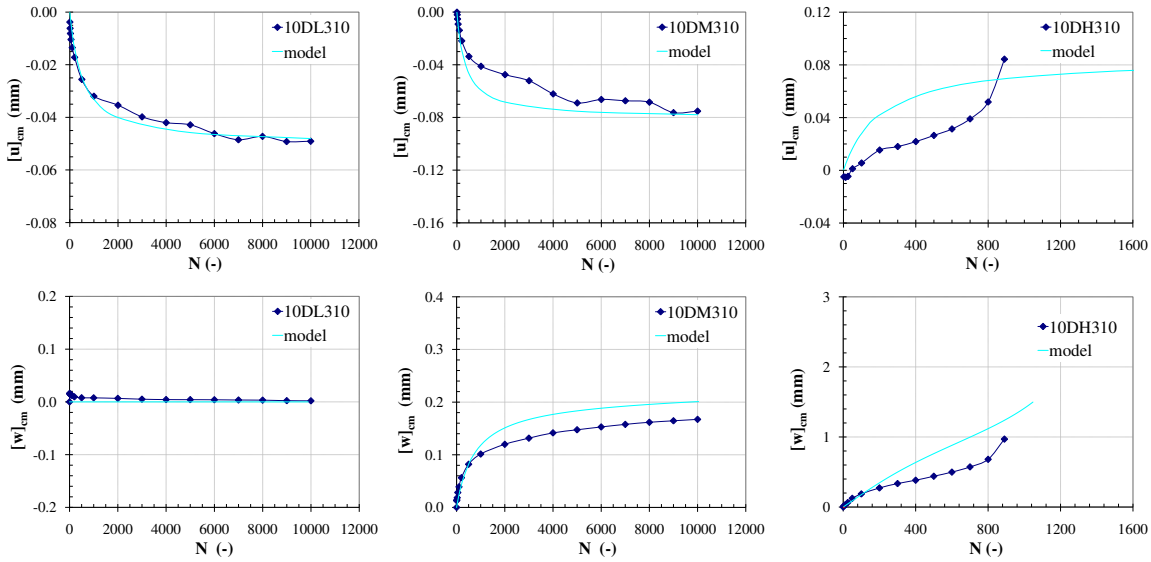

Figure 3.38: Comparison between experimental data and the model prediction, $\sigma_n = 310$ kPa, cyclic CNL tests on dense sand ($I_{D0} \approx 90\%$), $\Delta\tau = 10$ kPa with rough plate

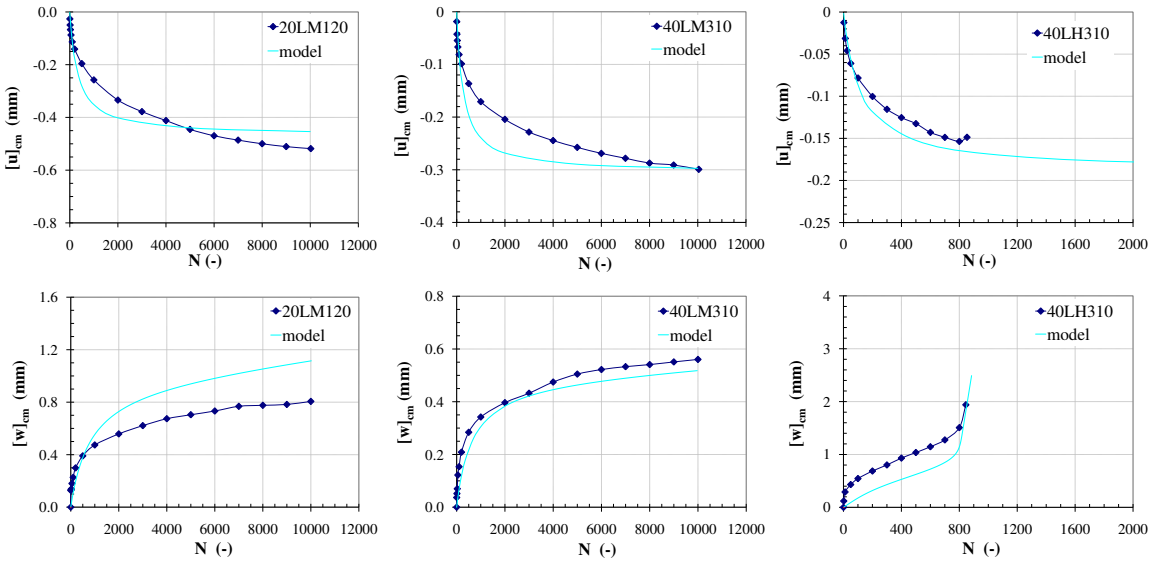

Figure 3.39: Comparison between experimental data and the model prediction, $\sigma_n = 120$ and 310 kPa, cyclic CNL tests on loose sand ($I_{D0} \approx 30\%$), $\Delta\tau = 20$ and 40 kPa with rough plate

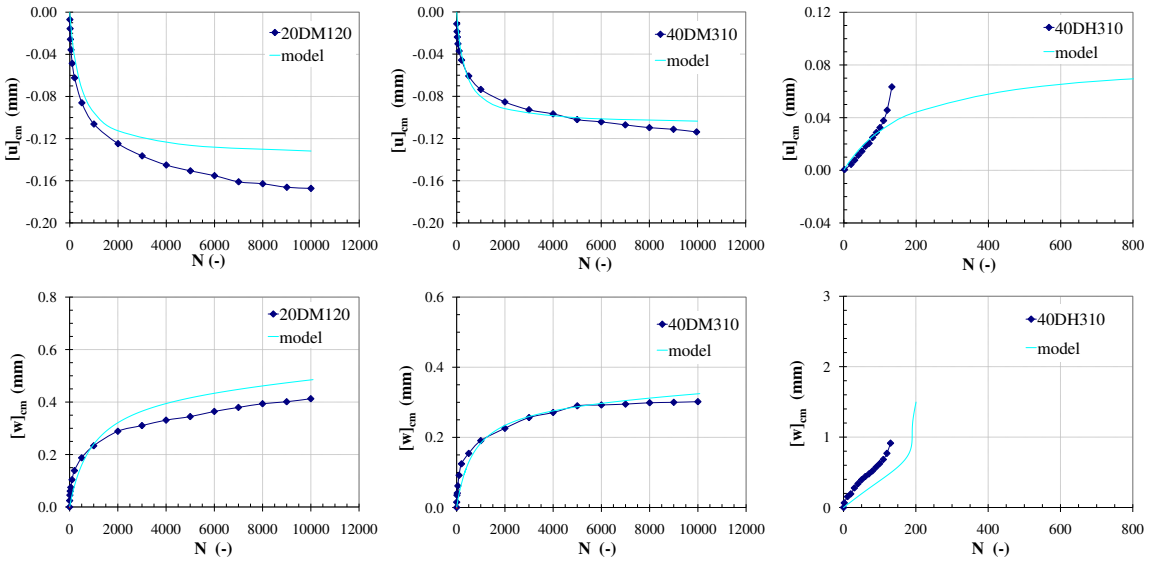

Figure 3.40: Comparison between experimental data and the model prediction, $\sigma_n = 120$ and 310 kPa, cyclic CNL tests on dense sand ($I_{D0} \approx 90\%$), $\Delta\tau = 20$ and 40 kPa with rough plate

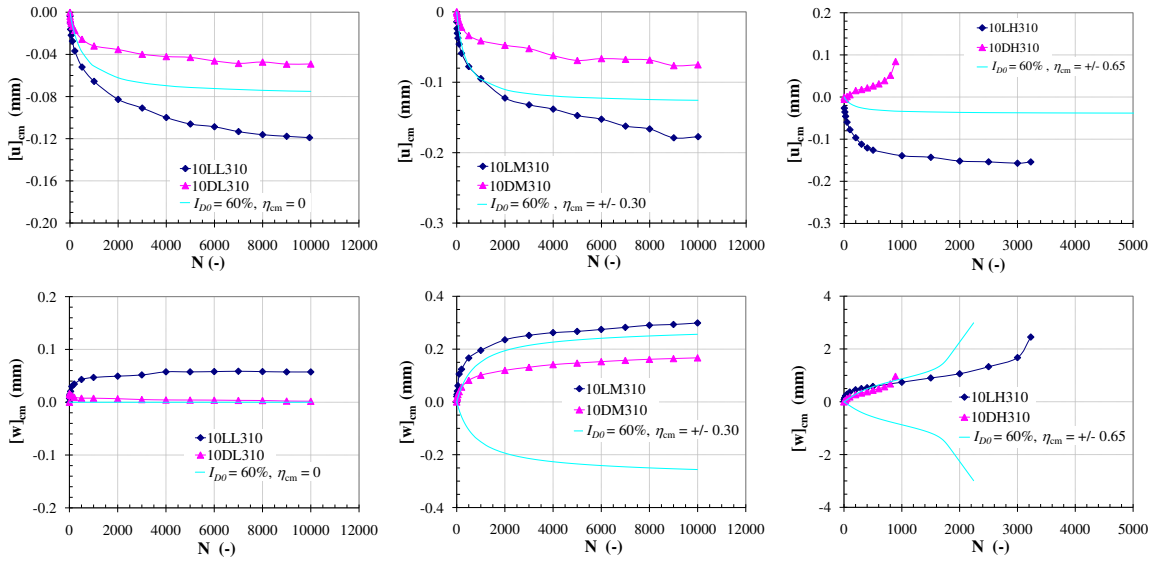

Figure 3.41: Interpolation of cyclic CNL tests, $\sigma_n = 310$ kPa, $I_{D0} = 90\%$, $\Delta\tau = 10$ kPa with rough plate

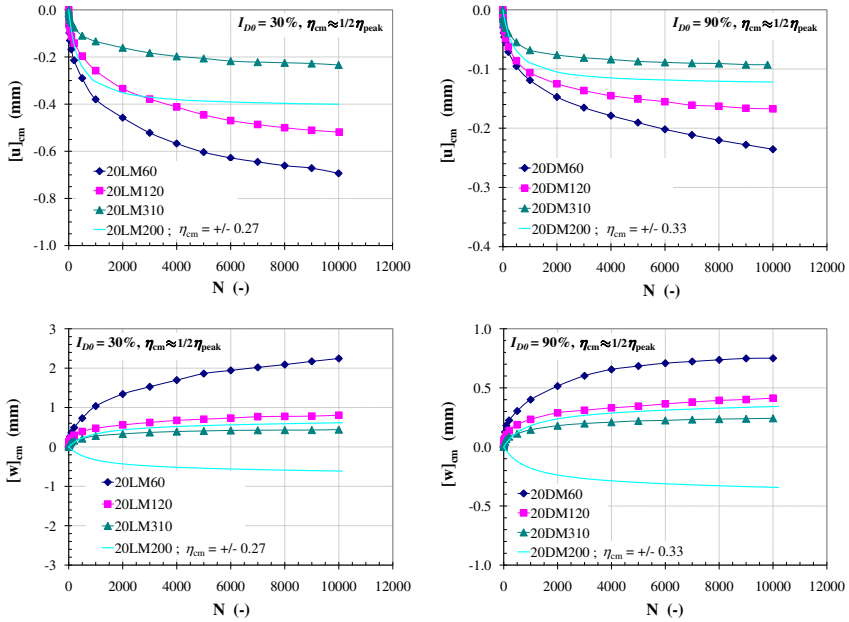

Figure 3.42: Interpolation of cyclic CNL tests, σ_n = 200 kPa, $\Delta\tau$ = 20 kPa with rough plate: (left) on loose sand ($I_{D0} \approx 30\%$), $\eta_{\text{cm}} = \pm$ 0.27 ; (right) on dense sand ($I_{D0} \approx 90\%$), $\eta_{\text{cm}} = \pm$ 0.33

3.3.4 Validation of the identification (CNL) model to the variation of cyclic amplitude and CNS condition

A simplication of the model for varying the cyclic amplitude and CNS condition is also derived from the analytical formulations of CNL condition. This is verified by the parameters of the constitutive law which is capable of connecting the cycles of different characteristics, using finite increments themselves in the parts of complete analytical formulations. The extension of CNL analytical formulations to the variation of cyclic amplitude is first considered. Then the modification of CNL analytical formulations by taking into account the effect of k is applied for CNS condition.

- **Procedure for modeling the variation of cyclic amplitude**

Once various cyclic amplitudes are applied in succession (ΔN), the corresponding state parameters for the accumulation rate of displacements are associated. Kaggwa et al. [1991] proposed the procedure for analyzing effects of irregular cyclic loading (changing the amplitude of cycles in succession) by evaluating the equivalent number (N_{eq}) of the uniform stress cycles. The meaning of N_{eq} is the number of cycles at the following loading package with the corresponding state parameters (e.g. η_{i}, $\Delta\eta_i$) that would cause the same displacements which result from the previous package of loading with the corresponding state parameters (e.g. $\eta_{\text{i-1}}$, $\Delta\eta_{i-1}$). Figure 3.43 shows the evaluation of N_{eq} when various cyclic amplitudes are applied in succession.

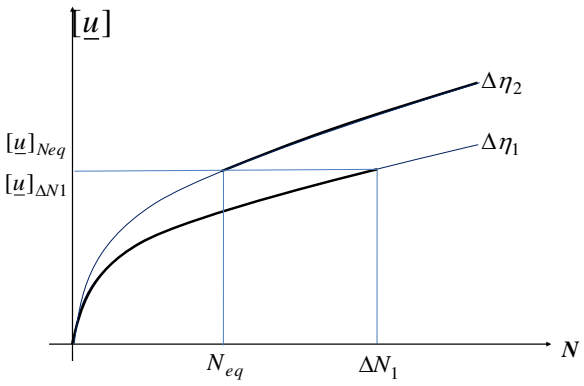

Figure 3.43: Evaluation of equivalent number of cycles at different cyclic stress conditions

To evaluate the incremental displacemments due to cyclic loading package in succession (ΔN_i), the procedures are the following;

1. Initialization:

$$\forall\ I_{D0} \text{ and/or } \gamma_{\mathrm{d}0},\ \sigma_{n0},\ \eta_{\mathrm{cm}},\ \Delta\eta_0$$

$$[u]_{\mathrm{cm}\,1} = [u]_{\mathrm{cm}\,0},\ [w]_{\mathrm{cm}\,1} = [w]_{\mathrm{cm}\,0},\ \gamma_{\mathrm{d}0} = \gamma_{\mathrm{d}1},\ \eta_{\mathrm{cm}\,1} = \eta_{\mathrm{cm}\,0},\ \Delta\eta_0 = \Delta\eta_0$$

   For $i = 1$ to I_M; 1^{st} package (ΔN_1)

2. Iterative search of N_{eq} at the beginning of step i for:
   - $[u]_{\mathrm{cm}\,i}$ corresponding to $[u]_{\mathrm{cm}\,i-1}$ or $\gamma_{\mathrm{d}\,i-1}$ for the parameters $\sigma_{n\,i}$, $\eta_{\mathrm{cm}\,i}$ and $\Delta\eta_i$
   - $[w]_{\mathrm{cm}\,i}$ corresponding to $[w]_{\mathrm{cm}\,i-1}$ for the parameters $\sigma_{n\,i}$, $\eta_{\mathrm{cm}\,i}$ and $\Delta\eta_i$

   It is worth noting that N_{eq} for $[u]_{\mathrm{cm}\,i}$ are different from N_{eq} for $[w]_{\mathrm{cm}\,i}$.

3. Compute increment of $\Delta[u]_{\mathrm{cm}\,i}$ and $\Delta[w]_{\mathrm{cm}\,i}$ resulting from $N_{eq} + \Delta N_i$ with analytical formulations

4. Update accumulation of displacements at the end of loading package i by:

$$[u]_{\mathrm{cm}\,i+1} = [u]_{\mathrm{cm}\,i} + \Delta[u]_{\mathrm{cm}\,i}$$

$$[w]_{\mathrm{cm}\,i+1} = [w]_{\mathrm{cm}\,i} + \Delta[w]_{\mathrm{cm}\,i}$$

- **Procedure for modeling CNS cyclic interface**

In case of CNS condition the procedures are carried out in a different way. Along the CNS direct shear path, a finite increment of the variables is considered, at an incremental level, as a combination of a CNL incremental path and of an oedometric incremental path according to the formal schemes described in Figure 3.44. It can be noted that the memory parameter is $[u]_{\mathrm{cm}}$.

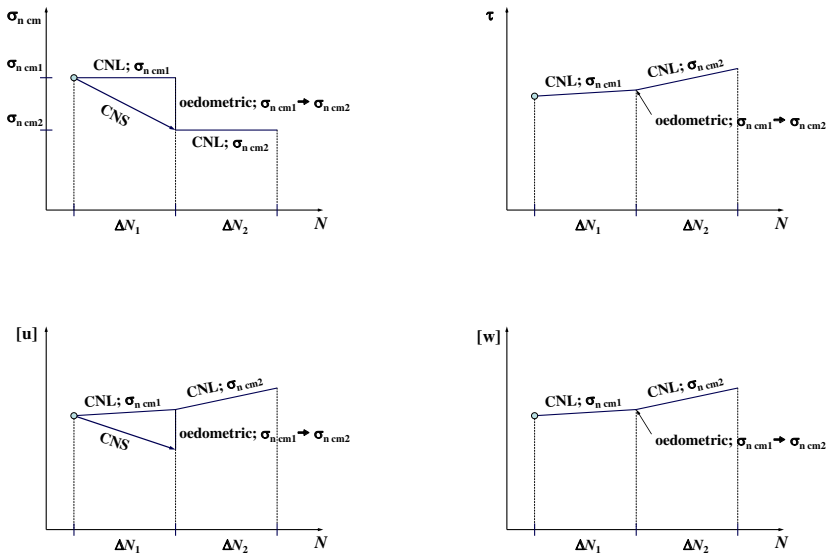

Figure 3.44: Schemes of a combination of a CNL incremental path and of an oedometric incremental path

To model CNS cyclic interface more satisfactorily, some modifications by considering the effect of k are applied as follows:

- The N interval of interest is discretized into finite incremental N_i steps with $\sum N_i = N$, $i_{\max} = I_M$
- The effect of k on the interpolation or weight functions (W_c and W_c) is taken into account by imposing the multiplicative factor on η_{cm2} which can be rewritten as:

$$\eta^*_{\mathrm{cm2}} = \eta_{\mathrm{cm2}} \exp\left(\frac{-k}{1000}\right) + \left[1 - \exp\left(\frac{-k}{1000}\right)\right] \eta_{\mathrm{cm}} \tag{3.61}$$

- Due to the variation of σ_n, the variation of $[u]_{\mathrm{cm}}$ has to be interpreted by taking into account the contribution of passive part and the variation of the sample height. Figure 3.45 shows the interpretation of $\Delta[u]_{\mathrm{cm}}$ due to the effect of the imposed normal stiffness (k) and the normal stiffness of sample during shear loading ($k_{\mathrm{n\,sam}}$). The relationship between $\Delta[u]_{\mathrm{cm}}$ in case of CNL and of CNS can be expressed as:

$$\Delta[u]_{\mathrm{cm\,CNS}\,i} = \frac{k_{\mathrm{n\,sam}}}{k_{\mathrm{n\,sam}} + k} \Delta[u]_{\mathrm{cm\,CNL}\,i} \tag{3.62}$$

  Using this result 3.62, an expression for the variation in normal stress ($\Delta\sigma_{\mathrm{n}}$) is obtained as:

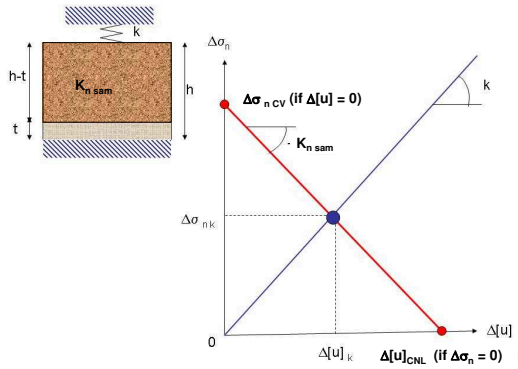

Figure 3.45: Interpretation of the $\Delta[u]_{\mathrm{cm}}$ due to the effect of the external imposed normal stiffness (k) and of proper normal stiffness of the sample ($k_{\mathrm{n\,sam}}$)

$$\Delta\sigma_{\mathrm{n\ cm}\,i} = \frac{k * k_{\mathrm{n\,sam}}}{k_{\mathrm{n\,sam}} + k} \Delta[u]_{\mathrm{cm\,CNL}\,i} \tag{3.63}$$

Figure 3.46 can also clarify the proccedure of the evaluation of the incremental displacements as well as the variation in normal stress in case of cyclic CNS condition.

As can be seen from the flowchart, this explicit method is easily implemented. However, the step size (ΔN_i) effect has to be taken into account. When the model contains a very large step size, the efficiency of explicit integration is compromised severely. To overcome this deficiency, a smaller step size is used. Figure 3.47 shows the effect of step size for σ_{n0} = 100 kPa, $\eta_{\mathrm{cm0}} = 0.50$, k = 1000 kPa/mm on dense sand. It is evident that the evolution of σ_{n0} and η_{cm0} with a smaller step size ($\Delta N_i = 10$) is more steady in the first five hundred cycles than that with a larger step size ($\Delta N_i = 200$).

Eventually, a simple analytical formulation of N at the critical state (N_{crit}: the number of cycles cannot evolve further) is proposed. This can be achieved by taking into account the influence of I_{D0}, σ_{n0}, η_{cm0}, $\Delta\tau$ and k. Regarding the results of cyclic tests, N_{crit} for σ_{n0} = 100 kPa on both densities are summarized in Figure 3.48. With increasing k and $\Delta\tau$, N_{crit} decrease significantly. It is worth noting that η_{max} is limited within the range of $\eta_{\mathrm{max}} < \eta_{\mathrm{crit}}$.

For the sake of simplicity, N_{crit} at $\eta_{\mathrm{cm}} = 0$ will first be formulated as a function of k for each $\Delta\eta$ as:

$$\text{for loose sand} \quad N_{\mathrm{crit\_0}} = [20.237\ln(\Delta\eta) + 18.049]\ln(k) + [-174.63\ln(\Delta\eta) - 155.45] \tag{3.64a}$$

$$\text{for dense sand} \quad N_{\mathrm{crit\_0}} = [9650\ln(\Delta\eta) + 6624.8]\ln(k) + [-83377\ln(\Delta\eta) - 57458] \tag{3.64b}$$

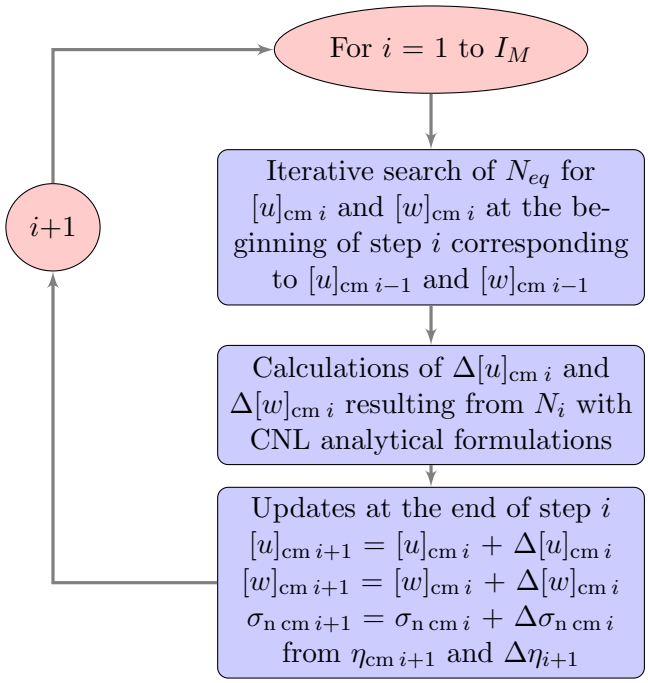

Figure 3.46: Procedure for evaluating the incremental variation of displacemments and normal stress in CNS condition

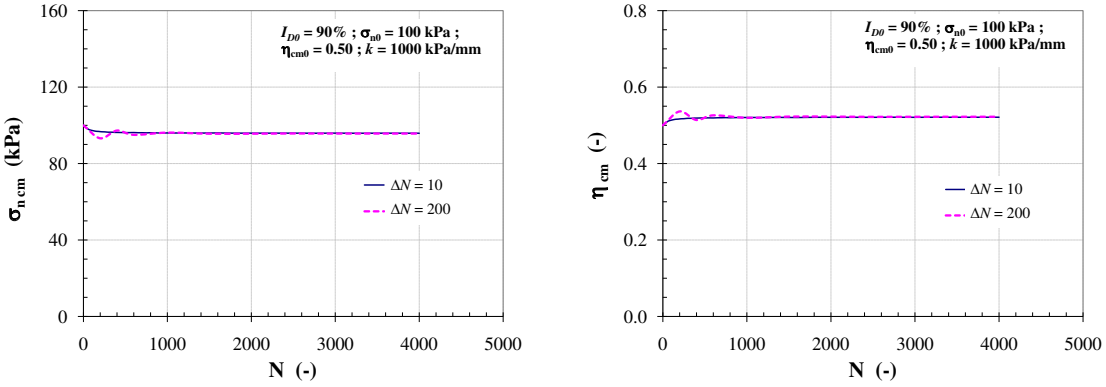

(a) (b)

Figure 3.47: Step size effect ($\Delta N_i = 10$ and $\Delta N_i = 200$) on the results of cyclic CNS test, $\sigma_{n0} = 100$ kPa, $\eta_{\mathrm{cm}0} = 0.50$, $k = 1000$ kPa/mm on dense sand

By taking into account the influence of σ_{n0}, the coefficient derived from experimental data can simply be given as:

$$\text{for loose sand} \quad C_{\sigma n0} = 1.5411 \ln(\sigma_{n0}) - 6.1637 \tag{3.65a}$$

$$\text{for dense sand} \quad C_{\sigma n0} = 1E-7 \, (\sigma_{n0})^{3.4512} \tag{3.65b}$$

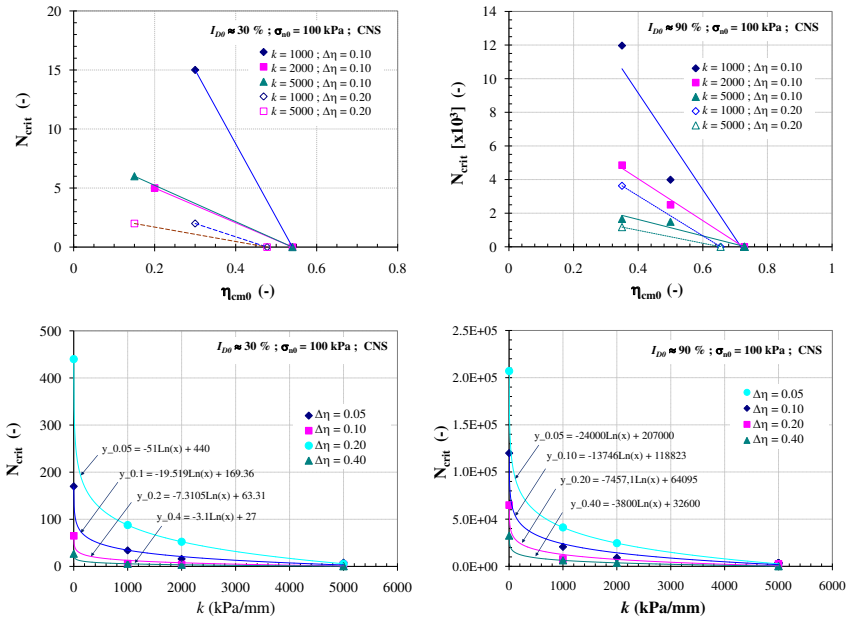

Figure 3.48: Summary of N_{crit} for $\sigma_{n0} = 100$ kPa ; (left) on loose sand ($I_{D0} \approx 30\%$) ; (right) on dense sand ($I_{D0} \approx 90\%$)

Finally, the formulation of N_{crit} for a given η_{cm} is expressed as:

$$N_{\text{crit}} = C_{\sigma n0} \left(\frac{N_{\text{crit\_0}}}{-\eta_{\text{crit}}} \right) (\eta_{\max} - \eta_{\text{crit}}) + 1 \tag{3.66}$$

3.3.5 Checking of the proposed analytical models for validation

The results of model prediction of the tests, in which the sequence and amplitude of two consecutive packages are changed, are summarized in Figure 3.49 and 3.50. It can be seen that the model predictions of $[w]_{\text{cm}}$ on loose sand starting with whether smaller amplitude or bigger amplitude are quite overestimated while model predictions of $[u]_{\text{cm}}$ are sastisfactory. On dense sand, particularly $[u]_{\text{cm}}$ in case of $10\_20DM120$, the intensity of the second package is slightly underestimated, this is due to $\eta_{\max}$ of the second package close to η_{car}. However, the model reproduces, with good accuracy, the rate of the intensity of $[u]_{\text{cm}}$ and $[w]_{\text{cm}}$

in other cases. The results of model prediction in overview are reasonably close to the experimental results.

In addition, to demonstrate the applicability of the proposed model in predicting cyclic loading with various packages, the supplementary cases in which five packages each 2,000 cycles are consecutively applied. Two series of amplitude variations ($\Delta\tau$ = 10, 20, 40, 60 and 80 kPa) are applied on both densities. The level of η_{cm} is set at 0.34 (in very contractive range) so as to clarify the size effect of cycles. Figure 3.51 shows the overview of the supplementary cases.

From the results of model prediction as shown in Figure 3.52, starting with the biggest package ($\Delta\tau$ = 80 in case of $S1$) causes the reduction in rate of displacement intensity of the subsequent packages on both densities. It can be seen that at the final number of cycles the accumulation of the displacement is much less influenced by the sequence of the packages of cylic amplitude.

Interestingly, the series starting with the biggest package provides considerable $[w]_{\text{cm}}$ on loose sand. This is due to the size of cyclic loading (η_{max} close to η_{peak}). From experimental point of view, the farthest displacement that the interface could undergo is approximately of 6-7 mm, and this only occurs when testing with low level of initial σ_n. It seems ambiguous if this series could be carried out in practice. On dense sand, the dilative behaviour hardly occurs even though η_{max} touches η_{car}.

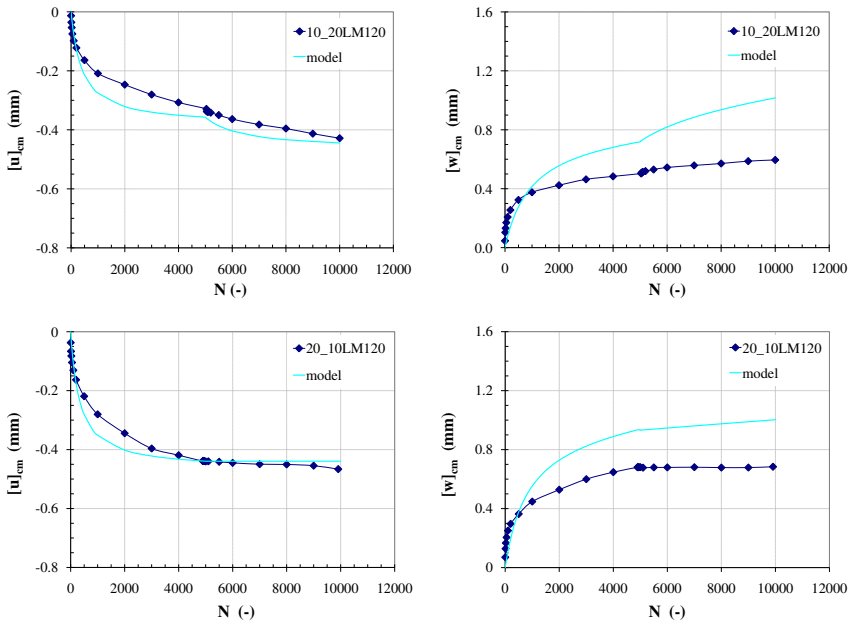

Figure 3.49: Comparison between experimental data and the model prediction, σ_n = 120 kPa, cyclic CNL tests on loose sand ($I_{D0} \approx 30\%$), cyclic loading package in succession $\Delta\tau$ = 10 and 20 kPa with rough plate

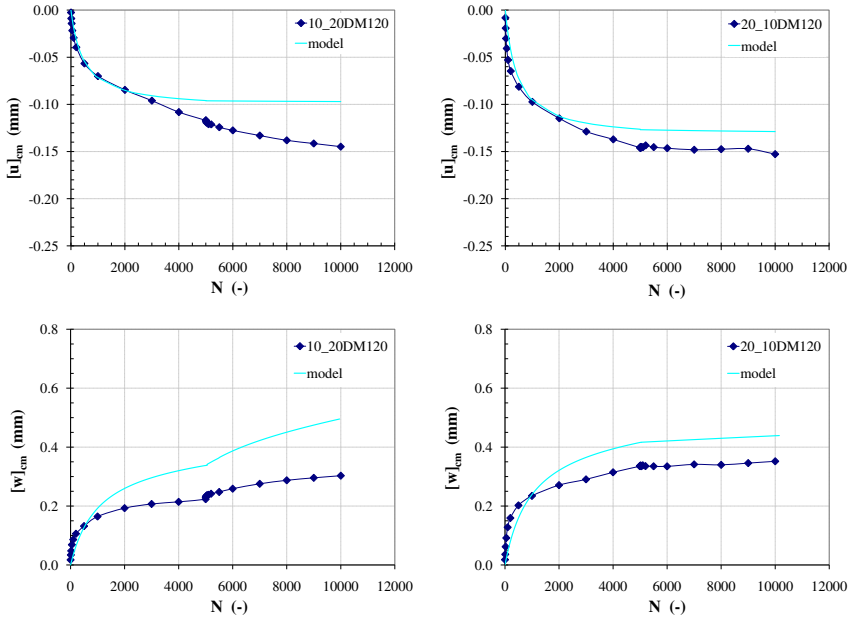

Figure 3.50: Comparison between experimental data and the model prediction, σ_n = 120 kPa, cyclic CNL tests on dense sand ($I_{D0} \approx 90\%$), cyclic loading package in succession $\Delta\tau$ = 10 and 20 kPa with rough plate

In case of CNS condition, the significant feature is the reduction of normal stress as a function of N. Here, the results of model prediction of the reduction in normal stress relative to the variation of normal displacement as a result of imposing the stiffness k are only be presented. Modeling of the mean cyclic shear displacement ($[w]_{\text{cm}}$) will be presented in the future. Figure 3.53 typically shows the comparison between experimental data and model prediction with k = 1000 kPa/mm, σ_{n0} = 100 kPa, η_{cm} = 0.35 and $\Delta\tau$ = 10 kPa on dense sand. The signifiant reduction in normal stress as a function of N is well reproduced on loose sand in case of k = 1000 kPa/mm, σ_{n0} = 310 kPa, η_{cm} = 0.30 and $\Delta\tau$ = 10 kPa (Figure 3.54). The results of model prediction relative to the reduction in normal stress as a function of N are close to the experimental results. The proposed model well reproduces the reduction in normal stress influenced by k, η_{cm} and $\Delta\tau$. However, in case of loose sand in which the tests can be carried out with a small number of cycles the reduction rate of normal stress reproduced by the proposed model is quite underestimated especially in the first five cycles (see Figure 3.55). All features of interface model in CNS condition are shown in Appendix **E**.

Figure 3.56 and 3.57 show the model prediction of N_{crit}. It can be seen that N_{crit} from the model prediction are in accordance with experimental data. However, at $\eta_{\text{cm0}} = 0$ on both densities, N_{crit} from model prediction would be underestimated. The overall agreement between model prediction and experimental data is satisfactory.

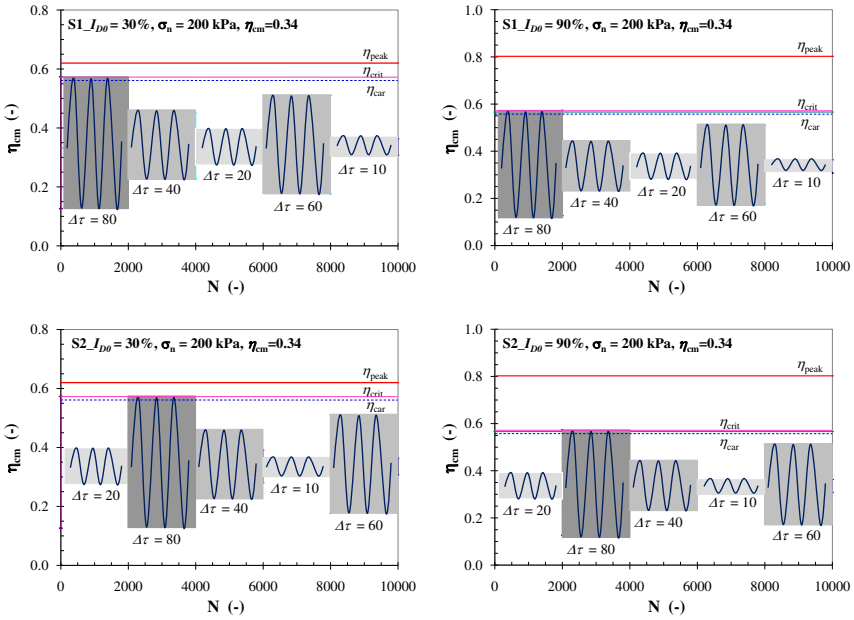

Figure 3.51: Sequence of cylic loading packages, $\sigma_n = 200$ kPa, cyclic CNL tests with rough plate ; (left) on loose sand ($I_{D0} \approx 30\%$): (right) on dense sand ($I_{D0} \approx 90\%$)

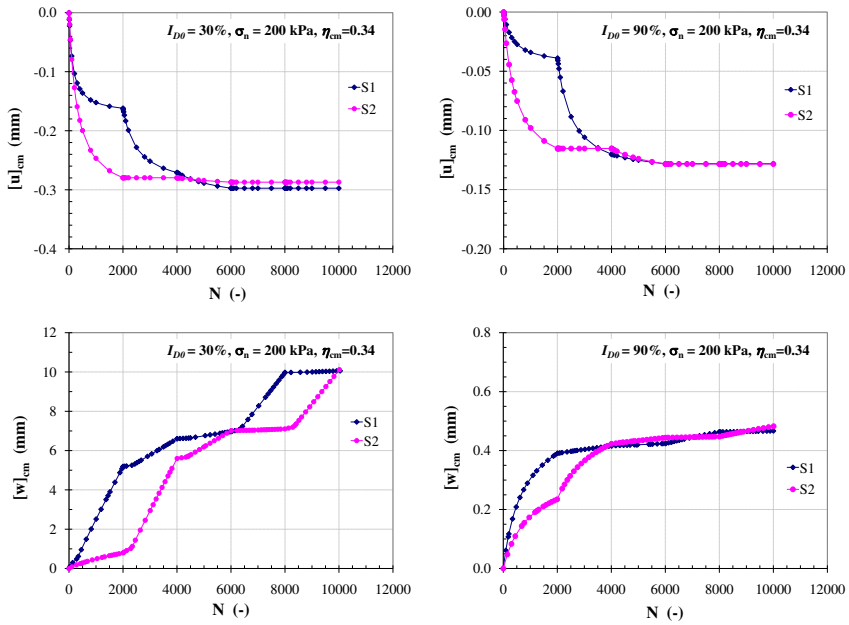

Figure 3.52: Model prediction of cylic loading packages in succession, $\sigma_n = 200$ kPa, $\eta_{\text{cm}} = 0.34$, cyclic CNL tests with rough plate ; (left) on loose sand ($I_{D0} \approx 30\%$): (right) on dense sand ($I_{D0} \approx 90\%$)

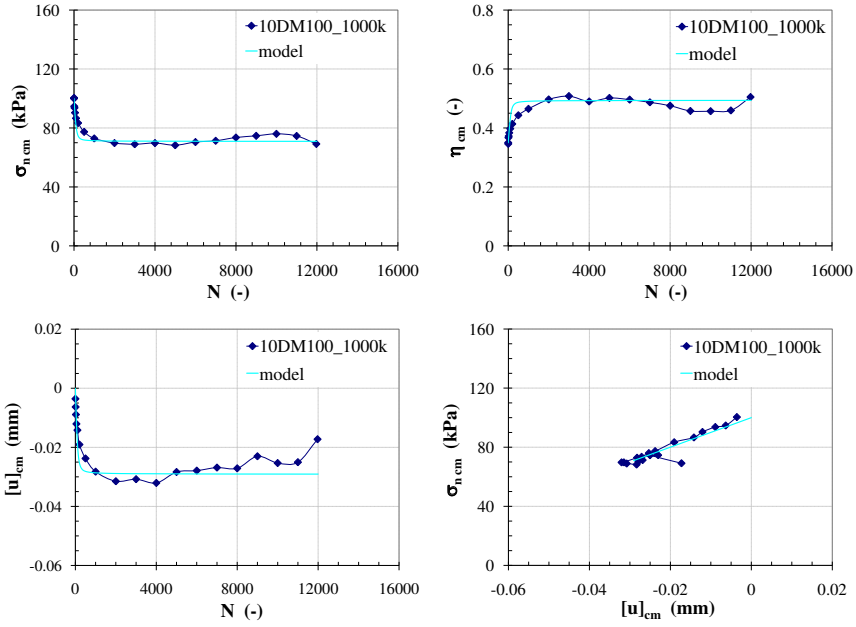

Figure 3.53: Comparison between experimental data and the model prediction, cyclic CNS test with $k = 1000$ kPa/mm, $\sigma_{n0} = 100$ kPa, $\eta_{\text{cm}0} = 0.35$, $\Delta\tau = 10$ kPa, rough plate on dense sand ($I_{D0} \approx 90\%$)

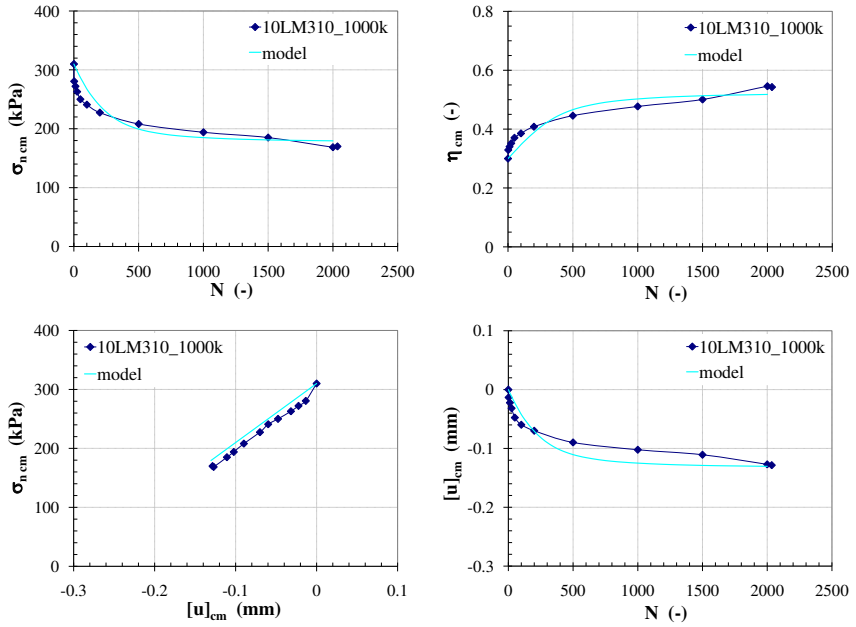

Figure 3.54: Comparison between experimental data and the model prediction, cyclic CNS test with $k = 1000$ kPa/mm, $\sigma_{n0} = 310$ kPa, $\eta_{\text{cm}0} = 0.30$, $\Delta\tau = 10$ kPa, rough plate on loose sand ($I_{D0} \approx 30\%$)

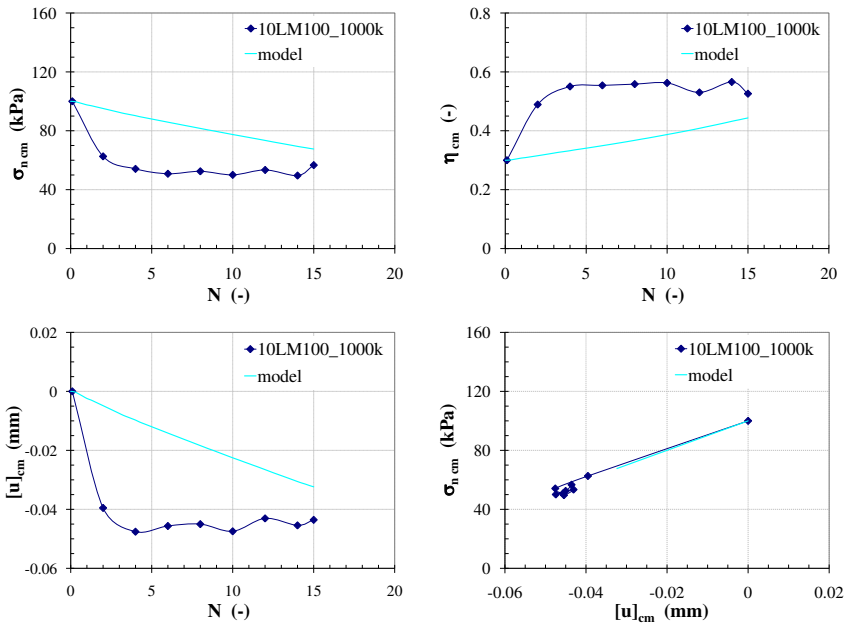

Figure 3.55: Comparison between experimental data and the model prediction, cyclic CNS test with $k = 1000$ kPa/mm, $\sigma_{n0} = 100$ kPa, $\eta_{\text{cm}0} = 0.30$, $\Delta\tau = 10$ kPa, rough plate on loose sand ($I_{D0} \approx 30\%$)

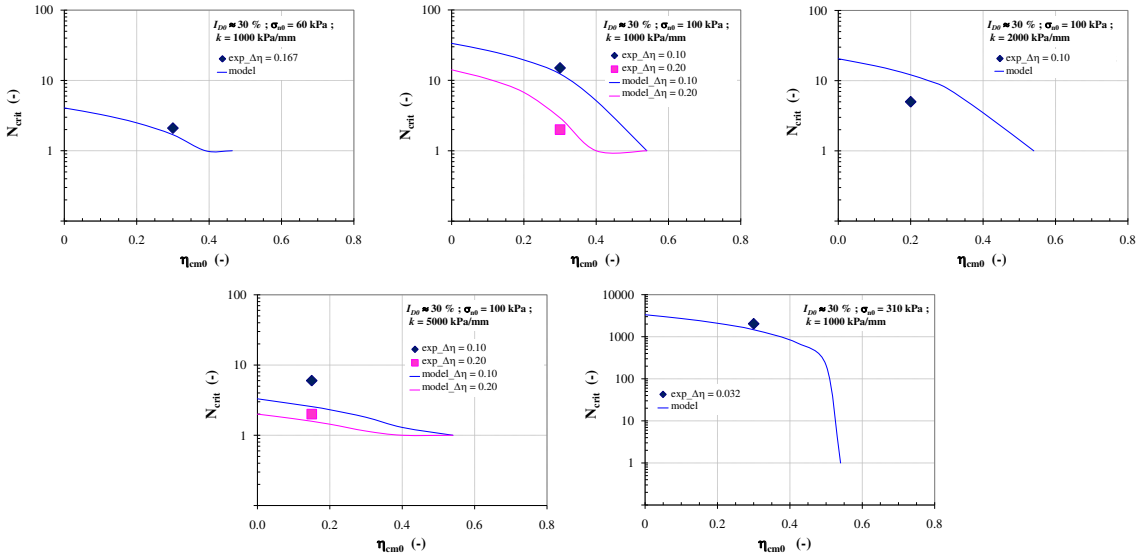

Figure 3.56: Comparison between experimental data and the model prediction of N_{crit} on loose sand $I_{D0} = 30\%$

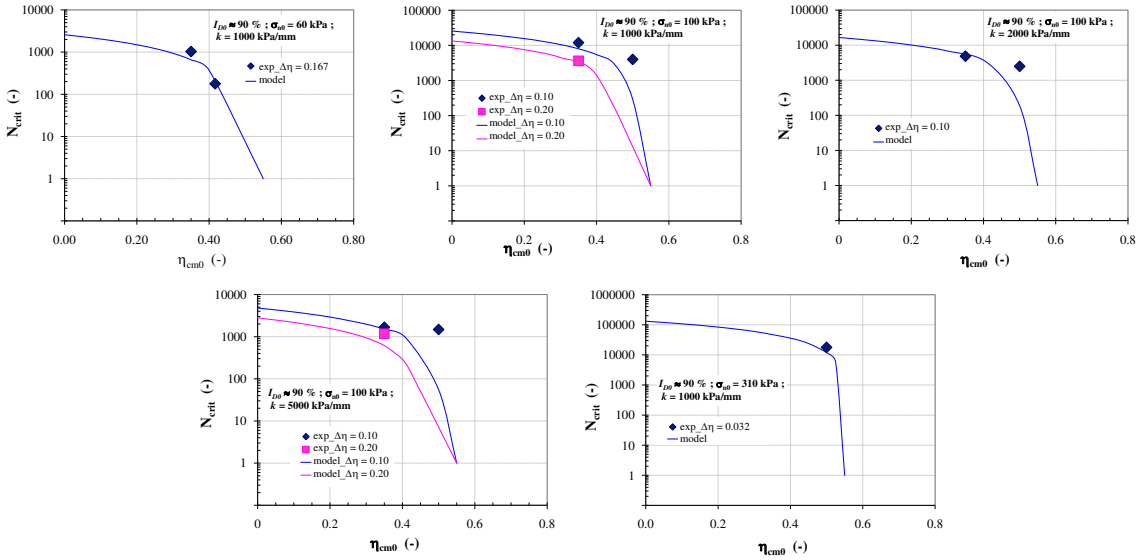

Figure 3.57: Comparison between experimental data and the model prediction of N_{crit} on dense sand $I_{D0} = 90\%$

3.4 Conclusions

The model presented here is an analytical-proposed model in which only four parameters for identification (i.e. I_{D0}, σ_n, η_{cm} and $\Delta\eta$) are derived from experimental data. The single memory parameter is $[u]_{\text{cm}}$ (or $\gamma_{\text{d}\,\sigma n}$). Then the extension of the identification (CNL) model to the variation of cyclic amplitude and CNS is also proposed for the validation purpose. The proposed model is capable of interpreting the behaviour of cyclic granular soil-structure in both CNL (analytically) and CNS (by finite analytically increments) conditions. The predictions of the model have been compared with the experimental data and the accordance is generally satisfactory. All of the main features of interface behaviour under a large number of cycles, i.e. contraction, dilation, the critical state of stress that the number of cycles cannot evolve further and more importantly the reduction in normal stress due to the accumulation of contraction in case of CNS condition are taken into account.

Chapter 4

Finite element modeling

4.1 Introduction

In this chapter, the FE Plaxis 2D (version 8.2) program is applied in a few examples to model the interaface behaviour. This FE program has been used increasingly for modeling geomechanical projects with several constitutive models. The well known and simple Mohr-Coulomb approach taking into account five parameters (E, ν, c, ϕ and ψ) is chosen to use. The analysis in this chapter is mainly oriented to highlight the mechanisms existing within the direct shear test considered as element test, as well as during the load transfer mobilization of the loaded piles. Preliminary Plaxis implementation of monotonic soil-structure interface direct shear tests is first presented for providing the applicability of this software and also focuses the possible defaults of the direct shear tests. Then, an implementation of some centrifuge model tests on pile carried out at the IFSTTAR in Nantes (France) within the SOLCYP project is typically presented.

4.2 Direct shear box

This study attempts to illustrate preliminary Plaxis implementation of soil-structure interface direct shear tests (e.g. Arslan [2005]). In this section, a simple implementation of monotonic CNL and CNS interface direct shear tests is presented. In Plaxis, interfaces are normally modeled with Mohr-Coulomb model. This model is a perfectly elastoplastic model involving five input parameters, i.e. E and ν for soil elasticity, φ and c for soil plasticity, and ψ as an angle of dilatancy, and provides a first reliable approximation of soil behaviour (Brinkgreve et al. [2008]). The Mohr-Coulomb criterion used to desribe the interface behaviour can be distinguished as:

- For elastic part (with a small displacement), the shear stress τ is given by:

$$\tau < \sigma_n \tan \varphi_i + c_i \tag{4.1}$$

- For plastic part (with an occurrence of permanent displacement), τ is then given by:

$$\tau = \sigma_n \tan \varphi_i + c_i \tag{4.2}$$

where φ_i and c_i are the friction angle and cohesion of the interface.

The strength of interface which mainly depends on the roughness surface are relative to the strength of a soil adjacent to the interface according to the reduction factor for interface friction (R_{inter}) :

$$c_i = R_{\text{inter}} \cdot c_{\text{soil}} \tag{4.3a}$$

$$\tan \varphi_i = R_{\text{inter}} \tan \varphi_{\text{soil}} \leq \tan \varphi_{\text{soil}} \tag{4.3b}$$

$$\psi_i = 0\,^\circ \quad \text{for} \quad R_{\text{inter}} < 1, \quad \text{otherwise} \quad \psi_i = \psi_{\text{soil}} \tag{4.3c}$$

4.2.1 Monotonic CNL direct shear box

- Boundary conditions

The interface direct shear is modeled by using plane - strain model with 15-node elements. A steel shear box containing a sand sample of the sand - structure interface has a dimension of $\phi = 60$ mm with sample height of 20 mm. Figure 4.1 illustrates the simplified configuration of interface direct shear test in case of CNL condition. The interfaces are created between steel shear box-sand, steel palte-sand and steel palte-steel shear box. In this situation the stress and the prescribed displacement are uniformly distributed on the shear box. The left hand side of the steel plate is set by vertical fixities so as to allow the upper part (shear box) displacing horizontally whereas the bottom and the right hand side boudaries are fully fixed. A medium mesh is sufficient for this simple geometry. The steady pore pressure is not taken into account because these tests are carried out with dry sand. Six points close to the interface (i.e. the first three points are positioned above the interface line and the rest are positioned within the interface zone) are chosen from the midle to the right side of the shear box for representing the stress - displacement curves.

- Material properties

The material properties used in this study are derived from monotonic CNL direct shear tests. The interface stiffness is set equal to the elastic soil stiffness. Therefore, the interface stiffness $E = E_{\text{ur}}$ where E_{ur} is proportinal to σ_n. On the basis of monotonic CNL tests the model parameters for Mohr-Coulomb model are summarized in Table 4.1. The steel plate has the same properties as steel shear box. Three values of model parameters on each density are derived from three levels of initial normal stress $\sigma_n = 60$, 120 and 310 kPa, respectively. The model parameters for steel-steel interface are also defined, which

will not affect the model results too much. The influence of surface roughness is able to be represented by R_{inter}. To model the interface with very rough plate $R_{\text{inter}} = 0.80$ is then be held in this study. It is worth noting that the interface thickness has never been defined in Plaxis, a virtual thickness factor is then defined. This is a purely numerical value (0.10 by default). From experimental observations, the deformations and thus the associated dilatancy commonly take place within the interface shear zone (very thin zone). To optimise the numerical performance on the interface, the value of virtual thickness factor = 0.010 is then defined.

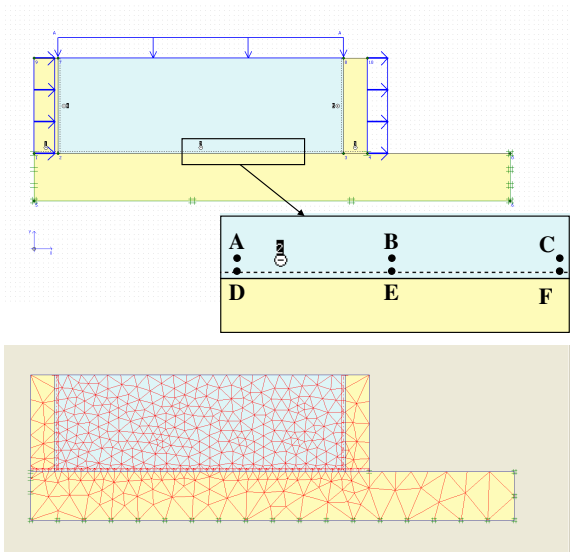

Figure 4.1: Simplified configuration of an interface direct shear test at CNL condition

Table 4.1: Material parameters for Fontainebleau sand

Parametrs (Unit)	Loose sand	Dense sand	Steel box/plate	steel-steel interface
Material model	Mohr-Coulomb	Mohr-Coulomb	Linear elastic	Linear elastic
γ_{dry} (kN/m^2)	14.74	16.55	60	-
γ_{sat} (kN/m^2)	20	20	0	-
E_{ref} (kN/m^2)	1680, 2240, 4260	2010, 4240, 9330	2.1E07	2.1E07
ν	0.30	0.30	0.15	0.15
c_{ref} (kN/m^2)	0.10	0.10	-	0.10
φ (°)	30	38	-	5
ψ (°)	0	8	-	0
R_{inter}	0.80	0.80	-	0.05

- Model procedures for monotonic CNL tests

The value of the applied loads and prescribed displacement can be specified in the input program. These procedures can be activated or deactivated in the calculation program by

means of the staged construction option. The calculation of all phases can be done by means of the staged construction propcess. All monotonic tests the prescribed shear displacement is set at 40 mm. The calculation procedures are typically listed in Table 4.2. Figure 4.2 also shows the distribution of vertical displacement due to an application of normal stress on the sample. It is also found that the distribution of normal stress is less pronounced at the bottom corners.

Table 4.2: Loading procedures for monotonic CNL test with σ_n = 120 kPa

Phase	Calculation type	loading input	load (kPa)	Displacement (mm)
1	Plastic	Staged construction	120	inactive
2	Plastic	Staged construction	120	+ 40

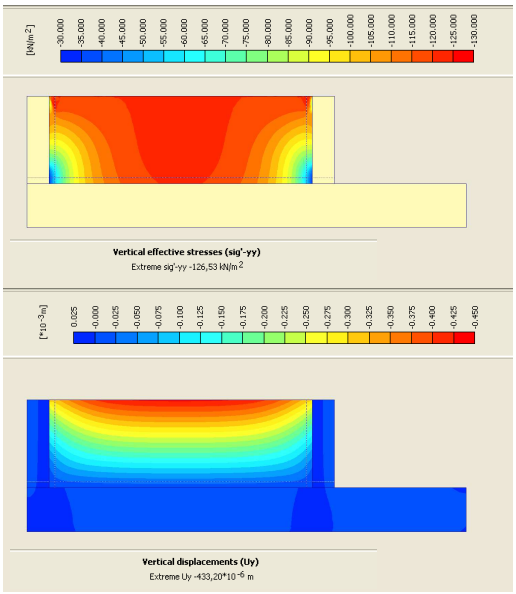

Figure 4.2: Distribution of vertical displacement due to an application of normal stress σ_n = 120 kPa on dense sand

- Analysis of results

The results of monotonic CNL tests are typically shown in Figure 4.3. It can be seen that the vertical displacement during shearing does not show the significant dilative behaviour at the interface line. When considering each point selected for representing the stress - displacement curves, all points also show very small dilation as shown in Figure 4.4. Two points ("A" and "B" above the interface line) at the middle would provide more dilation than the rest but the shear stress is too small. It seems that a simple Plaxis Mohr-Coulomb model is not fully successful in describing the normal displacement of the interface direct shear tests. A more advanced model is therefore required. This will be done in the future. However, in the following figures, as far as the interface strength is concerned, point "F"

positioned within the interface zone is supposed to be representative for describing the interface model.

Figure 4.4 then shows the results of monotonic CNL tests in comparison with the experimental data on both densities. It can also be seen that dense sand on which Mohr-Coulomb model does not include softening behaviour, so after reaching the peak shear stress, the stress level still evolves constantly. Whereas on loose sand the obtained results from Mohr-Coulomb model are close to the experimental results.

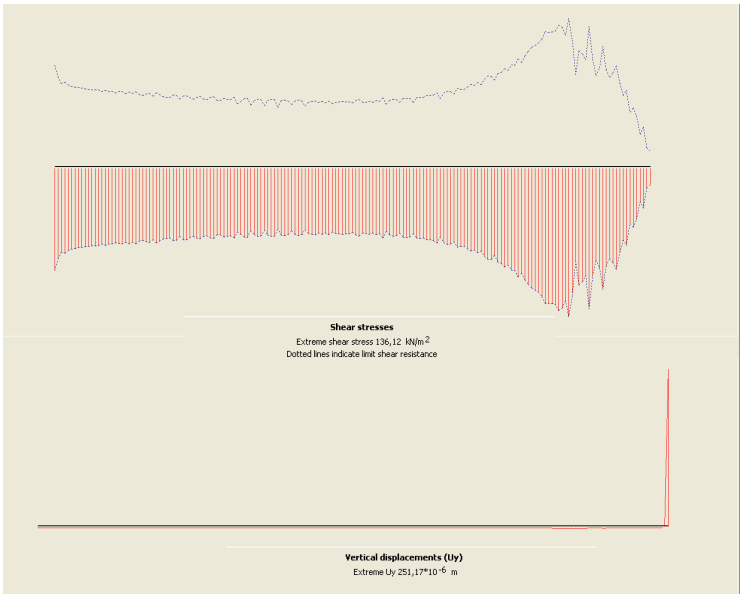

Figure 4.3: Shear stress and vertical displacement as a result of monotonic CNL condition, $\sigma_n = 120$ kPa on dense sand

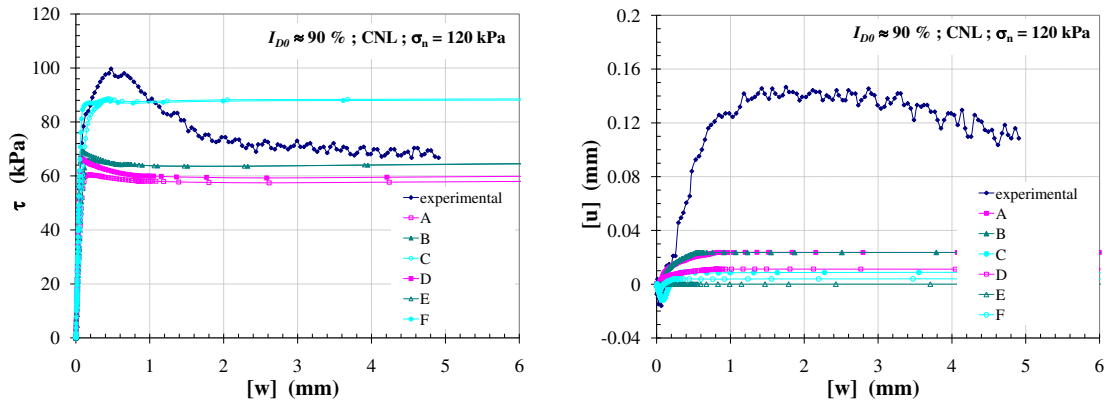

Figure 4.4: Shear stress and vertical displacement at each point of monotonic CNL condition, $\sigma_n = 120$ kPa on dense sand

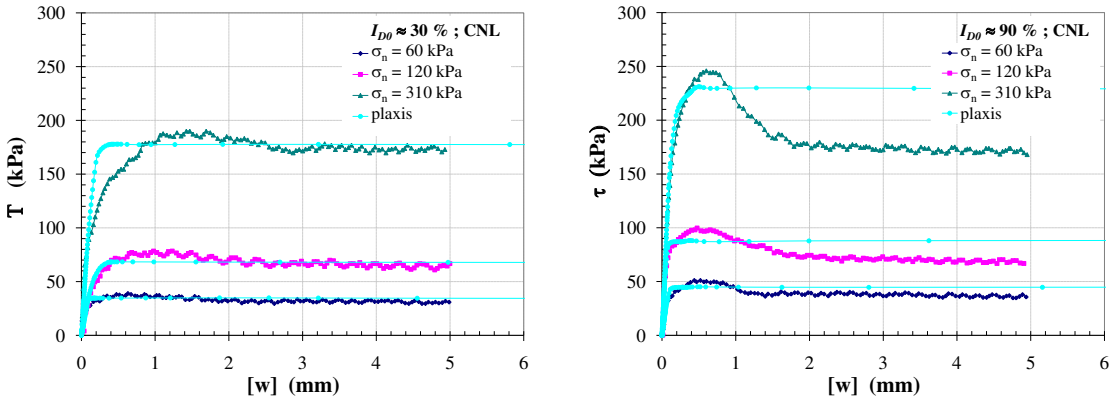

(a) (b)

Figure 4.5: Results of monotonic CNL tests: (a) loose sand ; (b) dense sand

4.2.2 Monotonic CNS direct shear box

- Boundary conditions

Imposing a prescribed normal stiffness in Plaxis has never been a direct input. There are a few ways making this task close to the experimental tests by modifying the the top cap of the sample as an imposed normal stiffness and loading application. Figure 4.6 shows the modified configuration of monotonic CNS tests. However, these are few fundamental issues which would be modified in the future in order to get the reliable results.

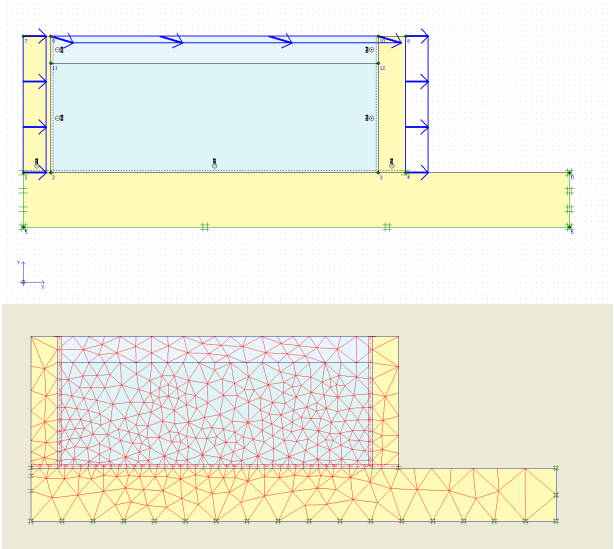

Figure 4.6: Modified configuration of an interface direct shear test at CNS condition

- Material properties

The material properties used are the same as monotonic CNL direct shear tests. The general material properties of top cap are the same as steel plate except the elastic stiffness. The elastic stiffness of top cap (E) modified as an imposed stiffness is expressed as:

$$\Delta\epsilon = \frac{\Delta[u]}{h} = \frac{\Delta\sigma}{E} \tag{4.4}$$

and then the imposed normal stiffness (k) is given as:

$$k = \frac{\Delta\sigma}{\Delta[u]} = \frac{E}{h} \tag{4.5}$$

where h is the height of top cap.

- Model procedures for monotonic CNS tests

Unlike CNL tests, the value of the prescribed vertical displacement is specified instead of the applied loads in the input program. In each case, the prescribed vertical displacement is derived from the displacement (adjustable according to the elastic stiffness of top cap, E) due to an applied load from CNL tests (the 1^{st} phase : load application). The calculation procedures are typically listed in Table 4.3 for σ_{n0} = 100 kPa, k = 1000 kPa/mm on dense sand. Figure 4.7 shows the distribution of normal stress on the sample due to the prescribed vertical displacement in case of σ_{n0} = 100 kPa, k = 1000 kPa/mm on dense sand. It can be seen that at the upper and bottom corners there are respectively more and less concentrations in normal stress due to the prescribed vertical displacement. During shearing phase, the prescribed vertical displacement is kept constant so as to describe the variation of normal stress.

Table 4.3: Loading procedures for monotonic CNS test with k = 1000 kPa/mm , σ_{n0} = 100 kPa on dense sand

Phase	Calculation type	loading input	Displacement (mm)
1	Plastic	Staged construction	-4.6E-07 (↓) for top cap
2	Plastic	Staged construction	-4.6E-07 (↓) and +40 (→) for top cap +40 (→) for shear box

- Analysis of results

Figure 4.8 typically shows the stress paths at each point of monotonic CNS tests for σ_{n0} = 100 kPa, k = 1000 kPa/mm. Again, it can be seen that point "C" and "F" respectively positioned above and within the interface zone can well represent stress paths according to the initial conditions. These two points can describe the reduction of normal stress associated with the shear stress during shearing load on loose sand. Whereas the reduction of normal stress associated with the shear stress occurs at the beginning of shear loading and consequently the stress state increases significantly on dense sand.

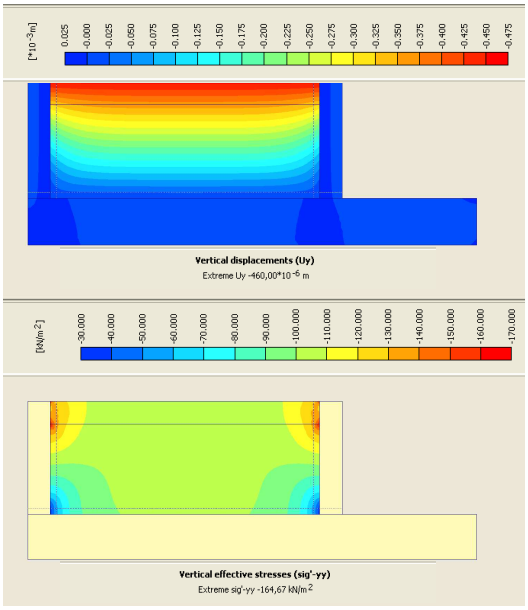

Figure 4.7: Distribution of normal stress due to a prescribed vertical displacement $\sigma_{n0} \approx$ 100 kPa on dense sand

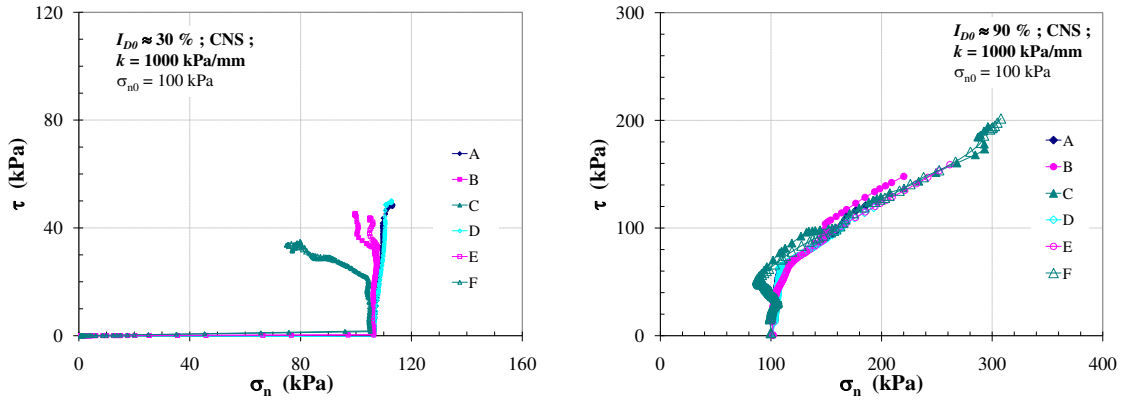

Figure 4.8: Stress paths of monotonic CNS tests with $k = 1000$ kPa/mm , $\sigma_{n0} = 100$ kPa : (a) loose sand ; (b) dense sand

Figure 4.9 also shows the computational results and the experimental data. It can be seen that the model can reasonably describe the variation of normal stress associated with shear stress which depends on the initial conditions. However, on dense sand the stress state continues to gradually increase according to the prescribed shear displacement. To propery describe monotonic CNS direct shear tests with Plaxis, more advanced model would be considered.

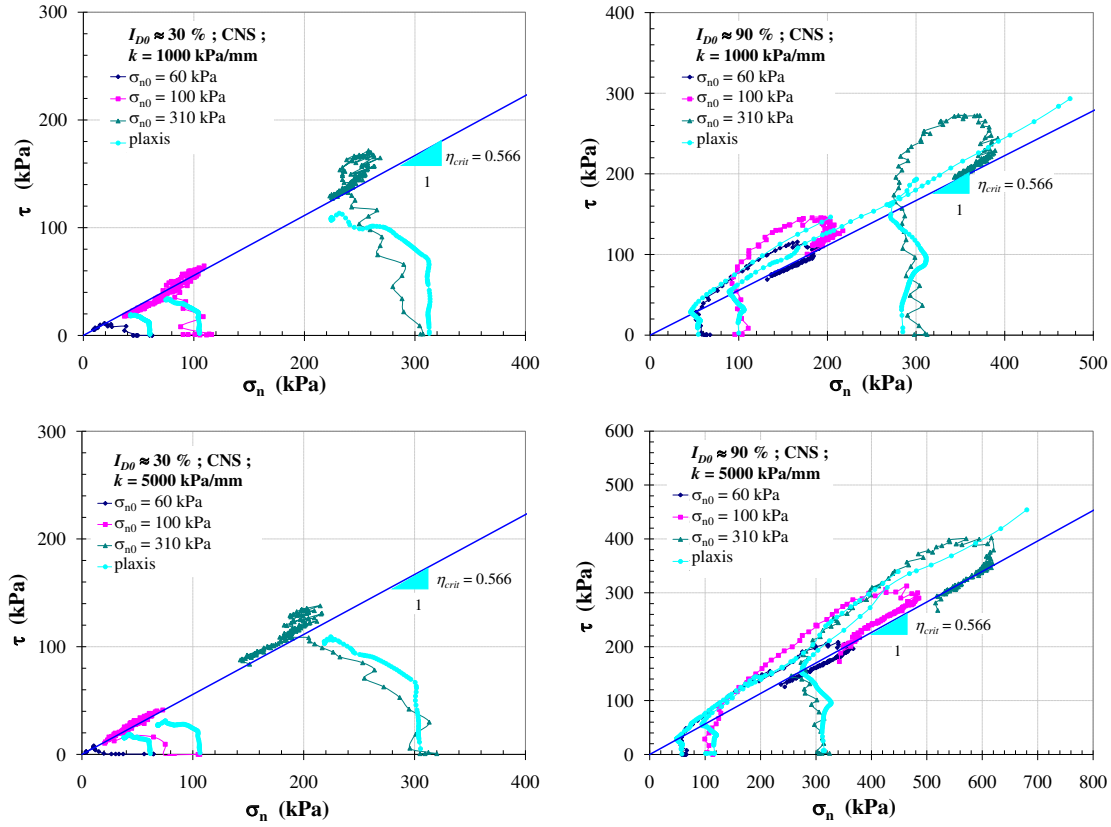

Figure 4.9: Stress paths of monotonic CNS tests with $k = 1000$ and 5000 kPa/mm , $\sigma_{n0} = 100$ kPa : (a) loose sand ; (b) dense sand

4.3 Centrifuge pile tests

In this section some of numerical modeling exercises based on experiments carried out in the IFSTTAR centrifuge in the SOLCYP project (ANR part) are presented. The physical modeling test in centrifuge, with a scale of 1/23, is subjected to a centrifugal acceleration of $23*g$. Figure 4.10 shows the details of the experimental setup. The container, equipped with the instrumentation and the actuator applying the load, is placed in the rotating nacelle of the centrifuge. An acceleration of $23g$ is applied at the level of - 240 mm from the surface of the reconstitued sand sample, corresponding to a radius of 4.943 m with respect to the axis of the centrifuge. Table 4.4 summarizes the physical prototype of the model and vice versa, with $N = 23$.

First, the monotonic tests in tension (pull-out test) is typically modeled with the geometric scale $1/N$ as shown in Table 4.5. To model the centrifuge model tests with Plaxis $2D$ the boundary conditions are summarized as follows:

- Units: mm, kN, kN/mm, kN/m^2, kN/m^3, Day.

It is worth noting that the fictitious time is used to represent the pile head force.

- 2D axisymmetric, y axis of revolution oriented upwards, x axis radial elements 15 nodes.

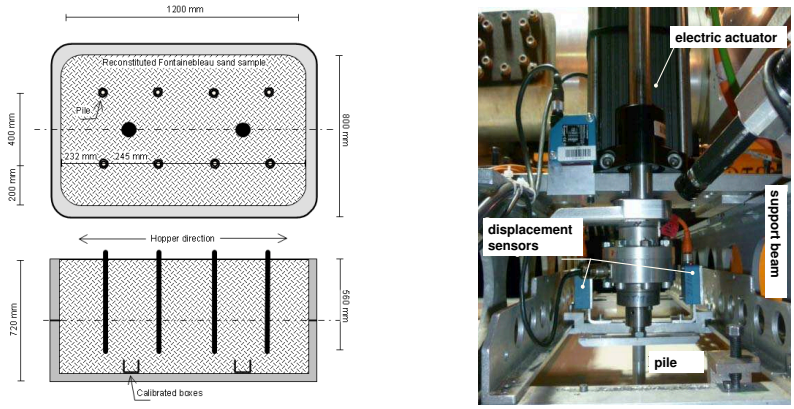

Figure 4.10: Details of the experimental setup of centrifuge pile tests at the IFSTTAR in Nantes (France) within the SOLCYP project

Table 4.4: Scale factors of centrifuge model tests

Physical parameter	Scale factor (scale model/scale prototype)
acceleration	N
length	$1/N$
displacement	$1/N$
deformation	1
force	$1/N^2$
mass	$1/N^3$
strength	N
stress	1
weight	$1/N^2$
density	1

- For the gravity "1/N" naturally during the growing in "g".
- The model pile, aluminum, has a length of 590 mm with an embedding of 560 mm (above the surface of 30 mm) and a diameter of 18 mm, all leading to a weight of 0.405 kg.
- For the purpose of monotonic calculation, the soil is first divided into three layers:

Table 4.5: Summary of centrifuge model tests

Load type	Prototype		Model	
	force a (MN)	displacement b (mm)	force a/N^2 (kN)	displacement b/N (mm)
Tension	2.12	30	4	1.30
Compression	3.25	28	6.10	1.22

  - Top layer; depth 0 to 240 mm
  - Middle layer; depth: 240 to 560 mm (pile tip)
  - Bottom layer; depth: 560 to 690 mm (under the pile tip)
- The studied area has dimensions height: 720 mm, diameter.
- The pile (radius of 9 mm) is divided into two sections:
  - Top section; depth: 0 to 240 mm in the soil
  - Bottom section; depth: 240 to 560 mm in the soil
- Two clusters of soil are determined, adjacent to the pile with the thickness of 9 mm, respectively, top and bottom sections for the purpose of cyclic calculation. An interface is placed against the pile in these two clusters, extended 10 mm below the tip. The deep layer between 690 and 720 mm is only for the mesh, then it will be inactivated.
- Mesh is generated by default.
- Pore pressure is zero.
- Weight initialization of soil under $1g$: K_0 procedure is only activated in the bottom layer (all other layers inactive).

All details for pile modeling are presented in Figure 4.11. The force acting on the pile head is linear, placed on the edge of the pile (9 mm in radius). The value of F_y is expressed in kN/mm, and will be called "Time" resulting from of using the facility of Plaxis, and then is given as:

$$\text{Time} = \pi \cdot 18 F_y \tag{4.6}$$

Because "Time" is proportional to $\sum -M_{\text{stage}}$.

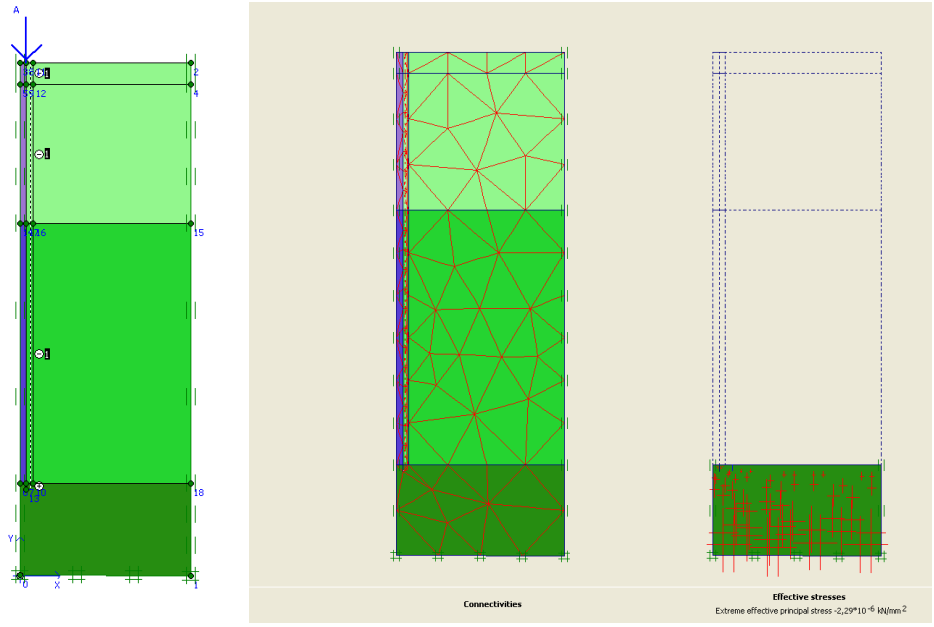

Figure 4.11: Geometry model for pile tests

Physical and mechanical properties of soil and structure elements are determined by using dimentional analysis in scaling definition. On the basis of centrifuge tests, these parameters of soil model are then determined from the level -240 mm relative to the surface (an application of acceleration of $23g$), corresponding to a radius of 4943 mm with respect to the axis of the centrifuge.

Soil parameters derived from dimentional analysis in scaling are:

- Specific weight is derived from initial state (dense case) in the prototype: $\gamma_d = 1704$ kg/m^3. For $1g$, $\gamma_d/1g = 1.6716\text{E-}08$ kN/mm^3. For each layer, γ_d can be given as:
  - Top layer; 0 - 240 mm : $\gamma_d/1g = 1.6310\text{E-}08$ kN/mm^3
  - Middle layer; 240 - 560 mm : $\gamma_d/1g = 1.7257\text{E-}08$ kN/mm^3
  - Bottom layer; 560 - 690 mm : $\gamma_d/1g = 1.8018\text{E-}08$ kN/mm^3
- Young's modulus is given according to the depth of each layer: $E = 4500$ kPa with reference stress $\sigma_i = 100$ kPa, $K_0 = n = 0.7$, results in $E = 5.45$ E-05*z + 0.0039 in kN/mm^2. It is worth noting that z is the opposite of y and taken into account from $y = 690$ mm (surface of the container). Figure 4.12 also shows the representation of Young modulus according to the depth.
- $\varphi = 40°$, $\psi = 14°$, $R_{\text{inter}} = 0.97$ and $c = 1$ kPa = 1e-6 kN/mm^3

  These interface parameters of soil are supposed to model the behaviour of dense sand. They differ from the parameters measured in Chapter 3, but they are necessary to

represent the results of the monotonic centrifuge pull-out pile test.

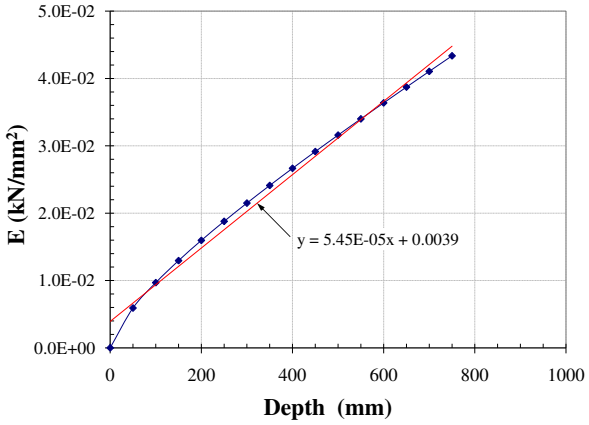

Figure 4.12: Young modulus (E) according to the depth

- Material parameters for aluminum pile are: $E = 67.5$ kN/mm^2, $\gamma/1g = 2.487$E-08 kN/mm^3 and $\nu = 0.34$.

Concerning the interfaces, in Plaxis model interface dilatancy is proportional to the deformations in the interface, in $1/t$ (t interface thickness). The thickness of interface should be reduced to increase the deformations therein and thus the associated dilatancy. In mode of "input", after preparing the model, the virtual thickness factor is changed to be 0.01 (by default: 0.1).

4.3.1 Modeling of pile pull-out load test

The pull-out test "$PC74TM$" is selected to typically model with Plaxis. It is the numerical model corresponding to the typical monotonic test carried out by the IFSTTAR. Point A is selected on the pile head, on the axis, to track the displacement. The procedures of calculations are:

- Phase 1: Set up the pile and adjacent soil (except top layer, because the pile emerges from the surface 30 mm) under $1g$. Staged construction, Activation of soil and interfaces
- Phase 2: Application of $23g$. Total multiplier, $\sum$ -$M_{\text{weight}} = 23$
- Phase 3: Pull-out load application on pile head (4 kN). Staged construction, a reduced-scale model is given as $F_y = 4/\pi/18 = 0.0707$ kN/mm.

  It can be noted that the stage of an application of $1g$ only optimizes the stability of the rearrangement sand grains subjected to centrifugal acceleration. At pull-out load application, it displays 4 for "Time" interval for F_y.

The results of centrifuge model test are summarized as follows:

- Application of $1g$ for the pile and adjacent soil as shown in Figure 4.13:
  - Maximum settlement of soil: -0.11 mm (very low because of high modulus), and pile : -0.052 mm
  - At interface; maximum $\sigma_n = 21.06\text{E-}6$ kN/mm^2 in comparison with γz: 1.24E-05 kN/mm^2 and maximum $\tau = 18.06\text{E-}6$ kN/mm^2 in comparison with $K_0 \gamma z \tan\varphi$: 7.3E-6 kN/mm^2
  - Saturated friction, slight dilatancy and considerable negative friction

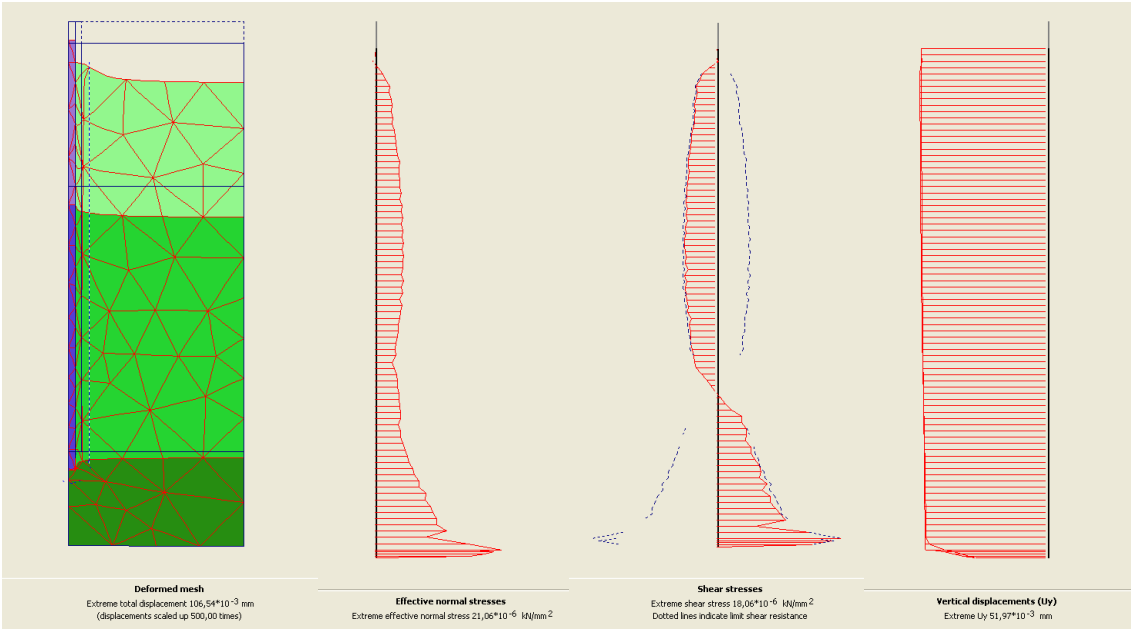

Figure 4.13: Phase1: Application of $1g$ for the pile and adjacent soil

- Application of $23g$ for all soil layers and the pile (Figure 4.14):
  - Maximum settlement of soil: -2.52 mm and pile : -1.16 mm
  - At interface; maximum $\sigma_n = 362.84\text{E-}6$ kN/mm^2, in fact 2/3 considered, in comparison with $23\gamma z$: 2.86E-04 kN/mm^2 and maximum $\tau = 294.82\text{E-}6$ kN/mm^2, in fact 2/3 considered, in comparison with $23K_0 \gamma z \tan\varphi$: 1.68E-4 kN/mm^2
  - Considerable negative friction and dilatancy
- Pull-out interface friction: the negative skin friction has disappeared, the normal and shear stresses are of the same sign. Summary verification on the distribution of τ: the average shear stress $\tau_{\text{avg}} \approx 131$ kPa or 1.31E-4 kN/mm^2, and $\tau_{\text{avg}} \cdot \pi \cdot 18 \cdot 560 = 4.15$ kN. This is in accordance with the centrifuge model test.

  After settling in $23g$, the pull-out loading of 4 kN is applied. In comparison with the centrifuge model test, Plaxis calculation provides a good agreement in the range of

pull-out loading of 4 kN as shown in Figure 4.15. However, a defect still exists as a result of a trend of a continuous increase of load-displacement.

Figure 4.16 shows the distribution of σ_n and τ along the pile under several loadings. The load acting on the pile tip as a function of loading on pile head is also presented in Figure 4.17. Since the application of loading in $23g$ is applied, the load acting on the pile tip resulting from pull-out loading of 4 kN is less pronounced.

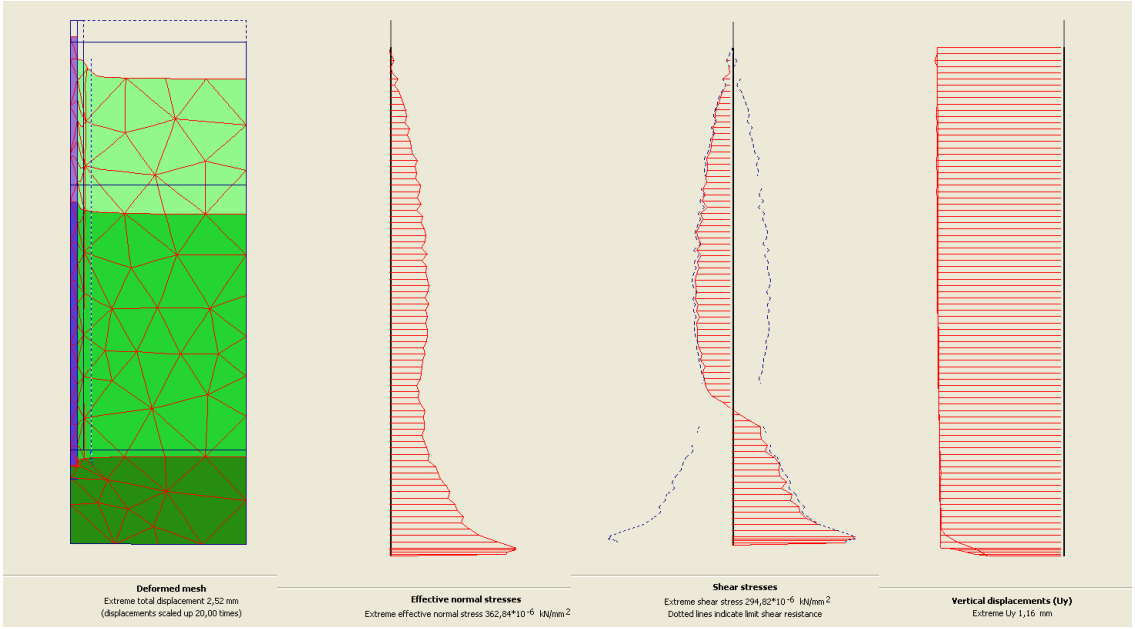

Figure 4.14: Phase2: Application of $23g$ for the pile and adjacent soil

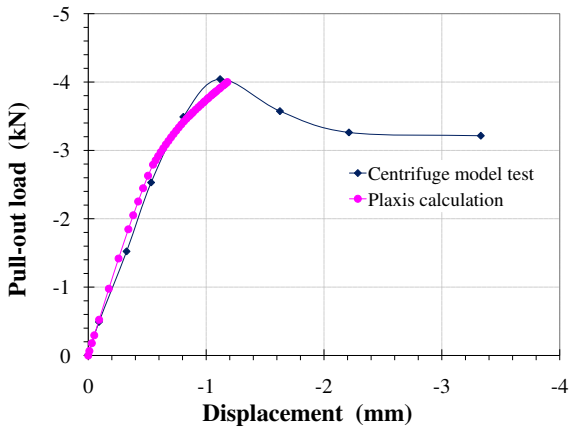

Figure 4.15: Comparison between centrifuge pile test and Plaxis calculation of pull-out load 4 kN on pile head for $PC74TM$

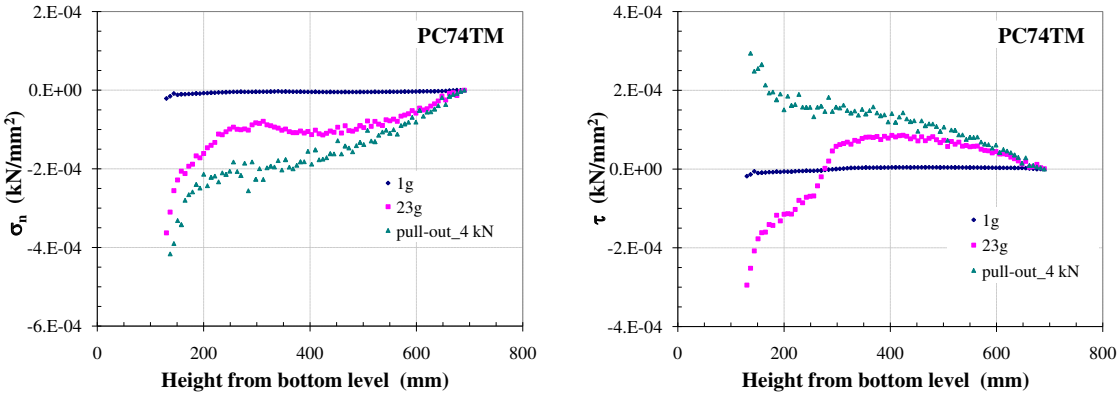

(a) (b)

Figure 4.16: Distribution of σ_n and τ acting along the pile shaft for $PC74TM$

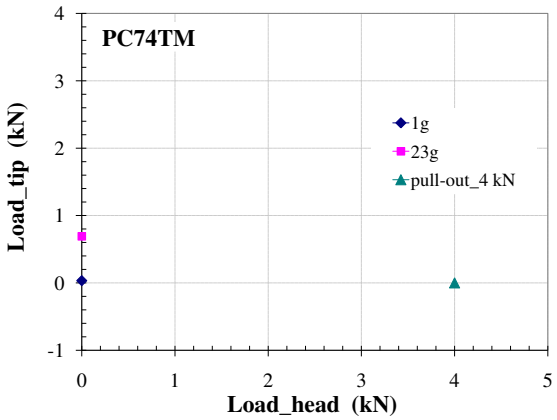

Figure 4.17: Load acting on pile tip as a function of loading on pile head for $PC74TM$

4.3.2 Modeling of pile pull-out load test (1^{st} cycle)

For cyclic model "PC84TC" is selected, neither properties of the pile nor mechanical and physical properties of the soil have changed. It refers to the cyclic pile test C075T05 carried out by the IFSTTAR. The first cycle of centrifuge test "PC74TM" is intended to model with the following extreme forces in tension (Table 4.6):

Table 4.6: Scale factors of centrifuge cyclic model test

PC84TC centrifuge test	prototype a (MN)	model 1/23 (kN)
Max tension force on pile head	1.587	$a/23^2 = 3$
Min tension force on pile head	0.529	$a/23^2 = 1$

To model pile under cyclic axial load, the geometry in the initial phase has been changed (Figure 4.18): 5 layers adjacent to the pile instead of 2 layers, so as to better distinguish the characteristics of cycles in terms of the depth.

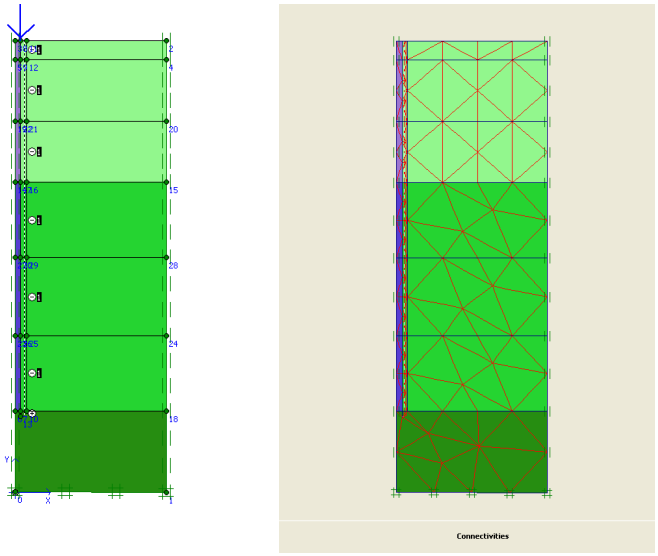

Figure 4.18: Geometry model for cyclic axial load test

- Calculation of loading in 1^{st} cycle

  At this stage, "Time" is still used to designate the force on pile head (kN), although "Time" is a gradual function. And the linear force in kN/mm will always be assigned manually under staged construction. From monotonic pull-out test, it will be necessary to "decode" Time in order that this variable represents the force on pile head even when it decreases during a cycle. Centrifuge modeling of pile under cyclic axial load is given in the following procedures:

  - Phase 1: Staged construction, Activation of sand and interfaces ($1g$), except at 30 mm above the adjacent pile
  - Phase 2: Total multiplier. $\sum$ -M_{weight} = 23
  - Phase 3: Staged construction, Activation of the linear force (0.0177 kN/mm), equivalent to a loading at pile head up to 1 kN. Time interval = 1 ($\sum$ Time = 1)
  - Phase 4: Staged construction, Activation of the linear force (0.0354 kN/mm), equivalent to a loading at pile head up to 2 kN. Time interval = 1 ($\sum$ Time = 2)
  - Phase 5: Staged construction, Activation of the linear force (0.0531 kN/mm), equivalent to a loading at pile head up to 3 kN. Time interval = 1 ($\sum$ Time = 3)

– Phase 6: Staged construction, Activation of the linear force (0.0354 kN/mm), equivalent to a loading at pile head up to 2 kN. Time interval= 1 (where $\sum$ Time = 4, although total force = 2 kN, but this will then be decoded)

– Phase 7: Staged construction, Activation of the linear force (0.0177 kN/mm), equivalent to a loading at pile head up to 1 kN. Time interval = 1 (where $\sum$ Time = 5, although total force = 1 kN, but this will then be decoded)

From calculation, the "Time" (F_y by using the facility of Plaxis) in the last two stages can be modified in order that Time increments higher than 3 are taken negatively, then afterwards led to 1 kN (Figure 4.19).

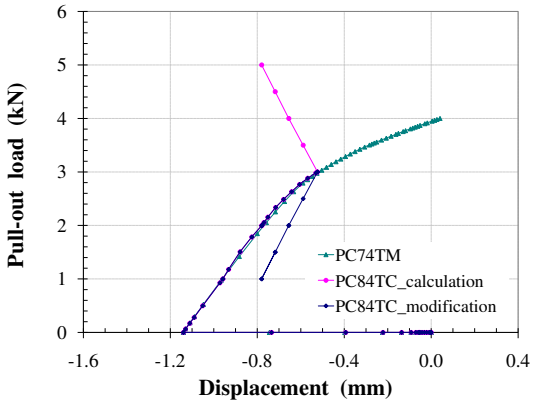

Figure 4.19: Initial pull-out load for cyclic axial load $PC84TC$

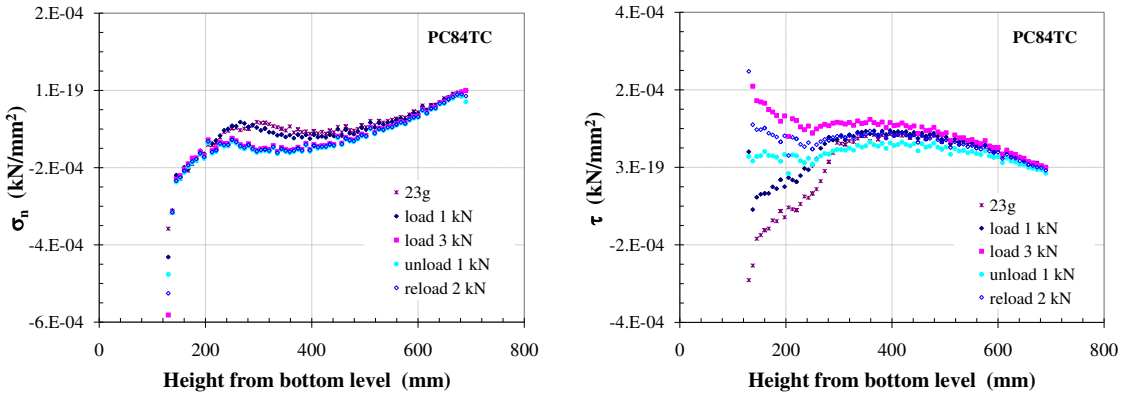

(a) (b)

Figure 4.20: Distribution of σ_n and τ along the pile shaft $PC84TC$ for $F_y = 1 \rightarrow 3 \rightarrow 1 \rightarrow 2$ kN

Figure 4.20 shows the distributions of the normal and shear stresses along the pile during loading up to 3 kN, unloading to 1 kN and then reloading to 2 kN. The normal stress increases significantly when the load acting on pile head varies between 1 and 3 kN due to a trend of dilation. Regarding the shear stress, the negative friction due to the application of $23g$ still exists under the loading of 1 kN and then disappears during the subsequent loading.

4.3.3 Modeling of pile pull-out load test (for further cycles)

Considering the simultaneous variation of σ_n and τ along the pile during the first cycle, and the pre-existence of a significant negative skin friction due to the application of $23g$. It seems useful to examine the cyclic path at various depths along the pile, in order to decide the parameters $\sigma_{\text{n cm0}}$, τ_{cm0}, $\Delta\tau$, and η_{cm0} to be taken into account as a function of depth. Figure 4.21 also shows the stress paths during the first cycle at sand-pile interface.

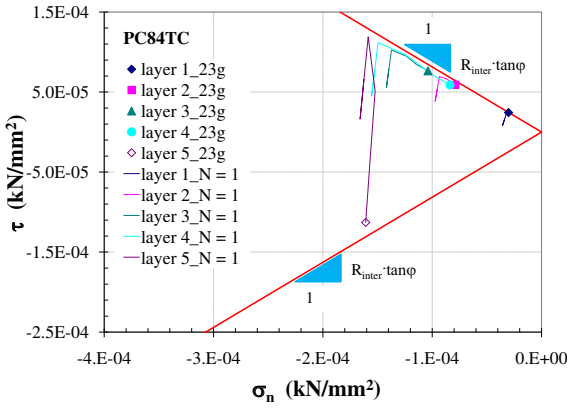

Figure 4.21: Stress paths along the pile shaft during the first cycle for each layer

The reduction of normal stress under CNS condition can be calculated, for each depth, for a given number of cycles, wherein k is the imposed normal stiffness expressed as:

$$k = \frac{2G}{R} \tag{4.7}$$

where;

$R = 9$ mm and G is a linear function with depth as E and $G = E/2/(1 + \nu)$

$E = 0.0039 + 5.45\text{E-}5{*}z$ (kN/mm^2) and $z = 690$ - y, height from the bottom level (mm)

The distribution of normal stiffness is also presented in Table 4.7

Table 4.7: Distribution of the normal stiffness (k) according to the depth in case of "PC84TC"

Layer (mm)	$\sigma_{\text{n cm0}}$ (kPa)	τ_{cm0} (kPa)	$\Delta\tau$ (kPa)	η_{cm0} (-)	E (kN/mm^2)	G (kN/mm^2)	k (kPa/mm)
1	38.5	19.3	18.0	0.50	6.571E-03	2.527E-03	5.616E+02
2	95.2	53.7	32.5	0.56	1.191E-02	4.581E-03	1.018E+03
3	141	78.1	48.4	0.55	1.785E-02	6.866E-03	1.526E+03
4	153	77.3	69.3	0.51	3.333E-02	1.282E-02	2.849E+03
5	172	28.5	104.2	0.17	3.115E-02	1.198E-02	2.662E+03

From Table 4.7, it can be found that the values of maximum stress ratio ($\eta_{\max}$) and the cyclic amplitued $\Delta\eta$ are higher in the upper part of these five layers. This indcates that these cycles are largely in contracting domain. It is interesting to consider the following cycles which show that the former is largely influenced by the initial negative skin friction, while the following cycles are "stabilized".

The pseudo-creep describing the cyclic evolution starts just after the application of the mean cyclic load (2 kN) at the pile head. According to the parameters shown in Table 4.7 and to the formulation of N_{crit} developed in Chapter 3 for dense sand, the local evolution of initial stress state ($\sigma_{\text{n cm0}}$, τ_{cm0} and η_{cm0}) to critical ($\sigma_{\text{n cm crit}}$, $\tau_{\text{cm crit}}$ and $\eta_{\text{cm crit}}$) condition can be calculated for each layer. Figure 4.22 shows the evolution of normal stress as a function of number of cycles. It can be seen that the reduction of normal stress significantly increases during the first 2,000 cycles and then the reduction rate is almost constant when N > 2000.

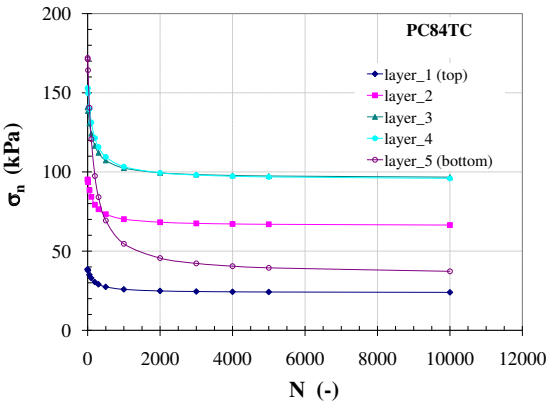

Figure 4.22: Evolution of σ_n along the pile shaft $PC84TC$ as a function of N

The more difficult task is to apply this change in normal stress along the pile shaft. For this purpose, a concentric soil layer of thickness equal to the pile radius has been defined for each horizontal layer. Then the facility developed in Plaxis is used to prescribe a volume change in a predefined cluster. The distribution of normal stress change is obtained by applying a distribution of volume change in these clusters. The definition of the distribution of

volume change is made by iterations as a volume change in a cluster has an influence in the neighbor clusters. In this case the distribution of normal stress acting on the pile shaft which is calculated after 18 iterations is presented in Table 4.8.

Table 4.8: Distribution of the normal stress calculated from the application of volume strain in predefined cluster adjacent to pile shaft in case of "PC84TC"

Layer	1	2	3	4	5
imposed ϵ_v	-3.31	-3.61	-4.08	-4.13	-6.39
σ_n	28.8	75.6	105.9	114.1	71,3
% σ_n	65.5	67.1	78.0	67.13	73.5

Figure 4.23 shows the cyclic pull-out load - displacement curve at pile head for 2,000 cycles of centrifuge model test in comparison with Plaxis calculation. In the phase where the load is constant (2kN), it is the mean cyclic load (pseudo-creep). The result of cyclic pseudo-creep from Plaxis calculation is close to the centrifuge model test. The distribution of normal and shear stresses acting on the pile shaft after the application of 2,000 cycles is also presented in Figure 4.24. It is found that under cyclic pull-out loading the stress state at pile tip is less prominent.

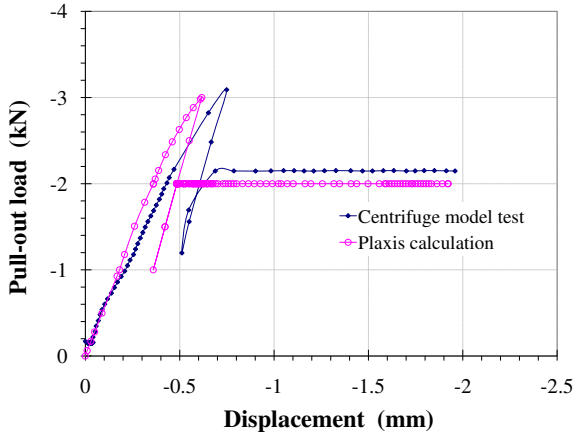

Figure 4.23: Comparison between centrifuge pile test and Plaxis calculation of cyclic pull-out load 2 kN for 2,000 cycles of $PC84TC$

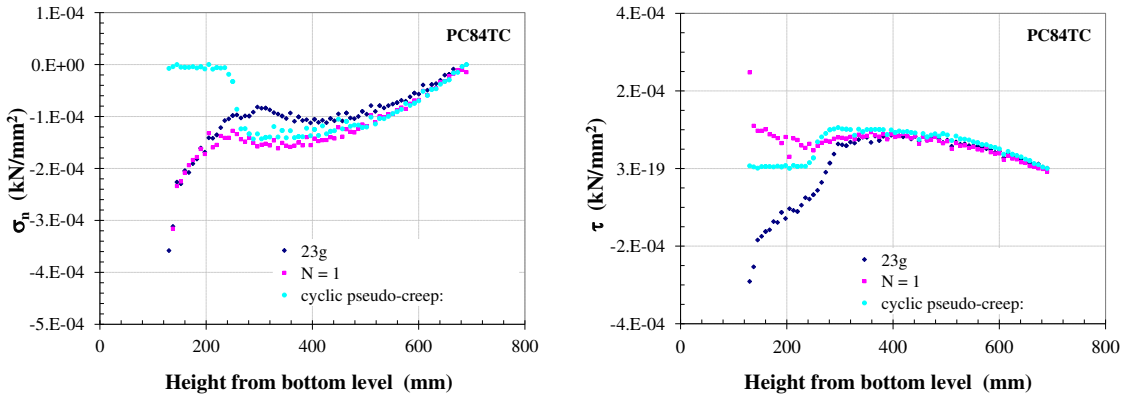

Figure 4.24: Distribution of normal and shear stresses acting on the pile shaft "PC84TC"

4.3.4 Modeling of pile compression load test

The monotonic compression loading of "PC74CM" is modeled in the same way as mentioned in pull-out test. After the application of $23g$, the compression load is then applied with $F_y = 6.1/\pi/18 = 0.1078$ kN/mm. Figure 4.25 shows the distribution of normal and shear stresses after applying the compression loading 6.1 kN. The negative skin friction disappears after applying the compression loading. The normal and shear stresses increase as a function of depth and these are considerable at pile tip in comparison with pull-out test (Figure 4.26).

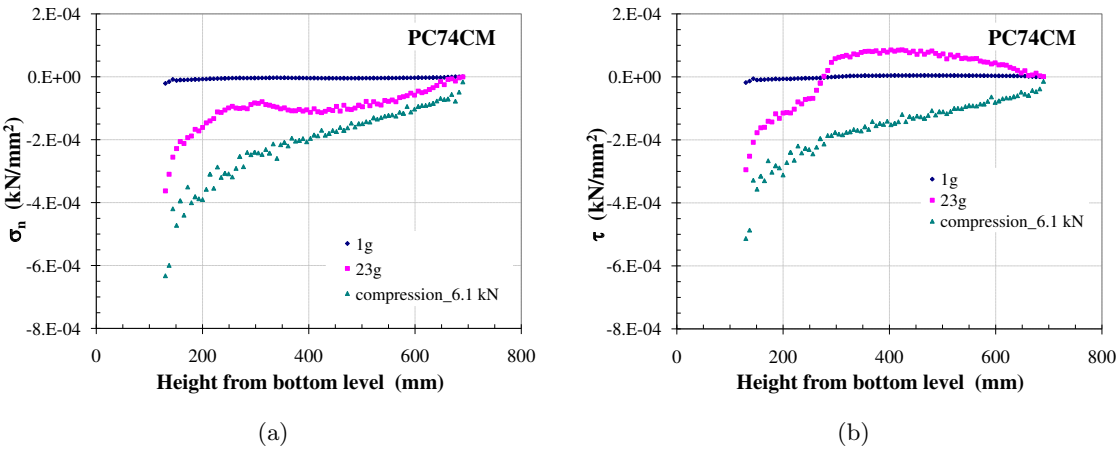

Figure 4.25: Distribution of σ_n and τ acting along the pile shaft for $PC74CM$

Again, the summary verification on the distribution of τ shows that the average shear stress $\tau_{\text{avg}} \approx 184$ kPa or 1.84E-4 kN/mm^2, and $\tau_{\text{avg}} \cdot \pi \cdot 18 \cdot 560 = 5.829$ kN. The agreement between Plaxis calculation and centrifuge model test is satisfactory.

Considering the displacement of pile head, after settling in $23g$, the result from Plaxis calculation is in accordance with centrifuge model test in the range of compression loading of 6.1 kN. A trend of continuous increase of load-displacement from Plaxis calculation still exists.

Figure 4.28 also shows the load acting on the pile tip as a function of loading on pile head. Since the application of loading in $23g$ is applied, the load acting on the pile tip resulting from compression loading of 6.1 kN is more prominent.

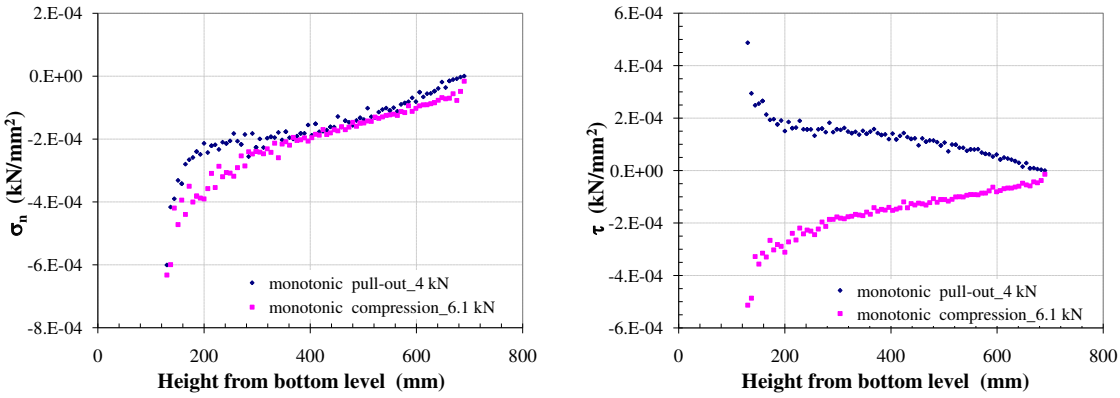

(a) (b)

Figure 4.26: Comparison of distribution of σ_n and τ acting along the pile shaft for pull-out ($PC74TM$) and compression ($PC74CM$) tests

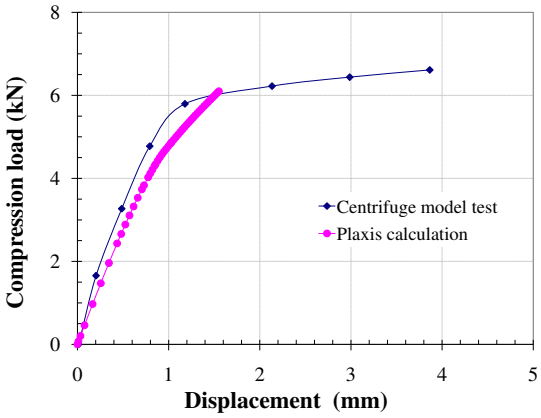

Figure 4.27: Comparison between centrifuge pile test and Plaxis calculation of compression load 6.1 kN

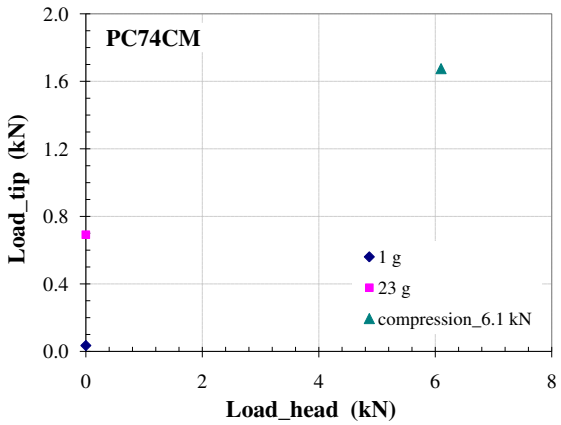

Figure 4.28: Load acting on pile tip as a function of loading on pile head for $PC74CM$

4.3.5 Modeling of pile compression load test (1^{st} cycle)

The procedure of modeling cyclic compression test is similar to that as described in cyclic pull-out test. Again, the first cycle of centrifuge test "PC74CC" is selected to typically model cyclic compression test. Table 4.9 shows the extreme forces in cyclic compression test.

Table 4.9: Scale factors of centrifuge cyclic compression test

PC74CC centrifuge test	prototype a (MN)	model 1/23 (kN)
Max compression force on pile head	1.904	$a/23^2 = 3.6$
Min compression force on pile head	0.635	$a/23^2 = 1.2$

Following the procedures for the first cycle as mentioned in cylic pull-out loading, the "Time" (F_y) is modified in order that Time increments higher than 3.6 are taken negatively, then afterwards led to 1.2 kN (Figure 4.29). Figure 4.30 shows the stress distribution along the shaft pile during the first cycle. Similarly to cyclic pull-out test, during the first cycle in compression the negative skin friction along the pile shaft disappear as a result of an increase of loading step.

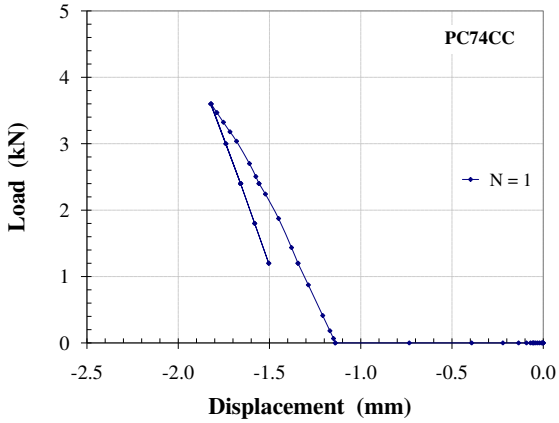

Figure 4.29: Initial compression load for cyclic axial load $PC74CC$

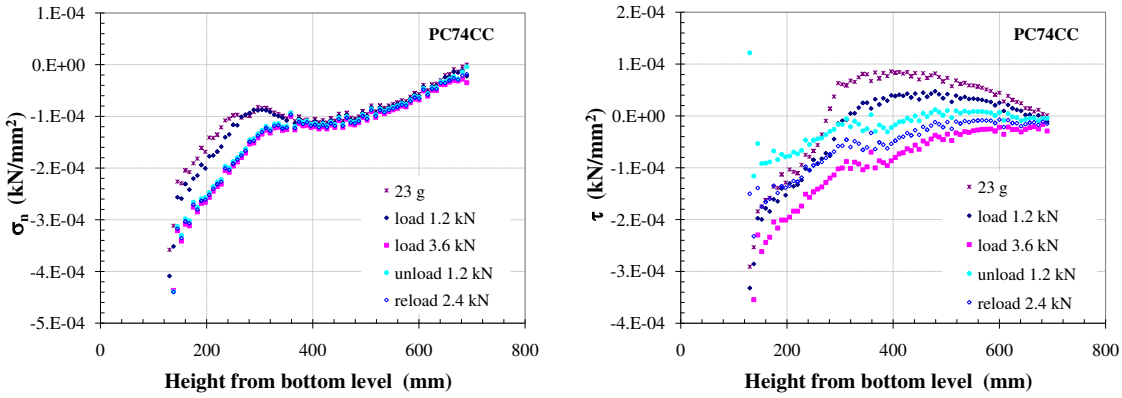

(a) (b)

Figure 4.30: Distribution of σ_n and τ along the pile shaft $PC74CC$ for $F_y = 1.2 \rightarrow 3.6 \rightarrow 1.2 \rightarrow 2.4$ kN

4.3.6 Modeling of pile compression load test (further cycles)

During the first cycle in compression, the stress state acting along the pile shaft varies. Figure 4.31 shows the stress paths during the first cycle. Similarly to cyclic pull-out load test, since $23g$ is applied, the stress state for each layer is close to the limit state. After the application of the first cycle, the stress state for each layer returns into the contractive domain. The pseudo-creep describing the cyclic evolution then starts from the mean cyclic load (2.4 kN) and the initial state can be given as shown in Table 4.10. It can be noted that τ_{cm0} and η_{cm0} are derived from the iterations.

The evolution of normal stress during cyclic loading until reaching the critical state is also derived from the iterations of volume strain application in predefined cluster adjacent to

the pile shaft. Table 4.11 shows the imposed volume strain in predefined cluster adjacent of pile shaft resulting in the variation of normal stress.

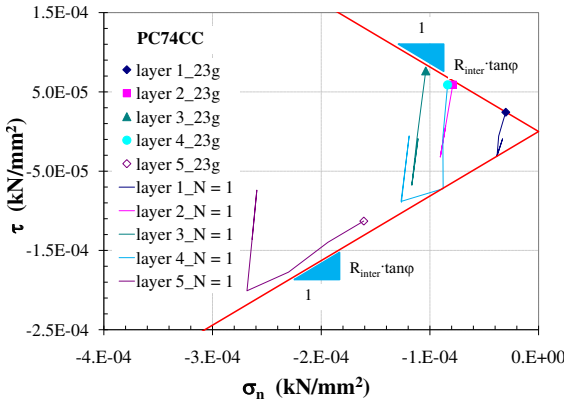

Figure 4.31: Stress paths along the pile shaft during the first cycle in compression for each layer

Table 4.10: Initial state of evaluating the cyclic evolution according to the depth in case of "PC74CC"

Layer (mm)	$\sigma_{\text{n cm0}}$ (kPa)	τ_{cm0} (kPa)	η_{cm0} (-)	$\Delta\eta$ (-)	η_{max} (-)
1	35.7	19.8	0.515	0.410	0.805
2	87.9	12.0	0.132	0.429	0.357
3	113.7	37.5	0.316	0.452	0.583
4	122.7	46.0	0.515	0.415	0.707
5	263.7	135.9	0.520	0.429	0.732

Table 4.11: Distribution of the normal stress calculated from the application of volume strain in predefined cluster adjacent to pile shaft in case of "PC74CC"

Layer	1	2	3	4	5
imposed ϵ_{v}	-2.45	-2.18	-2.17	-2.54	-2.61
σ_n	16.2	40.0	54.2	44.7	142.7
$\sigma_{n\ \text{crit}}$	22.6	14.3	44.1	77.8	168.3

Figure 4.32 shows the cyclic compression load - displacement curve at pile head for 2,000 cycles. The mean cyclic displacement at pile head begins from the mean cyclic load 2.4 kN. It can be seen that the displacement during the pseudo-creep phase in case of cyclic compression is less pronounced in comparison with cyclic pull-out load test. The difference between the numerical modeling and the centrifuge test is important in this case (compres-

sion). It is probably due to the point effect not suitably simulated at large stressess in Plaxis with Mohr-Coulomb model.

Figure 4.33 also shows the distribution of normal and shear stresses acting on the pile shaft after the application of 2,000 cycles. The reduction in normal stress increases as a function of depth after applying 2,000 cycles. The normal stress is even small in comparison with the application of 23g. The negative skin friction along the pile shaft disappears after applying 2,000 cycles and the skin friction along the pile shaft slighly decreases resulting from the reduction in normal stress.

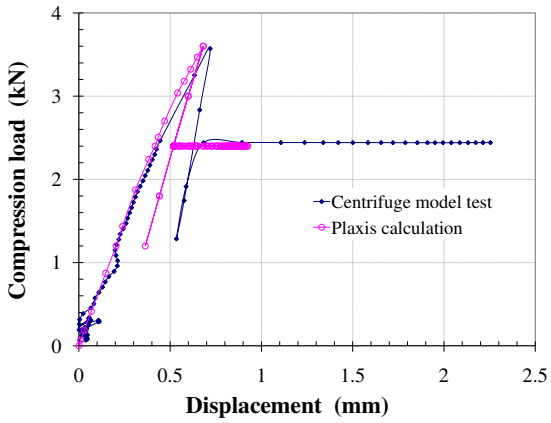

Figure 4.32: Comparison between centrifuge pile test and Plaxis calculation of cyclic compression load 2.4 kN for 2,000 cycles of $PC74CC$

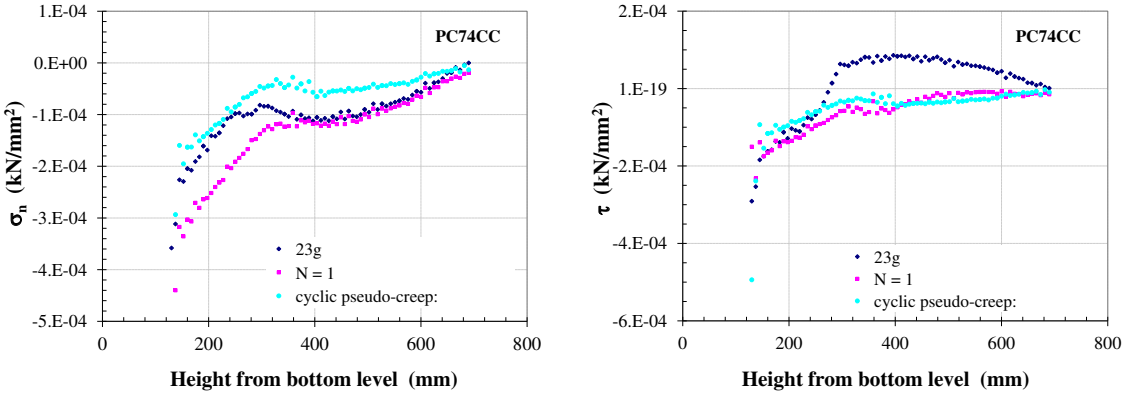

(a) (b)

Figure 4.33: Distribution of normal and shear stresses acting on the pile shaft "PC74CC"

4.4 Conclusion

FEM Program Plaxis, with the simplest constitutive model: Mohr-Coulomb with 5 parameters is used to model the interface behaviour. The first analysis devotes to model the behaviour of interface direct shear box. Since the model is 2D in plane strain, and not 3-D, the defaults (inhomogeneity) of the direct shear test are clarified, perhaps magnified. It is found that a simple Plaxis Mohr-Coulomb model is not fully successful in describing the normal displacement of the interface direct shear tests. As regards the interface strength, the obtained results from Mohr-Coulomb model are close to the experimental results.

The second part of our FEM simulations is related to pile tests. This deals with centrifuge model pile tests performed at the IFSTTAR in Nantes, France. Pull-out pile tests and compression pile tests, under monotonic and cyclic loading, are intended to model in order to develop an alternate methodology compared to the existing ones. In this part, the methodology uses the FEM program as a tool for managing the soil, the pile, and their equilibrium. The interface cyclic pseudo-creep developed in the framework of CNS curves function of the number of cycles is introduced. The complete approach would require the integrated curves along CNS paths. A simplified analysis, used in these computations, refers to the critical number of cycles (N_{crit}) previously developed and to a supposed law of evolution. Another simplification of this computation is to apply the drop of normal stress in one phase only, since the cyclic parameters evolve during this drop. This methodology is developed, but many refinements remain to be done.

Chapter 5

Calculation of real piles subjected to cyclic loading, for civil engineering projects

5.1 Introduction

Many efforts have been devoted for calculating real piles since many years: prediction of load transfer, head stiffness (relation load-displacement), stability/safety of piles axially loaded in the framework of civil engineering projects. The t-z method remains the favourite one of the most part of designers due to its simplicity. Another working method is the finite element or finite difference method, using suitable constitutive equations. The heaviness of the approach and the duration of computations represent a real obstacle against this kind of analysis. Both kinds of approaches need reliable soil and interface parameters. In addition modeling the real mechanisms of mobilisation of shaft and point resistance seems to be a fruitful working way. The work developed in this thesis would propose a compromise between these two extreme points of view. Nevertheless a lot of improvements of our analysis remain necessary.

5.2 Behaviour of real piles subjected to axial cyclic loading

In case of axially loaded piles, only considering the geometrical effect resulting in the intensity of stress transfer obviously inverse function of the current distance to the pile axis leads to give priority to the soil-structure interface. The interface is the locus of this load transfer mechanism by friction. In the radial direction, on one side, the pile is a nearly incompressible material. On the other side, the soil prescribes constraints which are in the radial direction not far from a pressuremetric one, and in the axial direction a shear stress-tangential relative displacement relation. These two constraints should be compatible

with a third constraint: the friction. From this step it is clear that interface shear paths at prescribed normal stiffness (CNS) should govern the load transfer.

The simple model of lateral friction developed by Boulon & Foray [1986] - Figure 1.16, formula (1.8)- gives an evaluation of the normal stiffness function of the pressuremetric modulus of the soil (E_p) and the radius of pile (R). For bored or cast in-situ piles, the pressuremetric modulus could be considered in a small deformation and is not far from the shear modulus (G). But for driven piles, large radial deformations are prominent and it is necessary to consider the real pressuremetric modulus (large strains). The range of parameters of CNS direct shear tests relevant to piles are at least the initial normal stress and the normal stiffness. The range of these parameters will be presented and discussed in the next section.

The finite element or finite difference method should be considered as a tool for modeling the volume load transfer from small distance to the pile axis (often at the limit strength) to the large ones (far from the soil strength), insuring in addition a precise local equilibrium (the minimum requirement of mechanics). Now, what about the constitutive equations? Modeling cyclic loading needs thinking at the cyclic mean paths when considering a large number of cycles, excepted if the confidence ratio on incremental constitutive equations reaches 100 %! For reducing computation time, the number of cycles (series of cycles) instead of time (within a single cycle) for integrating adequate constitutive equations and reducing computation time will be treated. For soil-structure interface, the related tests and models should describe the so-called "cyclic pseudo-creep" where the a progression of negative drop in normal stress occurs.

5.3 Determination of soil and interface parameters

The ordinary data of soil such as the distribution of weight density, water content, strength (c, φ, ψ) and stiffness (G for small strains, E_p for large strains) are necessary for the calculation of pile foundation. If the properties are known only at some depths, this distribution has to be interpolated or extrapolated. In case of G and E_p, using the power law of Kondner would be useful, assuming a classical K_0 (≈ 0.50) for bored piles and a high value (≈ 1 or 2) for driven piles. A linear approximation of soil modulus versus depth (see Young modulus (E) according to depth in previous chapter) represents a single and suitable choice.

Concerning the soil-pile interface, a small number of cyclic CNS tests according to the distribution of the main cyclic parameters along the pile (effective normal stress depending on the installation mode, mean initial shear stress, cyclic amplitude and normal stiffness) would be sufficient. These tests are supposed to indicate the negative drop in normal stress as a function of the number of cycles.

5.4 Model prediction of piles under cyclic axial loading

5.4.1 Initial state (pile installation)

This state is the result of the installation mode. For bored or cast in-situ piles, after the calculation of geostatic state (K_0), the domain of soil corresponding to the place of pile is generally replaced by the material of pile. If the pile is made of concrete the initial normal stress could slightly overpass the K_0 stresses because the concrete is initially liquid. For driven piles, the installation generates a large positive drop in normal stress as well as a strong negative skin friction. In these two cases (bored and driven methods), the operator has to find a strategy in order to take into account these features. For the normal stress, a positive volume change around the pile could be a fair solution. On the other hand, there is no very satisfactory solution for modeling the negative skin friction and its consequence in the surrounding soil. A simple way would artificially be to increase or decrease the weight density of the pile.

5.4.2 Characterizing the loading acting on pile head and along pile shaft

It is necessary to analyse and to simplify the probable head loading program of the pile, then the most severe sequences of cyclic loading would be selected. Only these extreme sequences which could drastically modify the long term pile capacity are considered.

The interface phenomena are privileged as the amplitude of the cycles within the soil itself rapidly decrease with the distance from the pile (see § 5.2). A formulation of cyclic pseudo-creep for modeling a large series of cycles is considered. If the formulations of volumetric pseudo-creep are available (e.g. Wichtmann [2005] and Wichtmann et al. [2005]), these formulations would also be used for the surrounding soil at large distance from the pile. However, it can be noted that the influence of surrounding soil at large distance from the pile remains relatively small.

A first preliminary FEM calculation seems necessary for roughly defining the local cycles along the pile shaft, due to the extreme loading previously defined. This calculation should then give the local cyclic parameters (mean cyclic normal stress, mean cyclic shear stress and cyclic amplitude). The normal stiffness which is a very important parameter still has to be investigated (§ 5.3).

5.4.3 Soil and soil-structure interface tests

.

From ordinary soil experiments whether under monotonic or cyclic loading, the informations (e.g. weight density, strength, stiffness) are obtained. Concerning the soil-structure interface, the informations resulting from the preliminary FEM calculation (§ 5.4.2) are useful for precisely defining a limited number of CNS tests supposed to properly cover the

range of local cyclic parameters. The main result of these tests is the negative drop in normal stress at some selected depths along the pile.

A simple interpolation is necessary for generating this drop at any level along the pile shaft by generalizing the results of the cyclic CNS tests. Before explaining the phases of the final FEM calculattion, it is useful to consider the way of using these cyclic CNS interface tests in full details. Figure 5.1 shows the typical cyclic CNS paths in stress plane. The cyclic CNS path starts from the initial stress state ($\sigma_{\text{n cm0}}$, τ_{cm}):

$$\eta_{\text{cm0}} = \frac{\tau_{\text{cm}}}{\sigma_{\text{n cm0}}}$$

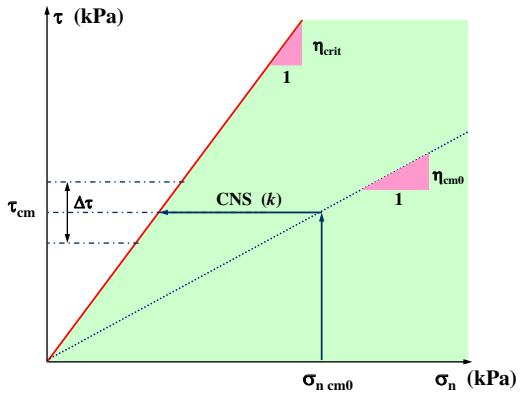

Figure 5.1: Typical cyclic CNS paths of soil-structure interface

The behaviour of the interface is always contractive as can be seen in the experimental section. Then, the center of cycles will progressively move to the "critical state" ($\sigma_{\text{n cm crit}}$, τ_{cm})

$$\sigma_{\text{n cm crit}} = \frac{\tau_{\text{cm}}}{\eta_{\text{crit}}} \tag{5.1}$$

It can be noted that the top of the cycles reaches the critical line before the center of cycles. For this reason, the rupture of the interface could overcome ealier, for $\sigma_{\text{n cm crit1}}$:

$$\sigma_{\text{n cm crit1}} = \frac{\tau_{\text{cm}} + \alpha\frac{\Delta\tau}{2}}{\eta_{\text{crit}}} \tag{5.2}$$

where: $0 < \alpha < 1$.

From the experimental point of view in this study, the coefficient α is not far from $\frac{\sqrt{2}}{2}$ which represents the "reduced efficient value" of the cyclic amplitude. Therefore, the maximum negative drop in normal stress ranges between $\Delta\sigma_{\text{n}}$ and $\Delta\sigma_{\text{n1}}$:

$$\Delta\sigma_{\mathrm{n}} \;=\; \sigma_{\mathrm{n\ cm\ crit}} - \sigma_{\mathrm{n\ cm0}} \;=\; \tau_{\mathrm{cm}} \left(\frac{1}{\eta_{\mathrm{crit}}} - \frac{1}{\eta_{\mathrm{cm0}}} \right) \tag{5.3}$$

$$\Delta\sigma_{\mathrm{n1}} \;=\; \sigma_{\mathrm{n\ cm\ crit1}} - \sigma_{\mathrm{n\ cm0}} \;=\; \frac{\tau_{\mathrm{cm}}}{\eta_{\mathrm{crit}}} \left(1 + \alpha \frac{\Delta\tau}{2\tau_{\mathrm{cm}}} \right) - \frac{\tau_{\mathrm{cm}}}{\eta_{\mathrm{cm0}}} \tag{5.4}$$

or it can be rewritten as:

$$\frac{\Delta\sigma_{\mathrm{n}}}{\sigma_{\mathrm{n\ cm0}}} \;=\; \frac{\eta_{\mathrm{cm0}}}{\eta_{\mathrm{crit}}} - 1 \tag{5.5}$$

$$\frac{\Delta\sigma_{\mathrm{n1}}}{\sigma_{\mathrm{n\ cm0}}} \;=\; \frac{\eta_{\mathrm{cm0}}}{\eta_{\mathrm{crit}}} - 1 + \alpha \frac{\eta_{\mathrm{cm0}}}{\eta_{\mathrm{crit}}} \cdot \frac{\Delta\tau}{2\tau_{\mathrm{cm}}} \tag{5.6}$$

Let us recall the whole set of 8 parameters governing the evolution of normal stress during a cyclic CNS test: roughness surface, I_{D0}, $\sigma_{\mathrm{n\ cm0}}$, τ_{cm}, $\Delta\tau$, $\Delta\sigma_{\mathrm{n}}$, N and k. For a given contact, density of soil, normal stiffness and according to Vashy-Buckingham theorem, these parameters can be reduced to 4 parameters:

$$\frac{\Delta\sigma_{\mathrm{n}}}{\sigma_{\mathrm{n\ cm0}}} \;,\; \frac{\Delta\tau}{\tau_{\mathrm{cm}}} \;,\; \eta_{\mathrm{cm0}} \;,\; N$$

Figure 5.2 gives an example of the presentation of the results of cyclic CNS tests directly related to the evolution of local normal stress along pile shaft under axial cyclic loading. This figure shows the reduced drop in normal stress as a function of the reduced cyclic shear stress and of the number of cycles. It can be seen that the lower limits range between $\frac{\Delta\sigma_{\mathrm{n}}}{\sigma_{\mathrm{n\ cm0}}}$ and $\frac{\Delta\sigma_{\mathrm{n1}}}{\sigma_{\mathrm{n\ cm0}}}$. These results have to be generalized to the other values of η_{cm0} and k.

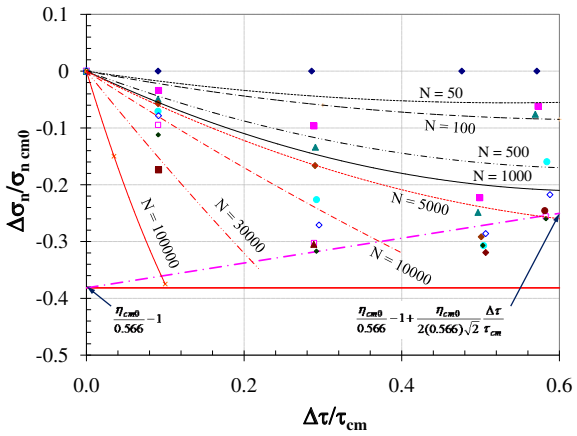

Figure 5.2: Typical results of CNS soil-structure interface shear tests directly related to the change in normal stress along pile shaft under axial cyclic loading; $I_{D0} = 90$ %, $\eta_{\mathrm{cm0}} = 0.35$, $k = 1000$ kPa/mm

5.4.4 FEM modeling the behaviour of a pile under axial cyclic loading

Having prepared this model, the successive phases of this process can be described in the following:

- Phase 1: Initialisation of the geostatic stresses of the FEM model.
- Phase 2: FEM modeling the pile installation.
- Phase 3: For each series of N cycles of the global loading, step to step, FEM calculation of 1 or 2 cycles of loading.
- Phase 4: Extraction of the local cyclic parameters along the pile shaft. Rough solution: at some selected points along the pile shaft (5 to 10). More refined solution: at each integration point along the pile shaft.
- Phase 5: Calculation of the local corresponding negative drop in normal stress by using the diagrams as typically shown in Figure 5.2.
- Phase 6: Implementation of these local drops in normal stress within the FEM model.
- Phase 7: If the series of the cycles is the last step, go to the next step, else return to Phase 3.
- Phase 8: Calculation of the new limit load of the pile under monotonic loading after these cyclic sequences.

General conclusions and perspectives

- **General conclusions**

The work developed in this thesis starts from the small amount of existing knowledge about soil-structure interfaces under cyclic loading. The reader should be convicted that the interface behaviour not only contains the stress limit (Mohr Coulomb or more sophisticated), but also a kinematic law.

For this reason, a direct shear testing machine for cyclic tests, measuring in 2-D changes in stress vector and related changes in relative displacement vector (4 variables) is developed. The direct shear test should be schematised as an element test including two parts: the interface itself of very small thickness (10 -12 D_{50} for sands) surrounded by a kind of buffer zone situated between the interface and the piston of the shear box. In case of direct shear at constant normal stress, the buffer does not evolve after applying the initial normal stress, but for constant normal stiffness, the test should be corrected according to the oedometric compressibility of the buffer. The direct shear test needs another correction due to the loss of sand between the box and the rough plate, inducing a parasite unexpected contraction. This shortcoming has been analysed and quantified.

Finally several series of monotonic and cyclic direct shear test between Fontainebleau sand and two kinds of plates (rough and smooth) were carried out. Only the tests on rough plate were deeply analysed and modeled. The key parameters are the density index (loose, dense), the initial normal stress (60 to 310 kPa), the initial stress ratio (shear to normal stress), the reduced amplitude (change in shear stress to normal stress), the external normal stiffness (zero for constant normal stress, CNL), and the number of cycles (10^4 when possible). The CNL tests were used for identification of parameters, and the CNS tests (constant normal stiffness > 0) were used for validation as well as special CNL test at variable amplitude. For each of these tests, a grain size analysis has been performed before and after test, by a classical sieve method and sometimes using a laser technique. These data have not been exploited due to the very small difference between original and sheared samples.

A rate type (phenomenological) model of interface behaviour under cyclic loading has been proposed. Due to the limited class of shear path (non negative prescribed normal stiffness), an analytical formulation of CNL tests, function of number of cycles, which should be considered as a pre-integrated interface law has also been proposed. Instead of considering

each detail of each cycle, the mean cyclic paths appearing like a pseudo-creep in the sense of Perzyna, the kernel being empty (pseudo-creep for any value of the parameters) are described. The single memory parameter is the mean cyclic normal relative displacement or the interface density under stress. The paths at prescribed normal stiffness (CNS) or CNL at various amplitude are incrementally integrated, but using finite analytical increments, which leads to spare a lot of computer time. This kind of integration is using the notion of the equivalent number of cycles. The step size effect has been studied. It is very important to notice that direct shear paths at prescribed normal stiffness are ever contractive (decreasing normal stress), and leading to the rupture (critical state) after a small or large number of cycles (N_{crit}).

After this study at the constitutive level, the structural studies related to soil-structure interfaces, using the FEM Plaxis, and the simplest constitutive model: Mohr-Coulomb with 5 parameters have been carried out. The first analysis has been devoted to model the shear box itself. Since the model is 2D in plane strain, and not 3-D, the defaults (inhomogeneity) of the direct shear test are clarified, perhaps magnified. Nevertheless the main features of the CNL and CNS shear tests are reproduced. The second part of our FEM simulations is related to pile tests. It deals with the centrifuge model pile tests performed at the IFSTTAR in Nantes, France. The pull-out and compression pile tests, under monotonic and cyclic loading, in order to develop an alternate methodology compared to the existing ones have been modeled. The existing ones are essentially the t-z method, and the more classical method based on well known constitutive equations, integrated step to step within each cycle. The methodology uses the FEM program as a tool for managing the soil, the pile, and their equilibrium. The contribution is to introduce the interface cyclic pseudo-creep here-above developed in the framework of CNS curves function of the number of cycles. The complete approach would require the integrated curves along CNS paths. A simplified analysis, used in these computations, refers to the critical number of cycles (N_{crit}) previously developed and to a supposed law of evolution. Another simplification of this computation is to apply the drop of normal stress in one phase only, since the cyclic parameters evolve during this drop. This methodology is developed, but many refinements remain to be done.

A last chapter is devoted to the calculation of real piles subjected to axial cyclic loading. Within this chapter the steps of modeling are listed according to a limited number of interface tests, after selecting them by a preliminary FEM simulation. The methodology exactly conforms to the one developed for our pile calculations.

- **Perspectives for future works**

The future perspectives opened by this thesis work are numerous. From the experimental point of view, it would be interesting to link the grain size evolution during cycles with the evolution of the normal relative displacement. Some tests with more various cyclic amplitudes would complete the small number of existing ones. The cyclic pseudo-creep is presently analytically formulated within an excel sheet. It would be useful to translate it in Fortran or C for using it directly in a FEM code. The analytical formulas describing CNL paths are using a large number of coefficients, which is not an obstacle, but a simplification of this analytical formulation is probably possible. At the structural level, calculating a pile requires several steps of dialogue between Plaxis and the rest of the world. It would

be important to made this exchange automatic. The methodology developed here for pile calculations needs to be improved by a refined mesh, by considering a larger number of horizontal layers beside the pile, and by integrating the changes in normal tress instead of proceeding in one step. In addition the complete procedure should be validated on several real piles.

References

Airey, D., Al-Douri, R., & Poulos, H. (1992). Esimation of pile friction degradation from shearbox tests. *ASTM Geotechnical Testing Journal*, *15(4)*, 388-392.

Al-Douri, R., & Poulos, H. (1992). Static and cyclic shear tests on carbonate sands. *ASTM Geotechnical Testing Journal*, *15(2)*, 138-158.

API, A. P. I. (1993). Foundation design. *RP 2A-LRFD-Section G*, 64-77.

Armand, G., Boulon, M., Papadopoulos, C., Basanou, M., & Vardoulakis, I. (1998). Mechanical behaviour of dionysos marble smooth joints: I, experiments. *Mechanics of jointed and Faulted Rock*, *Rossmanith (ed), Balkema, Rotterdam*, 159-164.

Arslan, H. (2005). Finite element study of soil structure interface problem. *The Electronic Journal of Geotechnical Engineering, EJGE*, *10*, Bundle C.

Aubry, D., Modaressi, A., & Modaressi, H. (1990). A constitutive model for cyclic behaviour of interfaces with variable dilatancy. *Computers and Geotechnics*, *9(1/2)*, 47-58.

Boulon, M. (1988). Contribution à la mécanique des interfaces sols-structures. application au frottement lateral des pieux. *Diplome d'Habilitation à Diriger des Recherches*, *Université Joseph Fourier, Grenoble, France*.

Boulon, M. (1989). Basic features of soil structure interface behavior. *Computers and Geotechnics*, *7*, 115-131.

Boulon, M., & Foray, P. (1986). Physical and numerical simulations of lateral shaft friction along offshore piles in sand. *The 3rd Int. Conf. On Numerical Methods in offshore piling*, *Nantes*, 127-147.

Boulon, M., Garnica, P., & Vermeer, P. (1995). Soil-structure interaction: Fem computations, mechanics of geomaterial interfaces. *Selvadurai A.P.S. and Boulon M.J. (editors)*, *Elseviers Science B.V.*, 147-171.

Boulon, M., Ghionna, V., & Mortara, G. (2003). A strain-hardening elastoplastic model for sand-interface under monotonic and cyclic loading. *Mathematical and Computer Modelling*, *37*, 623-630.

Boulon, M., & Nova, R. (1990). Modelling of soil-structure interface behaviour, a comparison between elastoplastic and rate type laws. *Computer and Geotechnics*, *9*, 21-46.

Boutrif, A. (1993). Mesure de comportement d'interface sol-structure à la boîte de cisaillement direct annulaire et modélisation. *Thèse de doctorat, Université Joseph Fourier, Grenoble*, *Grenoble, France*.

Brinkgreve, R., Broere, W., & Waterman, D. (2008). Plaxis 2d - manual.

D'Aguiar, S., Modaressi-Farahmand-Razavi, A., Lopez-Caballero, F., & Santos, J. (2008). Soil-structure interface modeling: Application to pile axial loading. *The 12th International Association for Computer Methods and Advances in Geomechanics (IACMAG)*, *Goa, India*, 957-965.

D'Aguiar, S., Modaressi-Farahmand-Razavi, A., Santos, J., & Lopez-Caballero, F. (2011). Elastoplastic constitutive modeling of soil-structure interfaces under monotonic and cyclic loading. *Computers and Geotechnics*, *38*, 430-447.

Dejong, J., Randolph, M., & White, D. (2003). Interface load transfer degradation during cyclic loading: a microscale investigation. *Soils and foundations*, *43(4)*, 81-93.

Desai, C., Drumm, E., & Zaman, M. (1985). Elasto-plastic analysis of the interface behavior between granular media and structure. *ASCE JGE*, *111(6)*, 793-815.

Desai, C., & Nagaraj, B. (1988). Modeling for cyclic normal and shear behavior of interfaces. *ASCE JGE*, *114(7)*, 1198-1217.

Fakharian, K., & Evgin, E. (1997). Cyclic simple shear behaviour of sand-steel interfaces under constant normal stiffness condition. *ASCE JGGE*, *123(12)*, 1096-1105.

Flavigny, E., & Nova, R. (1987). Viscous properties of geomaterials. *Geomaterials: Constitutive Equations and Modelling*, *Edited by Félix Darve, Elsevier Applied Science.*.

Garnica-Anguas, P. (1993). Simulation numérique du frottement entre solides par équations intégrales aux frontières et modèle d'interface non linéaire. application aux pieux. *Thèse de doctorat, Université Joseph Fourier, Grenoble*, *Grenoble, France*.

Gennaro, V. D., & Frank, R. (2002). Elasto-plastic analysis of the interface behavior between granular media and structure. *Computers and Geotechnics*, *29(7)*, 547-572.

Hammad, W. (1991). Modélisation non linéaire et étude expérimentale des bandes de cisaillement dans le sable. *Thèse de doctorat, Université Joseph Fourier, Grenoble*, *Grenoble, France*.

Hans, J., & Boulon, M. (2003). A new device for investigating the hydro-mechanical properties of rock joints. *Int. J. Numer. Anal. Meth. Geomech*, *27*, 513-548.

Heeres, O., Suiker, A., & de Borst, R. (2002). A comparison between the perzyna viscoplastic model and the consistency visoplastic model. *European Journal of Mechanics A/Solids*, *21*, 1-12.

Hicher, P., & Shao, J. (2002). Modèles de comportement des sols et des roches. *Tome 2: lois incrémentales, viscoplasticité, endommagement*, *ed Hermès-Lavoisier*.

Hoteit, N. (1990). Contribution à l'étude du comportement d'interface sable-inclusion et application au frottement apparent. *Thèse de doctorat, Institut National Polytechnique de Grenoble*, *France*.

Hu, L., & Pu, J. (2004). Testing and modeling of soil-structure interface. *ASCE, Journal of Geotechnical and Geoenvironmental Engineering*, *130(8)*, 851-860.

Johnston, I., Lam, T., & Williams, A. (1987). Constant normal stiffness direct shear testing for socketed pile design in weak rock. *Géotechnique*, *37(1)*, 83-89.

Kaggwa, W., Booker, J., & Carter, J. (1991). Residual strains in calcareous sand due to irregular cyclic loading. *Journal of Geotechnical Engineering*, *17(2)*, 201-218.

Karstunen, M., Yin, Z., Koskinen, M., Leoni, M., & Vermeer, P. (2008). Recent developments in constitutive modelling of soft clays. *The 12th International Association for Computer Methods and Advances in Geomechanics (IACMAG)*, *Goa, India, Invited keynote paper*.

Kelly, R. (2001). Development of a large diameter ring shear apparatus and its use for interface testing. *Ph.D. Thesis, University of Sydney*, *Australia*.

Kishida, H., & Uesugi, M. (1987). Tests of the interface between sand and steel in the simple shear apparatus. *Géotechnique*, *37(1)*, 45-52.

Liingaard, M., Augustesen, A., & Lade, P. (2004). Characterization of models for time-dependent behaviour of soils. *ASCE International Journal of Geomechanics*, *4(3)*, 157-177.

Liu, H., & Ling, H. (2008). Constitutive description of interface behaviour including cyclic loading and particle breakage within the framework of critical state soil mechanics. *Int. J. Numer. Anal. Meth. Geomech*, *32*, 1495-1514.

Liu, H., Song, E., & Ling, H. (2006). Constitutive modeling of soil-structure interface through the concept of critical state soil mechanics. *Mechanics Research Communications*, *33*, 515-531.

Luong, M. (1980). Stress-strain aspects of cohesionless soils under cyclic and transient loading. *International Symposium on Soils under Cyclic and Transient Loading*, *Zienkiewicz O.C. (eds); 7-11 January*, 315-324.

Messast, S., Boulon, M., Flavigny, E., & Labanieh, S. (2006). Modélisation constitutive du comportement cyclique des sables en condition drainée. *18ème Congrès Français de Mécanique*, *Grenoble*, 1-6.

Mortara, G. (2001). An elastoplastic model for sand-structure interface behaviour under monotonic and cyclic loading. *Ph.D. Thesis. Politecnico di Torino*, *Italy*.

Mortara, G., Boulon, M., & Ghionna, V. (2002). A 2-d constitutive model for cyclic interface behaviour. *International Journal for Numerical and Analytical Methods in Geomechanics*, *26*, 1071-1096.

Mortara, G., Mangiola, A., & Ghionna, V. (2007). Cyclic shear stress degradation and post-cyclic behaviour from sand-steel interface direct shear tests. *Canadian Geotechnical Journal*, *44*, 739-752.

Moutraji, J. (1992). Etude expérimentale et numérique du cisaillement direct silt-structure application à l'amélioration du frottement latéral dans les sols fins. *Thèse de doctorat, Université Joseph Fourier, Grenoble*, *France*.

Niemunis, A., Whichtman, T., & Triantafyllidis, T. (2005). A high-cycle accumulation model for sand. *Computers and Geotechnics*, *32*, 245-263.

Nova, R., & Wood, D. (1979). A constitutive model for sand in triaxial compression. *International Journal for Numerical and Analytical Methods in Geomechanics*, *3(3)*, 255-278.

Oumarou, T., & Evgin, E. (2005). Cyclic behaviour of a sand-steel plate interface. *Canadian Geotechnical Journal*, *42*, 1695-1704.

Owen, D., & Hinton, E. (1980). Finite elements plasticity: Theory and practice. *Pineridge Press Limited*.

Papadopoulos, C., Basanou, M., Vardoulakis, I., Boulon, M., & Armand, G. (1998). Mechanical behaviour of dionysos marble smooth joints: Ii, constitutive modeling. *Mechanics of jointed and Faulted Rock*, *Rossmanith (ed), Balkema, Rotterdam*, 165-170.

Pastor, M., Zienkiewicz, O., & Leung, K. (1985). Simple model for transient soil loading in earthquake analysis ii. non-associative model for sands. *Int. J. Numer. Anal. Meth. Geomech.*, *9(5)*, 477-498.

Perzyna, P. (1966). Fundamental problems in viscoplasticity. *Adv. Appl. Mech.*, *9*, 243-377.

Puech, A., Foray, P., Boulon, M., & Desrues, J. (1979). Calcul des pieux à l'arrachement à partir d'un modèle numérique en contraintes effectives-premiers résultats. *VII European Conf. on soils mechanics and foundation engineering*, *Brighton*, 227-232.

Samtani, N., Desai, C., & Vulliet, L. (1996). An interface model to describe viscoplastic behavior. *International Journal for Numerical and Analytical Methods in Geomechanics*, *20*, 231-252.

Schlosser, F., & Guilloux, A. (1981). Le frottement dans le renforcement des sols. *Revue Française de Géotechnique*, *16*, 65-79.

Shahrour, I., & Rezaie, F. (1997). An elastoplastic constitutive relation for soil-structure interface under cyclic loading. *Computers and Geotechnics*, *21(1)*, 21-39.

Stijn, F., Karg, C., Degrande, G., & Haegeman, W. (2007). A long term accumulation model for soils under low amplitude cyclic loading. *The 7th Colloque National AFPPS*, *Ecole Centrale Paris*.

Tabucanon, J., Airey, D., & Poulos, H. (1995). Pile skin friction in sand from constant normal stiffness tests. *ASTM GTJ*, *18(3)*, 350-364.

Uesugi, M., & Kishida, K. (1986). Influential factors of friction between steel and dry sands. *Soil and Foundations*, *6(2)*, 33-46.

Uesugi, M., Kishida, K., & Yasunori, T. (1989). Friction between sand and steel under repeated loading. *Soil and Foundations*, *29(3)*, 127-137.

Wichtmann, T. (2005). Explicit accumulation model for non cohesive soils under cyclic loading. *Ph.D. Thesis, Ruhr Universität Bochum*, *Germany*.

Wichtmann, T., Niemunis, A., & Triantafyllidis, T. (2005). Strain accumulation in sand due to cyclic loading: drained triaxial tests. *Soil Dynamics and Earthquake engineering*, *25*, 967-979.

Wichtmann, T., Niemunis, A., & Triantafyllidis, T. (2010). Strain accumulation in sand due to cyclic loading: On the effect of monotonic and cyclic preloading (miner's rules). *Soil Dynamics and Earthquake engineering*, *30*, 736-745.

Yin, Z. (2006). Modélisation du comportement visqueux de l'argile naturelle. *XXIVèmes Rencontres Universitaires de Génie Civil-Prix Jeunes Chercheurs*, 1-8.

Yin, Z., & Karstunen, M. (2008). Influence of anisotropy, destructuration and viscosity on the behavior of an embankment on soft clay. *The 12th International Association for Computer Methods and Advances in Geomechanics (IACMAG)*, *Goa, India*, 4728-4735.

Yoshimi, Y., & Kishida, T. (1981). A ring torsion apparatus for evaluating friction between soil and surfaces. *ASTM Geotechnical Testing Journal*, *4(4)*, 145-152.

Appendices

Appendix A

Analytical model of monotonic interface tests

A.1 Detail of functions at before-peak phase

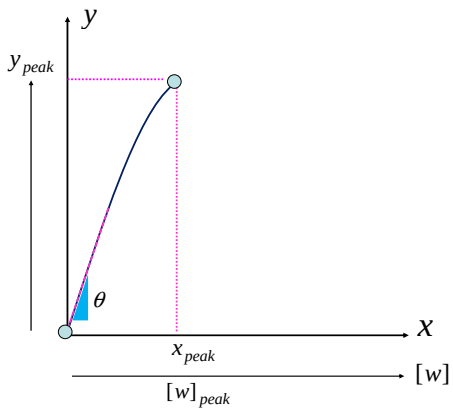

Figure A.1: Interface direct shear test at before-post peak

For $\eta([w])$, $\sigma([w])$ and $[u]([w])$ diagrams, a function defined by a polynomial function of degree three is given as:

$$y = A \cdot x^3 + B \cdot x^2 + C \cdot x + D \tag{A.1}$$

where

$y = \eta$ or σ or $[u]$

$y_{\text{peak}} = \eta_{\text{peak}}$ or σ_{peak} or $[u]_{\text{crit}}$

$x = [w]$

The derivative of a polynomial function is a quadratic function as;

$$y' = 3 \cdot A \cdot x^2 + 2 \cdot B \cdot x + C \tag{A.2}$$

if $x = 0$, $y = 0$ and $y' = \theta$ (the initial slope).

if $x = x_{peak}$, $y = y_{peak}$ (the peak value) and $y' = 0$.

$D = 0$

$C = \theta$

$$y' = 3 \cdot A \cdot x_{peak}^2 + 2 \cdot B \cdot x_{peak} + \theta = 0$$

$$y_{peak} = A \cdot x_{peak}^3 + B \cdot x_{peak}^2 + C \cdot x_{peak}$$

$$A = \frac{\theta}{x_{peak}^2} - 2\frac{y_{peak}}{x_{peak}^3} \tag{A.3}$$

$$B = -2\frac{\theta}{x_{peak}} + 3\frac{y_{peak}}{x_{peak}^2} \tag{A.4}$$

$$C = \theta \text{ (the initial slope)} \tag{A.5}$$

$$D = \begin{cases} 0 & \text{for } \eta([w]) \text{ and } [u]([w]) \\ \sigma_n & \text{for } \sigma([w]) \end{cases} \tag{A.6}$$

A.2 Detail of functions at post-peak phase

For $\eta([w])$ diagram, a function is defined by:

$$y = A \cdot \exp(-B \cdot x^2) \tag{A.7}$$

where

$x = [w] - [w]_{peak}$

let us define:

$$y = \left(\frac{\tau}{\sigma_n}\right) - \left(\frac{\tau}{\sigma_n}\right)_{\text{crit}}$$

The difference of stress ratio during the peak and critical value is expressed as:

$$y_M = \left(\frac{\tau}{\sigma_n}\right)_{\text{peak}} - \left(\frac{\tau}{\sigma_n}\right)_{\text{crit}} \tag{A.8}$$

and

$A = y_M$

Considering the point at 2% of y_M,

$$0.02 \cdot y_M = y_M \cdot \exp(-B \cdot x^2)$$

then

$$B = -\frac{\ln(0.02)}{x_1^2} \tag{A.9}$$

It can be noted that there is not so much difference in the range 1-5% of y_M.

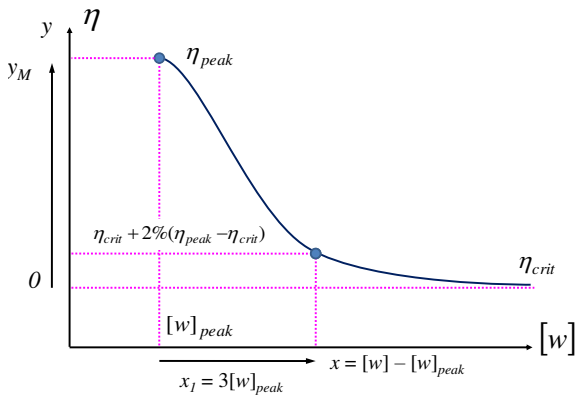

Figure A.2: Interface direct shear test at post-post peak of $\eta([w])$

$\sigma([w])$ and $[u]([w])$ diagrams are defined in the same function as, for instance,:

$$\frac{d\sigma_n}{d[w]} = \left[1 - \exp\left(-\frac{[w] - [w]_{peak}}{\upsilon}\right)\right] \cdot \beta_+ \tag{A.10}$$

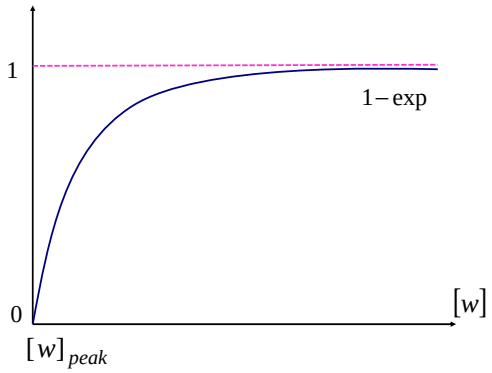

Figure A.3: Interface direct shear test at post-post peak of $\sigma([w])$ and $[u]([w])$

if

$$[w] = [w]_{peak} \rightarrow \frac{d\sigma_n}{d[w]} = 0$$

$$[w] = \infty \rightarrow \frac{d\sigma_n}{d[w]} = \beta_+$$

The evaluation of υ can be expressed as:

$$\left[1 - \exp\left(-\frac{[w] - [w]_{peak}}{\upsilon}\right)\right] \cdot \beta_+ = n \cdot \beta_+ \tag{A.11}$$

where n is the constant which $n = 0.95$ is held in this study.

Then

$$\upsilon = -\frac{[w]_{peak}}{\ln(1-n)} = \frac{[w]_{peak}}{2.9957} \tag{A.12}$$

From A.10, the evolution of σ_n is then expressed as:

$$\sigma_n = \beta_+[w] - [w] \cdot \exp\left[-\frac{[w] - [w]_{peak}}{\upsilon}\right] \cdot (-\upsilon) + C_1 \tag{A.13}$$

by imposing $\sigma_n = \sigma_{\text{peak}}$ for $[w] = [w]_{peak}$, and substituting υ in A.13, the constant C_1 is derived:

$$C_1 = \sigma_{\text{peak}} - \beta_+[w]_{peak} - \beta_+ \cdot \frac{[w]_{peak}}{2.9957} \tag{A.14}$$

Therefore, the evolution of σ_n as a function of $[w]$ is

$$\begin{aligned}\sigma_n = \sigma_{\text{peak}} + \ & \beta_+ \cdot ([w] - [w]_{\sigma\ \text{peak}}) \\ & - \beta_+ \cdot \left(\frac{[w]_{\sigma\ \text{peak}}}{2.9957} \right) \cdot \left[1 - \exp\left(([w] - [w]_{\sigma\ \text{peak}}) \cdot \frac{2.9957}{[w]_{\sigma\ \text{peak}}} \right) \right]\end{aligned} \tag{A.15}$$

Appendix B

Results for Monotonic CNL and CNS tests

B.1 Monotonic CNL tests on loose sand ($I_{D0} \approx 30\%$)

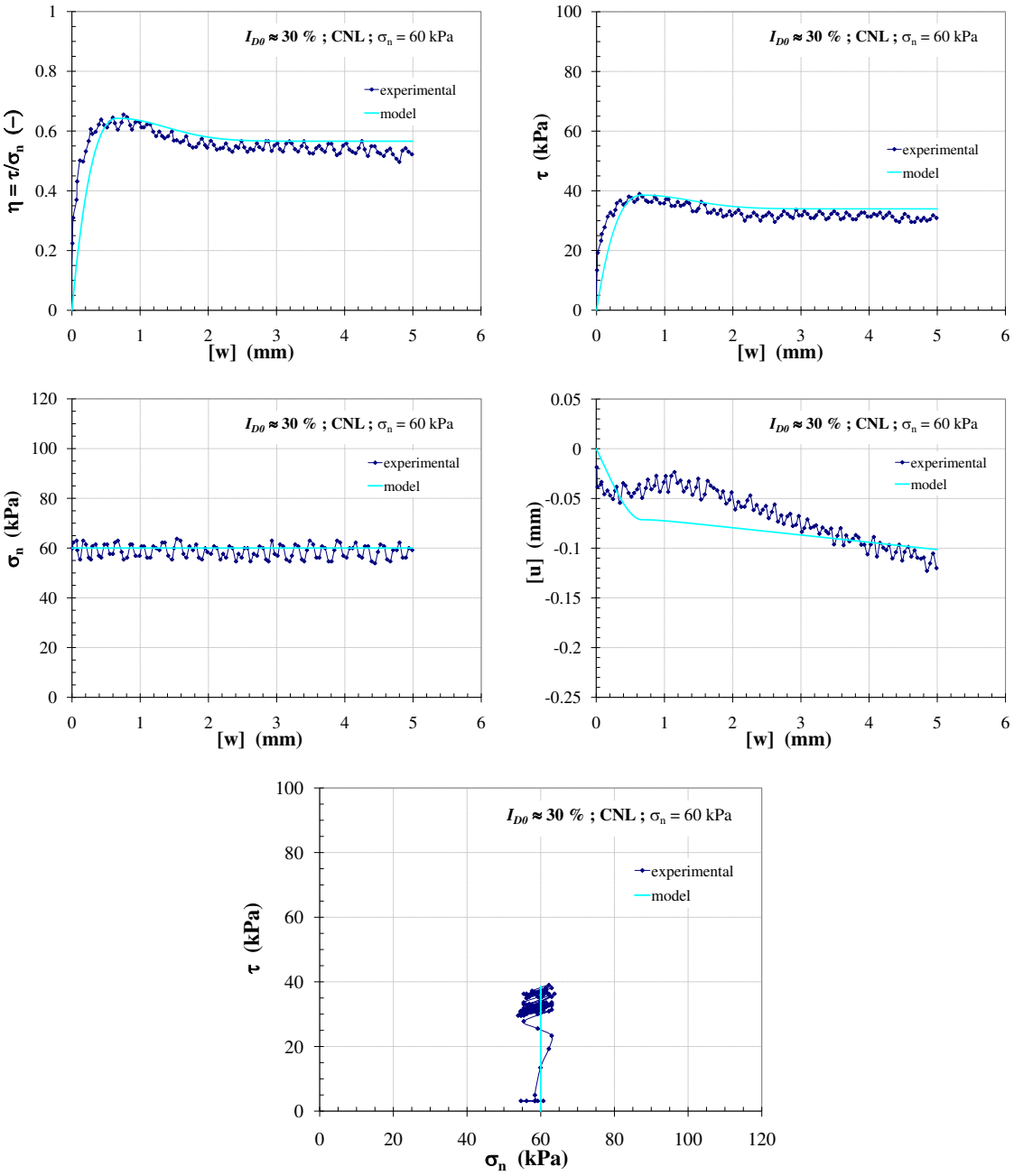

Figure B.1: Comparison between experimental data and the model prediction, $\sigma_n = 60$ kPa, CNL test on loose sand ($I_{D0} \approx 30\%$) with rough plate

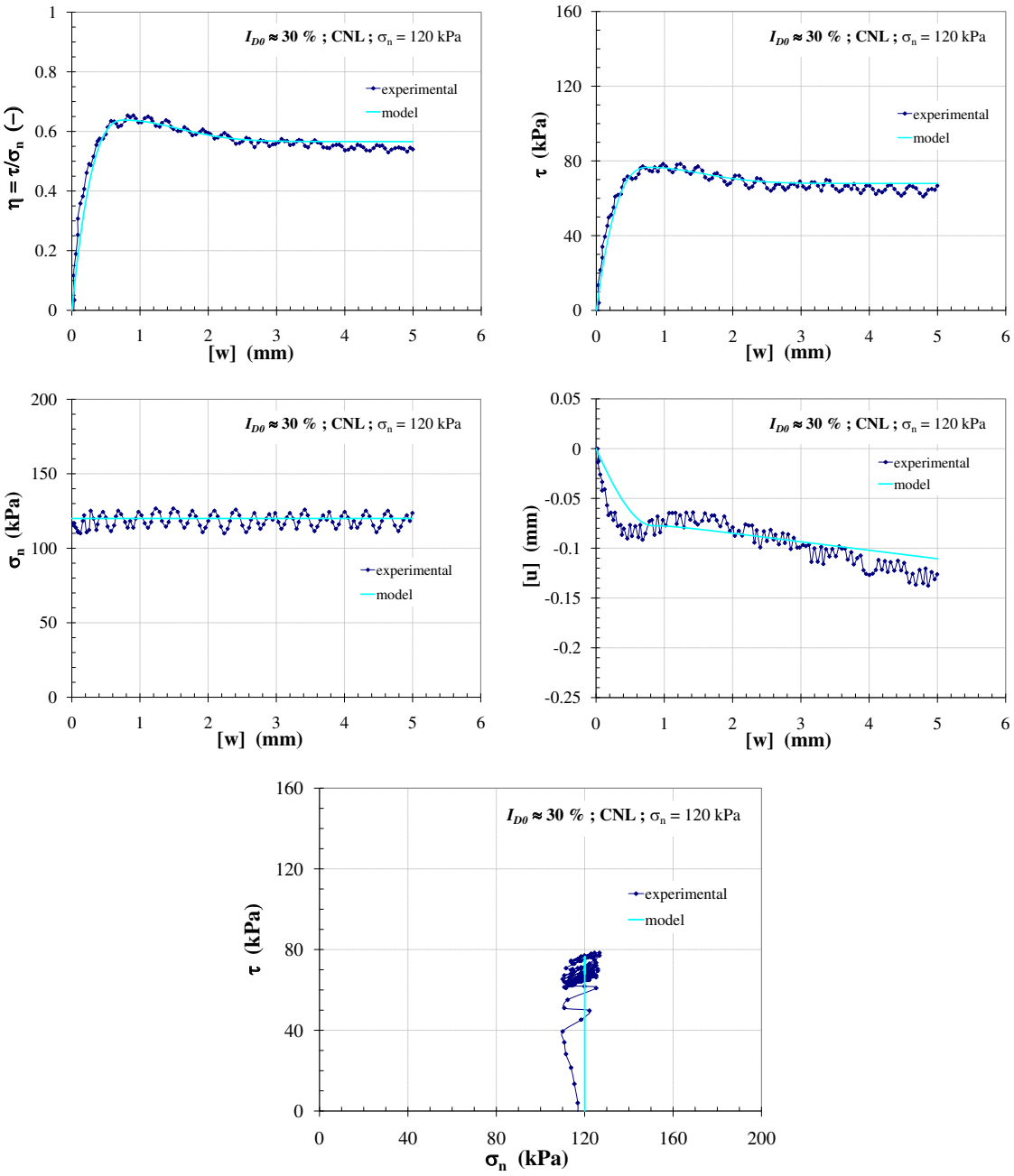

Figure B.2: Comparison between experimental data and the model prediction, $\sigma_n = 120$ kPa, CNL test on loose sand ($I_{D0} \approx 30\%$) with rough plate

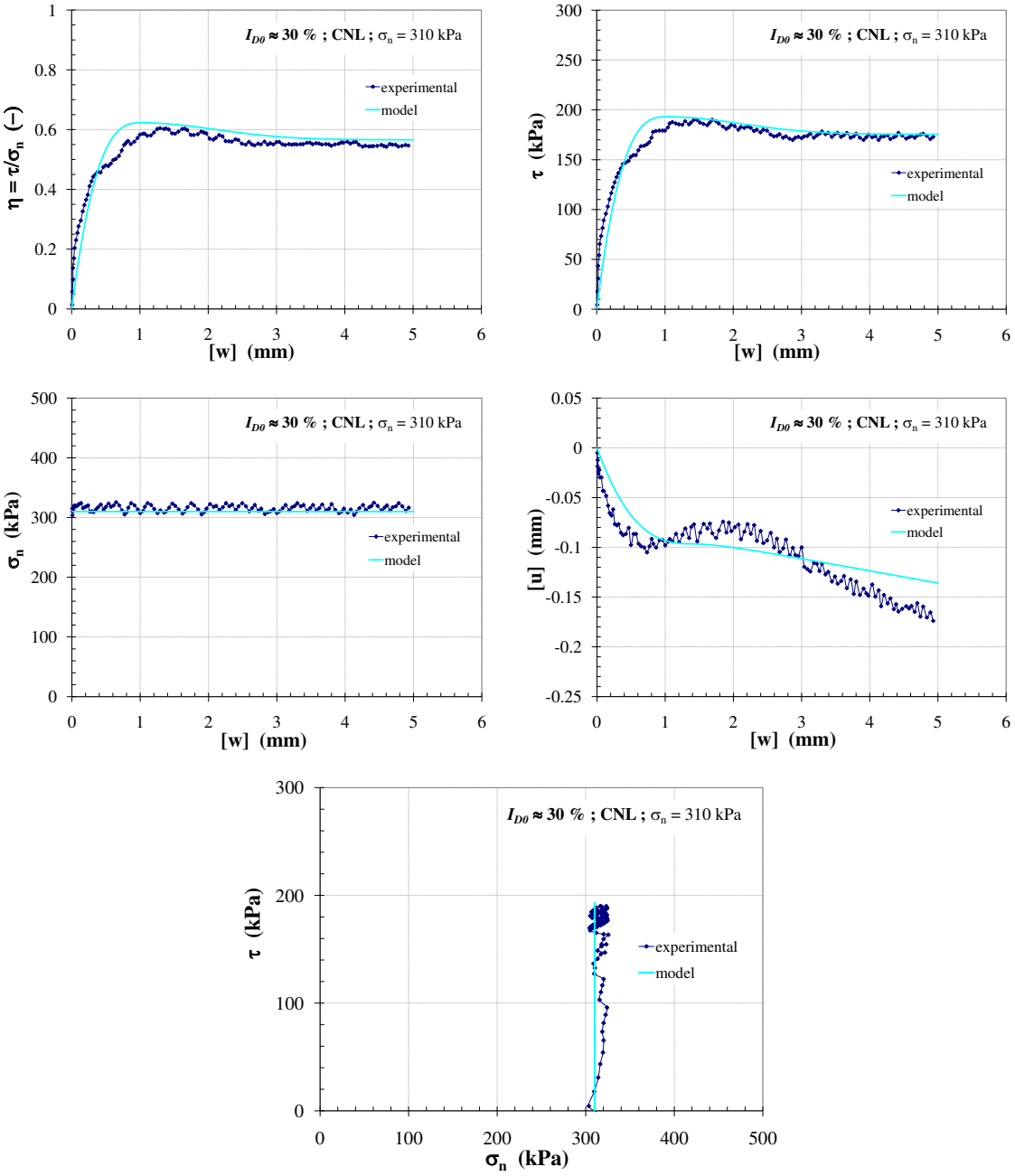

Figure B.3: Comparison between experimental data and the model prediction, $\sigma_n = 310$ kPa, CNL test on loose sand ($I_{D0} \approx 30\%$) with rough plate

B.2 Monotonic CNL tests on dense sand ($I_{D0} \approx 90\%$)

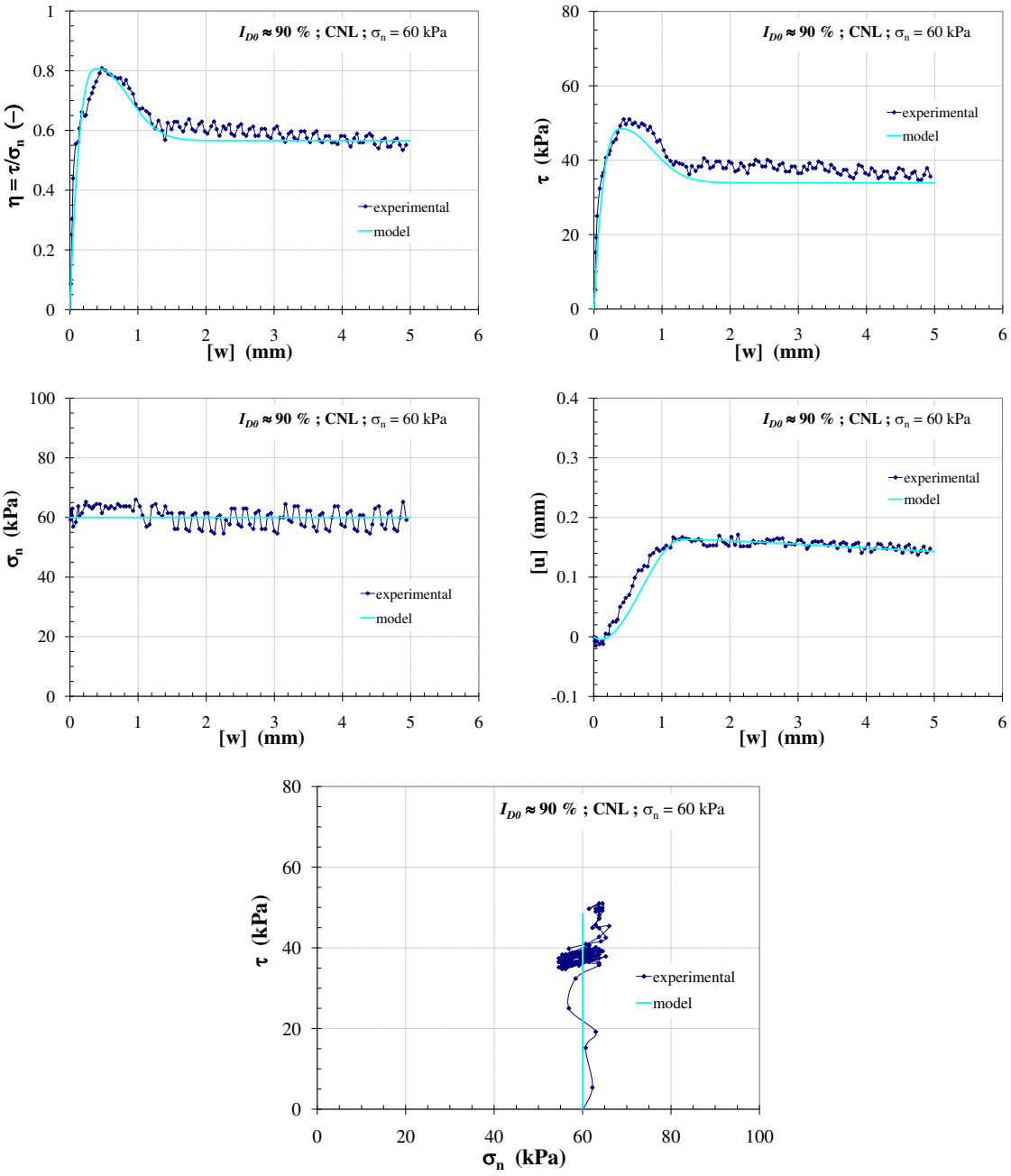

Figure B.4: Comparison between experimental data and the model prediction, $\sigma_n = 60$ kPa, CNL test on dense sand ($I_{D0} \approx 90\%$) with rough plate

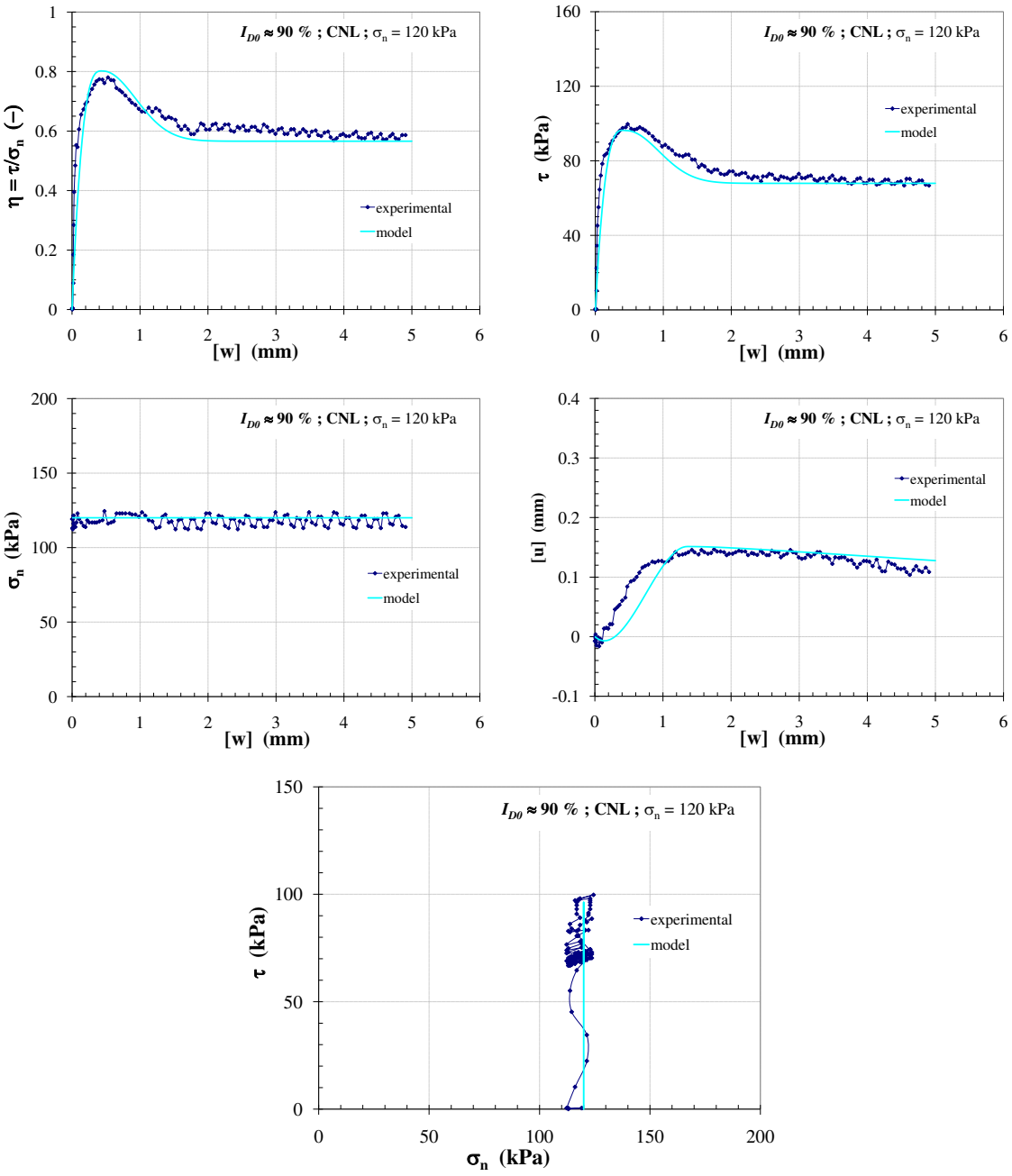

Figure B.5: Comparison between experimental data and the model prediction, $\sigma_n = 120$ kPa, CNL test on dense sand ($I_{D0} \approx 90\%$) with rough plate

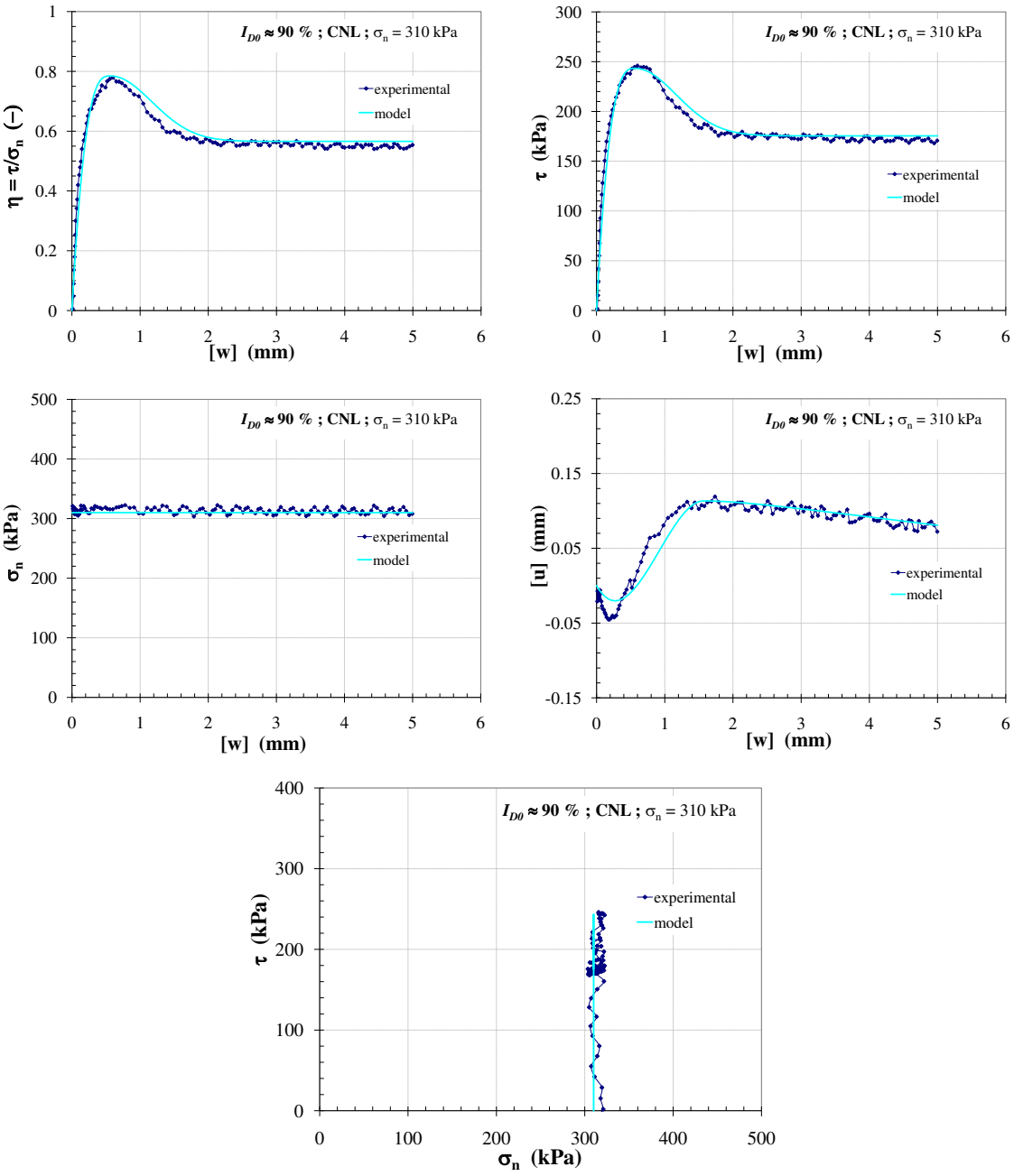

Figure B.6: Comparison between experimental data and the model prediction, $\sigma_n = 310$ kPa, CNL test on dense sand ($I_{D0} \approx 90\%$) with rough plate

B.3 Monotonic CNS tests on loose sand ($I_{D0} \approx 30\%$)

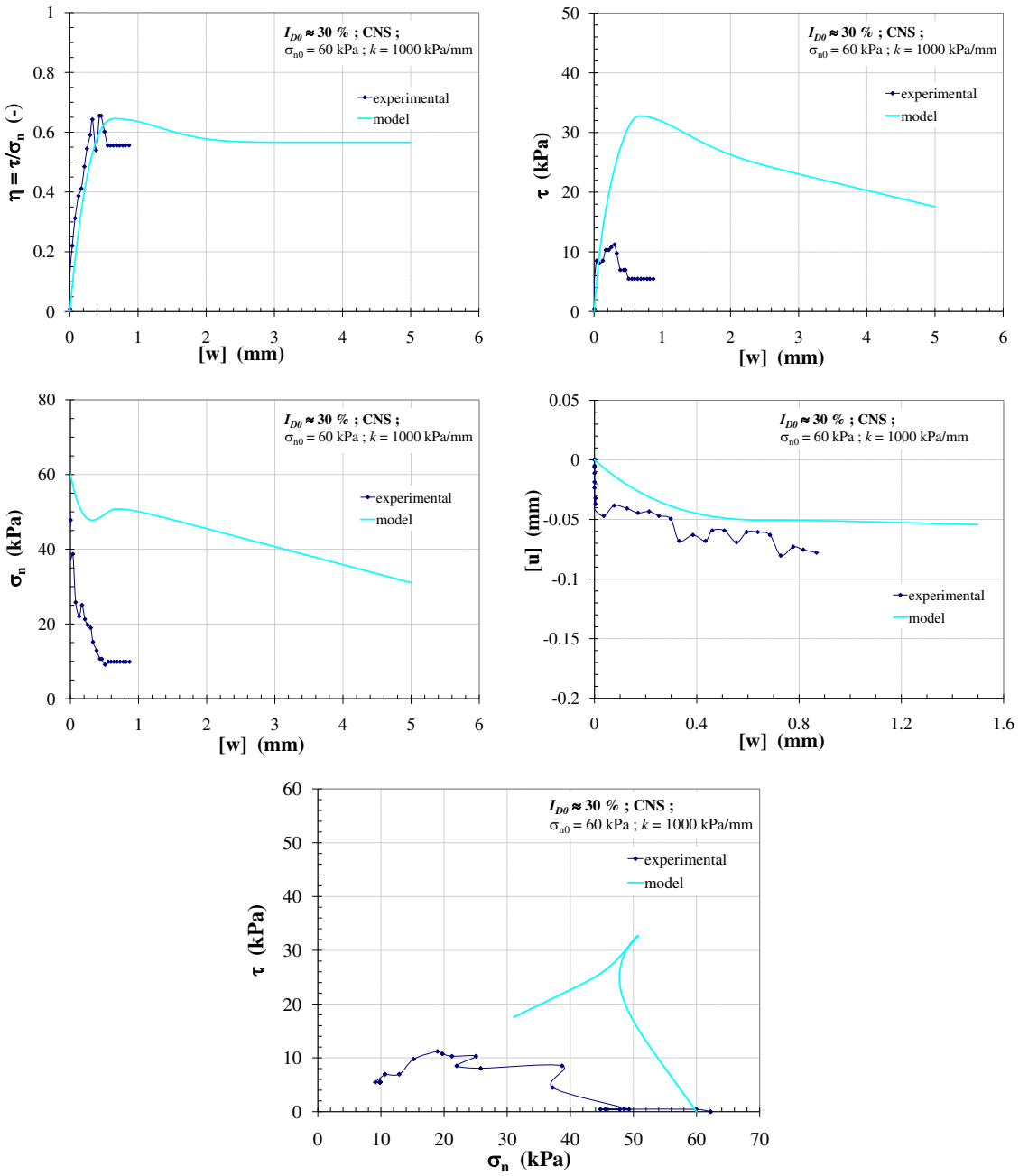

Figure B.7: Comparison between experimental data and the model prediction, $\sigma_{n0} = 60$ kPa, CNS ($k = 1000$ kPa/mm) test on loose sand ($I_{D0} \approx 30\%$) with rough plate

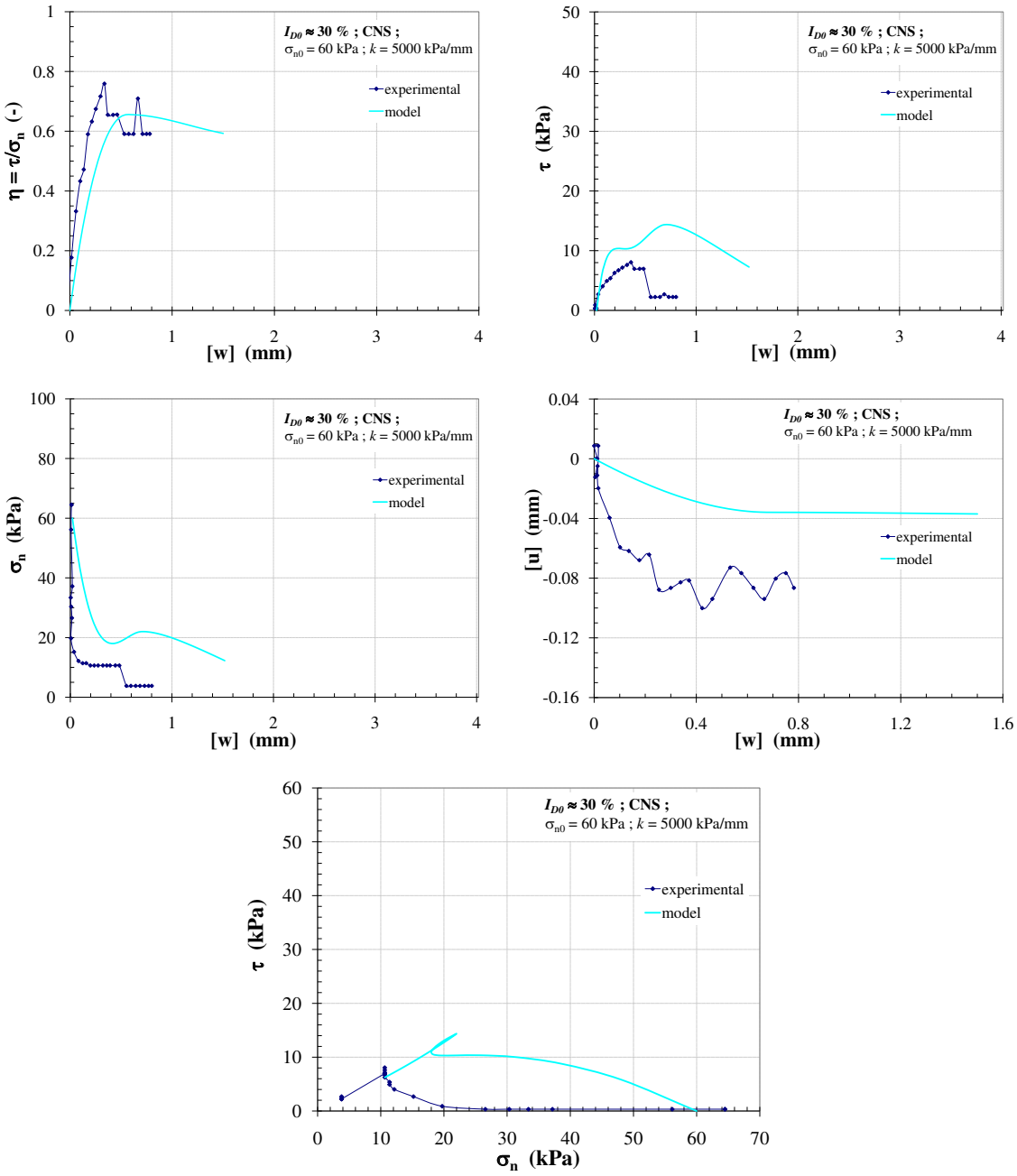

Figure B.8: Comparison between experimental data and the model prediction, $\sigma_{n0} = 60$ kPa, CNS ($k = 5000$ kPa/mm) test on loose sand ($I_{D0} \approx 30\%$) with rough plate

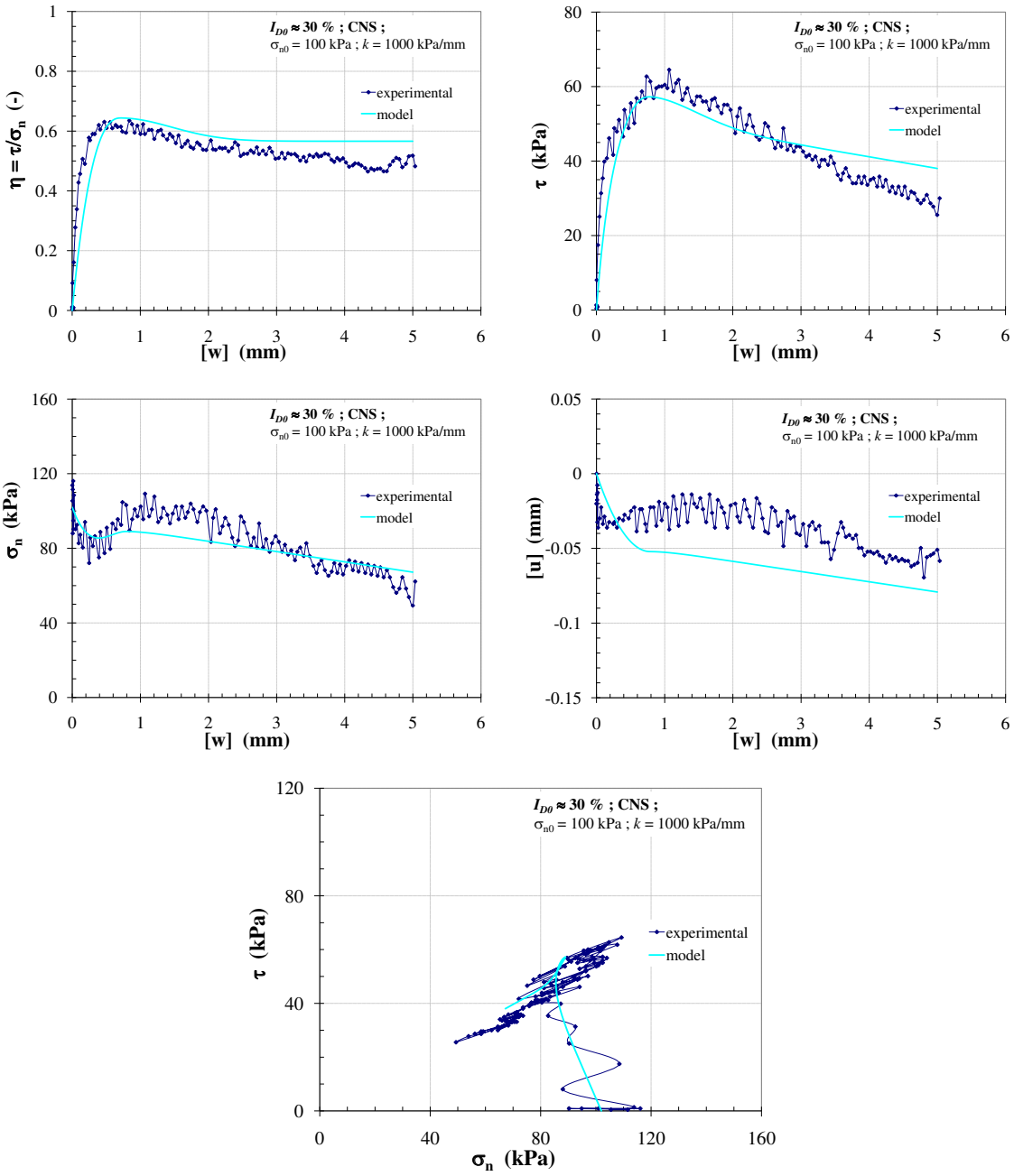

Figure B.9: Comparison between experimental data and the model prediction, $\sigma_{n0} = 100$ kPa, CNS ($k = 1000$ kPa/mm) test on loose sand ($I_{D0} \approx 30\%$) with rough plate

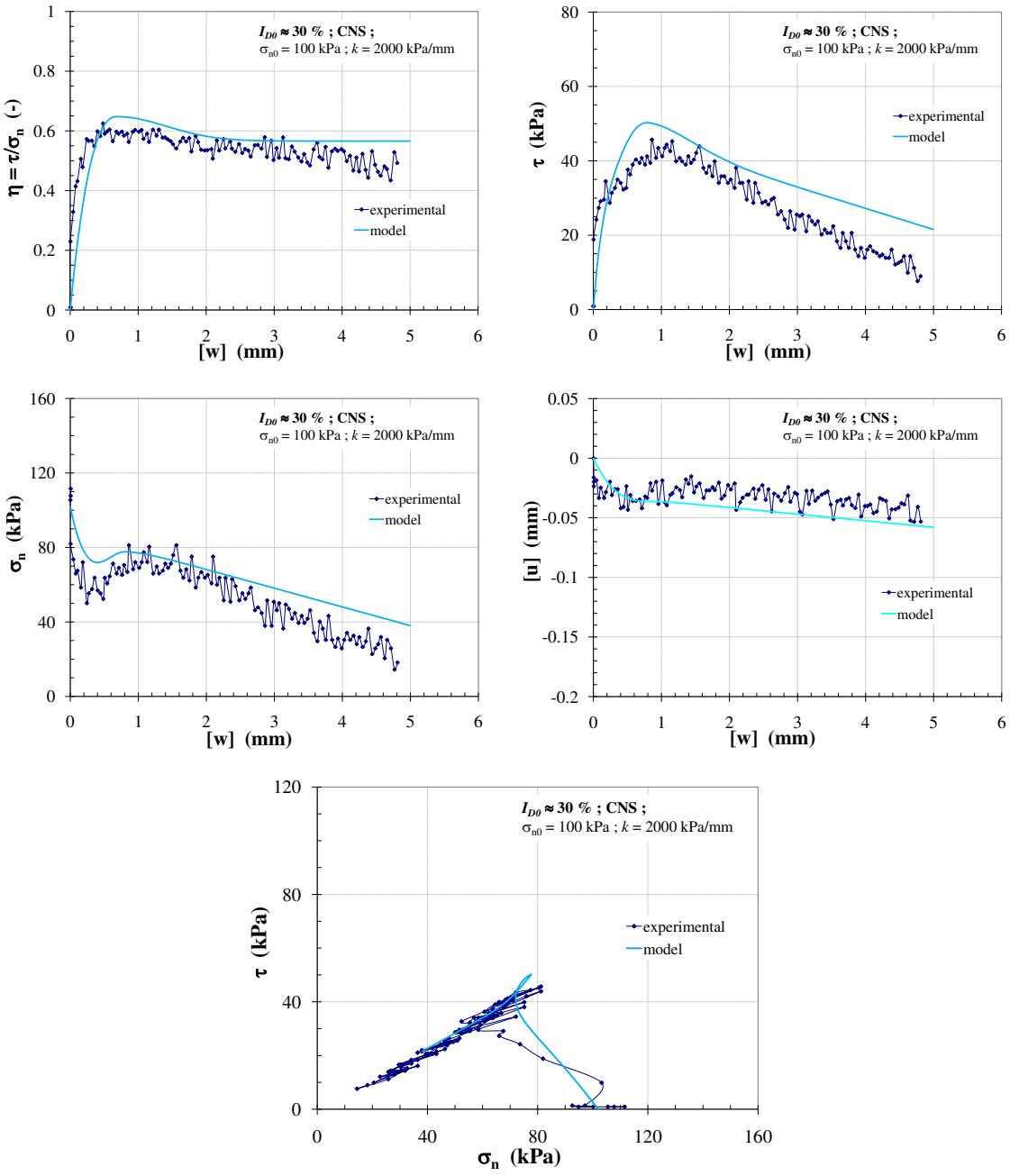

Figure B.10: Comparison between experimental data and the model prediction, $\sigma_{n0} = 100$ kPa, CNS ($k = 2000$ kPa/mm) test on loose sand ($I_{D0} \approx 30\%$) with rough plate

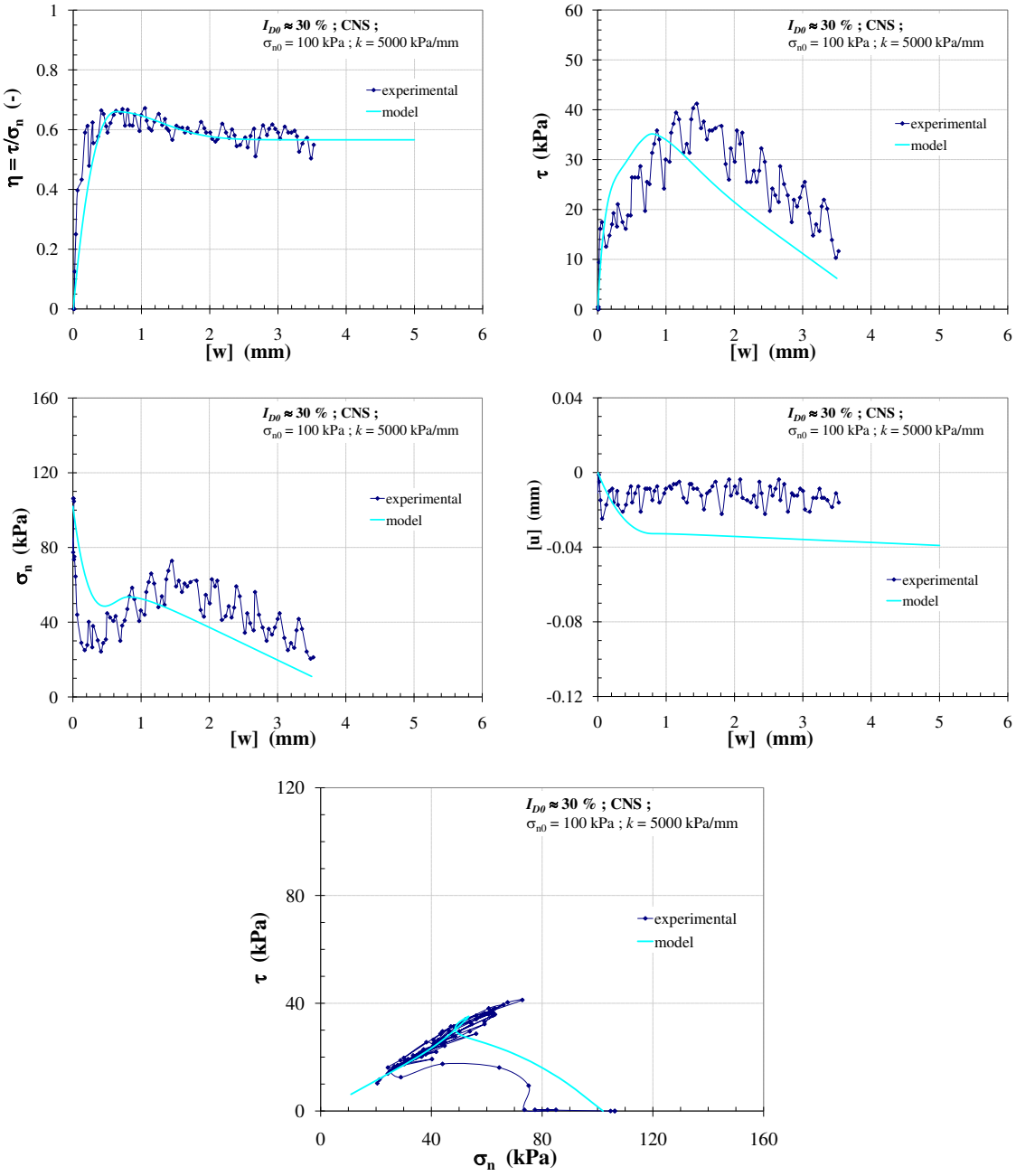

Figure B.11: Comparison between experimental data and the model prediction, $\sigma_{n0} = 100$ kPa, CNS ($k = 5000$ kPa/mm) test on loose sand ($I_{D0} \approx 30\%$) with rough plate

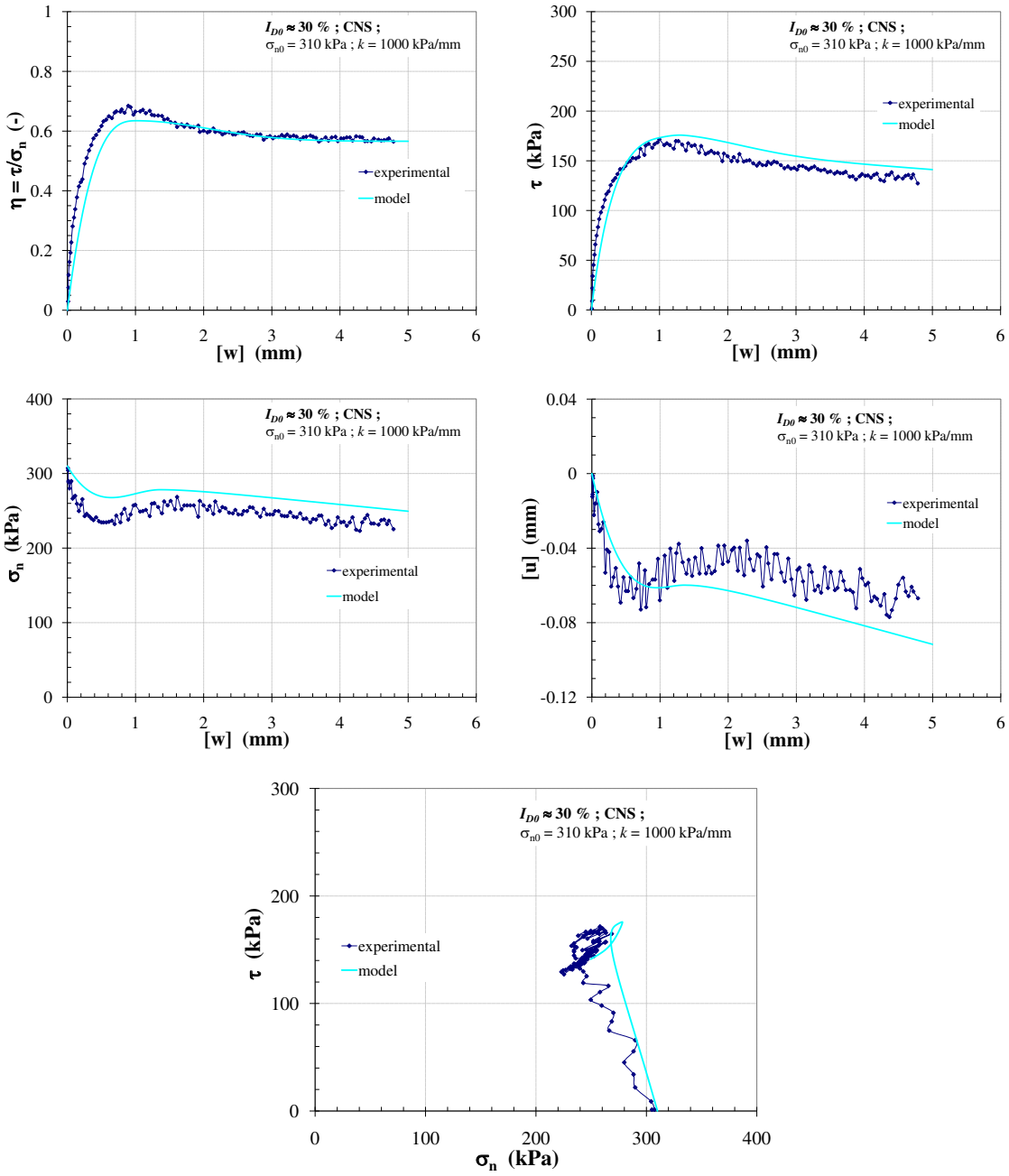

Figure B.12: Comparison between experimental data and the model prediction, $\sigma_{n0} = 310$ kPa, CNS ($k = 1000$ kPa/mm) test on loose sand ($I_{D0} \approx 30\%$) with rough plate

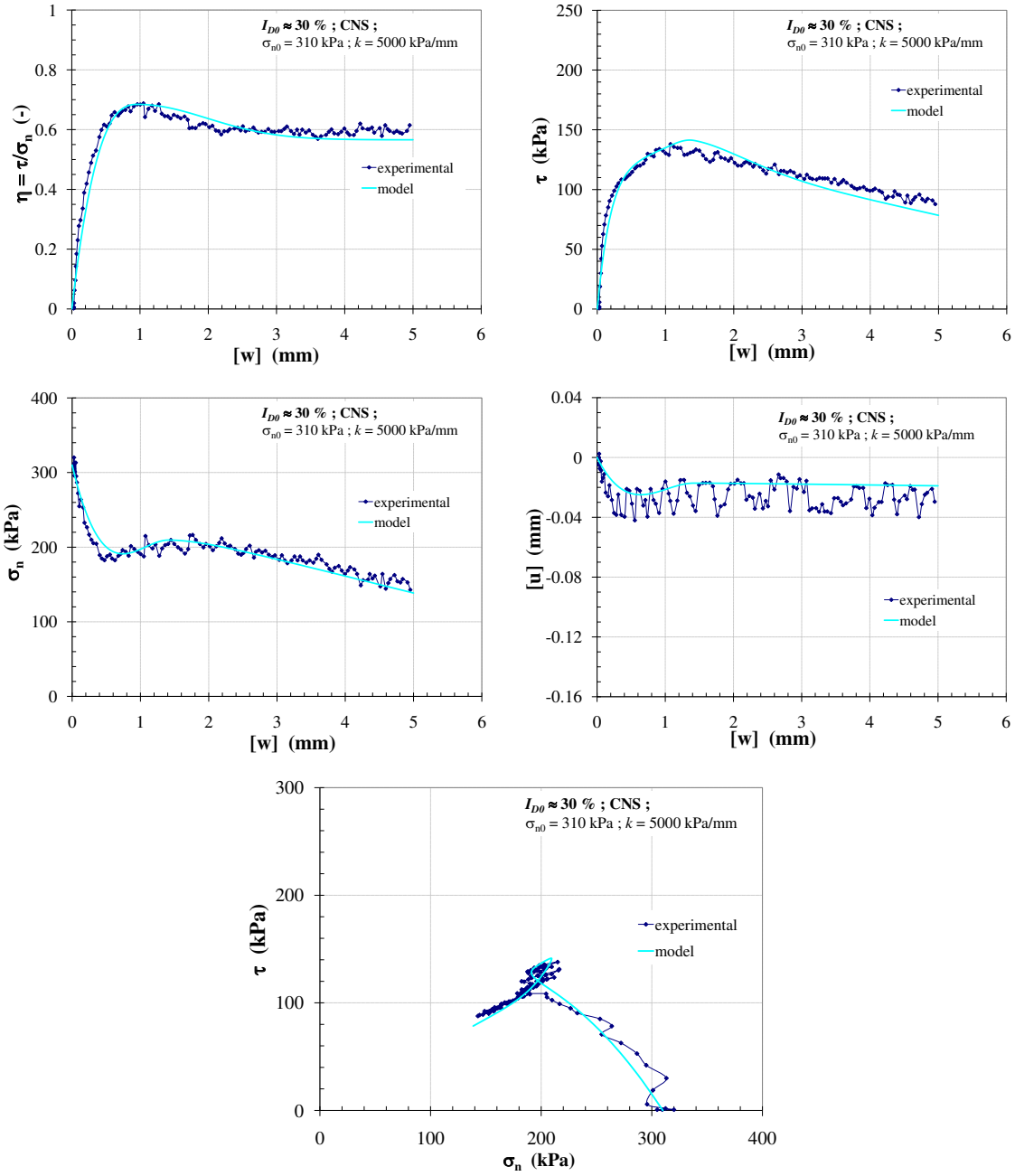

Figure B.13: Comparison between experimental data and the model prediction, $\sigma_{n0} = 310$ kPa, CNS ($k = 5000$ kPa/mm) test on loose sand ($I_{D0} \approx 30\%$) with rough plate

B.4 Monotonic CNS tests on dense sand ($I_{D0} \approx 90\%$)

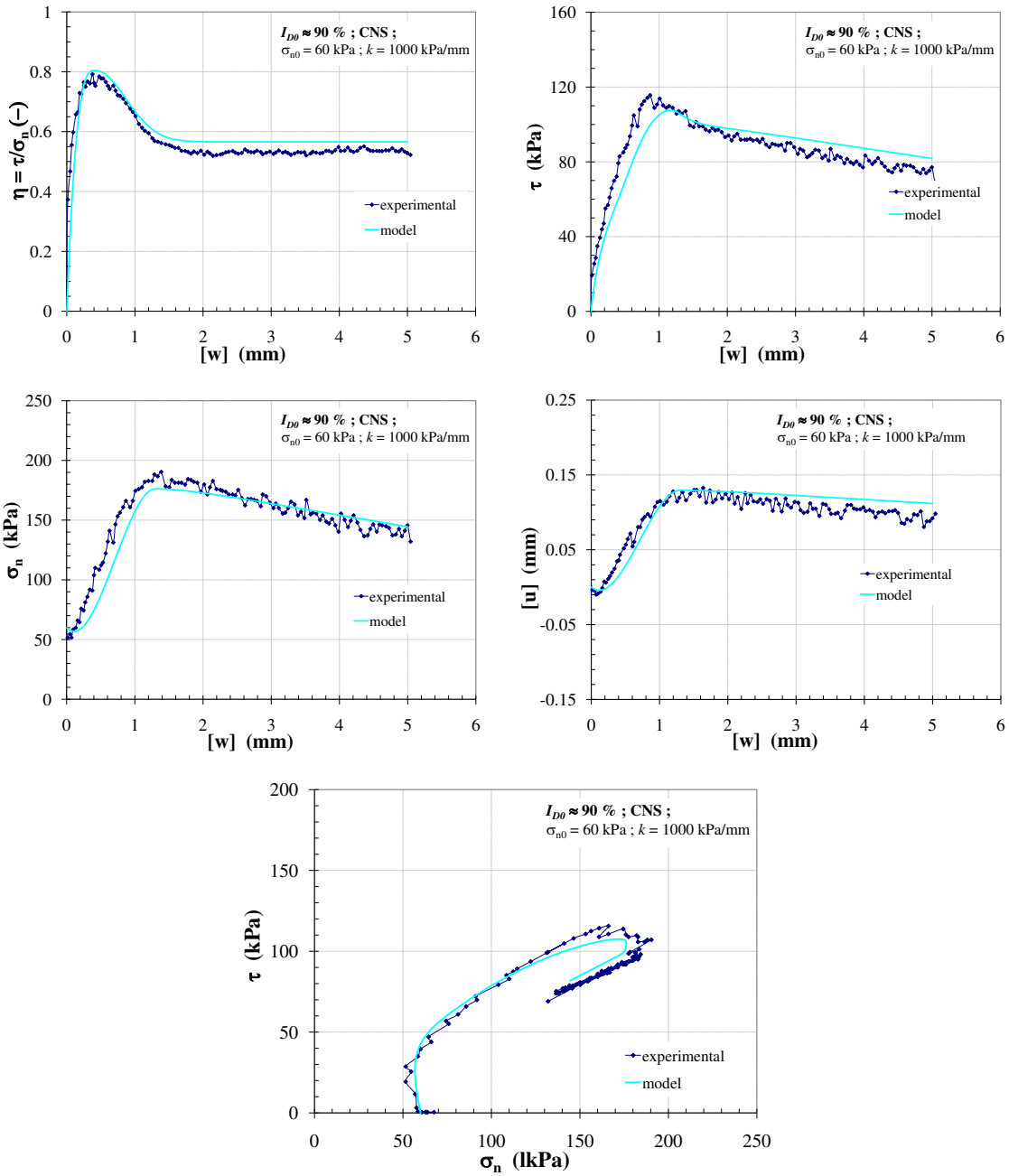

Figure B.14: Comparison between experimental data and the model prediction, $\sigma_{n0} = 60$ kPa, CNS ($k = 1000$ kPa/mm) test on dense sand ($I_{D0} \approx 90\%$) with rough plate

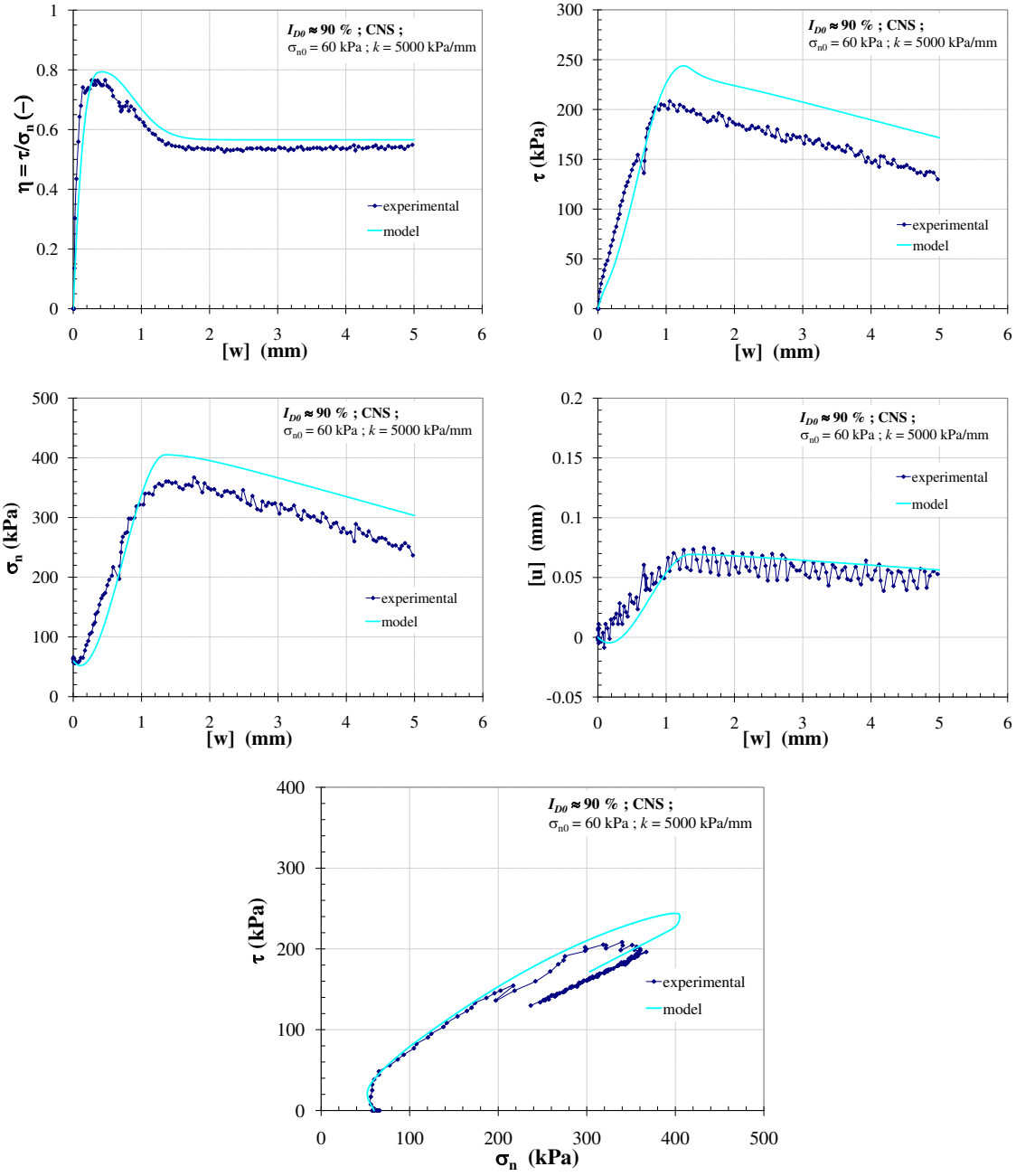

Figure B.15: Comparison between experimental data and the model prediction, $\sigma_{n0} = 60$ kPa, CNS ($k = 5000$ kPa/mm) test on dense sand ($I_{D0} \approx 90\%$) with rough plate

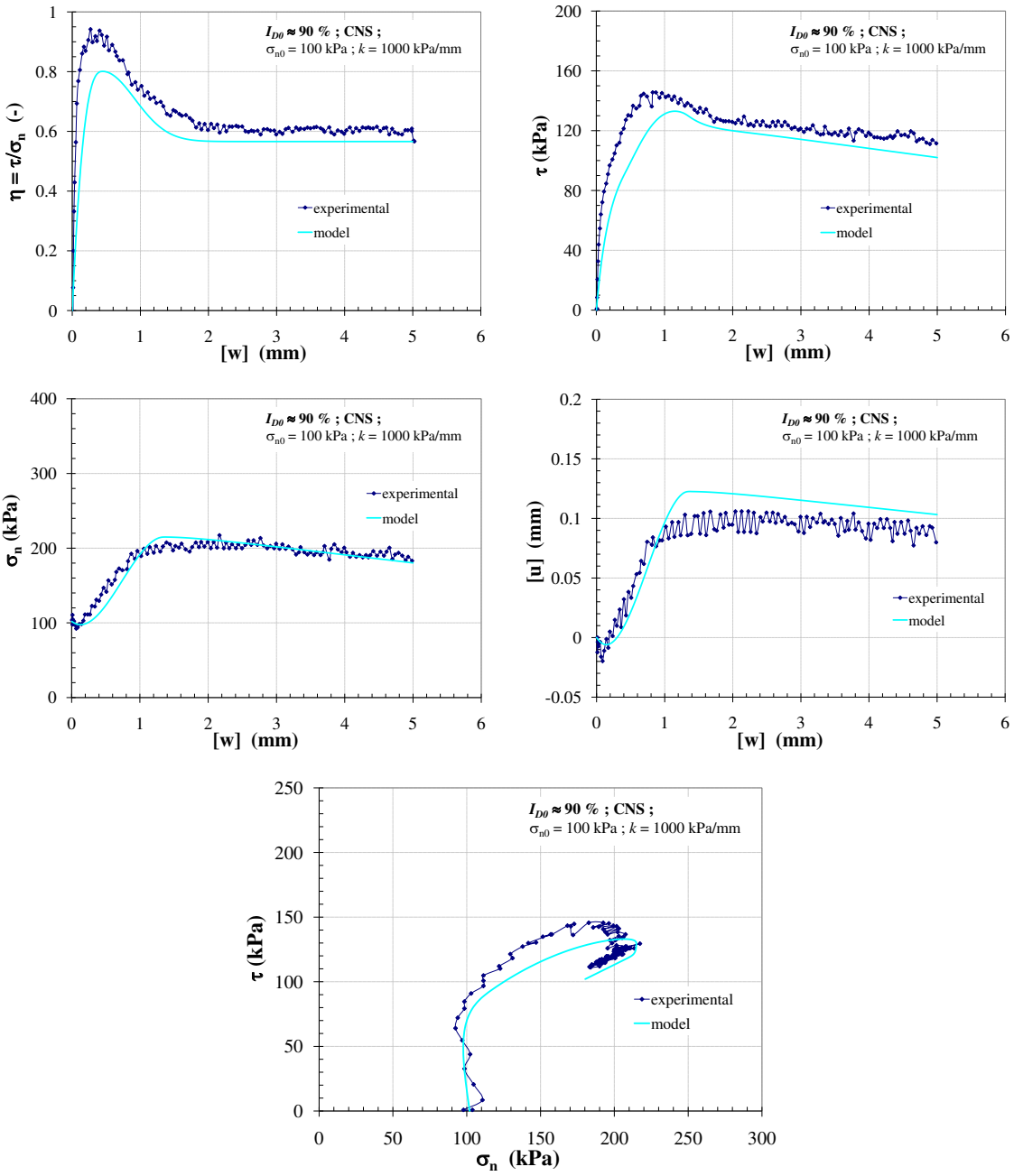

Figure B.16: Comparison between experimental data and the model prediction, $\sigma_{n0} = 100$ kPa, CNS ($k = 1000$ kPa/mm) test on dense sand ($I_{D0} \approx 90\%$) with rough plate

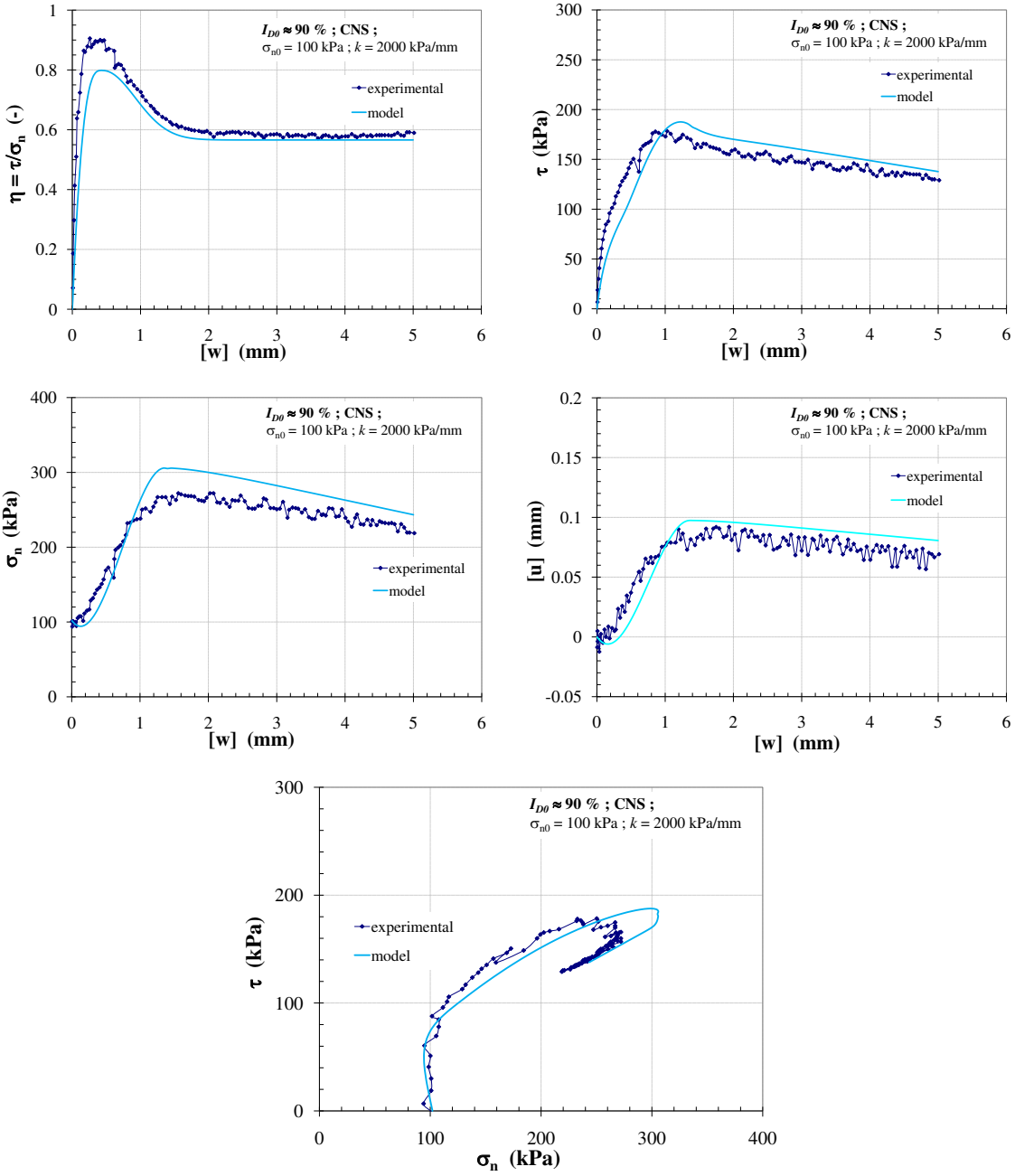

Figure B.17: Comparison between experimental data and the model prediction, $\sigma_{n0} = 100$ kPa, CNS ($k = 2000$ kPa/mm) test on dense sand ($I_{D0} \approx 90\%$) with rough plate

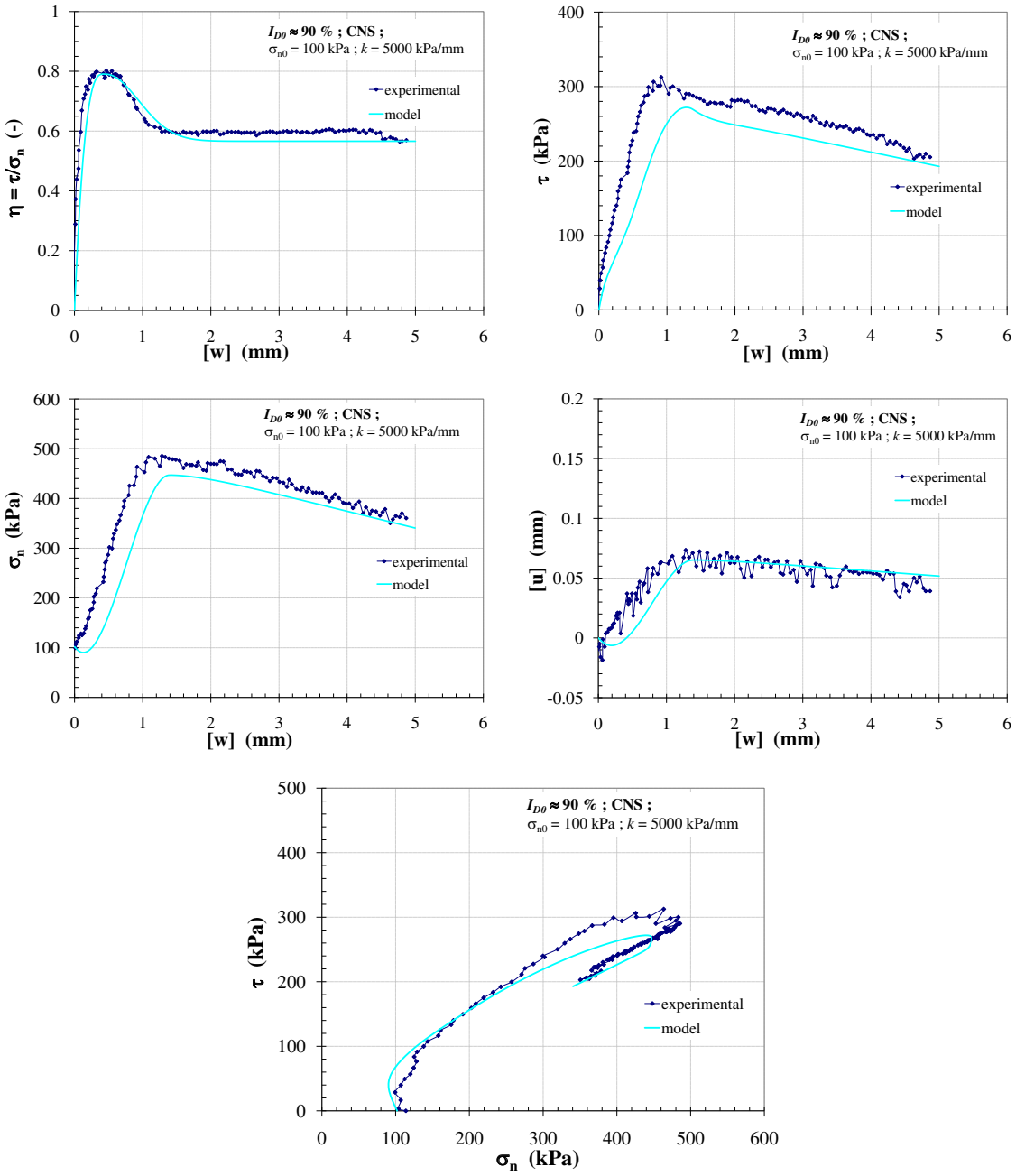

Figure B.18: Comparison between experimental data and the model prediction, $\sigma_{n0} = 100$ kPa, CNS ($k = 5000$ kPa/mm) test on dense sand ($I_{D0} \approx 90\%$) with rough plate

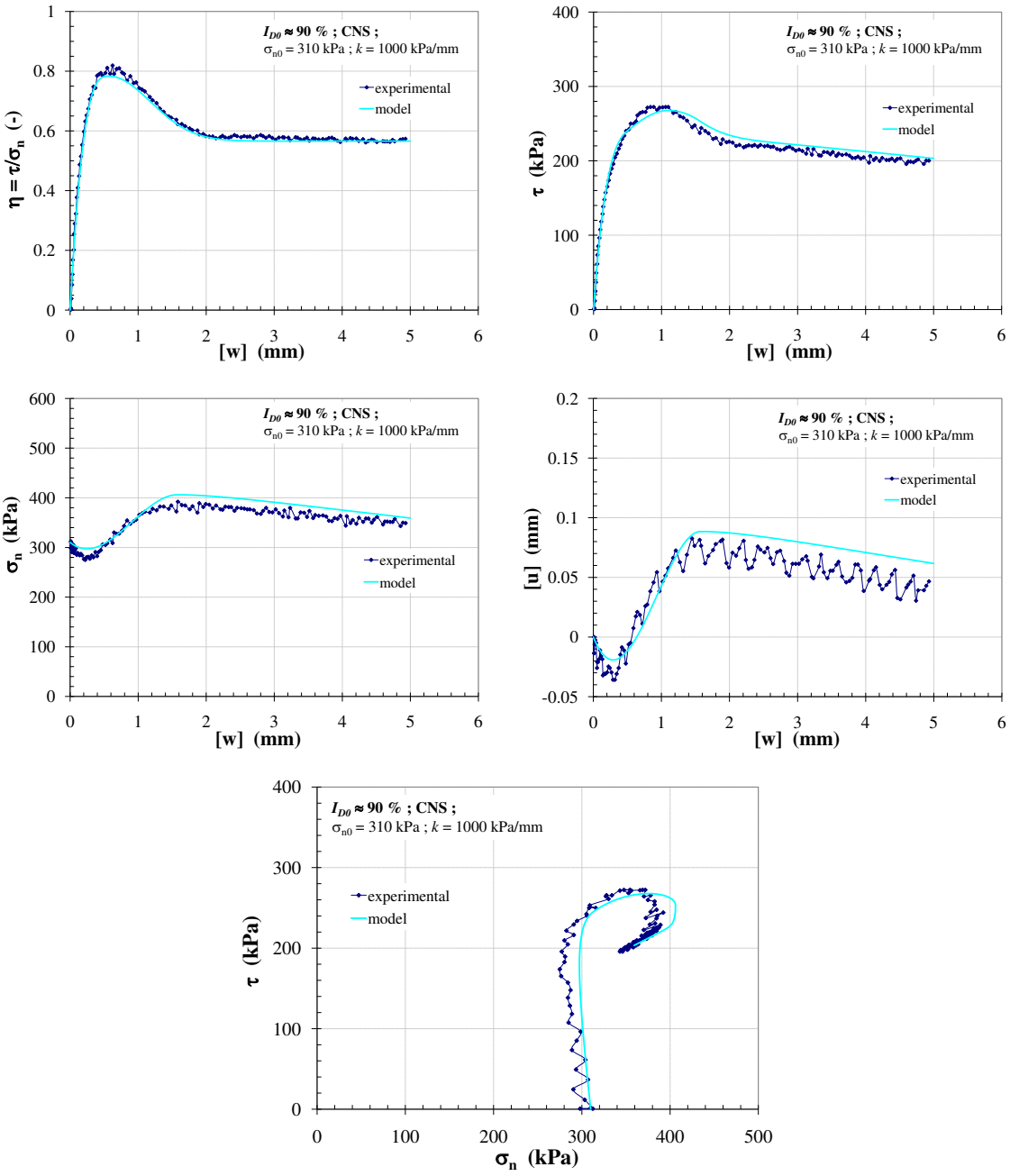

Figure B.19: Comparison between experimental data and the model prediction, $\sigma_{n0} = 310$ kPa, CNS ($k = 1000$ kPa/mm) test on dense sand ($I_{D0} \approx 90\%$) with rough plate

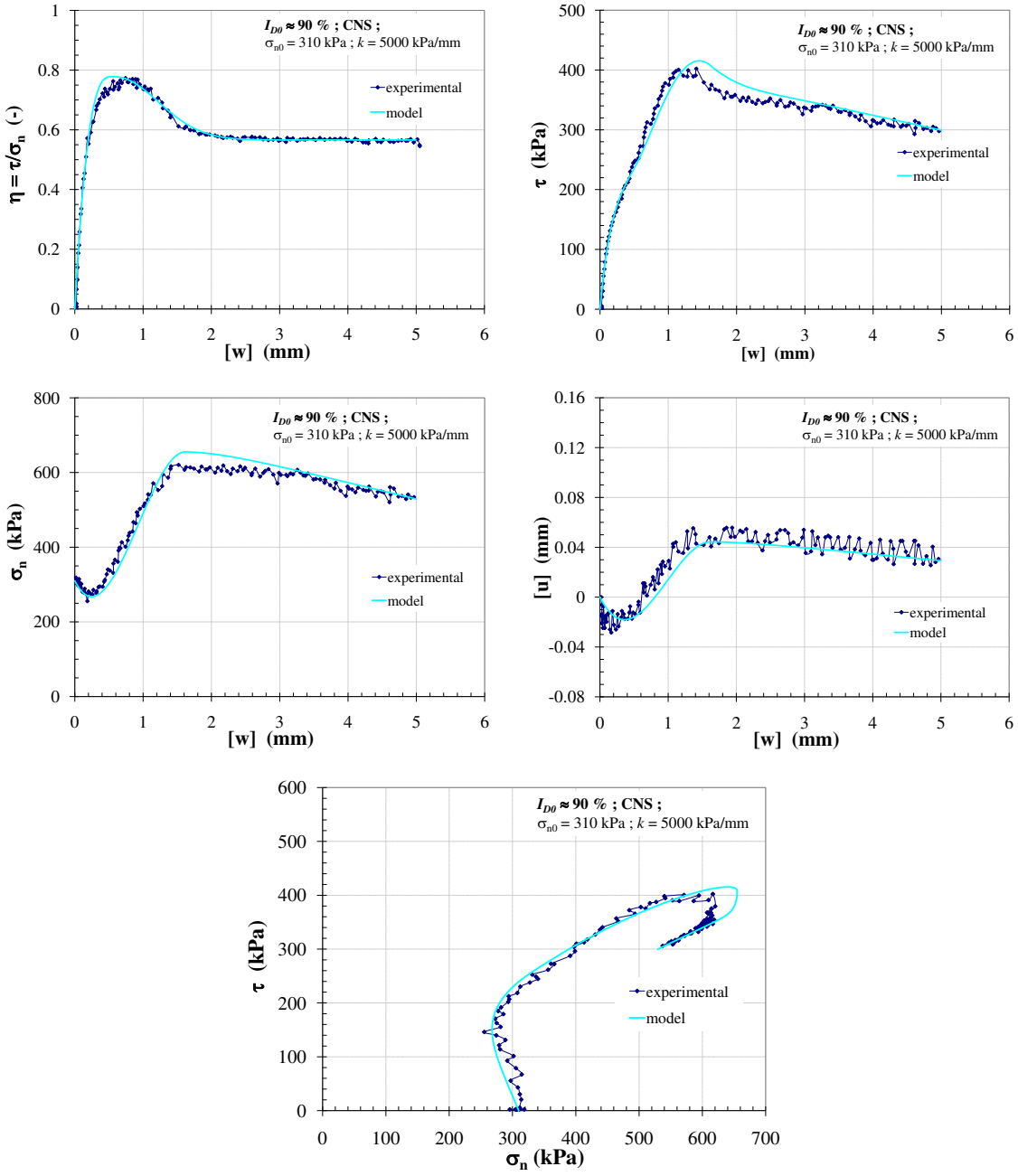

Figure B.20: Comparison between experimental data and the model prediction, $\sigma_{n0} = 310$ kPa, CNS ($k = 5000$ kPa/mm) test on dense sand ($I_{D0} \approx 90\%$) with rough plate

Appendix C

Cyclic interface models

C.1 Constitutive interpolations

- Term of W_c, "contraction" : 5 conditions are described as:
  - 1^{st} condition: for $\eta_{\text{cm}} = 0 \rightarrow W_c = \bar{a}$ with $0 < \bar{a} < 1$ (contacting for $\eta_{\text{cm}} = 0$)
  - 2^{nd} condition: for $|\eta_{\text{cm}}| = \eta_* \rightarrow W_c = 1$
  - 3^{rd} condition: for $|\eta_{\text{cm}}| = \eta_{\text{peak}} \rightarrow W_c = 0$
  - 4^{th} condition: for For $|\eta_{\text{cm}}| = \eta_* \rightarrow W_c' = 1$
  - 5^{th} condition: for $|\eta_{\text{cm}}| = \eta_{\text{peak}} \rightarrow W_c' = 0$

W_c is expressed as a polynomial function of degree 4 in η_{cm},

$$W_c = a + b\,|\eta_{\text{cm}}| + c\eta_{\text{cm}}^2 + d\,\left|\eta_{\text{cm}}^3\right| + e\eta_{\text{cm}}^4 \tag{C.1}$$

The first condition gives $a = \bar{a}$.

In case of $W_c' = 0$, the 4^{th} and 5^{th} conditions require the multiplicative factors $(|\eta_{\text{cm}}| - \eta_*)$ and $(|\eta_{\text{cm}}| - \eta_{\text{cm}})$ with the power ≥ 1, in W_c'. Therefore, W_c' is given as:

$$W_c' = (|\eta_{\text{cm}}| - \eta_{\text{peak}})(|\eta_{\text{cm}}| - \eta_{\text{peak}})(e\,|\eta_{\text{cm}}| + f) \tag{C.2}$$

And by integrating;

$$\begin{aligned} W_c = {} & \frac{e}{4}\eta_{\text{cm}}^4 + \frac{\left|\eta_{\text{cm}}^3\right|}{3}\left(f + e\left(\eta_{\text{peak}} + \eta_*\right)\right) \\ & + \frac{\eta_{\text{cm}}^2}{2}\left(e\eta_{\text{peak}}\eta_* - f\left(\eta_{\text{peak}} + \eta_*\right)\right) + \eta_{\text{cm}} f \eta_{\text{peak}}\eta_* \end{aligned} \tag{C.3}$$

With the 2^{nd} and 3^{rd} conditions, the parameters e and f are expressed as:

$$e = \frac{4}{(\eta_{\text{peak}} - \eta_*)^3} \left[\frac{(1-\bar{a})(3\eta_* - \eta_{\text{peak}})}{\eta_*^2} + \frac{\bar{a}(3\eta_{\text{peak}} - \eta_*)}{\eta_{\text{peak}}^2} \right] \tag{C.4}$$

$$f = -\frac{2}{(\eta_{\text{peak}} - \eta_*)^3} \left[\frac{(1-\bar{a})\eta_{\text{peak}}(2\eta_* - \eta_{\text{peak}})}{\eta_*^2} + \frac{\bar{a}\eta_*(2\eta_* - \eta_{\text{peak}})}{\eta_{\text{peak}}^2} \right] \tag{C.5}$$

- Term of W_d, "dilation" : the following conditions are described as:
  - 1^{st} condition: for $\eta_{\text{cm}} = 0 \rightarrow W_d = 0$
  - 2^{nd} condition: for $|\eta_{\text{cm}}| = \eta_* \rightarrow W_d = 0$
  - 3^{rd} condition: for $|\eta_{\text{cm}}| = \eta_{\text{peak}} \rightarrow W_d = 1$
  - 4^{th} condition: for $\eta_{\text{cm}} = 0 \rightarrow W_d' = 0$
  - 5^{th} condition: for $|\eta_{\text{cm}}| = \eta_{\text{peak}} \rightarrow W_d' = 0$

W_d is expressed as a polynomial function of degree 4 in η_{cm},

$$W_d = a + b\,|\eta_{\text{cm}}| + c\eta_{\text{cm}}^2 + d\,|\eta_{\text{cm}}^3| + e\eta_{\text{cm}}^4 \tag{C.6}$$

In case of $W_d = 0$ and $W_d' = 0$ for $\eta_{\text{cm}} = 0$, the 1^{st} and 4^{th} conditions require the multiplicative factor η_{cm}^2 in W_d and η_{cm}^2 in W_d.

The 2^{nd} condition requires the multiplicative factor $(|\eta_{\text{cm}}| - \eta_*)$ with the power ≥ 1, in W_d. Therefore, W_d is given as:

$$W_d = e\eta_{\text{cm}}^2\,(|\eta_{\text{cm}} - \eta_*|)\,(|\eta_{\text{cm}}| - f) \tag{C.7}$$

and then

$$W_d' = e(4\,|\eta_{\text{cm}}^3| - 3\eta_{\text{cm}}^2(\eta_* + f) + 2\eta_{\text{cm}}\eta_* f) \tag{C.8}$$

Then the 3^{rd} and 5^{th} conditions can impose

$$f = \eta_{\text{peak}} \frac{4\eta_{\text{peak}} - 3\eta_*}{3\eta_{\text{peak}} - 2\eta_*} \tag{C.9}$$

$$e = -\frac{3\eta_{\text{peak}} - 2\eta_*}{\eta_{\text{peak}}^3(\eta_{\text{peak}} - \eta_*)^2} \tag{C.10}$$

C.2 Correlation between $\eta_{\mathbf{cm}}$ and $\eta_{\mathbf{cm2}}$

Two conditions are defined as the following:

- if $\frac{\eta_{\max}}{\eta_{\text{peak}}}$ is very small $\rightarrow \eta_{\text{cm2}} \approx \eta_{\text{cm}}$
- if $\frac{\eta_{\max}}{\eta_{\text{peak}}} \rightarrow 1$ then $\eta_{\text{cm2}} \rightarrow \eta_{\text{peak}}$

By imposing $x = \frac{\eta_{\max}}{\eta_{\text{peak}}}$, $y = \frac{\eta_{\text{cm2}}}{\eta_{\text{cm}}}$ and $\Delta = \frac{\eta_{\text{peak}}}{\eta_{\text{cm}}} - 1$. The conditions for defining the correction (see Figure C.1) are:

1. $y = 1$ for $x = 0$
2. $y = 1 + \Delta$ for $x = 1$
3. $y' = 0$ for $x = 0$
4. $y' = 0$ for $x = 1$

   In addition, it turns out that y has to be forced close to unity for the low values of x. This is achieved by imposing an additional condition:

5. $y = 1 + \Delta/3$ for $x = 2/3$

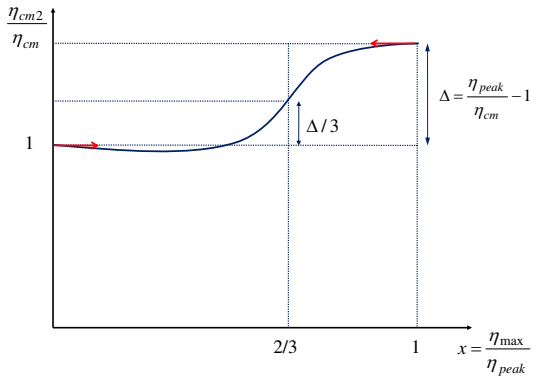

Figure C.1: Amplifying η_{cm} in a controlled manner, η_{cm2} in the direction of η_{peak}

Finally, the interpolation consists of a polynomial of degree 4 (for 5 conditions):

$$y = -\frac{33}{4}\Delta x^4 + \frac{29}{2}\Delta x^3 - \frac{21}{4}\Delta x^2 + 1 \tag{C.11}$$

or

$$\eta_{\mathrm{cm2}} = \eta_{\mathrm{cm}} + (\eta_{\mathrm{peak}} - \eta_{\mathrm{cm}}) \left[-\frac{33}{4} \left(\frac{\eta_{\mathrm{max}}}{\eta_{\mathrm{peak}}} \right)^4 + \frac{29}{2} \left(\frac{\eta_{\mathrm{max}}}{\eta_{\mathrm{peak}}} \right)^3 - \frac{21}{4} \left(\frac{\eta_{\mathrm{max}}}{\eta_{\mathrm{peak}}} \right)^2 \right] \tag{C.12}$$

C.3 Curve of $p_{\mathbf{max}}(\Delta\eta)$

To express the maximum of the hyperbolic function with oblique asymptote, let $p = y$ and $\Delta\eta = x$ and the function is expressed as

$$y = ax + b + \frac{\alpha}{c - x} \tag{C.13}$$

where $c < 0$, and $\alpha = -bc$ for $x = 0$ and $y = 0$ (see Figure C.2).

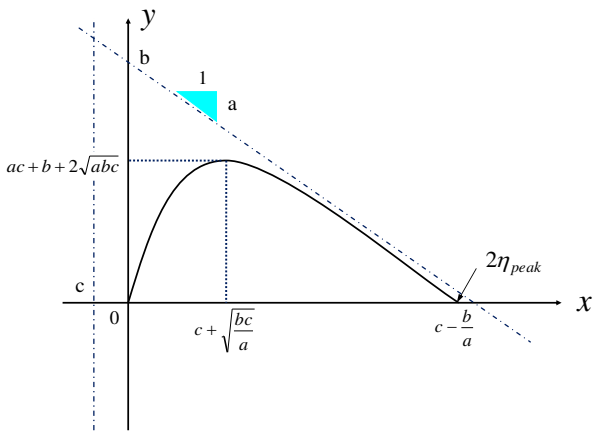

Figure C.2: Limit of $p_{\mathrm{max}}(\Delta\eta)$ for a given $|\eta_{\mathrm{cm}}|$

Then, the above expression can be rewritten as:

$$y = ax + b - \frac{bc}{c - x} \tag{C.14}$$

with the conditions, $y = 0$ for $x = \beta$ and $y' = 0$ for $x = \delta$.

Then β corresponds to $2\eta_{\mathrm{peak}}$ and δ corresponds to p_{max}

$$\beta = c - \frac{b}{a} \tag{C.15a}$$

$$\delta = c + \sqrt{\frac{bc}{a}} \tag{C.15b}$$

To represent the the hyperbolic function of $p_{\max}(\Delta\eta)$, δ is chosen to substitute x in C.14:

$$y = a\left(c + \sqrt{\frac{bc}{a}}\right) + b + \frac{bc}{\sqrt{\frac{bc}{a}}} \tag{C.16}$$

Finally, the hyperbolic function with oblique asymptote is

$$y = ac + b + 2\sqrt{abc} \tag{C.17}$$

A parabola passing through the origin and having its vertex on $p_{\max}(\Delta\eta)$ is proposed as:

$$p(\Delta\eta), |\eta_{\rm cm}|) = \alpha(\Delta\eta)^2 + \beta\Delta\eta + \gamma \tag{C.18}$$

when

- passing the origin $\rightarrow \gamma = 0$
- passing the vertex $(k) \rightarrow p_{\max}(\Delta\eta_{\max})$

and then this parabola can be written as

$$p_{\max} = \alpha\Delta\eta_{\max}^2 + \beta\Delta\eta_{\max} \tag{C.19}$$

The derivative of C.17 as

$$\frac{dp}{d(\Delta\eta)} = 2\alpha\Delta\eta + \beta \tag{C.20}$$

then gives α and β as the following

$$\alpha = -\frac{p_{\max}}{\Delta\eta_{\max}^2} \tag{C.21a}$$

$$\beta = 2\frac{p_{\max}}{\Delta\eta_{\max}} \tag{C.21b}$$

Finally, function of p $(\Delta\eta)$, $|\eta_{\rm cm}|)$ can be expressed as:

$$p = -\frac{p_{\max}}{\Delta\eta_{\max}^2} \cdot \Delta\eta^2 + 2\frac{p_{\max}}{\Delta\eta_{\max}} \cdot \Delta\eta \tag{C.22}$$

or it can be rewritten

$$p = p_{\max} \cdot \frac{\Delta\eta}{\Delta\eta_{\max}}\left(2 - \frac{\Delta\eta}{\Delta\eta_{\max}}\right) \tag{C.23}$$

Appendix D

Cyclic CNL tests

D.1 Cyclic CNL tests on loose sand ($I_{D0} \approx 30\%$) with rough plate

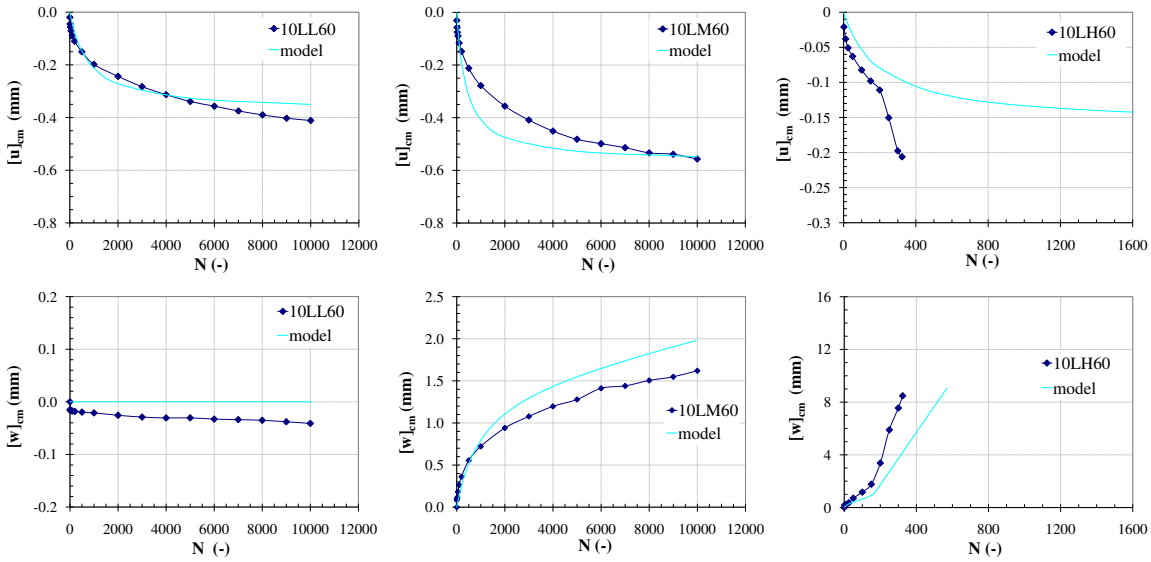

Figure D.1: Comparison between experimental data and the model prediction, $\sigma_n = 60$ kPa, $\Delta\tau = 10$ kPa

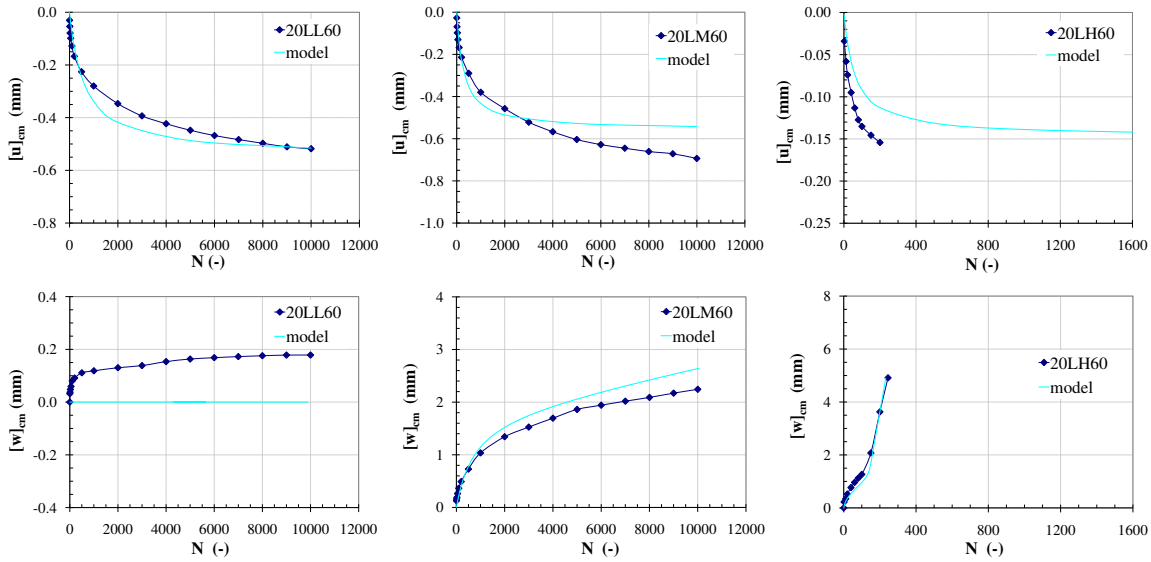

Figure D.2: Comparison between experimental data and the model prediction, $\sigma_n = 60$ kPa, $\Delta\tau = 20$ kPa

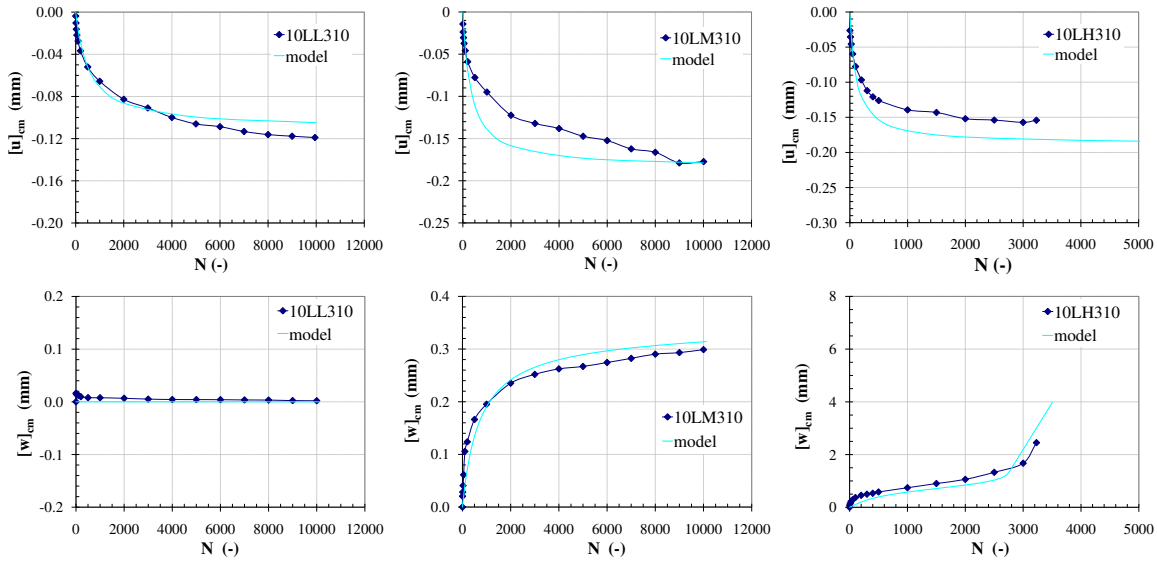

Figure D.3: Comparison between experimental data and the model prediction, $\sigma_n = 310$ kPa, $\Delta\tau = 10$ kPa

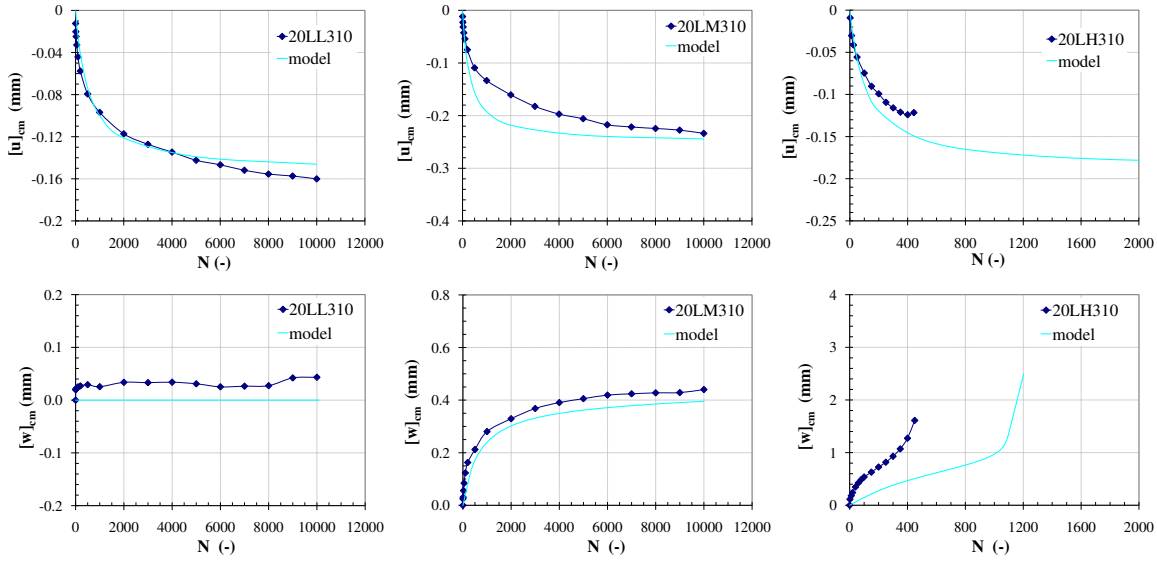

Figure D.4: Comparison between experimental data and the model prediction, $\sigma_n = 310$ kPa, $\Delta\tau = 20$ kPa

D.2 Cyclic CNL tests on dense sand ($I_{D0} \approx 90\%$) with rough plate

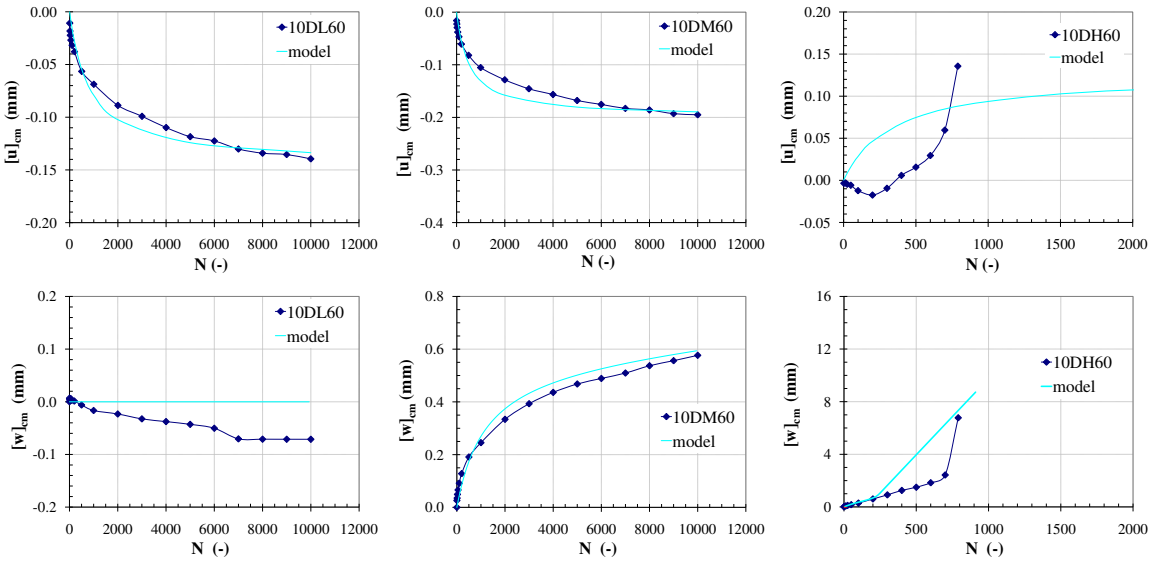

Figure D.5: Comparison between experimental data and the model prediction, $\sigma_n = 60$ kPa, $\Delta\tau = 10$ kPa

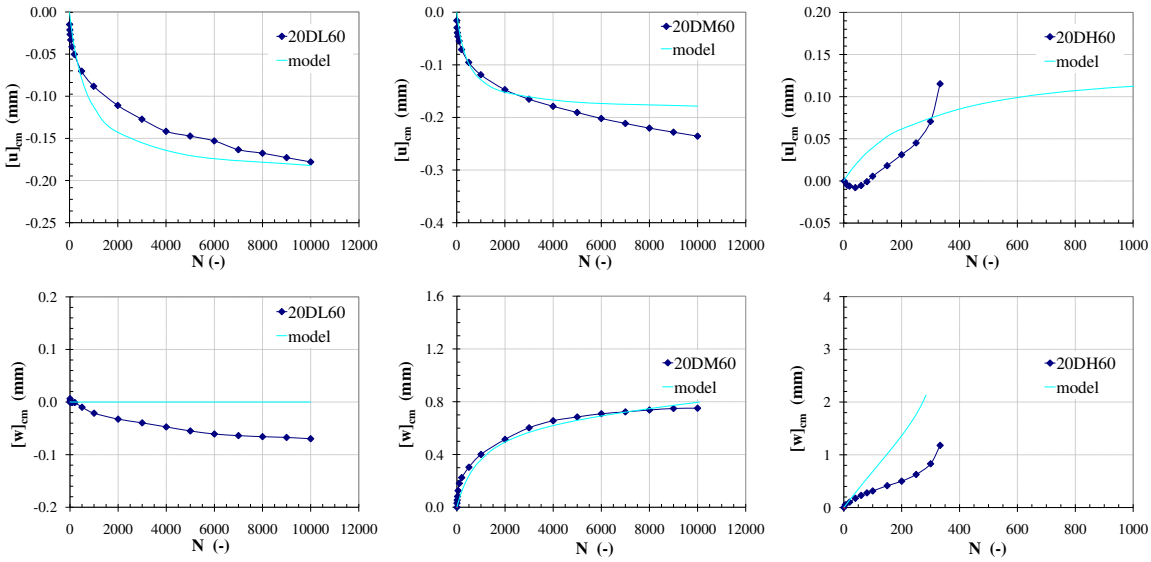

Figure D.6: Comparison between experimental data and the model prediction, $\sigma_n = 60$ kPa, $\Delta\tau = 20$ kPa

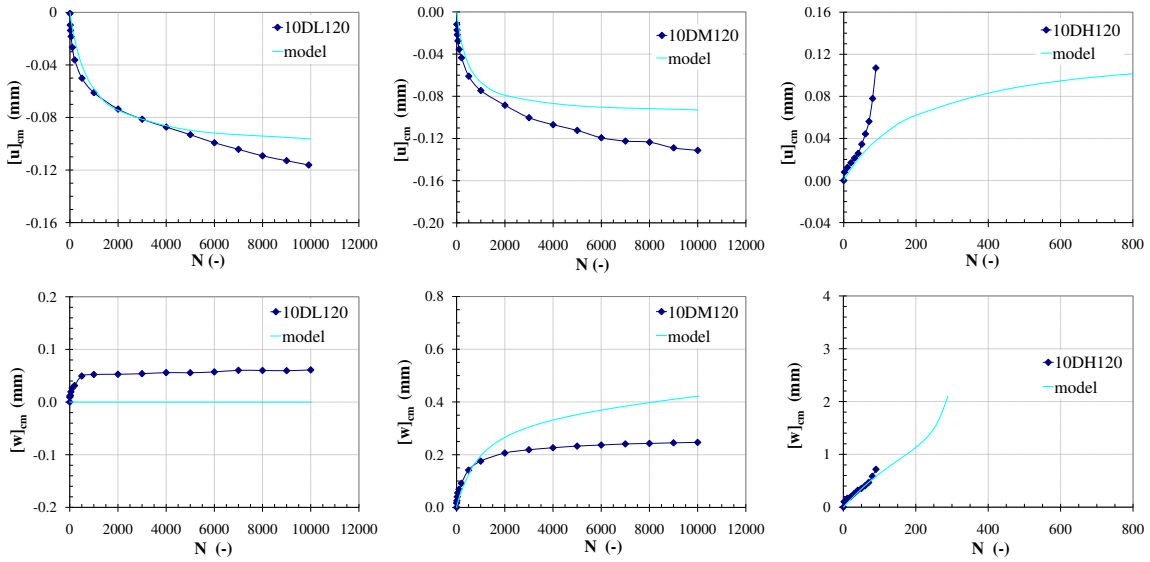

Figure D.7: Comparison between experimental data and the model prediction, $\sigma_n = 120$ kPa, $\Delta\tau = 10$ kPa

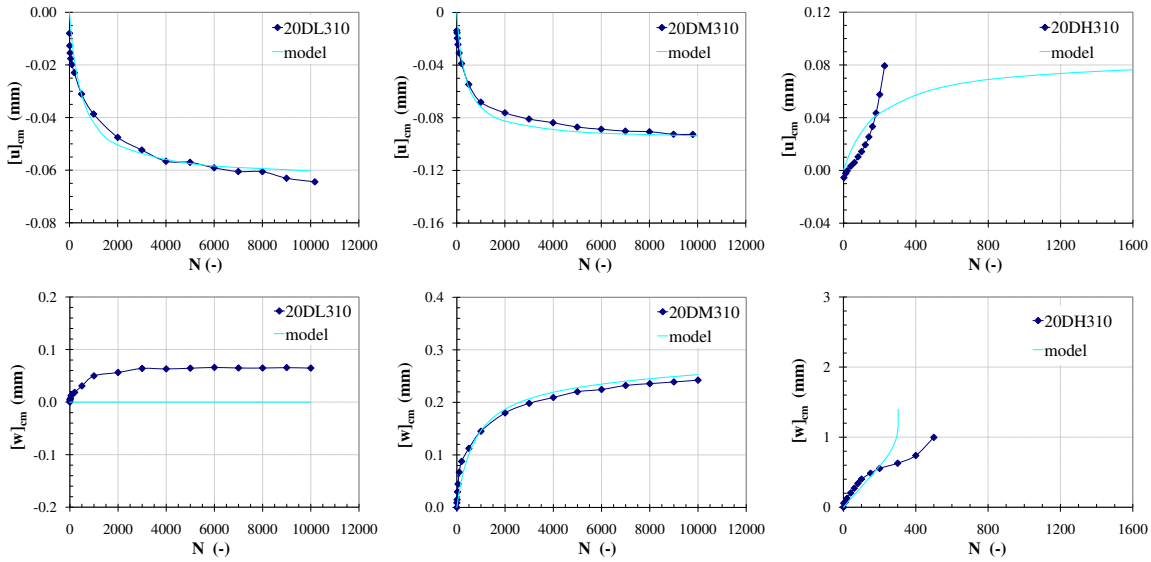

Figure D.8: Comparison between experimental data and the model prediction, $\sigma_n = 310$ kPa, $\Delta\tau = 20$ kPa

Appendix E

Cyclic CNS tests

E.1 Cyclic CNS tests on loose sand ($I_{D0} \approx 30\%$) with rough plate

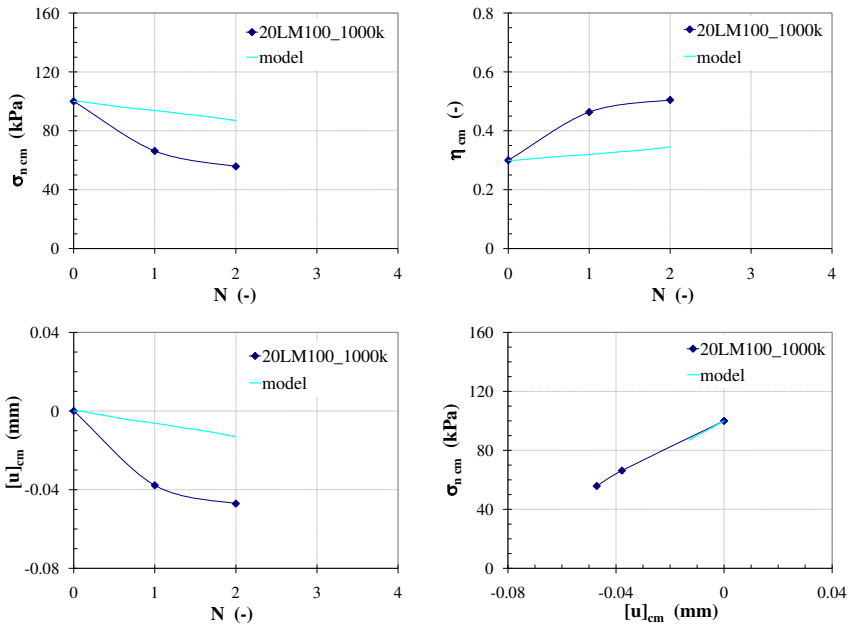

Figure E.1: Comparison between experimental data and the model prediction, $k = 1000$ kPa/mm, $\sigma_{n0} = 100$ kPa, $\eta_{\mathrm{cm}0} = 0.30$, $\Delta\tau = 20$ kPa

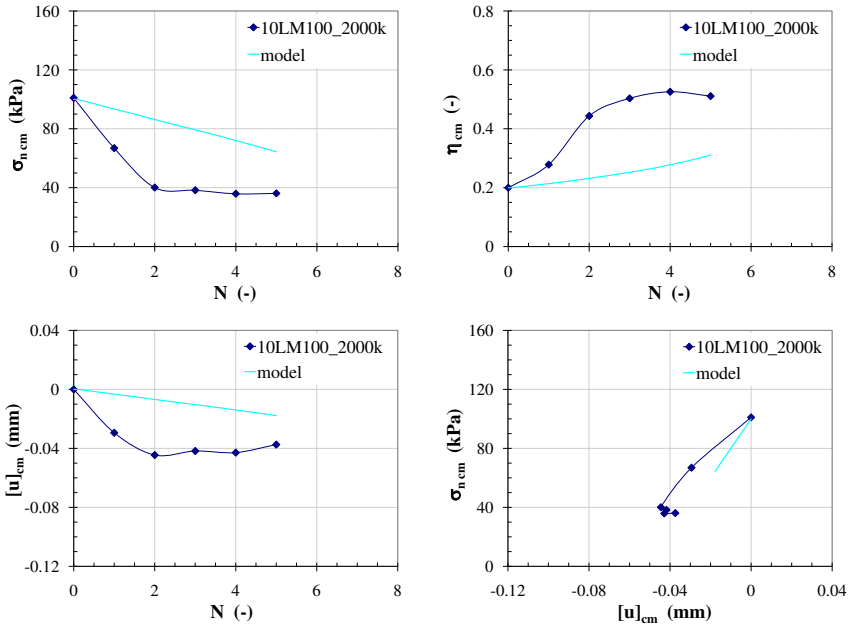

Figure E.2: Comparison between experimental data and the model prediction, $k = 2000$ kPa/mm, $\sigma_{n0} = 100$ kPa, $\eta_{\mathrm{cm}0} = 0.20$, $\Delta\tau = 10$ kPa

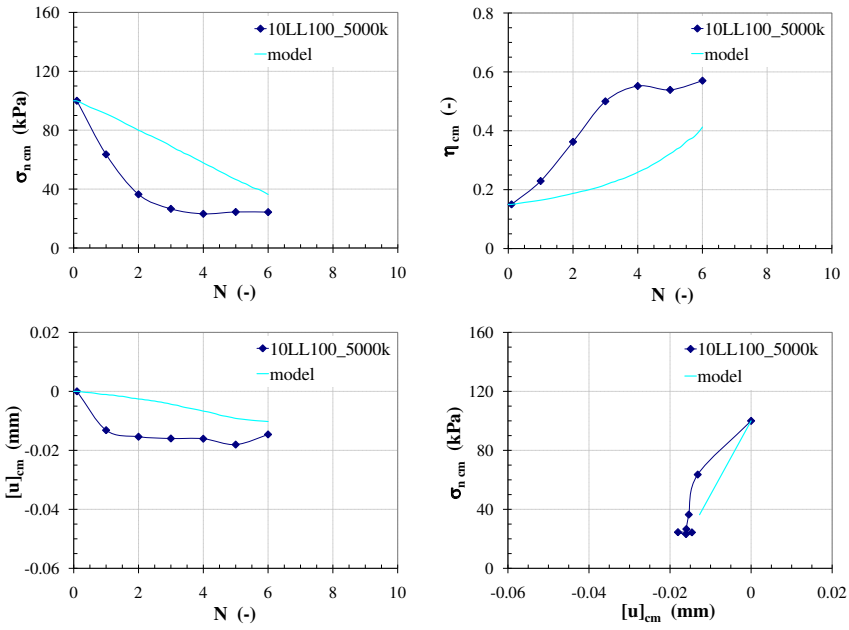

Figure E.3: Comparison between experimental data and the model prediction, $k = 5000$ kPa/mm, $\sigma_{n0} = 100$ kPa, $\eta_{\text{cm}0} = 0.15$, $\Delta\tau = 10$ kPa

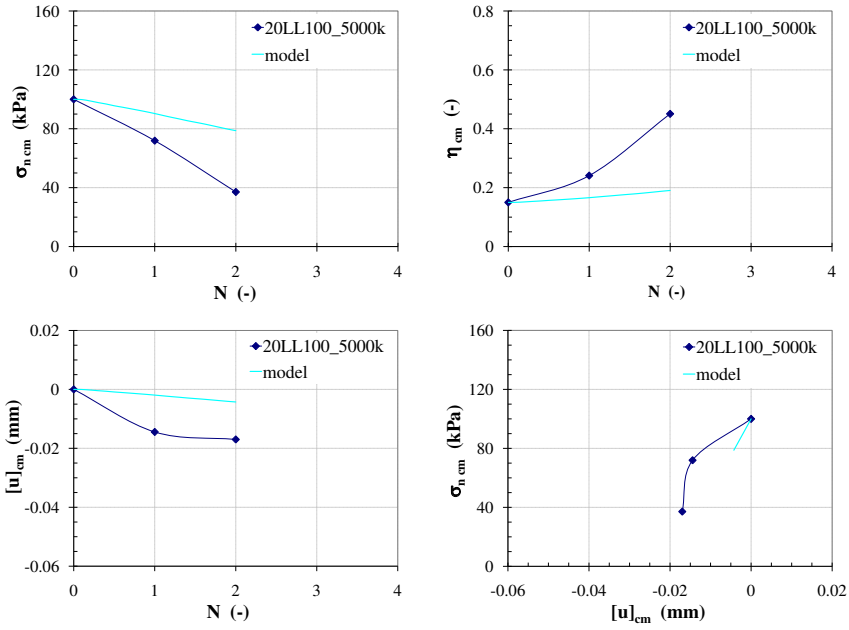

Figure E.4: Comparison between experimental data and the model prediction, $k = 5000$ kPa/mm, $\sigma_{n0} = 100$ kPa, $\eta_{\text{cm}0} = 0.15$, $\Delta\tau = 20$ kPa

E.2 Cyclic CNS tests on dense sand ($I_{D0} \approx 90\%$) with rough plate

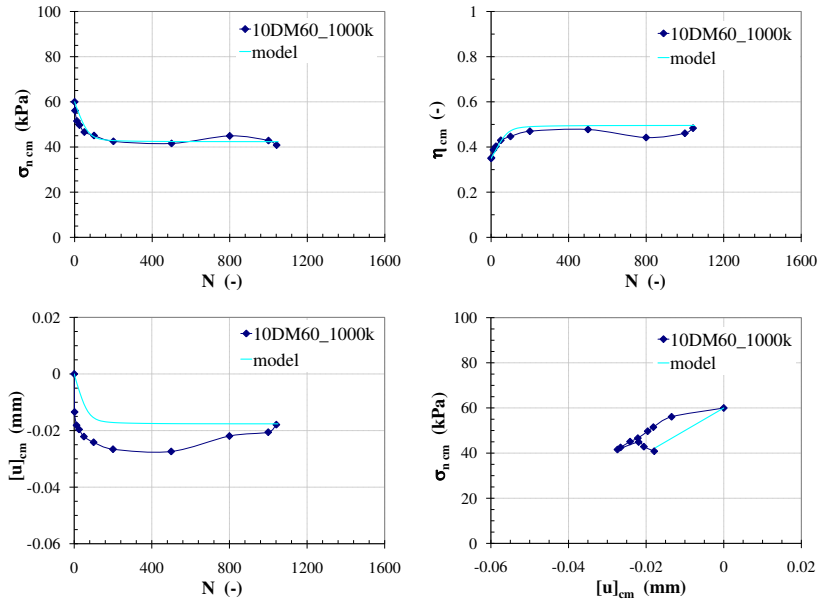

Figure E.5: Comparison between experimental data and the model prediction, $k = 1000$ kPa/mm, $\sigma_{n0} = 60$ kPa, $\eta_{\mathrm{cm}0} = 0.35$, $\Delta\tau = 10$ kPa

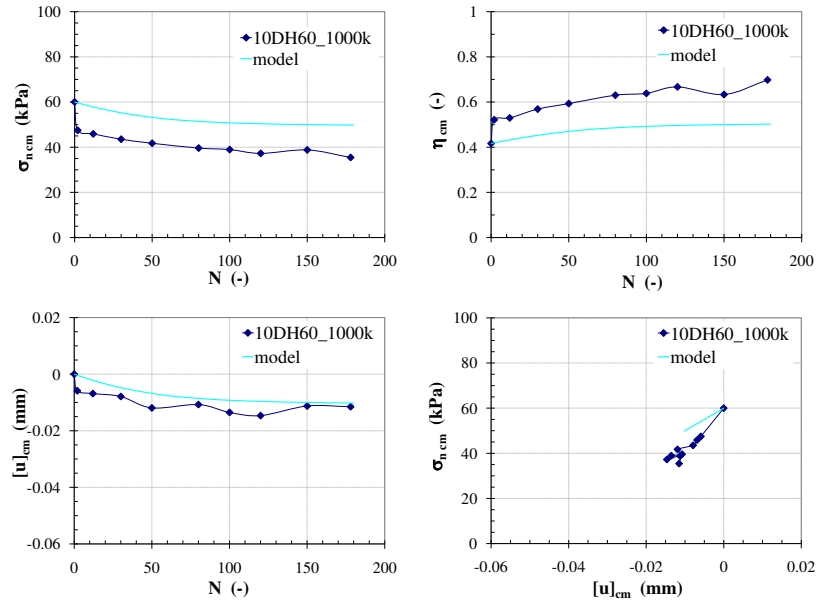

Figure E.6: Comparison between experimental data and the model prediction, $k = 1000$ kPa/mm, $\sigma_{n0} = 60$ kPa, $\eta_{\mathrm{cm}0} = 0.42$, $\Delta\tau = 10$ kPa

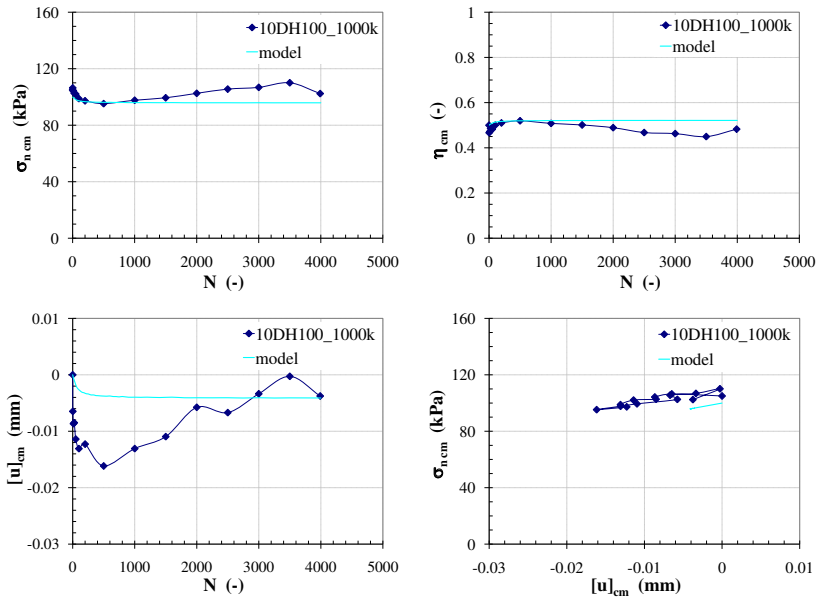

Figure E.7: Comparison between experimental data and the model prediction, $k = 1000$ kPa/mm, $\sigma_{n0} = 100$ kPa, $\eta_{\mathrm{cm}0} = 0.50$, $\Delta\tau = 10$ kPa

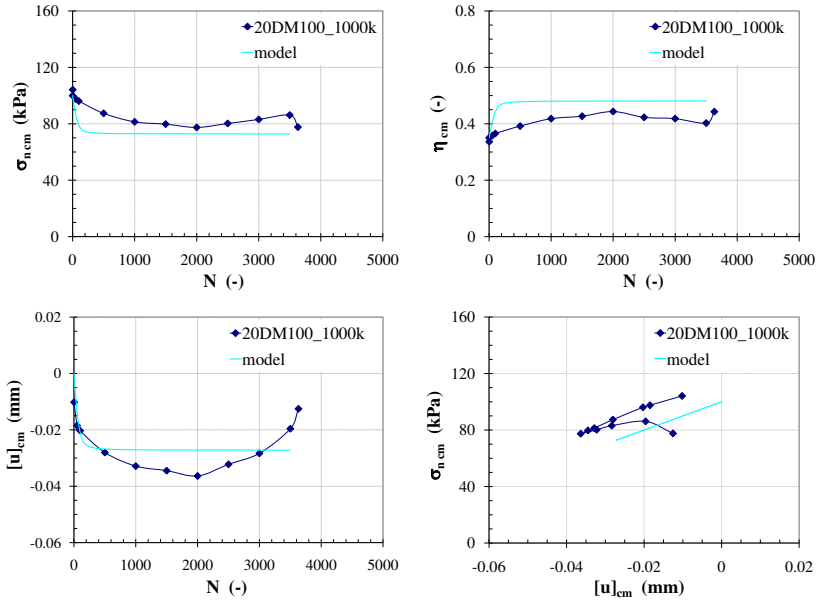

Figure E.8: Comparison between experimental data and the model prediction, $k = 1000$ kPa/mm, $\sigma_{n0} = 100$ kPa, $\eta_{\mathrm{cm}0} = 0.35$, $\Delta\tau = 20$ kPa

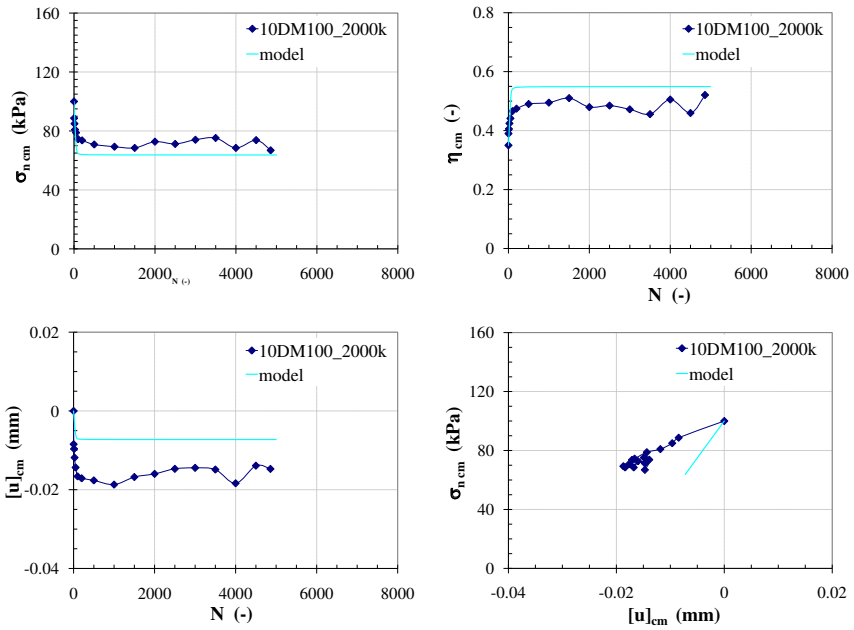

Figure E.9: Comparison between experimental data and the model prediction, $k = 2000$ kPa/mm, $\sigma_{n0} = 100$ kPa, $\eta_{\mathrm{cm}0} = 0.35$, $\Delta\tau = 10$ kPa

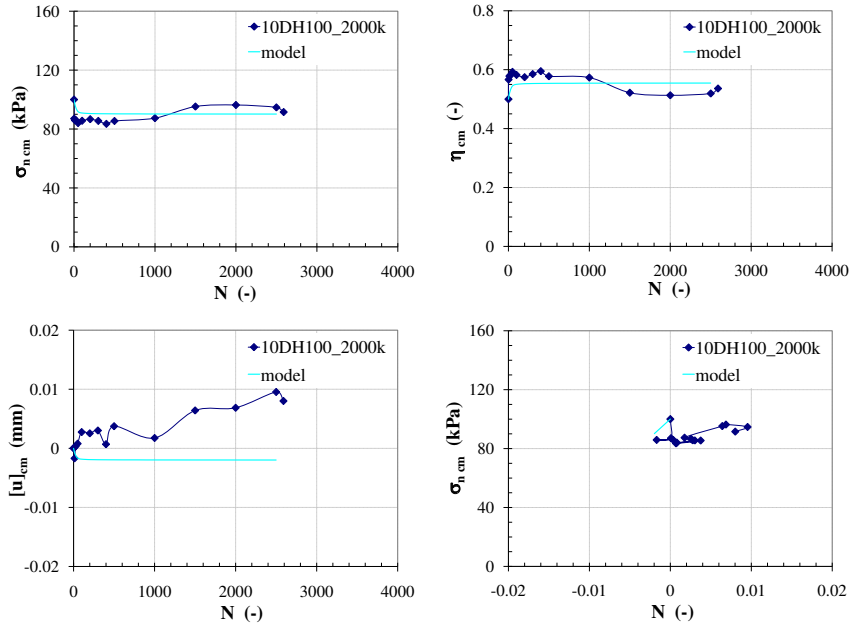

Figure E.10: Comparison between experimental data and the model prediction, $k = 2000$ kPa/mm, $\sigma_{n0} = 100$ kPa, $\eta_{\mathrm{cm}0} = 0.50$, $\Delta\tau = 10$ kPa, rough plate on dense sand ($I_{D0} \approx 90\%$)

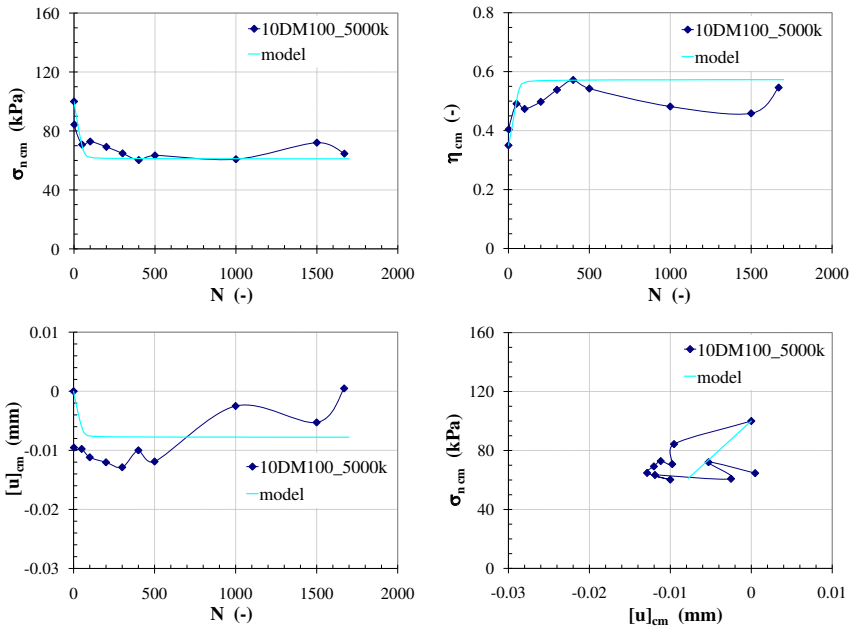

Figure E.11: Comparison between experimental data and the model prediction, $k = 5000$ kPa/mm, $\sigma_{n0} = 100$ kPa, $\eta_{\mathrm{cm}0} = 0.35$, $\Delta\tau = 10$ kPa

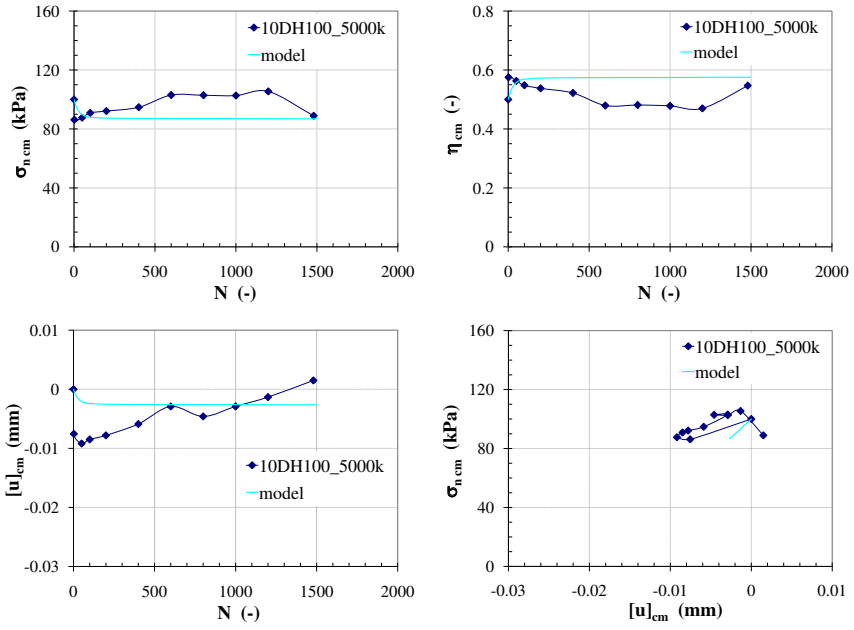

Figure E.12: Comparison between experimental data and the model prediction, $k = 5000$ kPa/mm, $\sigma_{n0} = 100$ kPa, $\eta_{\mathrm{cm}0} = 0.50$, $\Delta\tau = 10$ kPa

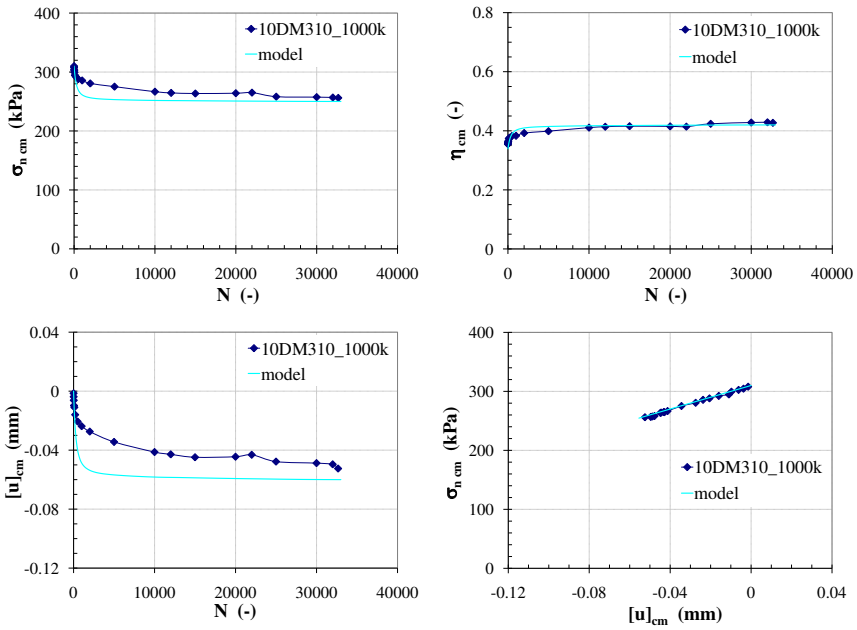

Figure E.13: Comparison between experimental data and the model prediction, $k = 1000$ kPa/mm, $\sigma_{n0} = 310$ kPa, $\eta_{\text{cm}0} = 0.35$, $\Delta\tau = 10$ kPa

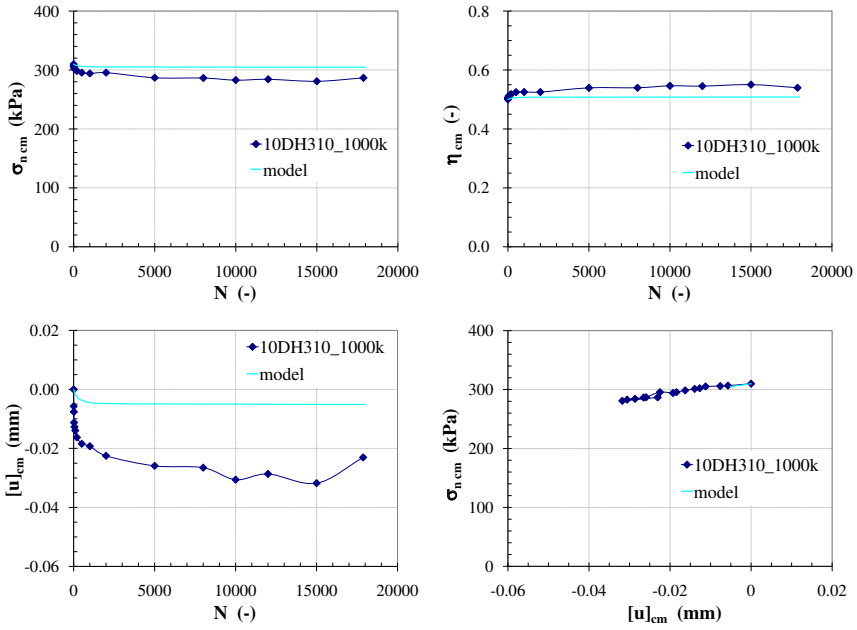

Figure E.14: Comparison between experimental data and the model prediction, $k = 1000$ kPa/mm, $\sigma_{n0} = 310$ kPa, $\eta_{\text{cm}0} = 0.50$, $\Delta\tau = 10$ kPa

Appendix F

Résumé français étendu de la Thèse

Résumé en français

UNIVERSITÉ DE GRENOBLE

THÈSE
Pour obtenir le grade de
DOCTEUR DE L'UNIVERSITÉ DE GRENOBLE
Spécialite: **Matériaux Mécanique, Génie Civil, Electrochimie**
Arrêté ministériel: 7 août 2006

Présentée par

SURIYAVUT PRA-AI

Thèse dirigée par **Pierre FORAY** et
codirigée par **Marc BOULON**

préparée au sein du **Laboratoire 3S-R**
dans **l'École Doctorale Ingénierie-Matériaux Mécanique Environnement Energétique Procédés Production (I-MEP2)**

Behaviour of soil-structure interfaces subjected to a large number of cycles. Application to piles

Thèse soutenue publiquement le **28.02.2013**,
devant le jury composé de:

M. Isam SHAHROUR
Professeur à Polytech Lille, Laboratoire Génie Civil et Géo-Environement, (Rapporteur)
M. Eric VINCENS
Maître de conférence à l'Ecole Centrale de Lyon, Laboratoire LTDS, (Rapporteur)
M. Fabrice EMERIAULT
Professeur à l'INP Grenoble, Laboratoire 3S-R, (Examinateur)
M. Jean CANOU
Chercheur à l'ENPC, Laboratoire NAVIER-CERMES, (Examinateur)
M. Alain PUECH
Directeur Scientifique à FUGRO Geo Consulting, (Invité)
Directeur Technique ANR et Programme National SOLCYP

Titre de la thèse

Essais et modélisation du cisaillement cyclique sol-structure à grand nombre de cycles. Application aux pieux

Sommaire

Introduction générale

La problématique des interfaces sol-structure est communément présente dans de nombreux problèmes géotechniques, fondations superficielles, fondations sur pieux, parois moulées, renforcement des sols, oléoducs, tunnels… Le récent développement des installations liées à l'énergie, renouvelable ou non (plateformes off-shore, éoliennes, hydroliennes,…) amène les professionnels à s'intéresser de manière accrue aux effets des sollicitations cycliques à grand nombre de cycles, d'autant qu'aucune recommandation nationale ni internationale ne permet de quantifier la dégradation cyclique, les laissant sans guide dans leurs travaux de conception.

La thèse, tentant d'apporter une contribution à ce vide scientifique et technique, est composée de 5 chapitres, comme indiqué au sommaire ci-dessus.
Le premier chapitre fait une revue bibliographique des travaux expérimentaux et de modélisation de la littérature, caractérisant et quantifiant la notion d'accumulation cyclique lors du cisaillement direct cyclique à contrainte normale constante et à rigidité normale imposée.
Le second chapitre décrit tout d'abord la machine de cisaillement direct développée dans le cadre de la thèse, permettant de réaliser et d'enregistrer automatiquement un grand nombre de cycles (typiquement 10 000), avec l'asservissement adéquat permettant de suivre n'importe quel chemin de cisaillement. L'ensemble et le détail des cycles des essais de cisaillement, entre sable de Fontainebleau et plaque rugueuse ou lisse, à contrainte normale constante ou à rigidité normale imposée, est enregistré, puis interprété.
Au troisième chapitre, relatif à la modélisation constitutive, est exposée une formulation analytique des essais de cisaillement direct monotones (à contrainte normale constante et à rigidité normale imposé) et cycliques à contrainte normale constante, ainsi que des compressibilités. Il est largement fait appel à l'interpolation, sur la densité, les contraintes normales, les niveaux cycliques moyens, et l'amplitude cyclique. Dans un second temps, les essais cycliques à rigidité normale imposée sont modélisés par incréments analytiques finis basés sur les formulations précédentes, la variable de mémoire étant la densité d'interface. De même pour des essais à amplitude variée.
Le quatrième chapitre est consacré à la modélisation par éléments finis, utilisant le logiciel PLAXIS. C'est tout d'abord une modélisation de l'essai de cisaillement direct sable-plaque rugueuse monotone lui-même, en 2-D déformation plane, dans une boite légèrement rugueuse, avec un sable lâche ou dense, et selon un chemin à contrainte normale constante ou à rigidité normale imposée. Les hétérogénéités sont bien identifiées, mais globalement, les chemins sont conformes à l'expérience. Puis sont modélisés 2 essais de pieu modèle centrifugés sollicités cycliquement, l'un en traction, l'autre en compression. La dégradation cyclique à l'interface sable-pieu est simulée à partir de la modélisation à rigidité normale imposée développée au troisième chapitre.
Le cinquième et dernier chapitre propose une méthodologie, basée sur les résultats des troisième et quatrième chapitre, permettant de modéliser, moyennant un petit nombre d'essais et un temps de calcul acceptable, le comportement de pieux réels chargés cycliquement.
Des conclusions générales sont tirées de ces travaux, et les perspectives de travaux ultérieurs sont proposées.

Chapitre 1. Etude bibliographique des interfaces sol-structure sous chargement cyclique

Dans cette revue bibliographique, on décrit d'abord le concept de cisaillement direct, essai élémentaire (homogène ? comment ?) simulant le comportement mécanique d'une fraction du contact sol-structure, et les dispositifs expérimentaux développés par les chercheurs à cette fin : cisaillement plan unidirectionnel, cisaillement(s) annulaire(s), cisaillement plan bi-directionnel. La question de l'épaisseur d'interface est abordée et discutée. Puis vient une présentation des variables mesurables d'interface, à comparer aux variables utilisées pour rendre compte du comportement volumique des sols : les déplacements relatifs qui tenant lieu des déformations du comportement volumique, et les composantes de vecteur contrainte, analogues des composantes de tenseur contrainte du comportement volumique. Puis sont évoqués les facteurs classiquement mis en avant, qui influent sur le comportement des interfaces sol-structure (sols essentiellement granulaires) : la compacité du sol, la rugosité de la plaque censée simuler la structure, le niveau de contrainte, la résistance des grains (sable

siliceux versus sable carbonaté), et enfin le chemin de cisaillement direct. Sont soulignés le rôle et la représentativité de tout premier ordre des chemins de cisaillement direct à rigidité normale imposée (externe, ne pas confondre avec la rigidité normale interne, ou compressibilité, d'une interface). De même, la contractance, toujours observée pour un petit nombre de cycles sur ces chemins, est rapportée. S'agissant de sollicitations cycliques (le sujet de cette thèse), les publications abordant le cisaillement direct et les sollicitations cycliques sont en nombre fort restreint, voire inexistantes lorsqu'on examine le grand nombre de cycles. Par ailleurs, les essais réalisés concernent généralement de grands cycles. En l'absence de résultats couvrant bien le champ de cette thèse, nous avons cité les travaux de grande qualité produits par Wichtmann, concernant une série consistante d'essais triaxiaux cycliques sur sable, et nous nous en sommes largement inspirés (figure 1). Accumulation de déformation a pour cet auteur le sens de déformation irréversible après cycles.
La seconde partie de ce chapitre est consacrée aux lois constitutives d'interfaces sol-structure. Sont évoqués les modèles phénoménologiques et les modèles élasto-plastiques, ainsi que les modèles de pseudo-fluage cyclique. Le formalisme du pseudo-fluage cyclique est issu des travaux fondateurs de Perzyna, sur son modèle élasto-visco-plastique. Hormis l'élasticité du matériau, ce modèle fait appel à trois ingrédients : une loi d'écoulement visco-plastique, un noyau visqueux, défini à partir de l'espace des contraintes, séparant les zones à et sans déformations visco-plastiques, et enfin un paramètres scalaire de viscosité.

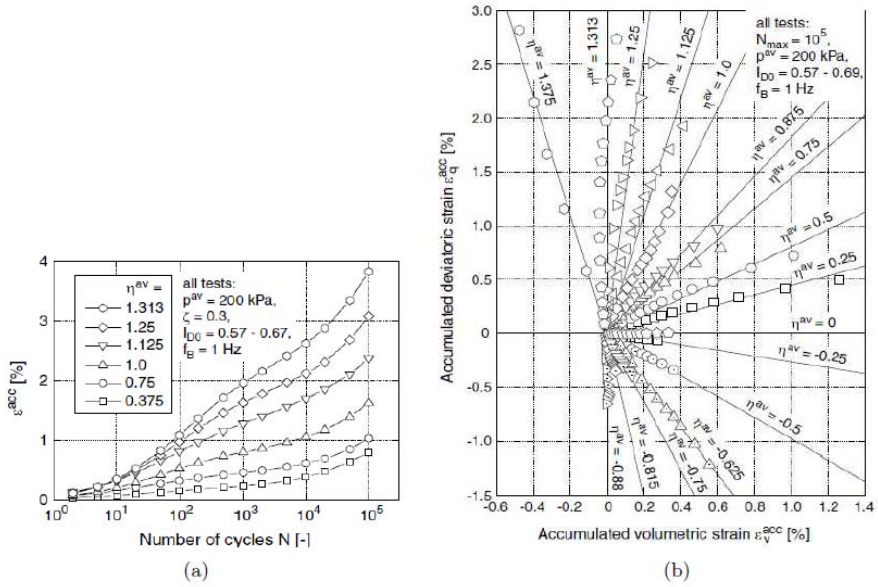

Figure 1. Essais triaxiaux cycliques : a) accumulation de la norme de déformation ε_{acc} fonction du nombre de cycles, pour différents taux de déviateur cyclique moyen. b) relation entre déformation déviatoire accumulée ($\varepsilon_{acc\ q}$) et déformation volumique accumulée ($\varepsilon_{acc\ v}$) selon le taux de déviateur cyclique moyen ($\varepsilon_{acc\ v}$ >0 contractant), d'après Whichtmann (2005).

Chapitre 2. Essais de cisaillement direct d'interfaces

2.1. La machine d'essai, les mesures

La machine d'essai est une boîte de cisaillement direct traditionnelle, modifiée pour répondre aux besoins de l'étude. La masse morte génératrice de la contrainte normale a été remplacée

par un moteur électrique double sens, asservi de manière à respecter la consigne correspondant au chemin de cisaillement direct souhaité (figure 2). La demi-boîte inférieure a été remplacée par une plaque rugueuse simulant la rugosité de la structure en contact avec le sol (situé dans la demi-boîte supérieure). Les forces normale et de cisaillement sont mesurée par 2 capteurs de force équipés de jauges de déformation, dûment étalonnés. Les déplacements relatifs sol/plaque sont mesurés par 2 LVDT également dûment étalonnés, l'un pour le déplacement relatif normal, l'autre pour le déplacement relatif tangentiel. En outre, un LVDT supplémentaire mesure le déplacement vertical de la demi-boîte supérieure, à titre de contrôle. Une carte analogique digitale permet la communication entre la machine et l'ordinateur (asservissement et mesure).L'essai est piloté par un programme idoine, écrit en langage C, ,qui affiche à l'écran les valeurs utiles en temps réel. L'ensemble des mesures est acquis et stocké dans un fichier texte. Ce dispositif permet de réaliser un cisaillement direct monotone ou cyclique. Dans les deux cas, la contrainte normale initiale est appliquée à vue. Ensuite le chemin de cisaillement direct est choisi. Dans le cas cyclique, l'opérateur choisit 2 seuils de contrainte de cisaillement l'un maximum et l'autre une minimum. Enfin le cisaillement est déclenché et la suite de l'essai est alors automatique, à vitesse relative tangentielle choisie au préalable et constante, éventuellement inversée (automatiquement) lors des cycles. On peut enchaîner, sans rupture des mesures, plusieurs séquences, telle que variation de contrainte normale, et/ou cisaillement.

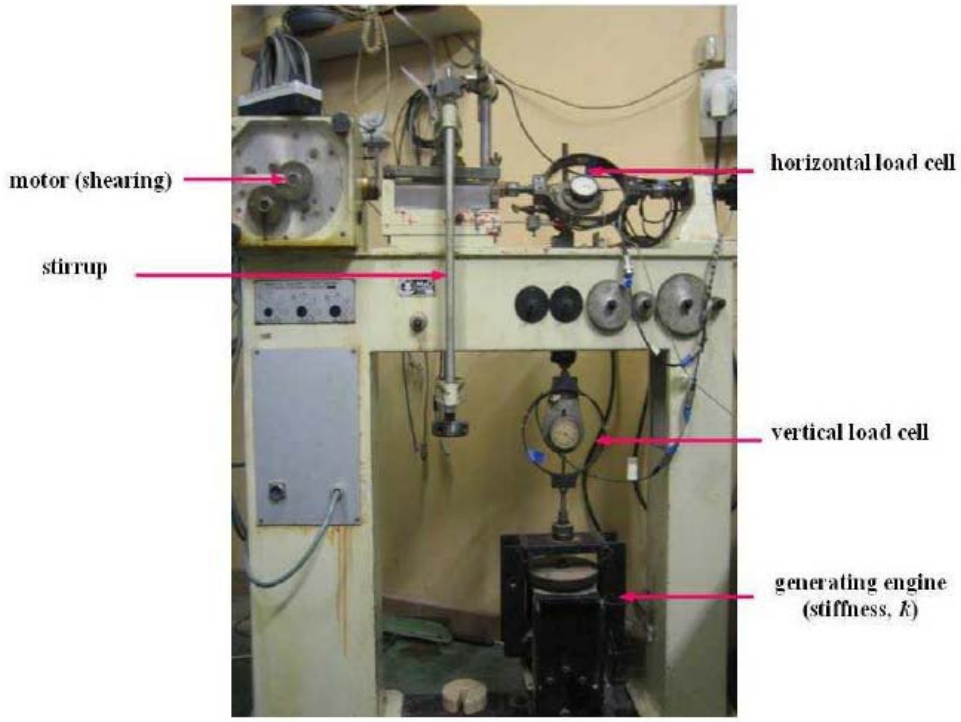

Figure 2. La boîte de cisaillement direct modifiée, le moteur générateur de la contrainte normale, les 2 capteurs de force (normale et tangentielle).

Les variables mesurées sont, en fonction du temps t, les déplacements relatifs sol/plaque normal $[u(t)]$ et tangentiel $[w(t)]$, les contraintes normale $\sigma_n(t)$ et de cisaillement $\tau(t)$, le déplacement relatif vertical boîte/plaque. Le déplacement relatif tangentiel $[w(t)]$ est toujours imposé (t = temps). Les chemins possibles sont le chargement et le déchargement pseudo-oedométrique (en contrainte normale), et le cisaillement résultant de la consigne (1), soit :

$$C = \Delta\sigma_n - k\Delta[u] \qquad (1)$$

- à contrainte normale constante (k = 0)
- à rigidité normale imposée (k > 0)
- à volume constant (encore appelés à dilatance empêchée) (k → ∞)

L'asservissement est généralement réalisé avec un écart $\Delta\sigma_n = \pm 5kPa$.

2.2. Les matériaux, sable et plaque rugueuse

Le sable testé est le sable de Fontainebleau standard NE34, réputé « uniforme » en raison de son C_u ,utilisé dans le cadre SOLCYP, dont les propriétés physiques sont indiquées tableau 1, et dont la courbe granulométrique est représentée figure 3. Les plaques rugueuses simulant le

D_{50} (mm)	G (g/cm^3)	$\rho_{d\,max}$ (g/cm^3)	$\rho_{d\,min}$ (g/cm^3)	e_{max}	e_{min}	$C_u = D_{60}/D_{10}$
0.23	2.65	1.72	1.42	0.866	0.545	1.72

Tableau 1. Propriétés physiques du sable de Fontainebleau NE34.

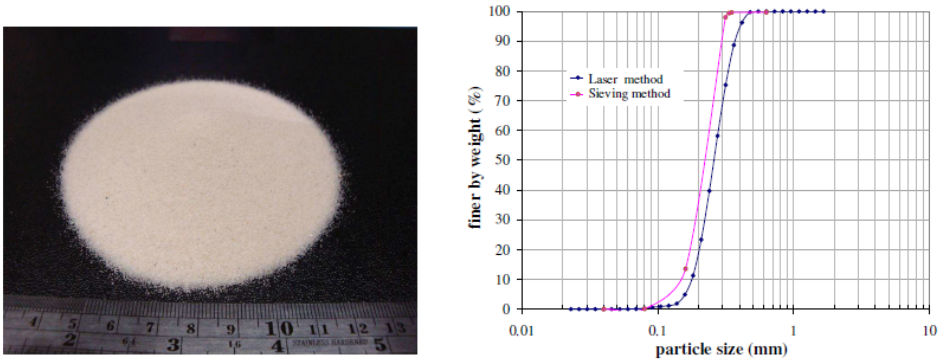

Figure 3. Sable de Fontainebleau, aspect et courbe granulométrique.

matériau structural (le pieu par exemple) sont de 2 types. La plaque « rugueuse »est une plaque rigide d'acier (épaisseur 1 cm) sur laquelle a été collé, à l'araldite, du sable de Fontainebleau NE34. Cette plaque est restaurée tous les 10 essais, compte tenu de l'arrachement éventuel de grains, réduisant progressivement sa rugosité. L'étude morphologique de ces plaques a conduit aux paramètres R_{max} = 0.2 mm, ou R_n = 0.87, ce qui les classe comme « très rugueuses ». Le second type de plaque est la même plaque d'acier, non couverte par du sable, et dite « plaque lisse » (R_{max} = 14 µm, ou R_n = 0.06).

2.3. Mode opératoire

Nous avons testé 2 types d'échantillons sable-structure : avec sable dense et avec sable lâche. Dans tous les cas, la préparation de l'échantillon est délicate, et faite en insérant un clinquant

de laiton de 0.30 mm d'épaisseur entre la plaque et la boîte (figure 4), compte tenu du d_{50} du sable (0,23 mm), et du fait que la boîte se rapproche de la plaque lors de l'application de la contrainte normale nominale initiale relative à l'essai. La densité faible (I_{D0} ≈ 30 %) est obtenue par déversement du sable d'une faible hauteur de chute, tandis que la densité élevée (I_{D0} ≈ 90 %) nécessite un compactage à l'aide d'une aiguille vibrante. Chaque essai est constitué des phases successives suivantes, après préparation de l'échantillon:

- Montée en contrainte normale jusqu'à la contrainte normale initiale
- Réglage des paramètres de l'essai
- Cisaillement direct selon le chemin choisi
- Arrêt du cisaillement par l'opérateur au terme du but de l'essai (cas monotone : déplacement relatif tangentiel maximum ; cas cyclique, nombre maximum de cycles ou, si « rupture » avant terme, déplacement relatif tangentiel maximum atteint (≈ 15 mm).
- Dans le cas cyclique, cisaillement final de grande amplitude, afin d'évaluer la résistance de l'interface après les cycles.
- Réduction de la contrainte normale jusqu'à 0 kPa
- Arrêt de l'essai proprement dit
- Démontage du piston de la boîte de cisaillement
- Extraction de la partie supérieure de l'échantillon de sable
- Prélèvement de la zone d'interface (épaisseur ≈ 10 à 12 $d_{50,}$ échantillon E_{f1})
- Prélèvement et pesage du sable « perdu » entre la demi-boîte inférieure et la plaque au cours de l'essai (échantillon E_{f2}, en quantité très faible !).
- Analyse granulométrique des échantillons E_{f1} et E_{f2}.

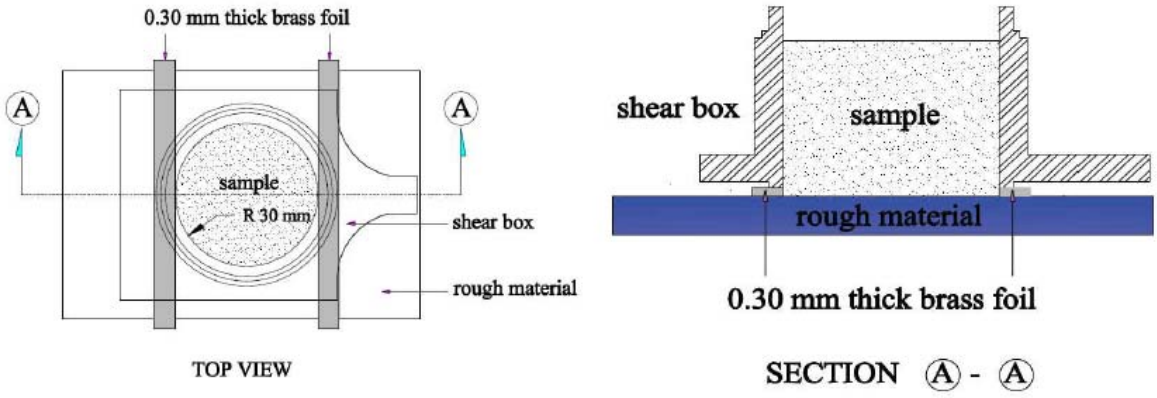

Figure 4. Dispositions d'espacement boîte/plaque lors de la préparation de l'échantillon d'interface sable-structure

2.4. Correction du biais expérimental

Le d_{50} du sable étant de l'ordre de 0,23 mm, et l'espacement initial boîte/plaque, hors contrainte normale, étant de 0,30 mm, on peut imaginer qu'il existe une « perte de sable » au cours du cisaillement, malgré l'uniformité importante de granulométrie du sable, et le rapprochement boîte/plaque lors de l'application de la contrainte normale initiale (entrainement de la demi-boîte inférieure par frottement sable/boîte). Ce biais, faible mais mesurable, rapporté par de nombreux auteurs, est inhérent à l'essai de cisaillement direct

matériau granulaire/structure. Il crée une contractance fictive parasite qui doit absolument être quantifiée et doit corriger le déplacement relatif normal $[u]$. Nous disposons de la masse finale de sable « perdu », en fin d'essai (§ 2.3). Il s'agit alors d'affecter localement (entre début et fin de cisaillement) ce biais global. Entre l'affectation proportionnelle au temps courant de l'essai, et l'affectation proportionnelle au déplacement relatif tangentiel cumulé en valeur absolue, nous avons choisi la seconde option, semblant plus physique. Les résultats d'essais sont donc présentés corrigés en ce qui concerne le déplacement relatif normal $[u(t)]$.

2.5. Interprétation des essais

2.5.1. Poids volumique et épaisseur d'interface

La zone d'interface étant d'épaisseur très faible (on admet généralement ≈ 5 à 10 d_{50}, Boulon (1988), Hoteit (1990)) par rapport à l'épaisseur d'échantillon de sable (≈ 2 cm), nous avons résolument interprété l'échantillon de sable comme formé de 2 couches séparément homogènes : la couche d'interface, au contact de la structure, et le reste de l'échantillon, couche « tampon » en quelque sorte. La couche tampon n'est pas soumise au cisaillement, elle ne subit que des déformations oedométriques sous l'effet des seules variations de contrainte normale. La couche d'interface est par contre soumise au chargement dans son ensemble, variation de contrainte normale et variation de contrainte de cisaillement (figure 5). Ceci n'est bien entendu qu'un schéma, l'épaisseur étant une valeur moyenne pour l'échantillon. Se pose alors la question de la détermination de l'épaisseur de cette zone d'interface : comment identifier cette épaisseur ? Nous avons utilisé les essais de cisaillement direct monotones CNL, à plusieurs niveaux de contrainte normale, et à plusieurs densités initiales. L'idée directrice est que l'épaisseur d'interface est peu dépendante de la densité initiale et du niveau de contrainte normale, du moins tant que les grains ne sont pas broyés. Par ailleurs la densité critique doit être atteinte dans l'interface lors de grands déplacements relatifs tangentiels.

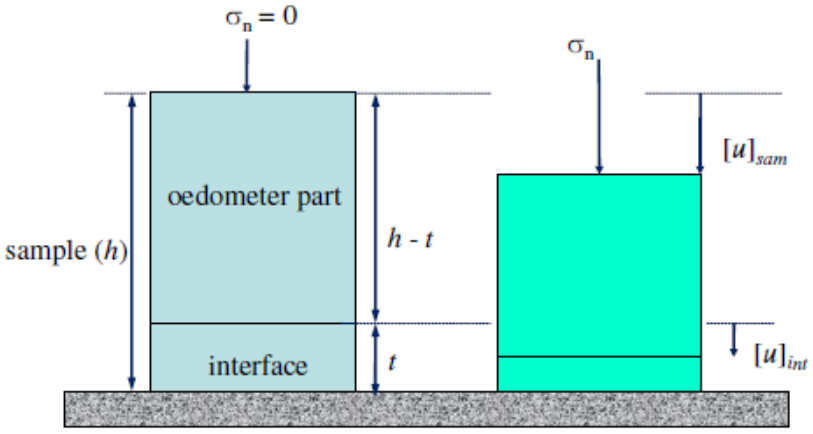

Figure 5. Hypothèse des zones séparément homogènes dans l'échantillon de sol (épaisseur h) situé dans la boîte de cisaillement : au contact de la structure , l'interface (épaisseur t), au dessus, le « tampon » oedométrique (épaisseur h-t).

Les figures 6 et 7 montrent le test de cette hypothèse, qui se révèle fructueuse. Néanmoins, l'épaisseur d'interface semble dépendre de la densité initiale (grains plus libres de leurs mouvements à densité initiale faible ?). Nous retiendrons pour l'interprétation de nos essais,

les valeurs indiquées au tableau 2. On retiendra pour la suite que les poids volumiques indiqués sont des **poids volumiques sous contrainte,** résultant du poids volumique intial γ_{d0} et du déplacement relatif normal d'interface $[u]$.

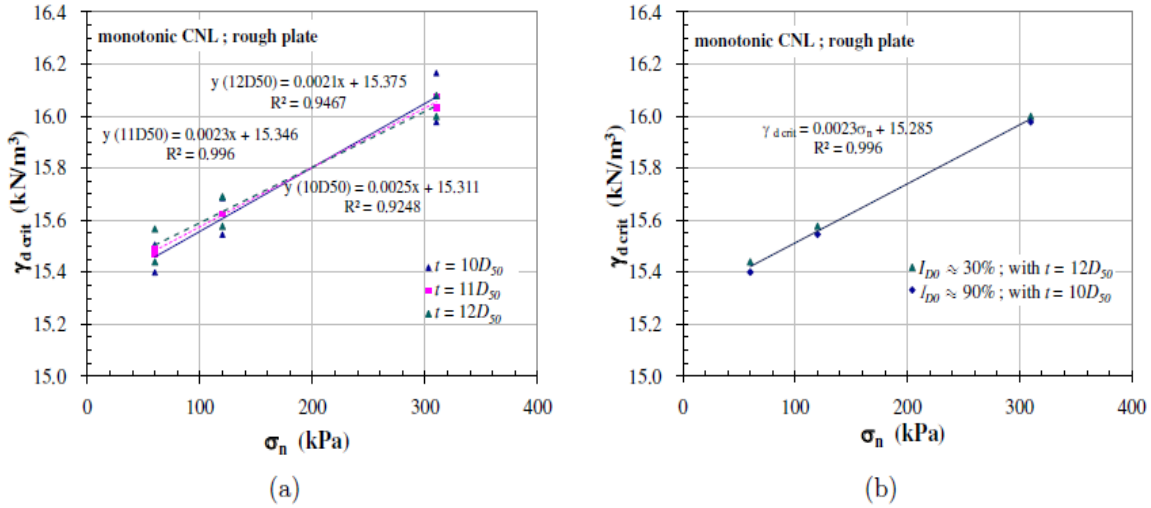

Figure 6. Poids volumique d'interface (cas plaque rugueuse) selon plusieurs hypothèses d'épaisseur d'interface : a) densités initiales faible et forte confondues. b) valeurs optimales différentes pour densités initiales faible et forte.

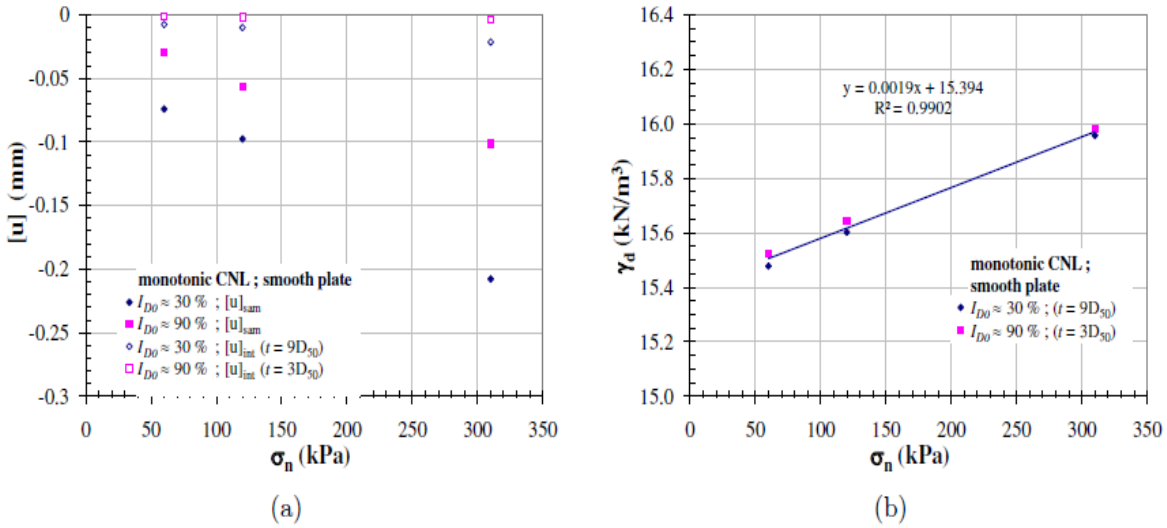

Figure 7. Déplacement relatif normal et poids volumique d'interface (cas plaque lisse) selon plusieurs hypothèses d'épaisseur d'interface : a) déplacement relatif (échantillon et interface) densités initiales faible et forte. b) valeurs optimales pour densités initiales faible et forte.

Plaque	I_{D0} = 90 %	I_{D0} = 30 %
Rugueuse	10 d_{50}	12 d_{50}
lisse	3 d_{50}	9 d_{50}

Tableau 2. Epaisseurs d'interface identifiées par examen des valeurs critiques sur chemins CNL, selon la densité initiale et la contrainte normale initiale.

2.5.2. Pseudo-fluage cyclique et chemin cyclique moyen

L'idée de base ayant prévalu à l'origine de cette étude a été de considérer les déplacements relatifs irréversibles accumulés au cours des cycles comme un pseudo-fluage cyclique, le nombre de cycles tenant lieu de temps fictif. C'est la raison pour laquelle nos essais ont été (pré)interprétés en fonction de la **notion de chemin cyclique moyen**. Les essais sont ainsi présentés interprétés en termes de variables déplacement relatif cyclique moyen normal $[u]_{cm}$ et tangentiel $[w]_{cm}$, en fonction du nombre de cycles (ou = 10000 cycles) et des autres paramètres (§ 2.6.1). L'évolution des rigidités normale et tangentielle, de la résistance d'interface, et de la granulométrie est également visée.

2.6. Programme d'essais et quelques résultats typiques

2.6.1 Programme d'essais

Le programme d'essais de base couvre, conformément au § 2.2, 2 types de contacts (rugueux et lisse), et 2 types de chemins, à contrainte normale constante (CNL, k = 0, en vue de l'identification des paramètres constitutifs), et à rigidité normale imposée (CNS, k > 0, en vue de la validation du modèle constitutif), pour chacun 10 000 cycles, sauf cas de rupture prématurée. La définition des paramètres de ces essais est basée sur la notion de « plans d'expérience ». Les tableaux suivants (3 à 5) donnent les paramètres clés de ces essais, à savoir :

- l'indice initial de densité I_{D0}
- la contrainte normale cyclique moyenne initiale σ_{ncm0}
- les seuils de contrainte de cisaillement ($\tau_{\min} < \tau < \tau_{\max}$)
- le rapport de contraintes cycliques moyennes (cisaillement à normale) η_{cm0}
- l'amplitude cyclique ($\Delta\tau = \tau_{\max} - \tau_{\min}$, $\Delta\eta_0 = \dfrac{\Delta\tau}{\sigma_{ncm0}}$)

En outre, un petit nombre d'essais CNL complémentaires, à amplitude cyclique variée au cours de l'essai, ont été menés à bien, aux fins de validation tableau 6)..

2.6.2. Résultats typiques

Le déplacement relatif tangentiel reste identiquement nul (aux parasites d'acquisition près) lorsque les cycles sont centrés ($\eta_{cm0} = 0$). Il est hautement remarquable, pour les applications, que les **essais CNS sont toujours contractants**, ce qui explique le concept traditionnel (souvent faussement interprété) de dégradation cyclique (ce n'est pas le coefficient de frottement qui est dégradé, croyance courante facile (dégradation de rugosité), mais le niveau de contrainte normale, ce qui est plus difficile à conceptualiser!).

Tableau 3. Série d'essais CNL, plaque rugueuse

N°	I_{D0} (%)	σ_n (kPa)	level of η_{cm} (-)	τ (kPa)	η_{cm} (-)	$\Delta\tau$ (kPa)
10LL60	30	60	0	$-5 < \tau < 5$	0	10
10LM60	30	60	$\approx 1/2\eta_{peak}$	$10 < \tau < 20$	0.25	10
10LH60	30	60	$\approx 9/10\eta_{peak}$	$25 < \tau < 35$	0.50	10
10LL120	30	120	0	$-5 < \tau < 5$	0	10
10LM120	30	120	$\approx 1/2\eta_{peak}$	$30 < \tau < 40$	0.29	10
10LH120	30	120	$\approx 9/10\eta_{peak}$	$55 < \tau < 65$	0.50	10
10LL310	30	310	0	$-5 < \tau < 5$	0	10
10LM310	30	310	$\approx 1/2\eta_{peak}$	$83 < \tau < 93$	0.28	10
10LH310	30	310	$\approx 9/10\eta_{peak}$	$170 < \tau < 180$	0.57	10
10DL60	90	60	0	$-5 < \tau < 5$	0	10
10DM60	90	60	$\approx 1/2\eta_{peak}$	$15 < \tau < 25$	0.33	10
10DH60	90	60	$\approx 9/10\eta_{peak}$	$32 < \tau < 42$	0.62	10
10DL120	90	120	0	$-5 < \tau < 5$	0	10
10DM120	90	120	$\approx 1/2\eta_{peak}$	$45 < \tau < 55$	0.40	10
10DH120	90	120	$\approx 9/10\eta_{peak}$	$85 < \tau < 95$	0.75	10
10DL310	90	310	0	$-5 < \tau < 5$	0	10
10DM310	90	310	$\approx 1/2\eta_{peak}$	$100 < \tau < 110$	0.34	10
10DH310	90	310	$\approx 9/10\eta_{peak}$	$50 < \tau < 60$	0.71	10
20LL60	30	60	0	$-10 < \tau < 10$	0	20
20LM60	30	60	$\approx 1/2\eta_{peak}$	$5 < \tau < 25$	0.25	20
20LH60	30	60	$\approx 9/10\eta_{peak}$	$15 < \tau < 25$	0.42	20
20LM120	30	120	$\approx 1/2\eta_{peak}$	$25 < \tau < 45$	0.29	20
20LL310	30	310	0	$-10 < \tau < 10$	0	20
20LM310	30	310	$\approx 1/2\eta_{peak}$	$78 < \tau < 98$	0.28	20
20LH310	30	310	$\approx 9/10\eta_{peak}$	$160 < \tau < 180$	0.55	20
20DL60	90	60	0	$-10 < \tau < 10$	0	20
20DM60	90	60	$\approx 1/2\eta_{peak}$	$10 < \tau < 30$	0.33	20
20DH60	90	60	$\approx 9/10\eta_{peak}$	$25 < \tau < 45$	0.58	20
20DM120	90	120	$\approx 1/2\eta_{peak}$	$35 < \tau < 55$	0.37	20
20DL310	90	310	0	$-10 < \tau < 10$	0	20
20DM310	90	310	$\approx 1/2\eta_{peak}$	$95 < \tau < 115$	0.34	20
20DH310	90	310	$\approx 9/10\eta_{peak}$	$210 < \tau < 230$	0.71	20
40LM310	30	310	$\approx 1/2\eta_{peak}$	$68 < \tau < 108$	0.28	40
40LH310	30	310	$\approx 9/10\eta_{peak}$	$140 < \tau < 180$	0.52	40
40DM310	90	310	$\approx 1/2\eta_{peak}$	$85 < \tau < 125$	0.34	40
40DH310	90	310	$\approx 9/10\eta_{peak}$	$190 < \tau < 230$	0.68	40

Tableau 4. Série d'essais CNS, plaque rugueuse

N°	I_{D0} (%)	σ_n (kPa)	k (kPa/mm)	level of η_{cm0} (-)	τ (kPa)	η_{cm} (-)	$\Delta\tau$ (kPa)
10LM60_1000k	30	60	1000	$\approx 1/2\eta_{peak}$	$13 < \tau < 23$	0.30	10
10LM100_1000k	30	100	1000	$\approx 1/2\eta_{peak}$	$25 < \tau < 35$	0.30	10
20LM100_1000k	30	100	1000	$\approx 1/2\eta_{peak}$	$20 < \tau < 40$	0.30	20
10LM100_2000k	30	100	2000	$\approx 1/3\eta_{peak}$	$15 < \tau < 25$	0.20	10
10LL100_5000k	30	100	5000	$\approx 1/4\eta_{peak}$	$10 < \tau < 20$	0.15	10
20LL100_5000k	30	100	5000	$\approx 1/4\eta_{peak}$	$5 < \tau < 25$	0.15	20
10LM310_1000k	30	310	1000	$\approx 1/2\eta_{peak}$	$88 < \tau < 98$	0.30	10
10DM60_1000k	90	60	1000	$\approx 1/2\eta_{peak}$	$16 < \tau < 26$	0.35	10
10DH60_1000k	90	60	1000	$\approx 1/2\eta_{peak}$	$20 < \tau < 30$	0.42	10
10DM100_1000k	90	100	1000	$\approx 1/2\eta_{peak}$	$30 < \tau < 40$	0.35	10
10DH100_1000k	90	100	1000	$\approx 2/3\eta_{peak}$	$45 < \tau < 55$	0.50	10
20DM100_1000k	90	100	1000	$\approx 1/2\eta_{peak}$	$25 < \tau < 45$	0.35	20
10DM100_2000k	90	100	2000	$\approx 1/2\eta_{peak}$	$30 < \tau < 40$	0.35	10
10DH100_2000k	90	100	2000	$\approx 2/3\eta_{peak}$	$45 < \tau < 55$	0.50	10
10DM100_5000k	90	100	5000	$\approx 1/2\eta_{peak}$	$30 < \tau < 40$	0.35	10
10DM100_5000k	90	100	5000	$\approx 2/3\eta_{peak}$	$45 < \tau < 55$	0.50	10
20DM100_5000k	90	100	5000	$\approx 1/2\eta_{peak}$	$25 < \tau < 45$	0.35	20
10DM310_1000k	90	310	1000	$\approx 1/2\eta_{peak}$	$105 < \tau < 115$	0.35	10
10DH310_1000k	90	310	1000	$\approx 1/2\eta_{peak}$	$150 < \tau < 160$	0.50	10
10_20LM120	30	120	CNL	$\approx 1/2\eta_{peak}$	$30 < \tau < 40$	0.35	10
					$25 < \tau < 45$	0.35	20
20_10LM120	30	120	CNL	$\approx 1/2\eta_{peak}$	$25 < \tau < 45$	0.35	20
					$30 < \tau < 40$	0.35	10
10_20DM120	30	120	CNL	$\approx 1/2\eta_{peak}$	$45 < \tau < 55$	0.35	10
					$40 < \tau < 60$	0.35	20
20_10DM120	30	120	CNL	$\approx 1/2\eta_{peak}$	$45 < \tau < 55$	0.35	10
					$40 < \tau < 60$	0.35	20

Tableau 5. Série d'essais CNL et CNS, plaque lisse

N°	I_{D0} (%)	σ_n (kPa)	k (kPa/mm)	level of η_{cm0} (-)	τ (kPa)	η_{cm} (-)	$\Delta\tau$ (kPa)
10LL120	30	120	CNL	0	$-5 < \tau < 5$	0	10
10LM120	30	120	CNL	$\approx 1/2\eta_{peak}$	$20 < \tau < 30$	0.21	10
10LH120	30	120	CNL	$\approx 9/10\eta_{peak}$	$40 < \tau < 50$	0.38	10
20LM120	30	120	CNL	$\approx 1/2\eta_{peak}$	$15 < \tau < 35$	0.21	20
10DL120	90	120	CNL	0	$-5 < \tau < 5$	0	10
10DM120	90	120	CNL	$\approx 1/2\eta_{peak}$	$28 < \tau < 38$	0.28	10
10DH120	90	120	CNL	$\approx 9/10\eta_{peak}$	$50 < \tau < 60$	0.46	10
20DM120	90	120	CNL	$\approx 1/2\eta_{peak}$	$23 < \tau < 43$	0.28	20
10LL100_1000k	30	100	1000	0	$5 < \tau < 15$	0.10	10
10LL100_5000k	30	100	5000	0	$0 < \tau < 10$	0.05	10
10LM310_1000k	30	310	1000	$\approx 1/2\eta_{peak}$	$42 < \tau < 52$	0.15	10
10LM310_1000k	30	310	1000	$\approx 2/3\eta_{peak}$	$88 < \tau < 98$	0.30	10
10DM60_1000k	90	60	1000	$\approx 1/2\eta_{peak}$	$10 < \tau < 20$	0.25	10
10DM100_1000k	90	100	1000	$\approx 1/2\eta_{peak}$	$15 < \tau < 25$	0.20	10
10DM100_1000k	90	100	1000	$\approx 2/3\eta_{peak}$	$30 < \tau < 40$	0.35	10
10DH100_5000k	90	100	5000	$\approx 2/3\eta_{peak}$	$30 < \tau < 40$	0.35	10
20DH100_1000k	90	100	1000	$\approx 2/3\eta_{peak}$	$25 < \tau < 45$	0.35	20
20DH100_5000k	90	100	5000	$\approx 2/3\eta_{peak}$	$25 < \tau < 45$	0.35	20
10DH310_1000k	90	310	1000	$\approx 1/2\eta_{peak}$	$105 < \tau < 115$	0.35	10

I_{D0} (%)	σ_{ncm0} (kPa)	η_{cm0}	$\Delta\tau$ (kPa)	N
30	120	0,3	10 puis 20	5000 puis 5000
30	120	0,3	20 puis 10	5000 puis 5000
90	120	0,3	10 puis 20	5000 puis 5000
90	120	0,3	20 puis 10	5000 puis 5000

Tableau 6. Série de 4 essais CNL, plaque rugueuse, amplitude variée en cours d'essai

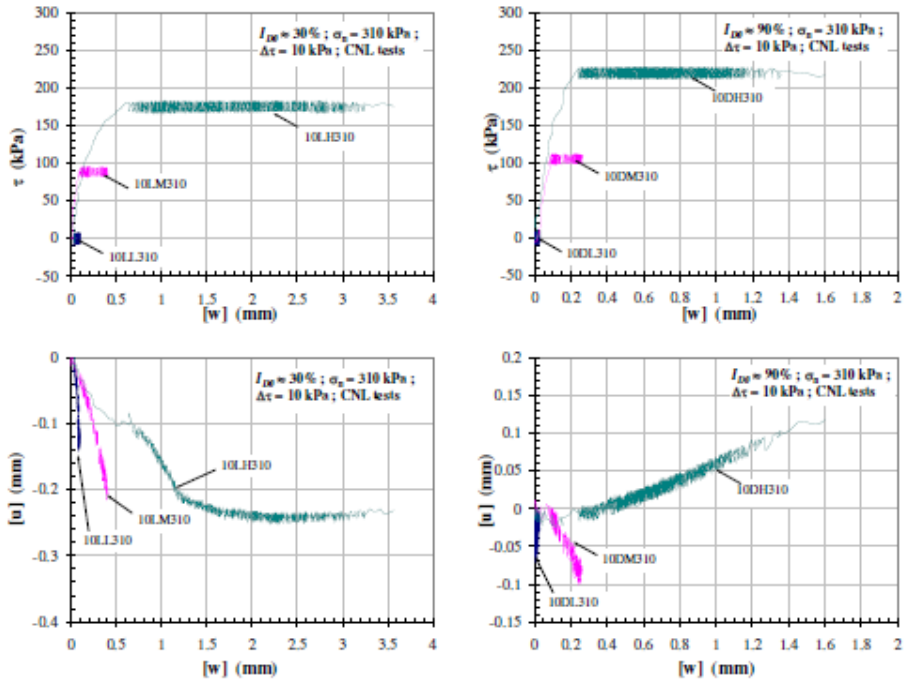

Figure 8. Essais CNL plaque rugueuse, σ_{ncm0} = 310 kPa, $\Delta\tau$ = 10 kPa, ID0 = 30 % (L…gauche), 90 % (D…droite). LL, DL (η_{cm0} = 0), LM, DM ($\eta_{cm0} \approx \eta_{pic}/2$), LH ($\frac{9}{10}\eta_{pic}$) contractants ; DH($\frac{9}{10}\eta_{pic}$) dilatant.

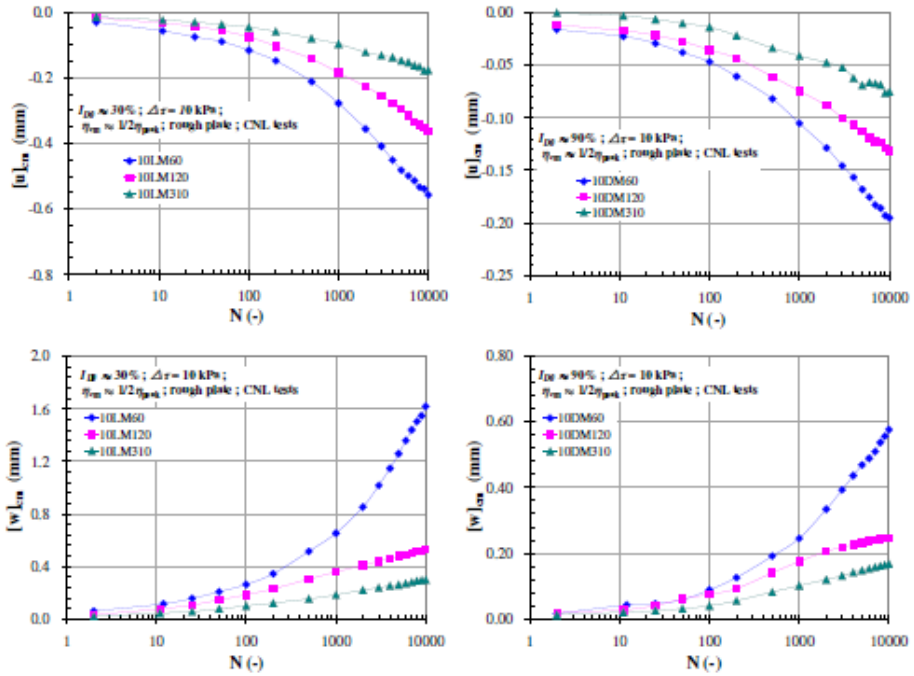

Figure 9. Essais CNL plaque rugueuse, σ_{ncm0} = 60, 120, et 310 kPa, $\Delta\tau$ = 10 kPa, I_{D0} = 30 % (à gauche) et 90 % (à droite). $\eta_{cm0} \approx \eta_{pic} / 2$. Tous contractants. Déplacement relatif tangentiel fonction décroissante de la contrainte normale initiale.

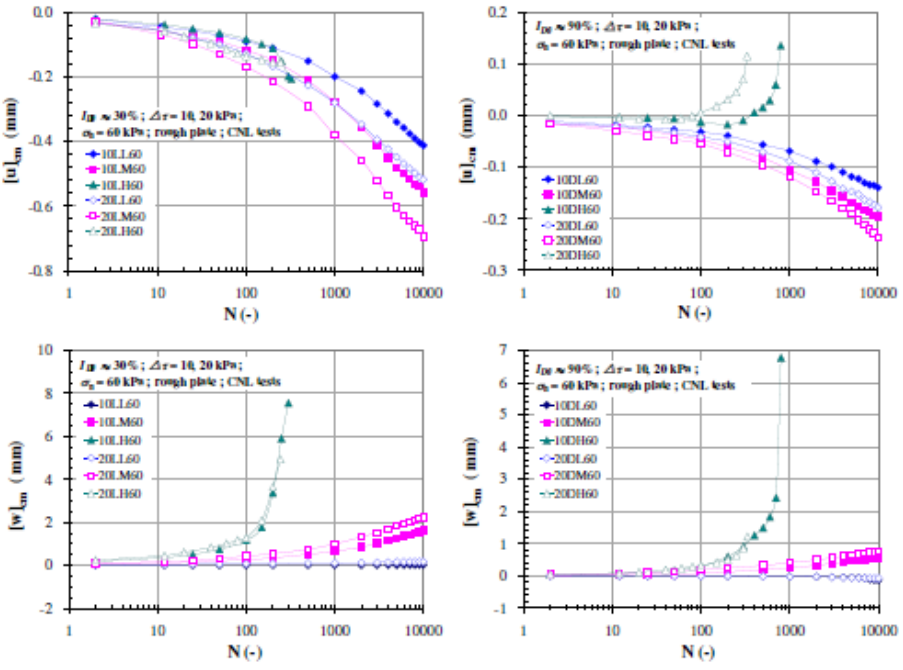

Figure 10. essais CNL, plaque rugueuse. σ_{ncm0} = 60 kPa, $\Delta\tau$ = 10 et 20 kPa, I_{D0} = 30 % (à gauche) et 90 % (à droite). Effet de l'amplitude cyclique.

Les influences de la densité initiale et du niveau cyclique moyen sont visibles figure 8 : dilatance seulement à densité et niveau cyclique moyen élevés. La figure 9, à cisaillement cyclique moyen similaire ($\eta_{cm0} \approx \eta_{pic} / 2$), montre l'influence du niveau de contrainte normale sur les déplacements relatifs normal et tangentiel. L'influence de l'amplitude cyclique se lit à la figure 10, comparant des essais CNL à même contrainte cyclique moyenne (60 kPa), à même amplitude cyclique (10 et 20 kPa), et à cisaillement cyclique moyen faible à fort. A tous les cisaillements cycliques moyens, une amplitude cyclique plus élevée accroit le déplacement relatif tangentiel. L'essai de cisaillement direct CNS typique est représenté figure 11. Le comportement d'interface sol-structure (rugueuse) sur chemin CNS est **toujours contractant**, conduisant à plus ou moins brève échéance, à l'état critique. Le nombre de cycles conduisant à cet état est d'autant plus élevé que la densité est plus forte, que la rigidité normale est plus faible, que le cisaillement cyclique moyen est plus faible, et que l'amplitude cyclique est plus faible. Le niveau de contrainte est également très influent, si l'on compare les nombres de cycles à la rupture aux figures 11 et 12, traduisant deux essais à mêmes paramètres, sauf le niveau de contrainte initial (respectivement 310 kPa, 2035 cycles, et 100 kPa, 2 cycles).

La figure 13, présentant des essais cycliques à amplitudes successives variées (5000 petits cycles suivis de 5000 grands cycles et l'inverse) montre l'influence prépondérante des grands cycles.

Les essais CNL avec plaque lisse exhibent les mêmes tendances que dans le cas rugueux, avec des spécificités remarquables (figure 14):

- le frottement limite est évidemment moindre,
- à nombre égal de cycles, et paramètres cycliques identiques, les déplacements relatifs sont sensiblement plus élevés, qu'il s'agisse du déplacement relatif tangentiel ou normal, ce qui est sans doute à mettre en relation avec une plus grande liberté de mouvements des grains.

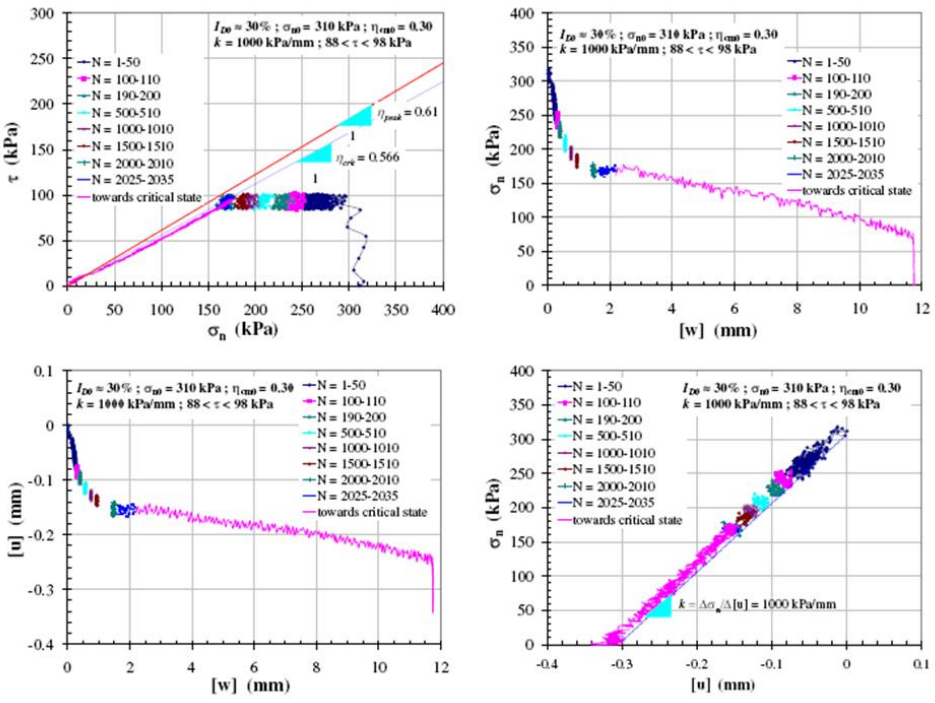

Figure 11. Essai CNS, plaque rugueuse, σ_{ncm0} = 310 kPa, $\Delta\tau$ = 10 kPa, η_{cm0} = 0,30, I_{D0} = 30 %. k = 1000 kPa/mm. Rupture (état critique) à 2035 cycles.

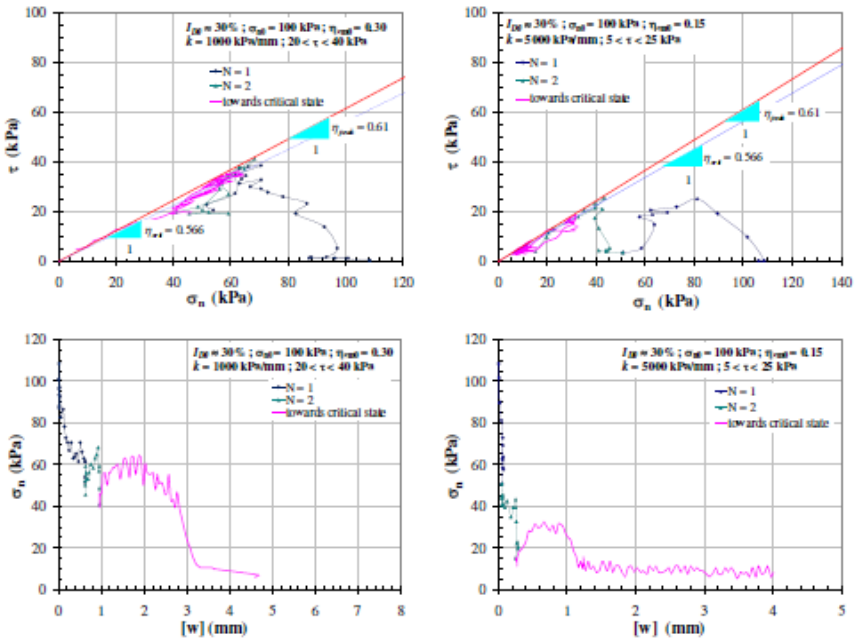

Figure 12. Essai CNS, plaque rugueuse, σ_{ncm0} = 100 kPa, $\Delta\tau$ = 20 kPa, η_{cm0} = 0,30, I_{D0} = 30 %. k = 1000 kPa/mm. Rupture (état critique) au bout de 2 cycles.

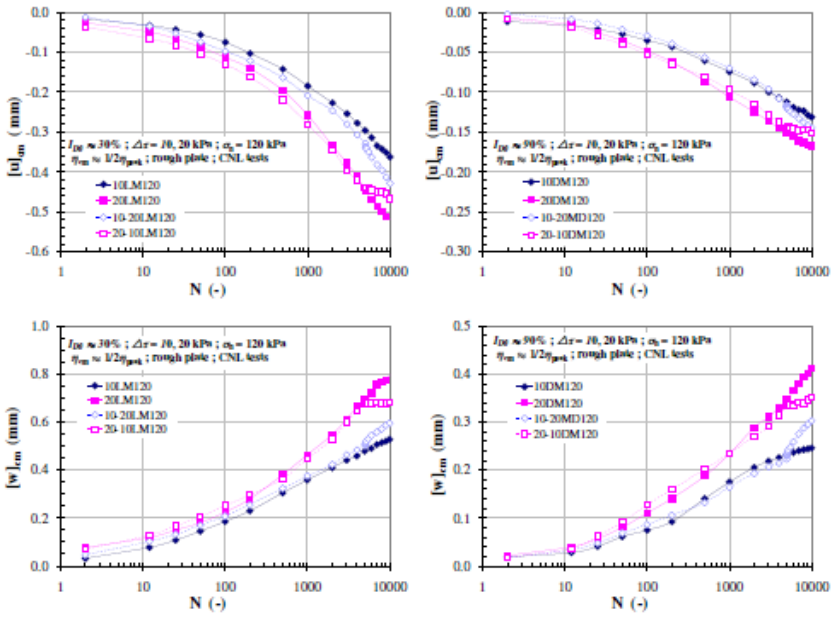

Figure 13. Comparaison d'essais cycliques CNL à amplitude variée, plaque rugueuse. σ_{ncm0} = 120 kPa, η_{cm0} = 0,30, à gauche I_{D0} = 30 %, à droite I_{D0} = 90 %. $\Delta\tau$ = 10 puis 20 kPa, et l'inverse.

On notera que l'essai à densité initiale forte et à niveau cyclique moyen élevé développe de la dilatance, même dans le cas de l'interface lisse.

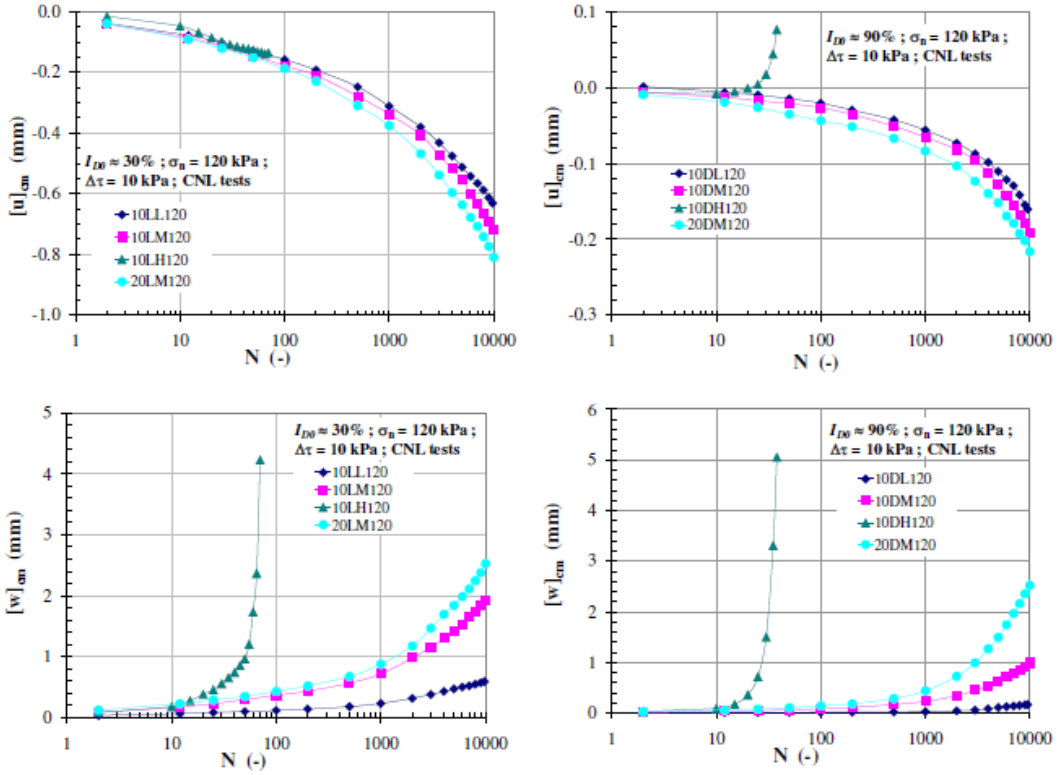

Figure 14. Essais CNL, plaque lisse. Déplacements relatifs tangentiels et normaux, contrainte normale initiale 120 kPa, densités faible (I_{D0} = 30 %) et forte (I_{D0} = 90 %), divers niveaux de cisaillement cyclique moyen.

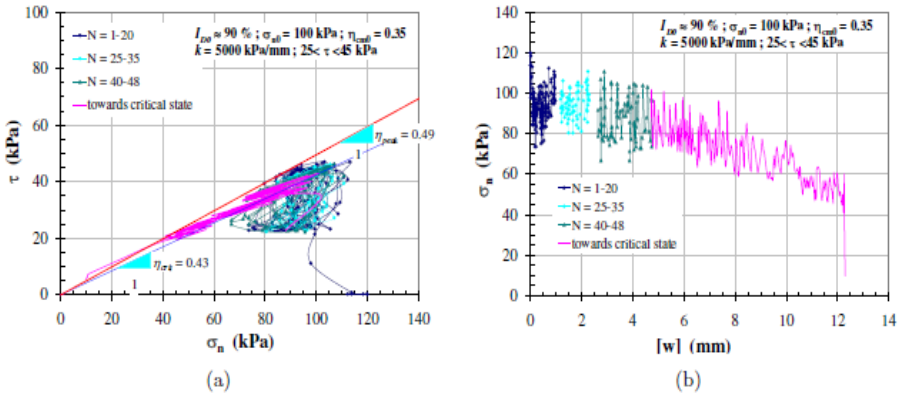

Figure 15. Essai CNS, plaque lisse, densité forte, contrainte normale initiale 100 kPa, k = 5000 kPa/mm. a) chemin de contraintes. b) Evolution de la contrainte normale en fonction du déplacement relatif tangentiel. Rupture à 48 cycles.

Concernant les chemins CNS, la tendance reste la même que dans le cas de la plaque rugueuse, contractance dans tous les cas, menant à la rupture (état critique) à plus ou moins brève échéance. Mais le nombre de cycles nécessaire pour atteindre la rupture est drastiquement plus faible que dans le cas rugueux (figure 15). La rupture intervient au bout de

48 cycles seulement dans le cas lisse, contre 1175 cycles dans le cas rugueux, les paramètres cycliques étant rigoureusement les mêmes (σ_{ncm0} = 100kPa, η_{cm0} = 0,35, $\Delta\eta$ = 0,2). Ceci dit, les taux de cisaillement limites sont plus faibles pour la plaque lisse (η_{pic} = 0,49 et η_{crit} = 0,43 dans le cas lisse, contre 0,61 et 0,57 dans le cas rugueux).
Les analyses granulométriques opérées après cisaillement ont été jugées trop peu discriminantes, même avec la technique laser, pour être exploitées, ainsi qu'en témoigne la figure 16 (essai à densités initiales faible et forte, même contrainte normale cyclique moyenne (310 kPa), même amplitude cyclique ($\Delta\tau$ = 10 kPa), et cisaillements cycliques moyens variés(η_{cm0} = 0,30 à 0,60).

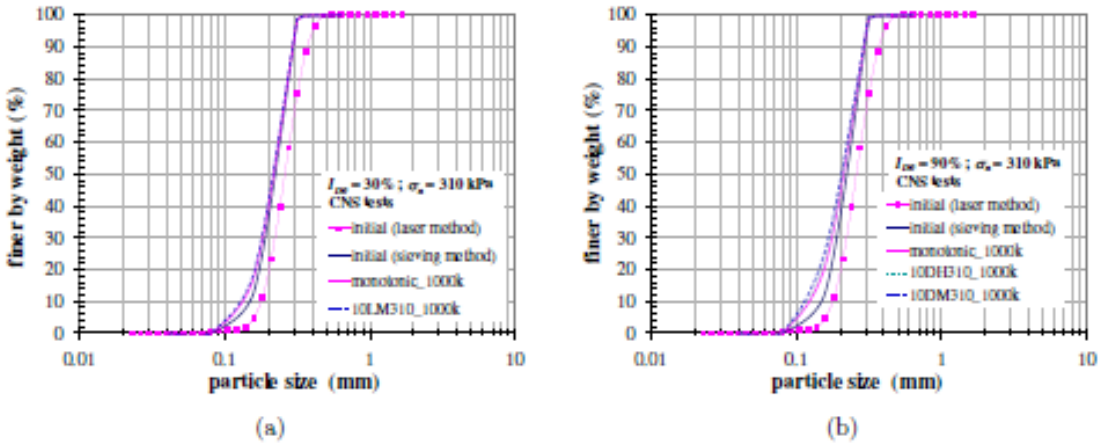

Figure 16 . Essais CNS, plaque rugueuse, σ_{ncm0} = 310 kPa, $\Delta\tau$ = 10 kPa, η_{cm0} variés (= 0,30 à 0,60), I_{D0} = 30 % et 90 %, k = 1000 kPa/mm. Analyses granulométriques avant et après cisaillement..

Chapitre 3. Modélisation constitutive des essais de cisaillement direct

3.1. Un modèle phénoménologique « pré-intégré »

En situation 2-D, la modélisation constitutive du cisaillement direct d'interface sol-structure consiste en la relation tangente entre réponse et sollicitation, ici entre les dérivées temporelles des vecteurs déplacement relatif (entre sol et structure) et contrainte (agissant sur l'interface), fonction du chemin suivi (c), et de paramètres de mémoire (m_i), soit :

$$\begin{pmatrix} \begin{bmatrix} \dot{u} \\ \dot{w} \end{bmatrix} \end{pmatrix} = f\left(\begin{pmatrix} \dot{\sigma}_n \\ \dot{\tau} \end{pmatrix}, c, m_i \right) \qquad (2)$$

Le chemin (tangent) de cisaillement est mesurable, par exemple, par le rapport des composantes de la sollicitation. Nous nous limiterons à **une classe de chemins**, dits à rigidité normale imposée non négative (§ 2.1). Parmi ces chemins, certains servent à l'identification du modèle, tandis que d'autres sont voués à la validation. Dès lors, si nous sommes en mesure de donner une formulation analytique (évidemment approchée) d'un chemin fini à c constant, et non plus de sa seule dérivée temporelle, nous considérerons cette formulation comme une

forme « pré-intégrée » de ce chemin sur un domaine fini de sollicitation, fonction des conditions initiales. Dans notre cas, la **mémoire** se réduit à **un seul paramètre, le poids volumique sous contrainte**, $\gamma_{d\ \sigma_n} = \gamma_{d0\ \sigma_n} (\frac{1}{1+[u]/t})$, directement déductible du déplacement relatif normal $[u]$, des conditions initiales, et de l'épaisseur d'interface t. Le poids volumique sous contrainte peut outrepasser le poids volumique maximum (conventionnel !).

3.2. Modélisation des essais monotones

Nous avons été en mesure de donner une formulation analytique de tous les essais monotones (à contrainte normale constante et à rigidité normale imposée). Nous présentons dans la thèse seulement des chemins d'identification, CNL et CNS, dans la mesure où, sauf chemins rarement suivis, à savoir variation de contrainte normale en cours d'essai CNL ou CNS, ou de rigidité normale imposée en cours d'essai CNS, les validations ne s'imposent pas. Au cas où de tels chemins seraient nécessaires, le paramètre de mémoire cité précédemment, $\gamma_{d\ \sigma_n}$ serait utilisé pour enchaîner des séquences de sollicitations, sous la forme d'incréments finis, formulés analytiquement. Les figures 17 et 18 présentent les paramètres clés des formulations analytiques respectivement pour les chemins CNL et CNS. La pente de la courbe $[u]-[w]$ du chemin CNL au-delà de $[w]_{crit}$ n'est pas classique, mais existe, surtout dans le cas d'une interface sol friable-structure (sables carbonatés par exemple). De même, la pente de la courbe $\sigma_n - [w]$ du chemin CNS existe principalement pour ce même type d'interface, la rupture des grains intervenant, bien que moindre, même pour des sables siliceux. Il s'agit donc d'identifier ces paramètres clés, avec leurs variations en fonction de l'indice de densité initiale I_{D0}, du niveau initial de contrainte σ_{n0}, et de la rigidité normale imposée k (3 paramètres). Nous avons repris, en les perfectionnant, les formulations de Hoteit (1990), Boutrif (1993), et Garnica Anguas (1993). La figure 19 présente la modélisation d'essais CNL entre sable de Fontainebleau et plaque rugueuse, à densités faible (30 %) à gauche, et forte (90 %) à droite.

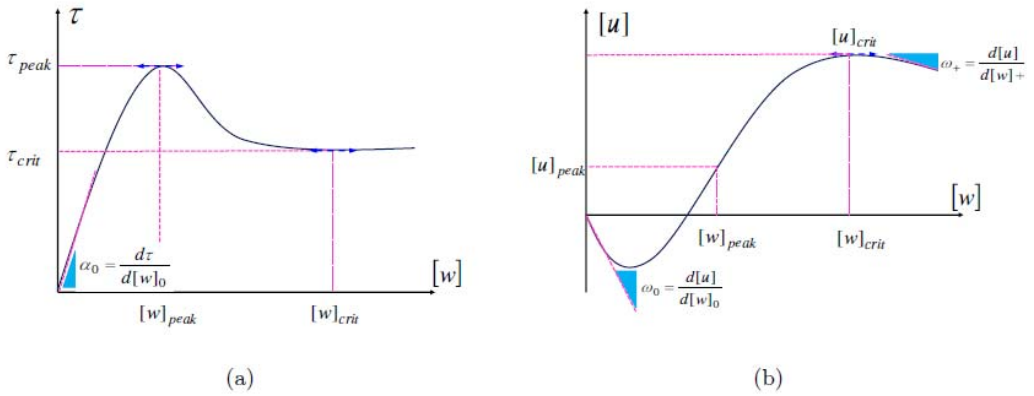

Figure 17. Paramètres clés de formulation des chemins CNL. a) courbe $\tau - [w]$. b) courbe $[u]-[w]$.

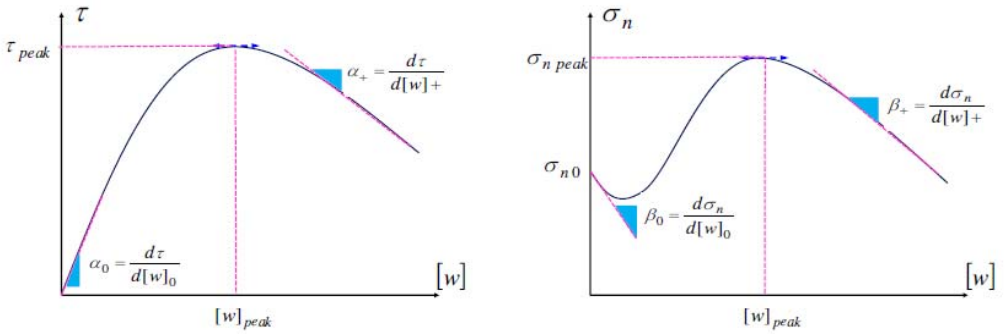

Figure 18. Paramètres clés de formulation des chemins CNS. a) courbe $\tau - [w]$. b) courbe $\sigma_n - [w]$.

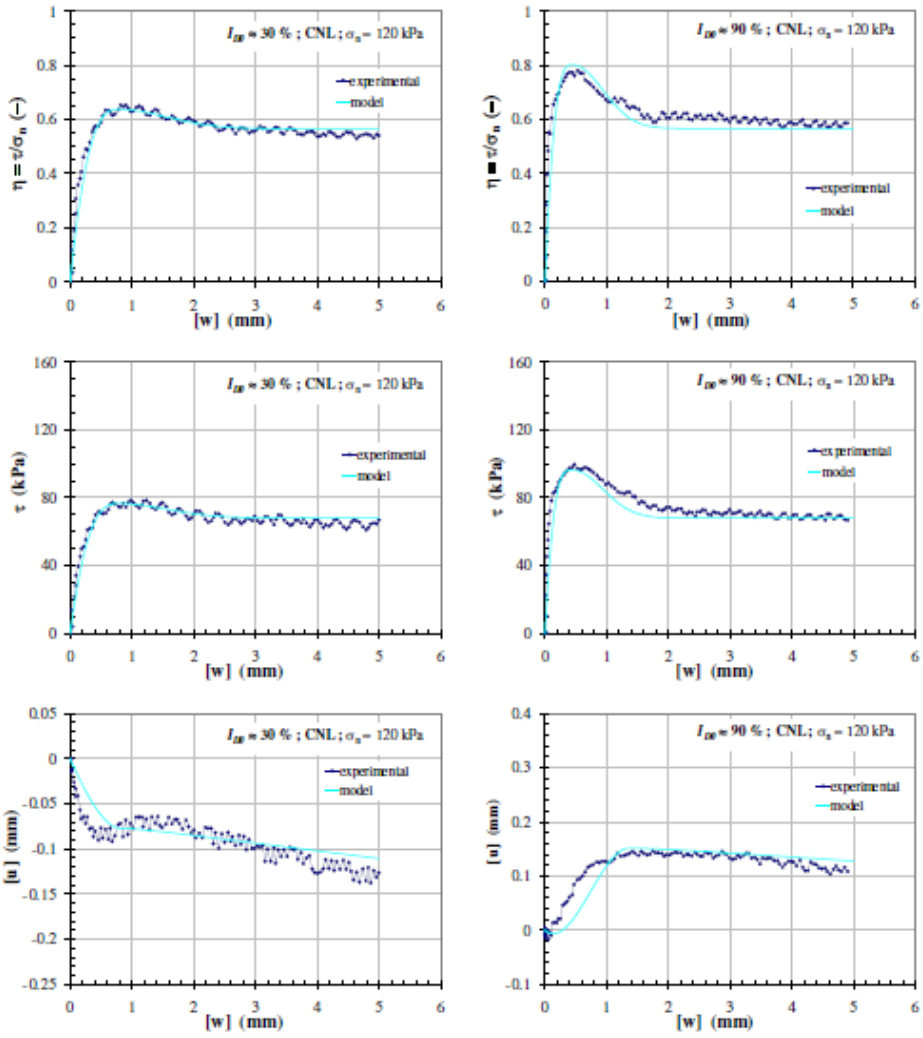

Figure 19. Comparaison entre essai et formulation analytique d'essais CNL, σ_{n0} = 120 kPa, densités faible (gauche) et forte (droite).

La figure 20 fournit la modélisation d'essais CNS entre sable de Fontainebleau et plaque rugueuse, à densités faible (30 %) à gauche, et forte (90 %) à droite, pour diverses valeurs de la rigidité normale imposée. Dans les 2 cas, figures 19 et 20, la contractance à densité faible et la dilatance à densité forte, lors de grands déplacements relatifs tangentiels, sont bien simulés.

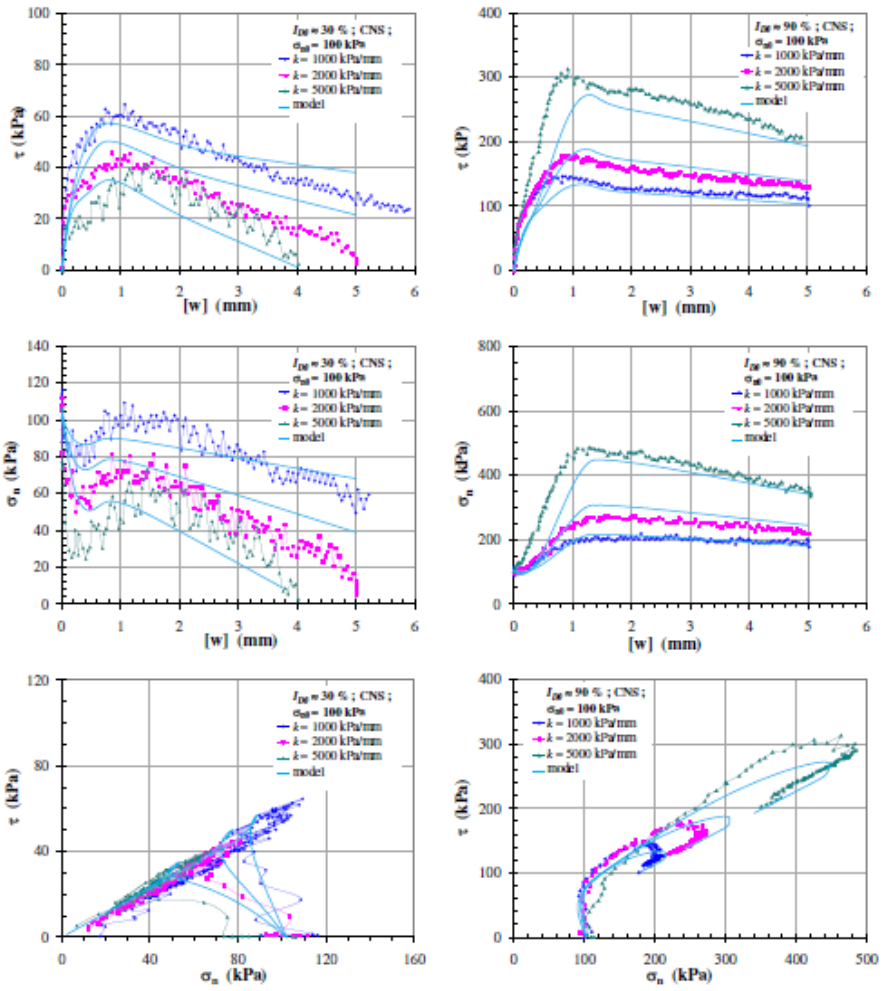

Figure 20. Comparaison entre essais et formulation analytique d'essais CNS, σ_{n0} = 100 kPa, densités faible (gauche) et forte (droite). k = 1000, 2000, et 5000 kPa/mm.

3.3. Modélisation des essais cycliques CNL d'identification

Rappelons les grands principes du modèle élasto-visco-plastique de Perzyna (1966) adapté au pseudo-fluage cyclique : Au cours des cycles, le vecteur incrément de déplacement relatif sol-structure est la somme d'une partie élastique indicée « e », et d'une partie cyclique moyenne

$$d[\underline{u}] = d[\underline{u}]_e + d[\underline{u}]_{cm} \tag{3}$$

indicée « cm ». La première partie, élastique, est classiquement écrite ($\underline{\underline{D_e}}$ matrice élastique) :

$$d[\underline{u}]_e = \underline{\underline{D_e}}^{-1} d\underline{\sigma} \tag{4}$$

tandis que le vecteur incrément de déplacement relatif visco-plastique (ici cyclique moyen), a pour expression (Γ paramètre scalaire de fluidité, F frontière entre comportements non visqueux et visqueux, Φ noyau visqueux (0 à l'intérieur, 1 à l'extérieur de F), $G(\underline{\sigma})$ potentiel visco-plastique, dont les dérivées partielles définissent la direction de l'écoulement visqueux, dN incrément de nombre de cycles):

$$d[\underline{u}]_{cm} = \Gamma\Phi(F)\frac{\partial G}{\partial \underline{\sigma}}dN \tag{5}$$

Dans notre cas, le noyau est vide, ce qui signifie que le pseudo-fluage existe quel que soit le niveau des paramètres cycliques. Par ailleurs le vecteur $[\underline{u}]_{cm}$ est directement exprimé analytiquement, par ses composantes $\begin{pmatrix}[u]_{cm}\\ [w]_{cm}\end{pmatrix}$, fonctions de N, qui traduisent en outre, de manière naturelle, la direction d'écoulement pseudo-visqueux. Le déplacement relatif irréversible $[\underline{u}]_{cm}$, déclaré pseudo-visqueux, est en fait une accumulation de déplacements relatifs plastiques.

3.3.1. Formulation analytique des chemins clés CNL de cisaillement cyclique

La base de notre interprétation est classique (figure 21), ce qui nous a conduit à détecter/identifier, les 3 sortes de pseudo-fluage (primaire, secondaire, et tertiaire), la vitesse

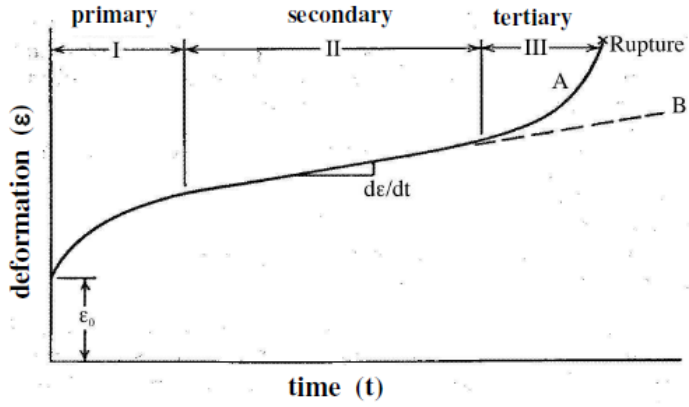

Figure 21. Le fluage, tel qu'il est classiquement décrit.

de pseudo-fluage s'entendant comme $\frac{\partial}{\partial N}$ au lieu de $\frac{\partial}{\partial t}$ (t = temps en fluage). Les paramètres de nos essais sont (§ 2.6.1) I_{D0}, σ_{ncm0}, η_{cm0}, $\Delta\eta_0$, et N. A l'examen attentif des essais, le plus souvent menés jusqu'à 10000 cycles, il est apparu les caractéristiques générales suivantes pour les composantes $[w]_{cm}$ et $[u]_{cm}$:

- La composante $[w]_{cm}$ est identiquement nulle pour des cycles centrés ($\eta_{cm0} = 0$).
- Le pseudo-fluage primaire existe pour les 2 composantes ($[w]_{cm}$ et $[u]_{cm}$), et pour tous les essais (noyau visqueux vide au sens de Perzyna).

- Le pseudo-fluage secondaire existe pour les 2 composantes dans les essais à valeurs modérées du cisaillement cyclique moyen réduit η_{cm0}. En outre ces essais (figure 22) sont toujours contractants ($[u]_{cm} < 0$).
- Concernant le déplacement relatif tangentiel cyclique moyen $[w]_{cm}$, le pseudo-fluage tertiaire existe aux valeurs élevées de η_{cm0}.
- Concernant le déplacement relatif normal cyclique moyen $[u]_{cm}$ aux valeurs élevées de η_{cm0}, on peut constater (figure 22) une dilatance (I_{D0} élevé), ou une contractance (I_{D0} faible), aboutissant à une valeur limite $[u]_{cm\ l}$ (en relation avec la densité critique sous contrainte $\gamma_{d\ crit\ \sigma_n}$, avec t épaisseur d'interface).

$$\gamma_{d\ crit\ \sigma_n} = \gamma_{d0\ \sigma_n} \left(\frac{1}{1+[u]_{cm\,l}/t}\right) \tag{6}$$

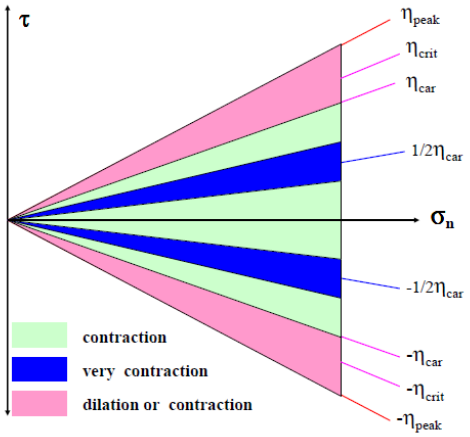

Figure 22. Les 3 « pôles » du comportement d'interface sable-structure, relativement au déplacement relatif normal cyclique moyen $[u]_{cm}$, en relation avec les résistances de pic et critique, et avec l'angle « caractéristique » (Luong, 1980).

- Le niveau de contrainte normale cyclique moyenne σ_{ncm0} agit directement sur les vitesses de pseudo-fluage cyclique, un peu à la manière d'un module (A contrainte faible vitesse élevée, et à contrainte élevée vitesse faible).
- L'amplitude cyclique réduite $\Delta\eta_0$ intervient comme un amplificateur, étant entendu que le pseudo-fluage cyclique s'éteint à amplitude cyclique nulle.

L'évolution de $[u]_{cm}$ est ainsi définie pour les pôles (nœuds en langage éléments finis):

- a) Cisaillement réduit modéré, c'est-à-dire $\eta_{cm0} = \eta^* = \eta_{car}/2$ par:

  $\gamma_{d\ \max\sigma_n\ N_f} = \gamma_d^*(\Delta\eta)^n$ constantes fonctions de σ_{ncm} et de I_{D0} ; N_f = 10000 cycles (7)

  Evolution hyperbolique $f(N) = \dfrac{N}{N_{50\%}+N}$, $N_{50\%}$ fonction de σ_{ncm}, I_{D0}, $\dfrac{\eta_{\max}}{\eta_{pic}}$ (8)

- b) Cisaillement réduit élevé, c'est-à-dire $|\eta_{cm0}| > \eta_{car}$

  $\gamma_{d\ crit\ \sigma_n}$ fonction de σ_{ncm} (§ 2.5.1). Ce poids volumique constitue une asymptote/N

Evolution hyperbolique comme en a)

- c) en outre, l'évolution de $[u]_{cm}$ pour $\eta_{cm0} = 0$ est liée à a) par le paramètre $\bar{a}$:

$$\gamma_{d \ \max \sigma_n N_f \eta_{cm}=0} = \bar{a}\gamma_d^*(\Delta\eta)^n \quad \text{avec } 0 < \bar{a} < 1, \ \bar{a} \text{ fonction de } \sigma_{ncm} \text{ et de } I_{D0} \text{ définir } N_f \qquad (9)$$

L'évolution de $[w]_{cm}$ ne requiert de formulation que dans les cas a et b :

- a) Cisaillement réduit modéré : Il s'agit de pseudo-fluages cycliques primaire et secondaire. Nous avons défini (figure 23) une asymptote (pente a, ordonnée à l'origine b dans le plan ($[w]_{cm}$-N), et une loi d'évolution hyperbolique y avec $N_{50\%}$ (C sur figure 23) double du précédent.

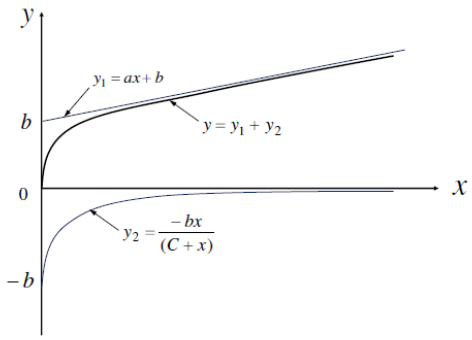

Figure 23. Définition de la fonction $[w]_{cm}(N)$, η_{cm0} modéré, pseudo-fluages cycliques primaire et secondaire, courbe y.

- b) Cisaillement réduit élevé, c'est-à-dire $|\eta_{cm0}| > \eta_{car}$: Le pseudo-fluage cyclique secondaire est pratiquement absent. Nous avons défini une pente initiale (y'_0), une

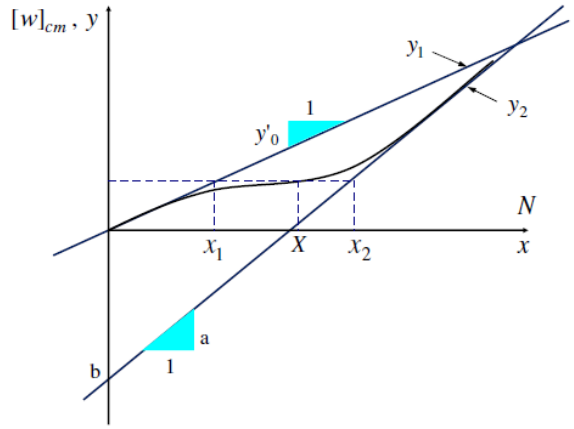

Figure 24. Définition de la fonction $[w]_{cm}(N)$, η_{cm0} élevé, pseudo-fluages cycliques primaire et tertiaire, secondaire pratiquement inexistant, courbe y interpolée entre y_1 et y_2.

asymptote (a et b), ainsi qu'une interpolation exponentielle entre ces 2 extrêmes (figure 24). Les paramètres $y_0^{'}$, a et b (paramètre courant p) sont fonctions de η_{cm0}, $\Delta\eta$ (figure 25), et σ_{ncm}. Pour $\Delta\eta < \Delta\eta_{\max}$, interpolations linéaire ou quadratique.

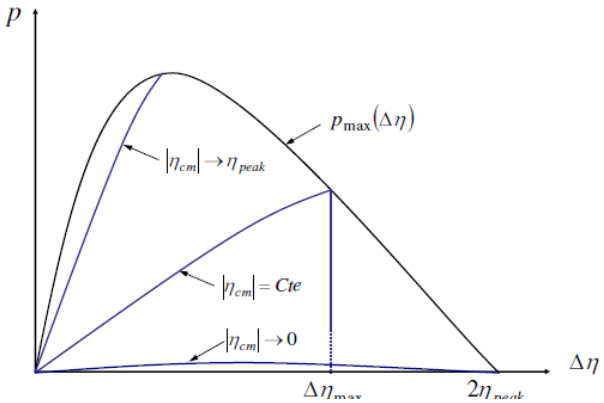

Figure 25. Limites et allure du paramètre p (= $y_0^{'}$/a / b), pseudo-fluages primaire et tertiaire, cas η_{cm0} élevé.

3.3.2. Interpolation constitutive

On se réfère ici au langage éléments finis. L'interpolation constitutive consiste en une interpolation entre les comportements clés (« nœuds » correspondant à $\left|\ \eta_{cm0}\ \right| = \eta_* = \eta_{car}/2$, $\left|\ \eta_{cm0}\ \right| \approx \eta_{crit}$, accessoirement $0 < \left|\ \eta_{cm0}\ \right| < \eta_*$) définis précédemment (§ 3.3.1).

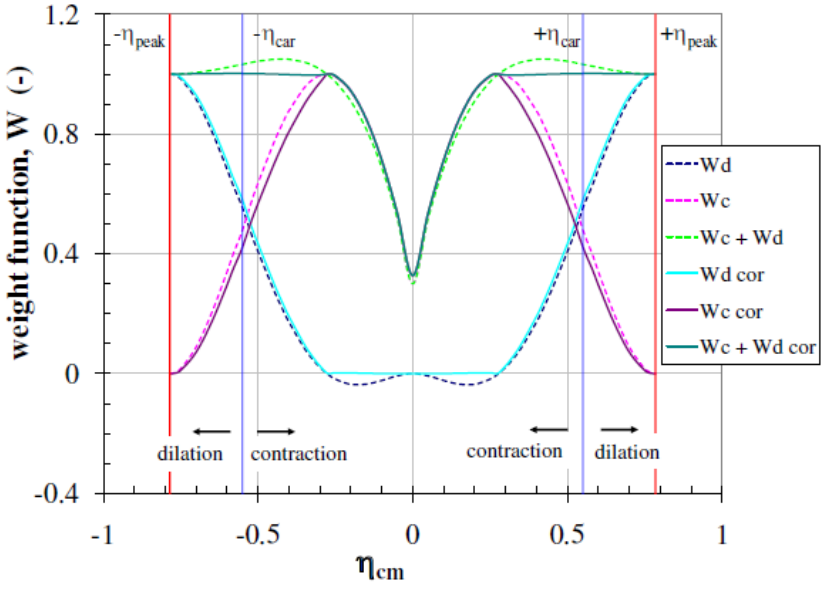

Figure 26. Les fonctions d'interpolation $W_{c\ corr}$ et $W_{d\ corr}$, pour $[u]_{cm}$ ($\bar{a} \neq 0$), cas dense ($I_{D0} = 90\%$) et niveau de contrainte élevé ($\sigma_{ncm0} = 310\ \ kPa$).

Nous avons construit des interpolations constitutives voisines pour $[u]_{cm}$ et $[w]_{cm}$, la différence provenant du paramètre $\bar{a}$, relatif aux chemins $\eta_{cm0} = 0$, avec $\bar{a} = 0$ pour $[u]_{cm}$ et $0 < \bar{a} < 1$ pour $[w]_{cm}$. Les fonctions d'interpolation sont relatives à un niveau de contrainte (car η_{pic} en dépend), et à un niveau de densité (pour la même raison). Deux fonctions d'interpolation dérivant du type hermitien sont utilisées : W_c (indice c comme contractant) centrée sur $\pm\eta_*$, et W_d (indice d comme dilatant) centrée sur $\pm\eta_{pic}$. La difficulté a été de générer une seule fonction analytique définie sur le domaine $\langle -\eta_{pic}, +\eta_{pic} \rangle$ pour chacune d'entre elles. D'autant plus qu'il s'agit d'une vraie interpolation sur les fractions de domaine $\langle -\eta_{pic}, -\eta_* \rangle$ et $\langle \eta_*, +\eta_{pic} \rangle$ (alors $W_c + W_d = 1$), tandis que sur la fraction de domaine $\langle -\eta_*, +\eta_* \rangle$, W_d n'intervient plus (alors $W_d \equiv 0$), et W_c varie entre $\bar{a}$ et 1. Nous avons utilisé une fonction de correction très voisine d'un « créneau », analytique elle aussi, pour parvenir à ce résultat. Les fonctions d'interpolation utilisées sont finalement $W_{c\ corr}$ et $W_{d\ corr}$. La figure 26 donne une représentation de ces fonctions dans le cas dense et pour le niveau de contrainte $\sigma_{ncm0} = 310\ \ kPa$.

3.3.3. Résultats comparés à l'expérience

Seuls les essais avec plaque rugueuse sont présentés ici. Les figures 27 (σ_{ncm0} = 120 kPa ; η_{cm0} faible, moyen, élevé ; faible amplitude cyclique ; I_{D0} = 30%) et 28 (σ_{ncm0} = 310 kPa ; η_{cm0} faible, moyen, élevé ; faible amplitude cyclique ; I_{D0} = 90%) montrent des résultats expérimentaux comparés aux courbes analytiques d'identification. On notera la valeur limite de $[u]_{cm}$ correspondant au poids volumique critique d'interface, pour η_{cm0} élevé.

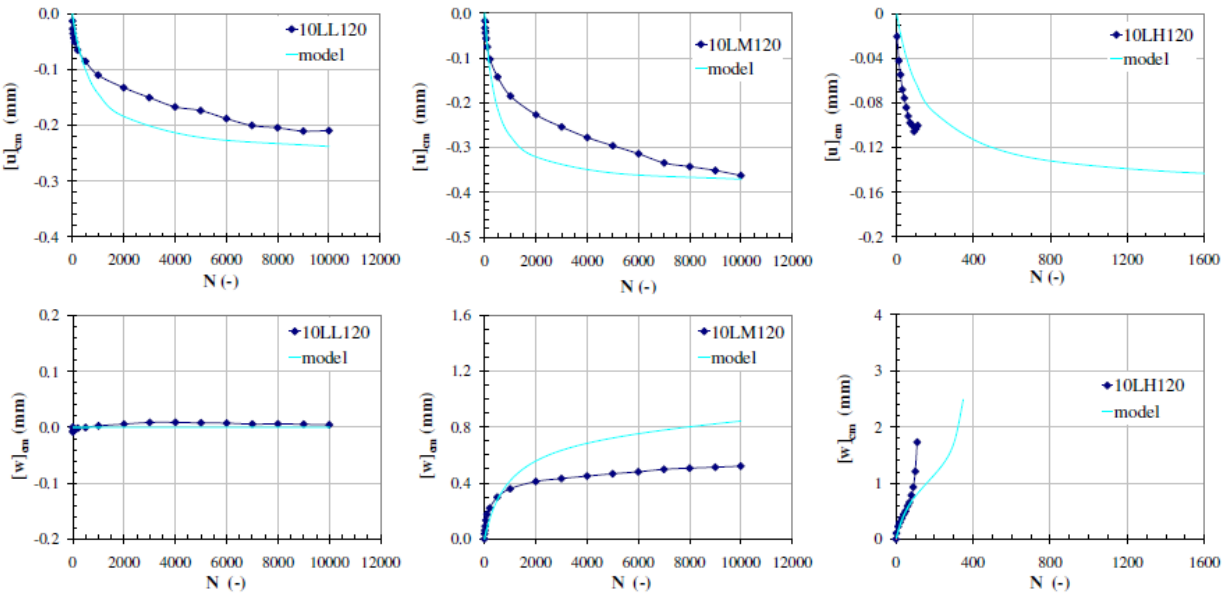

Figure 27. Essais CNL et identification analytique : σ_{ncm0} = 120 kPa ; η_{cm0} faible (= 0), moyen ($\approx \eta_{pic}/2$), élevé ($\approx 0.8 \times \eta_{pic}$); faible amplitude cyclique ($\Delta\tau$ = 10 kPa); I_{D0} = 30%.

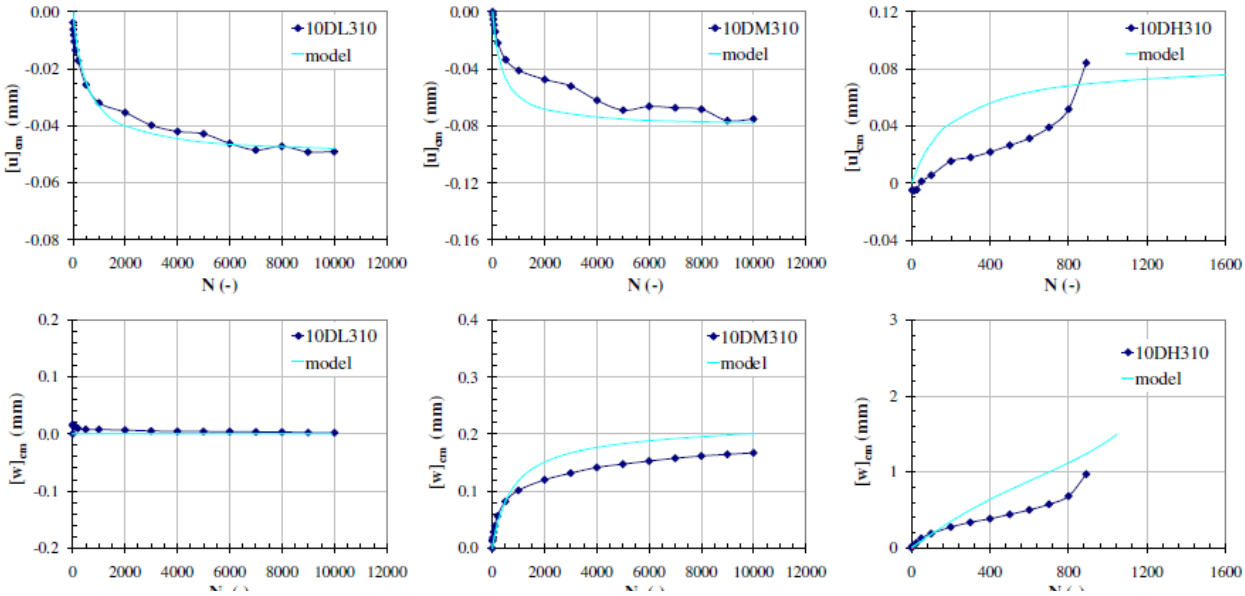

Figure 28. Essais CNL et identification analytique : σ_{ncm0} = 310 kPa ; η_{cm0} faible (= 0), moyen ($\approx \eta_{pic}/2$), élevé ($\approx 0.8\times\eta_{pic}$); faible amplitude cyclique ($\Delta\tau$ = 10 kPa); I_{D0} = 90%.

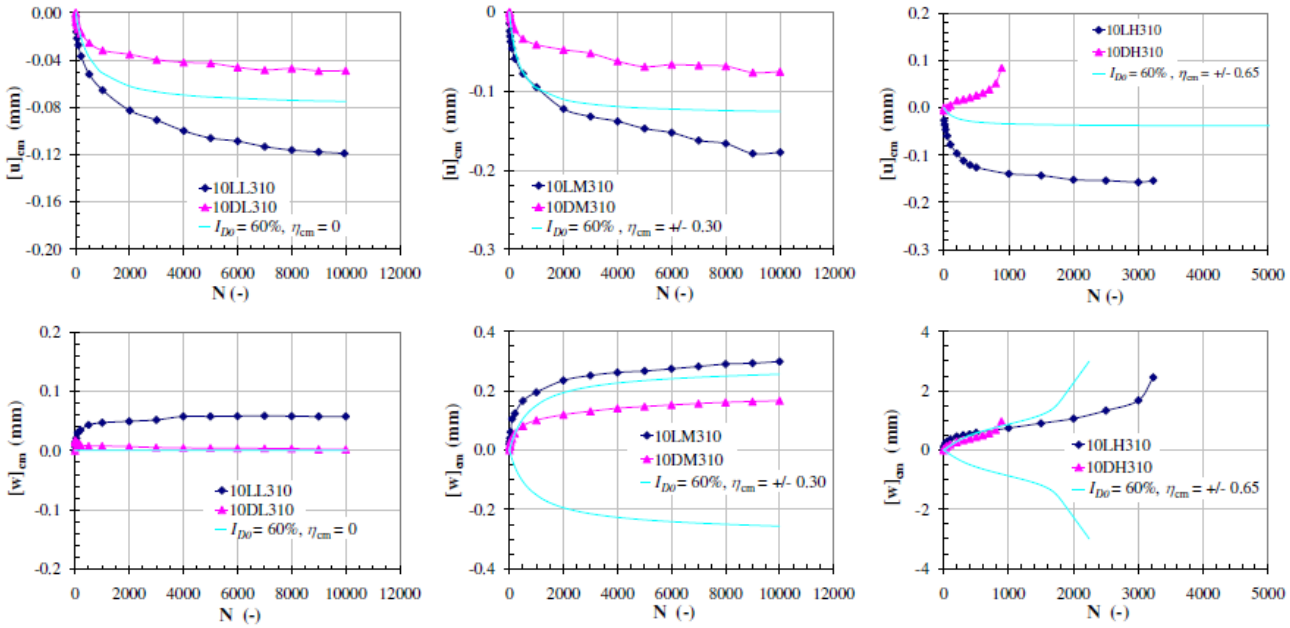

Figure 29. Généralisation analytique à un chemin CNL à densité moyenne (I_{D0} = 60%) par interpolation linéaire : σ_{ncm0} = 310 kPa ; η_{cm0} faible (= 0), moyen ($\approx \eta_{pic}/2$), élevé ($\approx 0.8\times\eta_{pic}$); faible amplitude cyclique ($\Delta\tau$ = 10 kPa).

Les formulations analytiques des essais CNL d'identification permettent un premier niveau de généralisation qui pourrait servir à la validation si d'autres essais existaient. On peut ainsi étendre ces résultats par interpolation linéaire sur la densité (figure 29 pour I_{D0} = 60%), quadratique sur le niveau de contrainte normale cyclique moyenne (figure 30 pour σ_{ncm0} = 200 kPa).

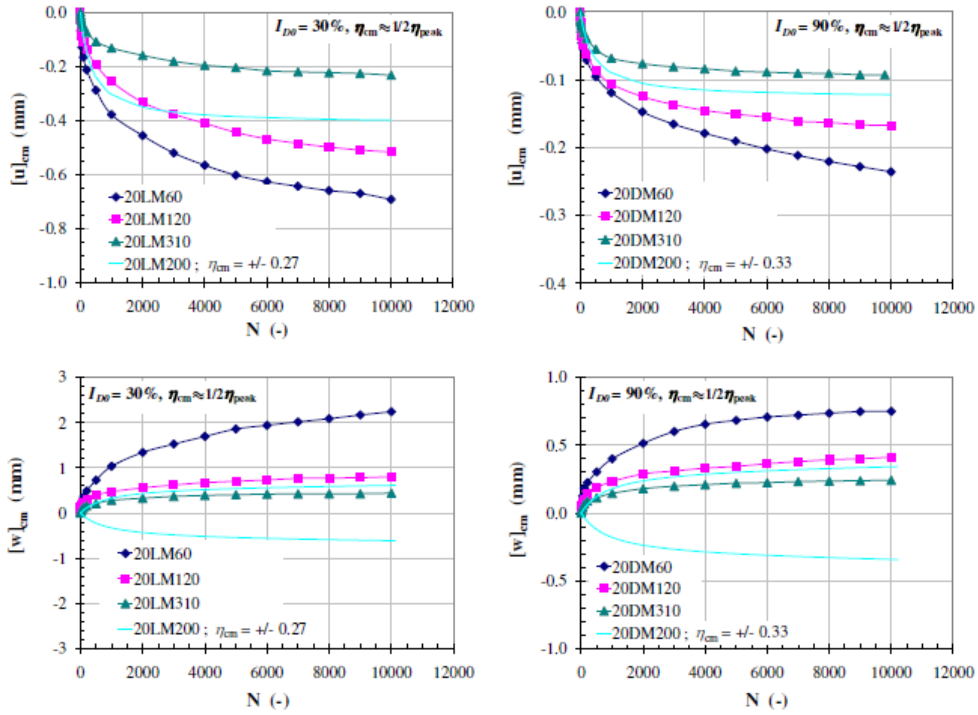

Figure 30. Généralisation analytique à un chemin CNL à niveau moyen de contrainte cyclique moyenne (σ_{ncm0} = 200 kPa) par interpolation quadratique : η_{cm0} moyen ($\approx \eta_{pic}/2$); amplitude cyclique moyenne ($\Delta\tau$ = 20 kPa). I_{D0} = 30% et 90 %.

3.4. Modélisation d'essais CNL à amplitude cyclique variée

Comme nous l'avons indiqué précédemment, les formulations analytiques sur chemin CNL fournissent $\begin{pmatrix} [u]_{cm} \\ [w]_{cm} \end{pmatrix}$ fonction des paramètres I_{D0}, σ_{ncm0}, η_{cm0}, $\Delta\eta_0$, et N. Comme la mémoire du comportement d'interface est représentée par $\gamma_{d\ \sigma_n}$ directement relié à $[u]_{cm}$, l'évolution de cette mémoire est immédiatement disponible sur de tels chemins. Ce n'est plus le cas lorsque le chemin CNL choisi inclut un changement de l'un des paramètres σ_{ncm0}, η_{cm0}, $\Delta\eta_0$ (par exemple plusieurs séries de cycles d'amplitude variée ou de niveaux moyens variés). Il s'agit alors de passer de la formulation analytique « précédente », à la formulation analytique « suivante », le lien entre celles-ci étant le paramètre de mémoire, démarche que nous expliquons ci-dessous. Néanmoins, notre analyse utilise des incréments analytiques finis ou pré-intégrés.

3.4.1. Nombre équivalent de cycles. Validation sur essais CNL à amplitudes variées

La figure 31 donne le principe de la recherche itérative du passage entre les 2 formulations, qui fait intervenir le « nombre équivalent de cycles » N_{eq} de la série dite « suivante »,

équivalent à l'évolution au cours des séries dites « précédentes » de cycles. Autrement dit, étant donné l'état atteint par l'interface au terme de la série (i-1), soit :

$$\Im_{i-1} = \{\mathrm{I_{D0}},\ \sigma_{ncm0},\ \eta_{cm0},\ \Delta\eta_{i-1},\ N_{i-1},\ [u]_{cm\ i-1},\ [w]_{cm\ i-1}\} \quad (10)$$

Nous recherchons l'état de début de la série de cycles i, à savoir :

$$\Im_i = \{\mathrm{I_{D0}},\ \sigma_{ncm0},\ \eta_{cm0},\ \Delta\eta_i,\ N_{eq\ i} \neq N_{i-1},\ [u]_{cm\ i} = [u]_{cm\ i-1},\ [w]_{cm\ i}\} \quad (11)$$

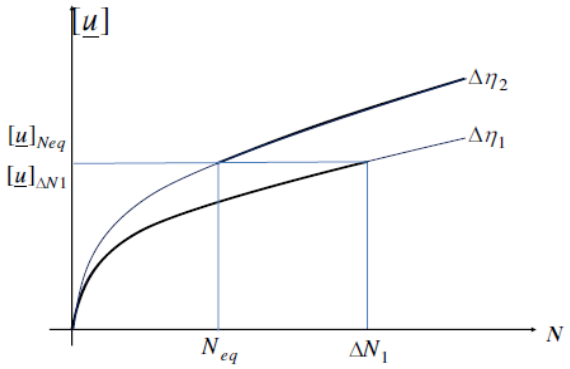

Figure 31. Principe d'évaluation du nombre équivalent de cycles, entre 2 séries successives de cycles de paramètres différents.

Il n'y a pas forcément coïncidence entre $[w]_{cm\ i}$ et $[w]_{cm\ i-1}$, ce que nous considérons comme secondaire. La figure 32 donne une comparaison expérience modélisation pour 2 séries successives de 5000 cycles, à σ_{ncm0} = 120 kPa), η_{cm0} moyen ($\approx \eta_{pic}/2$); amplitude cyclique moyenne ($\Delta\tau$ = 10 puis 20 kPa). I_{D0} = 30%.

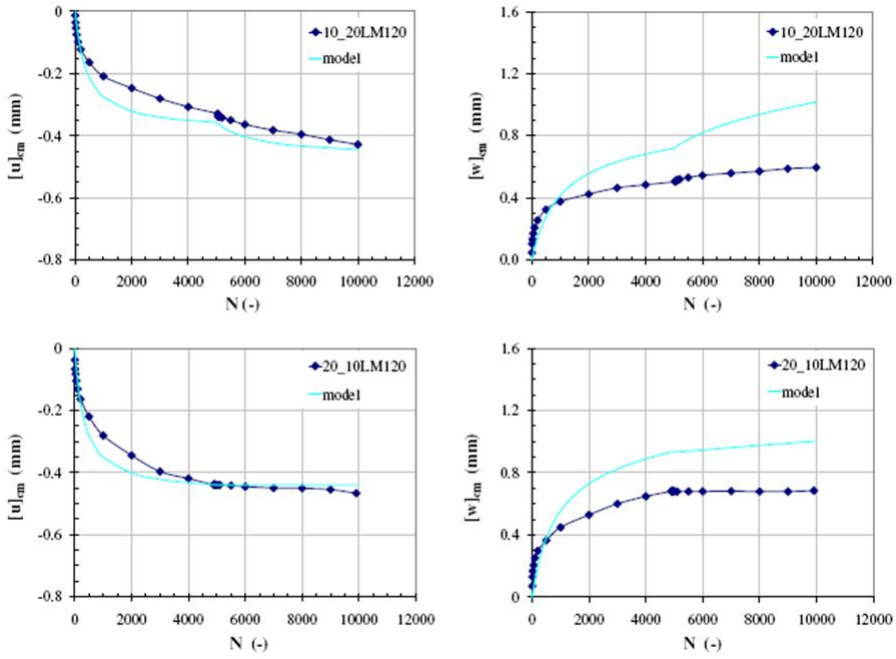

Figure 32. Comparaison expérience modélisation pour 2 séries successives de 5000 cycles, à σ_{ncm0} = 120 kPa , η_{cm0} moyen ($\approx \eta_{pic}/2$), amplitude cyclique moyenne ($\Delta\tau$ = 10 puis 20 kPa). I_{D0} = 30%.

3.4.2. Modélisation de chemins CNL possibles de type tempête

A titre d'exemple, des séries de cycles de type tempête sont modélisées figure 33, avec les paramètres σ_{ncm0} = 200 kPa , η_{cm0} = 0,34, I_{D0} = 90%, 2 séquences de chargement (S1 et S2) de chacune 5 séries d'amplitudes cycliques différentes.

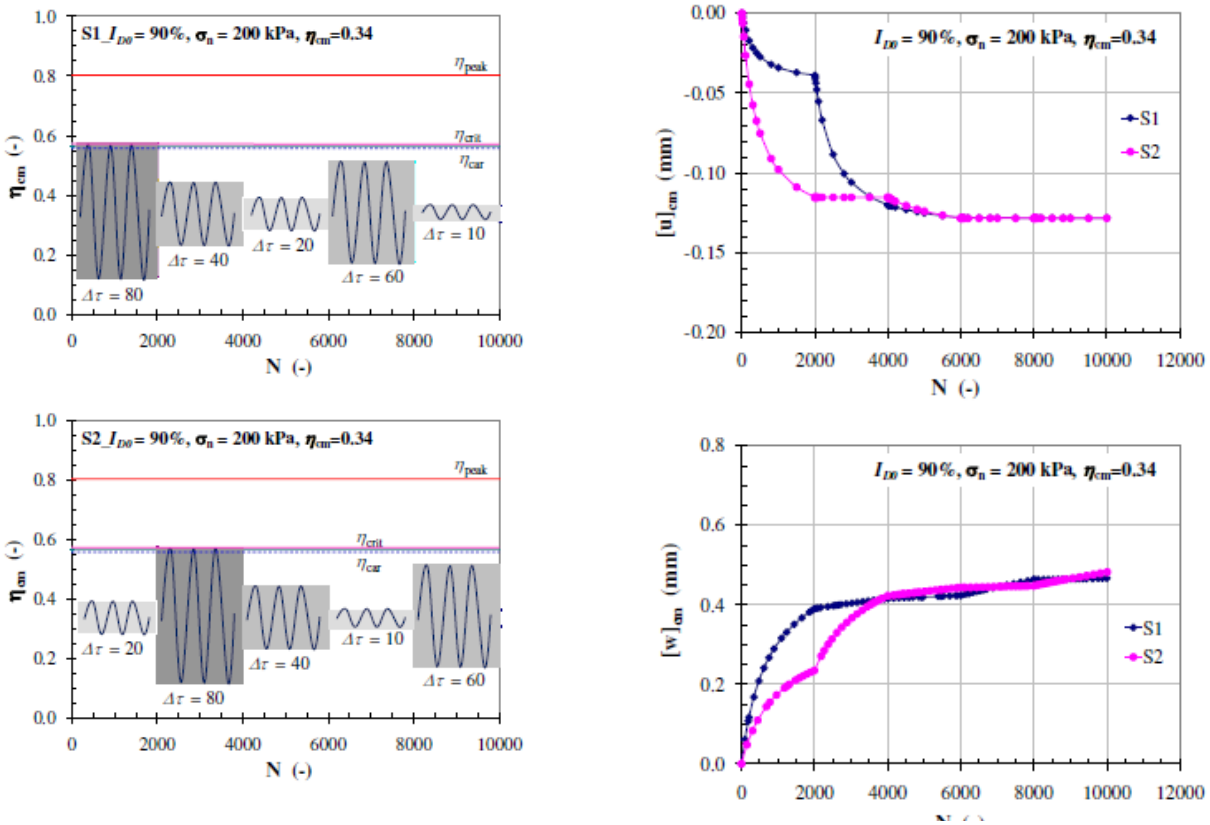

Figure 33. Deux séquences de chargement (S1 et S2) de chacune 5 séries d'amplitudes cycliques différentes, paramètres σ_{ncm0} = 200 kPa , η_{cm0} = 0,34, I_{D0} = 90%.

3.4. Modélisation des essais cycliques CNS

Dans le cas des chemins cycliques CNS, une complexité supplémentaire provient des variations possibles de la contrainte normale cyclique moyenne σ_{ncm}, ,et par conséquent du cisaillement cyclique moyen η_{cm} et de l'amplitude cyclique réduite $\Delta\eta$. Un incrément de chemin CNS se calcule donc comme la combinaison (on parle de « superposition ») d'un incrément CNL et d'un incrément pseudo-oedométrique (figure 34). Par ailleurs, le tampon oedométrique situé au dessus de l'interface, qui était considéré comme inerte pendant le cisaillement sur chemin CNL, devient actif, sa compressibilité (K_n) agissant en série avec la rigidité normale externe imposée k (figure 35) selon (12).

$$\Delta\sigma_{ncm\ \ CNS} = \frac{k * K_n}{K_n + k}\Delta[u]_{cm\ \ CNL} \quad \text{et} \quad \Delta[u]_{cm\ \ CNS} = \frac{\Delta\sigma_{ncm\ \ CNS}}{k} \qquad (12)$$

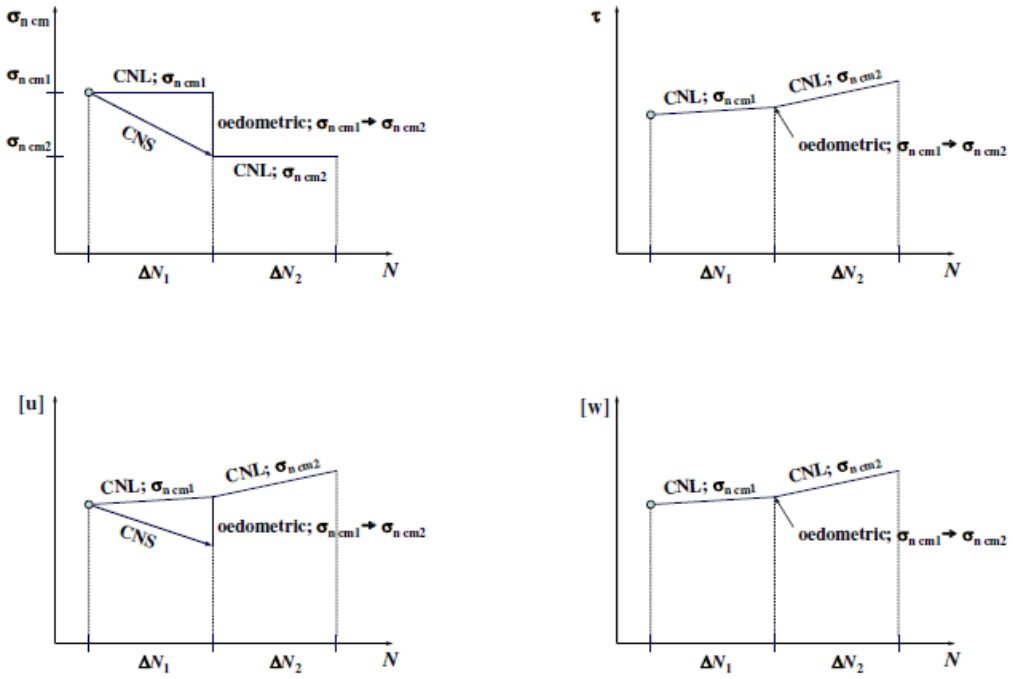

Figure 34. Incrément de chemin CNS = incrément de chemin CNL + incrément de chemin pseudo-oedométrique.

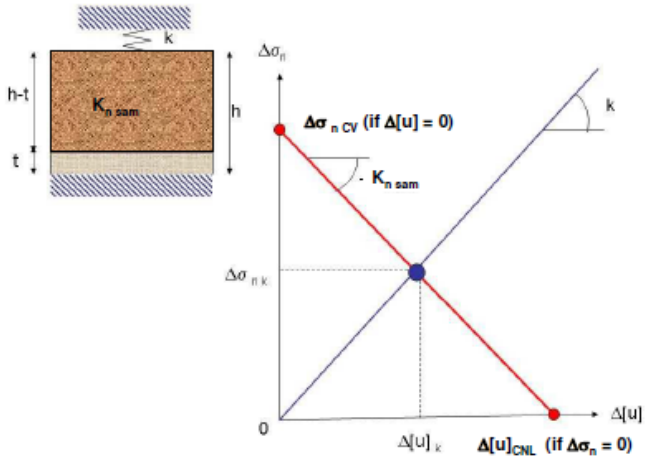

Figure 35. Correction du déplacement relatif normal d'interface, due à la compressibilité du tampon pseudo-oedomètrique sur chemin incrémental CNS.

3.4.1. Intégration par « incréments finis, pré-intégrés »

Nous avons poursuivi notre approche par incréments finis analytiques (donc pré-intégrés) de taille maxima compatible avec la stabilité d'intégration. La figure 36 montre l'effet du pas d'intégration, qui a été contrôlé dans tous nos résultats. Cette figure est relative à un échantillon initialement dense, pour lequel une intégration par pas de 200 cycles présente des

oscillations inacceptables, tandis qu'un pas de 10 cycles donne satisfaction. Dans le cas lâche, non représenté ici, une bonne stabilité d'intégration a conduit à des pas très faibles, parfois inférieurs à 1 cycle.

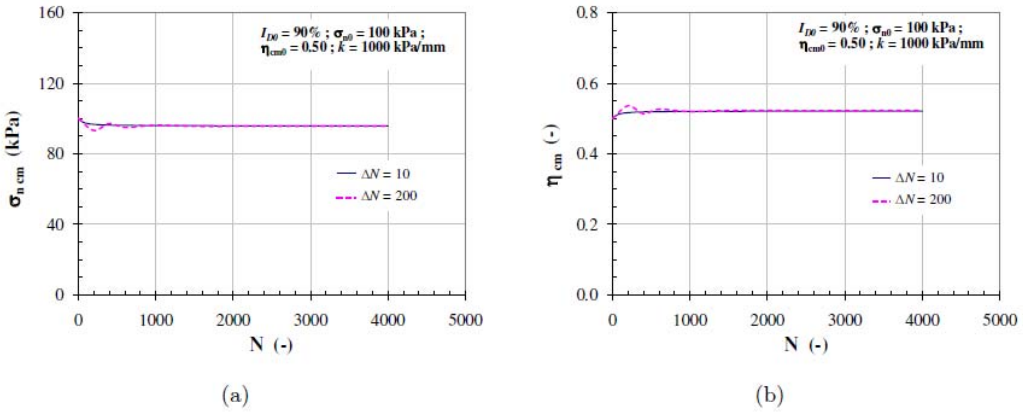

Figure 36. Caractère stable ou oscillatoire de l'intégration sur chemin CNS, selon la taille du pas d'intégration (σ_{ncm0} = 100 kPa , η_{cm0} = 0.50, $\Delta\eta_0$ = 0.1, I_{D0} = 90%).

3.4.2. Résultats comparés à l'expérience

L'intégration sur chemins CNS est d'autant plus aisée que plus le niveau de contrainte est plus élevé, que la densité est plus forte, et que le cisaillement cyclique réduit est plus faible. Les figures 37 et 38 montrent des cas bien simulés. Une information très intéressante et concise

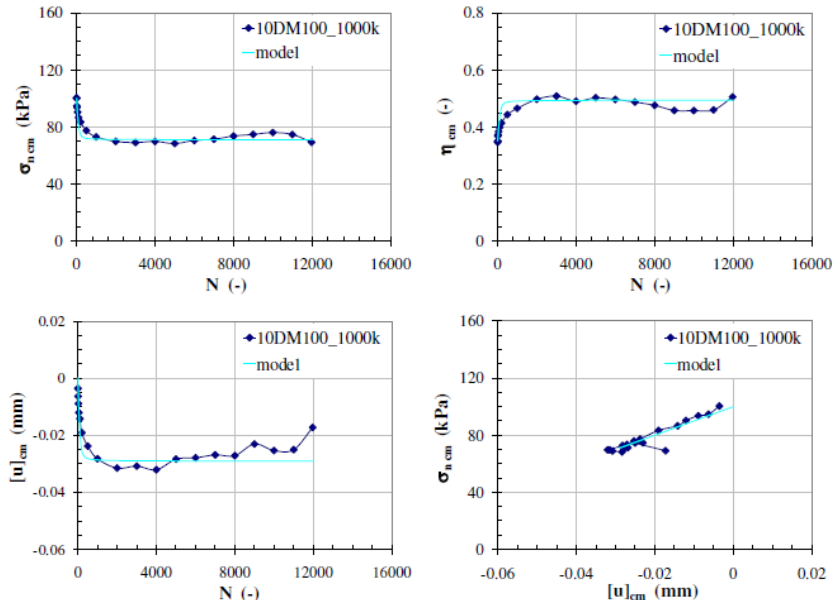

Figure 37. Chemin CNS , plaque rugueuse, ,essai et modélisation ; k = 1000 kPa/mm, σ_{ncm0} = 100 kPa , η_{cm0} = 0.35, $\Delta\eta_0$ = 0.1, I_{D0} = 90%.

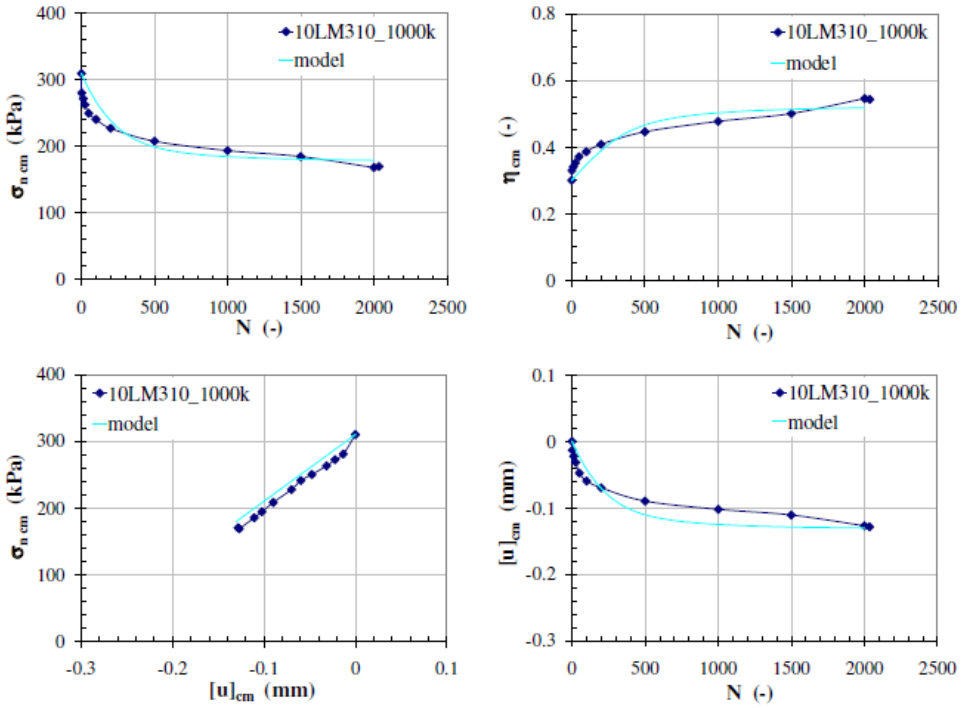

Figure 38. Chemin CNS , plaque rugueuse, essai et modélisation ; k = 1000 kPa/mm, σ_{ncm0} = 310 kPa , η_{cm0} = 0.30, $\Delta\eta_0$ = 0.032, I_{D0} = 30%.

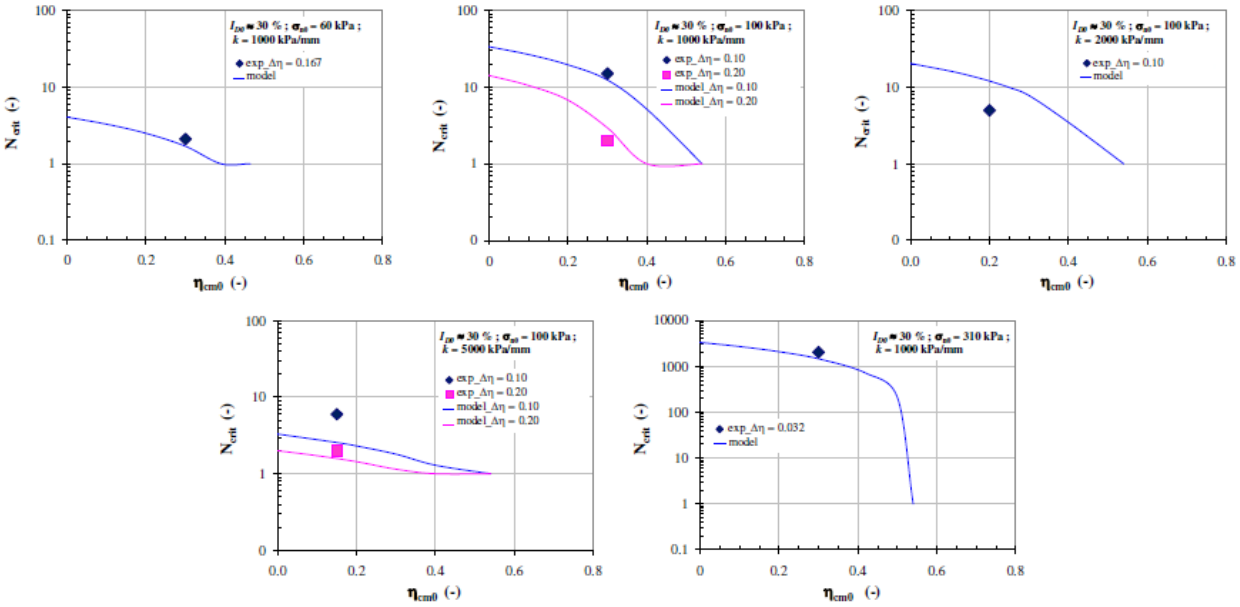

Figure 39. N_{crit} sur chemin CNS , plaque rugueuse, I_{D0} = 30%, essai et modélisation : Comparaison et modèle d'évolution.

consiste en la nombre de cycles menant à la rupture, ou à l'état critique, N_{crit}, sur chemin CNS qui, rappelons le, sont toujours contractant. Dans l'espace des contraintes, et selon nos essais, ces chemins sont horizontaux, c'est-à-dire à contrainte de cisaillement cyclique moyenne constante. Les figures 39 et 40 permettent une comparaison entre les cas lâche et dense, pour plaque rugueuse. Un résultat schématique : les valeurs de sont 100 fois plus élevées entre le cas dense et le cas lâche.

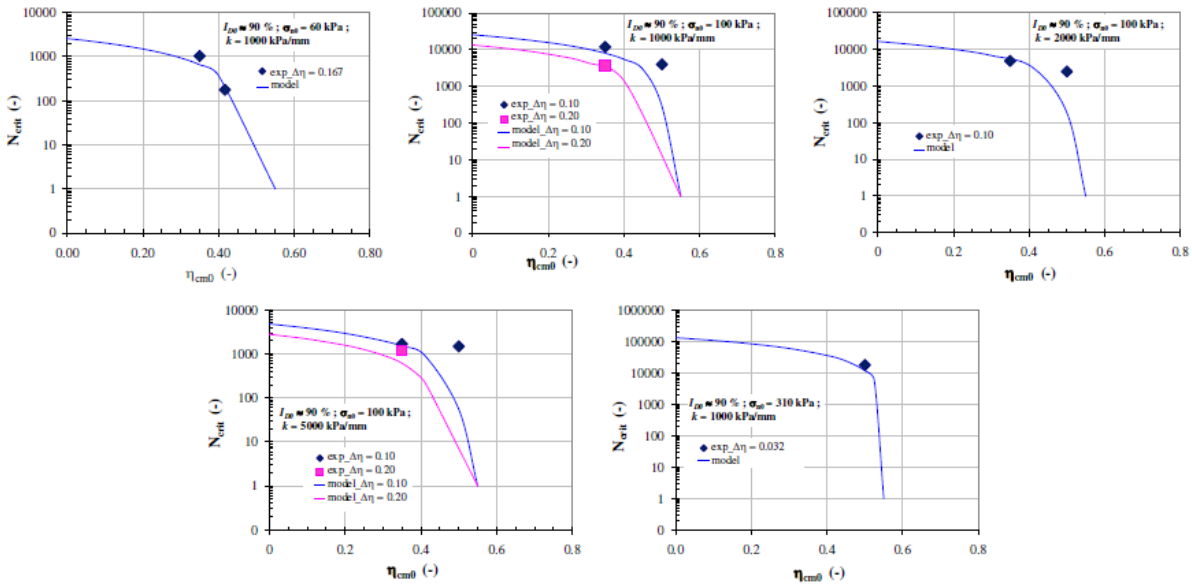

Figure 40. N_{crit} sur chemin CNS , plaque rugueuse, I_{D0} = 90%, essai et modélisation : Comparaison et modèle d'évolution.

Chapitre 4. Modélisation par la méthode des éléments finis

4.1. Introduction

Nous avons utilisé dans cette partie de la thèse le logiciel éléments finis PLAXIS, dédié à la géomécanique. Le modèle constitutif choisi est le plus simple, Mohr-Coulomb à 5 paramètres (E, ν, ,c, φ, ψ). En ce qui nous concerne, un des intérêts originaux du modèle structural PLAXIS est le traitement efficace des interfaces entre matériaux, en particulier des interfaces sol-structure.
Nous concevons la modélisation numérique guidée par le canevas suivant :

- Il s'agit d'abord d'identifier les mécanismes que nous supposons actifs dans l'expérience à modéliser.
- Puis il convient de classer ces mécanismes dans l'ordre hiérarchique d'importance que nous imaginons.
- Ensuite, nous devons implémenter ces mécanismes dans le modèle structural, autant que faire se peut, en privilégiant d'abord les plus importants.

- Enfin, il n'est pas inutile de lister les mécanismes négligés, en se demandant pourquoi ils l'ont été.

Nous avons tenté de modéliser, sur la base de ces idées, l'essai de cisaillement direct monotone, ainsi que des sollicitations cycliques axiales à grand nombre de cycles sur pieux modèles centrifugés.

4.2. Modélisation 2-D de l'essai de cisaillement direct sol-structure monotone à la boîte de cisaillement

Nous avons souhaité examiner, par modélisation numérique, les hétérogénéités si souvent décriées, de la boîte de cisaillement. Les essais d'Hoteit (1990) réalisés à l'aide d'un boîte carrée munie d'une plaque latérale de verre, et analysés par stéréophotogrammétrie, ont monté que la boîte fonctionnait selon 2 couches, l'une d'interface de faible épaisseur, et l'autre comme un tampon oedométrique, ce qui a motivé notre interprétation (§ 2.2.5).

Conformément au canevas ci-dessus, les aspects et mécanismes présents lors du cisaillement direct à la boîte sont, dans l'ordre hiérarchique :

- le caractère 3D de l'essai
- le frottement sol-plaque rugueuse et sol-boîte
- le chemin de cisaillement direct
- le frottement piston-boîte

Le caractère 3D de l'essai ne peut être simulé en 2D ; nous avons simulé l'essai en déformation plane, avec des éléments de volume T15, et des éléments d'interface J10. Les caractéristiques mécaniques du sable, de la plaque rugueuse, de la boîte et du piston sont indiquées au tableau 7. Des interfaces existent aux contacts sable plaque, sable boîte, et boîte plaque. La géométrie du modèle, le maillage, la sollicitation (verticalement contrainte normale sur le sable, horizontalement déplacement imposé de la boîte contenant le sable), et les points de contrôle (A à F) sont rapportés figure 41 pour le chemin CNL. L'hétérogénéité en terme de contrainte de cisaillement se manifeste figure 42. On constate une absence de pic de cisaillement (figure 43) et corrélativement, un déplacement relatif normal sous-évalué (C'est le plus grave défaut que l'on peut reprocher à cette modélisation). Le chemin CNS est modélisé avec la même géométrie de base et les mêmes caractéristiques mécaniques que le chemin CNL, mais la sollicitation supérieure est à déplacement imposé sur un piston compressible (figure 44), ce qui simule la rigidité normale imposée. Les principaux aspects du

Parametrs (Unit)	Loose sand	Dense sand	Steel box/plate	steel-steel interface
Material model	Mohr-Coulomb	Mohr-Coulomb	Linear elastic	Linear elastic
γ_{dry} (kN/m^2)	14.74	16.55	60	-
γ_{sat} (kN/m^2)	20	20	0	-
E_{ref} (kN/m^2)	1680, 2240, 4260	2010, 4240, 9330	2.1E07	2.1E07
ν	0.30	0.30	0.15	0.15
c_{ref} (kN/m^2)	0.10	0.10	-	0.10
φ (°)	30	38	-	5
ψ (°)	0	8	-	0
R_{inter}	0.80	0.80	-	0.05

Tableau 7. Caractéristiques mécaniques de volumes et d'interfaces utilisées pour modéliser l'essai de cisaillement direct monotone.

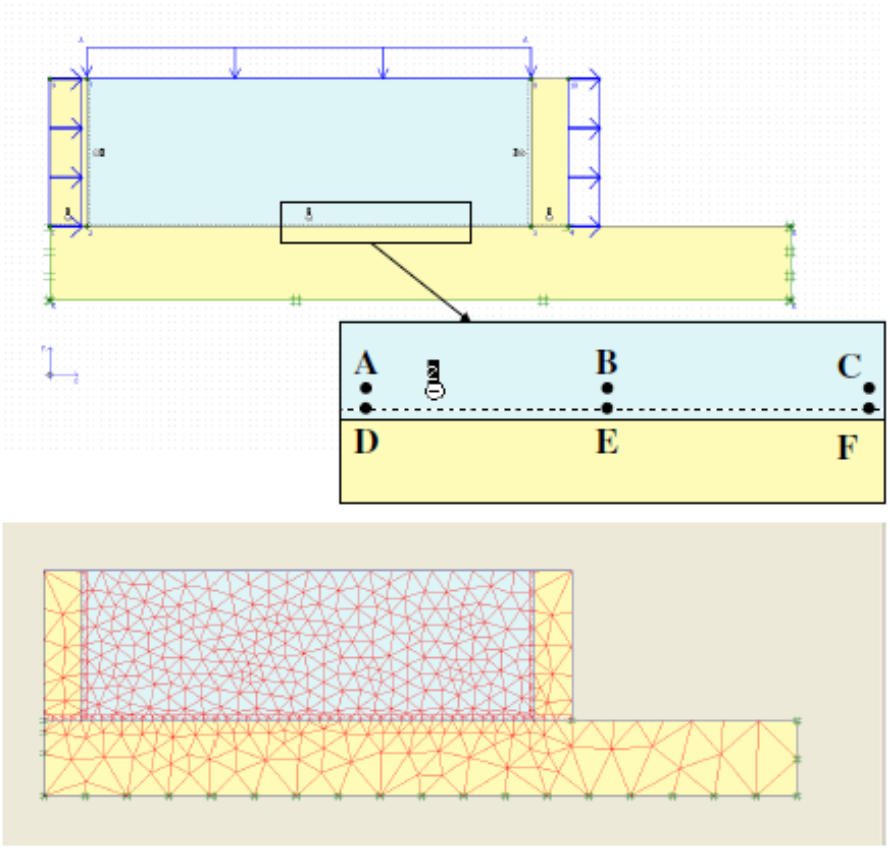

Figure 41. Modélisation de l’essai de cisaillement direct sur chemin CNL.

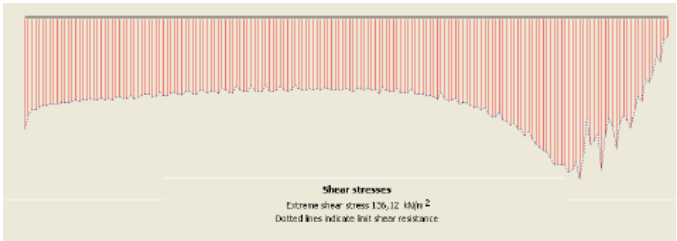

Figure 42. Hétérogénéité à l’interface sable plaque, du cisaillement simulé sur chemin CNL.

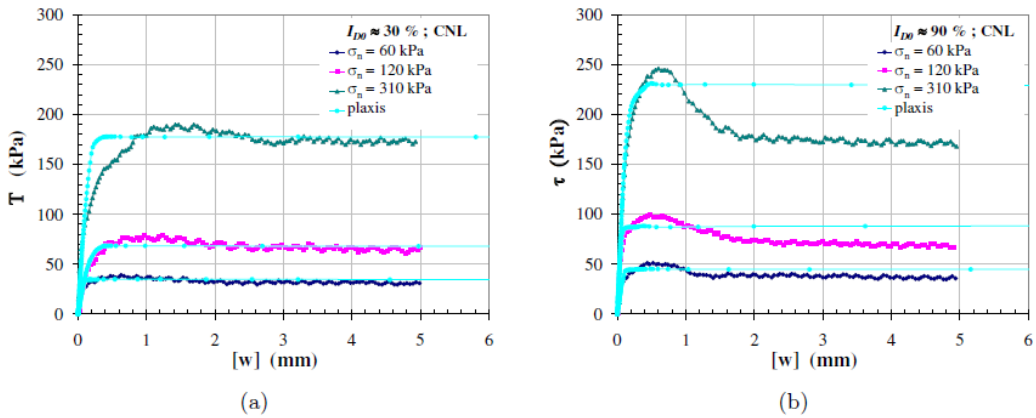

Figure 43. Modélisation de l’essai de cisaillement direct CNL (valeur globale moyenne de la contrainte de cisaillement). a) densité faible. b) densité forte.

cisaillement direct CNS sont rendus (figure 45), à savoir la dilatance à densité élevée, la contractance à densité faible, et ce quel que soit le niveau de contrainte normale (60 à 310 kPa). Par contre, le contraste pic palier et le retour vers l'origine le long de la ligne critique ne sont pas simulés, ce qui n'est pas inattendu avec un modèle constitutif de Mohr Coulomb.

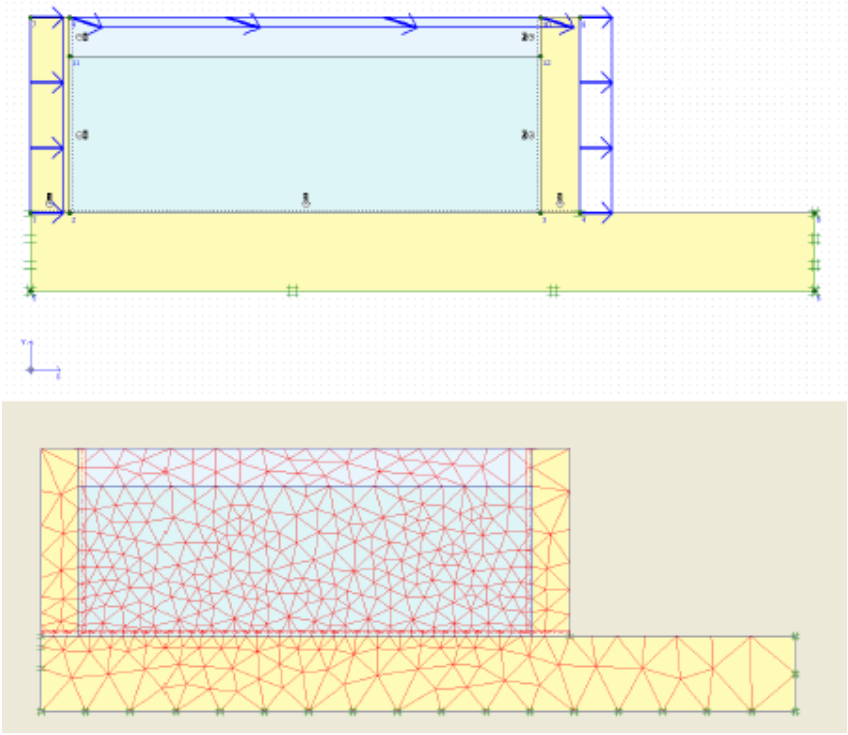

Figure 44. Modélisation de l'essai de cisaillement direct sur chemin CNS.

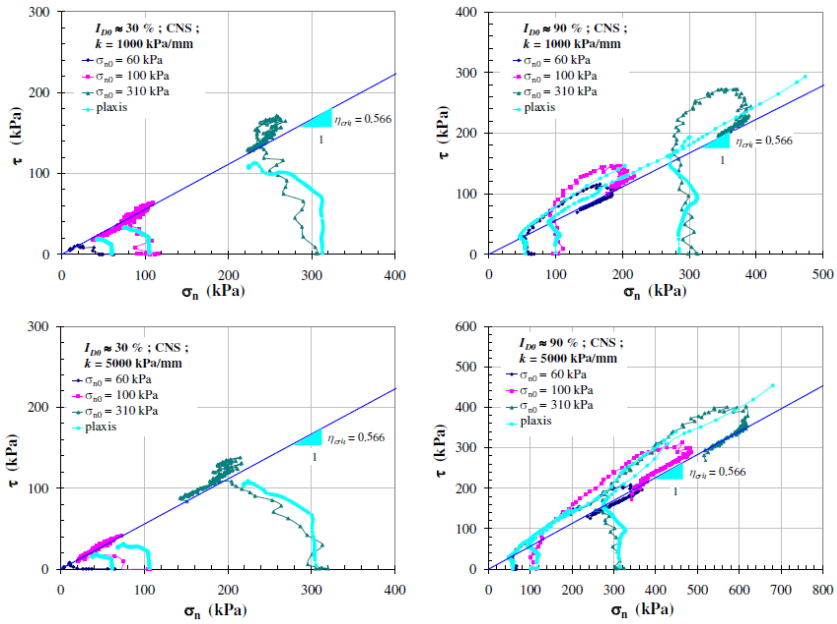

Figure 45. Modélisation de l'essai de cisaillement direct CNS (valeur globale moyenne des contraintes normale et de cisaillement). A gauche densité faible, à droite densité forte.

4.3. Modélisation des sollicitations cycliques à grand nombre de cycles

Nous avons pu procéder à ces modélisations grâce aux essais de pieux modèles centrifugés (23g) réalisés par l'IFSTTAR, et mis à disposition de la communauté SOLCYP. La figure 46 présente la nacelle de la centrifugeuse, et 8 pieux d'essai régulièrement répartis, ainsi qu'une vue du dispositif embarqué de chargement. Le tableau 8 donne les rapports de similitude pour

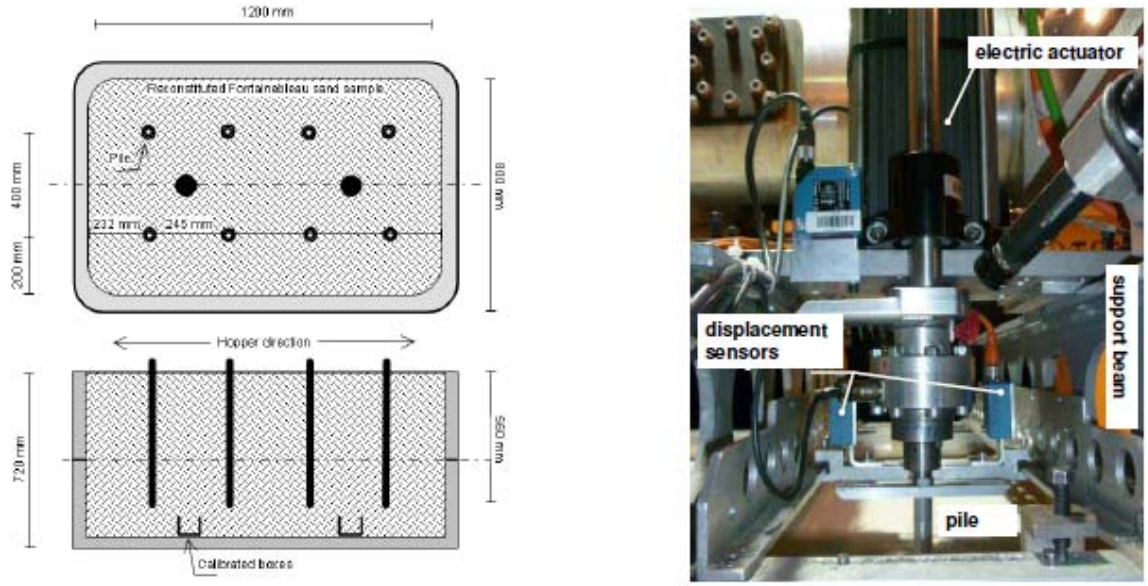

Figure 46. Dispositif expérimental d'essais de pieux modèles, échelle 1/23, à l'IFSTTAR, Nantes.

les diverses grandeurs physiques en jeu. Rappelons que les contraintes sont conservées entre le prototype et le modèle réduit. Les pieux modèles sont en aluminium, de diamètre 18 mm,

Physical parameter	Scale factor (scale model/scale prototype)
acceleration	N
length	$1/N$
displacement	$1/N$
deformation	1
force	$1/N^2$
mass	$1/N^3$
strength	N
stress	1
weight	$1/N^2$
density	1

Tableau 8. Rapports de similitude pour les diverses grandeurs physiques en centrifugeuse.

de longueur 590 mm (dont 30 mm en tête émergeant du sable de Fontainebleau de la nacelle, de masse 0,405 kg, et rugueux sur toute leur surface latérale. Les frontières du modèle sont, à la profondeur 690 mm pour la base, et au rayon 240 mm pour la frontière latérale. Selon les

données IFSTTAR, ce sable de Fontainebleau possède un angle de frottement de l'ordre de 40°, un angle de dilatance de 14°, et les caractéristiques d'interface mesurée à la boîte de cisaillement sont légèrement inférieures. Par ailleurs, les essais de pieu modèles sous sollicitations axiales monotones, en traction et compression ont donné les résultats résumés au tableau 9.

Load type	Prototype		Model	
	force a (MN)	displacement b (mm)	force a/N^2 (kN)	displacement b/N (mm)
Tension	2.12	30	4	1.30
Compression	3.25	25	6.10	1.09

Tableau 9. Résultats d'essais de pieux modèles centrifugés (23g) sous sollicitations axiales monotones en traction et compression.

Revenant au canevas exposé § 4.1, nous avons fait les choix suivants, en privilégiant la **simplicité** et la **rusticité**, compte tenu que nous avons placé la plus grande partie de notre énergie et de notre temps de travail dans nos essais de cisaillement direct cycliques. Il s'agit donc ici d'exposer une **méthodologie**, et de montrer sa **faisabilité**, étant entendu qu'il y aurait lieu de raffiner ultérieurement cette approche, à de nombreux points de vue, et notamment de rendre automatique le dialogue EXCEL-PLAXIS, par fichiers, ce qui est actuellement tout à la charge de l'opérateur :

- modélisation en axisymétrie, éléments de volume T15, et d'interface J10.
- pieu modélisé en éléments de volume, et sollicité par la force en tête.
- Sol (sable) modélisé selon 3 couches horizontales pour la sollicitation monotone, 6 couches horizontales pour la sollicitation cyclique
- interfaces sol pieu le long du fût et en pointe.
- modèle constitutif élasto-plastique de Mohr Coulomb (presque) classique pour le sable. Les aspects cycliques ne sont pas pris en compte dans le sol, car vu la géométrie, le cisaillement décroît très rapidement dans la direction radiale à partir du fût (en 1/r), ce qui limite naturellement ces effets.
- poids volumique du sol adapté, tenant compte de l'accélération imposée par la centrifugeuse, proportionnelle au rayon à partir de l'axe de rotation, et valant 23g à 240 mm de profondeur dans la nacelle.
- Module d'Young du sol adapté, linéaire par rapport à la profondeur dans la nacelle (figure 47), et approximation selon les moindres carrés par rapport à la loi de Kondner ($E = E_{ref}\left(\frac{\sigma_i}{\sigma_{ref}}\right)^n$). Ici, n = 0.7, σ_{ref} = 100 kPa, E_{ref} = 4500 kPa et σ_i contrainte moyenne, en kPa, résultant des contraintes pseudo-géostatiques (23g) et K_0 = 0.7 (car plusieurs cycles de centrifugation avant essai proprement dit).
- A un stade donné de la sollicitation en tête de pieu, PLAXIS fournit une approximation supposée acceptable des chemins cycliques locaux d'interface, par un calcul pas à pas d'un cycle entier. Par contre, le modèle constitutif de PLAXIS est insuffisant pour modéliser la contractance ou la dilatance cyclique. Donc l'ensemble des cycles imposés en tête de pieu est divisé en plusieurs séries, pour lesquelles on

calcule le premier cycle de la série à l'aide de PLAXIS, ce qui donne les informations locales pour la dite série.

- A l'interface sol-pieu le long du fût, on souhaite introduire les chemins de cisaillement direct cycliques CNS (localement $k = \frac{2G}{R}$, G module de cisaillement, R rayon du pieu) qui nous l'avons vu, sont toujours contractants. Introduire notre modèle de cisaillement cyclique comme modèle utilisateur a été impossible vu le temps imparti. Nous avons choisi une solution approchée, et simplifiée. Nous avons ainsi décidé d'utiliser les données de N_{crit} extraites de nos essais (Rappelons –figures 39 et 40, § 3.4.2- que N_{crit} représente pour un chemin CNS comme ceux de nos essais, le nombre de cycles nécessaire pour parvenir à l'état critique, à τ_{cm} et $\Delta\tau$ fixés). Le nombre de cycles N, entre 0 et N_{crit} , donne accès à la diminution de contrainte normale cyclique moyenne sur chemin CNS, soit $\Delta\sigma_{ncm}$, et accessoirement $\Delta\eta_{cm}$. La loi d'évolution en fonction de N est supposée, compte tenu de notre connaissance des chemins CNS.
- En toute rigueur, il conviendrait de générer $\Delta\sigma_{ncm}$ aux points d'intégration de l'interface, ce qui n'est pas possible actuellement dans PLAXIS. Mais il existe un moyen pour générer $\Delta\sigma_{ncm}$ par cluster (ensemble d'éléments), en y imposant une variation (diminution) locale de volume (ε_V). Nous avons donc créé dans PLAXIS un ensemble de clusters de très faible épaisseur, contigus au pieu, et de propriétés identiques à celles du sol, qui remplissent ce rôle. Ils seront nommés dans la suite « clusters de contrôle » et indicés i, de 1 à n_c.
- Les 2 modèles de pieux chargés cycliquement en traction et en compression utilisent exactement les mêmes données géométriques et mécaniques, à une différence près : en compression cyclique, le niveau des modules d'Young de la couche de sable située sous la pointe a été majoré pour tenir compte de la contrainte moyenne élevée dans cette zone.
- En traction comme en compression, le calcul est agencé selon les phases suivantes, impliquant un dialogue EXCEL-PLAXIS :

  0. Initialisation géostatique (1g) dans le module INPUT, selon la procédure K_0, pour la couche de sable située sous la pointe.
  1. Initialisation géostatique (1g) dans le module CALCULATION, pour tout le sol et pour le pieu métallique.
  2. Suite des phases, 2 à 5, dans le module CALCULATION. Et tout d'abord centrifugation du modèle (23g).

  3. Début du traitement de la série (S) de cycles, comportant N_s cycles identiques en tête. Application de la charge nominale moyenne en tête pour la série (s) de cycles actuellement traitée.
  4. Chargement en tête jusqu'à la charge maximum, puis minimum, puis **nominale moyenne**, et enfin à nouveau maximum[1].
  5. Extraction, depuis les n_c « clusters de contrôle », des paramètres locaux des cycles, stockage dans EXCEL.

  6. Calcul, dans EXCEL, des n_c chemins CNS correspondants aux paramètres extraits en phase 5. Ou, solution simplifiée, calcul des n_c valeurs N_{crit}

[1] Ceci afin de connaître les limites locales liées à un cycle en tête, car la première montée en charge suivie de la première descente en charge sont très influencées par l'état initial en fin de centrifugation sous 23g.

correspondantes. Calcul, dans chaque cluster de contrôle, des $\Delta\sigma_{ncm}$ (contractance, donc <0) correspondant aux N_s cycles de cette série (S).
7. Création, dans PLAXIS CALCULATION, de n_c cas de charge, correspondant chacun à ε_V unitaire (contractant = -1) dans l'un des clusters, =0 dans tous les autres.
8. Extraction, depuis les n_c « clusters de contrôle », des $\Delta\sigma_{ncm}$ correspondant à chaque cas de charge, stockage dans EXCEL.
9. Calcul, dans EXCEL, de la combinaison linéaire des n_c cas de charge de (7) permettant d'obtenir le champ des $\Delta\sigma_{ncm}$ définis en (6).

10. Création, dans PLAXIS CALCULATION, de la phase de pseudo-fluage cyclique modélisant les N_s cycles de la série (S), **à partir de la charge nominale moyenne en tête atteinte en (4)**. Il s'agit de la combinaison linéaire définie dans (9) des champs de ε_V définis en (7).
11. Si le résultat en termes de champ de $\Delta\sigma_{ncm}$ définis en (6) n'est pas tout à fait atteint, itération supplémentaire à partir du résultat atteint en (10)[2].
12. Passage à la série suivante de cycles en tête : retour en (3), sinon fin des calculs.

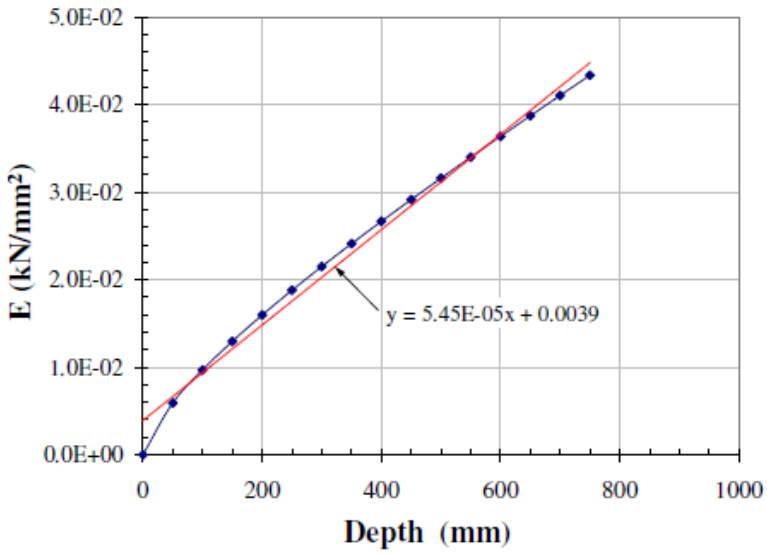

Figure 47. Module d'Young fonction de la profondeur dans la nacelle, approximation de la loi de Kondner.

4.3.1. Pieu modèle centrifugé en traction, monotone et cyclique

Nous avons modélisé l'essai monotone (tableau 9) et l'essai cyclique en traction CO7TO5. La figure 48 donne les résultats de l'application de l'accélération 23g sur la modèle. On note un frottement négatif très prononcé, comme dans une installation de pieu par fonçage ou battage, ce qui est dû au contraste de modules entre sol et pieu lors de ce type de chargement.

[2] En effet, dans PLAXIS (cf Reference Manual, § 4.7.6), pour des raisons qu'il serait trop long d'expliquer ici, une partie seulement de la variation de volume que l'on souhaite, est réellement imposée (de l'ordre de 50 %).

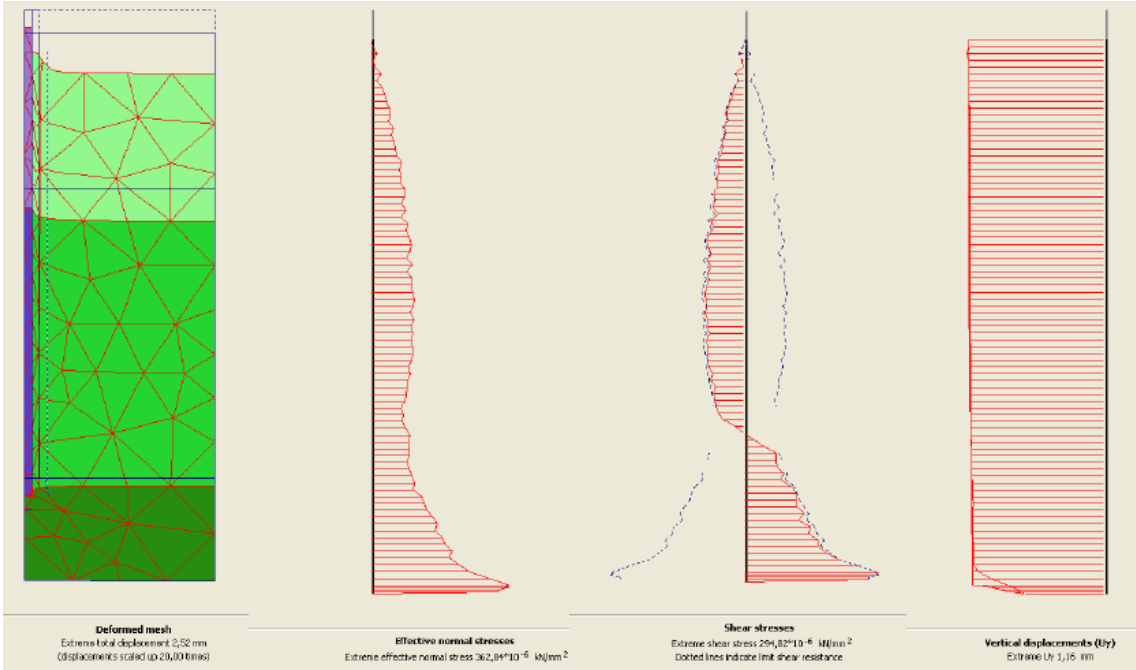

Figure 48. Maillage du modèle CO7TO5, application de l'accélération 23g sur le modèle : déplacements (amplifié 20 fois), contraintes agissant sur le fût, déplacement vertical du pieu.

La figure 49a représente le chargement du pieu en traction monotone jusqu'à 4 kN, après application des 23g. On note un déplacement en tête de 1.20 mm, voisin de celui mesuré en centrifugeuse (1.30 mm, tableau 9). La figure 49b donne la répartition entre effort en tête et force de pointe, à différents stades. La figure 50 fournit les distributions de contraintes normale et de cisaillement sur le fût, aux mêmes stades de chargement. L'intense frottement

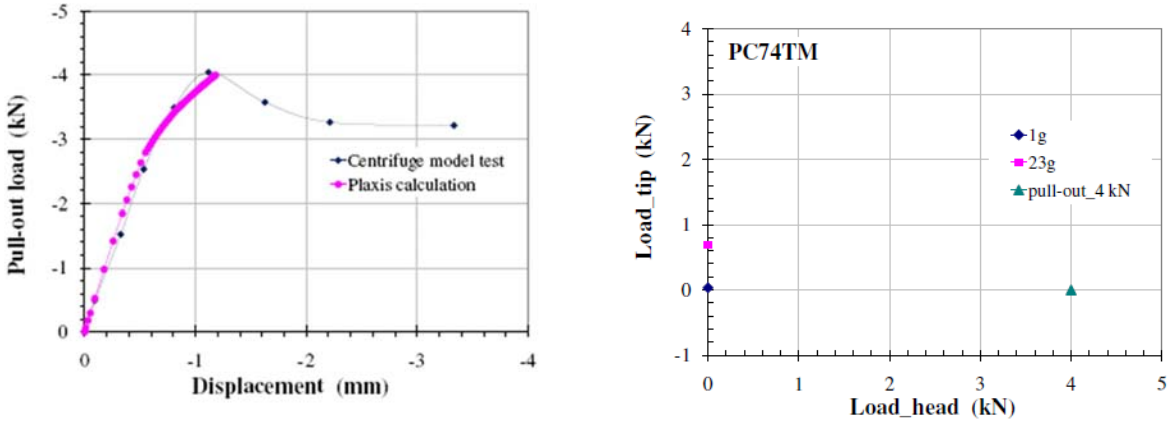

(a) (b)

Figure 49. Chargement monotone du pieu modèle en traction à 4 kN. a) charge-déplacement en tête. b) charge en pointe versus charge en tête ; pointe/tête ≈ 0 %..

négatif initial est confirmé. Le calcul cyclique est effectué avec 6 couches horizontales, dont 5 contigües au pieu (figure 51a). On réalise le parcours pas à pas du premier cycle (figure 51b), puis le pseudo-fluage cyclique au cours des 2000 cycles suivants. La figure 52 donne les chemins locaux de contraintes à diverses profondeurs, le long du pieu. On doit noter que ces

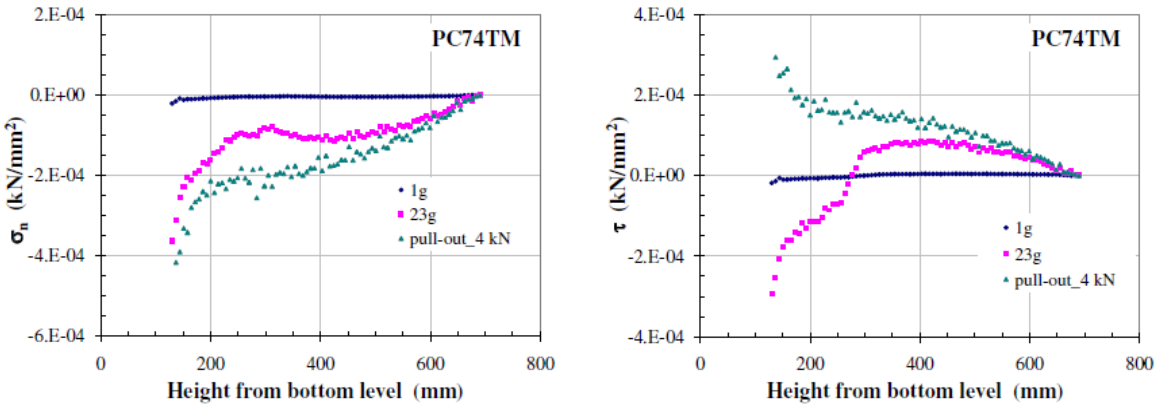

Figure 50. Chargement monotone du pieu modèle en traction . a) distribution des contraintes normales sur le fût. b) distribution des contraintes de cisaillement.

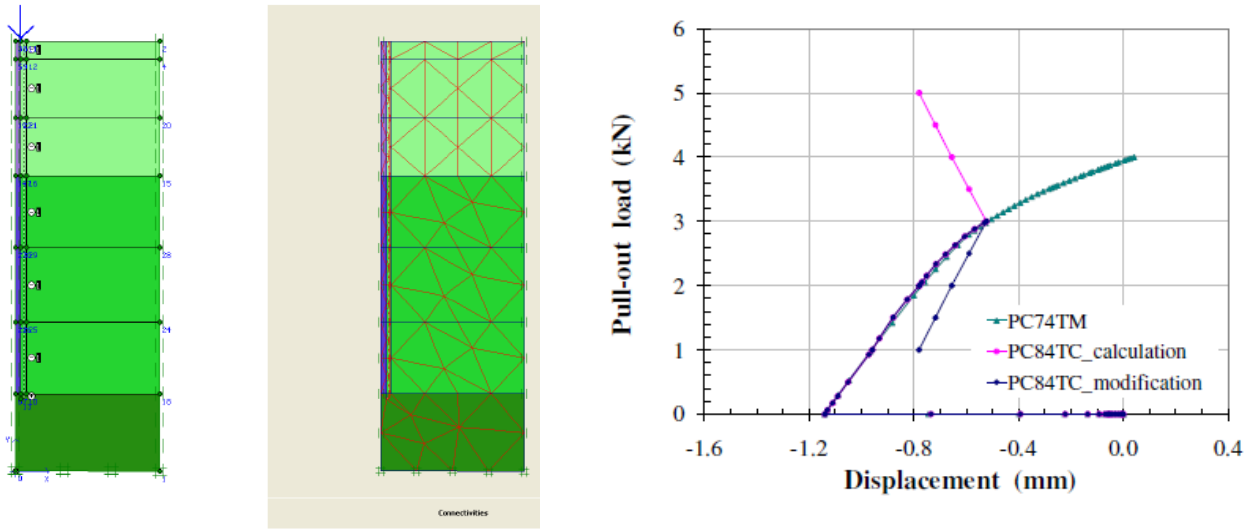

Figure 51. Chargement cyclique du pieu modèle en traction, modélisation de l'essai CO7TO5. a) maillage en 6 couches horizontales. b) charge en tête versus déplacement en tête, 1er cycle entre 1 et 3 kN (en bleu), comparaison au chargement monotone.

chemins sont d'autant plus amples en termes de cisaillement, que l'on se déplace de la tête vers la pointe du pieu. Le tableau 10 résume les paramètres cycliques de ces cycles, et la rigidité normale locale du massif de sable. La figure 53 donne les chutes de contraintes normales qui en découlent, en fonction du nombre de cycles, selon l'approche déduite de N_{crit}. Finalement, la figure 54 donne le déplacement cyclique moyen en tête de pieu résultant du pseudo-fluage cyclique au bout de 2000 cycles, tandis que la figure 55 compare les distributions de contraintes le long du pieu en traction, initialement (23g), au bout du premier

cycle, et au bout de 2000 cycles. La zone près de la pointe a perdu toute résistance. Le déplacement cyclique moyen atteint au bout de 2000 cycles est de l'ordre de 1.54 mm.

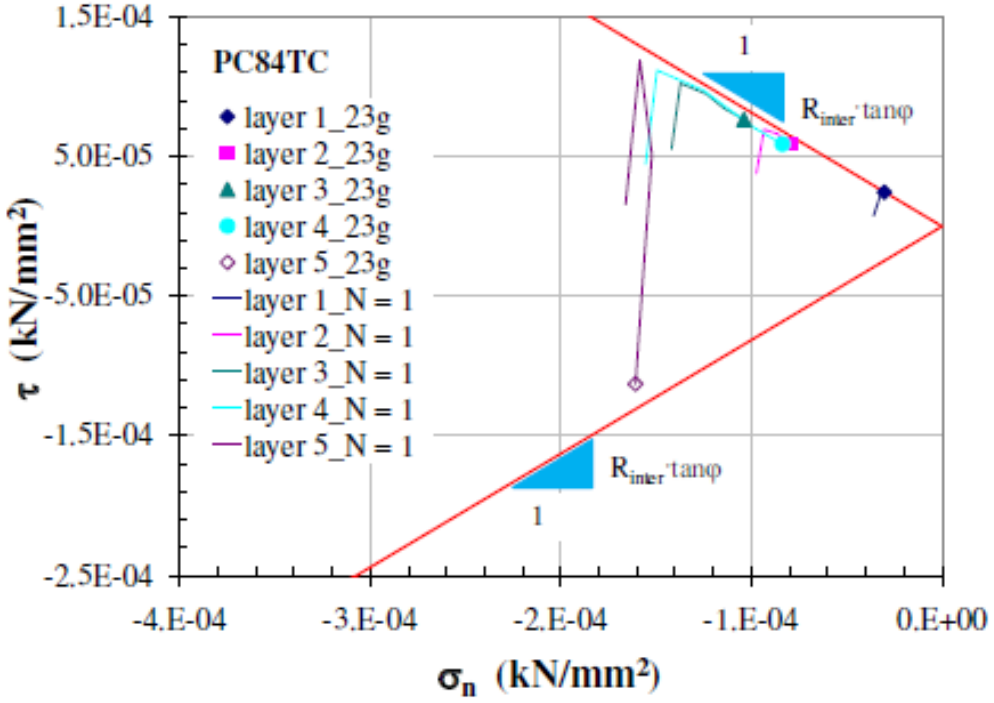

Figure 52. Chemins de contraintes au cours du premier cycle, sur le fût du pieu modèle en traction, modélisation de l'essai CO7TO5. layer 1 près de la surface libre de la nacelle, layer 5 près de la pointe du pieu.

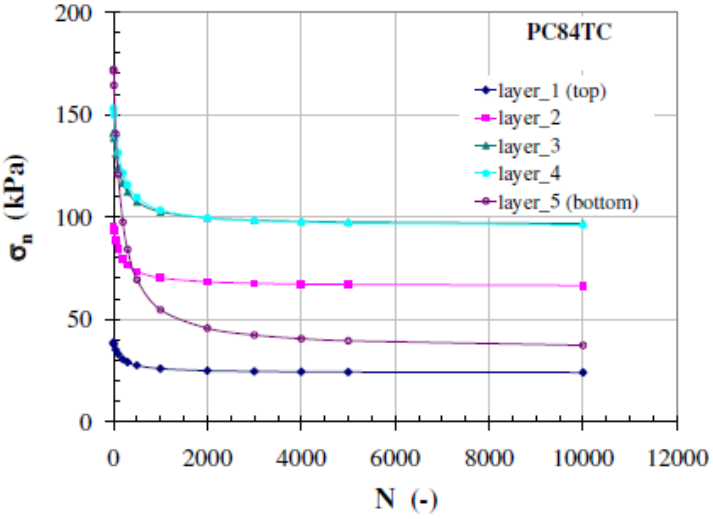

Figure 53. Pieu modèle en traction. Chutes de contraintes normales sur chemins CNS le long du pieu, en fonction du nombre de cycles, découlant des paramètres cycliques locaux, selon l'approche déduite de N_{crit}.

Layer (mm)	$\sigma_{n\ cm0}$ (kPa)	τ_{cm0} (kPa)	$\Delta\tau$ (kPa)	η_{cm0} (-)	E (kN/mm^2)	G (kN/mm^2)	k (kPa/mm)
1	38.5	19.3	18.0	0.50	6.571E-03	2.527E-03	5.616E+02
2	95.2	53.7	32.5	0.56	1.191E-02	4.581E-03	1.018E+03
3	141	78.1	48.4	0.55	1.785E-02	6.866E-03	1.526E+03
4	153	77.3	69.3	0.51	3.333E-02	1.282E-02	2.849E+03
5	172	28.5	104.2	0.17	3.115E-02	1.198E-02	2.662E+03

Tableau 10. Paramètres cycliques des cycles locaux le long du pieu en traction, au cours du premier cycle de force en tête, et rigidité normale locale du massif de sable.

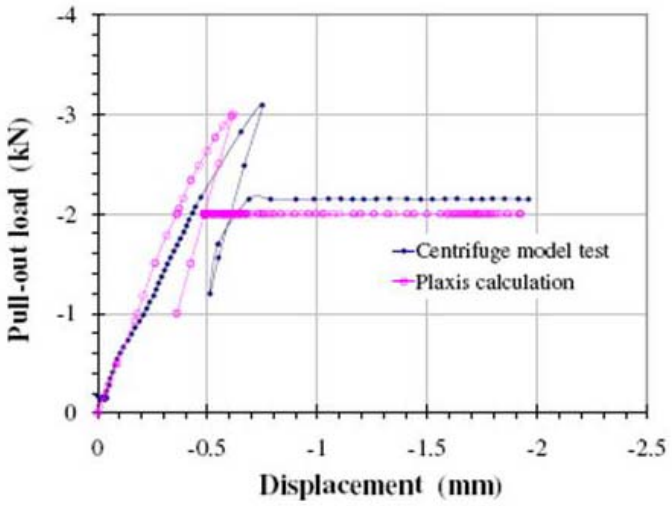

Figure 54. Pieu modèle en traction. Modélisation de l'essai CO7TO5 ; Force cyclique moyenne-déplacement cyclique moyen en tête de pieu résultant du pseudo-fluage cyclique au bout de 2000 cycles.

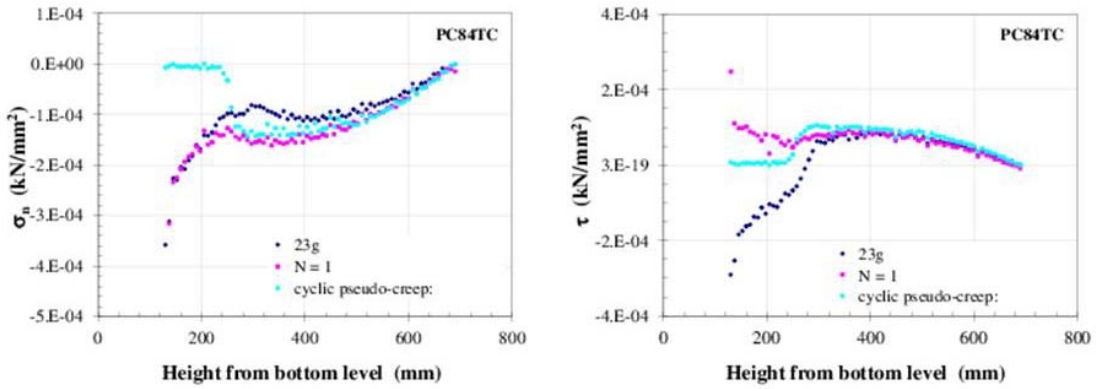

Figure 55. Modélisation de l'essai CO7TO5, traction cyclique. Distribution de contraintes le long du pieu initialement (23g), au bout du premier cycle, et au bout de 2000 cycles.

4.3.2. Pieu modèle centrifugé en compression, monotone et cyclique

Nous avons modélisé l'essai monotone (tableau 9) et l'essai cyclique en compression CO4TO7. Les résultats de l'application de l'accélération 23g sur la modèle sont évidemment identiques aux précédents, au déplacement du pieu, en tête notamment près, puisque le module d'Young de la couche située sous la pointe a été renforcé, compte tenu du niveau élevé de contrainte dans cette zone. On note de toutes manières un frottement négatif initial très prononcé, comme dans une installation de pieu par fonçage ou battage. La relation charge -tassement sous 6.1 kN est présentée figure 56, tandis que la distribution de contraintes fait l'objet de la figure 57. Le déplacement modélisé dû au chargement est de 1.51 mm, supérieur

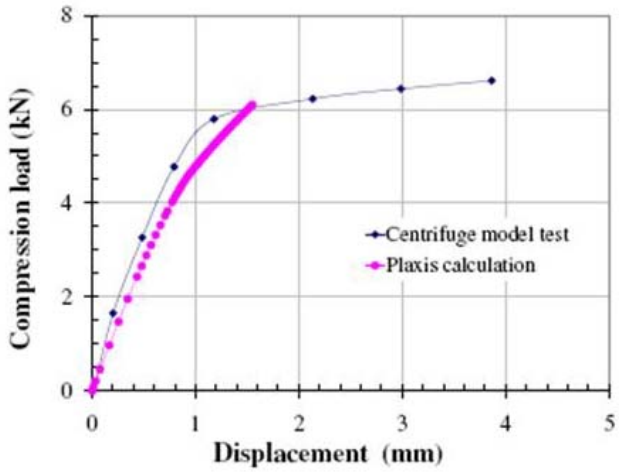

Figure 56. Modélisation de l'essai de compression monotone du pieu modèle centrifugé, courbe charge-tassement jusqu'à 6.1 kN.

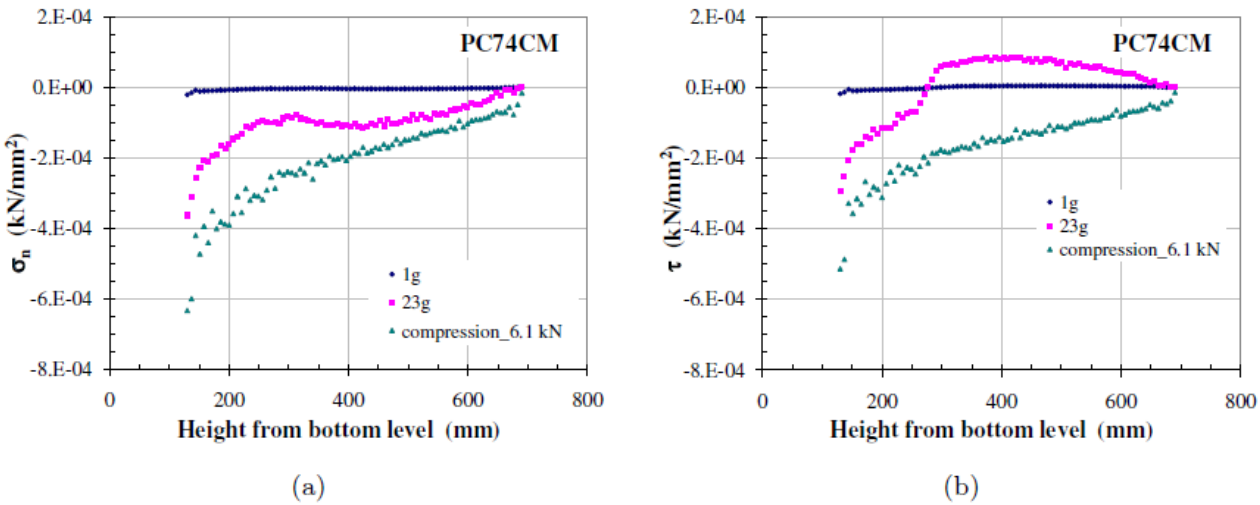

Figure 57. Modélisation de l'essai de compression monotone du pieu modèle centrifugé, distribution des contraintes normale et de cisaillement le long du fût.

à celui qui a été mesuré (tableau 9). La figure 58 compare les distributions de contraintes sous chargements monotones en traction (4 kN) et en compression (6.1 kN). On note que les contraintes normales sont voisines, excepté près de la pointe du pieu. Elle sont majorée en moyenne de 70 % près de la point du pieu, entre les cas traction et compression. La figure 59 donne la répartition entre forces en tête et de pointe pour le pieu en compression, depuis l'application de la gravité (1g).

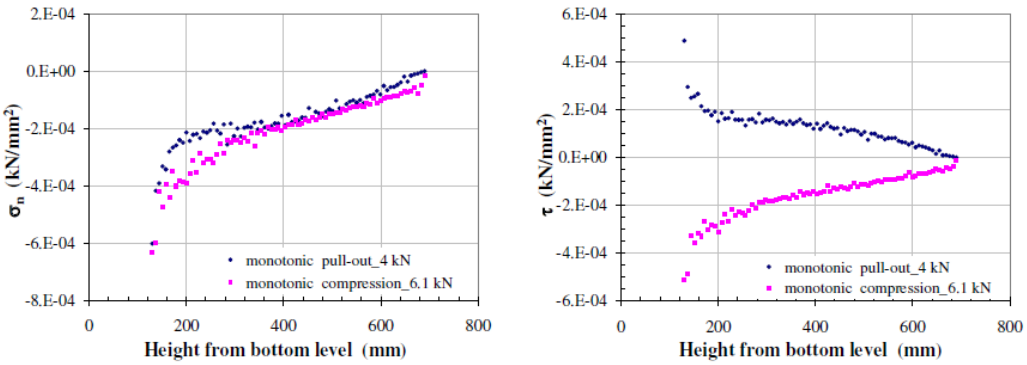

Figure 58. Distributions des contraintes normale et de cisaillement le long du pieu modélisé sous chargements monotones en traction (4 kN) et en compression (6.1 kN).

A la figure 60 est représentée la courbe charge-déplacement en tête lors du premier cycle, tandis que les répartitions de contraintes le long du fût sont indiquées figure 61. Les chemins de contraintes, à diverses profondeurs (couche 1 en surface, et 5 près de la pointe), sont visibles sur la figure 62. Les amplitudes cycliques sont importantes. Les caractères de ces cycles sont indiqués au tableau 11.

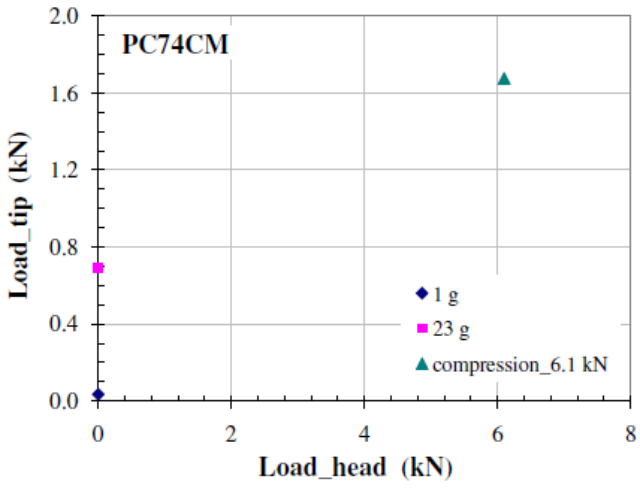

Figure 59 . Répartition entre forces en tête et en pointe pour le pieu modélisé en compression monotone (6.1 kN). Pointe/tête = 27.9 %.

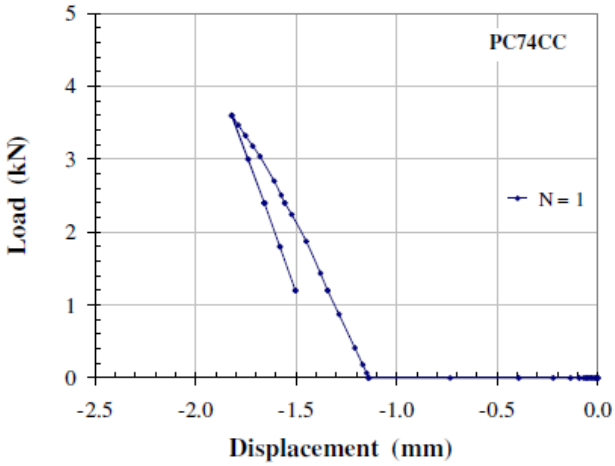

Figure 60. Modélisation de l'essai de pieu centrifugé en compression cyclique CO4TO7. Courbe charge-déplacement en tête lors du premier cycle (0, 1.2 kN, 3.6 kN, 1.2 kN, 2.4 kN). La recharge de 1.2 à 2.4 kN est pratiquement confondue avec la décharge correspondante.

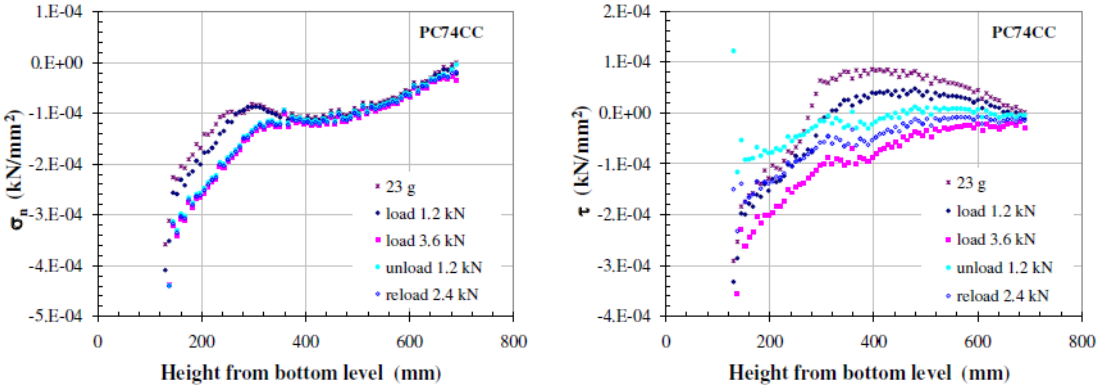

Figure 61. Modélisation de l'essai de pieu centrifugé en compression cyclique CO4TO7. Distribution de contraintes a) normale b) de cisaillement le long du fût, au cours du premier cycle de chargement.

Layer (mm)	$\sigma_{n\,cm0}$ (kPa)	τ_{cm0} (kPa)	η_{cm0} (-)	$\Delta\eta$ (-)	η_{max} (-)
1	35.7	19.8	0.515	0.410	0.805
2	87.9	12.0	0.132	0.429	0.357
3	113.7	37.5	0.316	0.452	0.583
4	122.7	46.0	0.515	0.415	0.707
5	263.7	135.9	0.520	0.429	0.732

Tableau 11. Modélisation de l'essai de pieu centrifugé en compression cyclique CO4TO7. Caractères du premier cycle de chargement, à diverses profondeurs.

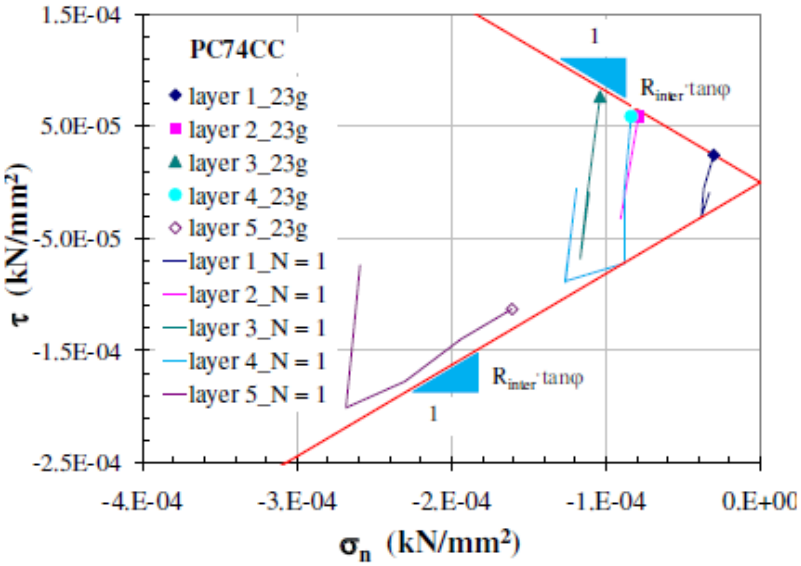

Figure 62. Modélisation de l'essai de pieu centrifugé en compression cyclique CO4TO7. Chemins de contraintes, à diverses profondeurs (couche 1 en surface, et 5 près de la pointe).

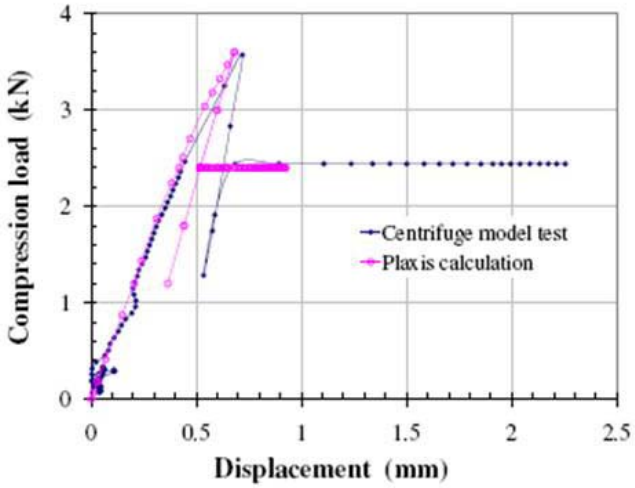

Figure 63. Modélisation de l'essai de pieu modèle centrifugé en compression cyclique CO4TO7 ; Force cyclique moyenne-déplacement cyclique moyen en tête de pieu résultant du pseudo-fluage cyclique au bout de 2000 cycles.

On atteint ainsi un déplacement cyclique moyen de 0.50 mm au bout de 2000 cycles. Cette valeur est à comparer à la valeur relative au pieu en traction cyclique, 1.54 mm. La figure 64 donne la distribution de contraintes le long du pieu au terme des 2000 cycles. La comparaison avec le pieu en traction cyclique est intéressante : Le niveau de contrainte normale près de la pointe décroit entre le 1er cycle et le dernier, mais reste important (≈ 150 kPa). D'où un frottement latéral qui reste conséquent après cycles dans le cas d'une sollicitation en compression. Cette analyse du pseudo-fluage cyclique relatif aux pieux est rustique, il s'agit à ce stade d'une méthodologie.

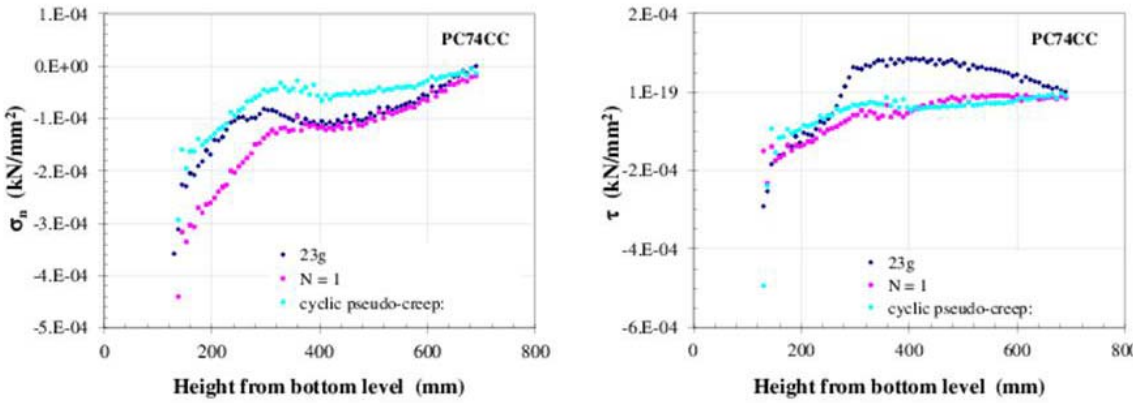

Figure 64. Modélisation de l'essai de pieu modèle centrifugé en compression cyclique CO4TO7. Distribution de contraintes a) normale b) de cisaillement le long du pieu au terme des 2000 cycles.

Chapitre 5. Calcul de pieux réels chargés cycliquement, pour les projets de génie civil

Le calcul des pieux sous sollicitation cyclique mobilise les géotechniciens depuis de nombreuses années, que ce soit pour le transfert de charge, pour la capacité limite, et pour la relation charge déplacement en tête. Les méthodes des courbes t-z et p-y ont la faveur des praticiens, en raison de leur simplicité. Le calcul pas à pas des cycles semble rédhibitoire au vu du temps de calcul, mais aussi de la fiabilité des lois constitutives cycliques traitées pas à pas, au-delà de quelques cycles. Le pseudo-fluage cyclique (le nombre de cycles agit comme un temps fictif) s'impose pour traiter le grand nombre de cycles. Encore s'agit-il d'utiliser des lois constitutives représentatives du phénomène. Les variables cycliques moyennes sont tout naturellement les variables du pseudo-fluage cyclique.
Pour avoir quelques chances d'être représentatif, tout calcul doit impérativement modéliser les mécanismes essentiels intervenant dans le sol et à l'interface sol-pieu. L'interface sol-pieu est le centre névralgique du transfert des contraintes entre le pieu et le sol. De plus, s'agissant de pieux sous chargement axial cyclique, la priorité doit être donnée à l'interface sol-pieu sachant que la diffusion des sur-contraintes dues au chargement du pieu se diffuse en 1/r à partir du fût, r étant la distance à l'axe du pieu. Par ailleurs, le sol contigu au pieu confine le pieu (et l'interface), et ce confinement se manifeste par la rigidité normale k du massif de sol, de l'ordre de $k = \frac{2G}{R}$ (G module de cisaillement du sol, et R rayon du pieu). Si bien que les chemins de cisaillement cycliques mobilisés le long du pieu sont à peu de chose près des chemins à rigidité normale imposée (CNS). Cette rigidité normale est généralement faible, mais présente, pour les pieux courants, de l'ordre de 1000 kPa/mm. Nous avons observé, d'après nos essais cycliques CNS, que ces chemins étaient toujours contractants, conduisant à une diminution de contrainte normale agissant sur le pieu. Ainsi, la dégradation du frottement, souvent (mais heureusement de moins en moins) considérée comme diminution du coefficient de frottement, correspond en fait à une réduction du niveau de contrainte normale.
La question de la modélisation du mode d'installation du pieu se pose bien évidemment. Elle est importante, et nos 2 calculs de pieux modèles centrifugés montrent, par exemple, que ce mode d'installation génère un frottement négatif influant sur la suite du chargement.

Après ces constatations, nous proposons la méthodologie suivante, impliquant un nombre minimum d'essais, pour modéliser le comportement d'un pieu sous chargement axial cyclique.

- Etat initial résultant du mode d'installation :
  - Dans le cas du pieu moulé, la solution la plus simple consiste à remplace le sol par le matériau pieu dans son emprise, le matériau pieu étant liquide en début d'opération, coefficient de Poisson voisin de ½.
  - Dans le cas du pieu foncé ou battu, on sait qu'il existe du frottement négatif avant tout chargement. Nos calculs de pieux modèles centrifugés ont opportunément mis en évidence un frottement négatif considérable. Pourquoi ne pas modéliser le fonçage ou le battage par une excursion en accélération verticale sur le modèle (1g $\rightarrow$ quelques g $\rightarrow$ 1g) ?
- Caractérisation du chargement du pieu, en tête et localement :
  - Il s'agit d'analyser le programme de chargement en tête probable du pieu, en le simplifiant sous forme de séries de cycles (valeur moyenne, amplitude), étant entendu que les séries les plus sévères seront les seules modélisées.
  - On privilégie délibérément les phénomènes d'interface lors de la modélisation cyclique ultérieure, c'est-à-dire que l'on utilisera un outil éléments finis ou différences finies mettant en œuvre une élasto-plasticité classique pour le sol.
  - On réalise un calcul préliminaire du pieu, avec quelques cycles traités pas à pas, afin de déterminer approximativement les paramètres cycliques locaux (contrainte normale cyclique moyenne, cisaillement cyclique moyen, amplitude cyclique).
- Essais de sol et d'interface sol-structure :
  - On suppose avoir à disposition les essais courants de sol, ou les informations équivalentes, censés fournir les distributions du poids volumique du sol, de la teneur en eau, de la résistance du sol, de la rigidité du sol (E_p, ou G notamment).
  - L'information concernant les paramètres cycliques locaux (§ précédent) permet de réduire le nombre, et de mieux cibler les paramètres, des essais de cisaillement direct cyclique caractérisant le pieu, le sol et le chargement du pieu. Il s'agira de quelques (3 à 5 ?) essais de cisaillement direct cycliques à rigidité normale imposée (CNS), selon les paramètres cycliques précédemment définis. La chute de contrainte normale au cours des cycles, et en fonction de la profondeur, est une information de première importance à extraire de ces essais. L'interpolation est un outil de grande qualité à manier sans modération, pour compléter ces données.
- Modélisation proprement dite du comportement du pieu sous chargement axial cyclique, à l'aide d'un logiciel structural éléments finis ou différences finies :
  - 0. Phase d'initialisation des contraintes géostatiques
  - 1. Phase de modélisation du mode d'installation du pieu
  - 2. Pour chaque série de cycles, Parcours pas à pas d'1 ou 2 cycles de chargement en tête
  - 3. Extraction des paramètres cycliques locaux
  - 4. Formulation des courbes de chute de contrainte normale fonction du nombre N de cycles de la série, relatives à ces conditions locales (Figure 65)
  - 5. Prescription de ces chutes de contrainte normale locale dans le logiciel structural, pour modéliser les N cycles de cette série.
  - 6. Si cette série de cycles est la dernière, passer à 7, sinon retourner à 2.

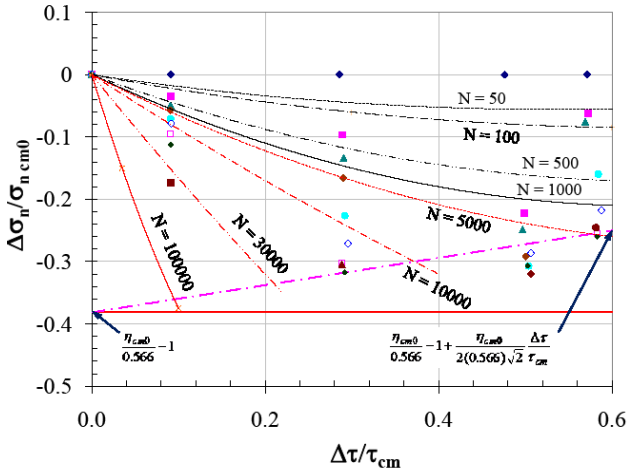

Figure 65. Résultats typiques d'essais d'interface sol-structure sur chemin CNS directement utilisable pour la modélisation de la chute de contrainte normale le long d'un pieu chargé cycliquement. I_{D0} = 90 %, η_{cm0} = 0.35, k = 1000 kPa/mm.

Conclusions générales et perspectives

Nous sommes partis d'une petite somme de connaissances internationales concernant le comportement des interfaces sol-structure sous sollicitations cycliques. La résistance d'interface n'est pas la seule information utile : les possibilités de dilatance et/ou contractance d'interface sont tout aussi utiles. Nous avons donc développé une modification de machine de cisaillement direct apte à réaliser des essais de cisaillement direct à rigidité normale imposée, pour des sollicitations cycliques à grand nombre de cycles (le plus souvent 10000).
Cette machine nous a permis de mener à bien plusieurs séries d'essais. Une série cohérente sable de Fontainebleau-plaque rugueuse à contrainte normale constante et à rigidité normale imposée, une série cohérente aussi, mais avec un nombre réduit d'essais, pour plaque rugueuse, et enfin une série encore plus limitée relative au sable de Loon-Plage, site sur lequel des essais de pieu grandeur réelle sous sollicitation cyclique sont disponibles dans le cadre SOLCYP (ANR et Programme National). Après tous ces essais, une analyse granulométrique de la zone d'interface a été faite, mais non exploitée. Les essais plaque lisse et Loon-Plage n'ont pas été exploités non plus. L'échantillon testé a été considéré comme formé de 2 couches, l'interface, de faible épaisseur d'une part, le tampon pseudo-oedométrique d'autre part, n'intervenant que lors des variations de contraintes normales. Ces essais ont été interprétés dans un premier temps en termes de variables cycliques moyennes, et de poids volumique d'interface sous contrainte.
En référence au modèle élasto-visco-plastique de Perzyna, nous avons modélisé analytiquement, d'une manière phénoménologique, les essais sable-plaque rugueuse sur chemin CNL (dits identification) en traitant d'abord les densités faible (I_{D0} = 30 %) et forte (I_{D0} = 90 %), les cisaillements cycliques moyens nul, moyen et élevé, et plusieurs niveau d'amplitude cyclique. Le paramètre de mémoire est le poids volumique d'interface sous contrainte (normale) ou le déplacement relatif normal d'interface. Les autres chemins CNL ont été générés par interpolation (rhéologique). Nous avons également modélisé les essais sur chemins différents (dits validation), en intégrant par pas analytiques pré-intégrés. Il s'est agit de chemins à amplitudes successives variées, et de chemins CNS, ceux-ci faisant appel aussi au comportement pseudo-oedométrique. L'effet de la taille du pas d'intégration a été examiné. Les comparaisons expérience-modèle sont généralement assez satisfaisantes.

Au terme de ces essais et de leur modélisation constitutive, nous nous sommes consacrés à la modélisation structurale en relation avec notre sujet, en utilisant le logiciel éléments finis PLAXIS 2D et sa loi constitutive opar défaut : l'élasto-plasticité à 5 paramètres.
Nous avons d'abord modélisé l'essai de cisaillement lui-même, en 2D (malheureusement pas en 3D), afin de détecter, lors d'une sollicitation monotone, les hétérogénéités de cisaillement, et de valider notre hypothèse de 2 couches globalement homogènes dans la boîte. Nous avons également modélisé les chemins CNL et CNS. Ces comparaisons sont assez satisfaisante.
Puis nous avons abordé la modélisation de pieux sous chargement axial cyclique. Il s'agit d'essais de pieux modèles centrifugés menés à bien par l'IFSTTAR à Nantes. Nous avons traité un cas de traction cyclique et un cas de compression cyclique, d'une manière que nous qualifions de rustique, disons « avec les moyens du bord ». Il est clair que le logiciel PLAXIS, pas plus que d'autres, ne possède pas la faculté de modéliser le grand nombre de cycles, avec les lois constitutives disponibles en bibliothèque. D'autre part, nous n'avons pas eu le temps matériel d'implémenter notre loi d'interface en tant que loi utilisateur. Nous avons donc du prendre une voie détournée. Nous avons travaillé en dialogue entre EXCEL et PLAXIS. Nous avons modélisé la chute de contrainte normale locale sur chemin CNS, issue de nos résultats sur le nombre de cycles conduisant à la rupture sur chemin CNS. Nous avons opéré par cluster le long du pieu, en imposant une variation de volume locale dans les dits clusters, d'où un déplacement irréversible (pseudo-fluage cyclique) en tête de pieu, à partir du déplacement moyen en tête au cours des premiers cycles.

De nombreuses perspectives de travaux futurs sont ouvertes par nos travaux. Au plan expérimental, nous n'avons traité que des cycles d'amplitude relativement faible. Il y aurait lieu de compléter nos essais par des cycles plus amples. Ces essais seraient de très longue durée, sachant que nos essais à 10000 cycles duraient déjà environ une semaine. Par ailleurs nous n'avons pas exploité nos essais avec plaque lisse, ni les résultats de l'évolution de granulométrie du sable de Fontainebleau due au cisaillement cyclique. Il est vrai que chaque échantillon de sable de la zone d'interface représente une très faible quantité (quelques grammes). En termes de modélisation constitutive, il y aurait sans doute lieu d'opérer quelques simplifications (réduction du nombre de paramètres) en reliant des coefficients vraisemblablement corrélés. Un travail très important pourrait être effectué sur le plan de la modélisation structurale des pieux sollicités cycliquement. Maillage plus élaboré, travailler au niveau des points d'intégration plutôt qu'au niveau de quelques clusters, automatiser les échanges entre PLAXIS et les données du pseudo-fluage cyclique en reprogrammant la loi d'interface cyclique en langage C, et enfin utiliser des chemins CNS réellement intégrés au lieu de la simplification apportée par N_{crit}, et un seul pas de pseudo-fluage cyclique. L'automatisation des échanges est possible, car elle a été réalisée dans la thèse de S. Levasseur

Annexes

L'annexe A contient le détail de calculs analytiques relatifs au modèle de cisaillement direct monotone.

L'annexe B contient les résultats expérimentaux de tous les essais de cisaillement direct monotones et cycliques réalisés, ainsi que leur modélisation constitutive.